

Proximal Soil Sensing

Progress in Soil Science

Series Editors:

Alfred E. Hartemink, *ISRIC – World Soil Information, Wageningen, The Netherlands*

Alex B. McBratney, *Faculty of Agriculture, Food & Natural Resources, The University of Sydney, Australia*

Aims and Scope

Progress in Soil Science series aims to publish books that contain novel approaches in soil science in its broadest sense – books should focus on true progress in a particular area of the soil science discipline. The scope of the series is to publish books that enhance the understanding of the functioning and diversity of soils in all parts of the globe. The series includes multidisciplinary approaches to soil studies and welcomes contributions of all soil science subdisciplines such as: soil genesis, geography and classification, soil chemistry, soil physics, soil biology, soil mineralogy, soil fertility and plant nutrition, soil and water conservation, pedometrics, digital soil mapping, proximal soil sensing, soils and land use change, global soil change, natural resources and the environment.

For further volumes:
<http://www.springer.com/series/8746>

Raphael A. Viscarra Rossel · Alex B. McBratney ·
Budiman Minasny
Editors

Proximal Soil Sensing



Springer

Editors

Dr. Raphael A. Viscarra Rossel
CSIRO Land & Water
Canberra, ACT 2600
Australia
Raphael.Viscarra-Rossel@csiro.au

Dr. Budiman Minasny
The University of Sydney
Faculty Agriculture, Food &
Natural Resources
John Woolley Building A20
Sydney, New South Wales 2006
Australia
budiman.minasny@sydney.edu.au

Prof. Alex B. McBratney
The University of Sydney
Faculty Agriculture, Food &
Natural Resources
John Woolley Building A20
Sydney, New South Wales 2006
Australia
alex.mcbratney@sydney.edu.au

ISBN 978-90-481-8858-1 e-ISBN 978-90-481-8859-8
DOI 10.1007/978-90-481-8859-8
Springer Dordrecht Heidelberg London New York

Library of Congress Control Number: 2010929695

© Springer Science+Business Media B.V. 2010

No part of this work may be reproduced, stored in a retrieval system, or transmitted in any form or by any means, electronic, mechanical, photocopying, microfilming, recording or otherwise, without written permission from the Publisher, with the exception of any material supplied specifically for the purpose of being entered and executed on a computer system, for exclusive use by the purchaser of the work.

Cover image courtesy Raphael Viscarra Rossel and Alex McBratney

Printed on acid-free paper

Springer is part of Springer Science+Business Media (www.springer.com)

Foreword

Proximal Soil Sensing: Looking, Touching, Feeling

Proximal sensing is the oldest activity in soil science and forms the very core of our professional existence as soil scientists. The first soil scientists looked at what everybody called just soil and – even though others had seen before what they were seeing – they, for the first time, became really excited and recognised the unique character of what their eyes revealed. The soil as a natural body was born.

To better understand and interpret what they were seeing, they used looking glasses to magnify the soil image and smelled, tasted, and squeezed the soil material to get a better idea about its features. They also learned the hard way that soil features could be exposed only by digging pits. This elementary proximal sensing resulted in flowery analogies – such as the assertion I recall from my field training as a student that ‘the feel of a loess soil was supposed to be comparable to that of the skin of an 18-year-old girl’.

Thus, at least four elementary forms of proximal sensing have been with us since the 19th century. This book convincingly illustrates that by now, thanks to modern technology, our sensing abilities reach way beyond what our human senses can accomplish. Some of these techniques have already been applied for decades in remote sensing from aeroplanes or satellites and have made significant contributions to soil and landscape science. But proximal sensing, as covered in this book, represents a special ‘niche’ as it defines tools that are available for field scientists who follow their own intuition and game plan as they move around in the field trying to unravel the secrets of Mother Earth, independent of a rigid flight plan or a satellite passover.

Fascinating new opportunities arise and are covered in this book: for instance, soil spectroscopy and hyperspectral sensing allow direct estimates of nitrogen, carbon, and the micronutrient contents of soil materials – in contrast to cumbersome and costly treatments associated with traditional wet chemistry. Electromagnetic induction and resistivity measurements allow a complete characterisation of soil layering, in stark contrast with traditional approaches where separate, isolated borings had to be somehow interpolated to form meaningful patterns.

At least two major advantages of proximal sensing stand out, while there are also some potential pitfalls. A major advantage is the fact that, finally, there can be

enough soil data to allow meaningful (geo)statistical analyses to ascertain spatial soil patterns. So far, major advances have been made in the theory of spatial analysis (as reported in this book), but practical application has often stalled because of lack of data as research projects did not provide funds to allow adequate sampling. A second advantage is the fact that soil scientists, using these techniques, increase their scientific fecundity, which make them more effective and interesting as partners in interdisciplinary land use programs. With easily accessible soil databases, user-friendly simulation models, and flashy geographical information systems, non-soil scientists can produce many soil-related products that may look attractive at first sight but often lack depth and scope. As is true in any science, soil scientists must stay ahead in their game, and the proximal sensing toolkit is of major assistance here.

There may be a potential problem, however, if techniques start to have a life of their own and when they become a goal in themselves rather than a means towards a broader purpose, which is the dynamic characterisation of soils for the benefit of all. That is why it would be wise for modern soil scientists with their sophisticated toolkits to recall and be inspired by the initial excitement of the first soil scientists, because even though we know a lot more about our soils now, its complexity and beauty are still way beyond our understanding.

The Netherlands

Johan Bouma

Preface

Our scientific understanding of soil – its unique qualities and functions – has been gained through long and arduous soil surveys complemented by careful chemical, physical, mineralogical, and biological laboratory analysis. These conventional methodologies continue to serve us well, but they can be expensive, complex, and time consuming and often only qualitative. The growing demand for good quality, inexpensive soil information underlines these shortcomings.

We need better information to solve pressing problems such as how to monitor the effects of climate change on soil, how to populate models of key processes, how to use precision agriculture for improving the sustainability and efficiency of food production, and how to assess and remediate contaminated land. These applications have prompted the development of more time- and cost-efficient quantitative approaches to soil analysis that complement, or replace, the more conventional laboratory techniques.

Sensors are becoming smaller, faster, more accurate, more energy efficient, wireless, and more intelligent. Many such devices can be used for proximal soil sensing (PSS), for example using ion-sensitive field effect transistors to measure soil pH and soil nutrients or using portable near-infrared spectrometers to measure soil properties like organic carbon content and mineral composition.

In this book, PSS is defined as the use of field-based sensors to collect soil information from close by (say within 2 m), or within, the soil body. Proximal soil sensors may be active or passive; they may be invasive, where there is direct sensor-to-soil contact, or non-invasive, measuring properties of the soil from above the surface. They may either measure the soil property directly or indirectly – by finding a proxy that is easier and cheaper to measure and developing a pedotransfer function. Frequently, the sensors are mounted on vehicles for on-the-go measurements. The rationale for PSS is that although it may produce results that are not as accurate – per individual measurement – as conventional laboratory analysis, it facilitates the generation of larger amounts of (spatial) data using cheaper, simpler, and less laborious techniques which, as an ensemble, may be highly informative. Moreover, the information is produced in a timely manner (that is, almost instantaneously).

This book reports on developments in PSS and high-resolution digital soil mapping presented at the First Global Workshop on High Resolution Digital Soil Sensing and Mapping held in Sydney in 2008. The workshop was held under the

auspices of the International Union of Soil Sciences (IUSS) and was hosted by the University of Sydney Faculty of Agriculture, Food and Natural Resources, with support from the Commonwealth Scientific Industrial Research Organisation (CSIRO) and Environmental Earth Sciences International (EESI Pty Ltd). The workshop attracted 90 soil scientists, agronomists, agricultural engineers, spectroscopists, statisticians, geostatisticians, and proximal and remote sensing specialists from 18 countries.

We have selected 36 chapters, arranged in sections, which represent the range of presentations made on various aspects of PSS. The book comprises an introductory section that sets the scene; a section on soil sensing and soil sampling; a section on soil (UV), visible, and infrared spectral sensing; one on soil electromagnetic induction and electrical resistivity sensing; one on radar and gamma radiometric sensing; one on multisensor systems and other sensors; and a final section on applications of PSS.

Australia

Raphael A. Viscarra Rossel
Alex B. McBratney
Budiman Minasny

Acknowledgements

We wish to acknowledge the University of Sydney, Australia's Commonwealth Scientific and Industrial Research Organisation (CSIRO), Environmental Earth Sciences International Pty Ltd, and the International Union of Soil Science (IUSS) for supporting the 1st Global Workshop on High-Resolution Digital Soil Sensing and Mapping. We thank the members of the scientific committee for their invaluable help in reviewing the papers and the Australian Collaborative Land Evaluation Program (ACLEP) for its financial support during the preparation of this book. We also thank Professor Johan Bouma for writing the foreword and succinctly providing the context of the book.

Contents

Part I Overview

1 Sampling for High-Resolution Soil Mapping	3
J.J. de Grujter, A.B. McBratney, and J. Taylor	
2 Development of On-the-Go Proximal Soil Sensor Systems	15
V.I. Adamchuk and R.A. Viscarra Rossel	
3 Diffuse Reflectance Spectroscopy for High-Resolution Soil Sensing	29
B. Stenberg and R.A. Viscarra Rossel	
4 High-Resolution Digital Soil Mapping: Kriging for Very Large Datasets	49
N. Cressie and E.L. Kang	

Part II Soil Sensing and Sampling

5 The Sun Has Shone Here Antecedently	67
A.B. McBratney and B. Minasny	
6 Proximal Soil Nutrient Sensing Using Electrochemical Sensors	77
C.R. Lobsey, R.A. Viscarra Rossel, and A.B. McBratney	
7 DIGISOIL: An Integrated System of Data Collection Technologies for Mapping Soil Properties	89
G. Grandjean, O. Cerdan, G. Richard, I. Cousin, P. Lagacherie, A. Tabbagh, B. Van Wesemael, A. Stevens, S. Lambot, F. Carré, R. Maftei, T. Hermann, M. Thörnelöf, L. Chiarantini, S. Moretti, A.B. McBratney, and E. Ben Dor	
8 iSOIL: An EU Project to Integrate Geophysics, Digital Soil Mapping, and Soil Science	103
U. Werban, T. Behrens, G. Cassiani, and P. Dietrich	
9 Conditioned Latin Hypercube Sampling for Calibrating Soil Sensor Data to Soil Properties	111
B. Minasny and A.B. McBratney	

10	Response Surface Sampling of Remotely Sensed Imagery for Precision Agriculture	121
	G.J. Fitzgerald	

Part III Soil UV, Visible, and Infrared Spectral Sensing

11	Mid- Versus Near-Infrared Spectroscopy for On-Site Analysis of Soil	133
	J.B. Reeves, G.W. McCarty, and W.D. Hively	
12	Determination of Soil Nitrate and Organic Matter Content Using Portable, Filter-Based Mid-Infrared Spectroscopy	143
	B.R. Jahn and S.K. Upadhyaya	
13	VNIR Spectroscopy Estimates of Within-Field Variability in Soil Properties	153
	K.A. Sudduth, N.R. Kitchen, E.J. Sadler, S.T. Drummond, and D.B. Myers	
14	Infrared Sensors to Map Soil Carbon in Agricultural Ecosystems	165
	G. McCarty, W.D. Hively, J.B. Reeves III, M. Lang, E. Lund, and O. Weatherbee	
15	Predicting Soil Carbon and Nitrogen Concentrations and Pasture Root Densities from Proximally Sensed Soil Spectral Reflectance	177
	B.H. Kusumo, M.J. Hedley, M.P. Tuohy, C.B. Hedley, and G.C. Arnold	
16	Diagnostic Screening of Urban Soil Contaminants Using Diffuse Reflectance Spectroscopy	191
	J.G. Bray, R.A. Viscarra Rossel, and A.B. McBratney	
17	Using Wavelets to Analyse Proximally Sensed Vis–NIR Soil Spectra	201
	R.A. Viscarra Rossel, R.M. Lark, and A.S. Ortega	
18	Mapping Soil Surface Mineralogy at Tick Hill, North-Western Queensland, Australia, Using Airborne Hyperspectral Imagery	211
	T. Cudahy, M. Jones, M. Thomas, P. Cocks, F. Agustin, M. Caccetta, R. Hewson, M. Verrall, and A. Rodger	

Part IV Soil Sensing by Electromagnetic Induction and Electrical Resistivity

19	Combining Proximal and Penetrating Soil Electrical Conductivity Sensors for High-Resolution Digital Soil Mapping	233
	D.B. Myers, N.R. Kitchen, K.A. Sudduth, S. Grunwald, R.J. Miles, E.J. Sadler, and R.P. Udawatta	

20	A Neural Network Approach to Topsoil Clay Prediction Using an EMI-Based Soil Sensor	245
	L. Cockx, M. Van Meirvenne, U.W.A. Vitharana, F.M.B. Vancoillie, L.P.C. Verbeke, D. Simpson, and T. Saey	
21	Field Determination of Soil Moisture in the Root Zone of Deep Vertosols Using EM38 Measurements: Calibration and Application Issues	255
	M.B. Hossain, D.W. Lamb, P.V. Lockwood, and P. Frazier	
22	Can the EM38 Probe Detect Spatial Patterns of Subsoil Compaction?	265
	G. Hoefer, J. Bachmann, and K.H. Hartge	
23	Changes in Field Soil Water Tracked by Electrical Resistivity	275
	A. Besson, I. Cousin, G. Richard, H. Bourennane, C. Pasquier, B. Nicoullaud, and D. King	
24	Is a Systematic Two-Dimensional EMI Soil Survey Always Relevant for Vineyard Production Management? A Test on Two Pedologically Contrasting Mediterranean Vineyards	283
	G. Coulouma, B. Tisseyre, and P. Lagacherie	

Part V Radar and Gamma Radiometric Sensors

25	Full-Waveform Modelling and Inversion of Ground-Penetrating Radar Data for Non-invasive Characterisation of Soil Hydrogeophysical Properties	299
	S. Lambot, E. Slob, J. Minet, K.Z. Jadoon, M. Vanclooster, and H. Vereecken	
26	Using Proximal Sensors to Continuously Monitor Agricultural Soil Physical Conditions for Tillage Management	313
	G. Richard, R. Rouveure, A. Chanzy, P. Faure, M. Chanet, A. Marionneau, P. Régnier, and Y. Duval	
27	Gamma Ray Sensor for Topsoil Mapping: The Mole	323
	F.M. van Egmond, E.H. Loonstra, and J. Limburg	
28	Gamma Ray Sensing for Cadmium Risk Assessment in Agricultural Soil and Grain: A Case Study in Southern Sweden	333
	M. Söderström and J. Eriksson	
29	Use of EM38 and Gamma Ray Spectrometry as Complementary Sensors for High-Resolution Soil Property Mapping	343
	M.T.F. Wong, K. Wittwer, Y.M. Oliver, and M.J. Robertson	

Part VI Multisensor Systems and Other Sensors

30 Field-Scale Draught Resistance and Soil Moisture Measurement in Australia Using a Tine-Based Force–Capacitance Sensing System	353
B.M. Whelan, Y. Sun, Q. Zeng, P. Schulze Lammers, and J. Hassall	
31 Sensor-Based Mapping of Soil Quality on Degraded Claypan Landscapes of the Central United States	363
N.R. Kitchen, K.A. Sudduth, R.J. Kremer, and D.B. Myers	
32 Proximal Sensing Methods for Mapping Soil Water Status in an Irrigated Maize Field	375
C.B. Hedley, I.J. Yule, M.P. Tuohy, and B.H. Kusumo	
33 Comparing the Ability of Multiple Soil Sensors to Predict Soil Properties in a Scottish Potato Production System	387
J.A. Taylor, M. Short, A.B. McBratney, and J. Wilson	
34 Spatial Variability and Pattern of Selected Properties of Agricultural Soils in the Czech Republic Measured by Indirect Proximal and Remote Sensing	397
M. Kroulik, J. Kumhalova, Z. Kviz, M. Zlinsky, M. Mimra, and V. Prosek	

Part VII Applications

35 Inverse Meta-modelling of Yield-Monitor Data for Estimating Soil-Available Water-Holding Capacities at a Farm Resolution of 10 m	413
M.J. Florin, A.B. McBratney, and B.M. Whelan	
36 Reconstructing Palaeotopography at the Beginning of the Weichselian Glacial Stage Using an Electromagnetic Induction Sensor	423
T. Saey, M. Van Meirvenne, D. Simpson, U.W.A. Vitharana, L. Cockx, and H. Vermeersch	
Postscript: Where to from Here?	435
Index	441

About the Editors

Raphael Viscarra Rossel is a scientist at the Commonwealth Scientific and Industrial Research Organisation (CSIRO) of Australia. He is developing methodologies to measure, model, and map soil using sensors and mathematical and statistical techniques to further our understanding of the different soil functions. He leads a collaborative initiative to develop a global soil diffuse reflectance spectral library. He is the inaugural chair of the International Union of Soil Science (IUSS) Working Group on Proximal Soil Sensing. E-mail: raphael.viscarra-rossel@csiro.au

Alex McBratney is pro-dean and professor of Soil Science in the Faculty of Agriculture Food & Natural Resources at the University of Sydney in Australia. He is director of the Australian Centre for Precision Agriculture and visiting professor at the National Soil Research Institute at Cranfield University in the United Kingdom, and honorary scientist with the Rural Development Administration in the Republic of Korea. He is joint editor-in-chief of the global soil science journal, *Geoderma*, and coeditor-in-chief of the book series *Progress in Soil Science*. Alex is a consummate pedometrist and soil scientist striving to understand soil variation in all its dimensions. E-mail: alex.mcbratney@sydney.edu.au

Budiman Minasny is a senior research fellow in the Faculty of Agriculture Food & Natural Resources at the University of Sydney in Australia. He was awarded the QEII Fellowship from the Australian Research Council to develop methodologies for creating a global soil map. His research interest is to link soil observations with process-based models and to develop empirical models to allow greater understanding of soil variation in space and time. E-mail: budiman.minasny@sydney.edu.au

Contributors

V.I. Adamchuk Department of Bioresource Engineering, McGill University, 21, 1111 Lakeshore Rd., Ste-Anne-de-Bellevue, Quebec, H9X 3V9, Canada, viacheslav.adamchuk@mcgill.ca

F. Agustin Curtin University, GPO Box U1987, Perth, WA 6845, Australia, afitchan@gmail.com

G.C. Arnold Landcare Research, Palmerston North, New Zealand

J. Bachmann Institute of Soil Science, Leibniz Universität Hannover, Herrenhäuser Str. 2, 30419 Hannover, Germany, bachmann@ifbk.uni-hannover.de

T. Behrens Institute of Geography, Physical Geography, Rümelinstraße 19-23, 72070 Tübingen, Germany, Thorsten.behrens@uni-tuebingen.de

E. Ben Dor University of Tel Aviv, Tel Aviv, Israel, bendor@post.tau.ac.il

A. Besson Unité de Science du Sol, INRA, Avenue de la Pomme de Pin, 45166 Olivet, France; Department of Environmental Sciences and Land Use Planning, Université Catholique de Louvain, Croix du Sud 2, BP 2, B-1348 Louvain-la-Neuve, Belgium, Arlene.Besson@orleans.inra.fr

H. Bourennane Unité de Science du Sol, INRA, Avenue de la Pomme de Pin, 45166 Olivet, France

J. Bray Faculty of Agriculture, Food and Natural Resources, University of Sydney, McMillan Building A05, Sydney, NSW 2006, Australia, jbray@eesi.biz

M. Caccetta CSIRO Exploration and Mining, Australian Resources Research Centre, PO Box 1130, Bentley, WA 6102, Australia, Mike.Caccetta@csiro.au

F. Carré JRC, Ispra, Italy, florence.carre@jrc.it

G. Cassiani Dipartimento di Geoscienze, University of Padova, 35127 Padova, Italy, giorgio.cassiani@unipd.it

O. Cerdan BRGM, Orléans, France, o.cerdan@brgm.fr

M. Chanet UR TSCF, 24 avenue des Landais, BP 50085, 63172 Aubiere Cedex, France, myriam.chanet@cemagref.fr.

A. Chanzy INRA, UMR EMMAH, Site Agroparc, 84914 Avignon Cedex 9, France, Andre.Chanzy@avignon.inra.fr

L. Chiarantini Gallileo Avionica, Firenze, Italy, leandro.chiarantini@galileoavionica.it

P. Cocks HyVista Corporation, PO Box 437, Baulkham Hills, NSW 1755, Australia, pac@hyvista.com

L. Cockx Department of Soil Management, Research Group Soil Spatial Inventory Techniques, Ghent University, Coupure 653, 9000 Gent, Belgium, liesbet.cockx@ugent.be

G. Coulouma INRA UMR LISAH, 2 place viala, 34060 Montpellier, France, coulouma@supagro.inra.fr

I. Cousin INRA, Orléans, France; Unité de Science du Sol, INRA, Avenue de la Pomme de Pin, 45166 Olivet, France, Isabelle.Cousin@orleans.inra.fr

N. Cressie Department of Statistics, The Ohio State University, 1958 Neil Avenue, Columbus, OH 43210-1247, USA, ncressie@stat.osu.edu

T. Cudahy CSIRO Exploration and Mining, Australian Resources Research Centre, PO Box 1130, Bentley, WA 6102, Australia, Thomas.Cudahy@csiro.au

J.J. de Gruijter Alterra, Wageningen University & Research Centre, P.O. Box 47, 6700 AA Wageningen, The Netherlands, jaap.degruijter@wur.nl

W.D. Hively Eastern Geographic Science Center, U.S. Geological Survey, Reston, VA 20192, USA, dean.hively@ars.usda.gov; USDA Hydrology & Remote Sensing Laboratory, Beltsville, MD, USA, dean.hively@ars.usda.gov

P. Dietrich UFZ – Helmholtz Centre for Environmental Research, Permoserstraße 15, 04318 Leipzig, Germany, peter.dietrich@ufz.de

S.T. Drummond Cropping Systems and Water Quality Research Unit, USDA Agricultural Research Service, 269 Agricultural Engineering Bldg., University of Missouri, Columbia, MO 65211 USA, Scott.Drummond@ars.usda.gov

Y. Duval INRA, UR Agronomie Laon-Reims-Mons, 2 Chaussée Brunehaut, Estrées-Mons, BP 50136, 80203 Péronne, France, Yves.Duval@laon.inra.fr

F.M. van Egmond The Soil Company, Leonard Springerlaan 9, 9727 KB Groningen, The Netherlands, egmond@soilcompany.com

J. Eriksson Department of Soil and Environment, the Biogeochemistry group, Swedish University of Agricultural Sciences, PO Box 7014, SE-750 07 Uppsala, Sweden, jan.eriksson@mark.slu.se

P. Faure UR TSCF, 24 avenue des Landais, BP 50085, 63172 Aubiere Cedex, France, pascal.faure@cemagref.fr

G.J. Fitzgerald Department of Primary Industries, 110 Natimuk Rd., Horsham, VIC 3401, Australia, glenn.fitzgerald@dpi.vic.gov.au

M.J. Florin Australian Centre for Precision Agriculture, Faculty of Agriculture, Food and Natural Resources, The University of Sydney, Sydney, NSW, Australia; Plant Production Systems, Wageningen University, Wageningen, The Netherlands, madeleine.florin@wur.nl

P. Frazier Eco Logical Australia, PO Box 1927, Armidale, NSW 2350, Australia paulf@ecoaus.com.au

G. Grandjean BRGM, Orléans, France, g.grandjean@brgm.fr

S. Grunwald GIS Core Research Laboratory, Department of Soil and Water Science, University of Florida, 2169 McCarty Hall, Gainesville, FL, USA, sabgru@ufl.edu

K.H. Hartge Institute of Soil Science, Leibniz Universität Hannover, Herrenhäuser Str. 2, 30419 Hannover, Germany

J. Hassall 'Kiewa', Gilgandra, NSW Australia, j.hassall@bigpond.com

M.J. Hedley Institute of Natural Resources, College of Science, Massey University, North Shore City, New Zealand, m.hedley@massey.ac.nz

C.B. Hedley Landcare Research, Manawatu Mail Centre, Private Bag 11052, Palmerston North 4442, New Zealand, HedleyC@LandcareResearch.co.nz; m.hedley@massey.ac.nz

T. Hermann University of Pannonia, Pannonia, Hungary, tamas.hermann@gmail.com

R. Hewson CSIRO Exploration and Mining, Australian Resources Research Centre, PO Box 1130, Bentley, WA 6102, Australia, Rob.Hewson@csiro.au

G. Hoefer Institute of Soil Science, Leibniz Universität Hannover, Herrenhäuser Str. 2, 30419 Hannover, Germany, hoefer@ifbk.uni-hannover.de

M.B. Hossain Precision Agriculture Research Group and Cooperative Research Centre for Irrigation Futures, University of New England, Armidale, NSW 2351, Australia, mhossai6@une.edu.au

K.Z. Jadoon Agrosphere (ICG-4), Institute of Chemistry and Dynamics of the Geosphere, Forschungszentrum Jülich GmbH, D-52425 Jülich, Germany, k.z.jadoon@fz-juelich.de

B.R. Jahn CSA Engineering Inc., 2565 Leghorn St., Mountain View, CA 94043, USA, bjahn@csaengineering.com

M. Jones Geological Survey of Queensland, 80 Meiers Road, Indooroopilly, QLD, 4068, Australia, Mal.Jones@dme.qld.gov.au

E.L. Kang Department of Statistics, The Ohio State University, 1958 Neil Avenue, Columbus, OH 43210-1247, USA, lei@stat.osu.edu

D. King Unité de Science du Sol, INRA, Avenue de la Pomme de Pin, 45166 Olivet, France

N.R. Kitchen Cropping Systems and Water Quality Research Unit, USDA Agricultural Research Service, University of Missouri, Columbia, MO 65211 USA, Newell.Kitchen@ars.usda.gov

R.J. Kremer USDA Agricultural Research Service, Agricultural Engineering Building, University of Missouri, Columbia, MO 65211, USA, Robert.Kremer@ars.usda.gov

M. Kroulik Department of Agricultural Machines, Czech University of Life Sciences, CZ-16521, Prague 6 – Suchdol, Czech Republic, kroulik@tf.czu.cz

J. Kumhalova CRI, CZ-161 06 Prague 6 – Ruzyně, Czech Republic, kumhalova@vurv.cz

B.H. Kusumo Institute of Natural Resources, College of Science, Massey University, New Zealand; Faculty of Agriculture, Department of Soil Science, University of Mataram, Lombok, Indonesia, b.h.kusumo@massey.ac.nz; bambanghk@gmail.com

Z. Kviz Department of Agricultural Machines, Czech University of Life Sciences, CZ-16521, Prague 6 – Suchdol, Czech Republic, kviz@tf.czu.cz

P. Lagacherie INRA UMR LISAH, 2 place viala – 34060 Montpellier, France, lagacherie@supagro.inra.fr

D.W. Lamb Precision Agriculture Research Group, Cooperative Research Centre for Irrigation Futures, University of New England, Armidale, NSW 2351, Australia, dlamb@une.edu.au

S. Lambot Earth and Life Institute, Université Catholique de Louvain, Croix du Sud 2, Box 2, B-1348 Louvain-la-Neuve, Belgium; Agrosphere (ICG-4), Institute of Chemistry and Dynamics of the Geosphere, Forschungszentrum Jülich GmbH, D-52425 Jülich, Germany, sebastien.lambot@uclouvain.be; s.lambot@fz-juelich.de

M. Lang USDA Hydrology & Remote Sensing Laboratory, Beltsville, MD, USA, megan.lang@ars.usda.gov

R.M. Lark Rothamsted Research Harpenden, Hertfordshire, AL5 2JQ, UK, murray.lark@bbsrc.ac.uk

J. Limburg Medusa Explorations, Verlengde Bremenweg 4, 9723 JV, Groningen, The Netherlands, han@medusa-online.com

C.R. Lobsey Australian Centre for Precision Agriculture, The University of Sydney, Sydney, NSW 2006, Australia, craig.lobsey@sydney.edu.au

P.V. Lockwood Precision Agriculture Research Group, University of New England, Armidale, NSW 2351, Australia, peter.lockwood@une.edu.au

E.H. Loonstra The Soil Company, Leonard Springerlaan 9, 9727 KB, Groningen, The Netherlands, loonstra@soilcompany.nl

E. Lund Veris Technologies, 601 Broadway, Salina, KS, USA, lunde@veristech.com

R. Maftei GIR, Bucharest, Romania, mafteir@yahoo.com

A. Marionneau Cemagref, UR TSCF, 24 avenue des Landais, BP 50085, 63172 Aubiere Cedex, France, anicet.marionneau@cemagref.fr

A.B. McBratney The University of Sydney, Faculty Agriculture, Food & Natural Resources, John Woolley Building A20, Sydney, New South Wales 2006, Australia, alex.mcbratney@sydney.edu.au

G. McCarty USDA Hydrology & Remote Sensing Laboratory, Beltsville, MD, USA, greg.mccarty@ars.usda.gov

R.J. Miles Department of Soil Environmental and Atmospheric Sciences, University of Missouri, 302 Anheuser-Bush Natural Resources Building, Columbia, MO, USA, milesr@missouri.edu

M. Mimra Department of Agricultural Machines, Czech University of Life Sciences, CZ-16521, Prague 6 – Suchdol, Czech Republic, mimra@tf.czu.cz

B. Minasny The University of Sydney, Faculty Agriculture, Food & Natural Resources, John Woolley Building A20, Sydney, New South Wales 2006, Australia, budiman.minasny@sydney.edu.au

J. Minet Earth and Life Institute, Université Catholique de Louvain, Croix du Sud 2, Box 2, B-1348 Louvain-la-Neuve, Belgium, julien.minet@uclouvain.be

S. Moretti University of Firenze, Firenze, Italy, sandro.moretti@geo.unifi.it

D.B. Myers Department of Soil and Water Science, GIS Core Research Laboratory, University of Florida, 2169 McCarty Hall, Gainesville 32611, FL, USA, myersdb@ufl.edu

B. Nicoullaud Unité de Science du Sol, INRA, Avenue de la Pomme de Pin, 45166 Olivet, France

Y.M. Oliver CSIRO Sustainable Ecosystems, Underwood Avenue, Floreat, WA 6014, Western Australia, yvette.oliver@csiro.au

A.S. Ortega Faculty of Agriculture Food & Natural Resources, The University of Sydney, Sydney, NSW 2006, Australia, a.ortega-andrade@usyd.edu.au

C. Pasquier Unité de Science du Sol, INRA, Avenue de la Pomme de Pin, 45166 Olivet, France

V. Prosek Department of Agricultural Machines, Czech University of Life Sciences, CZ-16521, Prague 6 – Suchdol, Czech Republic, prosek@tf.czu.cz

J.B. Reeves III USDA Environmental Management and Byproduct Utilization Laboratory, Beltsville, MD, USA, james.reeves@ars.usda.gov

P. Régnier INRA, UR Agronomie Laon-Reims-Mons, 2 Chaussée Brunehaut, Estrées-Mons, BP 50136, 80203 Péronne, France, Paul.Reginier@mons.inra.fr

G. Richard Unité de Science du Sol, INRA, Avenue de la Pomme de Pin, 45166 Olivet, France; INRA, UR272 Science du Sol, Centre de Recherche d'Orléans, 2163 Avenue de la Pomme de Pin, CS 40001, 45075 Orléans Cedex 2, France, Guy.Richard@orleans.inra.fr

M.J. Robertson CSIRO Sustainable Ecosystems, Underwood Avenue, Floreat, WA 6014, Western Australia, michael.robertson@csiro.au

A. Rodger CSIRO Exploration and Mining, Australian Resources Research Centre, PO Box 1130, Bentley, WA 6102, Australia, Andrew.Rodger@csiro.au

R. Rouveure UR TSCF, 24 avenue des Landais, BP 50085, 63172 Aubiere Cedex, France, raphael.rouveure@cemagref.fr.

E.J. Sadler Cropping Systems and Water Quality Research Unit, USDA Agricultural Research Service, 269 Agricultural Engineering Bldg., University of Missouri, Columbia, MO 65211 USA, John.Sadler@ars.usda.gov

T. Saey Research Group Soil Spatial Inventory Techniques, Department. Soil Management, Ghent University, Coupure 653, 9000 Ghent, Belgium, timothy.saey@gmail.com

P. Schulze Lammers Department of Agricultural Engineering, University of Bonn, Bonn, Germany, lammers@uni-bonn.de

M. Short Australian Centre for Precision Agriculture, The University of Sydney, John Woolley Building A20, Sydney, NSW 2006 Australia, michael.short@sydney.edu.au

D. Simpson Research Group Soil Spatial Inventory Techniques, Department. Soil Management, Ghent University, Coupure 653, 9000 Ghent, Belgium, davidgb.simpson@gmail.com

E. Slob Department of Geotechnology, Delft University of Technology, Stevinweg 1, 2628 CN Delft, The Netherlands, e.c.slob@tudelft.nl

M. Söderström Department of Soil and Environment, the Precision Agriculture and Pedometrics Group, Swedish University of Agricultural Sciences, PO Box 234, SE-532 23 Skara, Sweden, mats.soderstrom@mark.slu.se

B. Stenberg The Precision Agriculture and Pedometrics Group, Department of Soil and Environment, SLU, PO Box 234, SE-532 23 Skara, Sweden, Bo.Stenberg@mark.slu.se

A. Stevens Georges Lemaître Centre for Earth and Climate Research (TECLIM), Earth and Life Institute (ELI), UCLouvain, Place Pasteur, 3, 1348 LLN, Belgium

K.A. Sudduth Cropping Systems and Water Quality Research Unit, USDA Agricultural Research Service, University of Missouri, Columbia, MO 65211, USA, Ken.Sudduth@ars.usda.gov

Y. Sun Key Lab on Precision Agriculture System Integration Research, China Agricultural University, PO Box 63, Beijing, China, pal@cau.edu.cn

A. Tabbagh UMR Sisiphe, UPMC, Paris, France, alat@ccr.jussieu.fr

J. Taylor INRA, UMR LISAH et UMR ITAP, Batiment 21, 2 Place Pierre Viala, 34060 Montpellier, France, taylor@supagro.inra.fr

J.A. Taylor Australian Centre for Precision Agriculture, The University of Sydney, John Woolley Building A20, Sydney, NSW 2006, Australia, precision.agriculture@sydney.edu.au

M. Thomas Geoscience Australia, GPO Box 378, Canberra, ACT 2601, Australia, Matilda.Thomas@gc.gov.au

M. Thörnelöf ABEM, Sundbyberg, Sweden, mt@abem.se

B. Tisseyre Montpellier SupAgro UMR ITAP, 2 place viala–34060 Montpellier, France, tisseyre@supagro.inra.fr

M.P. Tuohy Institute of Natural Resources, College of Science, Massey University, North Shore City, New Zealand, m.tuohy@massey.ac.nz

R.P. Udawatta Center for Agroforestry and Department of Soil Environmental and Atmospheric Sciences, University of Missouri, 203 Anheuser-Busch Natural Resources Building, Columbia, MO, USA udawattar@missouri.edu

S.K. Upadhyaya Biological and Agricultural Engineering Department, University of California – Davis, Davis, CA 95616 USA, skupadhyaya@ucdavis.edu

M. Van Meirvenne Research Group Soil Spatial Inventory Techniques, Department Soil Management, Ghent University, Coupure 653, 9000 Ghent, Belgium, marc.vanmeirvenne@ugent.be

B. van Wesemael Université catholique de Louvain, Louvain-la-Neuve, Belgium, bas.vanwesemael@uclouvain.be

M. Vanclooster Earth and Life Institute, Université Catholique de Louvain, Croix du Sud 2, Box 2, B-1348 Louvain-la-Neuve, Belgium, marnik.vanclooster@uclouvain.be

F.M.B. Vancoillie Laboratory of Forest Management and Spatial Information Techniques, Ghent University, Coupure 653, 9000 Ghent, Belgium, frieke.vancoillie@ugent.be

L.P.C. Verbeke Geo Solutions, Veldkant 37, 2550 Kontich, Belgium, lieven.verbeke@geosolutions.be

H. Vereecken Agrosphere (ICG-4), Institute of Chemistry and Dynamics of the Geosphere, Forschungszentrum Jülich GmbH, D-52425 Jülich, Germany, h.verecken@fz-juelich.de

H. Vermeersch Research Group of Soil Spatial Inventory Techniques, Department Soil Management, Ghent University, Coupure 653, 9000 Ghent, Belgium, vermeersch_hans@yahoo.ca

M. Verrall CSIRO Exploration and Mining, Australian Resources Research Centre, PO Box 1130, Bentley, WA 6102, Australia, Michael.Verrall@csiro.au

R.A. Viscarra Rossel CSIRO Land and Water, Canberra, ACT 2600, Australia, raphael.viscarra-rossel@csiro.au

U.W.A. Vitharana Research Group of Soil Spatial Inventory Techniques, Department Soil Management, Ghent University, Coupure 653, 9000 Ghent, Belgium, vithara@hotmail.com

O. Weatherbee SpecTIR LLC, 8628 Brooks Drive, Suite 103, Easton, MD, USA, oweatherbee@spectir.com

U. Werban UFZ – Helmholtz Centre for Environmental Research, Permoserstraße 15, 04318 Leipzig, Germany, ulrike.werban@ufz.de

B.M. Whelan Australian Centre for Precision Agriculture, University of Sydney, Sydney, NSW 2006, Australia, b.whelan@sydney.edu.au

J. Wilson Soilessentials Ltd, Hilton of Fern, By Brechin, Angus, DD9 6SB, United Kingdom, jim@hiltonfern.co.uk

K. Wittwer CSIRO Land and Water, Underwood Avenue, Floreat, WA 6014, Western Australia, kathy.wittwer@csiro.au

M.T.F. Wong CSIRO Land and Water, Underwood Avenue, Floreat, WA 6014, Australia, mike.wong@csiro.au

I.J. Yule New Zealand Centre for Precision Agriculture, Institute of Natural Resources, Massey University, Palmerston North, New Zealand, I.J.Yule@massey.ac.nz

Q. Zeng Research Center for Precision Farming, China Agricultural University, Quinghua Donglu 17#, Beijing 100083, China, Qingmeng_zeng@yahoo.com

M. Zlinsky Department of Agricultural Machines, Czech University of Life Sciences, CZ-16521, Prague 6 – Suchdol, Czech Republic, zlinsky@tf.czu.cz

Part I

Overview

Chapter 1

Sampling for High-Resolution Soil Mapping

J.J. de Grujter, A.B. McBratney, and J. Taylor

Abstract When doing sensing for high-resolution soil mapping, one has to decide on the disposition of the sensor, which is a special case of spatial sampling. To optimise the pattern of measurements, a cost model and a quality model are proposed. The quality model reflects the coverage of the geographic space, and this is illustrated with some practical experiments. Optimisation of sensing patterns is worked out for two different types of sensing equipment. If the sensor variable differs from the target (management or decision) variable, then a model is needed to predict the target variable from the ancillary data. So in that case, one also has to decide how and where to sample for calibration data. This ‘calibration sampling’ differs from ‘sensor sampling’, as now coverage of the predictor space rather than the geographic space is important. In addition, the handling of extremes is an issue here. Existing methods for calibration sampling are reviewed and a suggestion is made for a new approach, based on fuzzy cluster analysis, which might avoid some of the shortcomings of existing methods.

Keywords Soil sampling · Calibration · Proximal sensing · Latin hypercube sampling · Fuzzy k -means · Cost modeling

1.1 Introduction

High-resolution soil mapping often needs some form of proximal sensing, and it should be realised that this is not complete enumeration. Proximal sensing enables measurement at high densities, but practical and financial constraints usually prevent sensing at sufficiently high resolution. Thus empty spaces will remain between the sensing locations, and proximal sensing can be seen as a form of soil sampling.

J.J. de Grujter (✉)

Alterra, Wageningen University & Research Centre, P.O. Box 47, 6700 AA

Wageningen, The Netherlands

e-mail: jaap.degruijter@wur.nl

Sampling for high-resolution soil mapping therefore will often be twofold: sensor sampling and calibration sampling. Sensor sampling is in order if

- the available prior information (detailed soil maps, soil sample data, remote sensing images, previous proximal sensing data, yield data, DEMs) is insufficient for the required mapping and
- sensing can produce data about the target variable, either directly (e.g. pH sensing) or indirectly via a model (e.g. lime requirement sensing).

Calibration sampling should be done if

- a model is needed for prediction of the target variable from the prior information and/or newly acquired sensing data and
- such a model is not yet available.

The flow diagram of Fig. 1.1 shows the various possibilities of data needs and their consequences for data acquisition.

Usually one has to decide on two different spatial sampling patterns: one for the sensing locations and one for the locations from which calibration data are to be collected. It should be realised that entirely different aims are involved, leading to different methods. The aim of sensor sampling is to enable mapping so that the pattern should have sufficient coverage of the geographic space. The aim of calibration sampling is to identify a useful model so that the pattern should have sufficient coverage of the predictor space.

Like the sampling itself, the aim of this chapter is twofold. Firstly, a reconnaissance of the problems of sensor sampling is aimed at, with a first attempt to optimise sensing patterns theoretically, supplemented with some field experiments. Secondly, we shall consider some existing and possible methods for calibration sampling, which will have mostly the character of a review on the basis of a priori considerations.

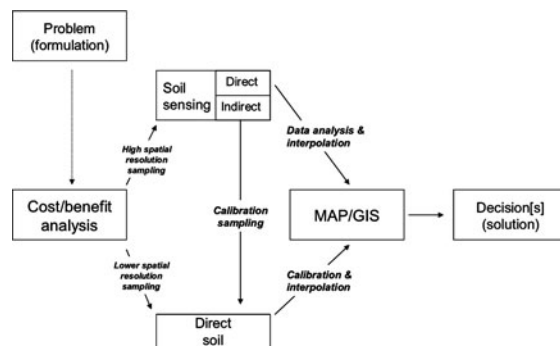


Fig. 1.1 Flow diagram of high-resolution digital soil sensing and mapping

1.2 Materials and Methods

1.2.1 Sensor Sampling: Some Theory

Sensor sampling will normally be done with a vehicle taking measurements at fixed intervals while driving along straight parallel lines, thus forming a regular grid of sample points. The size and the shape of this grid should be chosen such that the resulting sensing data will form the best starting point for interpolation onto the final grid at which the target variable is to be predicted, subject to a cost constraint. This needs a cost model and a quality model (see below). In cases where there is more than one sensor mounted on the vehicle, the measurements are generally not collocated, but we assume that the data will be transformed into collocated ones by post-processing.

For cost modelling and optimisation, we distinguish two types of equipments: sensors mounted on a vehicle that stops to take a measurement (type A) and sensors mounted on a vehicle that does not stop for measuring (type B). With type A we assume that the operator can choose the swathe width and the interval between measurements along the driving lines. With type B we assume that the measurement frequency is fixed and that the operator can choose the swathe width and the speed.

1.2.1.1 Optimisation for Equipment Type A

Assuming that we drive a sensing instrument along parallel lines through the field, with equal distance w between the lines and equal distance between sensing points h at the lines, a simple model of the variable costs is

$$C = \frac{c_d}{w} + \frac{c_m}{wh}, \quad (1.1)$$

where C is the variable sensing cost per hectare (€ ha^{-1}), c_d is the cost of driving per hectometre (€ hm^{-1}) and c_m is the cost of measuring per sensing point (w and h both given in hectometre). This model neglects boundary effects and driving between lines, which seems reasonable for large fields.

The patterns of sensing points that are best for spatial prediction, regardless of costs, are square grids, i.e. $w = h$. (Theoretically, triangular grids would be slightly more efficient, but these are not practical for routine application.) When we take costs into account, the optimal grid shape may be rectangular instead of square. To maximise the quality of the pattern, given a budget, we need a quality measure. Ideally we would define this in terms of prediction error variance, but that assumes that we have an explicit model of the spatial variation and knowledge of the relation between the sensor variable(s) and the target variable. In the absence of these, we can take recourse to a geometric measure that penalises large distances from prediction points to nearest sensing points. One such measure is the mean of the squared shortest distances (MSSD) of the prediction points to the sensing points (Brus et al.,

2003; de Gruijter et al., 2006, p. 153). If we take this as the quality measure, Q (ha), then the model is, by double integration of the squared distance between points over a rectangle

$$Q = \frac{w^2 + h^2}{12}. \quad (1.2)$$

Using Eqs. (1.1) and (1.2) one can minimise the costs under the constraint of a given quality requirement Q_r . It can be shown by the Lagrange multiplier technique that the optimal value of h equals [for non-negative D and $(R - \sqrt{D})$]

$$h = \sqrt[3]{R + \sqrt{D}} + \sqrt[3]{R - \sqrt{D}} - \frac{2}{3}r, \quad (1.3)$$

where $r = \frac{c_m}{c_d}$, $R = 6Q_r r - \left(\frac{2}{3}r\right)^3$ and $D = R^2 - \left(\frac{2}{3}r\right)^6$.

The optimal value of w follows by substitution in Eq. (1.2). Given the cost ratio r , the optimised spacing between driving lines is a function of the quality requirement. Graphs of this function are given in Fig. 1.2 for $r = 0.05$, 0.25 and 0.5 hm.

Note that for a given cost ratio r , the ratio of the two optimal spacings h/w is a function of the quality requirement Q_r . This function is given in Fig. 1.3 for $r = 0.05$, 0.25 and 0.5 hm. The graphs show that the stronger the quality requirement, the more the optimised grid shape approaches $h/w = 1$, i.e. the ideal of the square. As expected, the rectangles of the optimised grids become more elongated as the ratio of measuring cost and driving cost is smaller.

Two extremes in terms of the cost ratio r deserve special attention. One extreme occurs when the cost of measuring is negligible; then $r \approx 0$, and according to Eq. (1.3), also $h \approx 0$. This would mean that sensing is done at the smallest possible spacing along the driving lines, the latter being $w = \sqrt{12Q_r}$ hm apart. One

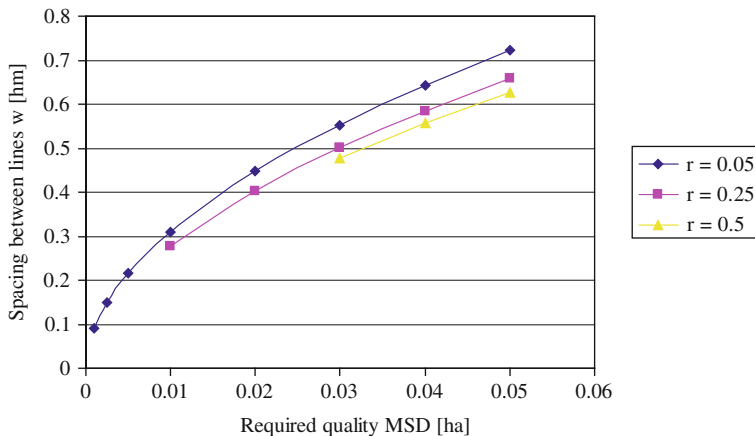


Fig. 1.2 Optimised spacing between driving lines w as a function of the required grid quality (MSSD), for cost ratios $r = 0.05$, 0.25 and 0.5 hm

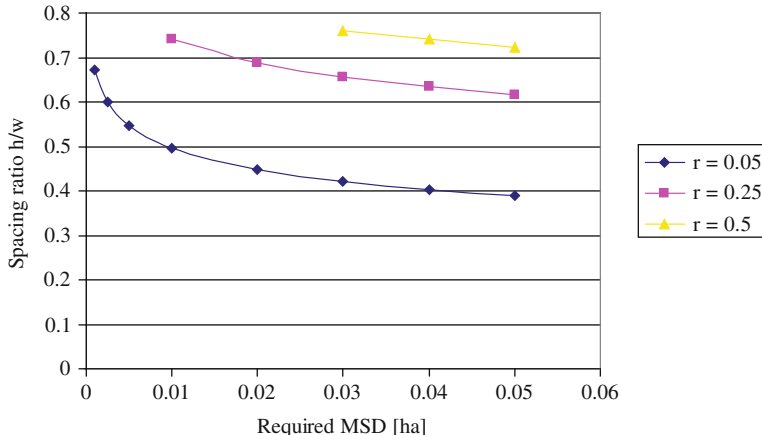


Fig. 1.3 Ratio of optimised spacings h and w as a function of the required grid quality (MSSD), for cost ratios $r = 0.05, 0.25$ and 0.5 hm

may ask if in such cases more efficient patterns can be formed by two perpendicular sets of equidistant parallel lines. The answer is negative because, to keep the investment at the same level, the spacing between the lines should be doubled and it can be shown that Q would then equal approximately $w^2/9$ instead of $w^2/12$.

The other extreme is when the cost of driving is negligible compared with measuring. The only concern is then to keep the sensing density as low as possible, under the constraint Q_r . The optimal grid shape is now square for any density so that [from Eq. (1.2)] $h = w = \sqrt{6Q_r}$.

The spacing between the lines cannot always be chosen freely because there may be controlled driving lines in the field, say w_m apart. In that case w is allowed to take only the values w_m or multiples of it. Given Q_r and a series of permissible values of w , optimisation can be done by calculating h from Eq. (1.2) and C from Eq. (1.1) for each value of w and selecting the (w, h) combination with the smallest C .

1.2.1.2 Optimisation for Equipment Type B

Assume that we drive the vehicle at speed v (m min^{-1}) while the sensor is measuring at frequency f (min^{-1}). A cost model in terms of time T (min ha^{-1}) needed for optimisation is now as follows:

$$T = \frac{1}{w \cdot v}. \quad (1.4)$$

The measuring interval along the lines h is determined by speed and frequency: $h = v/f$.

Minimising T , again under quality constraint Q_r , results in $w = h = \sqrt{6Q_r}$. So with this type of equipment one should always strive for a square grid, regardless of the quality requirement and the measuring frequency, as with type A when driving costs are negligible.

1.2.2 Sensor Sampling: Some Experiments

Three surveys were done in a 9.4-ha field located at 'The Lagoon' near Bathurst, New South Wales, on the flood plain of the Campbell River. Soil ranged from sandy, crusting, coarse textured profiles (Arenosols) with rock fragments on the higher elevations to heavy alluvial clays (Fluvisols) on the flats adjoining the river. The surveys were done with equipment of type B (non-stop driving) with an EM38 (horizontal): (1) fast driving in north-south direction; (2) slowly driving in north-south direction, half the speed but double swathe width of (1); and (3) same as (2) but in east-west direction. The driving lines were approximately straight, parallel and equidistant, two times farther apart with the slow surveys than with the fast one (13.3, 26.6 and 26.8 m on average). Figure 1.4 shows the swathe patterns for the three surveys.

The difference in speed caused differences in spacing between the measurements along the lines. The variable costs of the three surveys were approximately equal. See Table 1.1 for the key parameter values of the surveys. The numbers in brackets in this table are the expected parameter values after optimisation of the sampling design, given the same measuring frequencies and quality requirements as realised in the surveys.

The EC_a was mapped by ordinary kriging with the three datasets separately, and the mean kriging standard deviation was calculated. Figure 1.5 shows that, as expected, both the geographic pattern quality and the geostatistical pattern quality are better for the fast survey than for the slow survey, because the grid pattern is less elongated. This better quality was achieved with no extra costs.

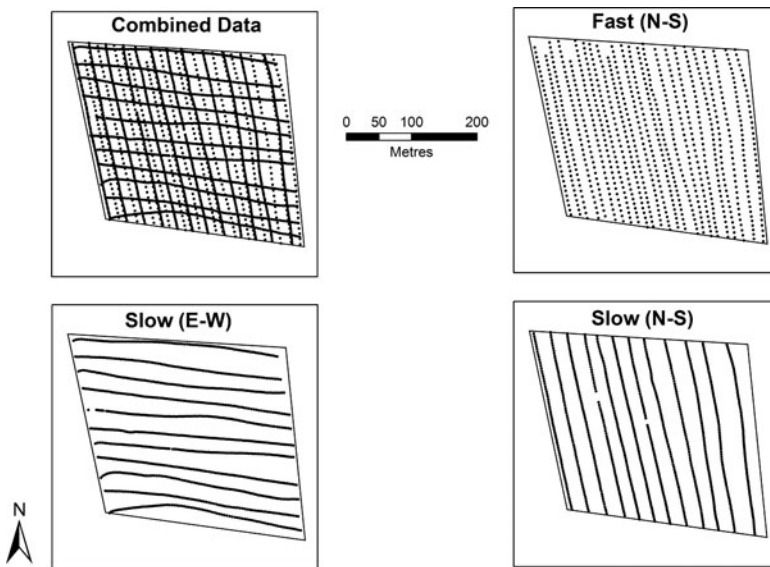


Fig. 1.4 Swathe patterns as applied in three sensing experiments

Table 1.1 Key parameter values of the three surveys

Survey parameter	Fast N–S	Slow N–S	Slow E–W
Swathe width, w (m)	13.3 (11.0)	26.6 (19.0)	26.8 (19.0)
Sample size, n	870	965	1035
Total line length (m)	7,080	3,540	3,520
Interval, h (m)	8.14 (11.0)	3.67 (19.0)	3.40 (19.0)
Frequency, f (min $^{-1}$)	24.2	24.7	28.8
Speed, v (m min $^{-1}$)	197 (267)	90.8 (469)	97.8 (547)
Time, T (min ha $^{-1}$)	3.82 (3.40)	4.13 (1.12)	3.82 (0.96)
Quality, Q (m 2)	20.3	60.1	60.8

Values for the optimised pattern are represented in brackets, given the same frequency and quality requirement as realised in the survey

Fig. 1.5 Geometric pattern quality Q (Eq. 1.2) versus geostatistical pattern quality (mean kriging standard deviation) for the surveys fast N–S, slow N–S and slow E–W (from left to right)

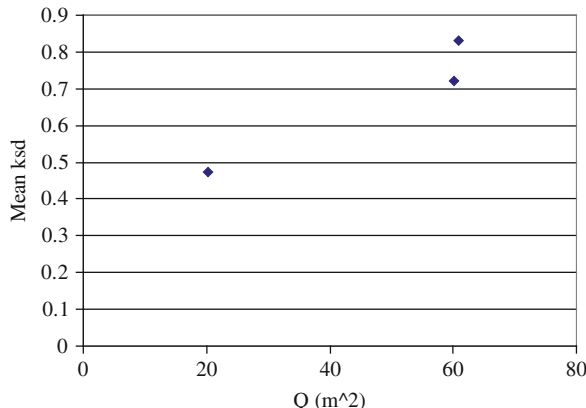


Table 1.1 shows that optimising the sensing pattern at the low-quality level of the slow speed surveys would decrease the survey time by about 75%. However, this could be achieved only with a more than four times higher speed of driving, which is clearly impractical. Optimising the sensing pattern at the higher quality level of the fast survey decreases the survey time much less than with the slow surveys (11%), and this would require a 36% higher driving speed. However, as the speed of the fast survey was already high from the point of view of sensing precision, such a speed-up might be at the cost of too much loss of data quality.

1.2.3 Calibration Sampling

As opposed to sensor sampling, in calibration sampling, aliquots are taken to the laboratory for measurements, and the total costs are therefore dominated by the

costs per aliquot, rather than the costs of going from one location to the other. Also, the sample size will be much smaller: some tens instead of hundreds or thousands.

From an optimisation point of view it seems practical to start from an affordable budget for calibration sampling, to derive the sample size from this, and to try to optimise the quality of the sample by choosing a pattern in the predictor space. Existing approaches to calibration sampling are the following: Latin hypercube sampling, response surface design, and model-based sampling for universal kriging. These are briefly reviewed below.

1.2.3.1 Latin Hypercube Sampling

Latin hypercube sampling (LHS) was developed by McKay et al. (1979) for random selection of a set of input values for a model, to generate outputs from which unbiased estimates of distribution parameters of the output can be made. It can also be used for sensitivity analysis. It has been shown that, under assumptions of monotonicity, this technique is more efficient for this purpose than are simple random sampling and stratified random sampling. See Fig. 1.6 for an example of LHS with two predictors and sample size 8.

Minasny and McBratney (2006) suggested the use of the technique for model calibration in the context of digital soil mapping (see also Chapter 9). Although LHS is suitable and widely used for the analysis of model output, i.e. when the model is already there, it is not clear whether it is also a suitable sampling method for model building and calibration. There are in fact reasons to expect otherwise.

Firstly, LHS is a *random* sampling technique, but for calibration, there is no need for random selection of predictor values, because inference on population parameters of the distribution of predictors is not the aim. Apart from being unnecessary, randomness is undesirable in this case because, even if a random design could be constructed that tends to produce sample configurations similar or close to the

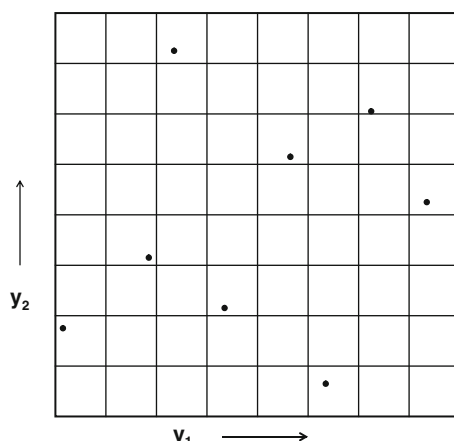


Fig. 1.6 Example of Latin hypercube sampling with two predictors and $n = 8$

configuration that is optimal for a given model structure, the randomness would generally cause deviations from this optimum.

Secondly, efficient calibration requires that values of predictors are taken at or near the extremes. Although LHS warrants that samples are taken near both extremes of each predictor individually, it can be expected that *combinations* of extremes of different variables (i.e. the corners of the hypercube) will rarely be selected. However, it is desirable to have such combinations in the calibration sample, especially when interaction effects are expected. For example, in the case of Fig. 1.4, none of the corner cells was selected, and it can be calculated that the probability of selecting two opposite corner cells is only 3.6%. This probability soon becomes negligible when the sample size or the number of predictors is increased. Note that any configuration that includes the four corners, favourable for calibration, is excluded by the Latin hypersquare constraint. Thus albeit LHS excludes samples that are really bad for calibration (all points concentrated around the centre of the sample space), there is a suspicion that the really good ones are avoided as well.

1.2.3.2 Sampling by Response Surface Methodology

Response surface methodology (Myers and Montgomery, 2002) was developed for designing efficient experiments in the context of optimising industrial processes and products. Fitzgerald et al. (2006) used this approach for spatial soil sampling, their aim being calibration of regression models. When used for sampling, response surface methodology tries to optimise sample configurations in predictor space, assuming a small number of predictors and a known, low-order model structure. Its applicability for high-resolution soil mapping seems therefore rather limited (see also Chapter 10).

1.2.3.3 Model-Based Sampling for Universal Kriging

Brus and Heuvelink (2007) used simulated annealing to optimise sample patterns for universal kriging of environmental variables. This method assumes that the predictors are linearly related to the target variable and that the variogram of the residuals is known. Little is known about the robustness of this approach against deviations from the model assumptions. An advantage is that the sample pattern is, in one step, optimised in both predictor space and geographic space. However, the assumed linearity and knowledge of the residual variogram will limit its applicability in practice. Furthermore, the sampling density will often be so low that optimisation of the sample pattern in predictor *and* geographic space would not much improve the precision of the spatial predictions over that gained by optimisation in predictor space alone.

1.2.3.4 Sampling by Fuzzy Cluster Analysis

Generally speaking, fuzzy cluster analyses create fuzzy subsets of objects, in which the objects have memberships varying between 0 and 1. In pedometric applications

of these techniques (McBratney and de Grujter, 1992), soil profiles have been taken as the objects and their memberships in fuzzy classes were mapped to produce soil maps with gradual transitions between those classes. However, one can also use these memberships for sampling purposes. If we take the data vectors in the predictor space as objects and apply fuzzy cluster analysis to them, then we can use their memberships in the fuzzy subsets to search for a sample pattern with suitable properties for calibration.

The method of fuzzy k -means (Bezdek, 1981) results in a user-selected number (k) of centroids in predictor space, which are optimised with a least squares criterion and can be seen as centres of gravity attracted by sub-regions with relatively high densities. If for each centroid we choose the predictor vector with the largest membership in the corresponding subset and allocate a sample point at the geographic location of that vector, then we have a sample of size k which is (in a least squares sense) representative of the distribution in predictor space. The sample points will tend to be located in high-density sub-regions. See Fig. 1.7 for an example of fuzzy k -means sampling with two predictors and sample size 8. Clearly, although the FKM samples will represent the multivariate distribution well, the corners with the extremes will remain systematically undersampled.

A remedy for this might be found with a modification of FKM (called fuzzy k -means with extragrades, FKME), developed by McBratney and de Grujter (1992) in order to enhance the predictive power of fuzzy class memberships. The core of this method is that, apart from the k regular subsets represented by a centroid, an extra fuzzy subset with multivariate extremes or outliers is created. The relative volume of this latter subset, i.e. the average membership in it, is chosen by the user. Thus a sampling method based on FKME could be first to choose the total sample size (say n) and then to decide on the number of extreme sample points

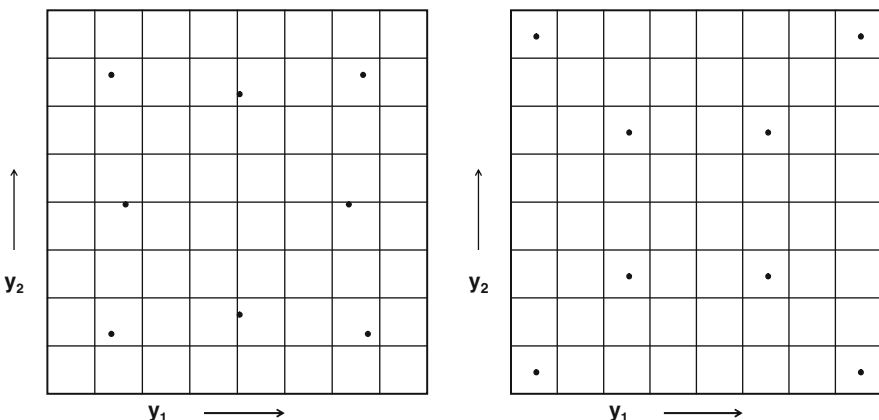


Fig. 1.7 Left: FKM sample with two predictors and with $n = k = 8$ (all sample points located at centroids). Right: FKME sample with $n = 8$, $k = 4$ and $e = 4$

(say e). FKME is then applied with $k = n - e$. Finally, the k locations with the largest membership in the respective regular subsets are selected and completed by the e locations with the largest memberships in the extra subset. See Fig. 1.7 for an example of FKME sampling with two predictors, $n = 8$, $k = 4$, $e = 4$, and average membership in the extra subset equal to 1/5. As expected, the four sample points near the centroids represent the central sub-region, while the four points with the largest membership in the outlier subset occupy the corners. A 50/50 division of the total sample size might be a reasonable choice in practical applications.

1.3 Results and Discussion

The models as proposed for the variable costs and for the quality of sensing grids seem to yield plausible results when used for optimisation. Two factors influence the size and the shape of optimised sensing grids: the ratio of costs of measuring and driving and the required grid quality in terms of spatial coverage. The costs ratio affects mostly the shape: the smaller the measuring costs relative to the driving costs, the more elongated the rectangles of the sensing grid (Fig. 1.3). The required quality level affects mostly the size. For instance, relaxing the quality requirement as root MSSD from 0.1 to 0.2 hm doubles the optimal swathe width from 0.3 to about 0.6 hm (Fig. 1.2).

Our review of existing approaches to calibration sampling revealed some shortcomings and limitations. The proposed alternative, FKME sampling, attempts to address these. It does not assume any specific knowledge of the model structure, but its coverage of the predictor space may work well in cases where there are several predictors, non-linearities and interaction effects. As a heuristic proposed on a priori grounds, FKME sampling needs proper testing before any final conclusions on its usefulness can be drawn.

1.4 Conclusions

1. As the fixed costs of sensing are typically (much) higher than the variable costs, the decision on whether or not to do it seems more important than how to do it, as long as the sensing grid is not too coarse.
2. The circumstances under which sensing is reasonable should be investigated in detail and quantitatively. Qualitatively, the principle underlying sensing seems to be that the measurement error is smaller than the short-range variation. Apart from experiments, quantitative analysis requires cost models and accuracy models that cover sensing, calibration and spatial prediction together.
3. There is ample room for improvement of calibration sampling, and as long as no sensor is available for direct measurement of the target variable, and calibration sampling is relatively expensive, more research on how to do it is warranted.

References

Bezdek JC (1981) Pattern recognition with fuzzy objective function algorithms. Plenum Press, New York, NY

Brus DJ, de Gruijter JJ, van Groenigen JW (2003) Designing spatial coverage designs by the k -means clustering algorithm. Proceedings of 8th international FZK/TNO conference on contaminated soil (ConSoil 2003), Gent, Belgium, pp 504–509

Brus DJ, Heuvelink GBM (2007) Optimization of sample patterns for universal kriging of environmental variables. *Geoderma* 138:86–95

de Gruijter JJ, Brus DJ, Bierkens MFP, Knotters, M (2006) Sampling for natural resource monitoring. Springer, Heidelberg

Fitzgerald GJ, Lesch SM, Barnes EM, Luckett WE (2006) Directed sampling using remote sensing with a response surface sampling design for site-specific agriculture. *Comput Electron Agric* 53:98–112

McBratney AB, de Gruijter JJ (1992) A continuum approach to soil classification by modified fuzzy k -means with extragrades. *J Soil Sci* 43:159–175

McKay MD, Beckman RJ, Conover WJ (1979) A comparison of three methods for selecting values of input variables in the analysis of output from a computer code. *Technometrics* 21:239–245

Minasny B, McBratney AB (2006) A conditioned Latin hypercube method for sampling in the presence of ancillary information. *Comput Geosci* 2:1378–1388

Myers RH, Montgomery DC (2002) Response surface methodology: process and product optimization using designed experiments, 2nd edn. Wiley, New York

Chapter 2

Development of On-the-Go Proximal Soil Sensor Systems

V.I. Adamchuk and R.A. Viscarra Rossel

Abstract To implement sustainable agricultural and environmental management, a better understanding of the soil at increasingly finer scales is needed. Conventional soil sampling and laboratory analyses cannot provide this information because they are slow and expensive. Proximal soil sensing (PSS) can overcome these shortcomings. PSS refers to field-based techniques that can measure soil properties from 2 m or less above the soil surface. The sensors may be invasive, or not, and may or may not be mounted on vehicles for on-the-go operation. Much research is being conducted worldwide to develop sensors and techniques that may be used for proximal soil sensing. These are based on electrical and electromagnetic, optical and radiometric, mechanical, acoustic, pneumatic, and electrochemical measurement concepts. This chapter reviews the latest of these technologies and discuss their applications.

Keywords Proximal soil sensing · Soil mapping · Sensor fusion · Electrical and electromagnetic sensors

2.1 Introduction

The implementation of sustainable agricultural and environmental management requires a better understanding of the soil at increasingly finer scales, e.g. for precision agriculture. Conventional soil sampling and laboratory analyses cannot provide this information because they are time consuming and expensive (Viscarra Rossel and McBratney, 1998). Proximal soil sensing can overcome these shortcomings because the techniques facilitate the collection of larger amounts of spatial data using cheaper, simpler, and less laborious techniques. PSS refers to field-based

V.I. Adamchuk (✉)

Department of Bioresource Engineering, McGill University, 21,1111 Lakeshore Rd.,
Ste-Anne-de-Bellevue, Quebec, H9X 3V9, Canada
e-mail: viacheslav.adamchuk@mcgill.ca

techniques that can be used to measure soil properties from a distance of 2 m or less above the soil surface. The sensors may be invasive, or not, and may or may not be mounted on vehicles for on-the-go operation.

Research is being conducted worldwide to develop sensors and techniques that may be used for proximal soil sensing (Hummel et al., 1996; Sudduth et al., 1997; Adamchuk et al., 2004a). For example, the use of electromagnetic induction (EMI) and electrical resistivity for measurements of soil electrical conductivity (Chapters 19, 20, 21, 22, 23, and 24); ground-penetrating radar (GPR) for measurements of soil water content (Chapter 25), proximal passive gamma ray spectrometry for measuring K, U, and Th (Chapters 27, 28, and 29); optical systems to estimate soil organic carbon and iron contents (Viscarra Rossel et al., 2008); diffuse reflectance spectroscopy using visible–near-infrared (vis–NIR) and mid-infrared (mid-IR) energies to estimate soil organic carbon (OC), clay content, mineral composition, and other soil properties (Chapters 3, 11, 12, 13, 14, 15, 16, 17, and 18); ion-sensitive field effect transistors (ISFETs) and ion-selective electrodes (ISEs) to measure soil pH, lime requirement, and soil nutrients (Chapter 6, Adamchuk et al., 2005; Viscarra Rossel et al., 2005) and mechanical draft systems for measuring soil strength (Hemmat and Adamchuk, 2008).

The aim of this chapter is to review the current development of proximal soil sensors and to discuss the applicability of on-the-go soil sensing to improve soil management.

2.2 Sensor Development Review

Global navigation satellite system (GNSS) receivers, used to locate and navigate agricultural vehicles within a field, have become the most common sensors in precision agriculture. In addition to determining geographic coordinates (latitude and longitude), high-accuracy GNSS receivers can measure altitude (elevation) and the data can be used to calculate slope, aspect, and other parameters relevant to the terrain. Maps of field terrain have been also used to determine landscape positioning in terms of the potential for water accumulation, runoff, soil erosion, and other soil-related processes.

When a GNSS receiver and a data logger are used to record the position of each soil sample or measurement, a map can be generated and processed along with other layers of spatially variable information. This method is frequently called a ‘map-based’ approach. Previously, several prototype on-the-go soil-sensing systems were developed for ‘real-time’ applications in which the generated sensor signal was used to control variable application rates without data recording. Although appealing, the real-time approach has limited applicability due to poorly understood relationships between sensor signal output and agro-economically optimised local needs. Furthermore, many management strategies (e.g. nitrogen fertiliser application) require multiple layers of georeferenced data and expert assistance for successful development of ‘prescription’ maps. Soil maps generated using on-the-go measurements can only serve as a part of this relatively complex decision-making process.

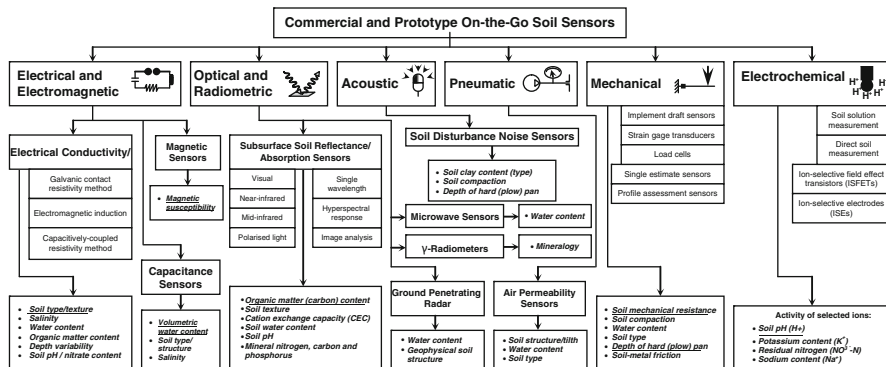


Fig. 2.1 General classification of on-the-go soil-sensing systems. Underlined soil properties are probably the easiest to distinguish

Although there is a large variety of design concepts, most on-the-go soil sensors being developed involve one of the following measurement methods: (1) electrical and electromagnetic sensors that measure electrical resistivity/conductivity or capacitance affected by the composition of the soil tested; (2) optical and radiometric sensors that use electromagnetic waves to detect the level of energy absorbed/reflected by soil particles; (3) mechanical sensors that measure forces resulting from a tool engaged with the soil; (4) acoustic sensors that quantify the sound produced by a tool interacting with the soil; (5) pneumatic sensors that assess the ability to inject air into the soil; and (6) electrochemical sensors that use ion-selective elements producing a voltage output in response to the activity of selected ions (e.g. hydrogen, potassium, nitrate).

An ideal soil sensor responds to the variability of a single soil attribute and is highly correlated with a corresponding conventional analytical measurement method. However, in reality, every sensor developed responds to more than one soil property and separation of their effects is difficult, or even not feasible. Figure 2.1 classifies types of on-the-go soil sensors according to corresponding agronomic soil properties affecting the signal. In many instances, an acceptable correlation between the sensor output and a particular agronomic soil property was found for a specific soil type, or when the variation of interfering properties was negligible.

2.2.1 Electrical and Electromagnetic Sensors

Electrical and electromagnetic sensors use electric circuits to measure the capability of soil particles to conduct and/or accumulate electrical charge. When using these sensors, the soil becomes part of an electromagnetic circuit and the changing local conditions immediately affect the signal recorded by a data logger. Several such sensors have become commercially available, e.g. sensors produced by Veris Technologies, Inc. (Salina, KS), Geonics Limited (Mississauga, Ontario, Canada),

Geocarta (Paris, France), Geometrics, Inc. (San Jose, CA), Dualem, Inc. (Milton, Ontario, Canada), and Crop Technology, Inc. (Bandera, TX).¹

One way to estimate soil electrical conductivity (EC_a) is by electromagnetic induction using, for example, a Geonics Limited EM38 meter. The transmitting coil induces a magnetic field that varies in strength with soil depth. The magnetic field strength can be altered to measure different soil depths to a maximum of 1.5 m. A receiving coil measures the primary and secondary induced currents in the soil and relates them to the soil electrical conductivity. Another instrument for mapping soil EC_a , the Veris 3100 mapping system, makes a more direct measurement (i.e. galvanic contact resistivity method). A set of coulter electrodes sends out an electrical signal through the soil. The signal is received by another set of coulter electrodes that measure the voltage drop due to the resistivity of the soil. Different spacing between coulters enables determination of EC_a for several depths, always starting at the surface. The capacitively coupled method has also been used to interface between an electrical conductivity sensor and soil. In each case, measured EC_a is called 'apparent' since it is different from the conventional solution-based test and the measurements relate to a bulk medium of soil containing different layers and inclusions of soil components with non-uniform conductive characteristics.

In addition to electrical resistivity/conductivity, some sensors based on electromagnetic induction can be used to measure magnetic susceptibility, which relates to variability of the gradient of the Earth's magnetic field near the surface. These magnetic susceptibility sensors can be used to map locations of artificial objects and/or iron-containing materials buried within the soil profile.

Alternatively, several researchers have used capacitor-type sensors to study soil dielectric properties. These sensors have been useful in mapping spatial variation in soil moisture (frequently in combination with the mechanical sensors described later). It appears that both conductive and capacitive soil characteristics, which can be measured on the go, are simultaneously affected by several agronomic soil attributes. For example, soil type (texture composition) significantly affects the output of most commercially available electrical resistivity/conductivity sensors. However, field variability of soil salinity, moisture, and some other parameters frequently interfere with this relationship.

2.2.2 Optical and Radiometric Sensors

Optical and radiometric sensors use electromagnetic energy to characterise soil. Optical sensors that use visible (vis: 400–700 nm) (Viscarra Rossel et al., 2008), near-infrared (NIR: 700–2,500 nm) (e.g. Chapters 3, 13, 15, 16, and 17), and/or

¹ The names of commercial entities are for illustration only, and additional suitable products may be offered by other companies.

mid-infrared (mid-IR: 2500–25,000 nm) (Chapters 3, 11 and 12) are being used as surrogates to enhance or replace conventional methods of soil analysis. These sensors measure the amount of light that is diffusely reflected from the soil after radiation containing all the pertaining frequencies illuminates it. Chapter 3 provides an overview of diffuse reflectance spectroscopy in the vis-NIR and mid-IR. Optical proximal soil-sensing systems, using either single or multiple wavelengths, have been developed by various researchers. For example, Shonk et al. (1991) developed an on-the-go sensor that used reflectance at 660 nm to predict soil organic matter (OM). Sudduth and Hummel (1993) used a full spectrum NIR sensor for predictions of soil OM, texture, and moisture. Shibusawa et al. (2001) developed a tine-mounted NIR sensor for taking measurements at a depth of 15 cm. Mouazen et al. (2005) also developed a tine-mounted NIR sensor, and more recently Christy (2008) developed an on-the-go spectrometer for in situ measurement and prediction of various soil properties, including soil OM, total carbon, total nitrogen, calcium, and magnesium. Calibration of all of these sensors appears to depend on geographic position (that is, prediction of soil properties varies from one region to another), and for some soil properties it relies on secondary correlations that may exist under certain conditions (e.g. coarse-textured soils at higher elevations of a field may have lower pH and residual nitrate compared to finely textured soils in lower areas).

Rather than using optical reflectance, some researchers are utilising ground-penetrating radar (GPR) to investigate wave propagation through the soil (e.g. Chapter 25). Changes in wave reflectance may indicate changes in soil density or existence of restricting soil layers. GPR has great potential for geophysics (in general) and agriculture (in particular), especially to support water management.

At the very short-wavelength (high frequency) end of the electromagnetic spectrum, there is potential for using γ -radiometric methods. All soils contain naturally occurring radioisotopes that can disintegrate and produce γ -rays. Gamma rays are suited to spectroscopic identification because the energy of each photon is characteristic of the isotope that produced it. Attenuation of γ -rays through the soil varies with bulk density and water content. The half thickness, i.e. the thickness of absorbing material that will reduce the radiation to half its value, is 10 cm for dry soil with a bulk density of 1.6 Mg m^{-3} so that 95% of measurable γ -radiation is emitted from the upper 50 cm of the soil.

Thallium-activated sodium iodide crystals, NaI(Tl), are mainly used as detectors in these systems, although thallium-activated caesium iodide crystals, CsI(Tl), are also available. Proximal γ -ray spectrometers typically use crystal detector packs of between 3 and 8 L and measure either 256 or 512 channels covering an energy spectrum from 0 to 3 MeV (Fig. 2.2).

The conventional approach to the acquisition and processing of proximal γ -ray data is to monitor three broad spectral windows or regions of interest (ROI) corresponding to potassium, uranium, thallium; a fourth measure is the total count over all channels. See Chapters 27, 28, 29, and 33. Recently, Viscarra Rossel et al. (2007) showed that the entire γ -ray spectrum (256 energy bands) could be used for prediction of various soil properties using multivariate calibration techniques.

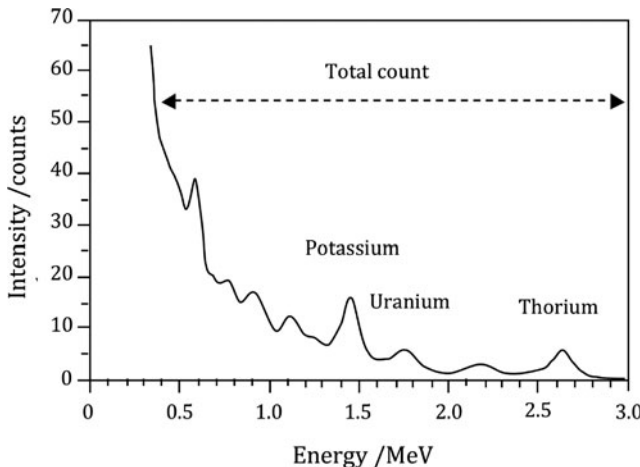


Fig. 2.2 Typical gamma ray spectrum and position of potassium, thorium, uranium, and total count regions of interest

2.2.3 Mechanical Sensors

Mechanical sensors can be used to estimate soil mechanical impedance (resistance), which is related to the spatially variable level of compaction. By nature, soil strength sensors measure resistance to soil failure. As such a sensor is dragged or pushed through the soil, it registers resistance forces arising from cutting, breaking, and displacing soil, as well as the parasitic (frictional and adhesive) forces that develop at the interface between the sensor and its surrounding soil. Normally, soil mechanical resistance is expressed in units of pressure and represents the ratio of the force required to penetrate the soil medium to the frontal area of the tool (normal to the direction of penetration) engaged with the soil.

Mapping total horizontal force (draft), and sometimes vertical force, applied to a traditional fixed-depth implement engaged with the soil can be viewed as the first step towards soil mechanical resistance sensing. Recorded measurements represent surrogate values affected by a variety of factors, including the type and shape of the tool working the soil, speed and depth of the operation, and surface conditions. Constructing a bulk soil strength sensor based on soil mechanics allows for better control of the type of soil failure it creates, and therefore produces more consistent measurements in diverse soil conditions. In any instance, bulk measurements reveal only spatial patterns of the underlying soil strength.

If a bulk soil strength sensor is actuated vertically (i.e. moved up and down) while mapping the field, the effective depth of engagement with soil will change from location to location. Assuming a relatively strong spatial structure, this approach allows assessment of soil variability associated with depth as well as location.

However, interpretation of variable-depth bulk soil strength measurements is not trivial and may include some subjective assumptions.

A vertically actuated cone penetrometer (which has been adopted as a standard tool; ASABE, 2006) is the most conventional method to detect change in soil penetration resistance with depth at a given location. Traditionally, this tip-based sensor has been used manually; automated versions increased the number of simultaneous point measurements and/or labour efficiency. However, for determining spatial variability across large agricultural fields, automated cone penetrometer sensors fail to provide economically justifiable mapping densities.

Single-tip horizontal sensors have been designed to generate high-resolution maps of horizontal soil penetration resistance obtained at a specific depth. Similar to the vertically actuated cone penetrometers, this method involves continuous logging of direct load measurements, which are frequently made using a load cell. Simultaneous deployment of multiple tips, each operated at a different depth, allows determination of spatial variability of soil mechanical resistance at any available depth as well as vertical variability in each part of a field. To avoid the expense of adding direct load-sensing tips, a single-tip horizontal sensor can be actuated vertically in a similar way as a bulk soil strength sensor.

In addition to a tip-based method, vertical distribution of soil mechanical resistance can be measured using an instrumented tine. This is done by measuring direct load applied to the tine at discrete depths and/or by measuring the degree of bending using strain gauge technology (i.e. a cantilever beam approach). The latter has also been used to map parameters of a (modelled) relationship between soil mechanical resistance and depth, rather than using discrete, measured values of this relationship.

In most field-mapping exercises, on-the-go sensing of soil strength under relatively constant travel speed has proven to be an economically viable alternative to the traditional point measurements. Sensor data frequently reveal strong spatial patterns with a relatively high degree of repeatability. However, published results from which an assessment of the benefits of variable tillage can be made are still limited. A number of investigators have searched for a depth where a local maximum in soil mechanical resistance occurs (indicating, for example, clay or a hard pan). Adjusting tillage depth according to the depth of a hard pan is potentially important economically.

As an example, Fig. 2.3 illustrates an instrumented system, developed at the University of Nebraska–Lincoln, which carries mechanical, electrical, and optical sensing components. The vertical blade, instrumented with an array of strain gauges, was designed to detect spatial and depth (5–30 cm) variability of soil mechanical resistance within a soil profile. Simultaneously, a capacitor-type sensor detects spatial variability in soil water. Finally, two sets of photodiodes and light-emitting diodes, protected with a sapphire window, are used to determine soil reflectance in the blue and red portions of the spectrum. This system is expected to help delineate field areas with potential compaction, excessive moisture, and/or low organic matter level. Potentially, several different soil treatment practices could be altered based on the data obtained.

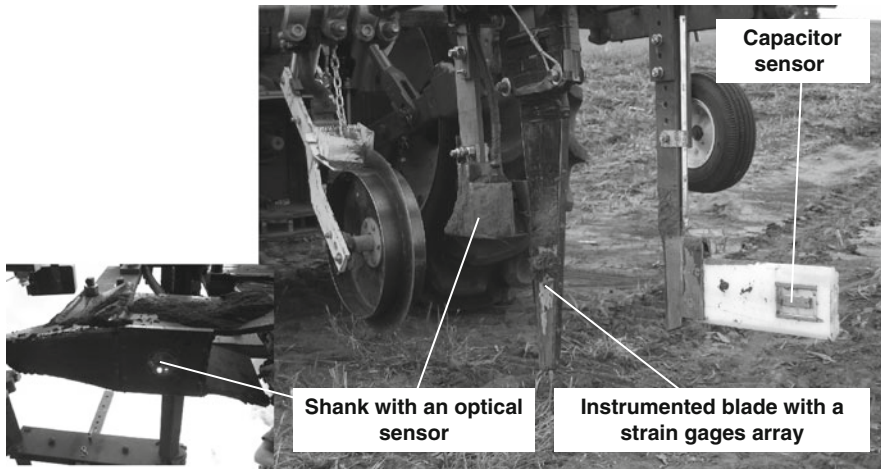


Fig. 2.3 Prototype system comprised of mechanical, electrical, and optical sensing components (University of Nebraska–Lincoln, Lincoln, Nebraska, USA)

2.2.4 Acoustic and Pneumatic Sensors

Alternatives to mechanical sensors are acoustic and pneumatic sensors, which can also serve to study the interaction between an implement and the soil. Acoustic sensors determine soil texture and/or bulk density by measuring the change in the level of noise caused by a tool's interaction with soil particles. Pneumatic sensors have been used, on the go, to measure soil–air permeability: the pressure required to force a given volume of air into the soil, at a certain depth, is compared to several soil properties, such as soil structure and compaction. At the present time, the relationship between sensor output and the physical state of soil is poorly understood, and additional research is needed. Because principles of acoustic and pneumatic sensors are conceptually different from the earlier described measurement principles, they may be good candidates for sensor fusion, in which multiple data streams are merged to improve the accuracy with which targeted soil attributes are predicted.

2.2.5 Electrochemical Sensors

Electrochemical sensors can provide crucial pieces of information needed for precision agriculture – soil nutrient availability and pH (Chapter 6). When soil samples are sent to a testing laboratory, a set of recommended laboratory procedures is performed. These procedures involve a sample preparation routine and then the measurement itself. Some measurements (especially of pH) are conducted using an ion-selective electrode (ISE), or an ion-selective field effect transistor (ISFET). Such electrodes detect the activity of specific ions (e.g. nitrate, potassium, or hydrogen in

case of pH). Several investigators have been trying to adopt existing soil preparation and measurement procedures to conduct laboratory-style tests on the go.

Adsett et al. (1999) developed a tractor-mounted, automated field-monitoring station for soil nitrate. The sensing system consisted of a soil sampler, a nitrate extractor unit, a flow cell, a controller, and a nitrate ISE. Loreto and Morgan (1996) also developed an automated system for on-the-go measurement of soil nitrate using a nitrate ISFET as the detector. Birrell and Hummel (2001) investigated the use of ISFETs and flow injection analysis (FIA) systems for real-time soil nitrate sensing. Viscarra Rossel and McBratney (1997) looked at the possibility of using a pH ISFET for the sensing component of an on-the-go soil pH and lime requirement measurement system. Viscarra Rossel et al. (2005) reported the development of a prototype soil pH and lime requirement measurement system made up of a soil sampling and sieving mechanism, a soil analyser using a pH ISFET, and data collection and measurement algorithms. Field testing of the prototype showed that the accuracies of soil pH measurements in 0.01 M CaCl_2 and in deionised H_2O were 0.37 and 0.60 pH units, respectively, and the accuracy of estimated lime requirements was 0.6 Mg ha^{-1} .

A commercial, automated soil pH-mapping system (Veris Soil pH Manager) uses two ISEs to directly determine the pH of naturally moist soil (Adamchuk et al., 1999). While travelling across a field, a soil sampling mechanism located on a mobile frame obtains a horizontal core sample of soil from a depth of about 10 cm and brings it into firm contact with the sensitive membranes and reference junctions of two combination ISEs. As soon as the output stabilises (approximately 10 s), the electrode surfaces are rinsed with water and a new sample is obtained. Each data point recorded using this method has a greater error than the laboratory analysis of a composite soil sample. However, increasing the sample density by more than 10 times means that a higher quality soil pH map can be generated for the same cost. An agro-economic analysis by Adamchuk et al. (2004b) showed that higher resolution maps can significantly decrease pH estimation errors and increase potential profitability of variable rate liming. Taking the cost of lime into account, a simulation of liming using 1 ha (2.5 acre) grid point sampling and automated mapping resulted in \$6.13 ha^{-1} higher net return than with no lime over a 4-year growing cycle in a corn–soybean rotation (based on 2004 commodity prices).

There is an ongoing effort to integrate additional ISEs to map soluble potassium and residual nitrate-nitrogen along with soil pH (Adamchuk et al., 2005; Sethuramasamyraja et al., 2008). The drawback of this approach is that it does not provide real-time ion extraction. The measurements therefore represent actual ‘snapshots’ of ion activity, which cannot be used to instantly calculate lime and fertiliser application doses based on current recommendations. Such prescription routines could be developed if the ion activity measurements are interpreted along with soil-buffering estimates (such as cation exchange capacity, or CEC) that can be derived from electrical conductivity and/or soil reflectance measurements. That reasoning is behind the development of the Veris Mobile Sensor Platform, which combines pH- and EC_a -mapping systems (Fig. 2.4).

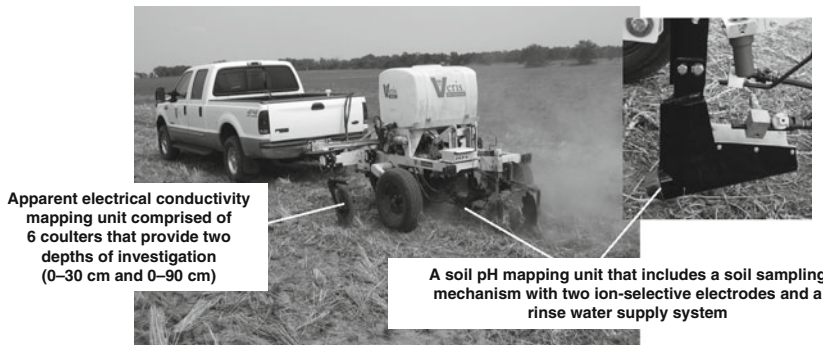


Fig. 2.4 The Veris Mobile Sensor Platform integrates soil electrical conductivity and pH-mapping units (Veris Technologies, Inc., Salina, Kansas, USA)

2.3 Sensor Applications

Producers would prefer a sensor that gave a reading in terms of existing prescription algorithms. Instead, commercially available sensors read out field topography, electrical conductivity, optical reflectance, or gamma radiation count – quantities that cannot be used directly since the final desired value depends on a number of physical and chemical soil properties – texture, organic matter, salinity, moisture content, temperature, and so on. Even so, these sensors do give valuable information about soil differences and similarities that makes it possible to divide a field into smaller and relatively homogeneous areas, often referred to as ‘management zones’.

These management zones could, for example, be defined according to the various soil types found within a field. In fact, EC_a maps usually reveal boundaries of certain soil series better than do conventional soil survey maps. Various anomalies such as eroded hillsides or ponding can also be easily identified on an EC_a map. Different levels of productivity observed in yield maps frequently correspond to different levels of EC_a , and often such similarities can be explained through differences in soil. In general, the EC_a maps indicate areas where further investigation to explain yield differences caused by soil is needed (Corwin and Lesch, 2003; Heiniger et al., 2003).

Current technology can delineate areas in a field that occupy specific landscape positions or have certain soil physical states, factors which typically result in similar growing environments (unless extra dissimilarities have been artificially added, such as through merged fields or non-uniform application of fertiliser).

2.3.1 Multisensor Data Fusion

Here, we define multisensor data fusion as the process of acquiring, filtering, correlating, and integrating relevant information from various sources, like sensors, databases, knowledge bases, and humans, into one representational format that is suited to agronomic and environmental decision making. When dealing with

multisensor data, their fusion can provide a number of advantages: (1) multiple sensors, revealing redundant information, can increase the robustness of the system; (2) the fusion of complementary information results in an information gain compared to that from a single source; (3) fusion from multiple sensors may provide more timely information, either because of the actual speed of operation of each sensor or because of the processing parallelism that may be achieved as part of the integration process; (4) operational performance is improved because any one sensor has the potential to contribute information when others are unavailable; (5) the attribute coverage is extended because one sensor can 'look' where another sensor cannot; (6) increased confidence in the measurements is acquired when multiple independent measurements are made on the same soil; and (7) increased dimensionality of the measurement space (i.e. different sensors measure different portions of the electromagnetic spectrum) reduces vulnerability to denial of any single portion of the measurement space.

Integrating different measurements from various sensors into a single mapping system is a current topic of investigation. The degree of association between different soil properties and conceptually different sensor outputs is not the same. Therefore, maps generated by different sensors can be integrated to improve their applicability. The best combination of sensors (whose outputs will be integrated) for mapping a field, and the corresponding optimum data-processing algorithm, will depend on the specific climatic and crop-growing conditions.

For example, in recent research (Sethuramasamyraja et al., 2008), the soil pH measurement equipment shown in Fig. 2.4 was expanded to simultaneously determine soluble potassium and residual nitrate (Fig. 2.5). Tested under laboratory conditions, the concept involved integration of different ISEs to measure the activity of hydrogen, potassium, and nitrate ions in aqueous solution. Although both pH and soluble potassium can be mapped on the go, such measurements are not sufficient by themselves to prescribe a dose of lime and potassium fertilisers: in many regions, measures of buffer pH and exchangeable potassium are required. Although some on-the-go mapping work has attempted to implement a solution-based method involving ion extraction (Viscarra Rossel et al., 2005), chemical extraction of ions while on the move presents technical difficulties. Knowledge of soil-buffering characteristics, determined using EC_a or other on-the-go method based on direct measurement of ion activities, can aid in developing these spatially variable soil treatment prescriptions.

For example, Fig. 2.6 illustrates, for 15 diverse Nebraska soils, relationships between measured and predicted buffer pH and exchangeable K values. In both cases, CEC was used to represent soil buffering through a multivariate regression analysis. The CEC itself was estimated using measured percentages of clay and organic matter content. Based on this example, it appears that, under certain conditions, a predictor of soil texture (most likely EC_a) and perhaps of organic matter content (optical reflectance) should be sufficient to determine site-specific soil-buffering characteristics; simultaneous measurements of soil pH and soluble K, obtained on-the-go, could then be used to determine needs for lime and potassium fertilisers based on existing recommendations.

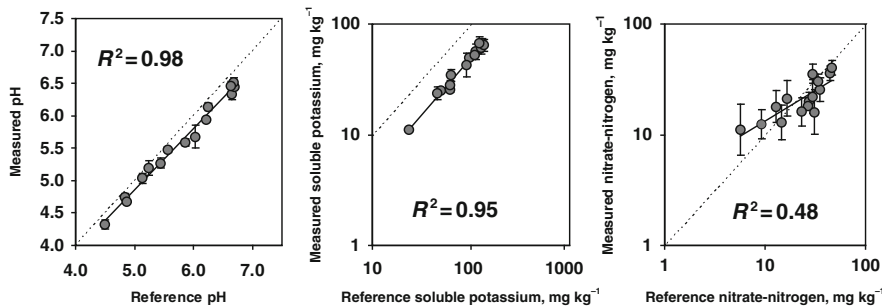


Fig. 2.5 Relationships between measured and reference soil pH (a), soluble potassium (b), and residual nitrate-nitrogen content (c). The measured estimates were obtained using the method cited and the reference measurements were conducted in a commercial soil laboratory

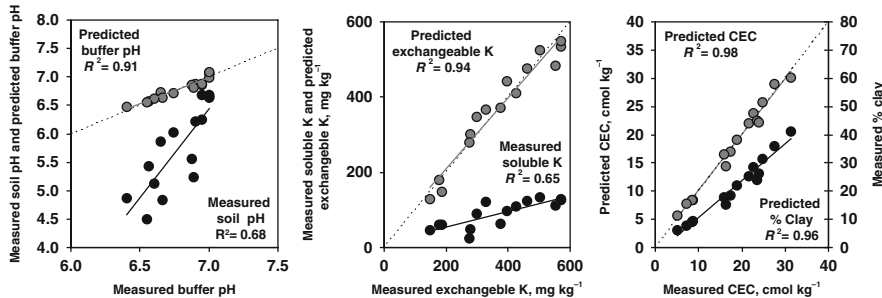


Fig. 2.6 Relationships between (a) measured soil pH/predicted buffer pH and measured buffer pH, (b) measured soluble K/predicted exchangeable K and measured exchangeable K, and (c) predicted CEC/percentage of clay and measured CEC. These measurements were obtained in several commercial soil laboratories for 15 Nebraskan soils

2.3.2 Sensor Deployment

From a practical viewpoint, successful deployment of an on-the-go soil sensor requires follow-up measurements of agronomic soil attributes in multiple field locations. These measurements are necessary to validate or define a new (field-specific) relationship between sensor outputs and soil parameters that guide decision-making processes. For example, EC_a and/or optical reflectance maps have been used to prescribe adaptive soil fertility sampling that would account for the spatial inconsistency of soil types, or to make point estimates of soil texture and organic matter content that would be used to calibrate these sensors to a given environment. If a high degree of association between sensor output and a given point estimate is discovered, an improved thematic soil map of an agronomic attribute may be produced. Currently, the process of prescribing guided sampling/point measurement locations includes a subjective component, which partially limits adoption by a lower level user of on-the-go sensing technology.

In our recent study (Adamchuk et al., 2008), it was discussed that a suitable set of guided samples should (1) be collected from relatively homogeneous field areas (i.e. away from the field boundary and away from locations where sensor outputs change significantly over short-distance intervals); (2) uniformly cover the entire range of sensor-based measurements; and (3) be spread across the entire field to assure representation of different soil conditions unaccounted for by sensor measurements.

Once multiple sensor logs and guided point measurements are obtained, spatial analysis is pursued to delineate field areas that may benefit from a differentiated treatment. This is typically done using a spatial clustering approach (supervised or unsupervised classification), which also relies on substantial subjective input from an expert. Development of automated routines to efficiently manage data obtained using on-the-go soil-sensing technology is another potential area for future investigations.

2.4 Conclusions

There is a need for thematic soil data layers to be used in soil assessment and management, e.g. for precision agriculture. Conventional soil survey cannot efficiently provide these data because the techniques are time consuming and expensive. Proximal soil sensing can be used to acquire spatial and temporal data cheaply and with less effort. This chapter reviewed the technologies, which are based on electrical and electromagnetic, optical and radiometric, mechanical, acoustic, pneumatic, and electrochemical methodologies, and discussed their applications.

References

Adamchuk VI, Morgan MT, Ess DR (1999) An automated sampling system for measuring soil pH. *Trans ASAE* 42:885–891

Adamchuk VI, Hummel JW, Morgan MT, Upadhyaya SK (2004a) On-the-go soil sensors for precision agriculture. *Comput Electron Agric* 44:71–91

Adamchuk VI, Morgan MT, Lowenberg-DeBoer JM (2004b) A model for agro-economic analysis of soil pH mapping. *Precis Agric* 5:109–127

Adamchuk VI, Lund E, Sethuramasamyraja B, Morgan MT, Dobermann A, Marx DB (2005) Direct measurement of soil chemical properties on-the-go using ion-selective electrodes. *Comput Electron Agric* 48:272–294

Adamchuk VI, Viscarra Rossel RA, Marx DB, Samal AK (2008) Enhancement of on-the-go soils sensor data using guided sampling. In: Proceedings of the 9th international conference on precision agriculture, Denver, Colorado, 20–23 July (2008), ASA-CSSA-SSSA, Madison, Wisconsin, USA (CD, 13 pp)

Adsett JF, Thottan JA, Sibley KJ (1999) Development of an automated on-the-go soil nitrate monitoring system. *Appl Eng Agric* 15:351–356

ASABE (2006) Soil cone penetrometer. S313.3 ASABE Standards, 53rd edn. ASABE, St. Joseph, Michigan

Birrell SJ, Hummel JW (2001) Real-time multi-ISFET/FIA soil analysis system with automatic sample extraction. *Comput Electron Agric* 32:45–67

Christy CD (2008) Real-time measurement of soil attributes using on-the-go near infrared reflectance spectroscopy. *Comput Electron Agric* 61:10–19

Corwin DL, Lesch SM (2003) Application of soil electrical conductivity to precision agriculture: theory, principles, and guidelines. *Agron J* 95:455–471

Heiniger RW, McBride RG, Clay DE (2003) Using soil electrical conductivity to improve nutrient management. *Agron J* 95:508–519

Hemmat A, Adamchuk VI (2008) Sensor systems for measuring spatial variation in soil compaction. *Comput Electron Agric* 63:89–103

Hummel JW, Gaultney LD, Sudduth KA (1996) Soil property sensing for site-specific crop management. *Comput Electron Agric* 14:121–136

Loreto AB, Morgan MT (1996) Development of an automated system for field measurement of soil nitrate. Paper No. 96–1087. ASAE, St. Joseph, Michigan

Mouazen AM, De Baerdemaeker J, Ramon H (2005) Towards development of on-line soil moisture content sensor using a fibre-type NIR spectrophotometer. *Soil Till Res* 80:171–183

Sethuramasamyraja B, Adamchuk VI, Dobermann A, Marx DB, Jones DD, Meyer GE (2008) Agitated soil measurement method for integrated on-the-go mapping of soil pH, potassium and nitrate contents. *Comput Electron Agric* 60:212–225

Shibusawa S, I Made Anom SW, Sasao A, Hirako S (2001) Soil mapping using the real-time soil spectrometer. In: Grenier G, Blackmore S (eds) *Precision Agriculture '01*, Proceedings of the 3rd European conference on precision agriculture, BIOS, Oxford, UK, pp 497–508

Shonk GA, Gaultney LD, Schulze DG, Van Scyoc GE (1991) Spectroscopic sensing of soil organic matter content. *Trans ASAE* 34:1978–1984

Sudduth KA, Hummel JW (1993) Soil organic matter, CEC, and moisture sensing with a portable NIR spectrophotometer. *Trans ASAE* 36:1571–1582

Sudduth KA, Hummel JW, Birrell SJ (1997) Sensors for site-specific management. In: Pierce FT, Sadler EJ (eds) *The state of site-specific management for agriculture*. ASA-CSSA-SSSA, Madison, Wisconsin, pp 183–210

Viscarra Rossel RA, McBratney AB (1997) Preliminary experiments towards the evaluation of a suitable soil sensor for continuous 'on-the-go' field pH measurements. In: Stafford J (ed) *Precision Agriculture '97*, Proceedings of the 1st European conference on precision agriculture, BIOS, Oxford, UK, pp 493–501

Viscarra Rossel RA, McBratney AB (1998) Soil chemical analytical accuracy and costs: implications from precision agriculture. *Aus J Exp Agric* 38:765–775

Viscarra Rossel RA, Gilbertsson M, Thylén L, Hansen O, McVey S, McBratney AB (2005) Field measurements of soil pH and lime requirement using an on-the-go soil pH and lime requirement measurement system. In: Stafford J (ed) *Precision agriculture: papers from the 6th European conference on precision agriculture*. Wageningen Academic Publishers, Wageningen, The Netherlands, pp 511–520

Viscarra Rossel RA, Taylor HJ, McBratney AB (2007) Multivariate calibration of hyperspectral γ -ray energy spectra for proximal soil sensing. *Eur J Soil Sci* 58:343–353

Viscarra Rossel RA, Fouad Y, Walter C (2008) Using a digital camera to measure soil organic carbon and iron contents. *Biosyst Eng* 100:149–159

Chapter 3

Diffuse Reflectance Spectroscopy for High-Resolution Soil Sensing

B. Stenberg and R.A. Viscarra Rossel

Abstract Diffuse reflectance spectroscopy in the visible–near-infrared (vis–NIR) and mid-infrared (mid-IR) is a practical analytical technique that can be used for both laboratory and in situ soil analysis. The techniques are sensitive to both organic and mineral soil composition. They are particularly well suited to situations where the primary (conventional) analytical method is laborious and costly or where a large number of analyses and samples are required, e.g. for high-resolution digital soil mapping or precision agriculture. This chapter will describe diffuse reflectance spectroscopy of soil in the vis–NIR (400–700–2,500 nm) and mid-IR (2,500–25,000 nm) portions of the electromagnetic spectrum. The theory of the mechanisms of absorbance in soil will be explained briefly, followed by aspects of data pretreatments, chemometrics, and multivariate calibrations. Finally, both laboratory and in situ applications are discussed and the focus of future research suggested.

Keywords Visible–near-infrared · Vis–NIR · Mid-infrared · Mid-IR · Diffuse reflectance spectroscopy · Diffuse reflectance spectrophotometers · FT-IR DRIFT

3.1 Introduction

Diffuse reflectance spectroscopy in the visible–near-infrared (vis–NIR) and mid-infrared (mid-IR) is gaining increasing interest for various soil applications, both for laboratory and in situ field analyses, including measurements made on the go. The reason for this is most certainly the potential to simplify procedures in the soil laboratory as the only sample preparation is drying and grinding. The sample is not affected by the analysis in any other way and no (hazardous) chemicals are required. In addition, scanning takes a matter of seconds, and several parameters can be measured from a single scan. This multi-parameter feature of diffuse reflectance

B. Stenberg (✉)

The Precision Agriculture and Pedometrics Group, Department of Soil and Environment, SLU, PO Box 234, SE-532 23 Skara, Sweden
e-mail: Bo.Stenberg@mark.slu.se

spectroscopy implies that one spectrum holds information about various soil constituents. Visible–NIR instruments can be robustly built and equipped with fibre optics for flexible sample presentation. Robust, portable mid-IR instruments are also starting to emerge. Thus, the hardware prerequisites for field measurements are basically fulfilled.

If all these were as simple and straightforward as it sounds, one may wonder why diffuse reflectance spectroscopy is not widely used in soil analysis – like it is for analysing grain and forage – or why the traditional soil auger has not yet been replaced by a portable spectrometer with a fibre optic attachment. The primary reason is that parameter values cannot be directly deciphered from the vis–NIR or mid-IR spectra. To be useful quantitatively, spectra have to be exactly related to a set of known reference samples through the calibration of a prediction model, and these reference samples have to be representative of the range of soils the model is intended for. In addition, environmental factors (e.g. soil water) influence spectra, which may, especially for in situ field measurements, cause problems.

In this chapter we intend to give an overview of diffuse reflectance spectroscopy in both the vis–NIR and the mid-IR, paying particular attention to what influences the spectra and what is, supposedly, measured in soil. The most common data treatment procedures and calibration techniques will also be presented. Examples of soil applications from both laboratory and field studies will be given and discussed and the focus of future research suggested.

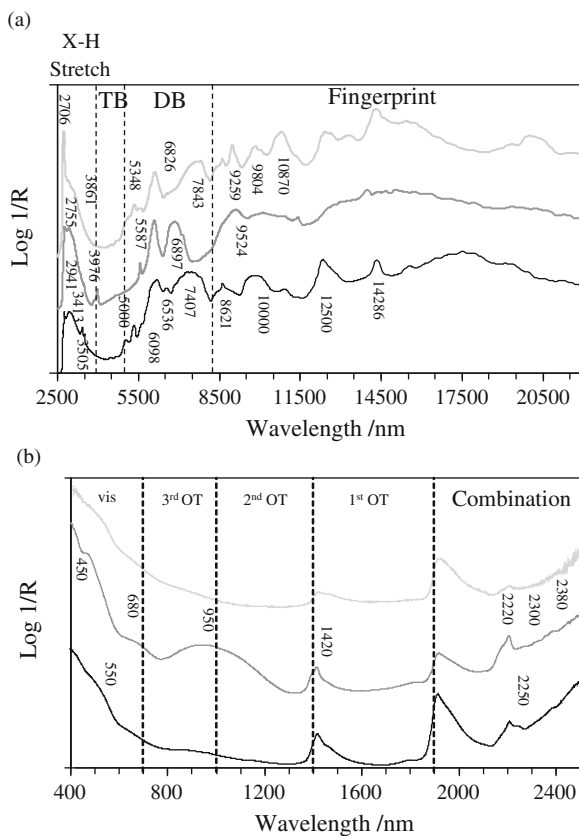
3.2 Fundamentals of Diffuse Reflectance Spectroscopy

When mid-IR radiation is directed onto a soil sample, it interacts with it and, if it has the right amount of energy, will induce fundamental vibrations of the organic and inorganic molecules in the soil. These molecular (fundamental) vibrations can be either stretching or bending vibrations and occur due to periodic displacement of the atoms with respect to one another. Stretching vibrations will usually occur at higher frequencies than bending vibrations as the restoring force acting on them will be greater than those in bending. In Fig. 3.1a, these stretching vibrations occur at wavelengths below 4,000 nm.

When NIR radiation interacts with a soil sample, it is only the overtones and combinations of the fundamental vibrations in the mid-IR that are detected. (Note that these also do occur in the mid-IR.) Molecular functional groups may absorb in the mid-IR with a range of overtones detected in both the mid-IR and NIR regions, getting weaker for each overtone order. Generally, the NIR region is characterised by broad, superimposed, and weak vibrational modes, giving soil NIR spectra fewer and broader absorption features than mid-IR spectra (Fig. 3.1b). In the visible region, electronic excitations are the main processes as the energy of the radiation is high.

To generate a soil spectrum, radiation containing all frequencies in a particular range is directed onto the sample. The principle is that a molecular bond will only absorb light with an energy quantum that corresponds to the difference between the two energy levels of a specific bond. As the energy quantum is directly related to

Fig. 3.1 Soil diffuse reflectance spectra. (a) The mid-IR (2,500–25,000 nm; 4,000–400 cm^{-1}) showing approximately the fingerprint, double-bond (DB), triple-bond (TB), and X–H stretch regions. Band assignments for organic functional groups taken from Ziechmann (1964), Russell et al. (1987), Skjemstad and Dalal (1987), and Baes and Bloom (1989); for minerals from Farmer (1974), van der Marel and Beutelspacher (1976), Russell (1987), and Nguyen et al. (1991). (b) The vis–NIR (400–2,500 nm; 25,000–4,000 cm^{-1}) showing approximately where the combination, first, second, and third overtone (OT) vibrations as well as the visible (vis) range occur



wavelength, or frequency, the effect on spectra is selective and can be used for analytical purposes. Those frequencies which are absorbed appear as a reduced signal of reflected radiation (R) and are displayed in percentage of the reflected radiation of a standardised white reference, which may then be transformed to apparent absorbance (A) through the relation $A = \log(1/R)$ (Fig. 3.1). The precise location of the absorption bands depends on the chemical matrix and environmental factors such as neighbouring functional groups and temperature, making it possible to detect a range of molecules that may contain the same type of bonds.

3.3 Soil Diffuse Reflectance Spectra

3.3.1 Vis–NIR

Due to broad and overlapping bands, vis–NIR spectra are visually much less resolved and difficult to interpret than the mid-IR (Fig. 3.1). Nevertheless, the vis–NIR region does contain useful information on organic and inorganic materials

in the soil. Absorptions in the visible region (400–780 nm) occur mostly due to electronic excitations and are primarily associated with minerals containing iron (e.g. haematite, goethite) (e.g. Sherman and Waite, 1985; Mortimore et al., 2004). Soil organic matter can also have broad absorptions in the visible region, dominated by humic acid (which is typically dark). Absorptions in the NIR (780–2,500 nm) result from the overtones of OH, SO₄, and CO₃ groups as well as combinations of fundamental features of H₂O and CO₂ (e.g. Clark, 1999). Absorption bands due to SOM in the NIR result from the stretching and bending fundamentals of N–H, C–H, and C–O groups in the mid-IR.

In the combination region of Fig. 3.1b, the weak absorption bands near 2,300 nm can, without any prior information on the sample, be rather difficult to interpret. For example, clay minerals like illite and smectite can show absorption in this region due to a combination of metal–OH bend plus O–H stretch, as can minerals containing Mg²⁺ like brucite (Viscarra Rossel et al., 2006b; Chapter 18). Carbonates have weak absorption peaks near 2,160 nm and also in the region between 2,300 and 2,500 nm, depending on the composition (Hunt and Salisbury, 1970). Soil organic matter can also have a weak combination band near 2,300 nm, which can sometimes be confused with hydroxyl and carbonate absorptions in minerals (Clark et al., 1990). The absorption doublet around 2,200 nm (Fig. 3.1b) is characteristic of kaolinite and is due to a combination of Al–OH bend plus O–H stretch. Other aluminosilicates, like illite and smectite, can also show absorption bands near 2,200 nm due to their Al–OH features. Other minerals, such as gibbsite, also show the typical Al–OH bend plus O–H stretch combination near 2,200 nm. These combination bands near 2,200 and 2,300 nm are useful diagnostic absorption features for clay mineral identification (Clark et al., 1990). The band near 1,920 nm represents the unique H–O–H bend and O–H stretch combination of molecular free water, vibrations of which are evident in structures of 2:1 minerals like smectite.

In the first overtone (OT) region (Fig. 3.1b), the only prominent absorption band is that near 1,400 nm, which can also be attributed to molecular water contained in various minerals, water attached to cellulose in organic materials, and to the first overtone of the O–H stretching vibration of kaolinite. Although not often visible, soil organic matter has a weak absorption band near 1,700 nm, which is due to the first overtone of the alkyl–CH₂ stretch fundamental at 3,413 nm. Carbonates also have a weak absorption band in the first OT region near 1,850 nm (Hunt and Salisbury, 1970).

In the third OT and visible regions, iron oxides show strong absorption features near 950 and 450 nm. The small absorbance peaks near 680 and 550 nm may be due to the iron chromophores found in haematite (red) and goethite (yellow), respectively (Mortimore et al., 2004).

3.3.2 *Mid-IR*

Soil mid-IR spectroscopy is particularly well suited for the analysis of soil organic matter (SOM) and mineral composition. Absorption features associated with both

organic functional groups and soil minerals can be readily identified in soil mid-IR spectra. In the fingerprint region (Fig. 3.1a), the dominant bands at 9,259, 12,500, and 14,286 nm are due to the fundamental SiO_2 stretching and bending vibrations of quartz (Russell, 1987). Bands near 8,621 and 10,000 nm may be attributed to mineral impurities and quartz, respectively. The $\text{Al}-\text{OH}$ vibration at 10,870 nm and the aluminosilicate lattice vibration at 9,804 nm are characteristic of kaolinite (Nguyen et al., 1991). The absorption band near 9,524 nm may be attributed to C–O stretch of polysaccharides in SOM (Skjemstad and Dalal, 1987).

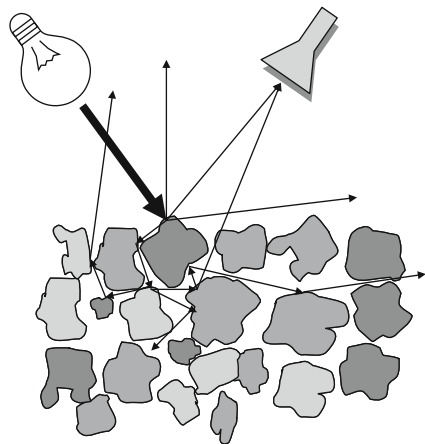
Many of the absorption bands in the double-bond (DB) region (Fig. 3.1a) are due to the fundamental vibrations of functional groups in SOM. The band near 7,843 nm may be attributed to a C–OH stretch in phenols, that near 7,407 nm to a stretch–bend combination of aliphatic groups, and the band near 6,826 nm to an aliphatic–CH stretch (Baes and Bloom, 1989). Bands near 6,536 and 6,098 nm are characteristic of humic acids rich in protein (Skjemstad and Dalal, 1987) and correspond, respectively, to an N–H deformation plus C=N stretch and a C=O stretch of amide groups (Stevenson, 1994). The absorption band near 6,897 nm (Fig. 3.1a) is most likely due to the bending vibration of the carbonate ion.

The double- and triple-bond regions (Fig. 3.1a) will also convey the overtones and combination vibration modes of quartz and other silicates in soil. The most characteristic of these are the combination bands of quartz and kaolinite in the region 5,000–5,880 nm. However, the absorption bands of kaolinite are often masked by the more intense group of three bands belonging to quartz, at 5,000, 5,348, and 5,587 nm (Nguyen et al., 1991). In the X–H stretch region (Fig. 3.1a), absorption bands at 3,861 and 3,976 nm may be assigned to combination vibrations of carbonate. The absorption bands at 3,413 and 3,508 nm are particularly useful for the detection of organic matter in soils, as this region is free of overlaps from other more intense vibrations. They may be attributed to alkyl– CH_2 symmetric and asymmetric stretches, respectively. The broad band near 2,941 nm may be attributed to O–H stretching vibrations of water molecules in the structure of 2:1 minerals. The absorption bands in the region between 2,631 and 2,778 nm may be attributed to O–H stretching vibrations of kaolinite and 2:1 layer aluminosilicates like smectite and illite. However, the latter only show poorly defined bands in this region, which are often masked by kaolinite and other clay minerals (van der Marel and Beutelspacher, 1976).

3.4 Mathematical Preprocessing of Spectra

Spectral preprocessing using mathematical functions are commonly used to correct for non-linearities, measurement and sample variations, and noisy spectra. In addition to chemical composition, spectra are also highly influenced by structural properties of the sample, which cause non-linear light scattering effects – hence the term *diffuse reflectance* spectroscopy. The key property of this phenomenon is that energy not reflected by the sample is not directly related to absorbance (Fig. 3.2). Most commonly, to attempt linearisation between absorbance and concentration,

Fig. 3.2 Illustration of diffuse reflectance. Incoming light from the left is scattered. Only a fraction of the reflected light reaches the receiving probe to the right. The rest is absorbed or lost



the measured reflectance (R) of the spectrum is transformed to $\log 1/R$ (Fig. 3.3). Other transforms include the Kubelka–Munk and the Dahm equations (Dahm and Dahm, 2007). Dahm and Dahm provide an excellent account of the theory of diffuse reflection in scattering and non-scattering samples.

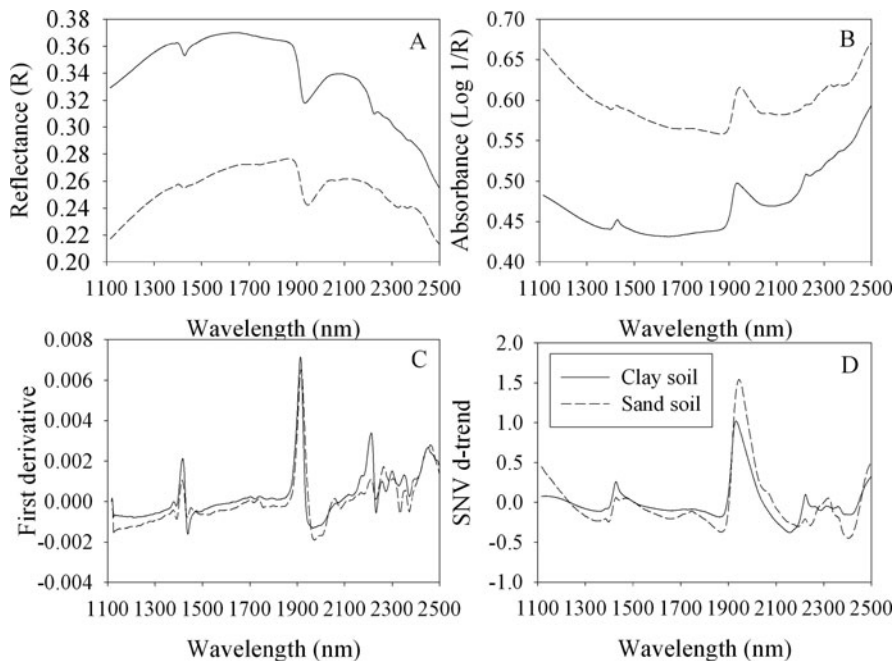


Fig. 3.3 The effect of spectral transformations and preprocessing on reflectance spectra (a). The $\log 1/R$ transformation is shown in (b), preprocessing of the $\log 1/R$ spectra using the first derivative is shown in (c), and the SNV with detrending is shown in (d)

The particle size distribution of the sample affects the degree of scattering. A coarser structure increases the scatter (reduces reflection), and as path length increases, the apparent absorbance also increases. To enhance the more chemically relevant peaks in the spectra (and reduce effects such as baseline shifts and overall curvature), various additional preprocessing transformations may be employed. For example, some of the more commonly used techniques include multiplicative scatter correction (MSC) (Geladi et al., 1985); simple additive baseline correction; the standard normal variate (SNV) transform (Fig. 3.3), with or without detrending (Barnes et al., 1989); first (Fig. 3.3) and second derivatives; and orthogonal signal correction (OSC) (Wold et al., 1998). Most spectroscopy-dedicated software includes a collection of techniques from which to choose (e.g. Viscarra Rossel, 2008). To reduce noise in spectral signals, commonly used smoothing algorithms include averaging of spectra, moving average and median filters, and the Savitzky–Golay transform (Savitzky and Golay, 1964). Because derivatives tend to amplify noise, a smoothing algorithm is often used in such cases. More recently, wavelets have been used to smooth and compress soil spectra, resulting in simpler and more robust calibrations (e.g. Chapter 17; Viscarra Rossel and Lark, 2009).

There is no one single or combination of preprocessing techniques that will work with all datasets. For soil samples, the type and amount of preprocessing required will be data specific. Nevertheless, the first and second derivatives calculated by difference are by far the most popular. Derivatives perform a baseline correction and enhance weak signals. The standard normal variate (SNV) combined with detrending has a similar effect, but the enhancement of weak signals is not as pronounced (Fig. 3.3).

3.5 Spectroscopic Multivariate Calibrations

Diffuse reflectance spectra of soil are largely non-specific due to the overlapping bands of soil constituents that are themselves varied and interrelated. This characteristic lack of specificity can be compounded by other unidentified soil components that are chemically reactive as well as by instrumental noise, drift, and scatter effects. All of these factors result in complex absorption patterns, and the challenge when acquiring data is to mathematically extract information from the spectra that is correlated with soil properties. In the end, the analysis of soil diffuse reflectance spectra will require the use of chemometric techniques and multivariate calibration (e.g. Martens and Naes, 1989). Chemometrics refers to mathematical or statistical techniques for treatment of chemical data, while multivariate calibration refers to the use of empirical data and prior knowledge to predict an unknown soil property \mathbf{y} from many spectroscopic measurements $\mathbf{x}_1, \mathbf{x}_2, \dots, \mathbf{x}_k$, simultaneously via a mathematical transfer function or model.

The most common calibration methods are stepwise multiple linear regression (SMLR) (e.g. Dalal and Henry, 1986; Ben-Dor and Banin, 1995), principal component regression (PCR), and partial least squares regression (PLSR). The main reason for the use of SMLR was the inadequacy of more conventional regression

techniques like multiple linear regression (MLR) and the ignorance of soil scientists of the existence of full-spectrum data compression techniques such as PCR and PLSR. Both of these techniques can cope with data containing large numbers of predictor variables that are highly collinear. PCR and PLSR are related techniques, and in most situations, prediction errors are similar. However, PLSR is often preferred because PLSR relates the response and predictor variables, meaning that the models explain more of the variance in response to fewer components, the models are more interpretable, and the algorithm is computationally faster. Increasingly we see the use of data-mining techniques such as neural networks (NN) (e.g. Daniel et al., 2003), multivariate adaptive regression splines (MARS) (e.g. Shepherd and Walsh, 2002), boosted regression trees (e.g. Brown et al., 2006), and regression rules (e.g. Minasny and McBratney, 2008); however, the outcome often only has limited advantages over PLSR. Viscarra Rossel (2007) combined PLSR with bootstrap aggregation (bagging-PLSR) to improve the robustness of the PLSR models and produce predictions with a measure of their uncertainty. Both MLR and PLS are linear models, while the data-mining techniques can handle non-linear data.

As with any other modelling, the selection of a validation procedure when performing spectroscopic multivariate calibrations is particularly important. For example, when using PCR or PLSR for calibration, leave-one-out or cross-validation is an adequate strategy for selecting the number of components (or factors) to use in the multivariate models. However, for accurate establishment of prediction performance, a representative, totally independent set of validation samples is required. To describe the accuracy, the explained variance (R^2) is the universal statistic. However, its dependence on range and its lack of a measure of prediction bias provide an over-optimistic view of the actual accuracy. Combined with an error estimate such as the root mean squared error (RMSE), it gives a more comprehensive view of the prediction error. Often the ratio of performance to deviation (RPD) is also given and facilitates the comparison between different parameters.

3.6 Spectroscopic Calibrations for Predictions of Soil Properties

3.6.1 *Visible–Near-Infrared (Vis–NIR) Calibrations*

Over the years, a large number of attempts to predict soil parameters with vis–NIR have been published. Most frequent are probably calibrations for total and organic carbon, followed by texture (especially clay content). According to a compilation of published explained variance statistics (Viscarra Rossel et al., 2006a) these two, together with total soil N, are also those with the best chance of success. Some other more-or-less frequently occurring parameters are pH, extracted P, K, Fe, Ca, Mg, and CEC, and also some properties that are dependent on various other soil properties such as lime requirement and mineralisable N (Table 3.1). Results for these are in general moderate or at least highly variable.

Table 3.1 Investigating the use of DRS for soil analysis in each of the visible (vis), near-infrared (NIR), mid-infrared (MIR), and vis–NIR. Data shown are average R^2 values of validation results for predictions of soil properties reported by various authors in the period 1986–2006

Soil property	Vis	Vis–NIR	NIR	MIR
<i>Chemical</i>				
Acid (exch.)	–	0.65 ^b	0.61 ^b	0.56 ^c
Al (exch.)	0.05 ^d	–	0.61 ^b	0.43 ^c
C (inorg.)	–	0.96 ^a	0.87 ^a	0.98 ^a
C (total)	–	0.89 ^a	0.91 ^a	0.95 ^a
C:N ratio	–	0.88 ^a	–	–
CEC	0.16 ^d	0.78 ^b	0.48 ^c	0.69 ^b
Ca (exch.)	0.35 ^d	0.80 ^a	0.45 ^c	0.89 ^a
Carbonate	–	–	0.69 ^b	0.95 ^a
EC	0.10 ^d	0.38 ^d	–	0.31 ^d
Fe (DTPA)	–	0.69 ^b	0.49 ^c	0.55 ^c
K (exch.)	0.29 ^d	0.52 ^c	0.47 ^c	0.36 ^d
LR	0.25 ^d	–	0.62 ^b	0.81 ^a
Mg (exch.)	–	0.76 ^b	0.59 ^c	0.76 ^b
N (NO_3^-)	–	0.63 ^b	0.04 ^d	0.06 ^d
N (total)	–	0.86 ^a	0.94 ^a	0.86 ^a
Na (exch.)	–	0.22 ^d	–	0.33 ^d
P (avail.)	0.06 ^d	0.81 ^a	0.10 ^d	0.14 ^d
pH _{Ca}	0.36 ^d	0.63 ^b	0.68 ^b	0.75 ^b
pH _w	0.36 ^d	0.61 ^b	0.62 ^b	0.66 ^b
Metal content: As, Cd, Cr, Cu, Hg, Ni, Pb, Zn	–	0.45–0.93 ^{c–a}	–	0.66–0.99 ^{b–a}
<i>Physical</i>				
Clay	0.43 ^c	0.76 ^b	0.64 ^b	0.78 ^b
Sand	0.47 ^c	0.70 ^b	0.59 ^b	0.84 ^a
Silt	0.31 ^d	0.59 ^c	0.41 ^c	0.67 ^b
Specific surface area	–	–	0.70 ^b	–
Air-dried water content	–	0.78 ^b	0.80 ^b	0.81 ^a
<i>Biological</i>				
Microbial biomass	–	0.60 ^c	0.75 ^b	0.69 ^b
Enzyme activity	–	–	0.55 ^c	0.70 ^b
Organic C	0.60 ^c	0.79 ^b	0.76 ^b	0.91 ^a
Microbial respiration rate	–	0.66 ^b	–	–

R^2 values for predictions of soil properties are classified as ^avery good (>0.81), ^bgood (0.61–0.8), ^cfair (0.41–0.6), and ^dpoor (<0.4)

That organic matter absorbs in the vis–NIR is not surprising, since most of the functional groups absorbing in this region are abundant in organic molecules. The strongly absorbing amide groups is expected to be active, which explains good results for total and organic N. Keep in mind, however, that the capacity of NIR to predict the N content of soil, which is generally well below 1%, depends on the close relation between the organic matter and the carbon content. Nevertheless, it

has been shown that NIR calibrations explain the variation of both organic C and N better than they explain each other (Chang and Laird, 2002; Fystro, 2002).

It has been frequently shown that vis–NIR relates better to organic matter than does NIR alone. Islam et al. (2003) reached considerably better results for Australian soils by including the visible region (350–700 nm) in their calibration. Similar observations were reported for Norwegian soils (Fystro, 2002). It is suggested that the brightness of the sample is an important feature in the visible region for it seems to indicate how well the organic C content can be predicted (Udelhoven et al., 2003). However, the opposite has been reported for US land resource areas (Chang et al., 2001) and south-eastern Australia (Dunn et al., 2002). Although it is generally true that dark soil has more organic matter, many soil properties – such as texture, structure, moisture, and mineralogy – also have an effect (Hummel et al., 2001), implying that darkness would only be a useful indicator within strictly limited geological types.

When it comes to soil texture, most of the focus has been on clay content. There are also several studies that suggest that NIR has a potential in mineralogical studies (Madejova and Komadel, 2001). To a large extent it is probably the absorption features of clay minerals that signal in the near-infrared region. Ben-Dor and Banin (1995) found the important bands for calibrations of clay content – and the related parameters, specific surface area (SSA) and cation exchange capacity (CEC) – to be related to both O–H in surface water and Mg–H, Al–H, and FeO–H in the mineral crystal lattice. Calibrations for SSA and CEC performed slightly better, which may be expected under such circumstances, as these parameters are better defined than clay. In addition the relevant features mentioned relate to surface area rather than particle size.

For precision agriculture, available P, pH, and lime requirement are important parameters. None of these have features that absorb in the vis–NIR; nevertheless there are examples of reasonably well-performing calibrations. Chang et al. (2001) suggested that correlations to organic matter and clay explain how pH is predicted by vis–NIR. Such indirect calibrations may lead to instability problems over a large variety of soils or a large geographical area.

Reeves et al. (1999) found that moving NIR calibrations from one site to another caused loss in precision to a much higher degree for pH (and some other indirectly predicted parameters) than it did for organic C and N. It must also be recognised that the calibrations for pH rarely perform better than an RMSE of one-third or one-half of a pH unit, which may be high for estimations of within-field variations of lime requirement, as the error may correspond to up to 10–15 t of lime/ha.

For available P, results are highly variable. Udelhoven et al. (2003) failed to predict CAL (calcium-acetate-lactate)-extractable P (Schuller, 1969) at the regional scale, but at the field scale CAL-extractable P was fairly well predicted. This was attributed to secondary correlations to other variables not measured in the study. Chang et al. (2001) found that Mehlich III extractable cations in general were better predicted than those extracted by NH₄OAc. Bogrekci and Lee (2005) and Maleki et al. (2006) hypothesise that P correlates with the near-infrared indirectly through different soil components that bind to phosphorus. If this is the case, it could also

explain the variable results, as there are a large variety of methods employed for available P that in some cases are fairly uncorrelated. Thus, also the correlation with P-containing soil component complexes would differ. This subject requires further investigation.

3.6.2 Mid-Infrared (Mid-IR) Calibrations

There are two main techniques for soil analysis using mid-IR spectroscopy: the pressed KBr method (e.g. Farmer, 1974) and the diffuse reflectance Fourier transform (DRIFT) technique (e.g. Nguyen et al., 1991). The KBr method has been conventionally used for soil mineral analyses (e.g. Farmer) and organic materials (Skjemstad and Dalal, 1987). Although the KBr technique provides a high degree of intensity and linearity, the technique is slow because each sample needs to be weighed, dispersed, and pressed. In recent years, the DRIFT technique has gained a lot of attention because it is highly sensitive to the organic mineral composition of soil, it demands much less sample preparation, and the collection of spectra is rapid (Nguyen et al., 1991). Accurate predictions of a range of soil properties that depend on the chemistry of the soil matrix can be achieved by combining mid-IR DRIFT with a multivariate calibration technique (e.g. PLSR) (Viscarra Rossel et al., 2006a).

Mid-IR has been shown to accurately predict soil organic carbon, total carbon, total nitrogen, exchangeable Ca and Mg, carbonate, pH, lime requirement, clay and sand content, and air-dried gravimetric water content (Table 3.1). Mid-IR with PLSR has also been used to rapidly, accurately, and inexpensively predict the concentration of organic carbon fractions in soil, including particulate organic carbon (POC) and charcoal (e.g. Zimmerman et al., 2006, 2007; Janik et al., 2007). Although mid-IR may be a valuable predictor of such fundamental properties (e.g. Chapters 11 and 12), predictions of soil properties dependent on soil structure, such as volumetric moisture retention, may not be possible (Tranter et al., 2008). Mid-IR is also unlikely to provide accurate predictions for soil properties that are dependent on soil solution chemistry, especially when concentrations are low – as for, for example, soil nitrate, available potassium, exchangeable Na, and available P (Table 3.1).

Table 3.1 shows that the mid-IR generally produces better predictions than does the NIR and the vis–NIR, and that the latter produce better predictions than does the NIR or visible alone. The studies summarised in Table 3.1 use surface and subsurface soils and report results collected from single soil types with few samples (e.g. Masserschmidt et al., 1999; Walvoort and McBratney, 2001) to many soil types from different continents (including tropical soils) with thousands of samples (Brown et al., 2006). Mostly, however, the studies include two to four different soil types and calibrations with 100–200 samples.

3.6.3 Generalisation and Limitations of Spectroscopic Calibrations

An important issue that receives little attention is the generalisation capacity of diffuse reflectance calibrations. There are several indications that the smaller the

geographical scale a calibration covers, the smaller the RMSE (explained variance is not a reliable parameter here as the range tends to increase with scale). The fewer calibrations required the better, but obviously there is a trade-off between accuracy and generalisation capacity. If the purpose is to map within-field variations for variable rate fertiliser applications or measure carbon sequestration, predictions need to be accurate.

Whilst attempting to develop an NIR calibration for clay content for all agricultural areas of Sweden, Stenberg et al. (2002) reduced the RMSE from 5.6 to 3.9% clay by dividing the dataset into six geographical sub-calibrations instead of one. In addition, for this particular dataset of 2,600 topsoil samples, it was not possible to make a satisfactory calibration for organic matter, sub-calibrations or not (RMSE $\sim 1.5\%$ SOM). However, it was shown that the calibrations improved significantly by removing the sandiest soils (Fig. 3.4). It was therefore hypothesised that signals in NIR bands from soil organic matter of sandy soils are masked by the scatter effects of, for example, quartz. This may also be the case for other soil constituents. Generally, more research is needed to investigate the effect of soil type on vis–NIR models. For example, it is improbable that the immense global variations in soil age and parent materials do not have a confounding effect.

Despite what was said about organic matter being spectrally very active over the vis–NIR region, it is often reported that organic matter signals are weak there (e.g. Viscarra Rossel and McBratney, 1998), particularly in soils that contain only a few percentage of organic matter and the rest is a highly variable mineral matrix. It may also be that the organic matter itself changes in quality with the amount in a way that influences spectra (Ben-Dor and Banin, 1995). This may explain why the range in organic carbon correlates with the RMSE in a number of published calibrations (Fig. 3.5a). Another problem with randomly sampled sample sets dealing with organic matter is the naturally high degree of skewness towards low values in

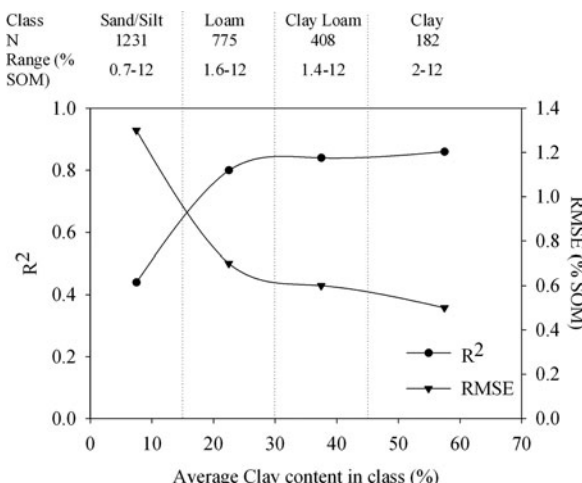


Fig. 3.4 The difference in calibration performance for soil organic matter (%SOM) between different clay classes

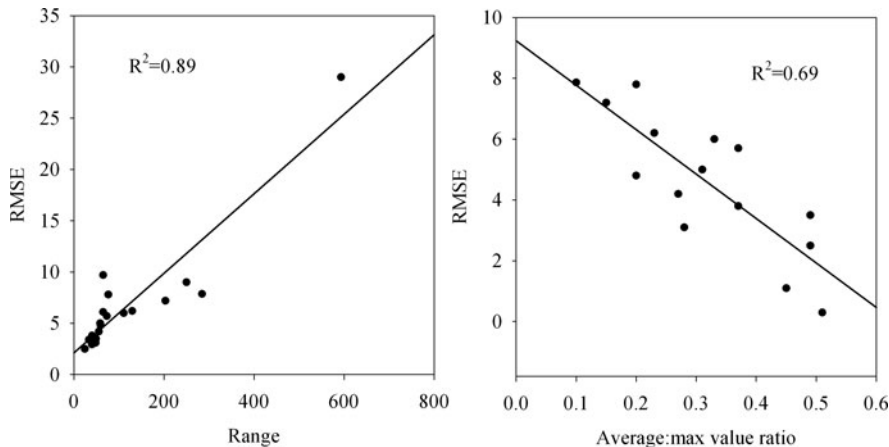


Fig. 3.5 Literature data of organic carbon (milligrams per gram) predictions with vis–NIR. (a) Correlation between range and RMSE ($n = 17$). (b) Correlation between average:max ratio and RMSE ($n = 15$)

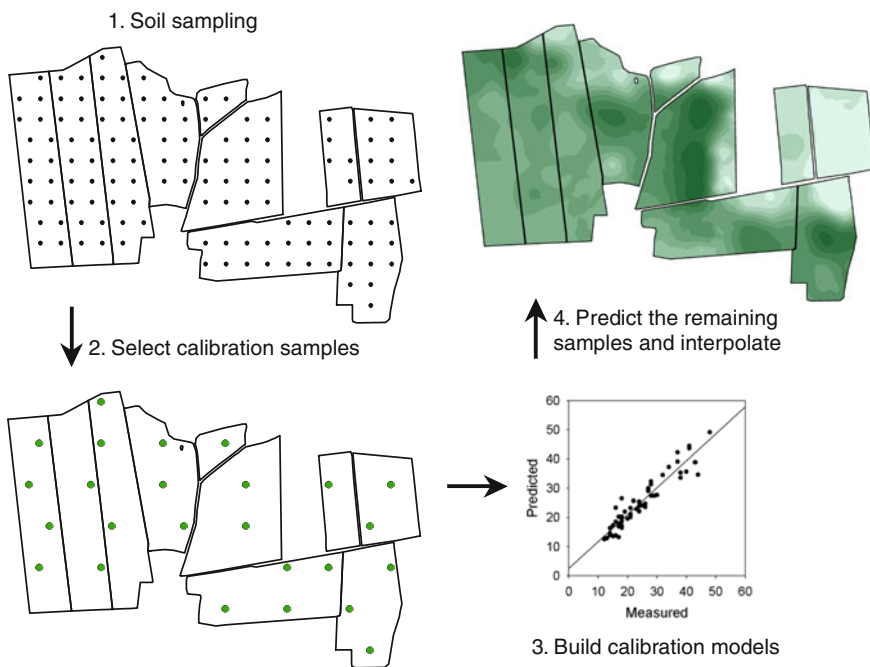


Fig. 3.6 An example of a farm soil mapping strategy. 1) Location of sample points (1.5 per ha), 2) selection of 25 calibration samples, 3) building the calibrations on these 25 samples and 4) use the calibration to predict the resulting samples and interpolate maps. © By permission of Johanna Wetterlind

agricultural soils. This is illustrated in Fig. 3.5b, where the ratio between the average and the highest value correlates negatively with the RMSE. A ratio of 0.5 suggests a moderately skewed dataset. The importance of a representative and evenly distributed calibration set is thus illustrated.

The relationships in Fig. 3.5 imply that more narrow calibrations may be required, at least for some parameters, to reach the accuracy required by the particular application. This is particularly so for spectrally inactive or weakly active soil properties, whose calibrations rely on correlations with spectrally active properties. In these circumstances, it can be presumed that calibrations at the field scale will have a better chance for success.

Recent data suggest that a consistent pattern can emerge with farm-scale calibrations. With calibration sets of 25 samples only, targeted from about 100 ha, it was possible to predict clay and organic matter with high precision (Fig. 3.6). Maps obtained by kriging of predicted data of approximately 1.5 samples per hectare improved the accuracy depending on validation samples; such kriging also changed the outcome of interpolated maps radically compared to those kriged from 0.5 samples per hectare as traditionally sampled (Wetterlind et al., 2008).

3.7 Proximal Soil Sensing Using Portable Spectrometers

Compared to diffuse reflectance analysis in the laboratory, in situ measurements with portable instruments in the field will need to access the full suite of new methods the technology has on offer (Chapter 14). This aspect is particularly germane for applications requiring high-resolution soil data, e.g. precision agriculture, especially if measurements are made on the go. Although Shonk et al. (1991) described an on-the-go spectroscopic soil sensor and Sudduth and Hummel (1993) described a prototype for a portable-field NIR sensor over 15 years ago, it is not until recently that results from on-the-go measurements of soil properties have been published (Christy et al., 2006; Mouazen et al., 2005; Shibusawa et al., 2001; Chapter 14). Assuming that instrumentation is robust enough for field operation, the first problems to overcome with field measurements are related to constructing a probe capable of delivering good reproducible spectra. Instability due to dust on the probe and variable distances between the sensor and soil have been experienced (Shibusawa et al., 2005; Shonk et al., 1991). Systems with soil-penetrating shanks – equipped with a fibre optic probe protected by a sapphire glass at the bottom that should be in close contact with the soil at all times – have been developed to prevent this (Christy et al., 2006; Mouazen et al., 2005; Stenberg et al., 2007). The fibre optic probe is in these cases connected to vis–NIR instruments. Generally, on-the-go predictions do not perform as well as those expected from a corresponding laboratory measurement. Probable reasons are variable environmental factors like soil water content, spectral contamination from plant residues and gravel, and the structure of the measured soil surface. Occasionally, loss of probe–soil contact due to shaking of the pulling vehicle has been shown to result in noisy spectra (Stenberg et al., 2007).

Automatic systems for identifying and filtering noisy and contaminated spectra are therefore sought.

Few studies tested the use of portable spectrophotometers to measure soil profiles, either *in situ* or *ex situ* by first extracting a soil core. Waiser et al. (2007) compared predictions of clay content using PLSR and vis–NIR spectra collected *ex situ* from soil cores at field moisture conditions (RMSE = 6.1%), smeared cores at field moisture conditions (RMSE = 7.4%), air-dried cores (RMSE = 4.1%), and air-dried ground soil (RMSE = 6.2%). Their conclusion was that vis–NIR could be used to estimate clay content of soil profiles *ex situ*. Ben-Dor et al. (2008) developed an accessory that can be attached to a vis–NIR fibre optic spectrophotometer and inserted down the drilled holes to measure soil spectra down the profile. They used it to make PLSR predictions of soil moisture, organic matter, carbonates, iron oxides, and specific surface area. They concluded that although their technique requires further and independent validations, there is good potential for *in situ* soil characterisation of soil using vis–NIR spectroscopy. Viscarra Rossel et al. (2009) evaluated *in situ* measurements of soil colour, mineral composition, and clay content using vis–NIR spectra from 10 different soil profiles that were derived from different parent materials. They report that (i) spectroscopic estimates of soil colour were in good agreement with Munsell book estimates; (ii) characterisation of soil mineral composition by vis–NIR was effective and in good agreement with XRD (in fact, the vis–NIR technique – with no sample preparation – detected iron oxides better); and (iii) PLSR predictions of clay content from the field-collected spectra (RMSE = 7.9%) were slightly more accurate than those from the laboratory-collected spectra (RMSE = 8.3%).

Water has a strong influence both in the NIR and in the mid-IR region. The strong absorption bands of water may mask peaks associated with other soil characteristics. Apparently mid-IR is more sensitive in this respect than vis–NIR (Chapter 11). Chang et al. (2005) compared calibrations on NIR spectra from air-dried and field-moist soil for several parameters. They found small differences, although calibrations on air-dried soils were always slightly better. The differences were larger for soil texture variables than for organic and inorganic C, soil N, CEC, and pH. On the other hand, Fystro (2002) found that PLS calibrations for SOM and total N made on spectra from coarse (<4 mm) field-moist soils (R^2 = 0.87 for C and 0.80 for N) outperformed those from the same air-dried samples (R^2 = 0.81 and 0.68, respectively). In addition to developing technical systems for the collection of high-resolution, high-quality spectra, the influence of environmental factors and the required actions to meet them have to be addressed in future research.

3.8 Conclusions

There is ample evidence that both vis–NIR and mid-IR diffuse reflectance spectroscopy have good potential for soil analyses and proximal sensing. Nevertheless, the techniques are still not widely used. The most probable reason for this is that despite all the ‘promising’ results, calibrations are still unreliable or cumbersome

to establish. Do we develop robust calibrations that will work over a large range of soil types but maybe with lower accuracies or smaller less robust calibrations with higher accuracies for a specific soil type? Research needs to focus on identifying the limitations of the techniques. Some of the inaccuracies of calibrations may arise from the lack of sufficient absorption features, particularly in the vis-NIR, and from large soil type diversity in the calibration sets. By explaining and identifying these, we may achieve the maximum generalisation capacity for the calibration of a particular soil property. Considering situations employing calibrations with very high accuracy, but with low generality, for a specific situation, there is also a need to develop soil-mapping strategies where not only the calibration as such but also the sampling scheme used and the selection and size of calibration and validation sets are considered. It is also important that the accuracy of the calibrations be evaluated in terms of the requirements of the intended application. It is essential that researchers quantitatively and qualitatively describe the distributions of soils included and the methods of calibration and most significantly the manner in which the validations are performed.

References

Baes AU, Bloom PR (1989) Diffuse reflectance and transmission Fourier transformation infrared (DRIFT) spectroscopy of humic and fulvic acids. *Soil Sci Soc Am J* 53:695–700

Barnes RJ, Dhanoa MS, Lister SJ (1989) Standard normal variate transformation and de-trending of near-infrared diffuse reflectance spectra. *Appl Spectrosc* 43:772–777

Ben-Dor E, Banin A (1995) Near-infrared analysis as a rapid method to simultaneously evaluate several soil properties. *Soil Sci Soc Am J* 59:364–372

Ben-Dor E, Heller D, Chudnovsky A (2008) A novel method of classifying soil profiles in the field using optical means. *Soil Sci Soc Am J* 72:1113–1123

Bogrekci I, Lee WS (2005) Spectral measurement of common soil phosphates. *Trans ASAE* 48:2371–2378

Brown DJ, Shepherd KD, Walsh MG, Dewayne Mays M, Reinsch TG (2006) Global soil characterization with VNIR diffuse reflectance spectroscopy. *Geoderma* 132:273–290

Chang CW, Laird DA (2002) Near-infrared reflectance spectroscopic analysis of soil C and N. *Soil Sci* 167:110–116

Chang CW, Laird DA, Mausbach MJ, Hurburgh CR (2001) Near-infrared reflectance spectroscopy – principal components regression analyses of soil properties. *Soil Sci Soc Am J* 65: 480–490

Chang GW, Laird DA, Hurburgh GR (2005) Influence of soil moisture on near-infrared reflectance spectroscopic measurement of soil properties. *Soil Sci* 170:244–255

Christy CD, Drummond P, Lund E (2006) Precision agriculture applications of an on-the-go soil reflectance sensor. In: Mulla D (ed) 8th international conference on precision agriculture, Minneapolis, MN, USA

Clark RN (1999) Spectroscopy of rocks and minerals, and principles of spectroscopy. In: Rencz N (ed) *Remote sensing for the earth sciences: manual of remote sensing*. Wiley, New York, NY, pp 3–52

Clark RN, King TVV, Klejwa M, Swayze G, Vergo N (1990) High spectral resolution reflectance spectroscopy of minerals. *J Geophys Res* 95:12653–12680

Dahm DJ, Dahm KD (2007) Interpreting diffuse reflectance and transmittance – a theoretical introduction to absorption spectroscopy of scattering materials. NIR Publications, Chichester, 286 pp

Dalal RC, Henry RJ (1986) Simultaneous determination of moisture, organic carbon and total nitrogen by near infrared reflectance spectrophotometry. *Soil Sci Soc Am J* 50:120–123

Daniel KW, Tripathi NK, Honda K (2003) Artificial neural network analysis of laboratory and in situ spectra for the estimation of macronutrients in soils of Lop Buri (Thailand). *Aust J Soil Res* 41:47–59

Dunn BW, Beecher HG, Batten GD, Ciavarella S (2002) The potential of near-infrared reflectance spectroscopy for soil analysis – a case study from the riverine plain of south-eastern Australia. *Aust J Exp Agric* 42:607–614

Farmer VC (1974) Vibrational spectroscopy in mineral chemistry. In: Farmer VC (ed) *The infra-red spectra of minerals*. Mineralogical Society, London

Fyistro G (2002) The prediction of C and N content and their potential mineralisation in heterogeneous soil samples using vis–NIR spectroscopy and comparative methods. *Plant Soil* 246:139–149

Geladi P, MacDougall D, Martens H (1985) Linearization and scatter-correction or near-infrared reflectance of meat. *Appl Spectrosc* 39:491–500

Hummel JW, Sudduth KA, Hollinger SE (2001) Soil moisture and organic matter prediction of surface and subsurface soils using an NIR soil sensor. *Comput Electron Agric* 32:149–165

Hunt GR, Salisbury JW (1970) Visible and near-infrared spectra of minerals and rocks. I. Silicate minerals. *Mod Geo* 1:283–300

Islam K, Singh B, McBratney A (2003) Simultaneous estimation of several soil properties by ultra-violet, visible, and near-infrared reflectance spectroscopy. *Aust J Soil Res* 41:1101–1114

Janik LJ, Skjemstad JO, Shepherd KD, Spouncer LR (2007) The prediction of soil carbon fractions using mid-infrared partial least square analysis. *Aust J Soil Res* 45:73–81

Madejova J, Komadel P (2001) Baseline studies of The Clay Minerals Society source clays: infrared methods. *Clays Clay Miner* 49:410–432

Maleki MR et al. (2006) Phosphorus sensing for fresh soils using visible and near infrared spectroscopy. *Biosys Eng* 95:425–436

Martens H, Næs T (1989) Multivariate calibration. Wiley, Chichester, 419 pp

Massersegmtd I, Cuelbas CJ, Poppi RJ, De Andrade JC, De Abreu CA, Davanzo CU (1999) Determination of organic matter in soils by FTIR/diffuse reflectance and multivariate calibration. *J Chemomet* 13:265–273

Minasny B, Mc Bratney AB (2008) Regression rules as a tool for predicting soil properties from infrared reflectance spectroscopy. *Chemomet Intell Lab Syst* 94:72–79

Mortimore JL, Marshall, L-JR, Almond MJ, Hollins P, Matthews W (2004) Analysis of red and yellow ochre samples from Clearwell Caves and Çatalhöyük by vibrational spectroscopy and other techniques. *Spectrochim Acta Part A* 60:1179–1188

Mouazen AM, De Baerdemaeker J, Ramon H (2005) Towards development of on-line soil moisture content sensor using a fibre-type NIR spectrophotometer. *Soil Till Res* 80:171–183

Nguyen TT, Janik LJ, Raupach M (1991) Diffuse reflectance infrared Fourier transform (DRIFT) spectroscopy in soil studies. *Aust J Soil Res* 29:49–67

Reeves JB, III, Mc Carty GW, Meisinger JJ (1999) Near infrared reflectance spectroscopy for the analysis of agricultural soils. *J Near Infrared Spectrosc* 7:179–193

Russell JD (1987) Infrared methods. Ch. 4. In: Wilson MJ (ed) *A handbook of determinative methods in clay mineralogy*. Blackie and Son, London

Savitzky A, Golay M (1964) Smoothing and differentiation of data by simplified least squares procedures. *Anal Chem* 36:1627–1639

Schuller H (1969) Die CAL-Methode, eine neue Methode zur Bestimmung des Pflanzenverfügbaren Phosphates in Böden. *Zeitschrift für Pflanzenernährung und Bodenkunde* 123:48–63

Shepherd KD, Walsh MG (2002) Development of reflectance spectral libraries for characterization of soil properties. *Soil Sci Soc Am J* 66:988–998

Sherman DM, Waite TD (1985) Electronic spectra of Fe^{3+} oxides and oxyhydroxides in the near infrared to ultraviolet. *Am Mineral* 70:1262–1269

Shibusawa S, Ehara K, Okayama T, Umeda H, Hirako S (2005) A real-time multi-spectral soil sensor: predictability of soil moisture and organic matter content in a small field. In: JV Stafford (ed) Precision agriculture '05, Papers presented at the 5th European conference on precision agriculture, Uppsala, Sweden, pp 495–502

Shibusawa S, I Made Anom SW, Sato HP, Sasao A (2001) Soil mapping using the real-time soil spectrometer. In: Gerenier G, Blackmore S (eds) ECPA 2001. Agro Montpellier, Montpellier, France, pp 485–490

Shonk JL, Gaultney LD, Schulze DG, Scoyer GEV (1991) Spectroscopic sensing of soil organic matter content. *Trans ASAE* 34:1978–1984

Skjemstad JO, Dalal RC (1987) Spectroscopic and chemical differences in organic matter of two vertisols subjected to long periods of cultivation. *Aust J Soil Res* 25:323–335

Stenberg B, Jonsson A, Börjesson T (2002) Near infrared technology for soil analysis with implications for precision agriculture. In: Davies A, Cho R (eds) Near infrared spectroscopy: Proceedings of the 10th international conference. NIR Publications, Chichester, pp 279–284

Stenberg B, Rogstrand G, Bölenius E, Arvidsson J (2007) On-line soil NIR spectroscopy: identification and treatment of spectra influenced by variable probe distance and residue contamination. In: JV Stafford (ed) ECPA 2007. Wageningen Academic, Skiathos, pp 125–131

Stevenson FJ (1994) Humus chemistry. Genesis, composition, reactions, 2nd edn. Wiley, New York, NY

Sudduth KA, Hummel JW (1993) Portable, near-infrared spectrophotometer for rapid soil analysis. *Trans ASAE* 36:185–193

Tranter G, Minasny B, McBratney AB, Viscarra Rossel RA, Murphy B (2008) Comparing spectral soil inference systems and mid-infrared spectroscopy predictions of soil volumetric moisture retention. *Soil Sci Soc Am J* 72:1394–1400

Udelhoven T, Emmerling C, Jarmer T (2003) Quantitative analysis of soil chemical properties with diffuse reflectance spectrometry and partial least-square regression: A feasibility study. *Plant Soil* 251:319–329

van der Marel HW, Beutelspacher H (1976) Atlas of infrared spectroscopy of clay minerals and their admixtures. Elsevier, Amsterdam

Viscarra Rossel RA, Mc Bratney AB (1998) Laboratory evaluation of a proximal sensing technique for simultaneous measurement of soil clay and water content. *Geoderma* 85:9–39

Viscarra Rossel RA, Walvoort DJJ, Mc Bratney AB, Janik LJ, Skjemstad JO (2006a) Visible, near infrared, mid infrared or combined diffuse reflectance spectroscopy for simultaneous assessment of various soil properties. *Geoderma* 131:59–75

Viscarra Rossel RA, Mc Glynn RN, Mc Bratney AB (2006b) Determining the composition of mineral–organic mixes using UV–vis–NIR diffuse reflectance spectroscopy. *Geoderma* 137:70–82

Viscarra Rossel RA (2007) Robust modelling of soil diffuse reflectance spectra by ‘bagging-PLSR’. *J Near Infrared Spectrosc* 15:39–47

Viscarra Rossel RA (2008) ParLeS: software for chemometric analysis of spectroscopic data. *Chemomet Intell Lab Syst* 90:72–83

Viscarra Rossel RA, Lark RM (2009) Improved analysis and modelling of soil diffuse reflectance spectra using wavelets. *Eur J Soil Sci* 60:453–464

Viscarra Rossel RA, Cattle SR, Ortega AS, Fouad Y (2009) In situ measurements of soil colour, mineral composition and clay content by vis–NIR spectroscopy. *Geoderma* 150: 253–266

Waiser TH, Morgan CLS, Brown DJ, Hallmark CT (2007) In situ characterization of soil clay content with visible near-infrared diffuse reflectance spectroscopy. *Soil Sci Soc Am J* 71:389–396

Walvoort DJJ, McBratney AB (2001) Diffuse reflectance spectrometry as a proximal sensing tool for precision agriculture. In: Grenier G, Blackmore S (eds) ECPA 2001. Agro Montpellier, vol 1, pp 503–507

Wetterlind J, Stenberg B, Söderström M (2008) The use of near infrared (NIR) spectroscopy to improve soil mapping at the farm scale. *Precis Agric* 9:57–69

Wold S, Antti H, Lindgren F, Ohman J (1998) Orthogonal signal correction of near-infrared spectra. *Chemomet Intell Lab Sys* 44:175–186

Ziechmann W (1964) Spectroscopic investigations of lignin, humic substances and peat. *Geochim Cosmochim Acta* 28:1555–1566

Zimmerman M, Leifeld Schmidt MW, Smith P, Fuhrer J (2006) Measured soil organic matter fractions can be related to pools in the RothC model. *Eur J Soil Sci* 58:658–667

Zimmerman M, Leifeld J, Fuhrer J (2007) Quantifying soil organic carbon fractions by infrared-spectroscopy. *Soil Biol Biochem* 39:224–231

Chapter 4

High-Resolution Digital Soil Mapping: Kriging for Very Large Datasets

N. Cressie and E.L. Kang

Abstract The ability to take many observations at precisely known spatial locations has given birth to precision agriculture and transformed traditional agriculture into a spatial science. An important aspect of precision agriculture is its intersection with pedometrics. Maps of soil properties are in great demand, but there is a point at which datasets from proximal soil sensors can, when very large, overload and ‘break’ the algorithms designed for production of the statistically optimal (kriging) maps. In this research, we present a geostatistical method that relies on highly flexible, nonstationary spatial covariances, for which exact kriging can be carried out for very large datasets (on the order of tens of thousands to hundreds of thousands of elements). The methodology is applied to total counts obtained from gamma radiometer readings in several fields of Nowley Farm, New South Wales, Australia.

Keywords Kriging · Fixed rank kriging · Gamma radiometer · Geostatistics · GRS spectrum

4.1 Introduction

Recently, agricultural practices have begun to exploit within-field heterogeneity to obtain higher yields and more environmental-friendly schemes for fertiliser and pesticide application. Global positioning systems (GPSs) installed in farm equipment can control the application of fertiliser and insecticides down to the metre scale, and they can provide closely spaced matching data on crop yields. Characterising within-field heterogeneity of a multitude of variables, including soil properties and

N. Cressie (✉)

Department of Statistics, The Ohio State University, 1958 Neil Avenue,
Columbus, OH 43210-1247, USA
e-mail: ncressie@stat.osu.edu

yields, has brought precision agriculture to the modern farmer. With this spatial precision comes the opportunity to make maps of the variables of interest. Geostatistics is a discipline which can provide maps of spatial predictions from noisy, incomplete data; it can also provide maps of prediction standard errors.

Advances in soil sensing and GPS technology are giving rise to increasingly larger datasets (of the order of 10,000 to more than 100,000 observations, as illustrated in many chapters in this book); moreover, each sampling point is known with almost pinpoint accuracy. And yet, gaps in the data always remain, and observations are inevitably noisy, so that any ‘smoothed’ map somehow has to adequately quantify these and other sources of uncertainty.

Kriging, or spatial best linear unbiased prediction (spatial BLUP), has become very popular in the earth, environmental, and soil sciences, where it is sometimes known as optimum interpolation. With its internal quantification of spatial variability through the covariance function (or variogram), kriging methodology is able to produce maps of optimal spatial predictions and associated prediction standard errors from incomplete and noisy spatial data (e.g. Cressie, 1993, Chapter 3). Solving the kriging equations directly for a dataset of size n involves inversion of an $n \times n$ variance–covariance matrix Σ , which typically requires $O(n^3)$ computations. Under these circumstances, straightforward kriging of very large-to-massive datasets is not possible.

It has been realised for some time that even a spatial dataset on the order of several thousands can, for kriging, result in computational breakdown. Ad hoc methods of subsetting the data were formalised by the moving window approach of Haas (1995), although the local covariance functions fitted within the moving window may yield invalid covariances at larger spatial lags. The variance–covariance matrix Σ is typically sparse when the covariance function has a finite range, in which case Σ^{-1} could be obtained using sparse matrix techniques. Barry and Pace (1997) were able to carry out kriging when $n = 916$ using a MATLAB routine based on the ‘symmetric minimum degree’ algorithm. Rue and Tjelmeland (2002) approximate Σ^{-1} to be sparse, approximating it to the precision matrix of a Gaussian Markov random field wrapped on a torus.

When datasets are very large (on the order of tens of thousands to hundreds of thousands), the general feeling is that kriging is not possible, and ad hoc local kriging neighbourhoods are typically used (e.g. Cressie, 1993, pp 131–134). One avenue of recent research has been to *approximate* the kriging equations (Nychka et al., 1996, 2002; Nychka, 2000; Furrer et al., 2006). Suggestions include giving an equivalent representation in terms of orthogonal bases and truncating the bases, doing covariance tapering, using approximate iterative methods such as conjugate gradient, and replacing the data locations with a smaller set of space-filling locations. Kammann and Wand (2003) take up this latter idea when fitting a class of spatial models they call geodadditive models.

Another approach has been to choose classes of covariance functions for which kriging can be done exactly, even though the dataset is massive. Huang et al. (2002) introduced a multi-resolution spatial model (MRSRM) that is mass balanced (across resolutions) and designed for processing very large amounts of spatial data. The

advantage of MRSM lies in the fact that it is able to capture nonstationary spatial dependence and to produce fast, optimal estimates using a change-of-resolution Kalman filter algorithm (Chou et al., 1994; Huang and Cressie, 2001). Later developments were given by Johannesson and Cressie (2004a) and Johannesson et al. (2007). In these papers, a multi-resolution spatial (and spatio-temporal) process is constructed explicitly so that (simple) kriging can be computed extremely rapidly, with computational complexity linear in the size of the data. An advantage of having a spatial model that allows exact computations is that there is no concern about how close approximate kriging predictors and approximate mean squared prediction errors are to the corresponding theoretical values. This puts the emphasis on having a highly flexible class of spatial models, from which one model is chosen that provides the best fit to the data.

When doing optimal spatial prediction (kriging) using exact methods, how flexible are the spatial covariance functions? For the multi-resolution models referred to above, the implied spatial covariances are nonstationary and ‘blocky’. To some extent, Tzeng et al. (2005) addressed this problem by ‘mixing’ or averaging the blocky predictions, but the underlying basis functions are still quite restrictive (effectively, piecewise linear and continuous). There are two requirements: positive definiteness of the covariance function implied by the model and computational ability to invert the matrix. For very large datasets, no satisfactory solution to satisfy these two requirements could, until recently, be found in the spatial statistics literature.

Cressie and Johannesson (2006, 2008) achieved orders-of-magnitude speed-ups for optimal spatial prediction by using covariance functions that were very flexible and could be chosen to be smooth or not (as determined by the type of spatial dependence exhibited by the n data). They showed how to define the $n \times n$ variance-covariance matrix Σ so that Σ^{-1} could be obtained by inverting $r \times r$ positive-definite matrices, where r is fixed (say $r = 100$). In this case, the number of computations per prediction location in the kriging equations is $O(n)$, which has the potential to be scalable – from large to very large to massive datasets. The result is a spatial BLUP (kriging) procedure they call ‘fixed rank kriging’ (FRK).

For completeness, we mention another approach to spatial prediction based on smoothing splines. In contrast to kriging, smoothing splines do not rely on a spatial stochastic process whose covariance function has to be modelled, fitted, and used for computing the optimal predictor. However, there are both knots and a smoothing parameter to be determined and, once again, the size of the dataset causes computational difficulties. Hastie (1996) and Johannesson and Cressie (2004b) developed low-rank spline smoothers for very large datasets.

In the following section we present the spatial stochastic process that leads to FRK. In Section 4.3, results from Cressie and Johannesson (2008) are given which show how kriging can be carried out for very large datasets. Finally, in Section 4.4, the results are applied to spatial prediction of a very large spatial dataset of total counts from gamma radiometer readings from Nowley Farm, New South Wales, Australia.

4.2 Spatial Covariance Function

In order to carry out FRK, we must specify the form of the (nonstationary) covariance function. In general, the covariance function $C(\mathbf{u}, \mathbf{v})$ has to be positive definite on $\mathbb{R}^d \times \mathbb{R}^d$. Often, $C(\mathbf{u}, \mathbf{v})$ is modelled as being stationary, in which case it then has to be a positive-definite function of $(\mathbf{u} - \mathbf{v})$. We take a different approach and try instead to capture the scales of spatial dependence through a set of r (not necessarily orthogonal) real-valued basis functions:

$$\mathbf{S}(\mathbf{u}) \equiv (S_1(\mathbf{u}), \dots, S_r(\mathbf{u}))', \quad \mathbf{u} \in \mathbb{R}^d,$$

where r is fixed and $\mathbf{S}(\cdot)$ is given. For any $r \times r$ *positive-definite* matrix \mathbf{K} and $\tau^2 \geq 0$, we specify

$$C(\mathbf{u}, \mathbf{v}) = \mathbf{S}(\mathbf{u})' \mathbf{K} \mathbf{S}(\mathbf{v}) + \tau^2 I(\mathbf{u} = \mathbf{v}), \quad \mathbf{u}, \mathbf{v} \in \mathbb{R}^d, \quad (4.1)$$

which is (straightforwardly) a positive-definite function and hence a valid covariance function (Cressie and Johannesson, 2008). The quantities \mathbf{K} and τ^2 are unknown parameters to be estimated.

An equivalent formulation of this spatial covariance model is to write

$$v(\mathbf{s}) = \mathbf{S}(\mathbf{s})' \boldsymbol{\eta} + \xi(\mathbf{s}),$$

where $\boldsymbol{\eta}$ is an r -dimensional random vector such that $E(\boldsymbol{\eta}) = \mathbf{0}$, $\text{var}(\boldsymbol{\eta}) = \mathbf{K}$, and $\xi(\cdot)$ is an independent, zero mean, white noise process with variance τ^2 . Then

$$\text{cov}(v(\mathbf{u}), v(\mathbf{v})) = \mathbf{S}(\mathbf{u})' \mathbf{K} \mathbf{S}(\mathbf{v}) + \tau^2 I(\mathbf{u} = \mathbf{v}),$$

which is Eq. (4.1). The role of the variance component $\xi(\cdot)$ is to capture the microscale structure of the spatial dependence as suggested by Cressie and Johannesson (2008). It is analogous to the ‘nugget effect’ in classical variogram models and largely addresses Jun and Stein’s (2008) criticism of these models.

Shi and Cressie (2007) and Cressie and Johannesson (2008) call $\mathbf{S}(\cdot)' \boldsymbol{\eta}$ the ‘Spatial Random Effects’ (SRE) model; Zhao et al. (2006), among others, have studied this model for $\mathbf{K} \propto I$. One of the contributions of this research is to show that a general positive-definite \mathbf{K} in Eq. (4.1) adds a great deal of flexibility to the spatial covariance model (4.1).

4.3 Kriging: Optimal Linear Spatial Prediction

In this section, we define and present the notation for *kriging*, and we equate it with best linear unbiased prediction (BLUP) in a spatial setting. When the spatial dataset is massive, exact computation of spatial BLUP is generally not possible. However, with the class of nonstationary spatial covariances given above, we can carry out

rapid computation of the kriging predictor (spatial BLUP) and the kriging standard error (root mean squared prediction error).

Let $\{Y(\mathbf{s}) : \mathbf{s} \in D \subset \mathbb{R}^d\}$ be a real-valued spatial stochastic process. We are interested in making inference on the Y -process based on data that have measurement error incorporated; consider the process $Z(\cdot)$ of actual and potential observations:

$$Z(\mathbf{s}) \equiv Y(\mathbf{s}) + \varepsilon(\mathbf{s}), \quad \mathbf{s} \in D, \quad (4.2)$$

where $\{\varepsilon(\mathbf{s}) : \mathbf{s} \in D\}$ is a spatial white noise process with mean zero and $\text{var}(\varepsilon(\mathbf{s})) = \sigma^2 v(\mathbf{s}) \in (0, \infty)$, $\mathbf{s} \in D$. In fact, the process $Z(\cdot)$ is known only at a finite number of spatial locations $\{\mathbf{s}_1, \dots, \mathbf{s}_n\}$; define the vector of available data to be

$$\mathbf{Z} \equiv (Z(\mathbf{s}_1), \dots, Z(\mathbf{s}_n))'.$$

The hidden process $Y(\cdot)$ is assumed to have a linear mean structure

$$Y(\mathbf{s}) = \mathbf{T}(\mathbf{s})' \boldsymbol{\alpha} + v(\mathbf{s}), \quad \mathbf{s} \in D, \quad (4.3)$$

where $\mathbf{T}(\cdot) \equiv (T_1(\cdot), \dots, T_p(\cdot))'$ represents a p -dimensional vector process of known real-valued covariates; the regression coefficients $\boldsymbol{\alpha} \equiv (\alpha_1, \dots, \alpha_p)'$ are unknown; and the random process $v(\cdot)$ has mean zero, $0 < \text{var}(v(\mathbf{s})) < \infty$, for all $\mathbf{s} \in D$, and spatial covariance function:

$$\text{cov}(v(\mathbf{u}), v(\mathbf{v})) \equiv \mathbf{C}(\mathbf{u}, \mathbf{v}); \quad \mathbf{u}, \mathbf{v} \in D,$$

which for the moment is left as general as possible.

If we define $\boldsymbol{\varepsilon}$, \mathbf{Y} , and v in an analogous manner to \mathbf{Z} , then the preceding equations imply a general linear model:

$$\begin{aligned} \mathbf{Z} &= \mathbf{T}\boldsymbol{\alpha} + \boldsymbol{\delta}, \\ \boldsymbol{\delta} &= \mathbf{v} + \boldsymbol{\varepsilon}, \end{aligned} \quad (4.4)$$

where \mathbf{T} is an $n \times p$ matrix of covariates $(\mathbf{T}(\mathbf{s}_1), \dots, \mathbf{T}(\mathbf{s}_n))'$. Observe that the error term $\boldsymbol{\delta}$ is made up of two mean-zero components, resulting in $E(\boldsymbol{\delta}) = \mathbf{0}$ and $\text{var}(\boldsymbol{\delta}) = \boldsymbol{\Sigma} \equiv (\sigma_{ij})$, where

$$\sigma_{ij} = \begin{cases} C(\mathbf{s}_j, \mathbf{s}_j) + \sigma^2 v(\mathbf{s}_j), & i = j \\ C(\mathbf{s}_i, \mathbf{s}_j), & i \neq j. \end{cases}$$

Upon writing $\mathbf{C} \equiv (C(\mathbf{s}_i, \mathbf{s}_j))$ and $\mathbf{V} \equiv \text{diag}(v(\mathbf{s}_1), \dots, v(\mathbf{s}_n))$, it is easily seen that

$$\boldsymbol{\Sigma} = \mathbf{C} + \sigma^2 \mathbf{V}.$$

No assumptions of stationarity or isotropy of the spatial covariance function have been made.

Interest is in inference on the Y -process, not the noisy Z -process. For point prediction, we wish to predict the Y -process at a location \mathbf{s}_0 , $\mathbf{s}_0 \in D$, regardless of whether \mathbf{s}_0 is or is not an observation location. Cressie (1993) (Section 3.4.5) shows that one particular formula for the kriging predictor of $Y(\mathbf{s}_0)$ is

$$Y^*(\mathbf{s}_0) = \mathbf{T}(\mathbf{s}_0)' \boldsymbol{\alpha}^* + \mathbf{k}(\mathbf{s}_0)'(\mathbf{Z} - \mathbf{T}\boldsymbol{\alpha}^*), \quad (4.5)$$

where $\boldsymbol{\alpha}^*$ is the generalised least squares estimator of $\boldsymbol{\alpha}$

$$\begin{aligned} \boldsymbol{\alpha}^* &= (\mathbf{T}' \boldsymbol{\Sigma}^{-1} \mathbf{T})^{-1} \mathbf{T}' \boldsymbol{\Sigma}^{-1} \mathbf{Z}, \\ \mathbf{k}(\mathbf{s}_0)' &= \mathbf{c}(\mathbf{s}_0)' \boldsymbol{\Sigma}^{-1}, \end{aligned}$$

and $\mathbf{c}(\mathbf{s}_0) \equiv (C(\mathbf{s}_0, \mathbf{s}_1), \dots, C(\mathbf{s}_0, \mathbf{s}_n))'$. The kriging standard error is the root mean squared prediction error of $Y^*(\mathbf{s}_0)$, given by

$$\begin{aligned} \sigma_k(\mathbf{s}_0) &= \{C(\mathbf{s}_0, \mathbf{s}_0) - \mathbf{k}(\mathbf{s}_0)' \boldsymbol{\Sigma} \mathbf{k}(\mathbf{s}_0) \\ &\quad + (\mathbf{T}(\mathbf{s}_0) - \mathbf{T}' \mathbf{k}(\mathbf{s}_0))' (\mathbf{T}' \boldsymbol{\Sigma}^{-1} \mathbf{T})^{-1} (\mathbf{T}(\mathbf{s}_0) - \mathbf{T}' \mathbf{k}(\mathbf{s}_0))\}^{1/2}. \end{aligned} \quad (4.6)$$

As the prediction location \mathbf{s}_0 varies over D , a kriging prediction map and a kriging standard error map, respectively, are generated. (In practice, prediction locations are finite in number and typically taken as nodes of a fine-resolution grid superimposed on D .)

Inspection of the kriging equations shows $\boldsymbol{\Sigma}^{-1}$ to be an essential component and the most obvious place where a computational bottleneck could occur. Now, for the class of covariance functions given by Eq. (4.1)

$$\boldsymbol{\Sigma} = \mathbf{S} \mathbf{K} \mathbf{S}' + \tau^2 \mathbf{I} + \sigma^2 \mathbf{V},$$

where $\mathbf{S} = (\mathbf{S}(\mathbf{s}_1), \dots, \mathbf{S}(\mathbf{s}_n))'$ is an $n \times r$ matrix. This model was proposed by Cressie and Johannesson (2008) in their discussion; note that when $\mathbf{V} = \mathbf{I}$, only $(\tau^2 + \sigma^2)$ can be estimated. In our case (Section 4.4), σ^2 is known, and hence τ^2 can be estimated even when $\mathbf{V} = \mathbf{I}$. Define $\mathbf{D} \equiv \tau^2 \mathbf{I} + \sigma^2 \mathbf{V}$, an $n \times n$ *diagonal* matrix. Hence, a Sherman–Morrison–Woodbury formula (e.g. Henderson and Searle, 1981) yields

$$\boldsymbol{\Sigma}^{-1} = \mathbf{D}^{-1} - \mathbf{D}^{-1} \mathbf{S} \{ \mathbf{K}^{-1} + \mathbf{S}' \mathbf{D}^{-1} \mathbf{S} \}^{-1} \mathbf{S}' \mathbf{D}^{-1}.$$

Note that this formula involves inverting either *fixed rank* $r \times r$ positive-definite matrices or the $n \times n$ *diagonal* matrix \mathbf{D} . Inspection of the kriging equations (4.5) and (4.6) reveals that for a fixed number of regressors p and a fixed rank r of the covariance model, the number of computations per prediction location is $O(n)$. Thus, through FRK, it becomes feasible to construct maps of kriging predictors and kriging standard errors based on very large quantities (hundreds of thousands) of spatial data. In principle, because FRK is scalable, it could be used to obtain maps for massive spatial datasets on the order of gigabytes, such as one might obtain from satellite data.

To implement FRK, as in classical geostatistics (e.g. Cressie, 1993, Chapter 2), detrended data are binned for computation of an empirical variance–covariance matrix estimator based on the method of moments. Estimates $\hat{\mathbf{K}}$ and $\hat{\tau}^2$ are obtained by minimising a Frobenius norm between the empirical variance–covariance matrix and a theoretical variance–covariance matrix. Substituting these estimated parameters into Eqs. (4.5) and (4.6), FRK predictions and FRK standard errors can be calculated. Details on the estimation procedure can be found in Cressie and Johannesson (2008).

4.4 Soil Properties on a Portion of Nowley Farm, New South Wales, Australia

Soil is a key factor affecting agricultural production. Soil maps at higher resolution are beneficial for both sound land management and profitable crop production.

In many current soil surveys, variations in soil attributes are measured by two sets of high-resolution geophysical tools that result in very large spatial datasets: a ground-based gamma ray spectrometer (GRS), or gamma radiometer, and electromagnetic (EM) instruments such as the EM38 and the EM31. GRSs measure broad radioactive emissions from elements such as potassium, uranium, and thorium in the top 40–60 cm of the soil. EM instruments penetrate deeper, measuring ground conductivity, which can indicate soil salinity and moisture variation. In this study, we analyse the *total count* for the full spectrum from a GRS.

Although the data collected with GRSs or EMs are spatially separated, it is the soil scientists' aim to generate spatially continuous maps of soil properties using these very large datasets. Usually, ad hoc (but computationally fast) smoothing methods such as the inverse distance weighting (IDW) method and the nearest neighbour smoothing (NNS) method are used, but they are unable to give prediction standard errors of the resulting soil maps. Moreover, they do not possess any statistical optimality properties. Based on the development in the previous section, FRK-based optimal spatial predictions of soil properties can be used for these very large datasets, whereas standard geostatistical methods either fail or yield unquantified approximations.

The study area from which the dataset was collected consists of three fields (F-Brigalow, 12-Brigalow, and Coda) covering about 2.66 km² of Nowley Farm (30.23°S, 150.24°E), New South Wales, Australia. The soils in this area can be described as Red Chromosols (Australian Soil Classification System, Isbell, 2002; Luvisols, Word Reference Base, FAO, 2006) in the west grading to Red Dermosols (Australian Soil Classification System, Isbell, 2002; Ferric Calcisols, Word Reference Base, FAO, 2006) and Sodosols (Australian Soil Classification System, Isbell, 2002; Solonetz, Word Reference Base, FAO, 2006) in the east, with a concomitant topsoil clay content decreasing from 40 to 10% in the east. The area is made up of two cropping fields and one field under pasture. More details can be found in Viscara Rossel et al. (2006). In the survey, EM31, EM38, and GRS were run

simultaneously on a single vehicle, which was driven along (approximately) evenly spaced swaths, 30–40 m apart, in the direction of tillage. All three sensors received location data from a single GPS mounted on the vehicle. Total count (TC) in counts per second (cps) from the GRS is the variable of interest in this chapter, since it integrates the entire spectrum and often shows strong spatial patterns. Ultimately, the three fields should perhaps be analysed separately because of different location and management characteristics. However, in what is to follow we assume that these differences are small enough to be absorbed into the spatial variability due to trend and spatial dependence.

The original TC dataset is made up of 34,266 data. Exploratory analysis indicated that measurement error variance on the original scale depended on the measured value, and hence a *shifted logarithmic transformation* was made; we define the adjusted count (AC) as $AC \equiv TC + 160$. The spatial analysis was carried out on the transformed variable, $Z \equiv \log(AC) = \log(TC + 160)$, and the transformed spatial dataset is $\mathbf{Z} \equiv \{Z(s_i) \equiv \log(TC(s_i) + 160), i = 1, \dots, n\}$, where $n = 34,266$. We fitted model (4.2) to the transformed data \mathbf{Z} , and the measurement error variance on the transformed scale was identified from an independent study to be $\sigma^2 = 0.0016$.

One of our goals in spatial prediction is to filter out the measurement error. Hence, we need to interpret this filtering on the original scale. Write

$$AC \equiv BC \cdot \exp(\varepsilon), \quad (4.7)$$

where $BC \equiv \exp(Y)$ is interpreted as the measurement error-free process corresponding to the adjusted count (AC) process. To make inference on the original scale, we define the smoothed count (SC), which is measurement error free and can be interpreted as the intensity function that gives rise to the observed counts, that is

$$E(TC|SC) = SC \quad (4.8)$$

and SC is independent of ε . To relate the process BC , in Eq. (4.7), to SC , let

$$BC = a \cdot SC + b. \quad (4.9)$$

From the relations $AC = TC + 160$, Eqs. (4.7), and (4.8), we have

$$\begin{aligned} E(TC|SC) &= E(AC - 160|SC) = E(BC \cdot \exp(\varepsilon)|SC) - 160 \\ &= a \cdot \exp(\sigma^2/2) \cdot SC + b \cdot \exp(\sigma^2/2) - 160. \end{aligned}$$

Setting $E(TC|SC)$ equal to SC , we obtain $a = \exp(-\sigma^2/2)$ and $b = \exp(-\sigma^2/2) - 160$. Thus

$$SC = \exp(\sigma^2/2) \cdot BC - 160 = \exp(\sigma^2/2) \cdot \exp(Y) - 160. \quad (4.10)$$

Although we fitted spatial models (4.1), (4.2), and (4.3) to data \mathbf{Z} and to the hidden process $Y(\cdot)$, our ultimate interest is in making inference on the original

scale. That is, we wish to predict the underlying smoothed count (SC) process given by Eq. (4.10).

Our geostatistical analysis proceeds on the transformed data Z . Trends in the spatial index $s = (x, y)'$ were visualised by randomly sampling 1,000 data and plotting $Z(s)$ versus x and $Z(s)$ versus y (the large amount of data makes visualisation problematic and necessitates taking a random sample); see Fig. 4.1. We observe a strong linear relationship between $Z(s)$ and the x -coordinate and similarly for the y -coordinate (although not quite as strong). Hence, in Eq. (4.4), we put $\mathbf{T}(s) = (1, x, y)'$ and we fitted $\alpha = (\alpha_1, \alpha_2, \alpha_3)'$ using ordinary least squares (OLS), as recommended by Cressie and Johannesson (2008). Then, estimation of \mathbf{K} and τ^2 was carried out on the OLS residuals; those estimates were substituted into Eqs. (4.5) and (4.6) to produce the kriging predictions and the kriging standard errors, respectively (on a log scale).

The basis functions (discussed in Section 4.2) we chose are made up of two scales of variation defined by a quadtree. The coarsest scale has 8 functions associated with it, and the second scale has 69. The centre points $\{\mathbf{v}_j\}$ of the basis functions are shown in Fig. 4.2.

Generally speaking, the basis functions should be multi-resolutional so that the covariance function model in Eq. (4.1) is able to capture multiple scales of variation. Shi and Cressie (2007) used wavelets. In what is to follow, our generic basis function is the bisquare function (e.g. Cressie and Johannesson, 2008):

$$S_j(\mathbf{u}) \equiv \begin{cases} (1 - (\|\mathbf{u} - \mathbf{v}_j\| / r_j)^2)^2, & \|\mathbf{u} - \mathbf{v}_j\| \leq r_j \\ 0, & \text{otherwise,} \end{cases}$$

where \mathbf{v}_j is one of the centre points of Fig. 4.2 and

$$r_j = (1.5) \times (\text{shortest distance between like-resolution centre points}).$$

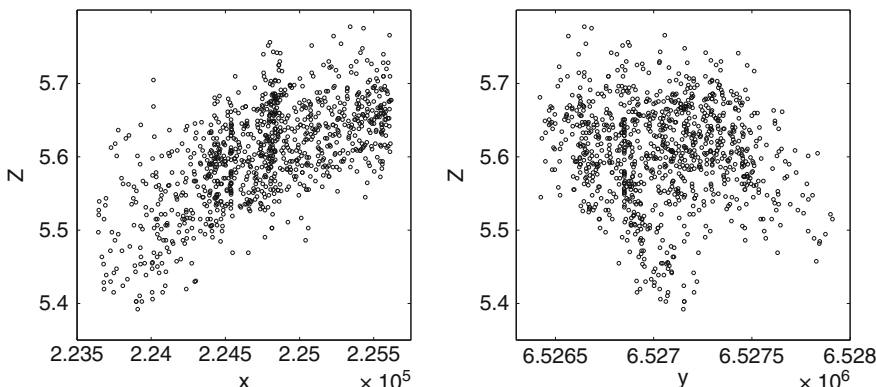


Fig. 4.1 Scatter plots of a size 1000, randomly sampled subset of the 34,266 data. The data $Z(s)$ are plotted against x (left-hand scatter plot) and y (right-hand scatter plot), where $s = (x, y)'$

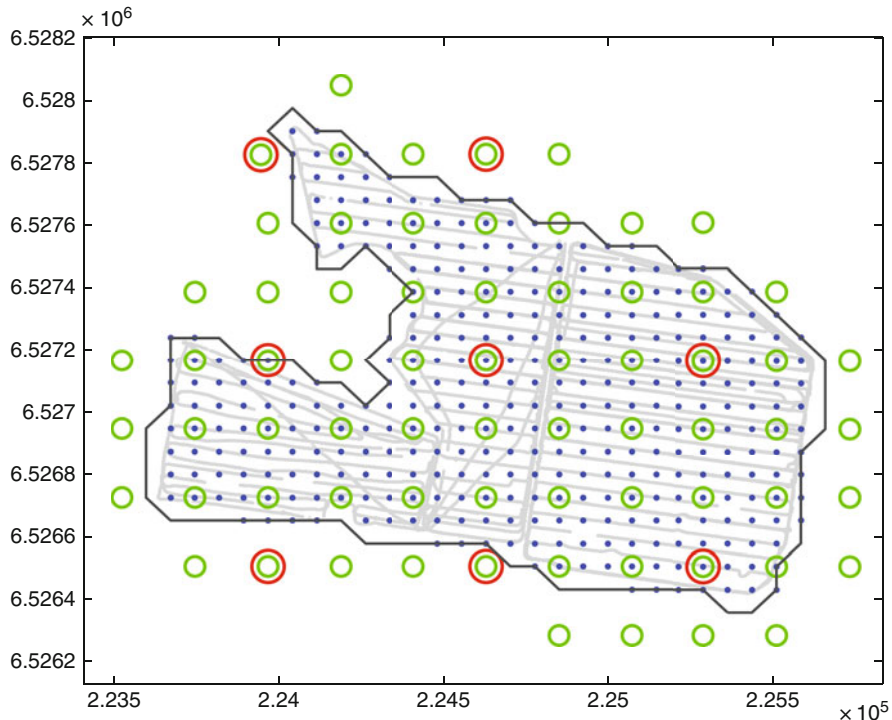


Fig. 4.2 Centre points of the first three scales from a quadtree. Units on the x -axis and the y -axis are in metres

For example, if \mathbf{v}_j is from scale 1, the shortest distance between centre points is 661.78 m and $r_j = 992.67$ m; if \mathbf{v}_j is from scale 2, the shortest distance between centre points is 220.59 m and $r_j = 330.89$ m.

To obtain estimates of \mathbf{K} and τ^2 that are not sensitive to edge effects, we recommend putting centre points of basis functions beyond region D but within a distance of its boundary that is less than or equal to $\min\{r_j/(1.5)\}$. From Fig. 4.2, there are a total of $r = 8 + 69 = 77$ basis functions used in our spatial analysis.

Cressie and Johannesson (2008) give a method for estimating parameters \mathbf{K} and τ^2 (σ^2 is assumed known) in our model based on a method of moments estimator of Σ , where recall that

$$\Sigma = \mathbf{SKS}' + \tau^2 \mathbf{I} + \sigma^2 \mathbf{V}.$$

Applying their method, the detrended residuals were binned with $M = 346$ bins to obtain an empirical covariance; we chose the bin centres as the centre points of the scale-3 grid (see Fig. 4.2). Because the spatial statistical analysis is done on a log scale, we chose $\mathbf{V} = \mathbf{I}$, and hence we have now specified everything for the estimation of \mathbf{K} and τ^2 . Finally, plugging the estimates into the kriging equations

(4.5) and (4.6), we obtain the kriging prediction $Y^*(\mathbf{s}_0)$ and the kriging standard error $\sigma_k(\mathbf{s}_0)$ on a log scale.

Figure 4.3 shows the 34,266 raw data (in units of counts per second). Recall that we added 160 to each datum and took the natural logarithm, resulting in the 34,266-dimension vector \mathbf{Z} . Further recall that for the dataset of total counts, our interest is in making inference on the smoothed count, SC, given by Eq. (4.10):

$$SC(\mathbf{s}) \equiv \exp(\sigma^2/2) \cdot BC(\mathbf{s}) - 160 = \exp(\sigma^2/2) \cdot \exp(Y(\mathbf{s})) - 160, \quad \mathbf{s} \in D.$$

Thus, we need to transform the predictions $\{Y^*(\mathbf{s}_0), \mathbf{s}_0 \in D\}$ back to the original scale, with an appropriate bias correction (e.g. Cressie, 2006), using the following formulas:

$$SC^*(\mathbf{s}_0) \equiv \exp(\sigma^2/2) \cdot \exp\{Y^*(\mathbf{s}_0) + (\sigma_k(\mathbf{s}_0))^2/2 - \mathbf{m}(\mathbf{s}_0)' \mathbf{T}(\mathbf{s}_0)\} - 160, \quad (4.11)$$

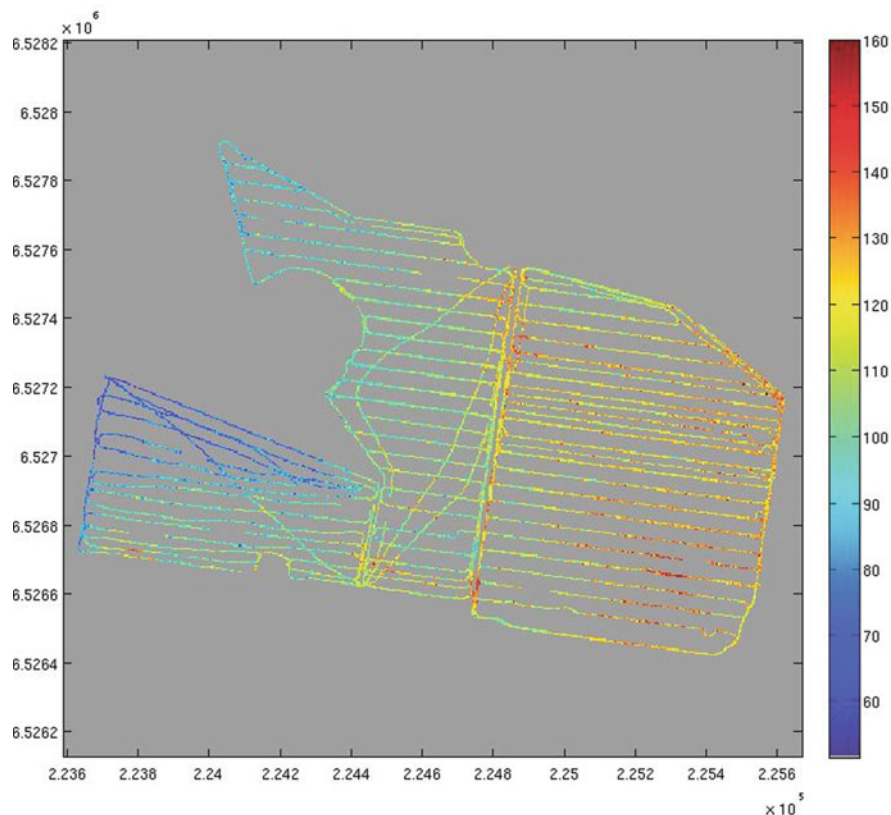


Fig. 4.3 Three fields of Nowley Farm, NSW, Australia. Shown are 34,266 γ -radiometer readings of total count (TC) in units of counts per second (cps). Units on the x-axis and the y-axis are in metres

$$\sigma_{SC,k}(\mathbf{s}_0) = \exp(\sigma^2/2) \cdot \exp\{\mathbf{T}(\mathbf{s}_0)'\boldsymbol{\alpha} + \text{var}(Y(\mathbf{s}_0))/2\} \cdot [\exp\{\text{var}(Y(\mathbf{s}_0))\} + \exp\{\text{var}(Y^*(\mathbf{s}_0))\} - 2\exp\{\lambda(\mathbf{s}_0)'\mathbf{c}(\mathbf{s}_0)\}]^{1/2}, \quad (4.12)$$

where

$$\mathbf{m}(\mathbf{s}_0)' = (\mathbf{T}(\mathbf{s}_0) - \mathbf{T}'\Sigma^{-1}\mathbf{c}(\mathbf{s}_0))'(\mathbf{T}'\Sigma^{-1}\mathbf{T})^{-1},$$

$$\lambda(\mathbf{s}_0)' = \{\mathbf{c}(\mathbf{s}_0) + \mathbf{T}(\mathbf{T}'\Sigma^{-1}\mathbf{T})^{-1}(\mathbf{T}(\mathbf{s}_0) - \mathbf{T}'\Sigma^{-1}\mathbf{c}(\mathbf{s}_0))\}'\Sigma^{-1},$$

$$\text{var}(Y^*(\mathbf{s}_0)) = \lambda(\mathbf{s}_0)'\Sigma\lambda(\mathbf{s}_0),$$

$$\mathbf{c}(\mathbf{s}_0) = \mathbf{SKS}(\mathbf{s}_0).$$

Then, from Eq. (4.11), we obtain the 512×512 -resolution map of $SC^*(\cdot)$ shown in Fig. 4.4. The FRK-based prediction standard errors $\sigma_{SC,k}(\cdot)$ (where the generalised least squares estimator $\boldsymbol{\alpha}^*$ is substituted for $\boldsymbol{\alpha}$) given by Eq. (4.12) are shown on the 512×512 -resolution map in Fig. 4.5. Overall, the FRK-predicted map (Fig. 4.4) captures the spatial variability in the original data (Fig. 4.3). It can be

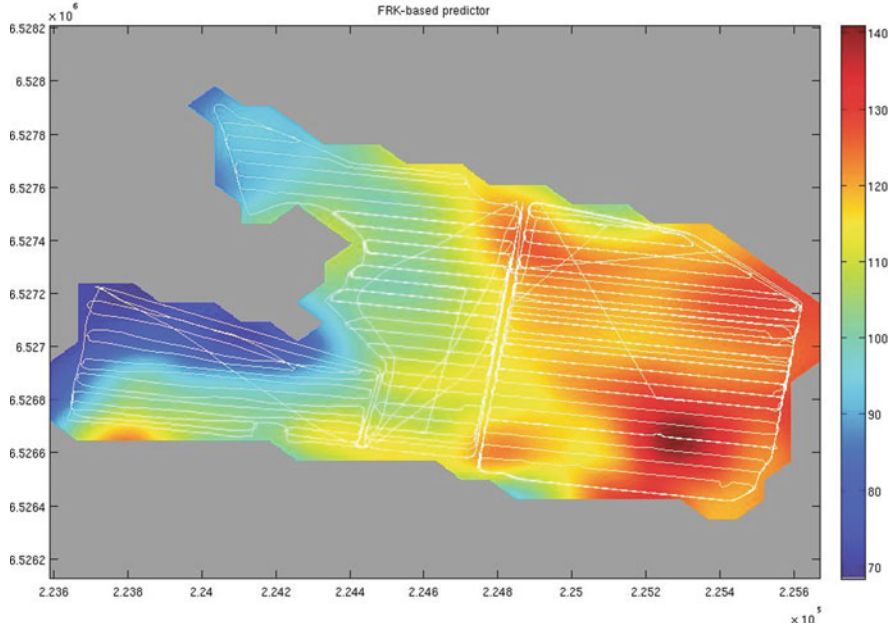


Fig. 4.4 Spatial predictions of SC, in cps. Units on the x -axis and the y -axis are in metres

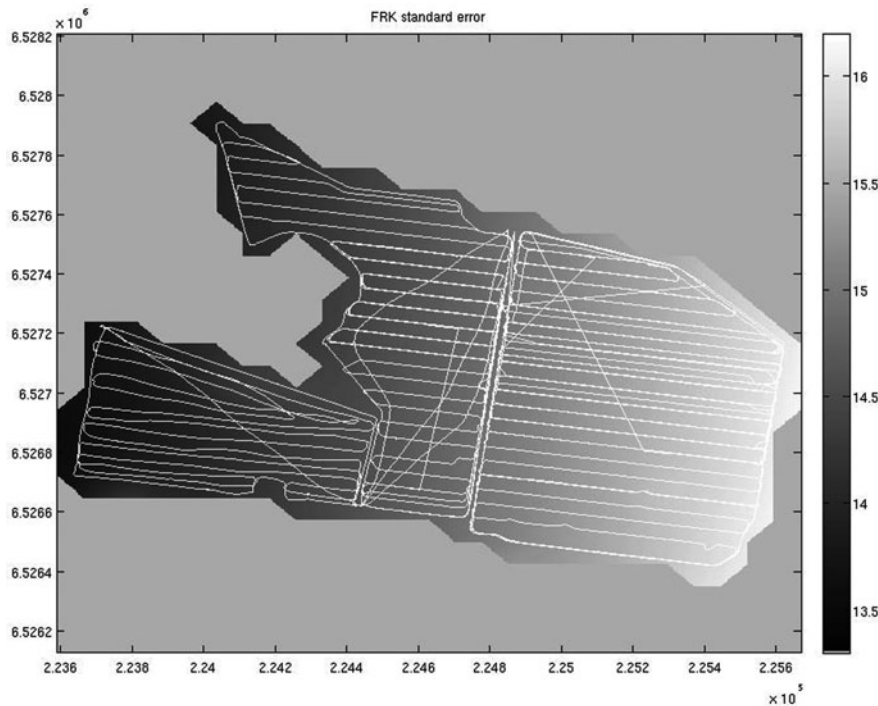


Fig. 4.5 Prediction standard errors, in cps. Units on the x -axis and the y -axis are in metres

seen in Fig. 4.5 that the prediction standard errors are dominated by the trend term, $\exp\{\mathbf{T}(\mathbf{s}_0)'\boldsymbol{\alpha}^*\}$.

The following timings were carried out in Matlab on a Linux machine with a Pentium 4 dual-core 3.0-GHz processor and 4 GB memory, and they were for computing $\mathbf{SC}^*(\cdot)$ and $\sigma_{\mathbf{SC},k}(\cdot)$ from 34,266 data at 114,266 prediction locations on the 512×512 -resolution grid. Timings for the computations, in seconds, are given in parentheses: \mathbf{S} (1.87 s), $\{\mathbf{S}(\mathbf{s}_0)\}$ (34.38 s), $\{Y^*(\mathbf{s}_0)\}$ (24.29 s), and $\{\sigma_k(\mathbf{s}_0)\}$ (50.17 s). Timings for estimation of parameters, in seconds, are given in parentheses: the binned empirical variance–covariance matrix (2.35 s) and $\hat{\mathbf{K}}$ and $\hat{\tau}^2$ (2.94 s).

4.5 Conclusions

Fixed rank kriging (FRK) is an optimal (best linear unbiased) spatial predictor that can be implemented on very large datasets. Because the computations are linear in the size of the dataset, the technology is in principle scalable to massive datasets on the order of gigabytes. The underlying spatial covariances are nonstationary and highly flexible. Given the measurement error variance σ^2 is known, we were able to model the hidden Y -process with microscale variance τ^2 and to estimate it. We

applied FRK to a soil-sensing dataset of total counts (TC) from a gamma radiometer. The application illustrates the following:

All the 34,266 data were used to produce Figs. 4.4 and 4.5.

- The covariance function we used was *nonstationary*.
- A matrix inversion of only a 77×77 positive-definite matrix was needed to produce these two figures.
- The map in Fig. 4.4 is the *optimal* predictor (for squared error loss) of smoothed counts (SC) on the 512×512 -resolution grid.

For complete details on the estimation of parameters or for more discussion on this methodology, such as choices of basis functions, readers are referred to Cressie and Johannesson (2006), Shi and Cressie (2007), and Cressie and Johannesson (2008).

Acknowledgements We would like to thank James Taylor and Alex McBratney for furnishing us with the Nowley Farm dataset and for answering a number of questions surrounding it. This research was supported by the National Science Foundation under grant number DMS-0706997 and the Office of Naval Research under grant number N00014-08-1-0464.

References

Barry RP, Pace RK (1997) Kriging with large data sets using sparse matrix techniques. *Commun Stat: Simul Comput* 26:619–629

Chou KC, Willsky AS, Nikoukhah R (1994) Multiscale systems, Kalman filters, and Riccati equations. *IEEE Trans Autom Control* 39:479–492

Cressie N (1993) Statistics for spatial data, Revised edn. Wiley, New York, NY

Cressie N (2006) Block kriging for lognormal spatial processes. *Math Geol* 38:413–443

Cressie N, Johannesson G (2006) Spatial prediction for massive datasets. Mastering the data explosion in the earth and environmental sciences. Proceedings of the Australian Academy of Science Elizabeth and Frederick White conference, Australian Academy of Science, Canberra, pp 1–11

Cressie N, Johannesson G (2008) Fixed rank kriging for very large datasets. *J R Stat Soc, Ser B* 70:209–226

FAO (2006) World reference base for soil resources, 2nd edn. FAO, Rome

Furrer R, Genton MG, Nychka D (2006) Covariance tapering for interpolation of large spatial datasets. *J Comput Graph Stat* 15:502–523

Haas TC (1995) Local prediction of a spatio-temporal process with an application to wet sulfate deposition. *J Am Stat Assoc* 90:1189–1199

Hastie T (1996) Pseudosplines. *J R Stat Soc Ser B* 58:379–396

Henderson HV, Searle SR (1981) On deriving the inverse of a sum of matrices. *SIAM Rev* 23: 53–60

Huang H-C, Cressie N (2001) Multiscale graphical modeling in space: applications to command and control. In: Moore M (ed) Spatial statistics: methodological aspects and some applications. Springer lecture notes in statistics, vol 159. Springer, New York, NY, pp 83–113

Huang H-C, Cressie N, Gabrosek J (2002) Fast, resolution-consistent spatial prediction of global processes from satellite data. *J Comput Graph Stat* 11:63–88

Isbell RF (2002) The Australian soil classification, Revised edn. CSIRO Publishing, Melbourne, Australia

Johannesson G, Cressie N (2004a) Variance-covariance modeling and estimation for multi-resolution spatial models. In: Sanchez-Vila X, Carrera J, Gomez-Hernandez J (eds) geoENV IV – Geostatistics for environmental applications. Kluwer Academic, Dordrecht, pp 319–330

Johannesson G, Cressie N (2004b) Finding large-scale spatial trends in massive, global, environmental datasets. *Environmetrics* 15:1–44

Johannesson G, Cressie N, Huang H-C (2007) Dynamic multi-resolution spatial models. *Environ Ecol Stat* 14:5–25

Jun M, Stein ML (2008) Nonstationary covariance models for global data. *Ann Appl Stat* 2: 1271–1289

Kammann EE, Wand MP (2003) Geoadditive models. *Appl Stat* 52:1–18

Nychka D (2000) Spatial-process estimates as smoothers. In: Schimek MG (ed) Smoothing and regression: approaches, computation, and application. Wiley, New York, NY, pp 393–424

Nychka D, Bailey B, Ellner S, Haaland P, O'Connell M (1996) FUNFITS: data analysis and statistical tools for estimating functions. North Carolina Institute of Statistics Mimeo Series, No. 2289, North Carolina State University, Raleigh, NC

Nychka D, Wikle C, Royle JA (2002) Multiresolution models for nonstationary spatial covariance functions. *Stat Mod* 2:315–331

Rue H, Tjelmeland H (2002) Fitting Gaussian Markov random fields to Gaussian fields. *Scand J Stat* 29:31–49

Shi T, Cressie N (2007) Global statistical analysis of MISR aerosol data: a massive data product from NASA's Terra satellite. *Environmetrics* 18:665–680

Tzeng S, Huang H-C, Cressie N (2005) A fast, optimal spatial-prediction method for massive datasets. *J Am Stat Assoc* 100:1343–1357

Viscará Rossel RA, Taylor HJ, McBratney AB (2006) Multivariate calibration of hyperspectral γ -ray energy spectra for proximal soil sensing. *Eur J Soil Sci* 58:345–353

Zhao Y, Staudenmayer J, Coull BA, Wand MP (2006) General design Bayesian generalized linear mixed models. *Stat Sci* 21:35–51

Part II

Soil Sensing and Sampling

Chapter 5

The Sun Has Shone Here Antecedently

A.B. McBratney and B. Minasny

What has been is what will be, and what has been done is what will be done; there is nothing new under the sun.

Ecclesiastes

Abstract Some scientific work can be so far ahead of its time that it is not taken up by contemporaries and is largely forgotten. High-resolution digital soil sensing and mapping is a classic example of this. The earliest work in this area can be found in three papers in 1925 and another in 1928 by the Rothamsted soil physicists Haines and Keen. This was not really followed up until the 1990s when precision agriculture became the focus. The major developments in these papers are disinterred. Haines and Keen were concerned with how tillage forces varied, in order to design efficient and effective tillage operations. The first paper described instrumentation – a dynamometer – capable of sensing soil strength (actually drawbar pull) and its real-time recording, which they designed and built. The second looked at soil uniformity ‘by means of dynamometer and plough’. They produced perhaps the first contour maps of a soil property at high (or any) resolution. The third paper dealt with the Rothamsted classical experiments which are now in their 167th year. The results of the Broadbalk experiment are shown as a perspective plot (familiar to all users of surface plotting programs) but constructed by quite different means. They found, perhaps to their surprise, that the signal of intrinsic soil differences in strength was heavily imprinted over the treatment effects even after 80 years of continuous wheat. In the fourth paper they recognised the need for a more light-weight, portable, and robust sensing system which they designed, built, and demonstrated, as well as a data-filtering technique based on the viscosity of oil in a sensor-recording system.

Keywords Draught force · EC_a soil properties · Sensor · Draft force · Conductivity · Electrical

A.B. McBratney (✉)

The University of Sydney, Faculty Agriculture, Food & Natural Resources, John Woolley Building A20, Sydney, New South Wales 2006, Australia
e-mail: alex.mcbratney@sydney.edu.au

5.1 Introduction

In 1925, before the age of digital computers and electronic sensors, Bernard Keen and William Haines conceived and built the first on-the-go soil strength sensor, made measurements and constructed the first high-resolution digital soil map, and discovered the reality and importance of soil spatial variation. For a biography of Keen, who wrote a classic text on soil physics (Keen, 1931), see Pereira (1982). Haines wrote a classic set of papers on soil physics, also published in the *Journal of Agricultural Science*.

5.2 High-Resolution Digital Soil Sensing and Mapping

A schematic diagram depicting the various components of high-resolution digital soil sensing and mapping (HRDSSM) is shown in Fig. 5.1. This book is intended to flesh out by means of example all the aspects depicted. Such a diagram, although perhaps incomplete, can only be drawn by considering the efforts of many scientists around the world and how the work of one group relates to another. There does seem to be a coherent framework for HRDSSM. What appears remarkable to us is that Haines and Keen in the 1920s first traced out a significant part of the methodology (that shown in black – as opposed to grey). How they did this is discussed further below.

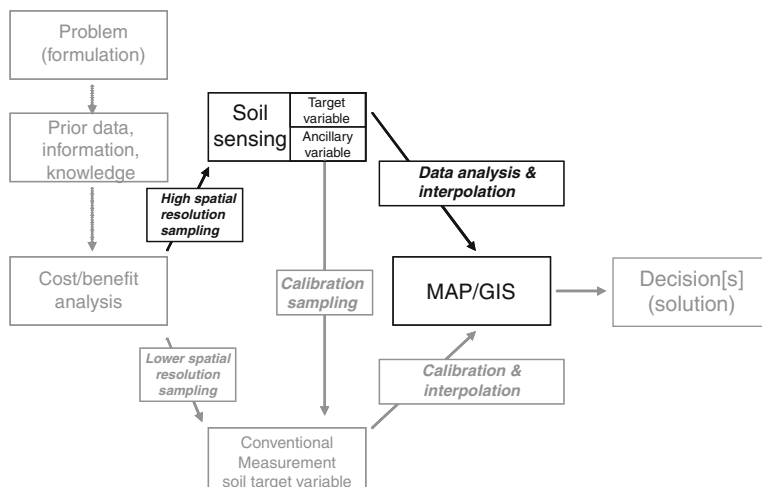


Fig. 5.1 A schematic diagram of high-resolution digital soil sensing and mapping (adapted from Fig. 1.1 in Chapter 1)

5.3 The Precocious and Prescient Contribution of Haines and Keen

5.3.1 The Rationale: Cultivation and Soil Strength

The rationale behind inventing the on-the-go soil strength meter was to measure the relative draughts of cultivation implements, to assess the impact of tillage and cultivation on soil structure, and to quantify short-range soil variation. The rationale has not really changed since. Chapters 26 and 30, *inter alia*, give up-to-date examples and there is a brief review of such sensors in Chapter 2.

5.3.2 The Sensor: A (Pre-electronic) Design for a Soil Draught Force Sensor

Keen and Haines (1925) built an instrument, based on a design by an automotive engineer, that measured the mechanical resistance that must be overcome by the applied force of drawing a tillage implement through soil. The first prototype was a simple spring balance: the instrument was an automated recording pressure gauge, indicating the pressure produced in an oil system by the pull between the two joints to which the instrument is hitched. This design was rather large but was suitable for measuring the draught force of tractor ploughs.

Later Haines and Keen (1928) designed and built a lighter, more portable version called the 'Rothamsted dynamometer' which was suitable for horse ploughs and was marketed by the Cambridge Instrument Company and which is shown in Fig. 5.2a and b. It was used in experiments in England and India.

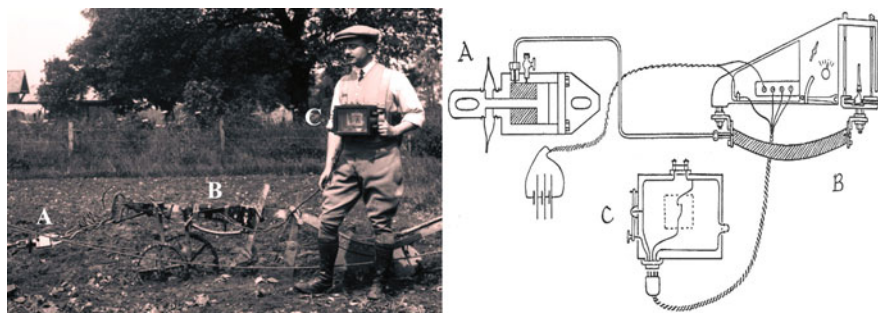


Fig. 5.2 *Left:* The Rothamsted dynamometer from 1928 in use in the field on a horse-drawn mouldboard plough. (Photograph courtesy of Rothamsted Experimental Station.) The sartorially elegant gentleman is believed to be B.A. Keen. *Right:* A schematic of the dynamometer. A, hydraulic link; B, recording device with Bourdon tube (http://en.wikipedia.org/wiki/Pressure_measurement); C, control box with Morse code tapping key for annotating records. A full description is given in Haines and Keen (1928). Figures from Haines and Keen (1928), used with permission

5.3.3 Data Logging: Analogue Data Recording

Recording was on a continuous strip chart with parallel records of drawbar pull (related to soil strength), depth of ploughing, and distance travelled (and thereby speed), as shown in Fig. 5.3.

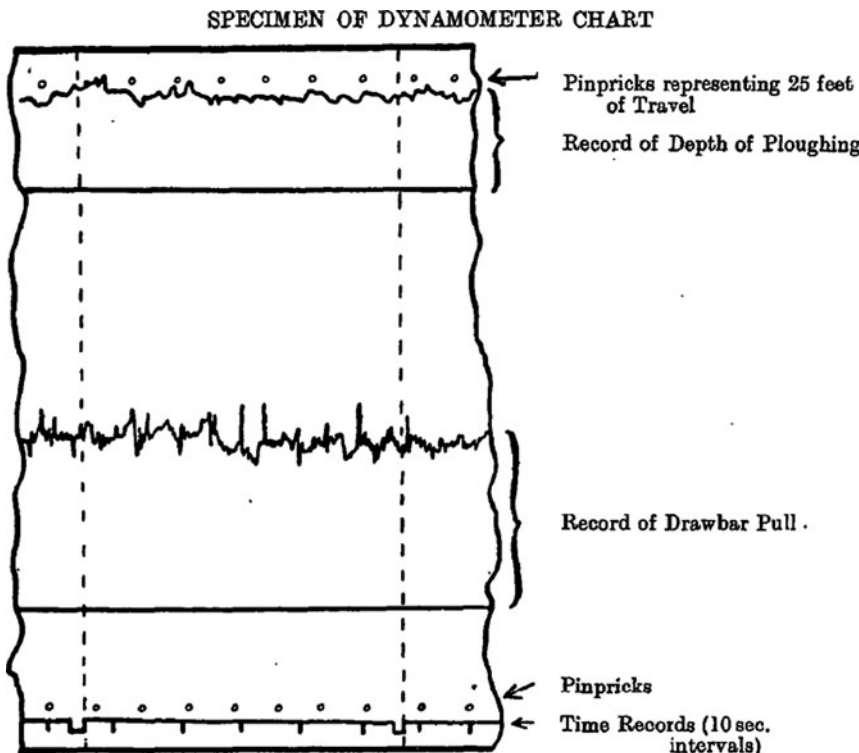


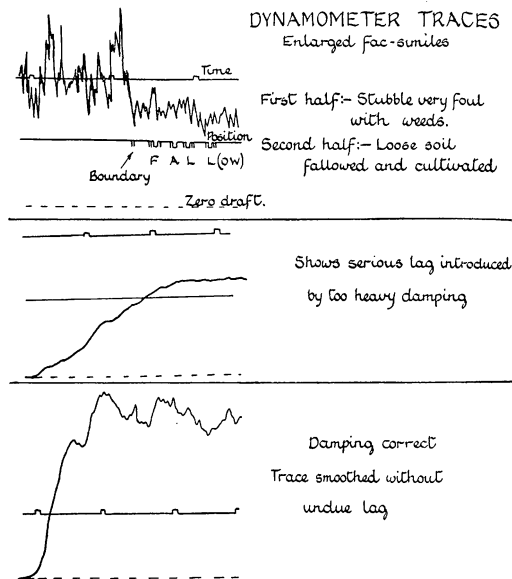
Fig. 5.3 Example of chart recording from Haines and Keen (1925a). The *dashed parallel vertical lines* represent field boundaries. Figure from Haines and Keen (1925a), used with permission

5.3.4 Data Analysis: Spatial Variation and Data Filtering

Haines and Keen (1925a) were the first to quantitatively document considerable amounts of short-range spatial variation in soil, invalidating the assumption that soil is in any sense uniform. They also postulated the origin of soil variation: 'the key is to be found in the observation that they remain constant from season to season. They are almost certainly the resultant of the age-long soil-forming processes'.

To handle the data, rather than using sophisticated time-series analysis or Kalman filtering, Haines and Keen (1928) found that the data could be smoothed during recording by using oil of an appropriate viscosity in the sensing system

Fig. 5.4 The effect of changing oil viscosity on the smoothing and delay of the recorded variation in soil mechanical resistance, from Haines and Keen (1928), used with permission



(see Fig. 5.4). The amount of detail in the record could then be controlled by the viscosity of the oil: a thin oil gave great detail, while thicker oil gave any desired degree of smoothing but with an undesirable time lag. A compromise was needed in order to give reasonable detail without appreciable time lag.

5.3.5 The Product: The First High-Resolution Digital Soil Map

The first experiment was on Sawyers field which had an area of 2.4 ha. It had received uniform treatment for many years and its soil was believed uniform too. The result from Sawyers field is shown in Fig 5.5. Haines and Keen (1925a) manually constructed a contour map based on average soil mechanical resistance values obtained for each plot. This is quite different from the methods that would be proposed today, for example by Cressie and Kang in Chapter 4. They called these ‘isodynes’ – contour lines of equal force or soil mechanical resistance. Haines and Keen (1925b) used their dynamometer to map soil mechanical resistance in the classical Rothamsted experiment plots. They also built a real 3D model (pre-GIS), shown in Fig. 5.6, of the soil mechanical resistance in one of the fields (the famous Broadbalk permanent wheat plots), and showed that the predominant factor was natural soil variation – and not ‘manuring’ – in spite of the long period (1843–1925) over which the soil had been cultivated. Much of the soil at Rothamsted is of the Batcombe and Hook series, which comprises silt to silty clay loam overlying clay with flints (Avery and Catt, 1995). These are probably Chromic Luvisols in the World Reference Base.

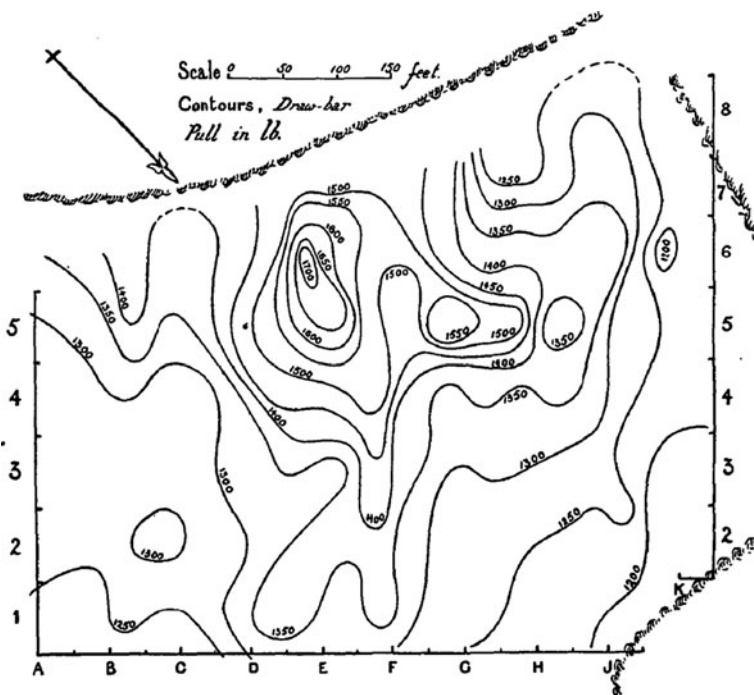


Fig. 5.5 Isodyne (contours of equal soil mechanical resistance) for Sawyers field, from Haines and Keen (1925a), used with permission. The map is constructed from 122 observations, each an average over a small area. The units of lb (pound force) can be converted to Newtons by multiplying by 4.448. The values range between 4.8 and 7.6 kN

5.4 Degrees of Separation

Nothing was reported in the literature on this kind of work for a very long time, and published work on on-the-go soil strength measurement seemed to begin afresh with Stafford and Hendrick (1985, 1988); since then, with the advent of site-specific soil and crop management, a number of other papers have been published. We list the ones we have discovered in Table 5.1, and they use a variety of technologies. We can define the *degree of separation* (dS) between two articles as ‘the number of papers that need to be sought for the two articles to meet’. For example, the dS between articles Alihamsyah et al. (1990) and Chung et al. (2006) is 1, as Alihamsyah et al. (1990) was cited by Chung et al. (2006). This is shown in row H, column M of Table 5.1. Another example is for Adamchuk and Christenson (2007) and Stafford and Hendrick (1988), where the dS is 2. In Adamchuk and Christenson (2007), no reference is given to Stafford and Hendrick (1988), but it gives reference to Adamchuk et al. (2001). In Adamchuk et al. (2001) there is a reference to Stafford and Hendrick (1988). So there are 2 degrees of separation between the two articles (shown in row E, column O of Table 5.1). The degrees of separation of the

Fig. 5.6 Physical block model of variation of soil mechanical resistance across the Broadbalk continuous wheat experiment in 1924, from Haines and Keen (1925b), used with permission



Table 5.1 Degrees of separation between papers on on-the-go soil strength measurement

	D	F	G	H	I	J	K	L	M	N	O
A	∞^a	∞									
B	1	∞									
C	1	∞	1	∞							
D	0	∞									
E	∞	1	1	∞	∞	2	3	2	3	∞	2
F	0	∞	∞	∞	1	2	2	2	∞	∞	2
G		0	∞	∞	∞	∞	1	2	∞	1	
H			0	∞	1	1	2	1	∞	2	
I				0	∞	∞	2	1	∞	2	
J					0	1	1	1	∞	1	
K						0	∞	1	∞	2	
L							0	∞	∞	2	
M								0	∞	1	
N									0	∞	
O										0	

A Keen and Haines (1925), B Haines and Keen (1925a), C Haines and Keen (1925b), D Haines and Keen (1928), E Stafford and Hendrick (1985/88), F Owen et al. (1987), G Glancey et al. (1989), H Alihamsyah et al. (1990), I Van Bergeijk et al. (1996/2001), J Adamchuk et al. (2001), K Hall and Raper (2005), L Mouazen and Ramon (2006), M Chung et al. (2006), N Watts et al. (2006), O Adamchuk and Christenson (2007)

^a ∞ as we possibly have not found all intervening papers this might be better expressed as >5

main papers on this topic are shown in a matrix in Table 5.1. The rows and columns are in chronological order and the lower half of the matrix is blank because earlier papers cannot refer to later ones. There appears to be a literature developing, but there is also a relatively high degree of non-citation – many of the cells show infinite separation. The most remarkable finding is that none of the early works of Haines and Keen appear to have been referenced in the scientific literature (see rows A, B, C, and D) until the Broadbalk measurements were repeated recently (Watts et al., 2006), and Watts et al.'s work seems to be separated in the citation sense from the main body of contemporary soil strength-sensing work (see column N).

Further study of the literature would no doubt show other early soil-sensing methodologies. For example, Murray Lark from Rothamsted has pointed out the paper by Broughton Edge (1931) as an early kind of electromagnetic induction apparatus.

5.5 Conclusions

- i. Haines and Keen appear to have invented high-resolution digital soil sensing and mapping in the 1920s.
- ii. Haines and Keen constructed the first on-the-go recording soil sensor and made high-resolution maps from the point data.
- iii. The work of Haines and Keen work was lost or seen as irrelevant until the new impetus given by precision agriculture in the 1990s when similar, but independent, work evolved again.
- iv. There is nothing new under the sun...

References

Adamchuk VI, Christenson PT (2007) Development of an instrumented blade system for mapping soil mechanical resistance represented as a second-order polynomial. *Soil Till Res* 95:76–83

Adamchuk VI, Morgan MT, Sumali H (2001) Application of a strain gauge array to estimate soil mechanical impedance on-the-go. *Trans Am Soc Agric Eng* 44:1377–1383

Alihamsyah T, Humphries EG, Bowers CG Jr (1990) A technique for horizontal measurement of soil mechanical impedance. *Trans Am Soc Agric Eng* 33:73–77

Avery BW, Catt JA (1995) The soil at Rothamsted. Lawes Agricultural Trust, Harpenden, Herts

Broughton Edge AB (1931) Geo-electrical prospecting by A.C. bridge methods. *Nature* 127:37–39

Chung SO, Sudduth KA, Hummel JW (2006) Design and validation of an on-the-go soil strength profile sensor. *Trans Am Soc Agric Biol Eng* 49:5–14

Glancey JL, Upadhyaya SK, Chancellor WJ, Rumsey JW (1989) An instrumented chisel for the study of soil-tillage dynamics. *Soil Till Res* 14:1–24

Haines WB, Keen BA (1925a) Studies in soil cultivation. II. Test of soil uniformity by means of dynamometer and plough. *J Agric Sci (Cambridge)* 15:387–394

Haines WB, Keen BA (1925b) Studies in soil cultivation. III. Measurements on the Rothamsted classical plots by means of dynamometer and plough. *J Agric Sci (Cambridge)* 15:395–406

Haines WB, Keen BA (1928) Studies in soil cultivation. IV. A new form of traction dynamometer. *J Agric Sci (Cambridge)* 18:724–732

Hall HE, Raper RL (2005) Development and concept evaluation of an on-the-go soil strength measurement system. *Trans Am Soc Agric Eng* 48:469–477

Keen BA (1931) The Physical properties of the soil. Longmans, Green & Co, London

Keen BA, Haines WB (1925) Studies in soil cultivation. I. The evolution of a reliable dynamometer technique for use in soil cultivation experiments. *J Agric Sci (Cambridge)* 15:375–386

Mouazen AM, Ramon H (2006) Development of on-line measurement system of bulk density based on on-line measured draught, depth and soil moisture content. *Soil Till Res* 86:218–229

Owen GT, Drummond H, Cobb L, Godwin RJ (1987) An instrumentation system for deep tillage research. *Trans Am Soc Agric Eng* 30:1578–1582

Pereira C (1982) Bernard Augustus Keen. 5 September 1890–5 August (1981) Biographical Memoirs of Fellows of the Royal Society 28:204–223. <http://tinyurl.com/2evp5x>

Stafford JV, Hendrick JG (1985) Dynamic control of pan rupturing tines. American Society of Agricultural Engineers paper No. 85–1547

Stafford JV, Hendrick JG (1988) Dynamic sensing of soil pans. *Trans Am Soc Agric Eng* 31:9–13

Van Bergeijk J, Goense D (1996) Soil tillage resistance as tool to map soil type differences. In: Robert PC, Rust RH, Larson WE (eds) Proceedings of the 3rd international conference on precision agriculture, ASA-CSSA-SSSA, Madison, Wisconsin, pp 605–616

Van Bergeijk J, Goense D, Speelman L (2001) Soil tillage resistance as a tool to map soil type differences. *J Agric Eng Res* 79:371–387

Watts CW, Clark LJ, Poulton PR, Powlson DS, Whitmore AP (2006) The role of clay, organic carbon and long-term management on mouldboard plough draught measured on the Broadbalk wheat experiment at Rothamsted. *Soil Use Manage* 22:334–341

Chapter 6

Proximal Soil Nutrient Sensing Using Electrochemical Sensors

C.R. Lobsey, R.A. Viscarra Rossel, and A.B. McBratney

Abstract Site-specific crop management requires the collection of high spatial resolution soil property data. Currently, electromagnetic (EM) induction or soil electrical resistance sensors, which measure soil electrical conductivity, are commonly used for this purpose. From the measurements, a number of related soil properties, e.g. clay content, are inferred. Although these techniques enable rapid, low-cost measurements that are able to capture within-field soil variability, they do not provide information on soil nutrient concentrations directly. This chapter reviews research conducted towards the development of proximal soil nutrient sensors using two forms of electrochemical sensors: ion-selective electrodes (ISEs) and ion-sensitive field effect transistors (ISFETs). It provides a brief introduction to electrochemical sensors and reviews their application for rapid low-cost soil analysis and proximal sensing. Over the last three decades, electrochemical sensors have been used in the laboratory to reduce the time, cost, and complexity of soil nutrient analysis. More recent studies suggest that ISEs and ISFETs have the potential to be used for rapid *in situ* soil analysis. However, the technologies have some limitations, particularly for on-the-go proximal soil sensing.

Keywords Proximal soil sensing · Ion-selective electrode (ISE) · Ion-sensitive field effect · Transistor (ISFET) · Nitrate · Sodium · Potassium · Phosphorus · pH

6.1 Introduction

Development of proximal soil sensors is important for improving the efficiency of crop production and raising our understanding of soil variability. These sensors should provide repeatable measurements and should be rapid, inexpensive,

C.R. Lobsey (✉)

Australian Centre for Precision Agriculture, The University of Sydney, Sydney, NSW 2006, Australia

e-mail: craig.lobsey@sydney.edu.au

and robust. A number of on-the-go proximal soil sensors are being developed (Chapter 2) and several are available commercially – for example, electromagnetic instruments (Sudduth et al., 2001), electrical conductivity systems (Lund et al., 1999), and a pH sensor (Adamchuk et al., 1999). However, proximal soil sensors for direct measurement of soil macronutrients are not yet commercially available.

Current methods to measure the variability of soil properties for continuous management have focused on the use of soil electrical conductivity (EC_a) measurements using either EM induction or electrical resistivity sensors (e.g. Sudduth et al., 2005). However, while these sensors provide rapid and low-cost measurements, they do not measure soil nutrient concentrations. Handheld ion-selective electrode (ISE) systems are available for low-cost analysis of soil macronutrients (e.g. Cardy meter); however, their performance for some important nutrients, such as nitrate, is questionable, and they still require manual pre-processing of each sample. With the economic and environmental gains expected from site-specific soil management, the development of proximal soil nutrient sensors is vital.

Initial research in on-the-go proximal nutrient sensing was targeted at soil pH (Viscarra Rossel and McBratney, 1997) and nitrate-N (Birrell and Hummel, 1997). Research into proximal sensing of soil pH has shown the most success (Adamchuk et al., 2007). Soil pH is relatively easy to measure and is important for management decisions through its effect on soil nutrient availability and as an indicator of soil health. There is also considerable scope for variable rate-liming and other site-specific management (Viscarra Rossel and McBratney, 2000). Similarly, considerable focus has been placed on the measurement of nitrate-N, which is an important nutrient for agronomic management. Environmental concerns about ground water nitrate leaching and high fertiliser prices have created a drive for optimal nitrogen application. This creates considerable scope for site-specific management and variable rate application of nitrogen.

This chapter reviews research on the development of electrochemical proximal soil sensors. It (i) includes a brief introduction to ion-selective electrodes (ISEs) and ion-sensitive field effect transistors (ISFETs); (ii) gives an overview of techniques for implementing on-the-go and in situ electrochemical soil nutrient measurements; and (iii) describes work to address some limitations of these sensors.

6.2 Proximal Soil Sensing Using Electrochemical Sensors

6.2.1 Electrochemical Sensors

Ion-selective electrodes are a potentiometric sensor for measuring ion activity in a solution. The sensing component of the ISE is an ion-selective membrane. Various membranes selective for pH and a range of soil nutrients (such as nitrate, sodium, potassium, and calcium) have been developed and are commercially available. ISEs for phosphate are not common; however, there are some research prototypes under evaluation for soil nutrient sensing (Kim et al., 2007a).

ISEs used for soil sensing come in three forms: (1) glass (e.g. pH electrode); (2) solid state (e.g. crystal based); and (3) liquid state (e.g. ionophore and PVC plasticiser). While ISEs differ in the construction of the sensing membrane, their mode of operation is similar. The electromotive force (emf) generated at the sensing surface is proportional to the log of the target ion activity in solution and is defined by the Nernst equation:

$$E = E_0 + \frac{2.3RT}{nF} \log_{10}(a_i),$$

where E is the measured potential of the system, E_0 is the offset potential, R is the gas constant, T is the absolute temperature, n is the charge on the ion, F is the Faraday constant, and a_i is the activity of the measured ion. ISFETs are a type of chemically sensitive field effect transistor that were first described by Bergveld (1972) and later by Matsuo and Wise (1974) and Esashi and Matsuo (1978). As the acronym suggests, ISFETs combine two well-established technologies – that of ion-selective electrodes (ISEs) and field effect transistors (FETs).

The ISFET is constructed like a metal oxide FET; however, the gate is replaced with an electrode that is in contact with the solution (electrolyte) to be analysed. Similarly, the insulating oxide (usually SiO_2) is in direct contact with the solution being measured (Fig. 6.1). The charge that develops on the oxide surface due to proton interaction controls the source–drain current (I_{ds}) of the FET, which is now indicative of the electrolyte pH.

Chemically modified field effect transistors (CHEMFETs) are ISFETs with specific membrane layers applied to the oxide insulator surface of the FET (Fig. 6.2), creating an ISFET selective to the target ionic species, e.g. a nitrate ISFET.

ISFETs and CHEMFETs have some advantages over standard ISEs. Firstly, the physical nature of the ISFET allows mass production of the sensors using micro-electronic manufacturing technology, with polyamide and membrane layers applied using rapid and repeatable techniques such as spin coating, film deposition, and

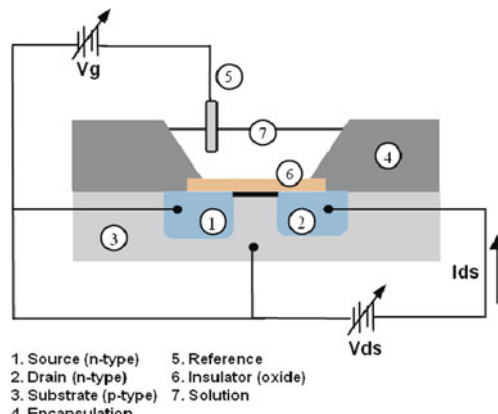
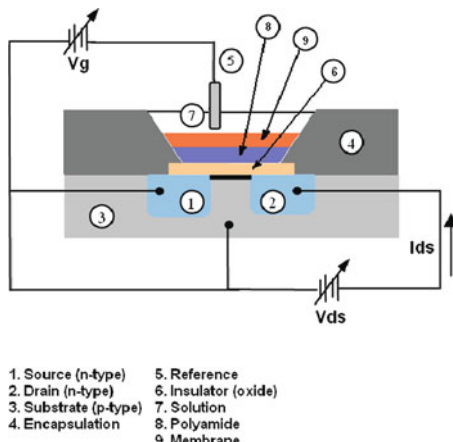


Fig. 6.1 ISFET construction

Fig. 6.2 Schematic of a CHEMFET showing layer deposition



photolithography. This also allows manufacturing of miniature sensors containing transducers for multiple ionic species. However, the benefits of miniaturisation – e.g. lower sample volumes, speed of measurement, in situ deployment – are countered by the requirement for a reference electrode, which for technical reasons cannot be miniaturised without sacrificing electrode lifetime and stability.

Currently, pH ISFETs are commercially available; however, CHEMFETs are more difficult to find. Their commercial development was driven by market focus on biomedical applications, but development was limited by factors such as biocompatibility (Bergveld, 2003). pH ISFETs are commonly used in food processing and medical science, where the vulnerability of glass membrane pH sensors makes them problematic (Bergveld, 2003). They have also been used for proximal soil sensing (Viscarra Rossel and McBratney, 1997). There has been limited use of CHEMFETs in environmental applications. CHEMFETs selective for nitrate, calcium, and potassium have been developed and evaluated for use in soil nutrient sensing (Artigas et al., 2001; Birrell and Hummel, 2001). Currently there are no commercially available CHEMFETs that are selective for ions targeted in soil nutrient analysis.

6.2.2 Soil Nutrient Analysis Using Electrochemical Sensors

The use of pH electrodes for measuring soil pH is a common and well-established technique. Research into the use of electrochemical sensors for measuring additional soil nutrients has been going on for decades, particularly after the introduction of the nitrate ISE by Orion research in the late 1960s (Orion nitrate ion electrode model 92-07). Initially, work was aimed at reducing the time and complexity of laboratory analysis and at replacing methods that required pre-treatment and extractions before analysis (e.g. in colorimetric analysis). This effort focussed on developing analytical methods that avoided the technical constraints of ISE measurements (such as interference, calibration, stirring, and response times) (Bremner et al., 1968;

Dahnke, 1971; Oien and Selmer-Olsen, 1969). These studies demonstrated that the concept was sound and that ISEs could successfully be used for low-cost soil nutrient analysis.

There was a renewed interest in electrochemical sensors for soil nutrient sensing in the 1990s, mostly due to the need for high spatial resolution soil information in precision agriculture. This created demand for sensors that could provide rapid, inexpensive, real-time measurement of soil properties, and preferably on-the-go. The use of electrochemical sensors for measuring soil nutrients was attractive for many reasons: they have a relatively fast response, they are rugged, they can measure directly in a soil slurry or in solution, they are relatively inexpensive, and they require little supporting hardware. While there has been some research on proximal soil sensing using other techniques – e.g. capillary zone electrophoresis (O’Flaherty et al., 2000) and spectroscopic techniques (Chapter 3) – most of the research on soil nutrient sensing has focused on electrochemical sensors. The main reasons are that the measurements provide direct measurements of soil nutrient concentrations and the measurements can be made directly in a soil slurry. A recent study reported that the nitrate ISE holds an advantage over colorimetric techniques as a candidate for soil sensing because it requires lower sample pre-treatment and has a fast response of 30–60 s (Domingue et al., 2005). Electrochemical sensors have been evaluated for stationary rapid soil analysis, i.e. static, in-field manual measurements or continuous deployment (Davenport and Jabro, 2001; Artigas et al., 2001). Research also suggests that they can be developed for autonomous, on-the-go operation (Adamchuk et al., 2003; Adsett et al., 1999; Viscarra Rossel et al., 2005).

6.2.3 PSS: Stationary In Situ Analysis

Proximal soil nutrient sensing provides real-time and continuous monitoring, opening the way for intelligent irrigation and fertiliser management systems (Artigas et al., 2001). Davenport and Jabro (2001) assessed the use of handheld Cardy ion meters for the direct measurement of soil nitrate, sodium, potassium, and pH. Two types of samples were used – silt loam and sand textures – and distilled water was added to the samples to provide a range of volumetric water contents. The resulting slurries were applied directly to the surface of the Cardy meters. The authors found that the handheld soil pH meter worked well on soil slurries and provided reliable measurements after more than 500 measurements. The Cardy potassium and sodium meters worked well in soils with volumetric water contents between 20 and 25% (potassium) and 20 and 30% (sodium), but the sodium ISE did not perform well with sandy soils. Durability of these ISEs was also lower and noticeable degradation of the membranes was evident after 300 measurements. The Cardy meter is not suitable for the measurement of soil nitrate-N (Davenport and Jabro, 2001).

Artigas et al. (2001) reported on the development and evaluation of pH, calcium, potassium, and nitrate ISFETs for use in real-time soil monitoring. The ISFETs were created with photo-curable polymeric membranes and soils were measured by directly inserting them into soil pots (which were subjected to different fertiliser

treatments) and the sensors were tested daily for 2 months. Over this period the sensitivity of all but the nitrate ISFET remained constant (the nitrate device's sensitivity decreased after the first month). The drift of the sensors was in the range of 2–4 mV per day (Artigas et al., 2001).

Viscarra Rossel and Walter (2004) developed a simple protocol for quantitative spatial field measurements of soil pH using an ISFET. To determine adequate times for field measurements, the kinetics of soil pH reactions in 1:5 suspensions of soil/0.01 M CaCl_2 (pH_{Ca}) and of soil/ H_2O (pH_{w}) were quantified. The accuracy of their 10-s field pH measurements was 0.34 pH units. Maps of field pH measurements in the laboratory and in situ (in the field) were compared, and the latter appeared to more accurately reflect the spatial structure of soil pH_{w} . Temporal measurements of field pH over 2 years were in good agreement.

6.2.4 PSS: *On-the-Go*

On-the-go proximal soil sensing must be rapid so as to allow data to be collected while a vehicle is traversing the field. In addition, sample collection and analysis needs to be automated to some degree. The advantage of on-the-go proximal soil sensing is that the number of samples is greater so that the accuracy need not be as great as for laboratory analysis where only few samples are measured.

A number of techniques have been explored for use in on-the-go sensing, and these will be discussed in some detail. In brief, direct soil measurement involves the direct insertion of the electrochemical sensors into a soil or a soil slurry, and this is the simplest method. Agitated soil measurement (ASM) involves the controlled addition of an extracting solution, followed by agitation of the slurry, and is similar to the chamber and batch methods. Chamber and batch methods require the sample to be delivered to a measurement chamber so that parameters are more tightly controlled, but the drawback is that complexity is increased. The final technique to be discussed – flow injection analysis (FIA) – separates the soil and analysis components and is called an ISFET-based FIA system.

6.2.4.1 Direct Soil Measurement

Currently there is only one commercial sensor for direct soil chemical measurement – the pH manager, which is a module of the Mobile Sensor Platform (MSP) commercialised by Veris Technologies, Inc. (Kansas, USA). It consists of a sample shoe which, while traversing a field, periodically brings a core of soil into direct physical contact with two pH electrodes (Adamchuk et al., 2006). While the primary advantage of this technique lies in its simplicity, and it performs well for soil pH mapping, its performance in the measurement of other soil nutrients is questionable. The feasibility of adapting this technique to the measurement of potassium, sodium, and nitrate on naturally moist soil samples has been explored (Adamchuk et al., 2005). Using the same sampling system as for pH measurements, the pH electrodes were replaced with ISEs selective for nitrate, potassium, and sodium; when

dealing with soluble potassium and residual nitrate, the system was capable of distinguishing between in-field areas of very low and high concentration levels. It is likely that some variability is introduced through inconsistent collection of sample cores, and its reliance on simple wetting of the soil surface probably results in non-uniform dilution factors which will affect the measured ion concentration. Similarly, upon wetting, some nutrient extraction would occur so that the ion concentration in the slurry would be in a dynamic state, with a time constant likely to exceed that of the electrode response. Finally, it must be noted that the technique is also physically harsh on the ISE membranes.

6.2.4.2 Agitated Soil Measurement (ASM)

The agitated soil measurement (ASM) technique (Sethuramasamyraja et al., 2005) was developed as a superior method, or modification, to the direct soil measurement technique. It involves using a controlled agitation environment similar to the batch method of Viscarra Rossel and McBratney (2003), but retaining some of the simplicity of the DM technique by using an open chamber. In implementing an ASM technique, Sethuramasamyraja et al. (2005) explored the use of a chamber-based measurement system which they referred to as an integrated agitation chamber module (IACM). ISEs selective for hydrogen, nitrate, and potassium ions are immersed in the soil extract solution, providing an environment more physically suited to the ISEs. They also observed the effects of various soil:water ratios, rinsing and extracting water quality, agitation, and the requirement for ionic strength adjustment (ISA). They reported that the best parameters for this system were agitated purified water extraction, a fixed soil:H₂O ratio of 1:1, and regular tap water for electrode rinsing. No ISA was necessary. Laboratory testing of the system (Sethuramasamyraja et al., 2008) using a modified soil-sampling shank on a Veris Mobile Sensor Platform was somewhat disappointing; it showed that while the ASM technique implemented with the IACM retained the benefits of reduced physical stress on the ISEs, there was no significant improvement in measurement performance over the original direct soil measurement technique. The authors suggest this could be due to the design of the IACM and the use of half-cell electrodes.

6.2.4.3 Batch/Chamber-Based Methods

An alternative approach that avoids some of these problems has been the use of batch-style processing and chamber-based analysis. Adsett and Zoerb (1991) developed a system for on-the-go soil nitrate measurement using an automated soil collection, metering, and delivery system. Nitrate was extracted using deionised water and analysed with a nitrate ISE. Although initial results were equivocal, they still demonstrated the feasibility of the technique. An improved design of the sampling system and electronics (Adsett et al., 1999) gave better results; however, field testing was still not particularly good. This system monitors the initial ion exchange kinetics, and by using calibrating samples, the initial sensor response is normalised

and soil nitrate concentration estimated. Laboratory testing gave estimates of nitrate with 95% accuracy in 6 s.

Loreto and Morgan (1996) developed an automated system for measuring field nitrate. The system augments various components to produce a complete on-the-go sample collection and analysis device. It included a sample wheel coring device that delivers a 50 g soil core to a sample cup on an indexing wheel. On the same indexing wheel, previous samples are simultaneously agitated and extracted using deionised water and then analysed using a solid-state nitrate electrode. Total sample measurement time is 20 s, with a new sample collected and processing initiated every 5 s. The system was tested in a soil bin, and despite relatively low correlation with a Lachat colorimetric analyser ($R^2 = 0.43$), the system showed good potential for on-the-go sensing.

Viscarra Rossel and McBratney (2003) developed a chamber-based system for on-the-go measurement of soil pH and lime requirement (LR). The system automatically collected soil, sieving it to a size fraction of < 2 mm, before measuring out a standard volume of soil. The soil was then delivered to a chamber containing a modified Mehlich buffer or 0.01 M CaCl₂ solution. The soil solution was agitated and analysed using a pH ISFET. This technique focussed on the chemistry of the system, in particular the online monitoring of the soil pH–buffer reaction. By monitoring the initial 15 s of the buffer reaction, these data could be used to predict buffer pH equilibrium and LR. Subsequently, Viscarra Rossel et al. (2005) developed an on-the-go soil pH and LR measuring system which automatically collected soil, sieved the sample, and measured and delivered it to an analytical chamber for real-time and on-the-go measurements.

Sibley et al. (2009) describe the field validation of a soil nitrate mapping system (SNMS) which was used to evaluate a nitrate extraction and measurement sub-unit (NEMS). The conceptual basis for this system follows that of Adsett and Zoerb (1991) with several design modifications. The study explored various data-processing methods (real number and integer number) and the use of soil moisture correction, and the NEMS results were compared with those of standard laboratory analysis for NO₃-N. Samples were processed in the NEMS by adding 15.1 g moist sub-sample to 58 mL of vigorously stirred distilled water for 6 s. The reported performance of the NEMS was excellent, with RMSE ranging from 2.23 to 3.73 mg kg⁻¹ depending on the data-processing method used. Sibley et al. suggest that although the sensor performance was robust under various field conditions (crops, soil groups, fertility types, and tillage), wider testing of the system is still required. They also found that the improvement gained from soil moisture correction is minimal and does not justify the additional hardware and expense required.

6.2.4.4 Flow Injection Analysis (FIA)

FIA can be used to measure low sample volumes, the analysis is rapid, and the electrochemical sensors can be frequently recalibrated to account for variation in their response. However, the sample injected into the FIA carrier stream must be

filtered, and precise control of injection times and flow rates is important. These add to the complexity of the system. Birrell and Hummel (2001) reported the development of a multi-ISFET nitrate sensor using an FIA system. They found that the FIA helps negate the long-term drift problems associated with ISFETs. A mechanical extraction system for proof-of-concept testing under laboratory conditions was also developed and tested. The system consisted of a soil-metering device and a rotating sample disc that progressed each sample through stages of soil collection, injection of extracting solution, and finally filtration. The filtered solution was then transferred and injected into the FIA carrier stream. It was reported that the automated extraction system was not particularly successful, likely due to variation in metered soil volume, variation in injection volumes into the FIA stream, and underestimation of actual soil nitrate due to incomplete extraction (Birrell and Hummel, 2001). However, the FIA system was capable of providing measurements of soil nitrate in manually extracted soil solutions with an R^2 greater than 0.9 in 1.25 s.

Price et al. (2003) refined and evaluated a core extraction procedure using the FIA system component developed by Birrell and Hummel (2001). The extraction system involved clamping a soil core between two filter discs and injecting an extracting solution (using a syringe pump) up through the filter soil core and filter assembly. The resulting extract was sampled and injected into the flow analysis stream and analysed using the FIA system. Sample response curves from the ISFET chip during the extraction and analysis process were recorded, and from these a series of data descriptors – such as response peak, slopes, and cumulative area-to-peak – were isolated. Stepwise multiple linear regression (SMLR) was performed on response descriptors, design variables (e.g. flow rates), and soil parameters to develop soil nitrogen prediction models. The authors concluded that the nitrate extract from the soil core was indicative of the soil nitrate concentration. They also suggested that a priori knowledge of soil type may be required if the ISFET technology were to make accurate real-time measurements of soil nitrate.

6.2.5 Addressing Limitations of Electrochemical Sensors for Proximal Soil Sensing

There are a number of limitations that must be faced in using electrochemical sensors for proximal soil sensing. The most significant arises from limited selectivity to the target ion, or ion interference. Most ion-selective membranes respond to a range of ions, with selectivity defined by selectivity coefficients. Response is defined by the Nikolsky equation (a modified form of the Nernst equation) shown below for a single interfering ion, where K_{ij}^{pot} represents the selectivity for an interfering ion with activity a_j and valence z :

$$E = E_0 + \frac{2.3RT}{nF} \log_{10} \left(a_i + K_{ij}^{\text{pot}} (a_j)^{n/z} \right).$$

While ion selectivity coefficients for most electrodes are typically acceptable for soil measurement of a single ion, problems arise when the aim is to measure multiple ions using a single extracting solution. High interfering ion activity occurs in commonly used extracting solutions, particularly when simultaneous analysis of multiple nutrients is being performed from a single batch extraction. Some limited work has been done in identifying ion-selective membranes compatible with certain nutrient-extracting solutions. Kim et al. (2007b) evaluated the compatibility of various ion-selective membranes and a cobalt rod-based ISE for simultaneous measurement of nitrate-N, available potassium, and available phosphorus in Kelowna extracting solution (0.25 M CH_3COOH + 0.015 M NH_4F). The ISE measurements in Kelowna extract were also compared with traditional laboratory measurements and, despite lower extracted quantities for phosphorus and potassium using the Kelowna buffer, the compatibility still allowed for simultaneous measurement of these soil nutrients.

Changes in sensitivity and sensor drift are other problems that must be addressed. Typically, this is done by performing frequent calibrations. Sensor drift is typically higher for ISFETs; however, the incorporation of ISFETs into an FIA system (e.g. Birrell and Hummel, 1997) addresses this problem. Sensor drift may severely limit the use of electrochemical sensors for in situ monitoring where frequent recalibration would be required for acceptable results. Sensor drift is also increased through exposure to soil extract or slurry, particularly when using nitrate sensors. It has been reported by several researchers (e.g. Adamchuk et al., 2005; Artigas et al., 2001) that nitrate sensitivity decreases considerably after exposure to soil and soil slurry.

Another problem with the use of ISEs in proximal soil sensing is durability. Recent work (Adamchuk and Lund, 2008) evaluates the use of an antimony electrode as a more durable alternative for pH sensing with the DSM technique. The measurement technique with glass pH electrodes may not be suitable in soils containing heavy impurities or coarser textures. Adamchuk and Lund report that the antimony electrode provides measurement results of similar quality with improved durability.

6.3 Conclusions

There is a growing body of literature demonstrating the feasibility of PSS using electrochemical sensors, and in some cases, successful systems have been demonstrated. Most of these studies tended to focus on constraints imposed by field operation, but there has been little work done in identifying and solving some of the fundamental issues associated with such measurements. There has also been only a small amount of work done on characterising the chemistry of the systems and the effect of variable environmental conditions, such as temperature. Finally, most work so far has been limited to soluble or plant-available ion concentration, with little focus on variable soil properties such as ion exchange kinetics. Due to the buffering nature of soil, information on both soluble and exchangeable components is critical for management decisions, e.g. for deciding whether to apply lime or fertiliser.

References

Adamchuk VI, Lund ED (2008) On-the-go mapping of soil pH using antimony electrodes. ASABE paper no. 083995, St. Joseph, Michigan

Adamchuk VI, Lund ED, Dobermann A, Morgan MT (2003) On-the-go mapping of soil properties using ion-selective electrodes. In Stafford JV, Werner A (eds) Precision agriculture. Wageningen Academic, Wageningen, pp 27–33

Adamchuk VI, Lund ED, Reed TM, Ferguson RB (2007) Evaluation of an on-the-go technology for soil pH mapping. *Precis Agric* 8:139–149

Adamchuk VI, Lund ED, Sethuramasamyraja B, Morgan MT, Dobermann A, Marx DB (2005) Direct measurement of soil chemical properties on-the-go using ion-selective electrodes. *Comput Electron Agric* 48:272–294

Adamchuk VI, Morgan MT, Brouder SM (2006) Development of an on-the-go soil pH mapping method: analysis of measurement variability. *Appl Eng Agric* 22:335–344

Adamchuk VI, Morgan MT, Ess DR (1999) An automated sampling system for measuring soil pH. *Trans ASAE* 42:885–891

Adsett JF, Thottan JA, Sibley KJ (1999) Development of an automated on-the-go soil nitrate monitoring system. *Appl Eng Agric* 15:351–356

Adsett JF, Zoerb GC (1991) Automated field monitoring of soil nitrate levels. In: Proceedings of the ASAE symposium on automated agriculture for the 21st century. Chicago, 16–17 December 1991, pp 326–335. American Society of Agricultural Engineers, St Joseph, MI

Artigas J, Beltran A, Jimenez C, Baldi A, Mas R, Dominguez C, Alonso J (2001) Application of ion sensitive field effect transistor based sensors to soil analysis. *Comput Electron Agric* 31:281–293

Bergveld P (1972) Development, operation, and application of ion-sensitive field effect transistor as a tool for electrophysiology. *IEEE Trans Biomed Eng* BM 19:342

Bergveld P (2003) Thirty years of ISFETOLOGY – what happened in the past 30 years and what may happen in the next 30 years. *Sens Actuat B-Chem* 88:1–20

Birrell SJ, Hummel JW (1997) Multi-sensor ISFET system for soil analysis. In: Precision agriculture '97. Volume II. Technology, IT and management. Papers presented at the 1st European conference on precision agriculture, Warwick University, UK, 7–10 Sept 1997, pp 459–468. Bios Scientific Publishers Ltd

Birrell SJ, Hummel JW (2001) Real-time multi ISFET/FIA soil analysis system with automatic sample extraction. *Comput Electron Agric* 32:45–67

Bremner JM, Bundy LG, Agarwal AS (1968) Use of a selective ion electrode for determination of nitrate in soil. *Anal Lett* 1:837–844

Dahnke WC (1971) Use of the nitrate specific ion electrode in soil testing. *Commun Soil Sci Plant Anal* 2:73–84

Davenport JR, Jabro JD (2001) Assessment of hand held ion selective electrode technology for direct measurement of soil chemical properties. *Commun Soil Sci Plant Anal* 32:3077–3085

Domingue KJ, Price RR, Mailander MP (2005) Real time soil nitrate sensing. ASAE paper no. 051031, St. Joseph, Michigan

Esashi M, Matsuo T (1978) Integrated micro multi ion sensor using field-effect of semiconductor. *IEEE Trans Biomed Eng* 25:184–192

Kim HJ, Hummel JW, Sudduth KA, Birrell SJ (2007a) Evaluation of phosphate ion-selective membranes and cobalt-based electrodes for soil nutrient sensing. In: Annual meeting of the American Society of Agricultural Engineers, ASAE, St Joseph, MI, pp 415–425

Kim HJ, Hummel JW, Sudduth KA, Motavalli PP (2007b) Simultaneous analysis of soil macronutrients using ion-selective electrodes. *Soil Sci Soc Am J* 71:1867–1877

Loreto AB, Morgan MT (1996) Development of an automated system for field measurement of soil nitrate. ASAE paper no. 96-1087, St. Joseph, Michigan

Lund ED, Colin PE, Christy D, Drummond PE (1999) Applying soil electrical conductivity technology to precision agriculture. In: Robert PC et al (eds) Precision agriculture. Proceedings. 4th International Conference, St. Paul, MN. 19–22 July 1998, ASA, CSSA, and SSA, Madison, WI

Matsuo T, Wise KD (1974) Integrated field-effect electrode for biopotential recording. *IEEE Trans Biomed Eng* 21:485–487

O'Flaherty BD, Barry EF, Cholli AL (2000) A rapid soil nutrient sensor device based on capillary zone electrophoresis. *J Environ Sci Health A – Tox/Hazard Subst Environ Eng* 35:189–201

Oien A and Selmer-Olsen AR (1969) Nitrate determination in soil extracts with the nitrate electrode. *Analyst* 94:888–894

Price RR, Hummel JW, Birrell SJ and Ahmad IS (2003) Rapid nitrate analysis of soil cores using ISFETs. *Trans ASAE* 46:601–610

Sethuramasamyraja B, Adamchuk VI, Dobermann A, Marx DB, Jones DD, Meyer GE (2008) Agitated soil measurement method for integrated on-the-go mapping of soil pH, potassium and nitrate contents. *Comput Electron Agric* 60:212–225

Sethuramasamyraja B, Adamchuk VI, Marx DB, Dobermann A, Meyer GE, Jones DD (2005) Analysis of an ion-selective electrode based methodology for integrated on-the-go mapping of soil pH, potassium, and nitrate contents. In: Annual meeting of the American Society of Agricultural and Biological Engineers, ASABE, Madison, WI, pp 1927–1935

Sibley KJ, Astatkie T, Brewster G, Struik PC, Adsett JF, Pruski K (2009) Field-scale validation of an automated soil nitrate extraction and measurement system. *Precis Agric* 10:162–174

Sudduth KA, Drummond ST and Kitchen NR (2001) Accuracy issues in electromagnetic induction sensing of soil electrical conductivity for precision agriculture. *Comput Electron Agric* 31:239–264

Sudduth KA, Kitchen NR, Wiebold WJ, Batchelor WD, Bollero GA, Bullock DG, Clay DE, Palm HL, Pierce FJ, Schuler RT, Thelen KD (2005) Relating apparent electrical conductivity to soil properties across the north-central USA. *Comput Electron Agric* 46:263–283

Viscarra Rossel RA, McBratney AB (1997) Preliminary experiments towards the evaluation of a suitable soil sensor for continuous, 'on-the-go' field pH measurements. Precision agriculture '97. Volume II. Technology, IT and management. Papers presented at the 1st European conference on precision agriculture, Warwick University, UK, 7–10 Sept 1997, pp 493–501

Viscarra Rossel RA, McBratney AB (2000) A two-factor empirical deterministic response surface calibration model for site-specific predictions of lime requirement. *Precis Agric* 2:163–178

Viscarra Rossel RA, McBratney AB (2003) Modelling the kinetics of buffer reactions for rapid field predictions of lime requirements. *Geoderma* 114:49–63

Chapter 7

DIGISOIL: An Integrated System of Data Collection Technologies for Mapping Soil Properties

G. Grandjean, O. Cerdan, G. Richard, I. Cousin, P. Lagacherie, A. Tabbagh, B. Van Wesemael, A. Stevens, S. Lambot, F. Carré, R. Maftei, T. Hermann, M. Thörnelöf, L. Chiarantini, S. Moretti, A.B. McBratney, and E. Ben Dor

Abstract The multidisciplinary DIGISOIL consortium intends to integrate and improve in situ proximal measurement technologies for assessing soil properties and soil degradation indicators, moving from the sensing technologies themselves to their integration and application in (digital) soil mapping (DSM). The core objective of the project is to explore and exploit new capabilities of advanced geophysical technologies for answering this societal demand. To this aim, DIGISOIL addresses four issues covering technological, soil science, and economic aspects: (i) development and validation of hydrogeophysical technologies and integrated pedogeophysical inversion techniques; (ii) the relation between geophysical parameters and soil properties; (iii) the integration of derived soil properties for mapping soil functions and soil threats; and (iv) the evaluation, standardisation, and industrialisation of the proposed methodologies, including technical and economic studies.

Keywords Soil properties · Sensing technologies · Geophysical techniques · Inference model · Water content

7.1 Introduction

The main objective of the European *FP7 Cooperation Work Program on Environment*¹ proposes to address global environmental issues in an integrated way by advancing our knowledge and capacities to develop new technologies for sustainable management of the environment and its resources. The DIGISOIL

G. Grandjean (✉)
BRGM, Orléans, France
e-mail: g.grandjean@brgm.fr

¹Framework Program 7.

project started in autumn 2008. As with the iSoil project (Chapter 8), it is defined according to the FP7 work program and addresses ‘technologies for data collection in (digital) soil mapping’. The multidisciplinary DIGISOIL consortium aims to integrate and improve in situ and proximal measurement technologies for the assessing soil properties and soil degradation indicators, moving from the sensing technologies themselves to their integration and application in (digital) soil mapping (DSM).

In order to assess and prevent soil degradation and to benefit from the different ecological, economic, and historical functions of the soil in a sustainable way, there is an obvious need for high-resolution, accurate maps of soil properties. The core objective of the project is to explore and exploit new capabilities of advanced geophysical technologies for answering this societal demand. To this end, DIGISOIL addresses four issues covering technological, soil science, and economic aspects (Fig. 7.1): (i) the validation of geophysical (in situ, proximal, and airborne) technologies and integrated hydrogeophysical inversion techniques (mechanistic data fusion); (ii) the relation between geophysical parameters and soil properties; (iii) the integration of derived soil properties for mapping soil functions and soil threats; and (iv) the evaluation, standardisation, and industrialisation of the proposed methodologies, including technical and economic studies.

7.2 Objectives

The purpose of the DIGISOIL project is to identify and bridge the technological gap and develop pertinent, reliable, and cost-effective geophysical mapping solutions. Considering the new equipment and signal processing developments offered by recent scientific investigations, the problem of performing soil data collections at the catchment scale using geophysical sensors can be foreseen in the near future, particularly for methods identified in the following tables (GPR, EMI, seismics, magnetics, and airborne hyperspectral) (Tables 7.1 and 7.2). Gravity-based and thermal-based methods will not be incorporated in DIGISOIL because of their low contribution to the characterisation of soil properties related to degradation processes. For gamma radiometrics, several investigations have already been carried out to study their potential for soil properties mapping (e.g. Viscarra Rossel et al., 2007). This technology has given satisfactory results and permits one to map types of clay minerals in the topsoil through the analysis of U, K, and Th anomalies in the gamma spectrum. We will not consider this method since it appears to be already used in the soil science community (Wilford and Minty, 2006). However, since the information provided by this technology has many interesting aspects, we will integrate it as potential auxiliary data in our mapping strategy. This context is therefore favourable for the development of DIGISOIL’s mapping tools and products in relation to DSM applications. With respect to these issues, the milestones of the DIGISOIL project are

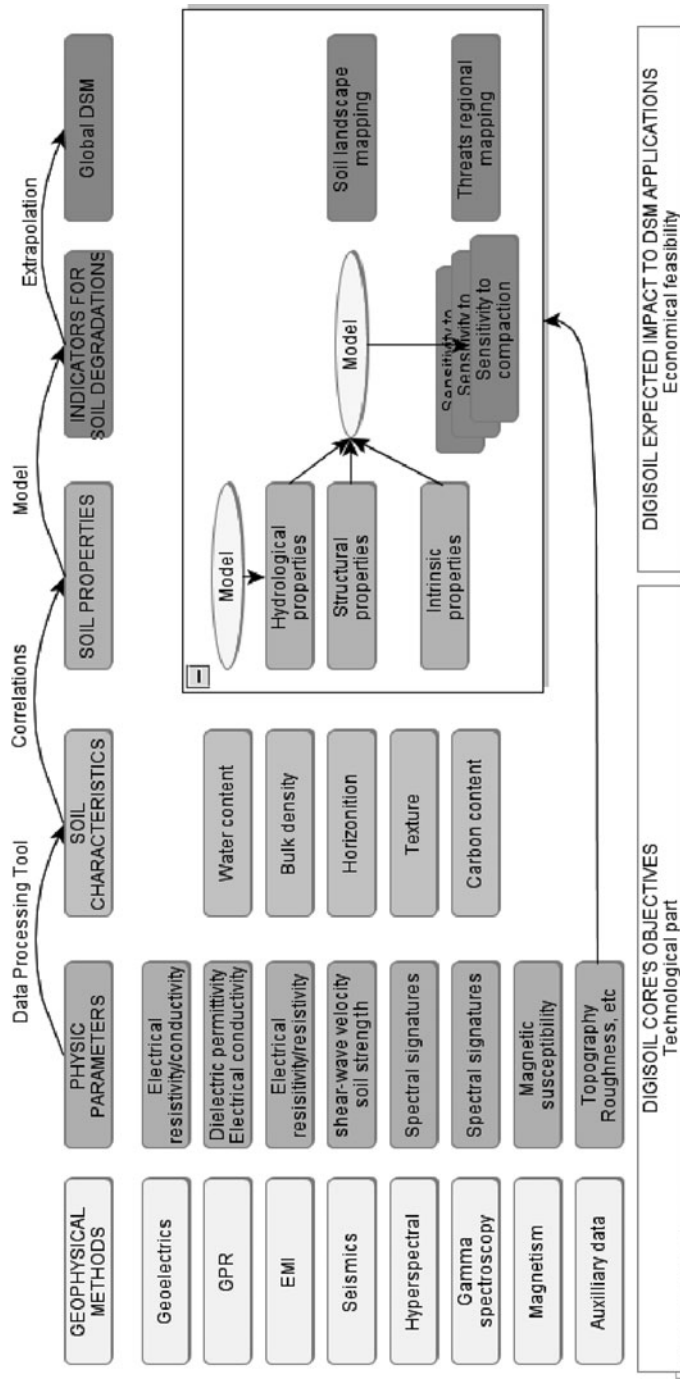


Fig. 7.1 DIGISOIL concept

Table 7.1 Common elements for the identification of risk areas

Soil threats				
Soil erosion	OM decline	Compaction	Salinisation	Landslide
<i>Soil properties</i>				
Soil texture	Soil texture/clay content	Soil texture	Soil texture	
Soil density		Soil density		
Soil hydraulic properties		Soil hydraulic properties	Soil hydraulic properties	
	Soil organic carbon	Soil organic matter		
<i>Soil-related parameters</i>				
Topography	Topography	Topography		Topography
Land cover	Land cover	Land cover		Land cover
Land use	Land use	Land use	Irrigation areas	Land use
Climate	Climate	Climate	Climate	Climate
Hydrological conditions				
Agro-ecological zone				Occurrence/density of existing landslides
		Groundwater information		
				Bedrock
				Seismic risk

1. To develop, test, and validate the most relevant geophysical technologies for mapping soil properties: geoelectric, seismic, GPR/EMI, magnetic, and airborne hyperspectral.
2. To establish correlations between the measured geophysical measurements and the soil properties involved in soil functions/threats (erosion, compaction, organic matter decline, salinisation, and shallow landslides) by using innovative data processing (inversion) and correlation protocols.
3. To evaluate the societal impact of the developed techniques by investigating their relevance to end-user needs, their technical feasibility, and their cost-effectiveness.
4. To produce an exploitation plan including the standardisation of the processes and the technical specifications of the developed methodologies describing the system components in terms of equipment (sensors, acquisition system,

Table 7.2 Potential influence of soil threats on functions of soils

Function of soil/soil threat	Biomass production	Storing, filtering and transformation	Bio diversity pools	Physical and cultural media	Raw material	Carbon pool	Geological and archaeological heritage
Erosion	x	x	x	x	x	x	x
Decline in organic matter	x	x	x	—	x	x	—
Contamination	x	x	x	x	x	x	x
Sealing	x	x	x	x	x	x	x
Compaction	x	x	x	x	—	x	x
Decline in soil biodiversity	x	x	x	—	—	x	—
Salinisation	x	x	x	—	—	x	—
Floods and landslides	x	x	x	x	x	x	x

x potential influence; – no influence

mobile vector), techniques (signal processing, inversion or fusion processes, specialisation), and operational protocols.

7.3 Strategy and Workplan

The DIGISOIL architecture is structured according to five items in relation to the above-cited objectives of the project:

1. *Identification of pertinent sensor technologies:* the capabilities of the different geophysical techniques will be investigated and technically adapted so as to characterise highly complex soil properties (spatial and temporal heterogeneities, low variations of properties, context-dependant, etc.). Two series of experiments will be carried out with a two-step feedback approach in order to analyse sequentially, and on different sites, the quality of the results and the efficiency of each technology.
2. *The data integration for estimating soil properties:* the conversion of geophysical parameters into soil properties and the derivation of soil threats are not straightforward. Most of the time, several indicators are necessary to reduce the uncertainty of the estimation. Studying the different correlation between indicators and possible soil properties should finally lead to an innovative methodology of fusion, guaranteeing a final assessment in terms of soil diagnostics (soil properties, threats, and soil functions).
3. *Testing and validation on selected sites:* the Commission policies have to deal with various European environments. For that reason, the sensor technologies will be tested on two series of sites: (i) second-order test sites for a specific

technique adaptation and (ii) first-order sites for testing the validity domain of different sensors at the same location. The latter have been selected in order to ensure a maximal geographical representativeness within Europe. For this validation task, classical *in situ* invasive sensors will be used.

4. *Evaluation of the proposed methodologies*: as the intent is oriented towards serving DSM applications, the results should be evaluated in terms of technical feasibility, maturity, and economical costs.
5. *Exploitation of the proposed methodology*: with respect to the Work Program's objectives, which stipulate that technologies developed in the Collaboration Program have to be finally exploited as European services, an exploitation plan, including technical specifications of the developed methodologies, will be presented.

7.4 From Soil Threats to Geophysical Properties

The DIGISOIL project can be seen as the setting up of operational techniques useful for implementing existing and emerging EU environmental legislation and policy – like the European Soil Thematic Strategy, which aims to protect soil functions and prevent soil degradation. Table 7.1 represents the main soil and soil-related parameters to be considered by member states for delineating risk areas. Since soil texture, soil water content, soil hydraulic properties, bulk density, and soil organic matter are involved in many soil functions, these properties have to be considered the first priority. Soils under threat cannot continue to perform all their environmental, economic, social, and cultural functions in the same way after being degraded (e.g. biomass production is not possible on sealed soils). The gradual loss of performance of soil functions depends on the severity of a threat, which can be gauged in terms of its intensity and duration. Depending on the type of threat, different soil functions may be affected (Table 7.2). In some cases more than one threat occur on a certain piece of land.

The combination of threats sometimes worsens their effect on soil functions. As illustrated in Fig. 7.1, which summarises the DIGISOIL concept, the core objectives of the program are focused on determining the most relevant soil properties, which in a second phase (and through the use of pedo- and hydro-models, as well as auxiliary data) will allow us to map soil threats and functions. In the last decades, geophysical prospecting applied to subsurface characterisation has been of an increasing interest, particularly in soil science. Major advances in this technological domain can be attributed to the development of integrated measuring systems, increasing computing power, equipment portability, and hardware/software diffusion. In this context, two kinds of technological platforms can be involved: ground-based and proximal technologies, working from the surface and from the air. Ground-based geophysical instruments are now equipped with digital signal processing and recording capabilities previously restricted to large corporate computing centres. This improved computational capacity has provided investigators with near real-time results that, in turn, drive improvements in instrument sensors and

Table 7.3 Main ground-based and airborne geophysical methods and related physical parameters. *Italics* indicate methods that will not be integrated into the DIGISOIL tool

Geophysical methods	Physical parameters
Ground-penetrating radar (GPR)	Dielectric permittivity, electric conductivity, magnetic permeability, frequency dependence of these electromagnetic properties
Seismic reflection and refraction	Volume and shear-wave velocities
Electromagnetic induction (EMI)	Electrical resistivity (electric conductivity and frequency dependence)
Electrical resistivity (geoelectric)	Electrical resistivity (almost zero-frequency)
<i>Gravity</i>	<i>Density</i>
Magnetics	Magnetic susceptibility and viscosity
<i>Airborne thermic</i>	<i>Surface temperature</i>
Airborne hyperspectral	Spectral reflectance
<i>Gammametry</i>	<i>Gamma spectrum (U, K, Th)</i>

processing algorithms. In a similar way, recent airborne geophysics has sparked strong interest due to the possibilities of civil airplanes equipped with optical, thermal, or hyperspectral sensors. The most common methods that take advantage of these enhancements, and their related parameters, are listed in Table 7.3.

Measuring the electrical resistivity of soil was proposed in the DIGISOIL project because it is closely related to several soil parameters and can be performed over areas of several hectares with high resolution (Panissod et al., 1997; Chapter 26, this volume). Up to now, the interpreting electrical measurements have remained difficult because the different influences soil parameters have on electrical resistivity are still hard to discriminate. There are numerous relationships between electrical resistivity and any one soil physical or chemical parameter. For example, there are linear (or more complex) correlations between electrical resistivity and soil temperature (Keller and Frischknecht, 1966), soil water content and salinity (Sen et al., 1988), soil cationic exchange capacity (Shainberg et al., 1980), soil texture (i.e. clay content), and soil porosity (Friedman, 2005). Other studies have demonstrated the influence of soil structure on electrical resistivity, such as the impact of bulk density or the effect of cracks (Samouëlian et al., 2003).

Spatial electrical investigations therefore enable us to describe soil structural heterogeneity, with the aim of delineating specific zones for use in precision agriculture or to map soil texture (Tabbagh et al., 2000) or salinity (Corwin et al., 2006). Nevertheless, despite these known relationships, it remains difficult to describe the effect of ancillary parameters on electrical resistivity, especially the effect of the soil structure (which changes quickly under the influence of water content and temperature). To address these issues, specific experiments will be conducted in the DIGISOIL project, such as taking measurements that should help describe the evolution of at least one or two parameters (assuming the others remain constant). As an example, Fig. 7.2 shows three electrical resistivity maps recorded on three dates when only the soil water content was supposed to vary (Besson et al., 2008).

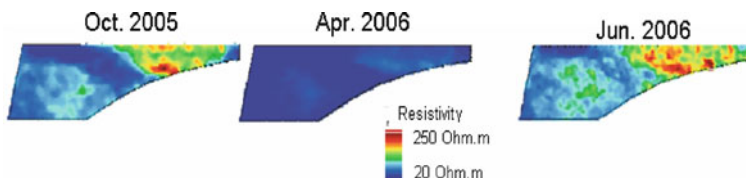
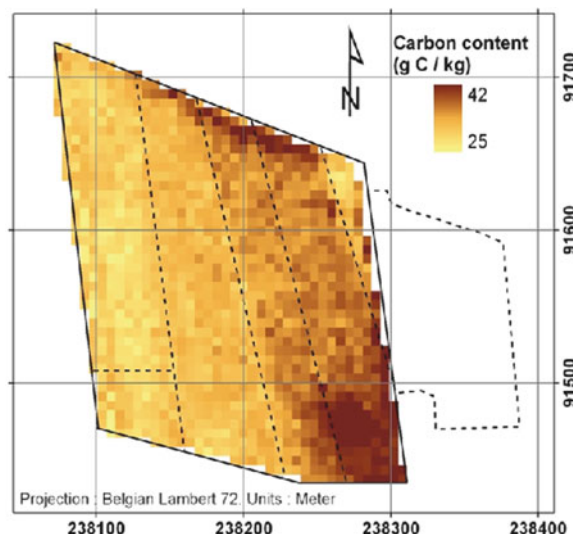


Fig. 7.2 Resistivity maps for three dates showing the impact of water saturation in soils on electrical resistivity (Besson et al., 2008)

Other studies will evaluate the possibility of using field spectroscopy (Chapter 11) to estimate carbon content (Stevens et al., 2006). Visible and near-infrared (VNIR) spectral analysis and diffuse reflectance analysis are techniques that can rapidly quantify various soil characteristics simultaneously (Ben-Dor and Banin, 1995; Viscarra Rossel et al., 2006). There are three types of VNIR techniques (Chapter 13), which operate at different spatial scales and in different environments: (1) laboratory spectroscopy (LS); (2) portable field spectroscopy (PS); and (3) imaging spectroscopy (IS). LS and PS rely on ground-based sensors (such as the FieldSpec Pro FR from Analytical Spectral Devices covering 350–2,500 nm). IS uses air- or space-borne sensors such as the Compact Airborne Spectrographic Imager or CASI (covering 405–950 nm) and the Shortwave Infrared Airborne Spectrographic Imager (SASI), covering 900–2,500 nm). Two different test sites in southern Belgium were monitored within the framework of the Belgian airborne imaging spectroscopy campaigns under the PRODEX program. The aim was to explore the capabilities of VNIR spectroscopy in the context of soil organic carbon (SOC) inventories and monitoring. The sites, Ortho in the Ardennes ($50^{\circ}8' N$, $5^{\circ}36' E$) and Attert ($49^{\circ}45' N$, $5^{\circ}44' E$), were overflowed with a CASI sensor in October 2003 when cereal fields had been ploughed, harrowed, and reseeded. Exactly 120 soil spectra from 13 bare fields were taken at Ortho and 40 from 10 bare fields at Attert using the FieldSpec Pro (ASD). At the same sites, topsoil (0–5 cm) samples were taken and analysed for moisture content and organic carbon content (the latter by wet oxidation). Furthermore, three bulk density samples were taken in each field in order to calculate the SOC stock in the ploughed layer (mean thickness 22 cm). Another dataset from a previous IS campaign near Attert, using both CASI and SASI sensors, was also analysed. We used both stepwise and partial least square (PLS) regression analysis to relate spectral measurements to SOC content. Root mean square error of prediction (RMSEP) for the ASD ranged from 2.4 to 3.3 g C kg⁻¹ depending on soil moisture content of the surface layer (Table 7.4). Imaging spectroscopy performed poorly, mainly due to the narrow spectral range of the CASI. Tests using both the CASI and the SASI performed better. The variation in soil texture and soil moisture content degrades the spectral response to SOC contents. Currently, RMSEP allows us to detect an SOC stock change of 1.9–4.4 g C kg⁻¹ or 4.2–9.9 Mg C ha⁻¹ in the upper 22 cm of the soil and is therefore still somewhat high, at least in comparison with changes in SOC stocks resulting from management or land conversion reported in the literature (0.3–1.9 Mg C ha⁻¹).

Table 7.4 PLS regression output statistics of the best model for each dataset

Data	Calibration			Validation			
	N	RMSEC ^a g C kg ⁻¹	RMSEC/SD	N	RMSEP ^b g C kg ⁻¹	RPD ^c	R ²
ASD	108	2.8	0.45	37	3.3	1.79	0.82
ASD ^d	77	1.7	0.25	24	2.4	2.33	0.90
CASI (Ortho)	94	3.0	0.93	32	4.4	1.08	0.44
CASI (Attert)	75	3.4	0.51	24	3.8	1.97	0.87
Casi+SASI	73	2.9	0.60	26	1.9	2.50	0.92

^aRoot mean square error of calibration^bRoot mean square error of prediction^cRatio of performance to deviation (RMSEP/SD)^dOnly including the dataset of dry soil surfaces**Fig. 7.3** Map of soil organic carbon content in a freshly ploughed field after land consolidation. The borders of the original fields that were joined are indicated with dashed lines (Stevens et al., 2006)

yr⁻¹; Freibauer et al., 2004). A detailed SOC map produced by IS reflected the patterns in SOC content due to the site's recent conversion from grassland to cropland (Fig. 7.3).

Accuracy of the spectral techniques is lower than that of most routine laboratory SOC analyses. However, the large number of samples that can be analysed by hyperspectral techniques outweighs the slight loss of precision compared to traditional chemical analyses. The greatest potential lies in airborne applications because imaging spectroscopy can cover a wide region almost instantaneously and

produce thousands of samples. Relatively poor detection levels are attributed to sensor characteristics (artefacts, noise, and limited spectral range) and factors affecting the soil spectral response (limited variability in SOC content, disturbing factors). The problem of disturbing factors will be addressed in the DIGISOIL project, through an experimental study of the effect of soil moisture, soil texture, and soil roughness on reflectance. Experiments on soil texture recovery, particularly well-suited for distinguishing between calcite and clayed minerals and using ULM's onboard sensors, have already begun (Fig. 7.4). Furthermore, specifications for airborne sensors as well as the optimal strategy for calibration and validation will be documented.

Ground-penetrating radar (GPR) is an increasingly used non-invasive and proximal electromagnetic (EM) sensing technology that can image the subsurface and identify its physical properties (Chapter 25). It is based on sending electromagnetic radiation (ultra-wideband VHF-UHF) into the soil and recording the reflected

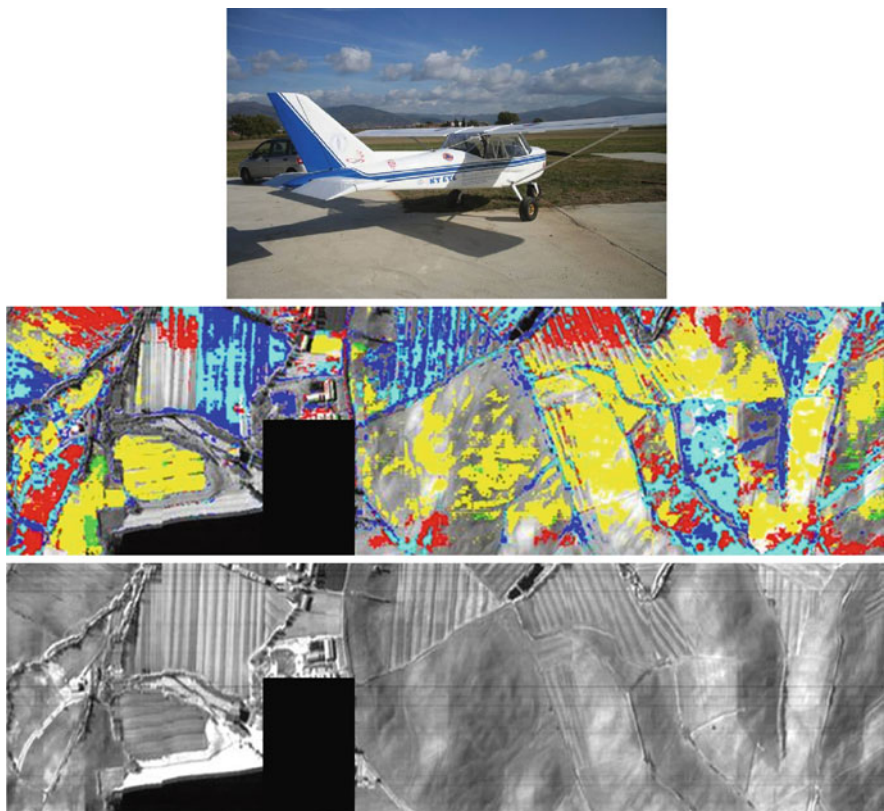


Fig. 7.4 ULM facility and resulting images: one based on Spectral Angle Mapper (SAM) classification; the second based on SWIR data where absorption bands of mineral clays (2.0–2.4 μm) are present (Univ. Firenze). *Red*: calcite, *green*: chlorite, *yellow*: illite, *blue*: illite-smectite, *cyan*: smectite

signals. In areas of agricultural and environmental engineering, GPR has been used to identify soil vertical structures, locate water tables, follow wetting front movement, identify soil hydraulic parameters, measure soil water content, assess soil salinity, monitor contaminants, and delineate soil compaction. Nevertheless, existing GPR techniques still suffer from major limitations due to simplifying assumptions on which they rely, particularly about EM wave propagation. In general, the radar system and antennas are not accounted for, ray approximation is applied to describe GPR wave propagation, and only the propagation time to reflectors is considered in signal processing algorithms. Reflection amplitude can also be used, but this is limited to the surface reflection for airborne GPR, and requires calibrations that are not practical for automated and real-time mapping. As a result, only a part of the information contained in the GPR data is usually used, and significant errors in the estimates are often introduced. To circumvent these shortcomings, Lambot et al. (2004) have recently developed a new approach: stepped-frequency continuous-wave monostatic off-ground GPR. The off-ground mode is particularly appropriate for real-time mapping of shallow subsurface properties. The radar system is based on ultra-wideband vector network analyser (VNA) technology. In contrast to classical GPR systems, the physical quantity measured by a VNA is exactly known and defined as an international standard. This permits the use of advanced full-waveform forward and inverse modelling techniques to estimate soil EM properties from the GPR signal, which intrinsically maximises information retrieval from the recorded data. In that respect, Lambot et al. (2004) developed a remarkably accurate EM model for their specific radar configuration, which included internal antenna and antenna–soil interaction propagation effects; they were able to exactly solve the three-dimensional Maxwell equations for wave propagation in multilayered media. Through GPR signal inversion, the approach has been successfully validated in a series of controlled hydrogeophysical experiments for electromagnetic soil characterisation (which included dielectric permittivity, electric conductivity, and frequency dependence of these quantities). GPR data inversion has been also integrated with hydrodynamic modelling to retrieve soil hydraulic properties from time-lapse radar data and to monitor the dynamics of continuous water content profiles (Lambot et al., 2006). In addition, the technique improves shallow subsurface imaging, which represents an important asset for determining high-resolution soil stratigraphy. Figure 7.5 shows an example of a field application where the developed method is used for real-time mapping of the soil surface dielectric permittivity and correlated water content, bridging the spatial scale gap between traditional soil sampling and remote sensing in hydrology.

To complement the above-cited techniques, DIGISOIL aims also to explore innovative geophysical methods for characterising specific soil properties. In particular, seismic methods will be tested in order to quantify the soil's mechanical modulus, a parameter closely related to soil compaction (Grandjean, 2006). Already validated in geotechnics for investigating zones tens of metres in extent, the challenge will be in adapting the methodology to small seismic devices, i.e. zones of several metres.

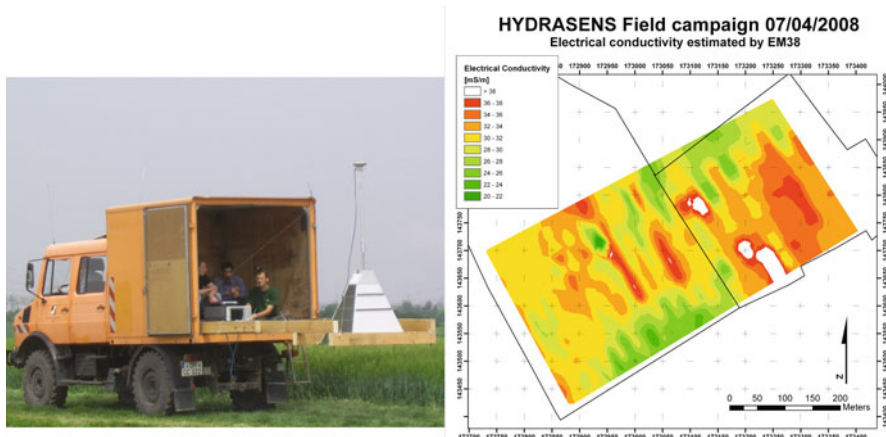


Fig. 7.5 Real-time mapping of soil surface water content with advanced GPR (Lambot et al., 2006)

7.5 Conclusions

In order to assess and prevent soil degradation, and to benefit from the different ecological, economic, and historical functions of the soil in a sustainable way, there is an obvious need for high-resolution, accurate maps of soil properties. The core objective of the project is to explore and exploit new capabilities of advanced geophysical technologies for answering this societal demand. Some geophysical techniques that will be carried out in the project are based on positive experiences in the domain and promise to fulfil the objectives of the project. Electrical and GPR measurements, hyperspectral imagery, and more innovative methods like seismic methods will be tested and technically adapted to soil properties mapping. An important output of the project will concern the use of related soil properties in an application dedicated to digital soil mapping (Chapter 5).

Acknowledgement The DIGISOIL project is financed by the European Commission under the 7th Framework Program for Research and Technological Development, Area 'Environment', Activity 6.3 'Environmental Technologies'.

References

Ben-Dor E, Banin A (1995) Near infrared analysis (NIRA) as a rapid method to simultaneously evaluate several soil properties. *Soil Sci Soc Am J* 59:364–372

Besson A, Cousin I, Bourennane H, Pasquier C, Nicoullaud B, Richard G, King D (2008) Discretization of spatial and temporal soil water variability into homogeneous zones based on electrical resistivity measurements at the field scale. *EUROSOIL congress 2008*, Soil, Society, Environment, 25–29/08/2008, Vienna

Corwin DL, Lesch SM, Oster JD, Kaffka SR (2006) Monitoring management-induced spatio-temporal changes in soil quality through soil sampling directed by apparent electrical conductivity. *Geoderma* 131:369–387

Freibauer A, Rounsevell MDA, Smith P, Verhagen J (2004) Carbon sequestration in the agricultural soils of Europe. *Geoderma* 122:1–23

Friedman SP (2005) Soil properties influencing apparent electrical conductivity: a review. *Comput Electron Agric* 46:45–70

Grandjean G (2006) A seismic multi-approach method for characterizing contaminated sites. *J Appl Geophys* 58:87–98

Keller GV, Frischknecht FC (1966) Electrical methods in geophysical prospecting. Pergamon, Oxford

Lambot S, Slob EC, van den Bosch I, Stockbroeckx B, Vanclooster M (2004) Modeling of ground-penetrating radar for accurate characterization of subsurface electric properties. *IEEE Trans Geosci Remote Sens* 42:2555–2568

Lambot S, Slob EC, Vanclooster M, Vereecken H (2006) Closed loop GPR data inversion for soil hydraulic and electric property determination. *Geophys Res Lett* 33:L21405, doi:10.1029/2006GL027906

Panissod C, Dabas M, Jolivet A, Tabbagh A (1997) A novel mobile multipole system (MUCEP) for shallow (0–3 m) geoelectrical investigation: the ‘Vol-de-canards’ array. *Geophys Prospect* 45:983–1002

Samouëlian A, Cousin I, Richard G, Tabbagh A, Bruand A (2003) Electrical resistivity imaging for detecting soil cracking at the centimetric scale. *Soil Sci Soc Am J* 67:1319–1326

Sen PN, Goode PA, Sibbit, A (1988) Electrical conduction in clay bearing sandstones at low and high salinities. *J Appl Phys* 63:4832–4840

Shainberg I, Rhoades JD, Prather RJ (1980) Effect of ESP, cation exchange capacity and soil solution concentration on soil electrical conductivity. *Soil Sci Soc Am J* 44:469–473

Stevens A, van Wesemael B, Vandenschriek G, Tychon B, Touré S (2006) Detection of carbon stock change in agricultural soils using spectroscopic techniques. *Soil Sci Soc Am J* 70:844–850

Tabbagh A, Dabas M, Hesse A, Panissod C (2000) Soil resistivity: a non-invasive tool to map soil structure horizonation. *Geoderma* 97:393–404

Viscarra Rossel RA, Walvoort D, McBratney AB, Janik L, Skjemstad J (2006) Visible, near infrared, mid infrared or combined diffuse reflectance spectroscopy for simultaneous assessment of various soil properties. *Geoderma* 131:59–75

Viscarra Rossel RA, Taylor HJ, McBratney AB (2007) Multivariate calibration of hyperspectral gamma-ray energy spectra for proximal soil sensing. *Eur J Soil Sci* 58:343–353

Wilford J, Minty B (2006) The use of airborne gamma-ray imagery for mapping soils and understanding landscape processes. In: Lagacherie P, McBratney AB, Voltz M (eds) Digital soil mapping: an introductory perspective. Elsevier Science, Amsterdam, 600 pp

Chapter 8

iSOIL: An EU Project to Integrate Geophysics, Digital Soil Mapping, and Soil Science

U. Werban, T. Behrens, G. Cassiani, and P. Dietrich

Abstract The Thematic Strategy for Soil Protection, prepared by the European Commission in 2006, concluded that soil degradation is a significant problem in Europe. Degradation is driven or exacerbated by human activity and has a direct impact on water and air quality, biodiversity, climate, and the quality of (human) life. High-resolution soil property maps are a major prerequisite for the specific protection of soil functions and the restoration of degraded soils, as well as for sustainable land use and water and environmental management. To generate such maps, a combination of digital soil mapping approaches and remote and proximal soil sensing techniques is most promising. However, a feasible and reliable combination of these technologies for the investigation of large areas (e.g. catchments and landscapes) and the assessment of soil degradation threats is still missing. There is insufficient dissemination – to relevant authorities as well as prospective users – of knowledge on digital soil mapping and proximal soil sensing from the scientific community. As a consequence, there is inadequate standardisation of the techniques. In this chapter we present the EU project iSOIL, which is funded within the 7th Framework Program of the European Commission. iSOIL focuses on improving and developing fast and reliable mapping of soil properties, soil functions, and soil degradation threats. This requires the improvement and integration of advanced soil sampling approaches, geophysical and spectroscopic measurement techniques, as well as pedometric and pedophysical approaches. Another important aspect of the project is the sustainable dissemination of the technologies and the concepts developed. For this purpose, guidelines for soil mapping on different scales, and using various methods for field measurements, will be written. Outcomes of the project's measurements will be implemented in national and European soil databases. The present state of knowledge and future perspectives will be communicated to authorities, providers of technologies (e.g. small and medium enterprises), and end-users.

U. Werban (✉)

UFZ – Helmholtz Centre for Environmental Research, Permoserstraße 15,
04318 Leipzig, Germany
e-mail: ulrike.werban@ufz.de

Keywords Geophysics · Geophysical transfer functions · Scorpan · Data mining · Sampling

8.1 Introduction

Soil erosion, decline in organic matter, local and diffuse contamination, sealing, compaction, decline in biodiversity, salinisation, floods, and landslides are serious threats to soil (Eckelmann et al., 2006). Soil degradation is accelerating, with negative effects on human health, natural ecosystems, climate, and the economy. In this context, the availability of high-resolution soil property maps is a major prerequisite for protecting and restoring soils. Existing databases for soils in Europe normally cannot provide such maps at sufficient resolution and coverage. Furthermore, these maps are often inconsistent and based on different soil mapping standards. Most soil properties are estimated in the field by soil surveyors, resulting in subjective, non-reproducible, and non-transferable data. Conventional, sample-based soil property mapping is time-consuming and expensive, and the data collected is only available for a few discrete points in a landscape. Thus, conventional soil mapping approaches are not reasonably applicable for large areas at high resolution and accuracy. The need to improve the current soil mapping toolbox has been recognised by the European Union as a result of its 'Thematic Strategy for Soil Protection' (European Commission, 2006).

The combination of geophysical methods and pedometrical techniques is one approach to improve the soil mapping toolbox. Various soil properties can already be mapped quasi-continuously in two dimension and in three dimension, using rapid and inexpensive methods (geophysics, infrared spectroscopy; see Chapters 3 and Chapter 19). However, the techniques available are deficient in terms of

- reliability and precision,
- the understanding of relationships between mapped soil parameters and relevant soil functions,
- transfer and application to large areas (e.g. catchments and landscapes), and
- the evaluation of soil degradation.

The EU project 'iSOIL: Interactions between soil related sciences – Linking geophysics, soil science, and digital soil mapping', financed by the European Commission within the 7th Framework Program, aims to overcome these deficiencies. The iSOIL consortium consists of 19 partners from 9 countries and contains universities, research organisations, and small- and medium-sized enterprises (<http://www.iSOIL.info>). The companion EU FP7 project is described in Chapter 7.

8.2 General Objectives

The focus of the iSOIL project is to develop new (and improve existing) strategies and innovative methods for generating accurate, high-resolution, soil property maps. At the same time, the developments should reduce costs compared to traditional soil mapping. The project tackles this challenge by integrating the following three major components:

- i. high-resolution, non-destructive geophysical, e.g. electromagnetic induction (Chapter 2), ground-penetrating radar (Chapter 25), magnetics (Chapter 20), seismics, and spectroscopic methods (Chapters 3, 11, 12, 13, 14, 15, 16, 17, and Chapter 18) and gamma spectroscopy (Chapters 27 and 28),
- ii. spatial interpolation and extrapolation concepts, e.g. geostatistics and machine learning (McBratney et al., 2003; Scull et al., 2003; Chapter 4), and
- iii. soil sampling and validation schemes to provide representative and transferable results (Brus et al., 2006; Behrens et al., 2009a; Chapters 1, 9, and 10).

Thus, within iSOIL we will develop, validate, and evaluate concepts and strategies for transferring measured physical parameter distributions into soil property, soil function, and soil threat maps of different scales, maps which are relevant to and demanded by the ‘Thematic Strategy for Soil Protection’ (European Commission, 2006). The final aim of the iSOIL project is to provide techniques and recommendations for high-resolution, economically feasible, and target-oriented soil mapping under realistic conditions.

8.3 Motivation of the Project

Global demand for low-cost, high-resolution digital soil maps can only be served partially at present (McBratney et al., 2003). Traditional soil sampling is labour-intensive, time-consuming, and very expensive. Additionally, only sparse datasets are generated. Scale, resolution, and information content of available soil class maps are not sufficient for applications such as GPS-based precision farming (Adamchuk et al., 2004). Soils are classified by soil surveyors using national, non-comparable, soil taxonomy systems instead of soil properties. As a result, soil maps are often not comparable.

Existing commercial single sensor systems are bound to a specific measurement depth. Relationships between sensor signals and soil properties are often non-linear and in some cases not understood. At the same time, new and emergent (geo-)physical techniques not yet in the commercial domain show promise for soil sensing.

Therefore, the following three topics are of major methodological interest, and we will briefly describe them.

8.3.1 Development of Geophysical Techniques

In recent years, various geophysical techniques have been developed for soil mapping based on the understanding that several soil properties correlate with physical parameters. For example, measurements of apparent electrical conductivity provide very useful soil information for precision farming (Chapter 19; Sudduth et al., 2001, 2005; Lück et al., 2002; Domsch and Giebel, 2004; Hedley et al., 2004; Werban, 2009). Maps prepared from radiometric surveys provide information about the parent soil and properties such as surface texture, weathering, leaching, soil depth, and clay types (Chapters 27, 28, and 29; Dickson et al., 1996; Viscarra Rossel et al., 2007; Wong et al., 2009). Extensive, geo-referenced soil maps for precision farming based on single geophysical sensors are commercially available, but only to a limited degree. Nevertheless, collection of integrated data from different techniques is currently only done at universities and research institutes, and most systems are still in the research stage. Further improvement in the integration of geophysical and meteorological sensors on platforms is needed. Combining multiple sensor data to derive a single soil property is the most promising approach to obtaining valid, high-resolution, and transferable results. However, exploring and developing emerging techniques, e.g. the derivation of mechanical properties using seismic methods and the characterisation of soil structures using spectral induced polarisation, is also part of iSOIL. Improvements of such techniques and development of concepts for platform integration are being sought (Chapters 31, 32, 33, and 34).

8.3.2 Development of Geophysical Transfer Functions

Since there is rarely a direct relationship between geophysical measurements and soil properties, a geophysical survey to generate a soil property map generally leads to ambiguous results. As in similar disciplines, such as well-log analysis (Doveton, 1986; Schön, 1997), it is expected that only suitable combinations of different geophysical quantities correlate unambiguously with the soil parameters of interest. At least in theory, searching for combinations that explain the soil parameter data should be equivalent to a principal component decomposition of the multi-parameter geophysical dataset. Even though a coherent view of how soil properties and soil state affect geophysical responses is lacking, a number of tentative constitutive laws exist linking certain geophysical properties to soil and rock properties (Chelidze and Gueguen, 1999; Rubin and Hubbard, 2005). Table 8.1 gives an overview of the main parameters acquired by geophysical methods and their related soil properties.

Development of geophysical transfer functions needs to be performed on the basis of both experimental results and theoretical work. In particular, two parallel lines of investigation need to be pursued: (i) the development of empirical and semi-empirical relationships between geophysical parameters and soil parameters, accounting for state variables (moisture content, salinity, and temperature), and (ii) the development of physically based relationships with the aid of numerical computation (pore scale models), including state variables. With the help of the

Table 8.1 Quantitative relationships of physical and soil parameters

ρ/σ	κ_M	v_{GPR}/ϵ_r	A_r/α	V_p	V_s	V_p/V_s	K	μs	γ	κ_h	$\tau, c, \rho_0, \rho_\infty$
θ	x		x	x	x	x				x	
S_w	x		x	x	x	x				x	
Φ	x		x	x	x	x				x	
ψ	x		x	x	x	x				x	
ρ_d				x	x	x	x	x			
TDS	x		x	x						x	
OC	x	x	x		x	x					
CC	x							x		x	
FeC	x										
T	x									x	
κ_h	x							x	x		

ρ , resistivity; σ , conductivity; κ_M , magnetic susceptibility; v_{GPR} , GPR velocity; ϵ_r , dielectric permittivity; A_r and α , GPR amplitude and attenuation; V_p , seismic P-wave velocity; V_s , seismic S-wave velocity; V_p/V_s , Poisson ratio; K , elastic bulk modulus, μs , shear modulus; γ , natural gamma-ray intensity; $\tau, c, \rho_0, \rho_\infty$, IP parameters; θ , vol. water content; S_w , saturation; Φ , porosity; ψ , water potential; ρ_d , density; TDS, total dissolved solids (salinity); OC, organic carbon content; CC, clay content (by cation exchange capacity); FeC, Fe content; T , temperature; κ_h , hydraulic conductivity

multi-parameter constitutive laws, geophysical measurements could then be used to map soil properties in a quick and efficient manner. This site-specific approach is the basis for an improved understanding of relationships and strategies for site-specific determination. Moreover, there is a need to investigate how flow and transport properties of soils could be assessed using geophysical parameters easily obtainable at the field scale.

8.3.3 Digital Soil Mapping

As most soil functions, soil threats, and environmental models (e.g. hydrological models) depend, in general, on soil properties, soil properties are the focus of the iSOIL project. Mapping soil properties is a more complex task than mapping soil classes in the field. Estimating soil properties in the field is limited by the soil surveyor's experience and is therefore subjective, susceptible to errors, and time-consuming. To overcome these shortcomings, (geo-)statistical and mathematical approaches have to be applied, as formulated in the scorpan paradigm introduced by McBratney et al. (2003), where a given soil property S can be mapped as a function of other soil properties s , climate c , organisms o , relief r , parent material p , age a , and space or spatial location n . Within the iSOIL project, new scorpan functions as well as environmental covariates will be tested.

Combining optimised sampling schemes (Chapter 1) with new and optimised data processing and digital soil mapping approaches could offer operational and economic benefits. Data collection would be based on improved and new geophysical measurements. Creating digital soil maps relies on data mining, geostatistics,

machine learning, and fuzzy logic. Thus, it is a challenge to not only find an optimal combination of geophysical sensors but also devise an accurate, optimised mapping technique that can cope with diverse levels of data availability and different landscape settings and can scale to map soil properties. The developed techniques and mapping tools need to be validated in terms of different soil functions and threats. Additionally, mapping and modelling approaches have to be tested at different landscape scales. Therefore, spatial data-mining approaches that operate across different scales have to be developed (Behrens et al., 2009b).

8.4 Structure of the Project

The project is structured as seven work packages (cf. Fig. 8.1). WP1 and WP2 develop and apply mobile measuring platforms by integrating existing geophysical, spectroscopic, and monitoring techniques and explore emerging technologies. WP3 will develop physically based transfer functions – so-called constitutive models – to establish site-specific relations between geophysical and soil parameters. The data generated by WP1–WP3 will be used in WP4 for digital soil mapping approaches. Furthermore WP4 will provide sampling schemes for WPs 1–3.

In terms of the expected impact of the project, it is necessary to demonstrate the capability of the technologies developed in WPs 1–4 to map soil functions, their suitability for different applications (e.g. management of soil threats, precision farming), and their economic feasibility for end-users. Therefore, the validation and selected application of soil property maps in soil threat models plays an essential role in the overall project. Field measurements, testing, and validation will be performed at field sites having different sizes and different threats. To indicate how the integrated framework might be applied at larger scales, a hierarchical design is

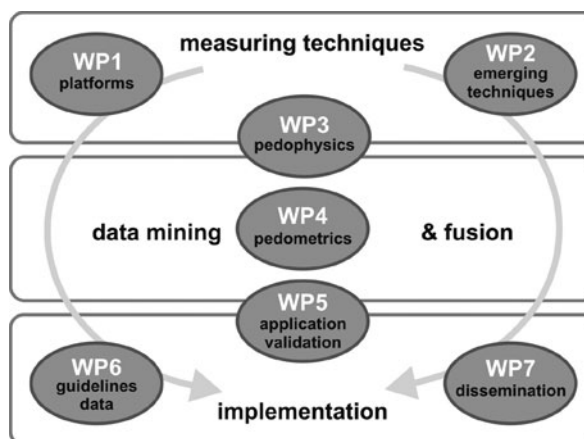


Fig. 8.1 Relation of the work packages to the overall tasks of the iSOIL project

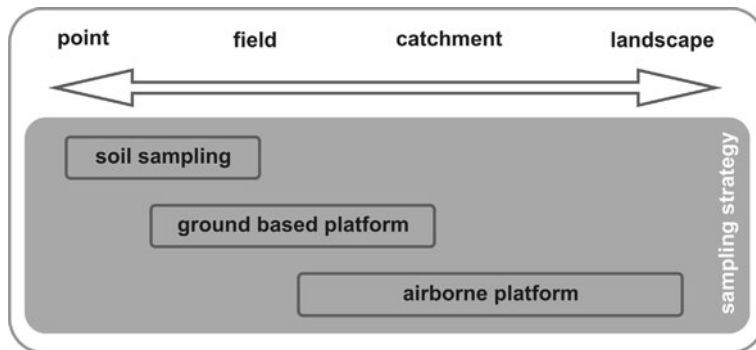


Fig. 8.2 Hierarchical iSOIL approach to data collection

chosen for the iSOIL project (cf. Fig 8.2). WP5 is responsible for the validation of the derived techniques and for exploring their application to studying soil threats. WP6 develops guidelines and standardisation, whereas WP7 prepares information for disseminating outcomes to end-users.

8.5 Conclusions

Within iSOIL we aim to assess and improve the integration of (multiple) geophysical datasets for digital soil mapping. One objective is the development of new, as well as improved, methods for mapping soil properties, including geophysical, spectroscopic, and monitoring techniques. In addition, different kinds of geophysical mapping technologies will be integrated into measuring platforms, allowing rapid (and economically feasible) mapping of large areas with multiple and complementary parameters. In this way, iSOIL will develop, validate, and evaluate necessary concepts and strategies for transferring measured physical parameter distributions into maps of soil properties and soil functions. Furthermore, iSOIL will develop sampling designs (for measurements, calibration, and validation) and pedometric approaches (for model and data integration, interpretation, mapping, and cross-scale analysis) to produce maps of soil properties, functions, and threats.

The major challenge within the iSOIL project is to seamlessly combine and integrate different measuring techniques, pedometric and geophysical approaches, enhanced DSM techniques, and subsequent modelling. We expect iSOIL will provide, at high acquisition rates, the most relevant soil properties, functions, and threats at high spatial resolution. The combined techniques will greatly improve digital soil maps and, in this way, planning and decisions related to soil.

Finally, iSOIL should provide realistic techniques and recommendations for high-resolution, economically feasible, and target-oriented soil mapping for a range of end-users. The project will transfer knowledge of concepts and technologies to authorities and small and medium enterprises in different European countries.

References

Adamchuk VI, Hummel JW, Morgan MT, Upadhyaya SK (2004) On-the-go soil sensor for precision agriculture. *Comput Electron Agric* 44:71–91

Behrens T, Scholten T (2006) Digital soil mapping in Germany – a review. *J Plant Nutri Soil Sci* 169:434–443

Behrens T, Schneider O, Lösel G, Scholten T, Hennings V, Felix-Henningsen P, Hartwich R (2009a) Analysis on pedodiversity and spatial subset representativity – the German soil map 1:1,000,000. *J Plant Nutri Soil Sci* 172(1):91–100

Behrens T, Zhu AX, Schmidt K, Scholten T (2009b) Multi-scale digital terrain analysis and feature selection for digital soil mapping. *Geoderma* 155(3–4):175–185

Brus DJ, de Grujter JJ, van Groenigen JW (2006) Designing spatial coverage samples using the *k*-means clustering algorithm. In: Lagacherie P, McBratney A, Voltz M (eds) *Digital soil mapping: an introductory perspective*. Develop Soil Sci 3. Elsevier, Amsterdam

Chelidze TL, Gueguen Y (1999) Electrical spectroscopy of porous rocks: a review. I. Theoretical models. *Geophys J Int* 137:1–15

Dickson BL, Fraser SJ, Kinsey-Henderson A (1996) Interpreting aerial gamma-ray surveys utilising geomorphological and weathering models. *J Geochem Explor* 57(1–3), 75

Doveton JH (1986) Log analysis of subsurface geology: concepts and computer methods. Wiley, New York, NY

Domsch H, Giebel A (2004) Estimation of soil textural features from soil electrical conductivity recorded using the EM38. *Precis Agric* 5:389–409

Eckelmann W, Baritz R, Bialousz S, Bielek P, Carre F, Houšková B, Jones RJA, Kibblewhite MG, Kozak J, Le Bas C, Tóth G, Tóth T, Várallyay G, Yli Halla M, Zupan M (2006) Common Criteria for Risk Area Identification according to Soil Threats. European Soil Bureau Research Report No.20, EUR 22185 EN, 94pp

European Commission (2006) Thematic strategy for soil protection communication. COM (2006) p 231

Hedley CB, Yule IY, Eastwood CR, Shepherd TG, Arnold G (2004) Rapid identification of soil textural and management zones using electromagnetic induction sensing of soils. *Aust J Soil Res* 42:389–400

Lück E, Eisenreich M, Domsch H (2002) Innovative Kartiermethoden für die teilschlagspezifische Landwirtschaft. In: Blumenstein O, Schachtzabel H (eds) *Stoffdynamik in Geosystemen*. Im Selbstverlag der Arbeitsgruppe Stoffdynamik in Geosystemen, Potsdam, 155pp

McBratney AB, Mendonça Santos ML, Minasny B (2003) On digital soil mapping. *Geoderma* 117(1):3–52

Rubin Y, Hubbard SS (2005) *Hydrogeophysics*. Springer, Dordrecht

Scull P, Franklin J, Chadwick OA, McArthur D (2003) Predictive soil mapping: a review. *Prog Phys Geogr* 27(2):171–197

Schön JH (1997) Physical properties of rocks: fundamentals and principles of petrophysics. In: Helbig K, Treitel S (eds) *Handbook of geophysical exploration – section i seismic exploration (on CD-ROM)*. Elsevier Science, Amsterdam

Sudduth KA, Drummond ST, Kitchen NR (2001) Accuracy issues in electromagnetic induction sensing of soil electrical conductivity for precision agriculture. *Comput Electron Agric* 31:239–264

Sudduth KA, Kitchen NR, Wiebold WJ, Batchelor WD, Bollero GA, Bullock DG, Clay DE, Palm HL, Pierce FJ, Schuler RT, Thelen KD (2005) Relating apparent electrical conductivity to soil properties across the north-central USA. *Comput Electron Agric* 46:203–237

Viscarra Rossel RA, Taylor HJ, McBratney AB (2007) Multivariate calibration of hyperspectral γ -ray energy spectra for proximal soil sensing. *Eur J Soil Sci* 58(1):343–353

Werban U, Kuka K, Merbach I (2009) Correlation of electrical resistivity, electrical conductivity and soil parameters at a long term fertilisation experiment. *Near Surf Geophys* 7:5–14

Wong MTF, Oliver YM, Robertson MJ (2009) Gamma-radiometric assessment of soil depth across a landscape not measurable using electromagnetic surveys. *Soil Sci Soc Am J* 73(4):1261–1267

Chapter 9

Conditioned Latin Hypercube Sampling for Calibrating Soil Sensor Data to Soil Properties

B. Minasny and A.B. McBratney

Abstract This chapter discusses methods for soil sampling that allow calibration of proximal sensor readings to soil properties. Conditioned Latin hypercube sampling (cLHS) was recently proposed as a method for sampling based on covariates obtained from proximal soil sensors. The method provides full coverage of the range of each variable by maximally stratifying the marginal distribution. A modification of cLHS was made so that it samples more on the edge of the distribution. This modification, called DLHS, is inspired by the D-optimality criterion in linear regression, where the design will place sample points on the corner of the distribution. We run a simulation to test the performance of cLHS. The simulation assumed a known form of the response function of EM38, EM31, and elevation to clay content. Results showed that when the form of the model is known, it is beneficial to place more sample points on the corners of the hypercube. When the form is unknown, conventional cLHS performs better.

Keywords Soil sampling · Calibration · Proximal sensor · Hypercube sampling

9.1 Introduction

An important aspect of soil sampling for high-resolution digital soil mapping is calibration (Chapter 1). There are several approaches to calibration sampling. The process usually involves surveying an area (a field) with on-the-go sensors, and soil sampling is required to provide calibration functions relating sensor readings (soil covariates) with soil properties. Once the calibration functions have been established, they are applied throughout the field to obtain high-resolution maps of soil properties. The goal of sampling in this application, according to Lesch (2005), is

B. Minasny (✉)

The University of Sydney, Faculty Agriculture, Food & Natural Resources,
John Woolley Building A20, Sydney, New South Wales 2006, Australia
e-mail: budiman.minasny@sydney.edu.au

selecting site locations that (1) can be used to optimise the fitting of a spatial regression model and (2) are representative of the total spatial variation for the targeted soil property or properties. A typical example is given by Lesch (2005), who developed an algorithm for the purpose of calibrating the electromagnetic induction (EMI) data to soil electrical conductivity and to clay content. The area was surveyed with an EMI equipment, and soil sampling was required to provide calibration functions relating EMI readings to soil clay content, water content, and electrical conductivity.

The design of calibration sampling aims to obtain a small number of samples so that they represent the predictor space effectively. Lesch (2005) developed an algorithm for calibration of electromagnetic induction (EMI) data. The sampling strategy not only covers a range of EMI values but also ensures a spreading of the location of the samples. The application of this sampling strategy is shown in Chapter 12. Hengl et al. (2003) proposed sampling along the principal components of the environmental covariates: the number of samples taken from each of the components is the proportion of the total variance described by each of the principal components. Other sampling designs for calibration are discussed in Chapter 1.

Minasny and McBratney (2006) argued that, for the purpose of spatial regression calibration, it would be beneficial to cover the range of values of each of the covariates using Latin hypercube sampling (LHS) (McKay et al., 1979). LHS is a procedure that ensures full coverage of the range of each variable by maximally stratifying the marginal distribution. LHS involves sampling n values from the prescribed distribution of each of k variables x_1, x_2, \dots, x_k . The cumulative distribution for each variable is divided into n equiprobable intervals. A value is selected randomly from each interval. The n values obtained for each variable are matched randomly with those of the other variables. This method does not require more samples for more dimensions (variables) (Fig. 9.1).

Another type of design optimised the variance of regression prediction using the so-called D-optimal design (St. John and Draper, 1979). The criterion used in generating D-optimal designs is to minimise the area of the confidence region for the linear model's parameter estimates or maximising the determinant of the information (covariance) matrix. The design adds 'axial' checkpoints and centre points or 'corners' of the distribution and is particularly useful if the model is linear. An example for two variables is given in Fig. 9.2.

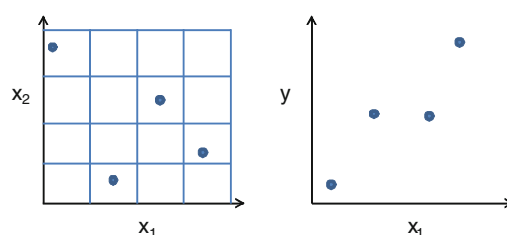
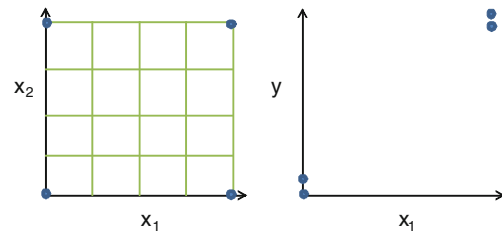


Fig. 9.1 Latin hypercube sampling for two covariates x_1, x_2 , and the assumed response to soil property y

Fig. 9.2 D-optimal design for an assumed two variables x_1 , and x_2 , and assumed response to soil property y



Inspired by the D-optimality criterion, we will modify the cLHS algorithm to place more sample points along the ‘axial’ or edge points of a hypercube. Then we will investigate its benefits for model calibration in a comparison with the conditioned Latin hypercube and simple random sampling.

9.2 Theory

A conditioned Latin hypercube sampling (cLHS) was proposed by Minasny and McBratney (2006) for sampling of existing covariates. We cannot directly apply conventional LHS to the multivariate distribution of covariates. Sample points selected by conventional LHS may represent combinations of the variables that do not exist in the real world (Fig. 9.3). Randomisation is used in this case as the distribution among the variables is not even, and some parts of the variable space might not correspond with existing soil.

For example, consider the EM38, EM31, and elevation data from Comet field in New South Wales, Australia (Fig. 9.4) (further examples will be given in Section 9.3). Figure 9.3 shows the scatter plot of the cumulative probability of EM38, EM31, and elevation as dots. Clearly, EM38 and EM31 are strongly

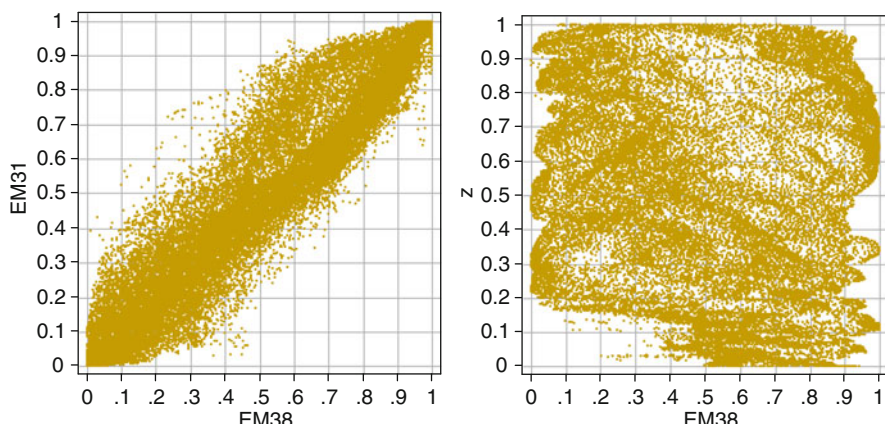


Fig. 9.3 Cumulative probability distribution of the EM38, EM31, and elevation data from the Comet field

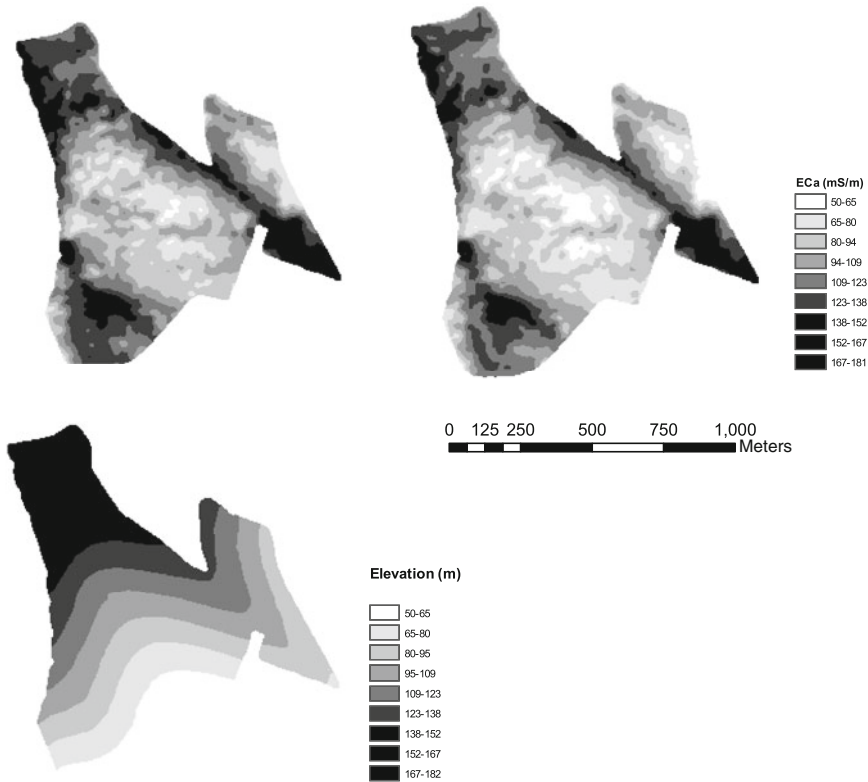


Fig. 9.4 EM38, EM31, and elevation from the Comet field

correlated, and the shape of the distribution between EM38 and elevation is uneven and some combinations do not exist.

The conditioned LHS algorithm attempts to select n observations (sites) from existing data which can form a Latin hypercube in the feature space. The algorithm solves an optimisation problem: given N sites with ancillary data (X), select n sample sites ($n \ll N$) so that the sampled sites x form a Latin hypercube. The method is a search algorithm based on heuristic rules combined with an annealing schedule.

The objective function to be minimised is an error criterion that counts the occupancy of the hypercube. First we define the sample size n , each component of X (size $N \times k$) is divided into n equally probable strata based on their distribution, and x (size $n \times k$) is a sub-sample of X . We define matrix η , which counts the number of x that fall into each of the defined strata:

$$\eta = \begin{bmatrix} \eta_{11} & \eta_{12} & \dots & \eta_{1k} \\ \vdots & \vdots & \ddots & \vdots \\ \vdots & \vdots & \ddots & \vdots \\ \eta_{n1} & \dots & \dots & \eta_{nk} \end{bmatrix}, \quad (9.1)$$

where the rows represent the strata s_1, \dots, s_n and the columns represents variables x_1, \dots, x_k . A true LHS will have values of 1 for all cells of matrix η ; we call this matrix η_o . The objective function is to minimise:

$$O = \|\eta - \eta_o\|. \quad (9.2)$$

A new conditioned LHS is proposed with importance placed on the ‘edge’ of the hypercube; we call it DLHS. We define parameter b , the importance of the edge of the distribution. For example, $b = 2$ means the edge of the distribution is twice more probable of being sampled than the rest. The objective is then to match the sampled matrix η to η_b :

$$\eta_b = \begin{bmatrix} b & b & b \\ 1 & 1 & 1 \\ \dots & \dots & \dots \\ b & b & b \end{bmatrix}. \quad (9.3)$$

We note that this is not a D-optimal design; it merely places importance on the edges of the hypercube.

9.3 Applications

We tested the LHS methods on the Comet field, situated in a property near Moree in the north-west of NSW. The area has been surveyed with on-the-go proximal soil sensors: EM38 (vertical mode), EM31, and elevation. The three variables were mapped at a resolution of 5×5 m using kriging with local variograms. The field is about 0.8 km^2 with 32,216 pixels.

For the purpose of this chapter, we postulated that we know the ‘true’ relationship between the proximally sensed covariates and the soil’s clay content (0–30 cm). Bulk electrical conductivity (EC_a) from EM38 and EM31 is assumed to have a positive correlation with the soil’s clay content (0–30 cm). This is in line with empirical observations and proposed theory on EC_a (McBratney et al., 2006). Elevation is assumed to have a negative correlation with clay content, which is a general feature observed in soil–landscape rules in erosional–depositional environments: areas at lower elevations tend to accumulate higher clay content. Both linear and nonlinear relationships between EC_a and elevation to clay content are postulated and given in Fig. 9.5.

The postulated ‘true’ clay content of the soil is a linear contribution from the three factors, with 50% from EM38, 25% from EM31, and 25% from elevation:

$$\text{True clay content (\%)} = 0.5f(\text{EM38}) + 0.25f(\text{EM31}) + 0.25f(z). \quad (9.4)$$

Normally distributed random numbers (mean = 0, variance = 1) were added to the ‘true’ clay content and represent measurement error and termed as ‘observed’ clay contents.

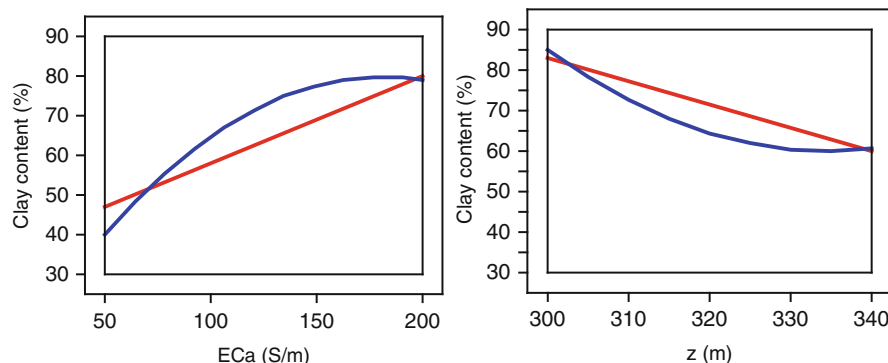


Fig. 9.5 ‘True’ linear and nonlinear models for the response of bulk electrical conductivity (EC_a) and elevation to the soil’s clay content

Three sampling methods are used to select samples of size 20 from the 32,216 data points:

- Conditioned Latin hypercube sampling (cLHS)
- Conditioned Latin hypercube sampling with importance (DLHS), where the edge of the hypercube is three times more likely to be sampled
- Simple random sampling (SRS)

The three sampling methods were performed 100 times (realisations). For each sampling method

- (1) Select 20 sample points from the whole data (32,216 sites)
- (2) Match the ‘observed’ clay for the 20 sample points
- (3) Fit a model predicting clay from the three covariates using either a linear or a quadratic function:
 - (a) a linear model, $\widehat{\text{Clay}} = \beta_0 + \beta_1 EM38 + \beta_2 EM38 + \beta_3 z$ on the linear relationships,
 - (b) a quadratic model, $\widehat{\text{Clay}} = \beta_0 + \beta_1 EM38 + \beta_2 EM38 + \beta_3 z + \beta_4 EM38^2 + \beta_5 EM38z + \beta_6 z^2$, on the quadratic relationships,
 - (c) a linear model, $\widehat{\text{Clay}} = \beta_0 + \beta_1 EM38 + \beta_2 EM38 + \beta_3 z$, on the quadratic relationships.
- (4) Apply the prediction model (a), (b), (c) to all data (32,216 sites)
- (5) Calculate the RMSE $\sqrt{1/n \sum_{i=1}^n (\widehat{y} - y)^2}$ for (a), (b), and (c).

9.4 Results and Discussion

Figure 9.6 shows an example of using DLHS where the edge of the distribution has a threefold greater probability of being sampled than the rest. We can see that DLHS samples more densely the edge of the distribution compared to cLHS (Fig. 9.7).

The sampling locations and position in the distribution of one sampling realisation of 20 sample points are given in Fig. 9.8.

Figure 9.9 shows the root mean squared error for predicting clay content using the three types of sampling. When the relationship between the covariates and clay content is known (i.e. linear or quadratic), DLHS produces lower RMSE than cLHS and SRS; thus it appears to be a better sampling method. However, when we fit a linear model to quadratic relationships, the conventional cLHS gives lower RMSE compared with DLHS. SRS shows the largest RMSE for all.

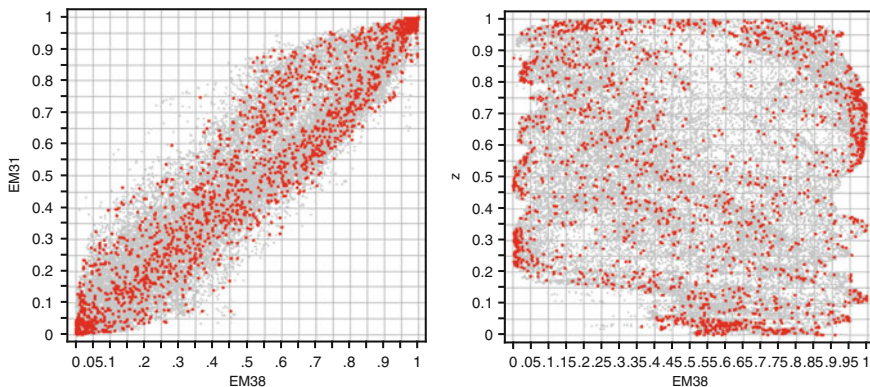


Fig. 9.6 Sample points selected using DLHS with 100 samples of size 20, where sampling at the edge of the distribution was given three times more probability than the rest of the distribution

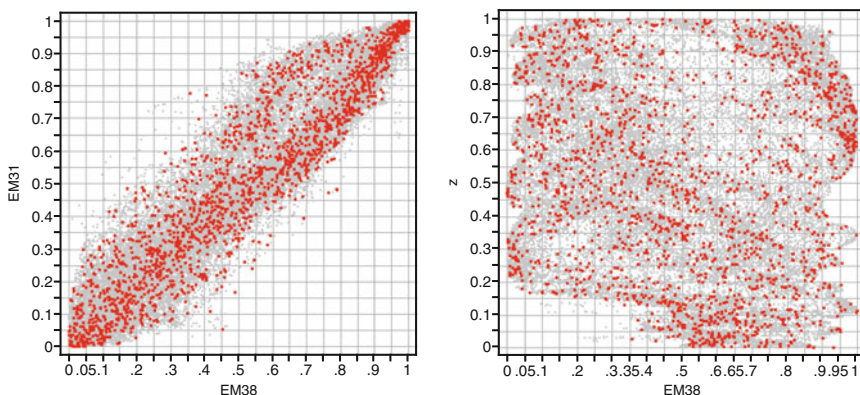


Fig. 9.7 Sample points selected using cLHS with 100 samples of size 20

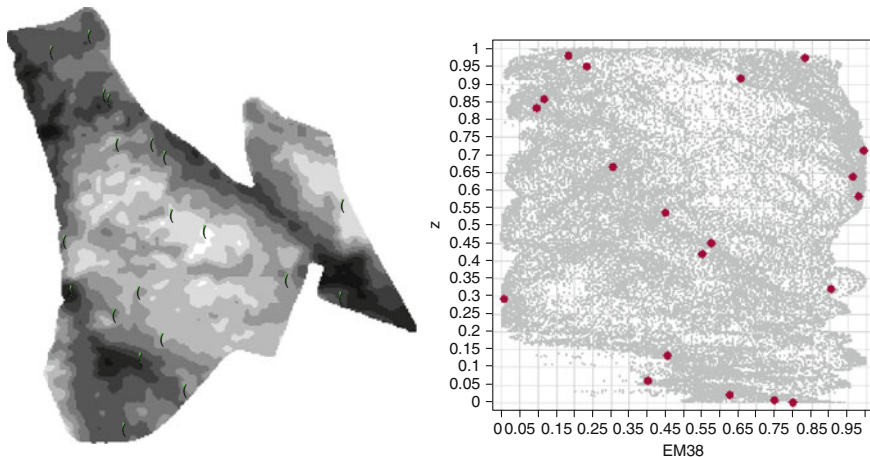


Fig. 9.8 Location of sample points selected using DLHS and their position in the distribution function

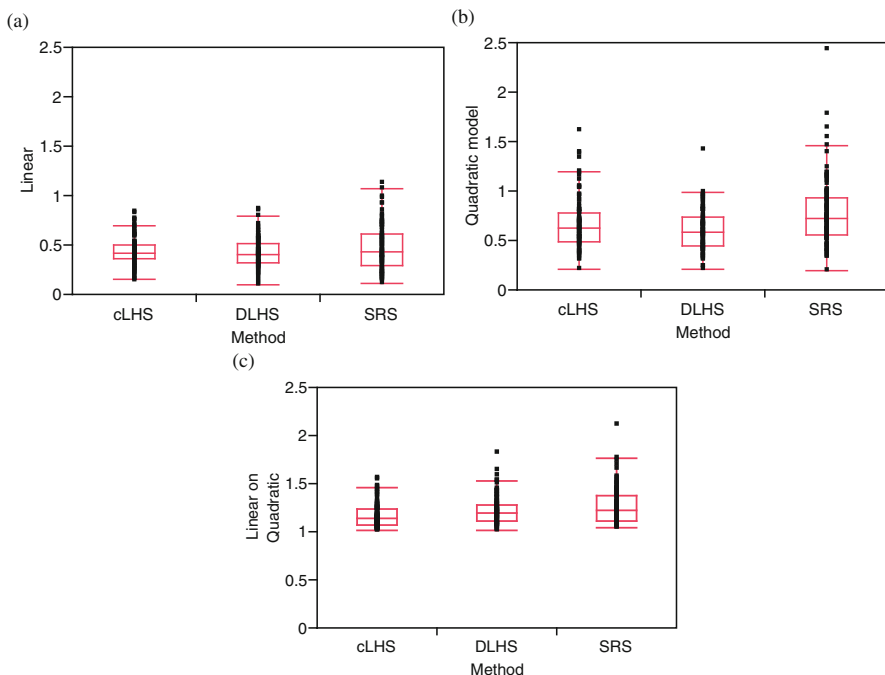


Fig. 9.9 RMSE for 100 realisations for the three sampling methods using (a) linear model, (b) quadratic model, and (c) linear model on quadratic relationship between the covariates and the soil's clay content

From these empirical results, we can conclude that if we know the relationships between covariates and soil properties (correct model assumption), sampling with emphasis on the edge of the distribution may be useful for calibration. However if the relationships are not known, but are assumed to be linear (incorrect model assumption), cLHS performs better as it ensures adequate ‘spread’ of data along the distribution. In real situations, most often we know little about the model structure, and it has to be inferred from the sample data as well.

The above exercise is by no means comprehensive and is intended to show the application of the cLHS method. One can use the D-optimal design for sampling with an assumed linear model and assuming the error to be spatially independent. Alternatively, a more sophisticated model which minimises the variance of universal kriging can be applied (Brus and Heuvelink, 2007). However, that model requires the form of the relationship to be known *a priori* and, in the case for universal kriging, the variogram of the residuals also needs to be assumed. While some relationships between covariates and soil properties are known and can be assumed to be linear, many relationships are dependent on the landscape and not known *a priori*. Furthermore, in digital soil mapping soil sampling is conducted for calibration of not only one soil property but several soil properties at once. Thus we believe that the cLHS method, which attempts to cover the whole multivariate distribution, works well for this purpose. Additional coverage at the edge of the distribution may be beneficial when we know the type of relationship – e.g. EC_a and clay content.

Finally, an important question about calibration sampling is, how good are predictions by the models inferred from the samples selected via the sampling method? Further work will include examining sampling method and choice of model structure in the simulation:

sampling → model selection → model fitting → prediction → validation.

Acknowledgement We thank Jaap de Gruijter for his comments and suggestions on the chapter.

References

Brus DJ, Heuvelink GBM (2007) Optimisation of sample patterns for universal kriging of environmental variables. *Geoderma* 138:86–95

de Gruijter JJ, McBratney AB, Taylor J (2008) Sampling for high resolution soil mapping. Global workshop on high resolution digital soil sensing and mapping. The University of Sydney, Australia, 5–8 February 2008

Lesch SM (2005) Sensor-directed spatial response surface sampling designs for characterising spatial variation in soil properties, *Comput Electron Agric* 46:153–180

McBratney AB, Minasny B, Whelan BM (2005) Obtaining ‘useful’ high-resolution soil data from proximally-sensed electrical conductivity/resistivity (PSEC/R) surveys. *Precision Agriculture* ’05. Stafford JV (ed) pp 503–510

McKay MD, Beckman RJ, Conover WJ (1979) A comparison of three methods for selecting values of input variables in the analysis of output from a computer code. *Technometrics* 21:239–245

Minasny B, McBratney AB (2006) A conditioned Latin hypercube method for sampling in the presence of ancillary information. *Comput Geosci* 32:1378–1388

St. John RC, Draper NR (1975) D-optimality for regression designs: a review. *Technometrics* 17:15–23

Chapter 10

Response Surface Sampling of Remotely Sensed Imagery for Precision Agriculture

G.J. Fitzgerald

Abstract Estimating biophysical characteristics of land surfaces using imagery or spatially contiguous datasets derived from proximal sensors requires developing statistically robust predictive models between the spatial data and ground features. These spatial datasets can contain thousands to millions of points or pixels, so determining the number and location of ground samples to calibrate models is critical. Zoning and co-kriging approaches have been used to identify sampling locations, but they suffer from either ambiguous location identification or the need for 60 or more ground points to produce robust models. In this study, the software ‘EC_e Sampling, Assessment, and Prediction’ (ESAP) was used to select sampling locations from high-resolution (4 m) imagery of a barley crop to develop a predictive regression model for biomass. A normalised difference vegetation index was derived from imagery of an 80 ha field near Rupanyup, Victoria, Australia in 2006. The ESAP software was originally developed to calibrate apparent soil electrical conductivity data to model soil salinity based on response surface theory, but any geo-located spatial dataset can be input. Results showed that the 12 ESAP-selected points produced a statistically significant regression model unbiased by spatial auto-correlation and was better able to predict biomass than models derived from 12 random points and a pooled model derived from 24 sample locations. The correlations between the selected pixels in the imagery and biomass ($r^2 = 0.38$) were not as high as from ground spectral data ($r^2 = 0.79$) collected coincident with biomass sampling, possibly due to misalignment between the imagery and ground data. Digital output from this approach could be used to map soil or plant properties, schedule variable rate applications of chemicals, or be used as inputs to soil and crop simulation models for more accurate site-specific modelling.

Keywords Remote sensing · ESAP · ENVI · NDVI · Vegetation index · Response surface

G.J. Fitzgerald (✉)

Department of Primary Industries, 110 Natimuk Rd., Horsham, VIC 3401, Australia

e-mail: glenn.fitzgerald@dpi.vic.gov.au

10.1 Introduction

Measuring biophysical and soil features across a landscape is not feasible without using some type of spatial dataset derived from sensors. Whether these sensors have direct contact with the surface being measured (Stenberg and Viscarra Rossel, Chapter 3) or sense remotely (e.g. imagers), they generally do not directly measure the parameter of interest. It is also not practically feasible to sample all points within the entire area of interest, so sampling routines and predictive equations must be developed to relate the sampled data to the larger area of interest. Number of samples, cost, and how to sample are all important variables (De Grujter et al., Chapter 1) and need to be optimised.

Remotely sensed imagery can provide valuable information about the spatial distribution of crop and soil characteristics. Fine-scale imagery of fields can contain millions of data points (pixels). If the objective is to develop a relationship between the imagery and ground data so that crop and soil characteristics can be mapped, then sampling issues (number and location of sites) become critical. The cost of physical sampling can limit the number of samples collected, but sufficient samples are required to produce a robust relationship between the imagery and biophysical measurements.

There are different techniques to relate ground data to imagery. Zone maps can be produced using classification routines commonly available in software, based either on the range of data values in the imagery or between imagery and ground data after regressions have been developed. One concern, however, is that regression statistics require sample independence. If they are not independent, then the correlation coefficients can be inflated and misleading (Stein et al., 2002). Thus, spatial autocorrelations must be removed or reduced to minimise their impact on the developed relationships. Techniques such as co-kriging can be used to account for spatial autocorrelations, but they require 60 or more points of ground data for model development (Lesch et al., 1995a).

The 'EC_e Sampling, Assessment, and Prediction' (ESAP) software was used here to select a small set of sites for directed ground sampling from imagery used as input. The software minimises the possibility of spatial autocorrelations in the model residuals by separating out the sampling locations as far as possible. It also provides for robust regressions by simultaneously selecting points with a large range of values from the imagery. The ESAP software assumes that a linear or low-order quadratic relationship exists between the input spatial dataset (imagery) and the ground data of interest. It was originally developed to direct soil sampling for calibration of electromagnetic induction data for estimation of soil salinity (EC_e) from apparent soil electrical conductivity (EC_a) survey data (Lesch et al., 2005, and reference therein). However, since it requires a spatial dataset as input, any geo-located data can be used. The theoretical and operational details of this software have been thoroughly described (Lesch et al., 1995a, b; Lesch et al., 2000; Lesch, 2005) and a more detailed description of the technique discussed here is presented in Fitzgerald et al. (2006).

The objective of this research was to use the ESAP software to provide geo-registered locations for plant biomass sampling based on input of imagery acquired over a field planted to barley and determine whether the predictive equation was statistically robust. Aerial imagery (normalised difference vegetation index, NDVI) was substituted for EC_a and crop biomass (dry) for EC_e in the ESAP software, allowing for the production of predictive maps of crop dry matter. Although plant data were used as the ground 'truth' data, soil characteristics or any spatially discrete dataset (geo-located) could be used.

10.2 Material and Methods

10.2.1 *Remote Sensing and Image Processing*

Multispectral imagery was acquired from a Cessna 206 flying at 3,050 m (10,000 ft) above an 80 ha barley field planted near Rupanyup, Victoria, Australia ($36^{\circ}41.1' S$, $142^{\circ}33.5' E$), on 8 August 2006 at 12:30 local time under clear skies. The imagery was collected from an MS3100 imaging system (Redlake Inc., San Diego, CA) custom designed with three narrow spectral bands centred at 670 (25), 720 (10), and 790 (25) nm with 8-bit resolution. Numbers in parentheses are bandwidths in nanometres. The imager had a $15^{\circ} \times 20^{\circ}$ field of view. Ground pixel resolution was about 1 m. Imagery was converted to reflectance using ground tarps of known reflectance located near the field.

The software ENVI (ITT, Boulder, CO) was used for all image processing. The 3-band image was converted to an NDVI using the 670 and 790 nm bands $[(790 - 670 \text{ nm})/(790 + 670 \text{ nm})]$. Trees, roads, canals, and other features not of interest were masked out. Because ESAP limits input data file size to 30,000 points, the number of pixels was reduced by resampling the 1 m pixels to 4 m and excluding NDVI values less than 0.53. This also ensured that locations would have plants available for ground sampling. These data were exported as text for input to the ESAP software.

10.2.2 *Directed Sampling*

The ESAP software is composed of several modules. The ESAP-RSSD (response surface sampling design) module assesses the input geo-located dataset and selects a subset of sites that are then used to direct ground sampling to the proper locations in order to build a predictive regression equation for all unsampled locations. Once the data are entered in the proper format (Lesch et al., 2000), the software provides the opportunity to remove outliers based on standard deviations from the mean. This is an iterative process that ends when there are no more outliers above 4 standard deviations (default) from the mean or a value selected by the operator. Sample designs are then produced that space the sample locations apart to minimise

spatial autocorrelations. Each sampling design is assigned an ‘optimisation criterion’ (Opt Cri) which is a measure of spatial uniformity of the sample design. The operator can choose the design with the lowest Opt Cri, or another if desired. Values below 1.30 are desirable (Lesch et al., 2000), although greater values can be acceptable even though they indicate more clustering of data points. The default setting selects 12 geo-registered calibration locations for sampling (6 and 20 can also be chosen), thus directing the user to these locations. Further details of the selection procedure and use of the software can be found in Lesch et al. (2000) and Fitzgerald et al. (2006).

The ESAP-RSSD software requires that the data meet two basic assumptions in order to produce accurate sampling designs (Lesch et al., 1995a, b): (1) A linear relationship must exist between the crop attributes (e.g. biomass) and the covariate (remotely sensed geospatial data) and (2) the residuals of the regression model between the crop attribute and the covariate must be spatially uncorrelated.

One feature of the software is its tendency to select points along the edges of the input dataset. This occurs because the software attempts to evenly distribute the data to reduce spatial autocorrelations. Although there is nothing inherently or statistically wrong about this, the input data must not contain anomalous data along edges (such as roads and houses) and thus require preprocessing to remove those features not related to the parameter(s) of interest.

10.2.3 *Ground Sampling*

Plant samples were collected from 24 ground locations 2 weeks after image acquisition. The barley plants were at growth stage DC 35 (five nodes) at sampling time (Zadoks et al., 1974). Exactly 12 of these locations were identified using the ESAP software (designated ‘ESAP’); 12 others were randomly selected sites using the random number function within Microsoft Excel (designated ‘RND’). These were used for validation of the data from the ESAP-selected locations. Ground points were located using a Trimble Ag132 GPS (Trimble Navigation Limited, Sunnyvale, CA). At each location, 1 m lengths of above-ground biomass were cut from four separate rows within a 2 m radius of the centre of each location in order to collect a representative sample to compare to the 4 m pixels. Plant matter was weighed, dried at 100°C, re-weighed, and dry matter (DM, g/m²) calculated.

Narrow-band remote sensing sensor data were also collected at the time of ground sampling from each of the 24 locations using a FieldSpec Pro spectroradiometer (Analytical Spectral Devices, Boulder, CO). These measurements represented about 1 m diameter areas of the crop and were radiometrically corrected to reflectance by measuring a white reference Spectralon plate (Labsphere, North Sutton, NH) immediately after each location measurement. This is a standard method for converting raw spectral data to reflectance. Reflectance is a physical measure of the amount of light reflected from a surface under prevailing lighting conditions and accounts for changes in atmospheric transmittance and sun angle.

10.2.4 Statistical Analysis and Mapping

The ESAP-Calibrate module was used to develop a regression relationship (a calibration) between the spatial dataset (NDVI) and the ground reference data (biomass). It was used to derive statistical parameters for four datasets [ESAP points, RND points, Pooled data (ESAP + RND), and the ground data]. The output included the Moran statistic for spatial independence (I_{MS}), root mean square error (RMSE), and predictive equations for developing a regression model to estimate dry matter (DM) biomass at all non-sampled locations ($DM = b_0 + b_1 \times NDVI$, where b_0 = intercept and b_1 = slope). Once the image was calibrated to biomass, an unsupervised IsoData classification routine available within ENVI was used to delineate zones within the image map produced.

10.3 Results and Discussion

Since the objective was to develop accurate predictive models for biomass, spatial autocorrelation was assessed to provide confidence that the regression coefficients were not inflated. Four different datasets were tested (Table 10.1) based on the biomass and NDVI data from the 24 locations (Fig. 10.1). Since the p -values ($p I_{MS}$) for the Moran statistic for the model residuals were not significant ($p > 0.05$) for any of these, the points chosen could be modelled as simple regressions without spatial bias. Note that the degree of spatial autocorrelation can be seen in the Pooled data. As the number of points in the model increased from 12 to 24 (and the mean distance between points decreased), the significance of the Moran statistic ($p I_{MS}$) decreased.

Correlation coefficients of NDVI vs. DM (Fig. 10.2, Table 10.1) show that the ESAP points provided statistically significant results ($p < 0.05$), although the relationship was not very robust ($r^2 = 0.38$). The regression between NDVI and DM with RND points was not statistically significant (n.s.). Pooling the ESAP and RND points showed a significant relationship ($p = 0.007$), but again the relationship was not strong ($r^2 = 0.28$). Other biophysical factors were calculated, such as leaf area index and plant nitrogen (N/m^2), and these had strong relationships to biomass (data not shown). When these were regressed against the ground-based and image-based NDVI, the data scatter and relationships were similar to biomass (so

Table 10.1 Regression statistics for predictive equations between NDVI and dry matter (DM, $g m^{-2}$)

DM prediction using	Slope	Intercept	R^2	p	RMSE	I_{MS}	$p I_{MS}$
ESAP-selected, 12 points	225.2	-40.2	0.38	0.030	27.9	-0.20	0.84
RND-selected, 12 points	-	-	0.06	0.46 n.s.	-	-0.26	0.84
Pooled, 24 points	206.9	-25.2	0.28	0.007	26.7	-0.04	0.46
Ground-measured (ESAP)	877.3	-572.9	0.79	0.0001	16.1	-	-

Fig. 10.1 Normalised difference vegetation index of 80 ha field. Symbols indicate sampling locations (\circ = ESAP, \bullet = RND). Brighter pixels indicate more plant biomass

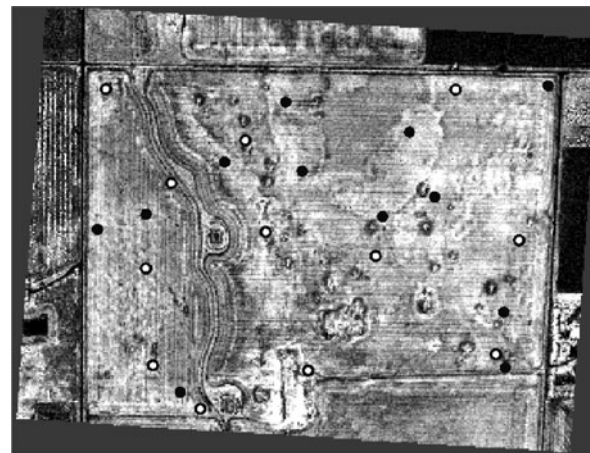
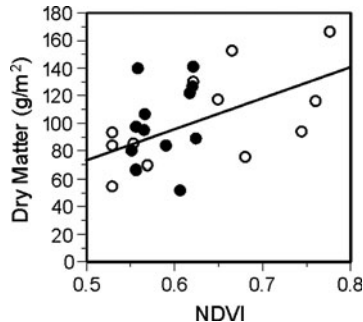


Fig. 10.2 Regression line for the ESAP (\circ) points with the RND (\bullet) points overlaid (not included in regression)



these would not have added to the discussion and are not presented, but could be predicted and mapped similarly to biomass).

The validity of the ESAP point selection process and the strength of the regression are two separate issues. Model validity can be assessed by comparing with an independently designed and sampled dataset, such as that provided by the 12 RND points. The DM values at the RND locations and the ESAP locations overlay each other, thereby representing the same data space (Fig. 10.2). Given that the slope and intercept of the ESAP and Pooled points are virtually the same (and not statistically different), there is confidence that the ESAP model properly describes the relationship and that the 12 points selected by ESAP were just as good as (or better than, in this case) the larger set of 24 points. The linear assumption of the relationship between NDVI and DM is shown to be valid by comparing the NDVI measured with the spectroradiometer directly over the sample locations with DM (Table 10.1, $r^2 = 0.79$). More comprehensive tests for assessing model robustness are presented in Fitzgerald et al. (2006), but since the results presented here showed the same trends as in the previous study, these tests were not duplicated.

It is possible for this directed sampling (or any modelling) approach to be statistically valid but produce equations that have low accuracy for the predicted variable because of data scatter. Data from the co-located ground NDVI and biomass samples showed that this relationship is fundamentally strong ($r^2 = 0.79$, Table 10.1). The weaker relationship between the imagery and ground data ($r^2 = 0.38$) is likely due to any or all of the following: inaccuracy of the DGPS (2 m accuracy), slight mis-registration in the data (1 pixel shift represented 4 m), the delay in ground sampling, or issues of scaling (Lovejoy et al., 2008). This last point is more critical when considering the ability of using imagery to estimate ground parameters. Scaling and sampling have not been well addressed in the remote sensing community and may represent the missing link in the ability to produce accurate maps derived from remote sensing.

The RND model chose values that did not result in a significant relationship between NDVI and DM (Table 10.1, Fig. 10.2). Although the distribution of points across the field was dispersed (Fig. 10.1), the actual range of values was more restricted than the ESAP-selected sites (Table 10.2). In addition to separating the sample locations in space, ESAP selects a wide range of data values to improve the predictive relationship developed. Including a greater range of values also reduces the chances of extrapolation errors beyond the model results. Random sampling cannot guarantee either spatial or value separation of points for development of optimal regression models.

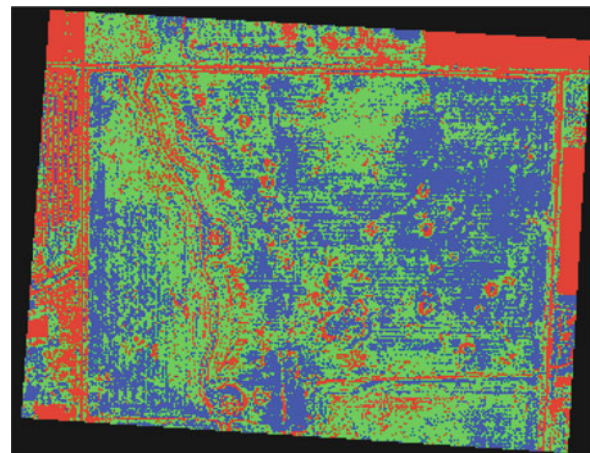
Since the model derived from the ESAP-selected locations was statistically significant and coincided with the Pooled dataset, the slope and intercept in Table 10.1 for the ESAP-selected data was applied to the NDVI image (Fig. 10.1) to derive a biomass map. A classification routine applied to the imagery emphasises differences across the landscape (Plate 10.1). The red colour shows known areas of soil including roads, bare areas around trees, fence lines, and dry stream channels. The green and blue areas were arbitrarily divided into low and high NDVI zones for display. A figure illustrating a continuously variable map is also possible and would look similar to Fig. 10.1.

The ESAP software maximises the probability that a sampling design will be generated that yields a regression model with spatially uncorrelated residuals. If the average sampling distance is less than the residual spatial correlation distance, then the residuals will show spatial dependence, inflating the correlation coefficient. Absent spatial dependence, this approach generates a simple regression model requiring few points for prediction of plant and soil characteristics across the landscape. Other indices relating to soil colour, texture, or chemical constituents could

Table 10.2 Univariate statistics (NDVI values) for ESAP, RND, and Pooled datasets

Dataset	Mean	Min	Max
ESAP points	0.64	0.53	0.78
RND points	0.59	0.55	0.63
Pooled points	0.61	0.53	0.78

Plate 10.1 Classified dry matter (DM) image (three zones). *Green* = low DM (72 g m^{-2} [11]), *blue* = high DM (106 g m^{-2} [12]), *red* = soil. Numbers in parentheses are class means and in square brackets standard deviations



be input regardless of sources, as long as they are geo-located and satisfy the model assumption of having a linear or near-linear relationship to the ground factor of interest.

10.4 Conclusions

Ground sampling and validation are the ‘missing links’ between remotely sensed imagery and quantified measures of ground features of interest. Sampling techniques that require many ground locations for validation are neither practical nor cost-effective and are unlikely to be put into wider practice. The advent of ever more readily available spatial datasets requires simpler tools for sampling. Although imagery was used here as an example, it should be noted that spatially contiguous datasets derived from any source, including proximal sensors, could be used as input and then calibrated to create useful maps of the parameter of interest.

The ESAP software presented here allows a spatial dataset to be calibrated by selecting 12 points within the dataset. It spatially distributes the data points to minimise, but not eliminate, the chance of spatial autocorrelations. It provides statistics for the user to understand the relationships and patterns in the data. It assumes that the spatial dataset (image) and ground data of interest (e.g. biomass) are linearly or nearly linearly related. It also requires geo-located points as input. The software is freely available and can be learned quickly.

This sampling strategy to link spatially explicit remotely sensed and ground data has the following advantages over other sampling methods:

- (1) Identifies unambiguous locations for sampling (unlike zoning);
- (2) Requires relatively few ground points to build the regression (calibration) model (unlike co-kriging);

- (3) Uses any spatially explicit dataset as input;
- (4) Minimises chance of spatial autocorrelations;
- (5) Produces continuously variable maps of the ground factor of interest.

Acknowledgements The author would like to thank the Our Rural Landscape project, a Victorian government initiative, for financial support. Hard work and dedication from Russel Argall and other technical staff made this chapter possible.

References

Fitzgerald GJ, Lesch SM, Barnes EM, Luckett WJ (2006) Directed sampling using remote sensing with a response surface sampling design for site-specific agriculture. *Comput Electron Agric* 53:98–112

Lesch SM, Strauss DJ, Rhoades JD (1995a) Spatial prediction of soil salinity using electromagnetic induction techniques: 1. Statistical prediction models: A comparison of multiple linear regression and co-kriging. *Water Resour Res* 31:373–386

Lesch SM, Strauss DJ, Rhoades JD (1995b) Spatial prediction of soil salinity using electromagnetic induction techniques: 2. An efficient spatial sampling algorithm suitable for multiple linear regression model identification and estimation. *Water Resour Res* 31:387–398

Lesch SM, Rhoades JD, Corwin DL (2000) The ESAP-95 version 2.01R User Manual and Tutorial Guide. Research Report No. 146. USDA-ARS. In: George E. Brown, Jr. (ed) Salinity Laboratory, Riverside, CA, <http://www.ussl.ars.usda.gov/lcrsan/esap95.pdf>. Accessed 9 Jul 2009

Lesch SM (2005) Sensor-directed response surface sampling designs for characterizing spatial variation in soil properties. *Comput Electron Agric* 46:153–179

Lovejoy S, Tarquis AM, Gaonac'h, H, Schertzer D (2008) Single and multiscale remote sensing techniques, multifractals and MODIS-derived vegetation and soil moisture. *Vadose Zone J* 7:533–546

Stein A, van der Meer F, Gorte B (2002) Spatial statistics for remote sensing. Kluwer Academic, Dordrecht

Zadoks JC, Chang TT, Konzak CF (1974) A decimal code for the growth stages of cereals. *Weed Res* 14:415–421

Part III

Soil UV, Visible, and Infrared

Spectral Sensing

Chapter 11

Mid- Versus Near-Infrared Spectroscopy for On-Site Analysis of Soil

J.B. Reeves, G.W. McCarty, and W.D. Hively

Abstract Research has demonstrated that for the determination of soil carbon, diffuse reflectance infrared Fourier transform spectroscopy (DRIFTS) is often more accurate and produces more robust calibrations than near-infrared (NIR) reflectance spectroscopy (NIRS) when analysing ground, dry soils. But DRIFTS is not considered feasible on non-dried samples due to the strong water absorptions in the mid-infrared. Also, mid-infrared spectrometers are generally either sealed from the ambient atmosphere or purged with CO₂-free dry air. While DRIFTS has been shown to be advantageous in the laboratory, if samples need to be ground and dried and instruments purged, it may not be practical for on-site analysis. The objective of this research was to determine the effect of ambient atmospheric conditions and soil state (ground, dried, etc.) on DRIFTS and NIRS calibrations for soil C and N. Results using a portable DRIFTS spectrometer over a wide range of ambient conditions demonstrated that purging is not necessary to obtain calibrations for C in soils equal to those obtained in the lab with dry or dried-ground samples. However, efforts with field-moist samples have demonstrated that while calibrations using DRIFTS can be developed with an accuracy equal to those obtained using NIRS, the calibrations may not be as robust and more research is needed. Comparing these results with results obtained using large-scale scanning such as remote imaging or in situ NIR (scanning on the fly with a tractor-drawn NIR unit) indicates that soil analysis in which the sample is analysed by both traditional analysis (combustion) and spectroscopic analysis as performed here results in better calibrations. However, a much smaller area of the total field is sampled. An important question that emerges is Which is more valuable, lots of lower quality information or much less information, but of perhaps much higher quality?

Keywords Soil analysis · Soil carbon · Soil nitrogen · Mid-infrared · Near-infrared · NIR

J.B. Reeves (✉)

USDA Environmental Management and Byproduct Utilization Laboratory,
Beltsville, MD 20705, USA
e-mail: james.reeves@ars.usda.gov

11.1 Introduction

Near-infrared (NIR) reflectance spectroscopy (NIRS) has been used for decades for the analysis of a wide variety of agricultural materials including grains and forages (Roberts et al., 2004). More recently mid-infrared (mid-IR) diffuse reflectance spectroscopy (DRIFTS) has been shown to be capable of such determinations, e.g. ground forages (Reeves, 1996), grains (Reeves and Delwiche, 1997), and soils (Janik et al., 1998; Reeves et al., 2001, 2002), without the customary KBr dilution pretreatment used in mid-infrared spectroscopy. The soil results have indicated DRIFTS to be more accurate than NIRS for the determination of C and spectral interpretation much easier due to the more advanced state of mid-IR spectral interpretation (Smith, 1999).

Recently, interest has greatly increased in the concept of sequestering carbon in soils to help remediate increasing atmospheric CO₂. The question of how soil C will be determined, if credits are given, has yet to be determined. It can be imagined that the ability to determine soil C on-site could be of benefit, e.g. one could do a quick survey of the field in order to determine the best locations for selecting samples for C analysis based on C variability. However, several interrelated questions remain to be answered if on-site analysis of samples – either as a preliminary survey, or even as a final means to determine the soil C content, or other measures such as N – is to be feasible, including what is the best spectral range to use, or even if such spectral methods are the best procedure? The objective of this work was to examine NIRS, DRIFTS, laboratory-based, field portable, and remote sensing spectroscopic-based methods under a variety of soil sample conditions [field-moist (FM), dried, and sieved but not ground (DRYSV), and dried, sieved, and ground (DRYSVGRN)] to determine the feasibility of on-site analysis of soils for total C and total N.

11.2 Materials and Methods

11.2.1 Soil Samples

In order to obtain as wide a range of C as possible, 67 soil cores (0–30 cm) were obtained from a site at the USDA Beltsville Agricultural Research Center (BARC) based on a previous mapping of carbon values (no consideration of N content was taken in the sampling design). Each core was sectioned into three sub-samples, 0–10, 10–20, and 20–30 cm, yielding 201 samples. After scanning FM, sub-samples were dried at 50°C for 2 days and crushed using a hammer mill. The crushed material was further ground in scintillation vials using a SampleTek vial rotator (SampleTek, Science Hill, KY). Finally, a set of 403 FM samples was obtained from five bare-soil (recently ploughed) fields on the Eastern Shore of Maryland and another 125 FM from the original site at BARC.

11.2.2 Compositional Determination

All C and N values (Table 11.1) were determined by combustion on samples which had been DRYSVGRD as indicated in Section 11.2.1 using either an Elementar Analysensysteme vario MAX CNS elemental analyser (Elementar Americas, Mt. Laurel, NJ) or a Leco TruSpec CN analyser (Leco Corp., St. Joseph, MI).

Table 11.1 Percent C and N values for all 201 soil samples examined

Variable	N	Mean	SD	Minimum	Maximum
Carbon	201	0.91	0.58	0.11	2.63
Nitrogen	201	0.13	0.09	0.02	0.39

11.2.3 Fourier Transform Spectrometer (FTS)

Dried and sieved, and DRYSVGRN samples were scanned (no KBr dilution) in the mid-IR from 4,000 to 400 cm^{-1} or in the NIR from 10,000 to 4,000 cm^{-1} (4 cm^{-1} resolution, 64 co-added scans) on a Digilab (Varian, Inc., Palo Alto, CA) FTS7000 FTS equipped with DTGS (deuterated triglycine sulfate) and InSb detectors and KBr and quartz beam splitters (mid-IR and NIR, respectively) by diffuse reflectance using a Pike (Pike Technologies, Madison, WI) AutoDiff autosampler (sample cups ~ 1 cm in diameter).

Field-moist, DRYSV, and DRYSVGRN samples were also scanned in the mid-IR on a Surface Optics Corporation model SOC-400 portable FTS (Fig. 11.1) from



Fig. 11.1 SOC-400 scanning samples under ambient conditions on-site

4,000 to 400 cm^{-1} at 8 cm^{-1} resolution using a rotating sample cup (approximate path 2 mm in width around an 8 mm diameter circle).

11.2.4 Non-FTS NIR Spectroscopy

Field-moist, DRYSV, and DRYSVGRN samples were also scanned in the NIR on an NIRSystems model 6500 scanning monochromator (FossNIRSystems, Eden Prairie, MN) from 400 to 2,498 nm (25,000–4,003 cm^{-1}) with data collected every 2 nm at a 10 nm bandwidth using a rotating sample cup ~4 cm in diameter.

11.2.5 Chemometrics

All calibration development was performed using SAS Ver. 9.12 PLS (Reeves and Delwiche, 2003). A total of 30 different spectral pre-treatments were tested, including multiplicative scatter correction and first and second gap derivatives with all spectra mean centred and variance scaled. Two types of calibrations were examined (1) using all samples in a one-out cross validation (Table 11.2 and Fig. 11.2) and (2) randomly splitting the samples into calibration samples and independent tests (Beltsville core samples only, Table 11.3 and Fig. 11.3).

Table 11.2 One-out calibration results using all 201 samples, with every four data points averaged

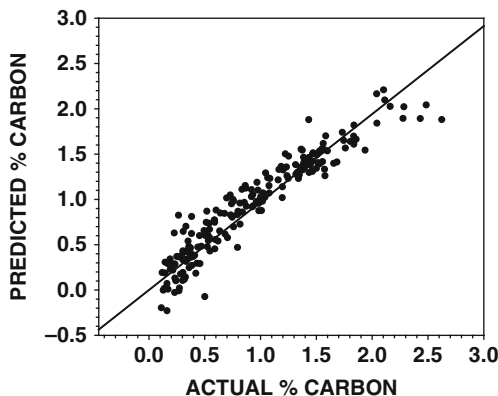
Analyte	DER	MSC	GAP	Factors	RMSD	CALR2
<i>NIRSystems 6500 with spinning cup</i>						
Samples scanned neat						
Carbon	2nd	Yes	8	9	0.155	0.928
Nitrogen	2nd	No	32	13	0.027	0.902
Samples scanned air-dried						
Carbon	2nd	No	32	13	0.153	0.931
Nitrogen	1st	No	64	13	0.030	0.881
Samples scanned air-dried and ground						
Carbon	1st	No	1	8	0.148	0.935
Nitrogen	1st	No	2	8	0.026	0.906
DIGILAB (VARIAN) FTS-7000 FTNIR						
Samples scanned air-dried						
Carbon	2nd	No	2	4	0.171	0.913
Nitrogen	2nd	No	32	4	0.025	0.912
Samples scanned air-dried and ground						
Carbon	1st	No	1	5	0.145	0.938
Nitrogen	1st	No	1	5	0.024	0.920

Table 11.2 (continued)

Analyte	DER	MSC	GAP	Factors	RMSD	CALR2
DIGILAB (VARIAN) FTS-7000 FTIR						
Samples scanned air-dried						
Carbon	2nd	No	1	3	0.175	0.909
Nitrogen	1st	Yes	2	5	0.029	0.882
Samples scanned air-dried and ground						
Carbon	1st	Yes	4	7	0.145	0.938
Nitrogen	2nd	Yes	8	4	0.027	0.899
SOC-400 Portable FTIR						
Samples scanned neat						
Carbon	1st	No	8	5	0.208	0.871
Nitrogen	1st	No	2	4	0.033	0.849
Samples scanned air-dried						
Carbon	1st	No	4	4	0.175	0.909
Nitrogen	1st	No	4	5	0.024	0.923
Samples scanned air-dried and ground						
Carbon	1st	Yes	16	8	0.140	0.942
Nitrogen	Non	No	0	12	0.023	0.927

DER, derivative type; MSC, multiplicative scatter corrected or non-corrected; RMSD, relative mean squared deviations; CALR2, calibration R^2

Fig. 11.2 SOC-400 FM calibration (1 DP av., 8 cm^{-1} resolution spectra)



11.3 Results and Discussion

The data in Table 11.1 show the composition of the 201 samples collected as cores at BARC and were typical of soils from the area. As shown, a wide range of values for both C and N were obtained with a high degree of correlation between the two analytes ($R^2 = 0.92$).

Table 11.3 Calibration results from 25 runs using 25% ($n = 50$) of samples as a randomly generated test set

Analyte	DER	MSC	GAPS	Factors	RMSD	VRMSD	CALR2	VALR2
<i>NIRSystems 6500 with spinning cup</i>								
Samples scanned neat								
Carbon	2nd	STR	64	13.28	0.163	0.181	0.920	0.901
Nitrogen	2nd	STR	32	10.12	0.028	0.035	0.893	0.822
Samples scanned air-dried								
Carbon	1st	STR	4	9.60	0.153	0.185	0.930	0.897
Nitrogen	2nd	MSC	8	4.04	0.032	0.037	0.863	0.813
Samples scanned air-dried and ground								
Carbon	1st	STR	2	7.24	0.151	0.203	0.931	0.879
Nitrogen	1st	STR	2	7.12	0.027	0.040	0.900	0.790
<i>DIGILAB (VARIAN) FTS-7000 FTNIR</i>								
Samples scanned air-dried								
Carbon	1st	STR	16	4.96	0.187	0.224	0.893	0.854
Nitrogen	1st	STR	16	4.92	0.030	0.036	0.872	0.821
Samples scanned air-dried and ground								
Carbon	Non	STR	0	8.80	0.177	0.204	0.906	0.878
Nitrogen	Non	STR	0	8.48	0.030	0.035	0.873	0.828
<i>DIGILAB (VARIAN) FTS-7000 FTIR</i>								
Samples scanned air-dried								
Carbon	2nd	STR	32	3.28	0.189	0.211	0.892	0.881
Nitrogen	2nd	STR	32	3.08	0.032	0.036	0.854	0.835
Samples scanned air-dried and ground								
Carbon	2nd	STR	16	3.80	0.163	0.187	0.920	0.899
Nitrogen	2nd	STR	16	3.68	0.029	0.033	0.887	0.860
<i>SOC-400 Portable FTIR</i>								
Samples scanned neat								
Carbon	1st	STR	8	4.32	0.224	0.286	0.851	0.752
Nitrogen	1st	STR	8	4.32	0.034	0.043	0.844	0.741
Samples scanned air-dried								
Carbon	1st	STR	32	4.00	0.185	0.194	0.897	0.893
Nitrogen	1st	STR	32	4.32	0.030	0.033	0.874	0.859
Samples scanned air-dried and ground								
Carbon	2nd	STR	64	5.00	0.149	0.177	0.932	0.913
Nitrogen	1st	STR	32	4.60	0.026	0.030	0.905	0.879

DER, derivative type; MSC, multiplicative scatter corrected or non-corrected; RMSD, relative mean squared deviations, VRMSD, validation set; CALR2/VALR2, calibration and validation R^2

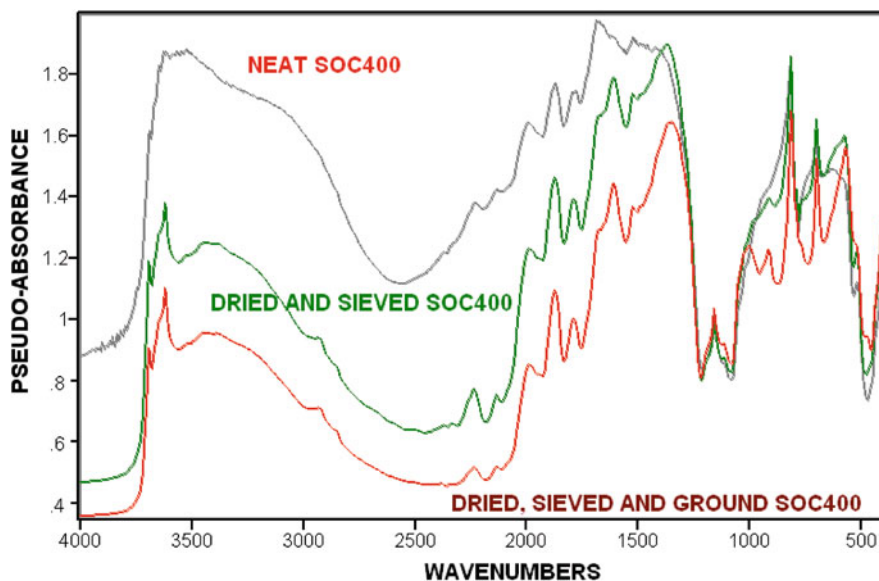


Fig. 11.3 Average spectra of 201 soil samples scanned on the SOC-400 in various physical states

The results in Table 11.2 show the effect of soil state, spectral range, and spectrometer used on calibrations for C using all 201 samples in a one-out cross validation. These are the best results one could expect for the determination of C in the samples in question. Examination of the data in Table 11.2 (results using different degrees of spectral averaging not shown) showed the following. (1) Averaging spectral data points (none, 1, 2, 4, etc.) generally had little effect on the results. (2) Calibrations for C were more accurate than those for N. (3) Effects of drying and grinding appeared dependent on the spectral range, spectrometer, and analyte in a complex fashion. (4) While drying, sieving, and grinding results in more accurate calibrations than drying and sieving alone, results were quite similar. (5) Results with the SOC-400 for FM samples (Fig. 11.2) were acceptable but not quite as good as for the NIRS6500 (but were quite similar for DRYSV and the best for DRYSVGRN samples). (6) Data for the SOC-400 were collected at 8 cm^{-1} resolution, based on previous work with DRYSVGRN samples. Higher resolution may be of advantage with FM samples where sharp water bands may exist and will be the subject of future research. (7) Patterns seen for N were similar to those found for C. (8) Overall, results supported the conclusion that the mid-IR can be used in the field to accurately determine the C and N content of soils, but further research is needed to assess how best to develop calibrations for FM samples, including whether higher resolution spectra would be of benefit.

Examination of average mid-IR spectra for the set of 201 soils (Fig. 11.3) shows that while considerable detail still exists in the spectra of the FM (neat SOC-400) samples, there is at least visually a loss of information. For example, peaks in the $2,900\text{--}3,000\text{ cm}^{-1}$ range due to organic matter (C–H and N–H bands) are no

longer apparent. The spectra also often appear very noisy due to the sharp water vapour bands in the mid-IR, something that higher resolution spectra might help reduce by deconvoluting the molecular signals. Comparing the SOC-400 spectra for DRYSVGRN samples to those produced by the FTS7000 (data not presented) demonstrated that the portable spectrometer produces very similar spectra and calibrations.

For the results in Table 11.3, samples were randomly selected for calibration ($n = 151$) and independent test sets ($n = 50$). This was done 25 times (25 random splits and PLS calibrations) and the results averaged. Examination of the data for soil carbon in Table 11.3 showed the following. (1) Results were very similar for DRYSV and DRYSVGRN samples for all spectrometers and spectral ranges examined, indicating that robust calibrations can be developed using any of the spectrometers studied. (2) Results for FM samples were significantly better for the NIRSystems 6500 than those achieved with the SOC-400 (Fig. 11.4). (3) Error (RMSDs) for the SOC-400 test set increased $\sim 30\%$ over those in Table 11.2 indicating a lack of robustness. (4) Comparison of the test set results for the SOC-400 for FM and DRYSVGRN samples indicated that the problem might be due to specific outliers which could not be accommodated by the calibration. While results for N followed similar patterns, overall it appears that the improvement using mid-IR over NIR was greater than that seen for C, with greater improvement in validation of R^2 and RMSD values indicating mid-IR-based calibrations to be more robust than NIR calibrations.

Efforts were also undertaken using a total of 729 samples (added additional sets from other studies) scanned FM on the SOC-400 to determine if better calibrations were possible. Preliminary results support the conclusion that variations in moisture, in combination with variations in C content, make samples appear more dissimilar in the mid-IR than in the NIR (e.g. increased spectral variance, resulting in a need for greater sample numbers and a more even distribution of C and moisture levels within the calibration set in order to produce a satisfactory mid-IR calibration). In particular, insufficient samples at higher C values ($>2\%$)

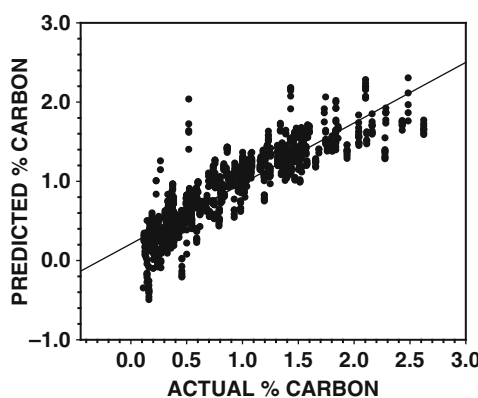


Fig. 11.4 SOC-400 FM test calibration (1 DP av., 8 cm^{-1} resolution spectra), results from 25 random runs

appeared to have a large effect on calibration robustness. Thus, results indicate that mid-IR calibrations for FM samples may be feasible, but greater attention will be needed in sample selection and calibration development. Other efforts, however, indicate no benefit in trying to reduce the influence of water by using only portions of the mid-IR spectra for such calibrations (unpublished data). Finally, other efforts, not discussed, have shown that excellent calibrations can be achieved using samples dried in the sun (unpublished data), and thus scanning of FM samples might not be necessary or even desirable except in cases such as the Veris on-the-go NIR system (<http://www.veristech.com/old/products/products.htm#NIR>, Veris Technologies, Salina, KS) or remote sensing where drying it is not feasible.

11.4 Conclusions

As a result of studies using mid-IR and NIR spectroscopy, the following conclusions can be drawn. (1) The greatest accuracy is achieved with DRYSVGRN samples. (2) What is removed (or not) by sieving has the potential to greatly affect the sample scanned versus the sample tested by combustion, or the sample scanned in the field (non-sieved) versus the sample scanned in the lab (sieved). (3) Results with a portable FTIR spectrometer were equal to those achieved with a research grade, benchtop instrument for samples in the same state. (4) Results achieved with a research-grade FTNIR were equal to those achieved with a similar grade, scanning monochromator. (5) It appears that it is possible to develop accurate and robust calibrations for soil C using FM samples and NIR spectra, but more work is needed to determine whether robust mid-IR calibrations for FM samples can be developed. (6) Considering the move to no-till, where surface litter will likely be considerable and soil C levels will vary with depth, only methods where samples are scanned after being obtained at various depths are likely to provide the information needed. In such cases, scanning sun-dried samples in the mid-IR using a portable instrument such as the SOC-400 or in the laboratory may be advantageous.

Finally, this study and results using remote sensing (see McCarty et al., Chapter 14) indicate that choices may need to be made between accuracy and quantity of data desired. Methods such as the Veris unit or images taken from planes have the capability of scanning much larger areas than can be done by coring. However, the results may not be as accurate due to problems such as matching a specific soil sample used for calibration to a specific soil area scanned. Recent developments in handheld NIR and mid-IR spectrometers such as the NIR-based Phazir (www.polychromix.com) or/and FTIR-based EXOSCAN (www.a2technologies.com) and other such instruments may help by allowing a larger area to be scanned on-site to better match spectra and reference data, but research will be needed to best determine how to do this. Other chapters in this volume of direct pertinence to this effort include Chapters 3, 12, 13, 14, 15, and 16, which also investigated various aspects of diffuse reflectance spectroscopy for soil analysis.

References

Janik LJ, Merry RH, Skjemstad JO, (1998) Can mid-infrared diffuse reflectance analysis replace soil extractions? *Aust J Exp Agric* 38:681–696

Reeves III JB (1996) Improvement in Fourier near- and mid-infrared diffuse reflectance spectroscopic calibrations through the use of a sample transport device. *Appl Spectrosc* 50:965–969

Reeves III JB, Delwiche SR, (1997) Determination of protein in ground wheat samples by mid-infrared diffuse reflectance spectroscopy. *Appl Spectrosc* 51:1200–1204

Reeves III JB, McCarty GW, Reeves VB (2001) Mid-infrared diffuse reflectance spectroscopy for the quantitative analysis of agricultural soils. *J Agric Food Chem* 49:766–772

Reeves III JB, McCarty GW, Mimmo TV, Reeves VB, Follet RF, Kimble JM, Galletti GC (2002) Spectroscopic calibrations for the determination of C in soils. *Transactions of the 17th World Congress of Soil Science, symposium 10, paper 398, 1–9*

Reeves III JB, Delwiche SR (2003) SAS partial least squares regression for analysis of spectroscopic data. *J Near Infrared Spectrosc* 11:415–431

Roberts CA, Workman Jr. J, Reeves III JB (eds) (2004) Near-infrared spectroscopy in agriculture, vol 44 in the series Agronomy. American Societies of Agronomy, Crop and Soil Science, Madison, WI

Smith B (1999) Infrared spectral interpretation: A systematic approach. CRC Press, New York, NY

Chapter 12

Determination of Soil Nitrate and Organic Matter Content Using Portable, Filter-Based Mid-Infrared Spectroscopy

B.R. Jahn and S.K. Upadhyaya

Abstract Soil nitrate content and organic matter are two important parameters that determine the amount of nitrogen available for plant growth. The goal of this study was to develop soil nitrate and organic matter sensing techniques, since traditional methods of determining soil organic matter and nitrate content are tedious, time-consuming, and expensive. Studies conducted at UC Davis have clearly shown that unmistakable nitrate peaks exist in the mid-infrared (MIR) spectra of soil pastes. In particular, the peak located at $1,390\text{ cm}^{-1}$ wave number is nitrate sensitive. However, this peak is broad and is influenced by carbonate/bicarbonate and organic matter peaks, which exist in the vicinity of the nitrate peak. Using wavelet analysis, we were able to isolate a single wave number, $1,350\text{ cm}^{-1}$, at which these interferences were minimal. However, if the soil contained a large amount of carbonates, a second wavelength located at $1,500\text{ cm}^{-1}$ was necessary to obtain a unique calibration equation. Using the absorbance values at these two wave numbers, nitrate-*N* concentrations of 14 different soils (6 Californian soils and 8 Israeli ones) could be determined using a single calibration curve with a coefficient of multiple determination (R^2 value) of 0.98. When only six Californian field soils were considered, the calibration equation resulted in an R^2 value of 0.95 with a standard error of 8 ppm. Moreover, preliminary tests indicated that soil organic matter can also be determined using MIR spectral response at two wave numbers ($1,383$ and $1,452\text{ cm}^{-1}$). The R^2 value for soil organic matter determination was 0.95 and the standard error was 0.25%. These results indicate that both soil nitrate content and organic matter can be determined using just a few wavelengths in the MIR region with sufficient accuracy for use in site-specific nutrient management.

Keywords Mid-infrared · MIR · Near infrared · NIR · Attenuated total reflection · ATR

S.K. Upadhyaya (✉)

Biological and Agricultural Engineering Department, University of California – Davis, Davis, CA 95616, USA

e-mail: skupadhyaya@ucdavis.edu

12.1 Introduction

Nitrogen is an important nutrient for crop production. Farmers typically apply uniform amounts of fertiliser in excess of what the crops need to prevent yield loss due to nutrient deficiency. However, nitrate is a highly mobile ion and easily leaches to the groundwater. Applying lower fertiliser amounts to areas within a field with limited yield potential will lead to a reduction in cost as well as less nitrate leaching. Fisher et al. (1993) have shown that, with variable rate application, approximately 25% reduction in fertiliser application can be achieved without any decrease in yield. However, soil organic matter content influences the amount of soil nitrate available through the mineralisation process. Therefore a nitrate management scheme should consider the amount of both soil mineral nitrogen (mostly nitrate) and organic matter content. Measurement of soil nitrate and organic matter content is a tedious, time-consuming, and expensive process. Rapid techniques of quantifying soil nitrate and organic matter content would save valuable time and money.

Adsett et al. (1999) used the nitrate-selective membrane approach to develop an on-the-go soil nitrate sensor. The calibration procedures for this system were tedious and possibly inaccurate due to changing potentials on the electrodes. Birrell and Hummel (2000) used ion-selective field effect transistors (ISFET) in a multi-ISFET sensor chip to measure soil nitrate. The advantages of using ISFET chips include fast response times and a need for low sample volumes. This technique has shown promise and is awaiting further improvements for field application. Kim et al. (2006) found that nitrate ion-selective membrane with tetradodecyl-ammonium nitrate (TDDA) was able to detect low concentrations of nitrogen when used in conjunction with Kelowna extractant. Chapter 6 provides a brief review of electrochemical sensing.

In the past, techniques to measure soil nitrate and organic matter content based on near-infrared (NIR) spectroscopy have received considerable attention due to the availability of inexpensive NIR instruments. However, NIR spectroscopy-based models tend to have (due to the nonuniqueness of the calibration curve) very limited ability to predict nitrogen content of soils that were not a part of the calibration set (Ehsani et al., 1999). The primary reason for this lack of robustness is due to the absence in the near-infrared region of absorbance (or reflectance) peaks due to nitrate.

In recent years, attenuated total reflection (ATR) coupled with mid-infrared (MIR) spectroscopy has shown great promise for detecting low concentrations of nitrate. The ATR technique applied to MIR spectra has advantages in terms of minimal sample preparation, even for low nitrate contents (<10 ppm $\text{NO}_3\text{-N}$), and increased sensitivity of nitrate peaks due to the fundamental modes of vibration of the nitrate molecule that occur in this region. In particular, the peak located at $1,390\text{ cm}^{-1}$ wave number is nitrate sensitive. However, this peak is broad and is influenced by carbonate/bicarbonate and organic matter peaks which exist in the vicinity of the nitrate peak. Linker et al. (2004) conducted MIR spectroscopic experiments with eight soils ranging in nitrate concentrations from 0 to 1,200 ppm

$\text{NO}_3\text{-N}$. Three of the eight soils were calcareous and required special considerations. When they excluded these three soils, they obtained very good results using partial least squares (PLS) (four components, standard error of 32 ppm $\text{NO}_3\text{-N}$). Including the three calcareous soils in the analysis caused the standard errors to increase approximately twofold. Jahn et al. (2006) and Jahn and Upadhyaya (2006) applied wavelet analysis technique to the experimental data collected at UC Davis, as well as data obtained by Linker et al. (2004), to develop a unique calibration equation. Using wavelet analysis they were able to isolate a single wavelength at which interference from carbonate/bicarbonate and organic matter was minimal. However, they did not verify the applicability of this wavelet-based technique to data from a grower's field.

The specific objectives of this study were (i) investigate the applicability of a nitrate calibration equation developed using FTIR/ATR spectroscopy to predict nitrate concentrations in a grower's field and (ii) determine the applicability of a rugged (i.e., no moving mirrors), fixed-filter spectrometer, suitable for field use, to sense soil nitrate and organic matter contents.

12.2 Materials and Methods

12.2.1 FTIR/ATR Spectrometer Tests

Four processing tomato fields that were owned and operated by the Button and Turkovich Farm in Winters, CA, were selected for this study. These four fields consisted of the following soil types: Yolo silt loam (Yolo Series – a fine-silty, mixed, superactive, nonacid, thermic Mollic Xerofluvents), Capay clay (Capay series – fine, smectitic, thermic Typic Haploxererts), Rincon silty clay loam (Rincon series – fine, smectitic, thermic Mollic Haploxeralfs), and Sycamore silty clay loam (Sycamore series – Fine-silty, mixed, superactive, nonacid, thermic Mollic Endoaquepts). Soil samples were obtained over four sampling periods. These periods were chosen to represent the variation in nitrate contents the tomato plants experienced during critical growing periods. The first set of samples was obtained after the pre-plant application of 8-24-6 (N-P-K) fertiliser at a rate of approximately 19 kg ha^{-1} . Approximately a week later, samples were again collected. Two other samples were obtained following the application a post-emergence fertiliser (UN-32 with 32%N) at the rate of about 168 kg ha^{-1} . Again, these two samples were spaced a week apart. Five samples were randomly collected from each field from the top 15 cm of soil for each of the four time periods, and each sample was split into three subsamples. The soil samples were oven dried at 55°C for 48 h. Then the samples were ground, sieved ($75 \mu\text{m}$), and finally mixed with distilled water on a 1:1 mass basis to form a paste. The pastes were stored in a refrigerator at 4°C for approximately 1 day, after which mid-IR spectra were collected. Soil samples were also sent to an analytical laboratory for nitrate analyses where a flow injection analysis technique was used. The nitrate concentrations for these soils varied from 14 to 189 ppm $\text{NO}_3\text{-N}$.

Table 12.1 Soil texture and CaCO_3 concentrations for soils from Israel

Soil name	Soil type	Clay (%)	Silt (%)	Sand (%)	CaCO_3 concentration (%)
Beit Shean	Calcareous clay	55	22	23	47
Bsor	Loam	15	9	76	13
Shaalabim	Clay	54	19	27	9
H1	Sandy	1	6	93	0
H2	Sandy	1	5	94	0
Germany	Loam	24	23	53	0
Columbia	Clay	N/A	N/A	N/A	1
Tourba	Peat	N/A	N/A	N/A	0

In addition to samples from these four fields, FTIR/ATR data obtained for two other soils in the USA and eight in Israel were also used for developing a single calibration equation. The two extra US soils belonged to Capay and Yolo series and were taken from the UC Davis Agricultural Experiment Station farms. The $\text{NO}_3\text{-N}$ content for US soil samples ranged from 0 to 200 ppm. Table 12.1 provides textural details of the eight Israeli soils used in this study. The Israeli soil samples were spiked with $\text{NO}_3\text{-N}$ concentrations in the range of 0–1,200 ppm. Three of the Israeli soils contained large amounts of calcium carbonate as shown in Table 12.1. Additional details of these soil samples and the techniques used to obtain their FTIR/ATR spectra can be found in Jahn et al. (2006).

12.2.2 Portable Filter-Based Spectrometer Tests

A portable mid-IR variable filter array (VFA) spectrometer manufactured by Wilks Enterprise¹ was used to obtain mid-IR spectra of field soil pastes described in Section 12.2.1. This rugged portable spectrometer, which contained no moving parts, also utilised the ATR technique and could provide continuous absorbance values in the 880–1,684 cm^{-1} range with a resolution of approximately 12 cm^{-1} . Figure 12.1 shows a photograph of this spectrometer.

12.2.2.1 Nitrate Experiments

The soil samples used for the nitrate experiments were the same ones as used in the FTIR/ATR spectroscopy experiments. Each sample was divided into 10 subsamples, and the spectrum of each subsample was obtained individually. Soil pastes were placed over the crystal and the ATR spectra were measured with 30 scans per sample. The spectra were corrected for added moisture, smoothed, and baseline corrected as described by Jahn et al. (2005).

¹Mention of a trade name is not an endorsement of the product over other similar products by the authors or the University of California.



Fig. 12.1 Wilks VFA Spectrometer with ATR crystal, used for collecting mid-IR spectra, compared with a floppy disk

12.2.2.2 Organic Matter Experiments

Organic matter was added in the form of humus to dry soil samples. Dried humus was mixed with soil samples to give organic matter concentrations from 0 to 5% in increments of 1%. Because of the residual nitrate content in these soils, this technique resulted in organic matter concentrations in the range of 2–7%. Sufficient soils corresponding to three of the four fields from the Button and Turkovich Farm were available for conducting these experiments. As in the case of nitrate experiments, distilled water was added to create a 1:1 paste. Each of the 18 soil samples (three field soils \times six levels) were subdivided into 10 subsamples and 30 mid-IR scans of each subsample were obtained using the VFA spectrometer. Similarly, these soil samples were sent to the analytical laboratory for determining the actual soil organic matter content.

12.3 Results and Discussion

12.3.1 FTIR/ATR Spectrometer Test Results

The development of the nitrate calibration equation using FTIR/ATR spectroscopy was explained previously by Jahn et al. (2005) and will not be detailed here. The basis of this equation relied on wavelet analysis to deconvolute mid-IR spectra of soil pastes. A 3-D plot of the wavelet-transformed MIR absorbance data as a function of wave number and scale is shown in Fig. 12.2. Note that the scale is related to the width of the Coiflet-3 wavelets used in transforming the absorbance data. The nitrate peak that occurs at $1,390\text{ cm}^{-1}$ wave number is marked with a circle in the figure. However, this peak is broad and is influenced by carbonate/bicarbonate and organic matter peaks in the vicinity of the nitrate peak. Additional analysis of the wavelet-transformed absorbance data by Jahn et al. (2006) indicated that

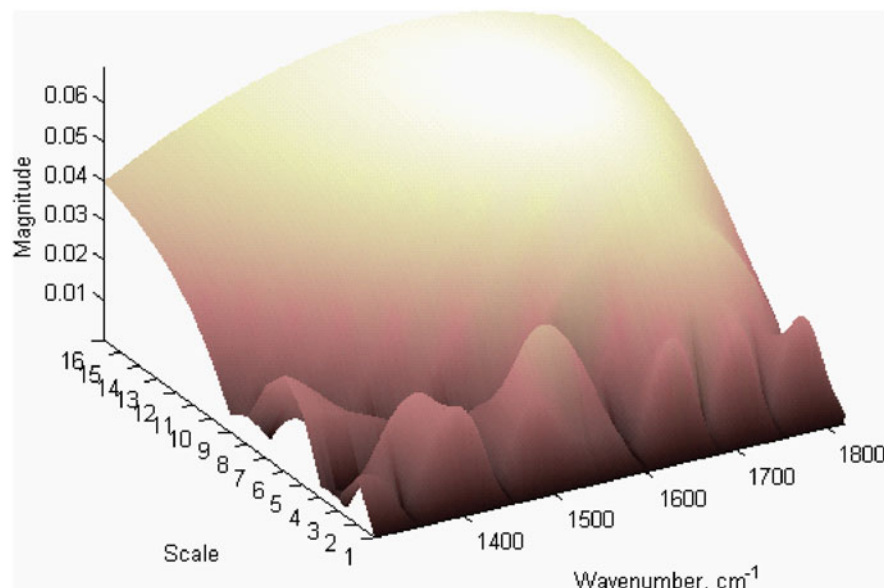


Fig. 12.2 Three-dimensional wavelet deconvoluted plot of a soil paste that contained 59 ppm $\text{NO}_3\text{-N}$. The nitrate peak is in the vicinity of $1,390 \text{ cm}^{-1}$

interferences from carbonate/bicarbonate ions and organic matter are minimal at a wave number of $1,350 \text{ cm}^{-1}$, if carbonate content of the soil samples is not too high (i.e., except for three Israeli soils – Beit Shen, Bsor, and Shaalabim – that contain high carbonate contents as shown in Table 12.1). However, if the soil contained a large amount of carbonate, a second wavelength located at $1,500 \text{ cm}^{-1}$ wave number was necessary to obtain a unique calibration equation. The laboratory and field data obtained in USA and Israel using 14 different soils were randomly split into calibration (124 samples) and validation (40 samples) sets. Figure 12.3 shows the calibration plot and Fig. 12.4 shows the validation plot. These plots are based on ATR absorbance values located at the two-point baseline- and water-corrected spectra of the soil paste at $1,350$ and $1,500 \text{ cm}^{-1}$ wave numbers.

The standard errors of calibration and validation were 41.8 and 40.1 ppm $\text{NO}_3\text{-N}$, respectively. These results show that nitrate can be predicted for 14 different soils using a single equation based on absorbance values at $1,350$ and $1,500 \text{ cm}^{-1}$. Including only the Californian soil samples (a total of 63 samples) with nitrate concentrations typical of those found in agricultural fields (0–200 ppm $\text{NO}_3\text{-N}$) in the analysis resulted in an R^2 value of 0.95 and standard error of approximately 8 ppm $\text{NO}_3\text{-N}$.

12.3.2 Filter-Based Spectrometer Test Results

MIR absorbance data due to nitrate and organic matter contents in the soil samples from farmers' fields were analysed and results are presented below.

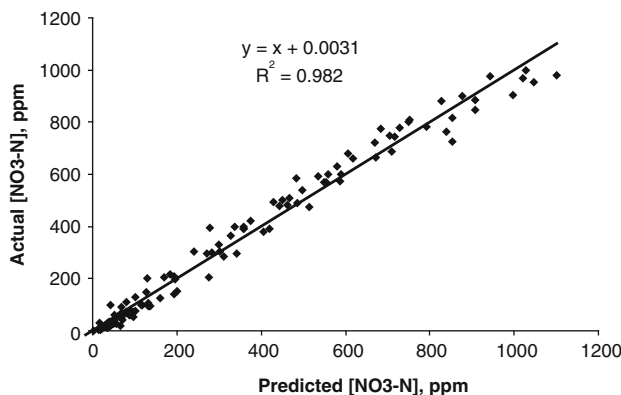


Fig. 12.3 Calibration plot based on 124 soil samples for all soil sets pooled together. The standard error of calibration was 41.8 ppm NO₃-N. Each point on the graph is an average of 10 subsamples

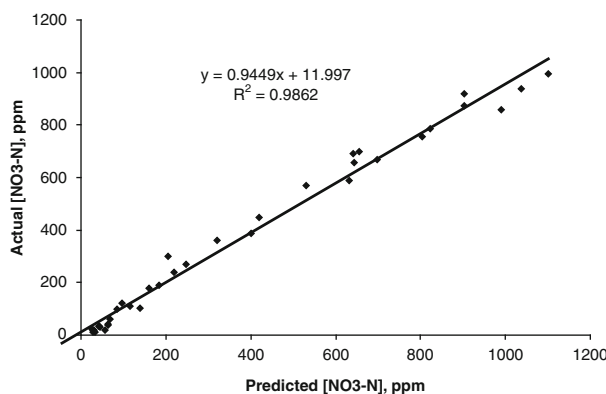


Fig. 12.4 Validation plot based on 40 soil samples for all soil sets pooled together. The standard error of validation was 40.1 ppm NO₃-N. Each point on the graph is an average of 10 subsamples

12.3.2.1 Nitrate Results

The results obtained using the filter-based portable device were not as accurate as the laboratory-based FTIR/ATR spectrometer results. One reason for the inferior predictive ability of the filter-based spectrometer is due to its poorer resolution compared with the laboratory-based spectrometer. Figure 12.5 shows the spectral responses of a soil sample containing 25 ppm of nitrate-N obtained using both the FTIR/ATR spectrophotometer and the filter-based spectrophotometer. The resolution of the filter-based spectrometer (12 cm^{-1}) is three times higher than the FTIR spectrometer used in the laboratory experiments (4 cm^{-1}). A statistical analysis of the VFA spectrometric data of the samples obtained from the four processing tomato fields described in Section 12.2.1 indicated that a one-term model based on

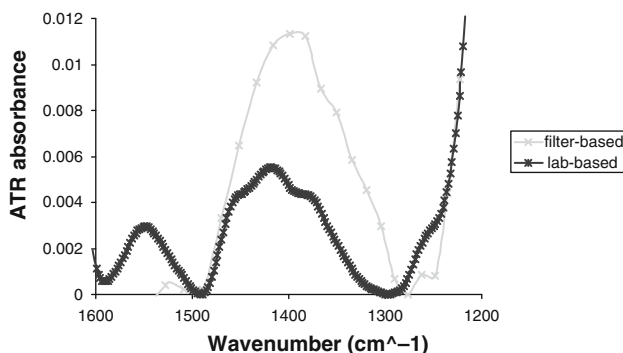


Fig. 12.5 Comparison of the spectra of a field soil sample containing 25 ppm $\text{NO}_3\text{-N}$ obtained using both the FTIR/ATR laboratory spectrophotometer and the filter-based spectrophotometers

the water- and baseline-corrected absorbance at $1,399\text{ cm}^{-1}$ resulted in a standard error of 25 ppm $\text{NO}_3\text{-N}$ with an R^2 value of 0.81. A plot of predicted versus actual nitrate concentration for this one-term model is shown in Fig. 12.6. Use of a second wavelength corresponding to wave number 992 cm^{-1} led to an improvement in R^2 to 0.94 and the standard error decreased to 14.9 ppm. Although the results were not as good as the ones obtained with the FTIR/ATR machine, it was encouraging to see detectable nitrate response using this filter-based spectrometer on field soils. Due to different optics, detector, and resolution, it is not surprising that the spectral characteristics from the filter-based spectrometer are discernable from those obtained from the FTIR spectrometer used. These results also indicate that some modifications (i.e., stronger source, better spectral resolution, higher sensitivity) of the filter-based spectrometer may make it better suited for detecting low nitrate concentrations.

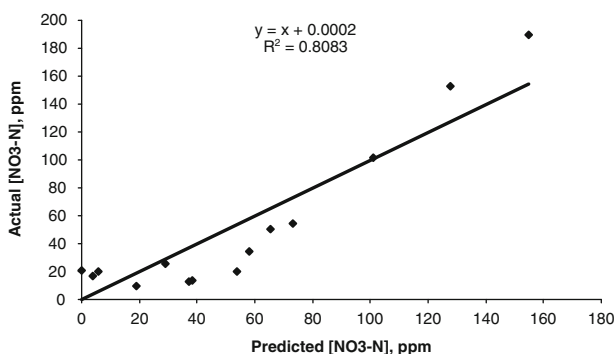


Fig. 12.6 Calibration plot of a one-term model based on the absorbance at $1,399\text{ cm}^{-1}$ for 16 soil samples from four growers' fields. These spectra were obtained from a filter-based spectrometer. The standard error of calibration was 25.0 ppm $\text{NO}_3\text{-N}$

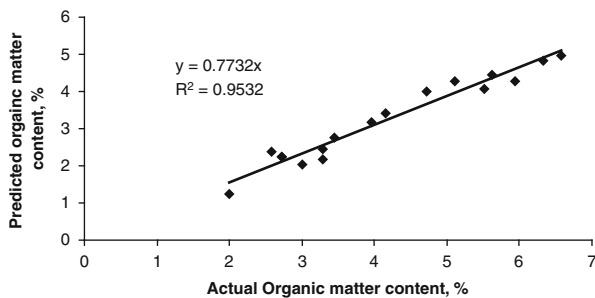


Fig. 12.7 Calibration plot for organic matter based on three fields. The standard error of calibration was 0.25% organic matter

12.3.2.2 Organic Matter Results

Figure 12.7 shows a plot of the organic matter calibration equation developed using absorbance values at two wave numbers located at $1,383$ and $1,452\text{ cm}^{-1}$ using a stepwise regression technique. The R^2 value was 0.95 and standard error was 0.25%. The $1,383\text{ cm}^{-1}$ peak could be due to nitrate and/or carbonate. Preliminary results shown in Fig. 12.7 indicate that this filter-based spectrometer shows promise for predicting organic matter concentrations.

12.4 Conclusions

The results of this study showed that a nitrate calibration equation could be successfully developed using FTIR/ATR spectroscopy to predict nitrate concentrations in 14 different soils. For large nitrate concentrations (up to 1,200 ppm $\text{NO}_3\text{-N}$), the standard error was approximately 40 ppm $\text{NO}_3\text{-N}$. For a smaller nitrate concentration range (0–200 ppm $\text{NO}_3\text{-N}$) typical of agricultural fields, the standard error was approximately 8 ppm $\text{NO}_3\text{-N}$. On the other hand, for a filter-based portable spectrometer, results were not as good as for the FTIR/ATR spectrometer. However, when a multiple linear regression model was developed based on the absorbance values at 992 and $1,399\text{ cm}^{-1}$ for soils from four agricultural fields, an R^2 of 0.94 and standard error of 14.9 ppm $\text{NO}_3\text{-N}$ were obtained. Moreover, the filter-based spectrometer also showed promise for predicting soil organic matter content. Based on a limited number of experiments and a range of organic matter from 0 to approximately 6%, a multiple linear regression calibration equation was developed resulting in an R^2 of 0.95 and a standard error of 0.25%.

Acknowledgement This project is supported by a US–Israel Binational Research and Development Fund (BARD Project US-3293-20c). The authors are also grateful to our Israeli collaborators, Dr Rafi Linker and Dr Avi Shaviv, for providing FTIR/ATR spectra of soil samples collected in Israel.

References

Adsett JF, Thottan JA, Sibley KJ (1999) Development of an automated on-the-go soil nitrate monitoring system. *Appl Eng Agric* 15(4):351–356

Birrell SJ, Hummel JW (2000) Membrane selection and ISFET configuration evaluation for soil nitrate sensing. *Trans ASAE* 43(2):197–206

Ehsani MR, Upadhyaya SK, Slaughter D, Shafii S, Pelletier M (1999) A NIR technique for rapid determination of soil mineral nitrogen. *Precision Agric* 1:217–234

Fisher KB, Peterson CL, Shropshire GJ, Dowding EA (1993) A spatially variable fertilizer applicator for wheat. *ASAE Paper No. 93-1074*. St. Joseph, MI

Jahn BR, Brooksby PA, Upadhyaya SK (2005) Wavelet-based spectral analysis for soil nitrate content measurement. *Trans ASAE* 48(6):2065–2071

Jahn BR, Linker R, Upadhyaya SK, Shaviv A, Slaughter DC, Shmulevich I (2006) Mid-infrared spectroscopic determination of soil nitrate content. *Biosystems Eng* 94(4):505–515

Jahn BR, Upadhyaya SK (2006) Development of mid-infrared based calibration equations for predicting soil nitrate, phosphate, and organic matter concentrations. *ASAE Paper No. 061058*. St. Joseph, MI

Kim H, Hummel JW, Birrell SJ (2006) Evaluation of nitrate and potassium ion-selective membranes for soil macronutrients sensing. *Trans of ASABE* 49(3):597–606

Linker R, Kenny A, Shaviv A, Singer L, Shmulevich I (2004) Wavebands selection for determination of nitrate in soil using mid-IR ATR spectroscopy. *Appl Spectrosc* 58(5): 516–520

Chapter 13

VNIR Spectroscopy Estimates of Within-Field Variability in Soil Properties

K.A. Sudduth, N.R. Kitchen, E.J. Sadler, S.T. Drummond, and D.B. Myers

Abstract Over the last three decades or more, researchers have estimated soil properties using visible and near-infrared (VNIR) diffuse reflectance spectroscopy (DRS), with varying results. Using VNIR DRS for estimating soil property variation within fields is particularly challenging, because in many cases the variation in the property of interest may be relatively small and because of the need to deal with spatially correlated data. In this study, we used VNIR DRS to estimate the variability in soil physical and chemical properties within a typical production field in north-east Missouri, USA. Soil samples were obtained to 15 cm depth on a 30 m grid spacing, plus at a number of random sampling locations. Laboratory analyses were conducted for sand, silt, and clay fractions, organic matter, pH, P, K, Ca, Mg, and cation exchange capacity (CEC). VNIR reflectance of dried and sieved samples was obtained in the laboratory using a spectrometer with a wavelength range from 350 to 2,500 nm. Partial least squares (PLS) regression was used to estimate soil properties from spectra, both for the full range and for subset wavelength ranges above and below 1,000 nm. A regression kriging approach was used to account for spatial dependence. We found that for these soils, an NIR-only instrument (1,000–2,500 nm) would be able to quantify CEC, organic matter, and texture with accuracy similar to that from a VNIR (350–2,500 nm) instrument. Some soil properties, including CEC and pH, were well estimated with PLS regression, while others, including organic matter, were not. Coupling regression kriging with PLS regression improved estimates in some cases, but was not as effective as has been reported in some other studies. More advanced calibration methods should be investigated for their ability to improve within-field VNIR DRS results on these soils.

Keywords Diffuse reflectance spectroscopy · Regression kriging · Precision agriculture · Soil sensing · Near infrared

K.A. Sudduth (✉)

Cropping Systems and Water Quality Research Unit, USDA Agricultural Research Service,
University of Missouri, Columbia, MO 65211, USA
e-mail: Ken.Sudduth@ars.usda.gov

13.1 Introduction

As agriculture has become a more information-intensive activity, from within-field scales (i.e. precision agriculture) to landscape and basin scales (i.e. digital soil mapping), the need for accurate, timely, and cost-effective quantification of soil properties through the use of sensors has increased. Optical diffuse reflectance spectroscopy (DRS) is one candidate soil sensing technology (Chapter 3) and has been investigated since at least the 1970s. Early research (prior to 1990) on this topic, as reviewed by Sudduth et al. (1997), can be categorised into three broad areas: (1) understanding how reflectance in satellite wavelength ranges could be related to soil properties; (2) building on earlier research using qualitative descriptors of soil colour to develop quantitative relationships between reflectance and soil properties; and (3) developing mobile reflectance sensors that could be used to control agronomic inputs, particularly the application rate of herbicides.

With the advent of precision agriculture and the concept of digital soil mapping, there has been renewed interest in optical DRS of soil properties. Researchers have collected spectra in the visible (VIS; 400–700 nm), near-infrared (NIR; 700–2,500 nm), and mid-infrared (MIR; 2,500–25,000 nm) for this purpose (Chapter 3). Viscarra Rossel et al. (2006) summarised recent research results and found that the MIR region generally provided more accurate results, a finding also reported in Chapter 14. Instrumentation for VIS and NIR (VNIR) DRS is less complex and expensive and at least one on-the-go VNIR soil sensor has become commercial (Christy, 2007). Research efforts continue towards adapting MIR technology for field use (Chapter 11).

Although most studies have developed calibrations using samples across a broad range (e.g. Sudduth and Hummel, 1991; Chang et al., 2001; Lee et al., 2009; Chapter 15), some have reported field-specific calibration efforts (Ge et al., 2007; Viscarra Rossel et al., 2006; Christy, 2007; Chapter 14). At field scales, one issue that becomes important is spatial dependence in the data. If only a few within-field sampling sites are employed, then it may be valid to assume that there is little or no spatial dependence. However, a denser sampling scheme (e.g. grid sampling) may create significant spatial autocorrelation in the data. Not including these effects in the model violates the usual assumption of statistical independence of the calibration residuals and can render the model suboptimal (Ge et al., 2007). For example, when Ge et al. (2007) applied the regression kriging approach to VNIR spectra for estimating within-field variations in soil properties, they found improved soil property estimates compared to a non-spatial principal component regression (PCR), particularly for those properties that were poorly estimated by PCR.

The purpose of this study was to determine the ability of VNIR DRS to estimate within-field variability in soil properties on a typical claypan soil field in north-central Missouri, USA. We anticipated that this application would be particularly challenging due to the relatively small variation in some soil properties, such as organic matter, that are commonly well estimated by VNIR DRS. We used a very spatially dense dataset and a methodology that might not be directly applicable for

practical implementation of VNIR DRS soil mapping where a minimum number of within-field calibration samples would be desired. However, this approach allowed us to obtain a ‘best case’ calibration that we can use as a baseline in future work evaluating calibration alternatives for claypan soil fields. Specific objectives of this study were (1) to identify the more predictive portion(s) of the VNIR spectrum for estimating claypan soil properties and (2) to compare non-spatial regression estimates to those obtained using regression kriging.

13.2 Materials and Methods

13.2.1 Study Site and Soil Sampling

Data were collected on a 35 ha research field located near Centralia, Missouri, USA (92.12°E, 39.97°N). The field was managed in a minimum tillage corn–soybean rotation. Soils are claypan soils of the Mexico (fine, smectitic, mesic aeric Vertic Epiqualfs) and Adco series (fine, smectitic, mesic aeric Vertic Albaqualfs). Surface textures range from a silt loam to a silty clay loam. The subsoil claypan horizon(s) are silty clay loam, silty clay, or clay and commonly contain as much as 50–60% smectitic clay.

The field was sampled on a 30 m grid to a 15 cm depth in the spring of 2001. An additional 24 soil samples were obtained at random locations to help define the short-range spatial structure. At each location, eight 1.5 cm diameter cores were obtained to 15 cm depth and composited. Samples were analysed for available P (Bray 1 extractable), exchangeable K, Ca, and Mg (ammonium acetate extractable), cation exchange capacity (CEC; sum of bases), organic matter (OM; loss on ignition), and pH, using standard University of Missouri procedures (Nathan et al., 2006). A rectangular 4 ha sub-field area was sampled on the same grid and analysed for a number of soil physical, chemical, and microbial properties as described by Jung et al. (2006). We used data from that study on 0–15 cm soil texture (clay, silt, and sand fraction) in this analysis.

13.2.2 Spectral Data Acquisition

Soil spectral reflectance data were obtained in the laboratory using an ASD FieldSpec Pro FR¹ spectrometer (Analytical Spectral Devices, Boulder, CO, USA). Air-dried, ground samples were used for reflectance data collection. The samples were illuminated by a halogen lamp and the reflected light was transmitted to the

¹Mention of trade names or commercial products is solely for the purpose of providing specific information and does not imply recommendation or endorsement by the US Department of Agriculture or its cooperators.

spectrometer through a fibre optic bundle. Spectra (350–2,500 nm) were recorded and output at a 1 nm interval. Each soil spectrum was the mean of 10 scans. Compensation for dark current variations was applied at the beginning of each data collection session and at least once every 30 min thereafter. A Spectralon (Labsphere Inc., North Sutton, NH) reflectance standard was scanned after every 10 soils and used to convert raw spectral data to decimal reflectance.

13.2.3 Analysis Procedures

Reflectance data were preprocessed to remove erroneous measurements and improve stability of the regression. Data from 350 to 499 nm and 2,451 to 2,500 nm were deleted due to their low signal-to-noise ratio, and the remaining 1951-point spectra were transformed from reflectance to absorbance ($\log 1/\text{reflectance}$). Preliminary analyses showed no consistent improvement with other data transformations (e.g. derivative, smoothing), so no other transformations were applied. Several observations identified as outliers by visual inspection or with missing data values were also removed. Data were randomly assigned on an 80–20 basis into calibration and test sets: 42 calibration and 13 test samples for texture and 299 calibration and 74 test samples for all other soil properties.

Although some have reported other methods to be superior in certain situations (Chapter 17), we chose to use partial least squares (PLS) regression, as implemented in Unscrambler version 9.1 (CAMO Inc., Oslo, Norway) to develop calibrations between soil properties and spectra. A 20-fold cross-validation procedure was used to select the number of PLS factors to use in the regression, increasing predictive capability and decreasing the potential for overfitting. These cross-validation results were used directly for evaluating the predictive capability of spectral regions. Models incorporating spatial dependence were constructed using the regression kriging approach described by Odeh et al. (1995). Semivariograms of measured soil data and of PLS regression residuals from the calibration set were fitted using GS+ version 5.1.1 (Gamma Design Software, Plainwell, MI, USA), which was also used to point-krige the residuals to test set locations. Estimated soil property values at the test set locations were given by the sum of the non-spatial PLS estimate and the kriged estimate of the spatial residual. Fit statistics derived from the independent test set were used for the regression kriging evaluation.

Model evaluation was based on coefficient of determination (R^2), root mean square error of prediction (RMSEP), and the ratio of standard deviation to RMSEP (RPD). RPD is useful when comparing results from datasets containing different degrees of variability. Chang et al. (2001) suggested that, as a general guideline, $RPD > 2.0$ or $R^2 > 0.8$ indicates success in estimating soil properties, $RPD < 1.4$ or $R^2 < 0.5$ shows unacceptable results, and calibrations with intermediate values may be improved to acceptable levels using different strategies. Results obtained with PLS, and PLS plus regression kriging, were further compared using difference maps of selected soil properties developed using the calibration dataset ($n = 299$).

13.3 Results and Discussion

13.3.1 Variability in Soil Properties

Soil property means were generally similar between the calibration and the test datasets (Table 13.1), as were standard deviations for all variables except P and clay fraction, indicating that the partitioning of observations into the two datasets was reasonable. The variation in many soil properties was quite low (CVs of $\sim 25\%$ or less). Variability in measured soil properties has often been higher (CVs of $\sim 50\%$ or more) in those wider-scale calibration studies, where good results have been reported (e.g. Chang et al., 2001; Lee et al., 2009).

Semivariograms fitted to the measured soil data showed varying degrees of spatial dependence (Table 13.2). Range parameters of these generally exponential semivariograms varied from 21 to 104 m, verifying that it was important to consider spatial dependence. Spatial structure was particularly well defined for texture fractions, which had very low nugget ratios. However, because the texture data were from a sub-field with $<15\%$ of the total field area, these results may not be directly comparable with other data. The highest nugget ratio in the measured data was for organic matter (OM). This may have been caused by the low relative accuracy of the OM lab analysis, where results were reported to only the nearest 0.1%.

Table 13.1 Descriptive statistics of soil property measurements

	Calibration dataset ^a			Test dataset ^b		
	Mean	SD	CV, %	Mean	SD	CV, %
Exch. Ca, mg kg ⁻¹	2,310	430	18.7	2,290	440	19.2
Exch. K, mg kg ⁻¹	80.4	30.4	38.0	80.8	31.2	38.9
Exch. Mg, mg kg ⁻¹	200	79	39.5	208	100	48.2
Av. P, mg kg ⁻¹	13.5	15.4	114.7	12.3	8.4	68.1
CEC, cmol _c kg ⁻¹	15.0	2.8	18.5	15.2	3.3	21.6
pH	6.2	0.50	8.0	6.2	0.58	9.4
Organic matter, %	2.0	0.35	17.1	2.1	0.34	16.4
Clay content, %	18.9	5.0	26.4	17.5	2.4	13.7
Silt content, %	73.5	5.5	7.4	76.3	4.1	5.3
Sand content, %	7.6	2.6	33.9	6.3	2.8	44.9

^a $n = 42$ for texture fractions, $n = 299$ for all other soil properties

^b $n = 13$ for texture fractions, $n = 74$ for all other soil properties

13.3.2 Predictive Capability of Spectral Regions

Regression analyses using PLS were completed for each soil property and each of three different spectral regions: (1) SR0, the complete spectrum from 500 to 2,450 nm; (2) SR1, from 500 to 1,000 nm; and (3) SR2, from 1,001 to 2,450 nm. We divided the spectrum in this manner due to instrumentation considerations. Below

Table 13.2 Semivariogram parameters for measured soil properties and VNIR regression residuals

	Measured data		Regression residuals	
	Nugget ratio, % ^a	Range, m	Nugget ratio, % ^b	Range, m
Ca	34	37	7.2	8
K	22	21	21	10
Mg	27	36	30	37
P	42	60	48	50
CEC	40	50	61	41
pH	26	104	65	40
Organic matter	50	59	68	80
Clay fraction ^b	4.4	71	100	—
Silt fraction	0.1	57	95	154
Sand fraction	0.1	45	98	154

^a Nugget ratio calculated as 100 (nugget/sill)^b Texture fraction data are from a 4 ha area vs. 35 ha area for other properties

about 1,000–1,100 nm, Si-based photodetectors are generally used, while at higher wavelengths other detector technologies, such as indium gallium arsenide (InGaAs), are required. Thus our division was based on the spectral range that could be sensed using a single detector. The specific division we chose (1,000 nm) was where the ASD spectrometer in this study switched from using its Si detector to the first of its two InGaAs detectors.

Generally, the same spectral range was best whether evaluation was on the basis of R^2 , RMSEP, or RPD (Table 13.3); only in one case (silt fraction) was there a

Table 13.3 Performance of various spectral ranges for estimating soil properties. **Bold** entries illustrate the best spectral range for each performance measure and soil property. Results from cross-validation analysis with $n = 42$ for texture fractions and $n = 299$ for other soil properties

	R^2			RMSEP ^a			RPD		
	SR0 ^b	SR1	SR2	SR0	SR1	SR2	SR0	SR1	SR2
Ca	0.72	0.64	0.63	204	234	233	2.12	1.86	1.86
K	0.32	0.29	0.28	21.5	22.6	22.2	1.41	1.37	1.37
Mg	0.73	0.58	0.71	36.7	46.9	38.6	2.15	1.73	2.10
P	0.31	0.31	0.27	10.7	10.9	11.4	1.44	1.44	1.40
CEC	0.73	0.63	0.72	1.4	1.6	1.5	1.96	1.67	1.92
pH	0.78	0.78	0.56	0.23	0.24	0.32	2.14	2.16	1.52
Organic matter	0.31	0.18	0.34	0.28	0.30	0.28	1.23	1.14	1.26
Clay fraction	0.49	0.49	0.56	3.59	3.96	3.31	1.39	1.30	1.51
Silt fraction	0.68	0.58	0.67	3.12	3.79	3.11	1.76	1.52	1.77
Sand fraction	0.04	0.02	0.28	2.53	2.59	2.37	1.03	1.02	1.12

^aUnits for RMSEP given in Table 13.1^bSR0: 500–2,450 nm; SR1: 500–1,000 nm; SR2: 1,001–2,450 nm

marginal difference. Best estimates were most often obtained with the full wavelength range, or in a few cases with the upper NIR spectral range, SR2. The trend towards better results with NIR data in the regression agrees with prior research (e.g. Sudduth and Hummel, 1991; Viscarra Rossel et al., 2006). There were cases (e.g. pH) where the SR1 estimation was as good as the SR0 estimation and considerably better than the SR2 estimation (Table 13.3). On the other hand, there were instances (e.g. silt) where SR0 and SR2 gave essentially equivalent results that were much better than those with SR1.

The importance of different wavelength ranges for different soil properties can also be illustrated by the PLS regression coefficients. To aid visualisation, the spectrum was first averaged to 40 nm resolution. Results with the averaged spectrum were generally within 3% (in RPD) of those with the original spectrum (data not shown). For pH, the largest regression coefficients were in the 500–700 nm range (Fig. 13.1), corresponding to the good SR1 estimate of pH (Table 13.3). For silt, larger regression coefficients were obtained from the NIR spectrum above 1,900 nm, corresponding to the good SR2 estimate of silt. This lack of consistency in optimum wavelength range makes it difficult to use a single-detector instrument when estimating a wide range of soil properties. For these soils, an NIR-only instrument would be able to quantify CEC, OM, and texture fractions as well (or almost as well) as a VNIR instrument. However, to achieve best results for all soil properties, a VNIR instrument would be needed.

The predictive capability of the VNIR DRS analysis varied among soil properties. Using RPD to compare across variables of different magnitudes, the most accurate estimates were obtained for exch. Ca, exch. Mg, pH, and CEC. Less

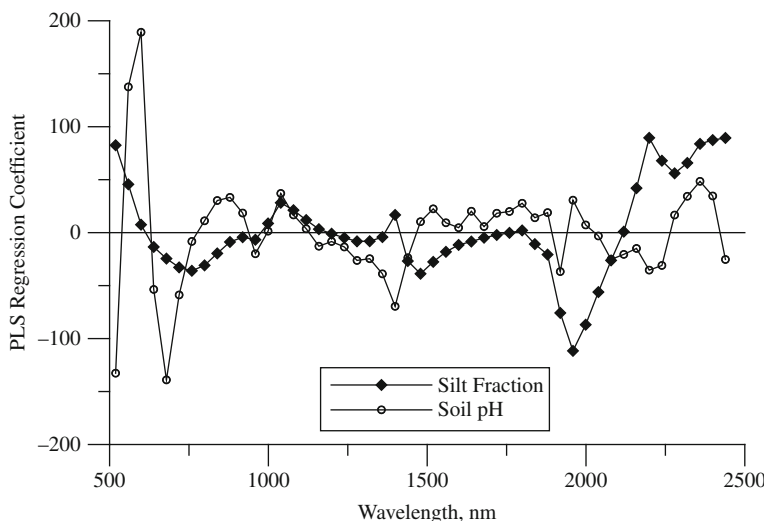


Fig. 13.1 PLSR coefficients for pH, which was well estimated with VIS data, and for silt fraction, which was well estimated by NIR data

accurate results were obtained for K, P, clay, and silt, while estimates of OM and sand were poor. The poor OM estimates were contrary to the many previous studies where OM (or organic carbon, OC) has generally been estimated quite well ($R^2 > 0.8$, $RPD > 2.5$; see literature review in Viscarra Rossel et al., 2006). On an absolute basis, OM errors were as good or better ($RMSEP = 0.28\text{--}0.30$) than those obtained in a number of other studies ($RMSEP \sim 0.30$, Viscarra Rossel et al., 2006; $RMSEP \sim 0.34$, Sudduth and Hummel, 1991; $RMSEP \sim 0.55$, Lee et al., 2009). In this case, poor relative estimates of OM, and also sand, were likely caused by the low standard deviations observed for those variables in the study field (Table 13.1).

13.3.3 Regression Kriging

For most soil variables there was an improvement with regression kriging (Table 13.4). Relatively large improvements were seen for Ca, K, and Mg, all of which had low nugget ratios, and therefore strong spatial structure, in their residual semivariograms (Table 13.2). Texture fractions showed little or no improvement, and their residual semivariograms had very high nugget ratios and little or no spatial structure, perhaps because the texture dataset was much smaller. Compared to results reported by Ge et al. (2007), regression kriging improvements were generally smaller. On the other hand, their regression results (by PCR rather than PLS) were generally poorer than those found in this study, and their overall regression kriging results were also poorer.

Figure 13.2 shows, for four selected soil properties, maps of actual, laboratory-measured data, and difference maps comparing (relative to the measured data) VNIR-PLS estimated data and VNIR regression kriging estimated data. In the case of exch. Mg, PLS estimates were good (Table 13.4), and there was also strong spatial

Table 13.4 Performance of PLS regression alone compared to PLS regression kriging. Validation results from separate test set ($n = 13$ for texture fractions, $n = 74$ for other soil properties)

	R^2		RMSEP ^a		RPD	
	PLS	PLS+RK	PLS	PLS+RK	PLS	PLS+RK
Ca	0.76	0.80	205	184	2.12	2.36
K	0.39	0.45	21.9	20.7	1.39	1.47
Mg	0.87	0.92	32.4	25.8	2.44	3.07
P	0.51	0.63	6.3	6.2	2.43	2.49
CEC	0.87	0.85	1.22	1.31	2.30	2.14
pH	0.84	0.88	0.24	0.20	2.08	2.50
Organic matter	0.55	0.55	0.23	0.23	1.52	1.52
Clay fraction	0.15	0.14	2.68	2.58	1.87	1.94
Silt fraction	0.63	0.62	1.79	1.84	3.07	2.99
Sand fraction	0.76	0.74	1.91	2.04	1.36	1.27

^aUnits for RMSEP given in Table 13.1

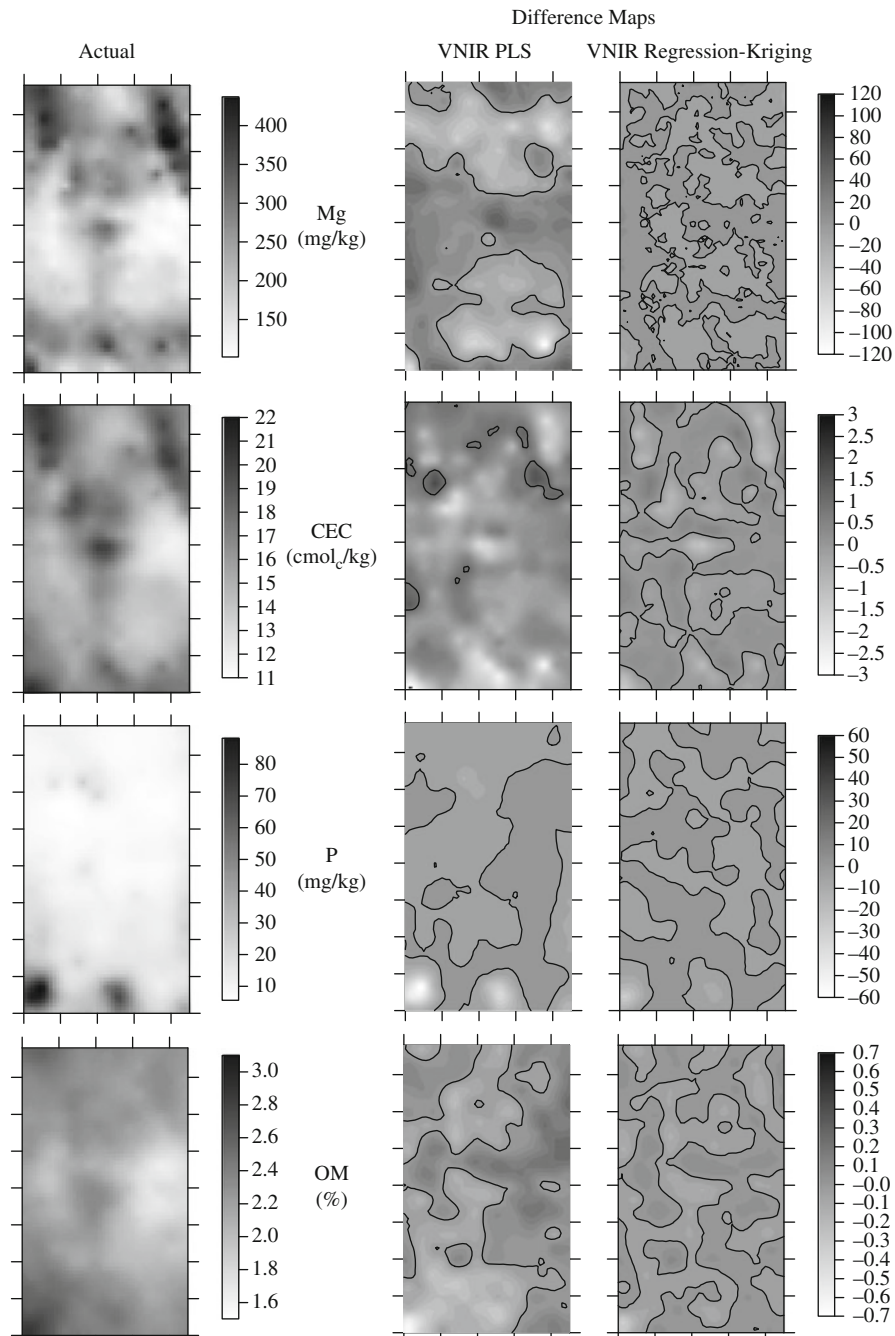


Fig. 13.2 Maps of selected soil properties from kriged lab analysis data (left), difference maps between lab data and kriged VNIR-PLS calibration (centre), and difference maps between lab data and regression kriging of VNIR-PLS calibration residuals (right). Zero lines are shown in the difference maps for reference

structure (Table 13.2). Thus, the PLS – actual differences were relatively small compared to the actual data range, while the regression kriging difference maps had a lower magnitude and a more random spatial structure. For CEC, PLS estimates were good, but there was little spatial structure to the residuals. Thus, the spatial structure of the two difference maps is similar, although the regression kriging appears to have removed some of the bias present in the PLS results. In the case of available P, PLS estimates were not good, but there was spatial structure to the residuals. Here, the regression kriging difference map has a lower magnitude and less structure than does the PLS difference map. Finally, in the case of OM, neither the PLS estimate nor the semivariogram was particularly predictive. The magnitudes of the differences seen in both maps were relatively large compared to the range of the actual data.

The usefulness of regression kriging for improving VNIR DRS estimates of soil properties was mixed. In some cases it provided a significant improvement over a non-spatial analysis, but in other cases it had little or no effect. An obvious drawback to practical application of the regression kriging approach is that measured soil data must be known at a high spatial density, contrary to the usual goal of using spectral data to estimate soil properties based on a few measurements. However, regression kriging was useful in this research, where we were interested in establishing a ‘best’ calibration for this dataset against which additional calibration approaches could be evaluated.

It is worthwhile to note that our evaluation of the predictive capability of the various spectral ranges and calibration methods was based solely on goodness-of-fit criteria – R^2 , RMSEP, and RPD – and that interpretations of whether a particular method was good were based on how well it represented the lab-measured data. Given the goals of this research, that approach seemed appropriate. However, a complete evaluation of the usability of VNIR DRS should also consider the intended uses of the soil property estimates and the accuracy needed for those particular uses.

13.4 Conclusions

Our goal in this study was to assess the ability of VNIR DRS to estimate the variability of selected soil properties within a typical claypan soil field. We found that some soil properties, such as CEC and pH, were well estimated with PLS regression, while others, such as OM, were not. Coupling regression kriging with PLS regression improved estimates in some cases, but was not as effective as has been reported in some other studies. Within-field estimation of soil properties with VNIR DRS is challenging, particularly so on claypan soil fields, due to the narrow range seen in some soil properties of interest. More advanced calibration methods, such as those used by Christy (2007), should be investigated for their ability to improve within-field VNIR DRS results on these soils.

References

Chang CW, Laird DA, Mausbach MJ, Hurlburgh Jr. CR (2001) Near-infrared reflectance spectroscopy – principal component regression analysis of soil properties. *Soil Sci Soc Am J* 65:480–490

Christy CD (2007) Real-time measurement of soil attributes using on-the-go near infrared reflectance spectroscopy. *Comput Electron Agric* 61:10–19

Ge Y, Thomasson JA, Morgan CL, Searcy SW (2007) VNIR diffuse reflectance spectroscopy for agricultural soil property determination based on regression-kriging. *Trans ASABE* 50:1081–1092

Jung WK, Kitchen NR, Sudduth KA, Anderson SH (2006) Spatial characteristics of claypan soil properties in an agricultural field. *Soil Sci Soc Am J* 70:1387–1397

Lee KS, Lee DH, Sudduth KA, Chung SO, Kitchen NR, Drummond ST (2009) Wavelength identification and diffuse reflectance estimation for surface and profile soil properties. *Trans ASABE* 52:683–695

Nathan M, Stecker J, Sun Y (2006) Soil testing in Missouri: A guide for conducting soil tests in Missouri. Extension circular 923, 4/06 revision. Missouri cooperative extension service, Columbia, MO. available online at: http://soilplantlab.missouri.edu/soil_soiltesting-inmissouri.pdf

Odeh IOA, McBratney AB, Chittleborough DJ (1995) Further results on prediction of soil properties from terrain attributes: heterotopic cokriging and regression-kriging. *Geoderma* 67:215–226

Sudduth, K.A., Hummel, J.W., (1991). Evaluation of reflectance methods for soil organic matter sensing. *Transactions of the ASAE* 34:1900–1909

Sudduth KA, Hummel JW, Birrell SJ (1997) Sensors for site-specific management. In: Pierce FJ, Sadler EJ (eds) *The State of Site-Specific Management for Agriculture*. ASA, CSSA, and SSSA, Madison, WI, pp 183–210

Viscarra Rossel RA, Walvoort DJJ, McBratney AB, Janik LJ, Skjemstad JO (2006) Visible, near infrared, mid infrared or combined diffuse reflectance spectroscopy for simultaneous assessment of various soil properties. *Geoderma* 131:59–75

Chapter 14

Infrared Sensors to Map Soil Carbon in Agricultural Ecosystems

G. McCarty, W.D. Hively, J.B. Reeves III, M. Lang, E. Lund, and O. Weatherbee

Abstract Rapid methods of measuring soil carbon – such as near-infrared (NIR) and mid-infrared (MIR) diffuse reflectance spectroscopy – have gained interest, but problems of accurate and precise measurement still persist as a result of the high spatial variability of soil carbon within agricultural landscapes. Tillage-based (meaning tine-mounted) and airborne-based spectral sensors offer the opportunity to effectively capture the spatial distribution of soil carbon within agricultural landscapes. We evaluated an airborne hyperspectral sensor covering the range 450–2,450 nm at 2.5 m spatial resolution and a tillage sensor covering the range 920–2,225 nm. We intensively sampled soils within five tilled agricultural fields within the flight path of the airborne sensor. The test fields were located on the Delmarva Peninsula in Maryland, USA. The quality of spectral data acquired by these field-based sensors was compared to laboratory-acquired spectral data in both NIR (1,000–2,500 nm) and MIR (2,500–25,000 nm) spectral regions for the soil samples taken at 304 geo-referenced locations within the fields. Partial least squares regression (PLSR) models developed from the three NIR spectral data sources were very comparable, indicating that the two field-based NIR sensors performed well for generating spatial data. Although the laboratory-based MIR calibration was found to be substantially better than the laboratory-derived NIR calibration, current instrumentation limitations favour the use of NIR for in-field measurements. A 2.5 m resolution soil carbon map was produced for an agricultural field using the airborne hyperspectral image and the PLS calibration. This new approach for mapping soil carbon will permit better assessment of soil carbon sequestration in agricultural ecosystems at the landscape scale. Such data can be used to improve the landscape models which account for biogeochemical and soil redistribution processes that occur within often complex topographic and management settings.

Keywords Mid-infrared diffuse reflectance spectroscopy · Near-infrared diffuse reflection spectroscopy · Partial least squares regression

G. McCarty (✉)

USDA Hydrology & Remote Sensing Laboratory, Beltsville, MD, USA

e-mail: greg.mccarty@ars.usda.gov

14.1 Introduction

Increasing carbon dioxide in the Earth's atmosphere has stimulated research to assess the role of terrestrial ecosystems in the global carbon (C) cycle. The terrestrial biosphere is an important component of the global C budget, but estimates of C sequestration in terrestrial ecosystems are partly constrained by the limited ability to assess the distribution of soil C storage. Croplands have good potential for sequestering atmospheric C if C-positive farming methods such as no-till, organic, and perennial cropping (Lal, 2004) are adopted, but current technologies for monitoring soil C sequestration in terrestrial ecosystems are not cost-effective or depend on laborious methods. Additionally, site-specific management of agricultural landscapes requires detailed information regarding the spatial distribution of soil properties across toposequences found in agricultural ecosystems (Hattfield, 2000).

Spatial assessment of soil carbon within agricultural landscapes requires intensive measurement and is important for understanding the dynamics of carbon within agricultural ecosystems. Errors in spatial assessment of soil C distribution within an ecosystem can result from inadequate or biased sampling of the landscape and from analytical errors in soil C measurements. The largest error is often that of sampling, which may be a poorly stratified reflection of real landscape variability or be too small in number to cover the actual range of soil C.

Diffuse reflectance spectroscopy offers a nondestructive means of measuring soil C based on the reflectance of illuminated soil (see Chapters 11, 12, 13, and 15). Both the near-infrared (NIR) and the mid-infrared (MIR) regions have been investigated using chemometrics for their use in quantifying soil C (Chapter 11; Janik et al., 1998; McCarty et al., 2002; McCarty and Reeves, 2006). Although MIR results are often superior (McCarty and Reeves, 2006), practical measurement technologies are generally more advanced in the NIR region. Most reported spectroscopic approaches involve field sampling, with subsequent laboratory analyses of both reflectance and soil chemical and physical properties.

For mapping soil carbon, remote sensing approaches have an obvious advantage – the spatially explicit nature of images – but a suitable means of quantification is needed. Chemometric approaches to quantification use large sample sets for calibration model development, sufficient to cover the range of properties expected in the sample population. This reduces interference in the calibration from spectral variance caused by sources unrelated to the property of interest. This differs from the customary approach within the remote sensing discipline of using end-member analysis, which is based on summation of pure spectra for components within the image. Such an approach can work well for scenes comprised of well-defined components such as mineral crystals. A classic example of this approach is mapping outcrops of minerals on land surfaces by use of hyperspectral imaging (Vaughan et al., 2005). However, because soil organic matter composition is not constant or well-defined, a similar end-member approach to quantification is not applicable because no defined end-member spectrum for soil organic matter can be generated.

Recent developments have led to a tillage-implement-based (tine-mounted) NIR sensor for detection of soil C in which reflectance measurements are made through

a sapphire window mounted on the bottom of a shank, which is then pulled through the soil (Christy et al., 2006). Airborne hyperspectral imaging spectrometers also hold promise as they can acquire a detailed spatial dataset of a soil. The aim of this study was to compare the ability to generate partial least squares regression (PLSR) models for tillage and airborne NIR sensors relative to those generated from standard laboratory-based NIR and MIR diffuse reflectance instruments. This study also tests the ability to generate PLS prediction maps for soil carbon using airborne hyperspectral images.

14.2 Materials and Methods

14.2.1 Soil Samples

In April 2007, 304 samples were collected from the plough layer (0–20 cm) of five bare soil fields (recently ploughed and generally vegetation-free) located on the Eastern Shore of Maryland, USA. Soils in this region are generally classified as acrisols using the Food and Agriculture Organization (FAO) soil classification system (<http://www.fao.org/docrep/W8594E/W8594E00.htm>). Sampling occurred in transects across the fields and corresponded to transects of NIR spectral data collected by the tillage-based sensor (see next section). Soil samples were dried at 50°C for 2 days and crushed using a hammer mill to pass through a 2 mm screen. The crushed material was further ground in scintillation vials containing two stainless steel rods and placed on a roller mill overnight. Soil C content of these samples was determined by dry combustion using a TruSpec CN analyser (Leco Corp, St. Joseph MI). None of the samples contained significant inorganic C. On the same day as field sampling, field-based spectral measurements were collected.

14.2.2 Spectral Measurements

14.2.2.1 Airborne Measurements

Hyperspectral image data were acquired with the AISA dual hyperspectral sensor system (Spectral Imaging Ltd, Finland) for simultaneous acquisition of visible–near-infrared (VNIR, 400–970 nm) and shortwave infrared (SWIR, 970–2,450 nm) data. The instrument measures reflected radiance in 178 spectral channels between 400 and 2,450 nm with approximately 10 nm resolution. The instrument is mounted on a tilting platform allowing for real-time compensation for aircraft motion. The aircraft was flown by the SpecTIR Corporation (Reno, Nevada, USA) at 1,800 m above the Earth's surface with a ground speed of 210 km h⁻¹. The images cover a swathe approximately 1 km wide (320 adjacent 2.5 m pixels; Fig. 14.1). Airborne reflectance data associated with soil sampling locations were extracted and spectra from nine neighbouring pixels centred on the sampling location were then averaged, resulting in average reflectance from an 81 m² area.

Fig. 14.1 An example of an airborne hyperspectral image collected in April 2007 on the Eastern Shore of Maryland, USA



A preliminary soil carbon prediction map was first generated using the raw (unfiltered) hyperspectral data. Before generation of the final soil carbon prediction map, spectra associated with each pixel in the image were smoothed by use of a low-pass filter which averages nine neighbouring pixels (kernel = 3) and assigns the average spectra to each of the central pixels. The smoothed spectra for the pixels were then used for PLS predictions. In this way, the approximate same degree of smoothing was applied to spectra used to develop the calibration as were used to generate the prediction data and the signal-to-noise ratios should be similar.

The airborne hyperspectral imager uses push-broom line scan technology which means that individual lines of data are obtained using the forward motion of the aircraft to sweep out a continuous strip image of the ground. One characteristic of this type of sensor is that a particular sensor array position will collect a line of data parallel to the flight path (Petrie, 2005). As a result, spectral variations due to internal instrument variances (associated with different sensor array positions) may appear as single pixel width bands in the unfiltered prediction image parallel to the flight path direction. To correct this banding error, we averaged spectra for the two pixels on both sides of the band and replaced the centre pixel value with the resulting spectrum. This operation was performed before spectral data were smoothed globally using the low-pass filter.

14.2.2.2 Proximal Measurements

Transects of NIR spectral data were collected using a tractor-mounted spectrophotometer built into a shank mounted on a toolbar and pulled behind the tractor.

Fig. 14.2 Pattern of soil sampling along transects generated by the tillage-based sensor. The size of the dots indicates relative differences in organic C content



Spacing between transects was 30 m on average (Fig. 14.2). Spectral measurements were acquired through a sapphire window mounted on the bottom of the shank. The spectrophotometer uses a tungsten halogen bulb to illuminate the soil and the reflected light is collected into a fibre optic cable for transmission to the spectrometer. An InGaAs photodiode array spectrometer (Model NIR-128L-1.7-USB, Control Development, Inc., South Bend, IN) was used to collect spectral data in the range 920–2,225 nm at a resolution of 6.35 nm. Shutters in the shank were manipulated to acquire dark and reference spectra at approximately 3–5 min intervals. The shank was pulled through the soil at approximately 7 cm depth at 6 km h^{-1} , acquiring approximately 20 spectra per second. Reflectance data associated with soil sampling locations were extracted using a Gaussian elliptical weighting algorithm to obtain a distance weighted average involving approximately five spectra for each location.

14.2.2.3 Laboratory Measurements

Oven-dried and sieved samples were scanned (64 co-added scans, four wave number resolution) in the near-infrared (NIR, 1,000–2,500 nm) and mid-infrared (MIR, 2,500–25,000 nm) regions on a Digilab Fourier transform spectrometer (FTS7000 FTS, Varian, Inc., Palo Alto, CA) equipped with DTGS (deuterated triglycine sulfate) and InSb detectors using a Pike (Pike Technologies, Madison, WI) AutoDiff auto-sampler (sample cups $\sim 1 \text{ cm}$ in diameter).

14.2.3 Chemometrics

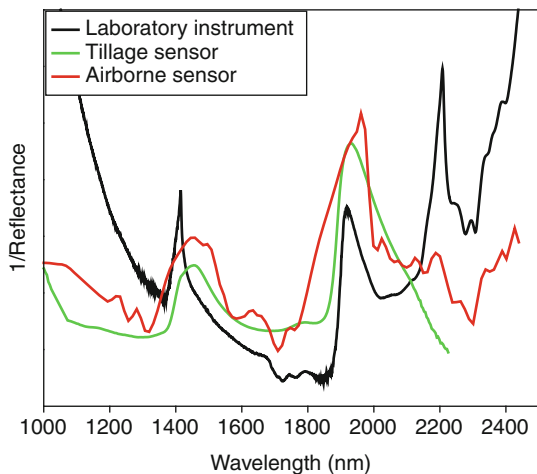
All calibrations were developed using the partial least squares (PLS) regression subroutines in SAS Ver. 9.12 PLS (Reeves and Delwiche, 2003). A total of 30 different

spectral pre-treatments were tested including multiplicative scatter correction and first and second gap derivatives with all spectra mean centred and variance scaled. The PRESS F test was used to select the number of factors used in the calibration. Calibration and independent validation sets were developed by randomly dividing the sample set into one-third for validation and two-thirds for calibration.

14.3 Results and Discussion

A comparison of averaged NIR spectrum ($n = 304$) for the laboratory, airborne-based, and tillage-based instruments is shown in Fig. 14.3.

Fig. 14.3 Averaged NIR spectra ($n = 304$) generated by the different near-infrared sensors



Substantial differences in spectral characteristics were observed among the methods. The tillage-based sensor generated spectra with the fewest amount of reflectance features discernable by visual inspection. Peaks around 1,400 and 1,900 nm associated with water were broader for the two field-based sensors. One notable difference is that the airborne sensor depends on natural sunlight, which is subjected to atmospheric filtering. This may account for the greater number of small-scale features evident in the spectra.

14.3.1 Calibration and Validation

The distribution of soil organic C contents within the sample set is shown by the histogram in Fig. 14.4 showing a near-normal distribution of samples with slight negative skewness.

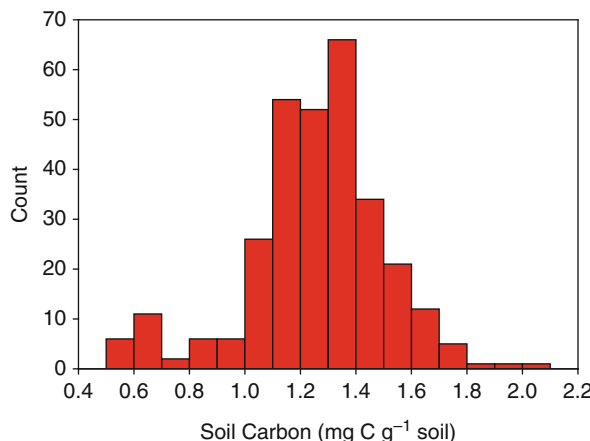


Fig. 14.4 Histogram showing the distribution of soil organic C contents within the 304 sample set used to develop NIR calibrations

Table 14.1 Calibration and validation statistics for PLSR models generated from the different spectral data sources

Source	Calibration		Validation	
	RMSD	R ²	RMSD	R ²
Airborne	0.15	0.64	0.17	0.54
Tillage	0.14	0.71	0.18	0.53
Lab. NIR	0.11	0.81	0.19	0.45
Lab. MIR	0.08	0.90	0.11	0.83

The PLS regression models for the NIR region generated a range of coefficients of determination (R^2) for prediction of soil organic C with the laboratory calibration outperforming those from tillage and airborne acquired data (Table 14.1). However, the validation statistics based on an independent sample set consisting of one-third of total samples indicated that the laboratory-based calibration was the least robust among the NIR calibrations.

Figure 14.5 shows the relationships between calibration and validation predictions for the MIR and NIR models. The laboratory NIR model provided the greatest difference in slope between calibration and validation sets, with the airborne and tillage NIR model performance between that of laboratory MIR and NIR. It is notable that the ability to quantify soil carbon by spectral measurements in the NIR region is considerably poorer in this study than what has been previously reported for other sets of soil ($R^2 = 0.90$, RMSD = 0.14% C for McCarty and Reeves, 2006). This may be due in part to a more limited range of soil C values within the current study (0.5–2.6% C with 73% of samples falling between 1.0 and 1.5% C).

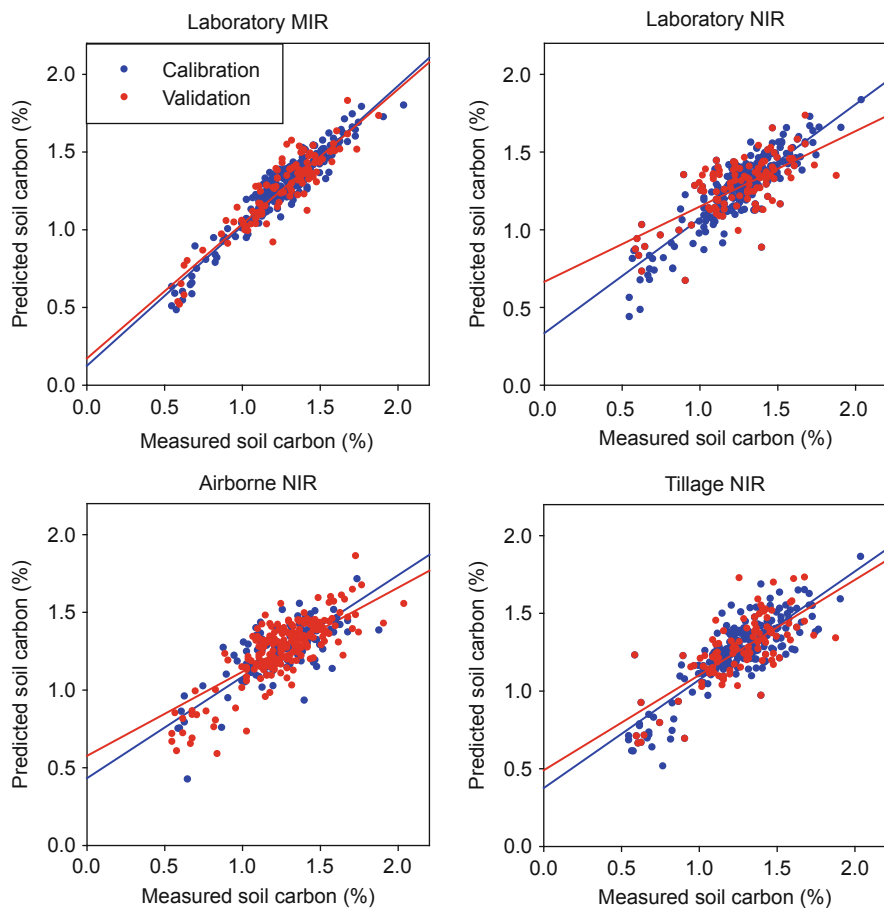


Fig. 14.5 Calibration data generated by partial least squared (PLS) regression models using the different spectral data sources

These data are consistent, however, with our previous findings that MIR outperforms NIR. This is likely due to the superior information contained within the MIR spectra (McCarty et al., 2002). Strong atmospheric absorption in portions of the MIR region is likely to preclude its use in remote sensing of soil carbon but not for in situ proximal soil sensing.

The under-performance of laboratory NIR during validation is interesting, since spectral data generated in the laboratory would be expected to have the least amount of noise. Additionally, there is a disparity in sample support for laboratory- versus field-scale spectral measurements. The laboratory data were collected from the actual sample analysed for carbon and therefore should have the lowest amount of error based on sample heterogeneity. The tillage-based spectral measurements would be expected to have additional error associated with global positioning

system (GPS) uncertainty during acquisition of the data, as well as the influence of soil moisture and aggregate structure. The airborne-based spectral data were smoothed to an average of nine 2.5 m pixels before analysis and may therefore be expected to require greater sample support than supplied by a single sampling point to account for spatial heterogeneity within the pixel.

14.3.2 Potential for Optimising Sampling Design

Interpolation between data transects created by the tillage-based sensor has been shown to create accurate maps of soil carbon (Christy et al., 2006). Operational spectral maps created by either the tillage or the airborne sensors could be used to design the optimal sampling strategy for a landscape with sampling stratification based on spatial analysis of spectral variance. Christy et al. (2006) described a protocol in which reflectance data are compressed using principal components analysis and then clustered using a fuzzy c-means algorithm. The algorithm was used to determine representative sample locations within each cluster based on minimal spatial variability. Acquired samples are then used to develop the calibration. This approach should generate a balanced sample set for the development of calibrations. McCarty and Reeves (2001) provided evidence that regional calibrations for soil properties can be developed and bias introduced by a location can be corrected by adding a few samples from the new location to the calibration set. This can provide a very efficient means of refining calibrations for the area of interest. By use of these calibration strategies, in conjunction with diffuse reflectance NIR sensors, it may be possible to efficiently measure soil carbon stocks within some agricultural ecosystems.

14.3.3 Remote Sensing of Soil Carbon

To generate a soil carbon prediction map, we applied the aircraft-based PLS calibration to the bare soil pixels within the hyperspectral image. The use of raw (unfiltered) spectra from individual pixels to generate predicted soil carbon content was found to result in high prediction variability between adjacent pixels. This resulted in a highly speckled soil carbon prediction map (Fig. 14.6).

Because PLS calibrations use all the spectrum, error due to poor signal-to-noise ratio or a single wave-band spike in any part of a spectrum (due perhaps to malfunction within the detector array) can cause substantial error in the carbon prediction. In the upper right corner of the unfiltered image (Fig. 14.6), one can see a nearly vertical strip along the flight path, and it represents a single position in the push-broom array of the imager. In another example, a clearly obvious recurring single wave-band spike in the spectra due to a faulty detector element at one position along the push-broom array caused a very marked striping pattern in the prediction map along the direction of flight. We found we could correct these detector errors by

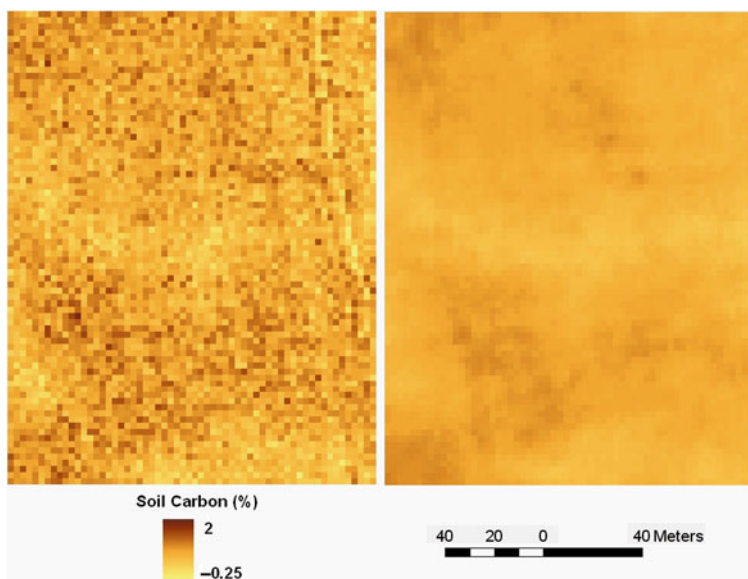


Fig. 14.6 Comparison of the variance in soil carbon predictions using raw and low-pass filtered pixel spectra

averaging spectra on either side of that position. We also found that subsequent data averaging using a low-pass filter improved PLS prediction of soil carbon.

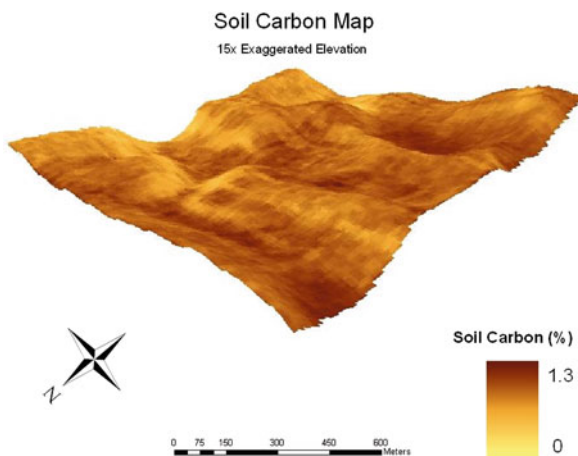
Figure 14.6 also illustrates the effect of this filtering on prediction continuity between adjacent pixels when compared to predictions using the unfiltered data. Statistical analysis of the prediction output showed that filtering eliminated negative prediction values and decreased the variance, but had little impact on the mean prediction value (Table 14.2).

The increased stability of PLS predictions using the low-pass filter is likely due to the better signal-to-noise ratio that results from spectral averaging, further indicating that non-smoothed spectra contain too much noise for stable predictions. The PLS calibration was produced using similarly averaged pixels, so the signal-to-noise ratio in spectra used to develop the calibration model was similar to those used to predict the unknown. The spatial averaging of spectra to gain improved signal-to-noise may be considered akin to co-adding multiple spectral scans to achieve the same

Table 14.2 Statistics on range, mean, and standard deviation for predicted carbon values (units, %C) between raw and filtered samples for the sample area shown in Fig. 14.6

Treatment	Min.	Max.	Mean	SD
Raw	-0.22	1.83	0.79	0.27
Filtered	0.36	1.12	0.78	0.12

Fig. 14.7 Soil carbon map, derived from hyperspectral image of bare soil, draped on a digital elevation model of an agricultural field



end. One effect of using filter averaging across the spatial dimension is the loss of some spatial definition in the soil carbon prediction. Another approach which may increase signal-to-noise and improve the ability to extract information from spectra involves the use of wavelets, which has proven to be faster than calibration by PLS (see Chapter 17).

Figure 14.7 shows a projection of the final soil carbon map on a lidar-derived digital elevation model (DEM) for the production field. The map shows a correspondence of soil carbon content with landscape position. The carbon pattern can be expected to be related both to biogeochemical gradients associated with landscape positions and to soil redistributions resulting primarily from agricultural activities.

14.4 Conclusions

This study demonstrates the potential utility of field-based sensors for measurement of soil organic C. An advantage of the tillage-based reflectance sensor is the ability to use it in untilled production fields with depth of sampling adjustable, thereby getting an improved estimate of C storage in no-till fields. Compare this with airborne or satellite sensors, for which soil C measurements are confounded by surface vegetation and crop residues. An obvious advantage of the aircraft-based reflectance sensor is its ability to rapidly return both intensive and extensive spatial datasets. Moreover, this study has found that calibration/validation approaches based on analysis of whole spectrum variance, such as partial least squares (PLS) regression, hold great promise to quantify soil organic matter. An obvious disadvantage is the need for bare soil images to detect soil carbon. The extent of interference from live or dead plant materials present in the image is unknown at this time.

References

Christy CD, Drummond P, Lund E (2006) Precision agriculture applications of an on-the-go soil reflectance sensor. Proceedings of the eighth international conference on precision agriculture, July 2006, Minneapolis, MN

Hatfield JL (2000) Precision agriculture and environmental quality: Challenges for research and education. Proceedings of a national workshop, precision agriculture and the environment: Research priorities of the nation, March 1999, Ames, IA

Janik LJ, Merry RH, Skjemstad JO (1998) Can mid infrared diffuse reflectance analysis replace soil extractions? *Aust J Exp Agric* 38:681–696

Lal R (2004) Soil carbon sequestration impacts on global climate change and food security. *Science* 304(5677):1623–1627

McCarty GW, Reeves III JB (2001) Development of rapid instrumental methods for measuring soil organic carbon. In: Lal R et al. (eds) *Assessment methods for soil carbon*. Lewis, Boca Raton, FL, pp 371–380

McCarty GW, Reeves III JB (2006) Comparison of near infrared and mid infrared diffuse reflectance spectroscopy for field-scale measurements of soil fertility parameters. *Soil Sci* 171:94–102

McCarty GW, Reeves III JB, Reeves VB, Follett RF, Kimble JM (2002) Mid-infrared and near-infrared diffuse reflectance spectroscopy for soil carbon measurement. *Soil Sci Soc Am J* 66:640–646

Petrie G (2005) Airborne pushbroom line scan: An alternative to digital frame cameras. *GeoInformatics* 8:50–57

Reeves III JB, Delwiche SR (1997) Determination of protein in ground wheat samples by mid-infrared diffuse reflectance spectroscopy. *Appl Spec* 51:1200–1204

Vaughan RG, Hook SJ, Calvin WM, Taranik JV (2005) Surface mineral mapping at Steamboat Springs, Nevada, USA, with multi-wavelength thermal infrared images. *Rem Sens Environ* 99:140–158

Chapter 15

Predicting Soil Carbon and Nitrogen Concentrations and Pasture Root Densities from Proximally Sensed Soil Spectral Reflectance

B.H. Kusumo, M.J. Hedley, M.P. Tuohy, C.B. Hedley, and G.C. Arnold

Abstract A modified soil probe for a portable spectroradiometer (ASD FieldSpecPro, Boulder, CO) was developed to acquire reflectance spectra (350–2,500 nm) from flat-sectioned *horizontal* (H method) soil surfaces of soil cores or from the *vertical* side (V method) of cylindrical soil cores. The spectra have been used to successfully predict soil carbon (C) and nitrogen (N) concentrations and root density. Partial least squares regression (PLSR) of the first derivative of the 5 nm space spectral data from method H against laboratory determined soil C and N concentrations produced calibrations that allowed quantitative estimates of C and N concentrations in unknown Pumice, Allophanic, and Tephric Recent soil samples (for C: R^2 validation = 0.76, RPD = 1.97; for N: R^2 validation = 0.84, RPD = 2.45). Compared to the H method, spectra acquired by the V method gave slightly more accurate predictions of soil C and N concentrations in Fluvial Recent soil (for C: R^2 cross-validation (cv) = 0.95 and 0.97, RPD = 4.45 and 5.80; for N: R^2 cross-validation = 0.94 and 0.96, RPD = 4.25 and 5.17, where the two values are for the H and V methods, respectively). Spectra acquired by the V method from drier soils in May produced a calibration against soil C and N concentrations that was capable of accurately predicting the soil C and N concentrations from spectra collected from wetter soils in November (C: R^2 validation = 0.97 and RPD = 3.43; for N: R^2 validation = 0.95 and RPD = 3.44). This indicates that a calibration dataset can have temporal robustness, which may reduce the number of calibrations that have to be performed. The root density predictions from spectra acquired by the H method were more accurate if soil types were separated into Allophanic soil (RPD = 2.42; R^2 cross-validation = 0.83) and Fluvial Recent soil (RPD = 1.99; R^2 cross-validation = 0.75).

Keywords Near-infrared · Carbon · Nitrogen · Root density · Pasture · In situ measurement

M.J. Hedley (✉)

Institute of Natural Resources, College of Science, Massey University,
North Shore City, New Zealand
e-mail: m.hedley@massey.ac.nz

G.C. Arnold is deceased.

15.1 Introduction

In response to increasing atmospheric carbon dioxide concentrations, more nations are proposing land-use changes to increase soil carbon (C) sequestration. Consequently, agricultural, and forestry management systems that produce a soil C change will need to be identified (Lal, 2008). Signatories to the Kyoto Protocol who adopt Article 3.4 will be allowed to offset greenhouse gas emissions with audited proof of increased soil C to 30 cm soil depth. Before we can determine the C sequestration ability of different plants (including their root systems) under different management regimes, we will need rapid field techniques for measuring soil organic matter content.

Near-infrared reflectance spectroscopy (NIRS) (see Chapter 3) is a rapid and non-destructive technique which has been successfully used to predict soil C and N in the laboratory (e.g. Chang and Laird, 2002) and in the field (e.g. Mouazen et al., 2007). NIRS has the potential to save time and cost in sample collection (see Chapters 11, 13, and 14). Moreover, in situ acquisition of reflectance spectra from soil cores offers the possibility of gaining quantitative information on plant root density (Kusumo et al., 2007; Kusumo et al., 2009). Such rapid techniques for measuring root density – without separating root and soil – are rare. Novel techniques using flatbed scanners have been proposed for speeding up the counting of separated roots (Pan and Bolton, 1991), and digital image acquisition methods have been proposed for analysing field root systems (Ortiz-Ribbing and Eastburn, 2003), but these techniques still need to separate roots from soil, and this remains a tedious procedure. Although fine root density and its turnover rate are highly correlated with soil organic matter synthesis (Guo et al., 2005), researchers will remain reluctant to measure root density unless they have access to a rapid technique for separating roots from soil.

This chapter reports the development and evaluation of a modified soil probe to acquire soil reflectance spectra for in situ measurement of soil C, N, and root density in pastoral soils, with the ultimate aim of high-resolution soil mapping.

15.2 Materials and Methods

15.2.1 Contact Probe Modification and Measurement Techniques

A modified soil probe was developed based on a commercial contact probe (Analytical Spectral Devices, Boulder, CO) by replacing the internal light source with a higher intensity (4.5°W) parabolic reflector halogen lamp. A round casting was developed (Fig. 15.1) which shielded the sensor from ambient light and avoided direct contact of the quartz probe window with the soil. The object–sensor distance was fixed at 30.5 mm. Two techniques were used to acquire soil reflectance spectra of cylindrical soil cores. Method H involved measurements made from a flat, sectioned horizontal soil surface and method V from the curved vertical wall. The

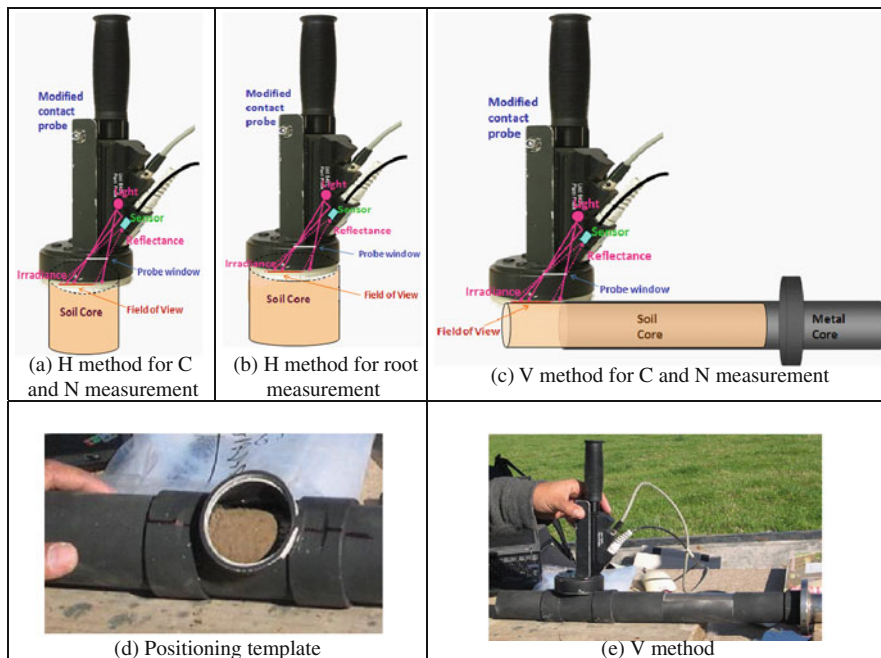


Fig. 15.1 Soil probe modification for horizontal (a, b) and vertical (c) measurement. Positioning template (d) for vertical method (e)

soil core was rotated 360°, giving a collection area of 561 mm² for the H method and 4707.4 mm² for the V method (Fig. 15.1).

15.2.2 Site Locations and Sample Collection

Using the H method, soil reflectance spectra and soil samples were collected in May and October 2006 from seven sites under permanent pasture; they were from the Taupo–Rotorua Volcanic Region of New Zealand and had been converted from forest to pasture 1, 3, and 5 years ago. Soils are classified into Pumice (Vitric Andosol, FAO-WRB soil classification), Allophanic (Vitric Andosol, FAO-WRB soil classification), and Tephric Recent soil (Vitric Cambisol, FAO-WRB soil classification) according to the New Zealand soil classification (Hewitt, 1998) and were mostly coarse in texture. A total of 30 soil samples were taken at each site, from 5 positions along each of 3 transects, and at 2 depths (37.5 and 112.5 mm), totalling 210 samples. The distance between transects was 20 m and that between sample points in each transect was 15 m. Soil cores were collected with a corer (46 mm diameter). After soil reflectance was acquired from the horizontal surface, a 15 mm soil slice was taken at each depth for laboratory measurements.

The V method was also evaluated for soil C and N content under permanent pasture; this was done on Fluvial Recent soil (Stagnic Fluvisol, FAO-WRB soil classification) in the Manawatu region in May 2007. A total of 17 soil cores were sampled from 3 transects (6 soil cores in a transect) at 6 depths at 50 mm intervals from 15 to 315 mm depth, totalling 102 samples. The distance between transects and between samples in a transect was 20 and 15 m, respectively. Field soil reflectance spectra were acquired from vertical surfaces of a 50 mm soil slice, which was subsequently analysed for total C and N. Another 18 cores (total 108 samples) were collected at the same site with the same intervals and depths in November 2007 in order to compare the H and V method and the temporal robustness of calibration and prediction.

Samples for root density assessment by method H were collected using a corer (80 mm diameter) at two permanent pasture sites on Ramiha silt loam (Allophanic soil) (Andic Cambisol, FAO-WRB soil classification) and Manawatu fine sandy loam (Fluvial Recent soil; Stagnic Fluvisol, FAO-WRB soil classification) in the Manawatu region. A total of 18 soil cores with 3 depths (15, 30, and 60 mm) were collected from each site, providing a total of 108 soil samples. The core positions were determined randomly in a paddock with a distance of 15 m between cores. After soil reflectance was recorded in each depth, a 3 mm soil slice (slice A) was collected for root density measurement. A further 3 mm soil slice (slice B, adjacent to root density samples) was collected from each depth for soil dry weight and soil moisture determination.

15.2.3 Measurement of Soil Properties

Soil cores were weighed field moist, crumbled, and allowed to air dry before reweighing. Soil moisture content was expressed as a fraction of air dry weight. Air dry soils were then ground to <500 μm particle size for total C and N analysis using a LECO FP-2000 CNS Analyser combustion method (Blakemore et al., 1987).

Root and soil were separated by wet sieving using sieve sizes of 710, 500, 355, 250, and 63 μm diameters. The roots retained on the first three sieves were bulked and dried for 3 days in a 50°C oven. Root density was reported in milligram dry root per gram soil (mg/g).

15.2.4 Spectral Pre-processing and Data Analysis

Exactly 10 replicates of the reflectance spectra were acquired from each soil sample using the purpose-built contact probe which was attached to the FieldSpecPro spectroradiometer by fibre optic cable. The instrument recorded spectra from 350–2,500 nm with a resolution of 1.4 nm for the region 350–1,000 nm and 2 nm for the region 1,000–2,500 nm. Software supplied with the instrument interpolated the data points to provide a uniform 1 nm resolution. Prior to regression analysis, spectral data were pre-processed by cutting those wave bands with noisy data (350–470

and 2,440–2,500 nm), smoothing the spectra with a Savitzky–Golay filter, reducing the data by taking every fifth spectral data point, calculating the first derivative, and then finally averaging the 10 replicates. SpectraProc V 1.1 software was used to pre-process the spectral data (Hueni and Tuohy, 2006), following which the data were imported into MINITAB 14 for principal component analysis (PCA) and partial least squares regression analysis (PLSR) of the first derivative of the reflectance spectra against the reference analytical data (C, N, and root density). A PCA score plot was used to observe the pattern of sample scattering and quantify the scatter by calculating the Euclidean distances of each sample to the centroid.

During PLSR processing, samples which had a standardised residual >2.0 were removed as outliers from the calibration and validation set. The accuracy of the models was tested internally using a leave-one-out cross-validation method and externally using a separate validation set.

15.2.5 Regression Model Accuracy

The ability of the PLSR model to predict soil properties was assessed using the following statistical procedure. The root mean square error (RMSE) was taken as the standard deviation of the difference between the measured and the predicted soil property values

$$\text{RMSE} = \sqrt{\frac{\sum (y_m - y_p)^2}{N}},$$

where y_m was the measured laboratory value, y_p the predicted value (of cross-validation or validation) from the PLSR model, and N the number of samples. RMSE calculated from cross-validation data was called RMSECV and that from validation data called RMSEP. Coefficient of determination (R^2) was calculated as the ratio of the sum of squares of the predicted values (either predicted values from cross-validation or validation as defined above) about the mean of the measured values to the sum of squares of the measured values (y_m) about their mean. RPD was the ratio of the standard deviation of measured values of soil properties to the RMSE and showed how much more accurate (as measured by the standard error) a prediction from the model was than simply quoting the overall mean. The variable RER was taken as the ratio of the range of measured values of soil properties to the RMSE, so that

$$\text{RPD} = \frac{\text{STDEV}(y_m)}{\text{RMSE}} \quad \text{and}$$

$$\text{RER} = \frac{\text{Max}(y_m) - \text{Min}(y_m)}{\text{RMSE}}.$$

Both cross-validation and test set validation were assessed using these equations. The best prediction model was that with the highest RPD, RER, and R^2 and the lowest RMSECV or RMSEP.

15.3 Results and Discussion

15.3.1 C and N Prediction of Taupo–Rotorua Allophanic, Pumice, and Tephric Recent Soil

The Taupo–Rotorua soil dataset had a wide range of total C (0.26–11.21%) and N (0.02–1.01%), even after excluding outliers. Mean total C and N values were 4.42 and 0.32%, respectively. Water content range was also large at 11–82%. The C:N ratio ranged from 9 to 30; high values indicated a low rate of organic matter decomposition, caused by the presence of residual forest trash in the areas recently (1–5 years) converted to pasture. The distribution of spectral samples on the PCA score plot (68% variance) is presented in Fig. 15.2.

The linear regression of predicted soil C and N concentrations against those measured by LECO (Fig. 15.3) was constructed as follows. Exactly 50% of the data (calibration set A) were used to build the PLSR calibration model of spectral reflectance (first derivative) and measured soil C and N. The calibration model was then used to predict the C and N concentrations of the remaining 50% (validation set B). This forms a calibration:validation set ratio of 1:1. The A and B sets were selected by two methods based on (1) chemical data – all soil samples were ranked from the lowest to the highest C or N content and odd- and even-ranked numbers were allocated to set A and B, respectively, and (2) spectral data – standardised Euclidean distances of all sample points from the centroid of the PCA score plot were calculated and the samples were ranked from the lowest to the highest standardised Euclidean distance. Odd- and even-ranked numbers were allocated to set A and B, respectively.

The H method of acquiring spectral reflectance gave a moderate prediction accuracy of soil C and N content despite the lack of sample preparation and the variably moist soil conditions for the field reflectance determination. Dataset selection technique had little influence on the accuracy of prediction (RPDs of 1.91–2.45 and R^2 validation of 0.74–0.84) (Fig. 15.3).

The soil texture variation of these mostly coarse textured soil types (Pumice, Allophanic, and Tephric Recent soil) may account for this moderate accuracy. Dalal and Henry (1986) found higher errors when predicting organic C and total N prediction in coarsely ground (<2 mm) compared to finely ground (<0.25 mm) soil samples. Barthes et al. (2006) found a less accurate prediction of total C and N of oven-dried <2 mm than oven-dried <0.2 mm particle size samples. In addition, 46% of samples contained more than 50% water (with a range of 11–82%), which may

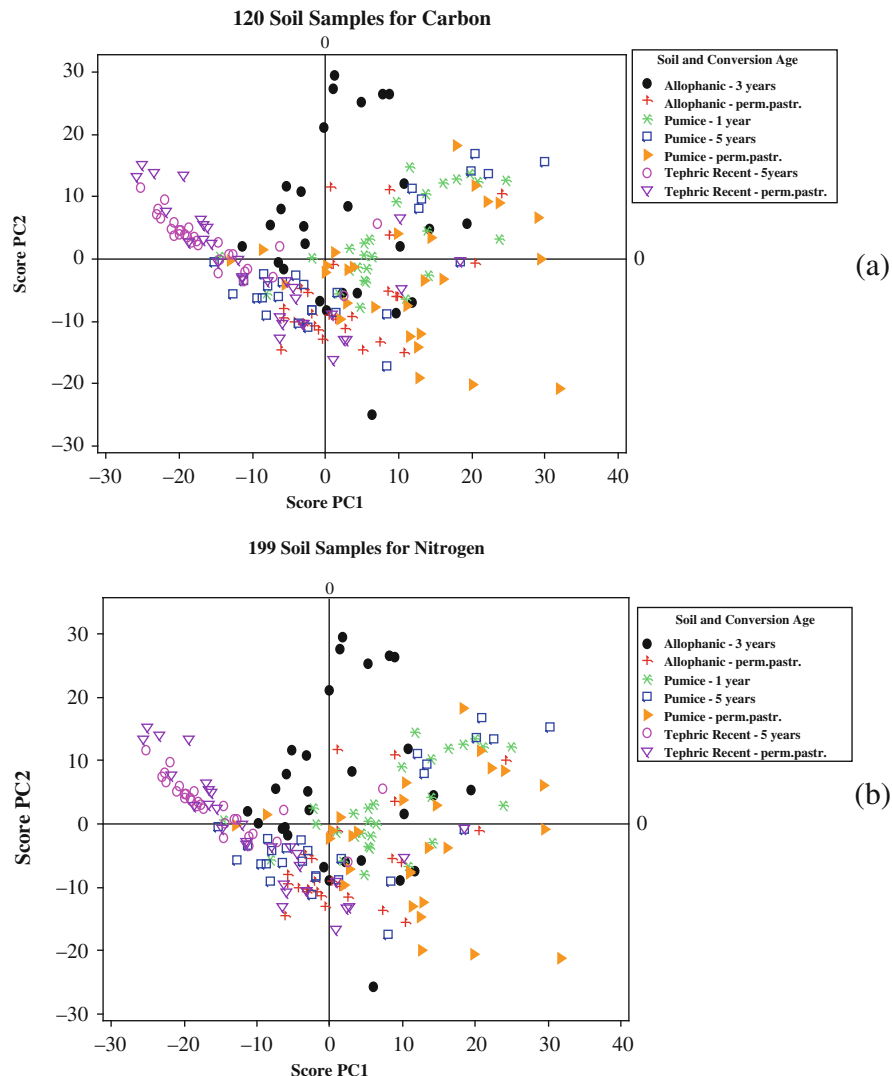


Fig. 15.2 A score plot of the first two principal components (PC1 and PC2) from a PC analysis of reflectance spectra (first derivative) acquired from soil samples with a range of ages since conversion from forest to pasture

have reduced accuracy because water can reduce the strength of important absorption features of C and N. Malley et al. (2002) reported less accurate prediction of organic matter and $\text{NH}_4\text{-N}$ with field moist soils than dry soils (dried at 40°C). Kooistra et al. (2003) also noticed a negative impact of water content on organic matter and clay content prediction.

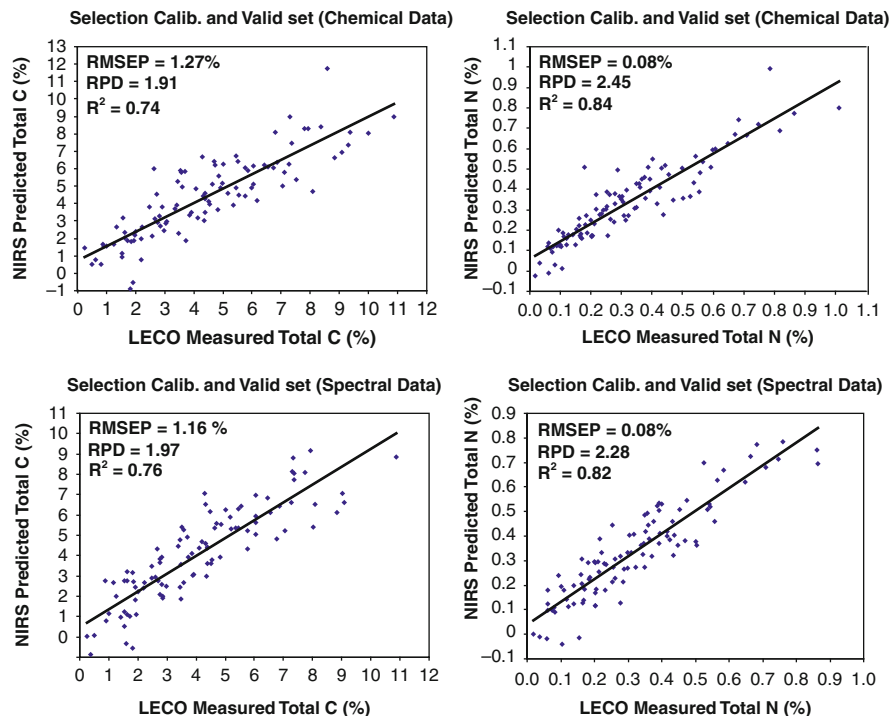


Fig. 15.3 Relationships between the C and N contents of Allophanic, Pumice, and Tephric Recent soil measured by LECO and predicted from their spectral reflectance (first derivative)

15.3.2 Comparison Between H and V Method for Fluvial Recent Soil

We found that reflectance spectra collected from the flat intact soil core target surface (H method) – especially those from the most shallow samples (15–65 mm) – were more influenced by root content than the V method (Fig. 15.4a, c, d). This difference between the two methods is illustrated by the shallow soil samples enclosed in the two circles of Fig. 15.4a. A spectrum with high reflectance collected by the H method (Fig. 15.4d) had high root content, largely because the larger number of root air voids caused higher reflection (Baumgardner et al., 1985). Method H records reflectance of soil and the exposed root, which is in contrast to the air-dried 2 mm sieved soil (from which some coarse roots were removed) used in the LECO measurement of soil C and N. Indeed, differences in the sample used for wet chemistry and spectroscopy can be a major source of calibration error (Mark and Workman, 2003).

Compared to the H method, the V method gave more accurate predictions of soil C and N concentrations in Fluvial Recent soil (with and without outliers) which is shown by higher RPD, R^2 , and RER and by lower error (RMSECV) (Table 15.1).

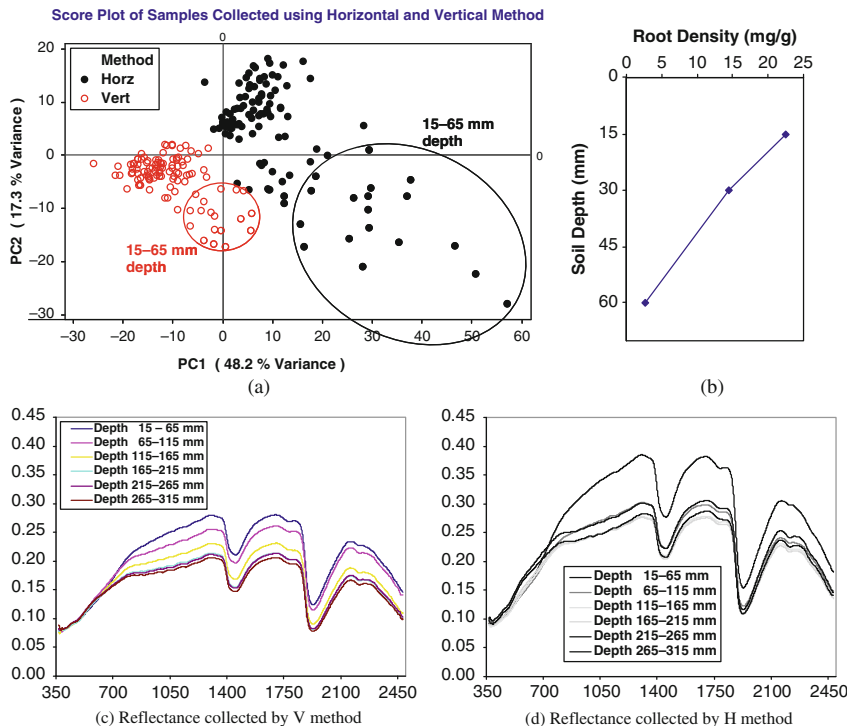


Fig. 15.4 (a) A score plot of the first two principal components (PC1 and PC2) from a PC analysis of reflectance spectra (first derivative) acquired from a range of soil depths (15–315 mm) under permanent pasture on a Fluvial Recent soil. (b) Root density decreased with depth, as did the reflectance from the same samples collected by the V (c) and H (d) methods

Table 15.1 Prediction of soil C and N concentrations in Fluvial Recent soil under permanent pasture (Spring–November 2007)

Method	Prediction values for C							
	<i>n</i>	Comp.	<i>R</i> ²	RMSECV (%)	RPD	RER	Bias	Slope
Horizontal ^a	108	5	0.88	0.45	2.90	11.05	0.0030	0.92
Vertical ^a	108	6	0.95	0.29	4.52	17.22	0.0042	0.96
Horizontal ^b	103	5	0.95	0.27	4.45	18.47	-0.0001	0.95
Vertical ^b	104	6	0.97	0.21	5.80	23.14	0.00066	0.97
Prediction values for N								
Horizontal ^a	108	3	0.90	0.04	3.11	12.27	0.00003	0.91
Vertical ^a	108	5	0.95	0.03	4.52	17.84	0.00028	0.96
Horizontal ^b	103	5	0.94	0.03	4.25	18.49	0.00022	0.96
Vertical ^b	104	6	0.96	0.02	5.17	21.17	0.00040	0.97

n, number of samples; Comp., component (factor or latent variable)

^aWithout removing outlier

^bOutliers removed

The soil core is rotated in the V method, and this results in a larger collecting area compared to the H method (Fig. 15.1). The V method is less influenced by the root content in the 15–65 mm depth. Also, reflectance recorded from the curved surface possibly includes less specular reflectance, and so this curved 5 cm long surface better represents the soil C and N variations of the core. The H method will provide representative C and N predictions for a 5 cm cylindrical soil sample only when it has a small vertical variation – for example in a mixed topsoil under intensive cultivation when it has little root content.

Water content of these samples was 20.7–53.6%. The C and N measured by the combustion method (LECO) were 0.27–5.20% and 0.02–0.50%, respectively.

15.3.3 Vertical Method on Fluvial Recent Soil Collected in Autumn (May)

The V method gave very accurate predictions of soil C and N concentrations for soil cores taken at the same site (Fluvial Recent soil) in autumn (May). This accuracy is expressed by high RPD, and R^2 values produced both in the internal validation (cross-validation) and in the external validation procedures using a 1:1 ratio of samples for the calibration set and validation set (see Fig. 15.5). Soil water content of the cores collected in May 2007 was drier (11.5–39.7%), but the C and N values determined by LECO were quite similar (0.31–5.43% C and 0.02–0.49% N), compared to November samples.

15.3.4 Is the Calibration Model Influenced by Temporal Variations in the Soil?

If the calibration of spectral data with soil C and N concentrations is stable over time then less effort will be required in re-calibrating the prediction model. It was considered that changes in soil colour, a feature of seasonal water table fluctuations, may influence the robustness of the calibration model.

The soil reflectance spectra collected in May were used as the calibration set to predict the soil C and N concentrations of the November samples and vice versa (May predict Nov, and Nov predict May) (Fig. 15.6). Even though the core samples taken in November were wetter and more mottled than those taken in May, accurate prediction of soil C and N concentrations could still be achieved. This indicates that the V method may be a temporally robust method for in situ measurement of soil C and N in this Fluvial Recent soil. This technique could facilitate high spatial resolution mapping of soil C and N to 30 cm soil depth, which would be helpful to soil C accounting researchers.

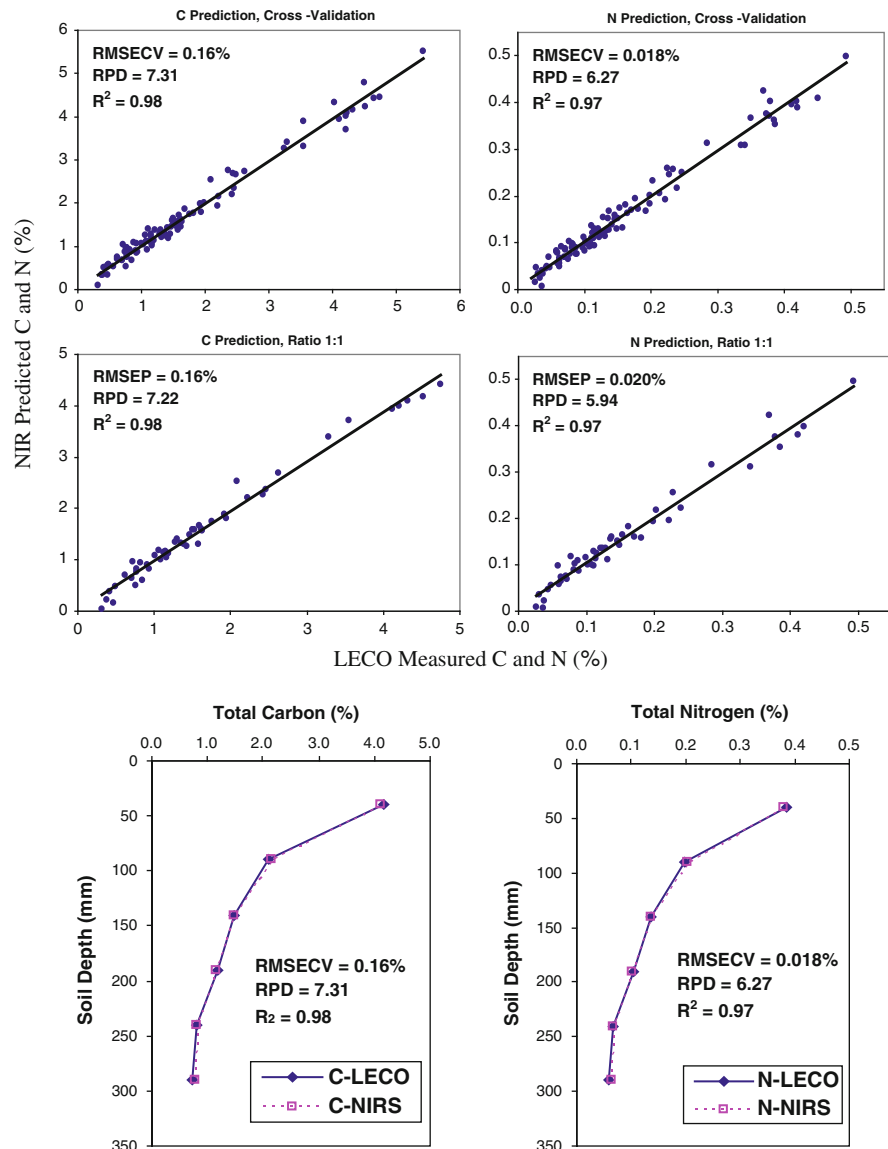


Fig. 15.5 Relationship between measured and predicted C and N (above and middle) and the mean of measured and predicted C and N with depth (bottom)

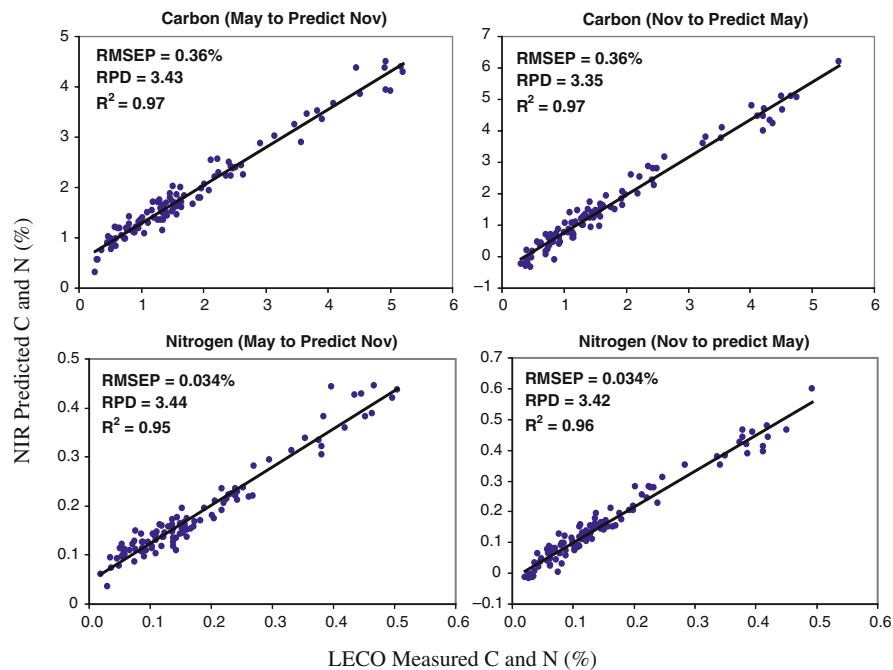


Fig. 15.6 The May PLSR calibration model can be used to predict soil C and N concentrations from spectra acquired in November (and vice versa)

15.3.5 Root Density Prediction on Ramiha and Manawatu Soil

The wide range of root density measured under permanent pasture on Allophanic (Ramiha) and Fluvial Recent (Manawatu) soil samples (2.27–23.10 and 1.53–37.03 mg dry root/g soil, respectively) could be predicted using the H method. Prediction was more accurate if the data from the two soil types were separated rather than grouped. The prediction of the amalgamated samples was 1.71 (RPD), 0.66 (R^2 cross-validation), and 0.86 (R^2 calibration). A better prediction was found in the Allophanic (Ramiha) soil (RPD = 2.42; R^2 cross-validation = 0.83; R^2 calibration = 0.99) than in the Fluvial Recent (Manawatu) soil (RPD = 1.99; R^2 cross-validation = 0.75; R^2 calibration = 0.99). The solid and open circles indicate the calibration and cross-validation data (Fig. 15.7a–c).

The first two principal components, which accounted for 53% of the variance in the spectral reflectance (first derivative), successfully differentiated Allophanic and Fluvial Recent soil (Fig. 15.7d). Samples with high root density tend to occur in the top left corner of the score plot diagram. Samples from each depth can also be distinguished, although some samples are close and overlapping, suggesting that they may have similar soil characteristics. Less overlapping samples from different depths can be found in the Manawatu soil, indicating that the spectral variations in this soil are relatively distinguishable. Many overlapping samples from the 30 and 60 mm depth

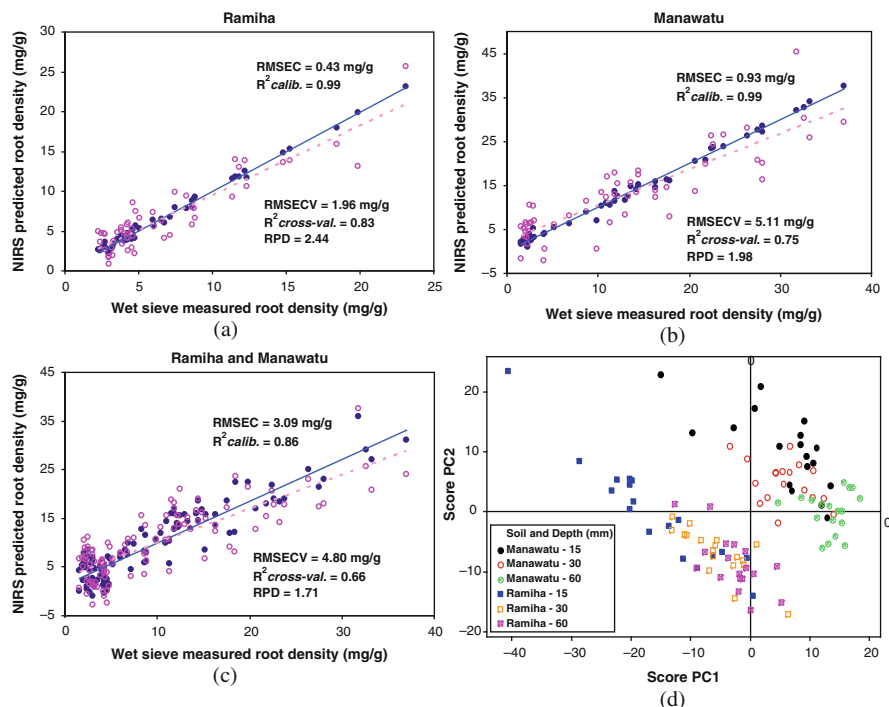


Fig. 15.7 (a, b, c) Linear relationship between wet sieved and NIRS predicted root density. (d) PCA score plot of the spectral reflectance of Ramiha and Manawatu soil

in Ramiha soil indicate that these samples may have similar characteristics, a view supported by there being no significant difference in root density between these two depths.

15.4 Conclusions

This study indicates that rapid in situ assessment of soil C, N, and root density using spectral reflectance from soil cores has considerable potential. The acquisition of reflectance spectra from the curved surface of a soil core (V method) gives more accurate predictions of soil C and N concentrations than acquisition of spectra from flat soil surfaces (H method). This method could facilitate high spatial resolution mapping of soil properties, measuring C and N within the soil profile and therefore providing a rapid field method for assessing the impacts of land-use change on soil organic matter stocks, as well as potential rates of soil organic matter synthesis via root density analysis.

Acknowledgement This work was made possible by funding support from the Fertilizer and Lime Research Centre (FLRC), Massey University, New Zealand.

References

Barthes BG, Brunet D, Ferrer H, Chotte JL, Feller C (2006) Determination of total carbon and nitrogen content in a range of tropical soils using near infrared spectroscopy: influence of replication and sample grinding and drying. *J Near Infrared Spec* 14:341–348

Baumgardner MF, Silva LRF, Biehl LL, Stoner ER (1985) Reflectance properties of soils. *Adv Agron* 38:1–44

Blakemore LC, Searle PL, Daly BK (1987) Methods for chemical analysis of soils. NZ Soil Bureau Scientific Report No. 80, Department of Scientific and Industrial Research, Lower Hutt, New Zealand

Chang CW, Laird DA (2002) Near-infrared reflectance spectroscopic analysis of soil C and N. *Soil Sci* 167:110–116

Dalal RC, Henry RJ (1986) Simultaneous determination of moisture, organic carbon, and total nitrogen by near infrared reflectance. *Soil Sci Soc Am J* 50:120–123

Guo LB, Halliday MJ, Siakimotu SJM, Gifford RM (2005) Fine root production and litter input: Its effects on soil carbon. *Plant and Soil* 272:1–10

Hewitt AE (1998) New Zealand Soil Classification. Landcare Research Science Series No. 1. Manaki Whenua, Lincoln, Canterbury

Hueni A, Tuohy MP (2006) Spectroradiometer data structuring, pre-processing and analysis – an IT based approach. *J Spatial Sci* 51(2):93–102

Kooistra L, Wanders J, Epema GF, Leuven SREW, Wehrens R, Buydens LMC (2003) The potential of field spectroscopy for the assessment of sediment properties in river floodplains. *Anal Chim Acta* 484:189–200

Kusumo BH, Hedley MJ, Hedley CB, Hueni A, Arnold GC, Tuohy MP (2009) The use of Vis–NIR spectral reflectance for determining root density: evaluation of ryegrass roots in a glasshouse trial. *Eur J Soil Sci* 60:22–32

Kusumo BH, Hedley MJ, Tuohy MP, Hedley CB, Arnold GC (2007) The use of diffuse reflectance spectrometry for in situ soil quality measurement. In: Currie LD, Yates LJ (eds) Designing sustainable farms: Critical aspects of soil and water management. Massey University, Palmerston North, 8–9 February 2007. Fertilizer and Lime Research Centre, Massey University, pp 158–169

Lal R (2008) Soils and sustainable agriculture. A review. *Agron Sustain Dev* 28:57–64

Malley DF, Yesmin L, Eilers RG (2002) Rapid analysis of hog manure and manure-amended soils using near-infrared spectroscopy. *Soil Sci Soc Am J* 66:1677–1686

Mark H, Workman J Jr (2003) Statistics in spectroscopy. Elsevier, San Diego, CA

Mouazen AM, Maleki MR, De Baerdemaeker J, Ramon H (2007) On-line measurement of selected soil properties using a VIS–NIR sensor. *Soil Tillage Res* 93:13–27

Ortiz-Ribbing LM, Eastburn DM (2003) Evaluation of digital image acquisition methods for determining soybean root characteristics. *Crop Management* (on-line), doi: 10.1094/CM-2003-0702-01-RS

Pan WL, Bolton RP (1991) Root quantification by edge discrimination using a desktop scanner. *Agron J* 83:1047–1052

Chapter 16

Diagnostic Screening of Urban Soil Contaminants Using Diffuse Reflectance Spectroscopy

J.G. Bray, R.A. Viscarra Rossel, and A.B. McBratney

Abstract There is increasing demand for cheap and rapid screening tests for soil contaminants in environmental consultancies. Diffuse infrared reflectance spectroscopy in the visible–near-infrared (vis–NIR) and mid-infrared (MIR) has the potential to meet this demand. The aims of this chapter are to develop diagnostic screening tests for heavy metals and polycyclic aromatic hydrocarbons (PAHs) in soil using vis–NIR and MIR diffuse reflectance spectroscopy. Cadmium, copper, lead, and zinc were analysed, as were total PAHs and benzo[a]pyrene. An ordinal logistic regression technique was used for predictions in the screening tests and to determine false-positive and false-negative rates. Zinc had the best prediction accuracy (89%) and copper predictions were consistently above 75%. Cadmium and lead were the least well predicted of the heavy metals (67 and 70%, respectively), and PAH predictions averaged 78.9%. MIR analysis (average prediction accuracy of 79.9%) was only slightly more accurate than vis–NIR analysis (average prediction accuracy of 77.1%), but the latter may currently be used in situ, thereby reducing cost and time of analysis and providing diagnosis in real time. Diffuse reflectance spectroscopy in the vis–NIR can substantially decrease both the time and the cost associated with screening for soil contaminants.

Keywords Soil contamination · Heavy metals · Diffuse reflectance infrared spectroscopy · Visible–near-infrared · Mid-infrared

16.1 Introduction

Soil contamination demands efficient methods for diagnosis and remediation. This is largely due to the health risks to both humans and ecosystems. Comprehensive assessments of contaminated land must include the identification of contaminants

J.G. Bray (✉)

Faculty of Agriculture, Food and Natural Resources, University of Sydney, McMillan Building A05, Sydney, NSW 2006, Australia
e-mail: jbray@eesi.biz

and a risk assessment of exposure. Public awareness has resulted in many government and public authorities finding themselves under increased pressure to ensure that any discovery of contaminated soils is publicly disclosed and remediated quickly and effectively. Therefore, efficient techniques for sampling and analyses have become necessary (Chuang et al., 2003). Heterogeneity of soil properties is an issue confronted by many researchers, such as Besson et al. in Chapter 23, and there is great difficulty in identifying both the extent of areas of contamination and the sources of the contaminants (Markus and McBratney, 1996). Other problems encountered may be simple – such as inaccessibility of soil due to surface sealing by roads, buildings, or other infrastructures – or more difficult (and frustrating) – such as restricted access to private land (Markus and McBratney, 1996). In sum, these are complex problems in need of rapid and simple solutions.

The Australian and New Zealand Conservation Council (ANZECC) has, in the past, used another method of determining soil contamination thresholds. These have been labelled ‘environmental investigation trigger values’ and in most cases differ from the National Health and Medical Research Council (NHMRC) values. The ANZECC trigger values for lead, zinc, copper, cadmium, benzo[a]pyrene (BaP), and total PAHs are 300, 200, 120, 3, 1, and 20 mg kg^{-1} , respectively (ANZECC, 1992). Total PAH covers the total concentration of the 16 PAHs that have been identified as particularly carcinogenic or mutagenic, and includes BaP (Xing et al., 2006).

The five contaminants listed above present definite challenges to those looking to efficiently diagnose, analyse, and rehabilitate contaminated sites. That their toxicity can vary rapidly over very short distances, particularly in industrial areas of urban landscapes, is also a challenge (Markus and McBratney, 1996). Urban and industrial land uses compete with one another in major cities, making it all the more important to ensure that urban soil remains clean enough for any use.

Despite their accuracy, many conventional methods of contaminant identification fall short because of their cost and long analysis time. Demand for rapid and cheap contaminant identification creates a niche for diffuse reflectance spectroscopy. The technology is simple to use and poses no health threats to the user, unlike other spectroscopic technologies, such as X-ray spectroscopy, which require protective equipment. Diffuse reflectance spectroscopy is non-destructive and a single scan, combined with some multivariate statistics, can measure several properties simultaneously (Viscarra Rossel et al., 2006; Upadhyayha et al. in Chapter 12). Perhaps most importantly, soil analysis can be completed within seconds at low cost. The aim of this research was to develop diagnostic screening tests for heavy metal and PAH contaminants in urban soil using vis–NIR and MIR diffuse reflectance spectroscopy.

16.2 Materials and Methods

16.2.1 Location

Two soil datasets were used for the experiment. The first consisted of 489 samples from the Sydney inner-west suburb of Glebe, New South Wales, Australia,

an area known to have concentrations of cadmium, copper, lead and zinc (Markus and McBratney, 1996). The second set was compiled from 65 samples with known PAH concentrations from a suburb in Melbourne, Victoria. Concentrations of heavy metals and PAHs were determined by atomic absorption spectrometry.

16.2.2 Diffuse Spectral Reflectance Measurements

Diffuse reflectance spectra of the soils were recorded in the vis–NIR range (350–2,500 nm) and in the MIR range (2,500–25,000 nm or 4,000–400 cm^{-1}). The spectrometers used were the vis–NIR AgriSpec (Analytical Spectral Devices, Boulder, Colorado, USA) and the FTIR Tensor 37 (Bruker Analytical Technologies). Spectra were collected over the vis–NIR range at 1 nm intervals (average of 10 scans per second) and over the MIR range (at 8 cm^{-1} resolution and 64 scans per second). A Spectralon white reference was used for calibrating the vis–NIR spectrometer, while spectroscopic-grade potassium bromide (KBr) was used for calibrating MIR spectrometer. Soil samples were ground to less than 2 mm diameter for the vis–NIR analysis and to less than 200 μm for the MIR analysis. The spectra of the PAH-contaminated soil were measured using only the vis–NIR spectrometer, since these samples were moist and volatile, making MIR analysis with the Tensor 37 and our current set-up difficult.

16.2.3 Statistical Analysis

Statistical analysis was carried out for both the vis–NIR and the MIR separately. The spectra were transformed to apparent absorbance or $\log(1/\text{reflectance})$ and a principal component analysis (PCA) was carried out to compress the spectra into fewer principal components, a technique similar to that of McCarty et al. (Chapter 14) and Kusumo et al. (Chapter 15). The first 10 principal components were retained and used as the independent variables in the analysis. Ordinal logistic regression (OLR) was used for the diagnostic screening of soil contamination. The selection of thresholds was based on current ANZECC guidelines, as outlined above. We also tested half, and double, the ANZECC threshold. Each dataset was randomly split into two independent datasets: two-thirds for training and the remainder for testing the models. The OLR models were derived using the training data and the models were independently tested using the remaining one-third testing dataset. The OLR models were thus used to predict whether the soils were contaminated or not based on the predetermined threshold.

16.2.4 Diagnostic Screening of Soil Contaminants

Two types of errors were principally considered from the analysis, namely type I or false positives and type II or false negatives. These types of errors were determined using contingency tables (Fig. 16.1).

		Actual condition	
		Absent	Present
Test result	Positive	Condition absent + Positive result = <i>False Positive</i>	Condition present + Positive result = <i>True Positive</i>
	Negative	Condition absent + Negative result = <i>True negative</i>	Condition present + Negative results = <i>False Negative</i>

Fig. 16.1 Contingency tables used for diagnostic screening of soil contamination

Type I errors occur when a sample is predicted to be contaminated but in fact it is not. Type II errors occur when samples that are contaminated are predicted to be free of contamination (Allchin, 2001). Thresholds may be varied to make the test either more restrictive or more sensitive, depending on the design of the experiment. In the development of diagnostic screening tests, it is clearly desirable to lower both the false-negative rate (FNR) and the false-positive rate (FPR) as much as possible.

16.3 Results and Discussion

16.3.1 Exploratory Data Analysis

Statistical distributions of the six soil contaminants studied are shown in Fig. 16.2, which shows highly skewed data for all contaminants. A feature of the heavy metal analysis was a strong correlation between contaminants within samples. That is, where lead contamination was present, there was an increased chance of copper and zinc contamination being present, and this can be attributed to previous industrial activity in Glebe (Markus and McBratney, 1996).

16.3.2 Spectroscopic Analysis

The mean absorbance of lead in the vis–NIR range at three soil concentrations is shown in Fig. 16.3a, namely high (greater than 500 mg kg^{-1}), low (less than 150 mg kg^{-1}), and moderate (150 – 500 mg kg^{-1}). The samples that fall into these categories are plotted onto a principal component score plot in Fig. 16.3b. Together, these two PCs account for 90.2% of the data variance.

While Fig. 16.3a shows very little spectral activity between 350 and 700 nm, clear peaks, characteristic of hydroxyl groups (1450 nm), water, and clay (1,950 and 2,250 nm), do appear. It is also clear in Fig. 16.3a that there is a difference in

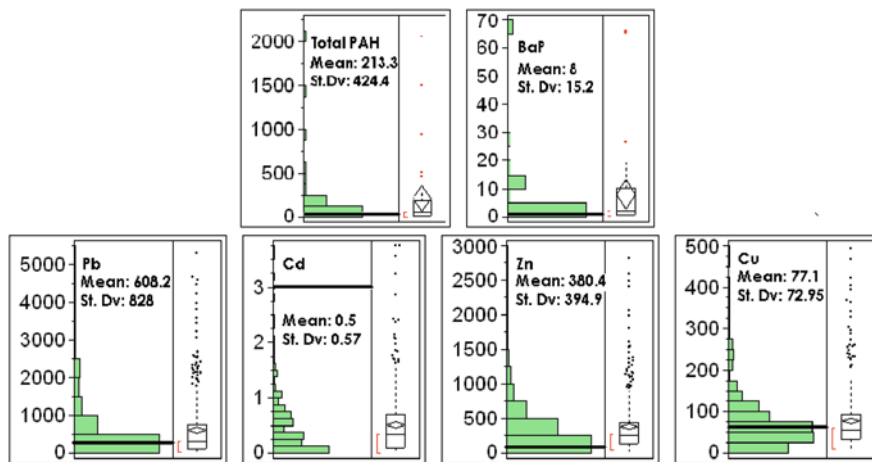
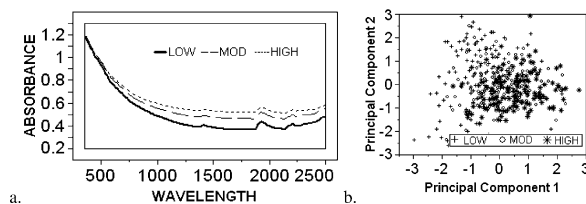


Fig. 16.2 Distributions, mean, and standard deviations of the soil contaminants. ANZECC thresholds are marked with a black line

Fig. 16.3 (a) Average vis–NIR absorbance of samples with lead contamination at low, medium, and high levels (wavelengths in nanometre). (b) Principal component (PC) score plot of the first two PCs



absorbance between samples with low and high contaminant concentrations. This is also evident in PAH samples and carries over to MIR analysis. Heavy metals and PAHs are not spectrally active in the visible or infrared portions of the electromagnetic spectrum. Spectroscopic diagnostic screening for heavy metal concentration, particularly lead, zinc, and copper, is possible because of their relationship with clay, iron, and organic matter (Turer et al., 2001). In this study, the heavy metal contaminants are well correlated to soil organic matter (Table 16.1). There is also some correlation between copper and clay content.

Table 16.1 Correlations between heavy metals, clay, and organic carbon

Analyte	Percentage of clay	%OC	Pb	Cd	Zn	Cu
Pb	0.05	0.35	1.00	0.23	0.42	0.09
Cd	-0.02	0.46	0.23	1.00	0.39	0.49
Zn	0.01	0.38	0.42	0.39	1.00	0.29
Cu	0.13	0.38	0.09	0.49	0.29	1.00

16.3.3 Diagnostic Screening Using Ordinal Logistic Regression

Figure 16.4 shows the contingency table of the OLR results for Pb contamination in both the vis–NIR and MIR spectra, given three different thresholds.

Figure 16.4 shows that, as thresholds increase, the true negatives increase while the true positives decrease. From this observation it is easy to see why the proportions of false positives decrease while the false negatives increase with an increase in threshold. This is to be expected given that at lower thresholds there is an increased likelihood of a sample being contaminated, while the reverse is expected at higher thresholds.

The analysis of zinc and copper produced similar results, albeit with greater changes in false positives and false negatives. Three ways of measuring the model's ability to predict contaminants were used. The first was accuracy, the second FPR, and the third FNR, and these values are shown in Table 16.2. Note that cadmium contamination was not present in a sufficient number of samples to carry out these analyses in full, while PAH samples were not analysed in the MIR range.

The FPR and FNR for both vis–NIR and MIR predictions (Table 16.2) show a decrease in FPR with an increase in threshold and an increase in FNR with an increase in threshold. The predictions of lead are the least accurate of the heavy metals analysed (Table 16.2), falling to below 68% in the vis–NIR analysis at the ANZECC threshold of 300 mg kg^{-1} . The difference in accuracy between vis–NIR

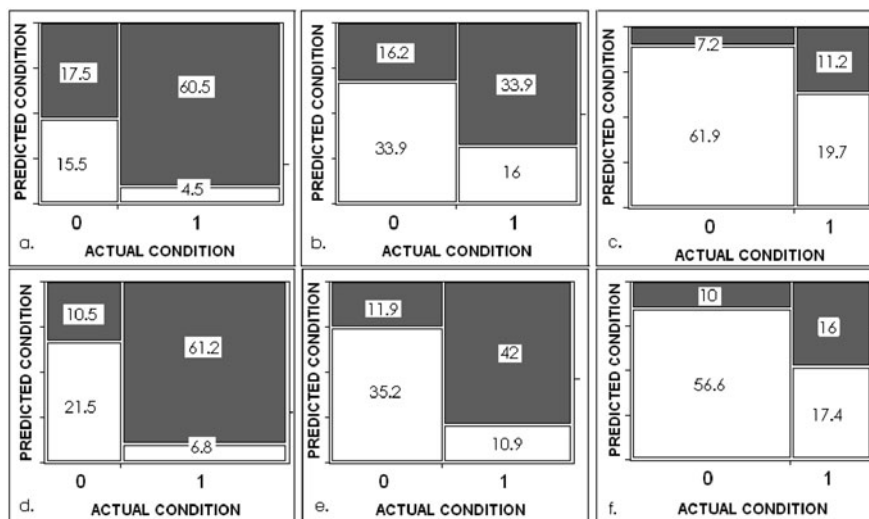


Fig. 16.4 Ordinal logistic regression results showing contingency tables for (a–c) vis–NIR and (d–e) MIR analysis of Pb at three different thresholds. From left to right, 150, 300, and 600 mg kg^{-1} . Percentage values are shown for each prediction. Grey indicates samples predicted to be contaminated, and white represents samples predicted to have non-contamination; column 0 represents samples that are known to be below the given thresholds, and column 1 represents samples that are contaminated

and MIR analyses at the ANZECC threshold and half the ANZECC threshold is noticeable for lead, with 10% difference at 300 mg kg⁻¹. However, the vis–NIR analysis is slightly more accurate at double the ANZECC threshold of 600 mg kg⁻¹.

The most accurate prediction of heavy metal presence was of zinc at the lowest threshold, where accuracies of 86 and 89.5% were found in the vis–NIR and MIR, respectively. Copper is the only element to have all six threshold predictions exceed 76% accuracy in Table 16.2.

The average accuracy of prediction for copper is 81.6%, exceeding that of zinc (78.9%), lead (75.9%), and total PAHs (78.9%). The copper analyses do have very high FNR values at the higher threshold of 120 mg kg⁻¹ (0.92). With just 2.5% of the soil samples above the ANZECC cadmium threshold, predictions for this contaminant were not considered as reliable as other analyses. This was despite the accuracy of predictions in both the vis–NIR and the MIR range, which were over 90% accurate. Previous research has failed to sufficiently quantify or qualify the presence of cadmium in soil (Wu et al., 2007), so it is surprising that this method has improved the accuracy of predicting cadmium in soil. With the exception of lead at a 600 mg kg⁻¹ threshold, all MIR predictions were more accurate than those of the vis–NIR, although these differences were as little as 1.3% for zinc at the highest threshold and 1% for the anomaly of Pb at the highest threshold. The best predictions were found at the lowest thresholds for all but the copper predictions from the vis–NIR data. The range in the accuracy of total PAH predictions is the greatest in Table 16.2. A 25% difference is apparent from half the ANZECC threshold of 10 mg kg⁻¹ to double the threshold at 40 mg kg⁻¹.

The FPR trend in Table 16.2 is fairly consistent, although a rare occurrence in the FPR *increasing with* the threshold for total PAH vis–NIR predictions is shown

Table 16.2 Selected contaminants and thresholds used to predict accuracy, false-positive rates (FPR), and false-negative rates (FNR)

Contaminant	Threshold (mg kg ⁻¹)	Vis–NIR predictions			MIR predictions		
		Accuracy (%)	FPR	FNR	Accuracy (%)	FPR	FNR
Pb	150	76.06	0.53	0.1	82.65	0.33	0.1
Pb	300	67.84	0.32	0.32	77.17	0.25	0.21
Pb	600	73.07	0.1	0.64	72.6	0.15	0.52
Zn	100	86.04	0.66	0.04	89.5	0.51	0.03
Zn	200	73.82	0.42	0.15	76.71	0.35	0.16
Zn	400	73.07	0.08	0.71	74.42	0.14	0.49
Cu	30	83.79	0.49	0.06	85.39	0.43	0.06
Cu	60	76.06	0.2	0.28	77.7	0.21	0.24
Cu	120	84.29	0.02	0.92	82.65	0.03	0.77
Total PAH	10	90.25	0.57	0			
Total PAH	20	80.48	0.88	0.03			
Total PAH	40	65.85	0.91	0.13			
BaP	0.5	75.91	0.5	0			
BaP	1	90.25	0.24	0.25			
BaP	2	65.9	0.44	0.26			

in Table 16.2. These results may be attributed to a lack of samples, particularly given that each threshold bracket had a very different number of samples. Accuracy was comparable between PAHs and heavy metals at the actual and half the actual thresholds, although the latter were better predicted at the highest threshold. On average, the MIR had lower false-positive and false-negative rates when compared with the vis–NIR.

These results suggest that further development could lead to practical applications in commercial industries. However, ways of improving predictions and reducing error values need to be investigated. Viability with regard to time and cost also needs to be explored.

16.4 Conclusions

- The soil contaminant studies do not exhibit characteristic spectral features. The spectroscopic screening tests work because of the interaction of the contaminants with other soil constituents that are spectrally active, such as clay, iron, and organic matter.
- Ordinal logistic regression can be used to develop diagnostic screening tests for soil contaminants. The technique produced accuracies consistently above 75% and up to 90%.
- There is a trade-off between the false-positive rate and false-negative rate, with the former generally decreasing with thresholds and the latter increasing with thresholds. Appropriate guidelines need to be formed regarding the acceptable levels of FPR and FNR.
- The MIR range (average prediction accuracy of 79.9%) was only slightly more accurate than the vis–NIR range (average prediction accuracy of 77.1%). However, this may be compensated by our current ability to use the vis–NIR *in situ*.

Acknowledgement We thank Julie Cattle and Dahmon Sorongan for the soil samples.

References

Allchin D (2001) Error types. *Perspect Sci* 9:38–58

Australian and New Zealand Environment and Conservation Council (1992) Australian and New Zealand guidelines for the assessment and management of contaminated sites, Canberra

Busch MP, Watanabe KK, Smith JW, Hermansen SW, Thomson RA (2000) False-negative testing errors in routine viral marker screening of blood donors. *Transfusion* 40:585–589

Chuang JC, Van Emon JM, Chou YL, Junod N, Finegold JK, Wilson NK (2003) Comparison of immunoassay and gas chromatography–mass spectrometry for measurement of polycyclic aromatic hydrocarbons in contaminated soil. *Anal Chim Acta* 486:31–39

Hua G, Broderick J, Semple KT, Killham K, Singleton I (2007) Rapid quantification of polycyclic aromatic hydrocarbons in hydroxypropyl- β -cyclodextrin (HPCD) soil extracts by synchronous fluorescence spectroscopy (SFS). *Environ Pollut* 148:176–181

Imray P, Langley A (1999) Health-based soil investigation levels. National Health and Medical Research Council, Canberra, ACT

Jensen H, Reimann C, Finne TE, Ottesen RT, Arnoldussen A (2007) PAH-concentrations and compositions in the top 2 cm of forest soils along a 120 km long transect through agricultural areas, forests and the city of Oslo, Norway. *Environ Pollut* 145:829–838

Markus JA, McBratney AB (1996) An urban soil study: heavy metals in Glebe, Australia. *Aus J Soil Res* 34:453–465

Turer D, Maynard JB, Sansalone JJ (2001) Heavy metal contamination in soils of urban highways: comparison between runoff and soil concentrations at Cincinnati, Ohio. *Water Air Soil Pollut* 132:293–314

Viscarra Rossel RA, Walvoort DJJ, McBratney AB, Janik LJ, Skjemstad JO (2006) Visible, near infrared, mid infrared or combined diffuse reflectance spectroscopy for simultaneous assessment of various soil properties. *Geoderma* 131:59–75

Wu Y, Ji JCJ, Gong P, Liao Q, Tian Q, Ma H (2007) A mechanism study of reflectance spectroscopy for investigating heavy metals in soils. *Soil Sci Soc Am J* 71:918–926

Chapter 17

Using Wavelets to Analyse Proximally Sensed Vis–NIR Soil Spectra

R.A. Viscarra Rossel, R.M. Lark, and A.S. Ortega

Abstract In this research we use the discrete wavelet transform to process visible–near-infrared (vis–NIR) diffuse reflectance spectra of soil. The aim was to transform the spectra into wavelet coefficients, some of which may be discarded, to obtain a more parsimonious representation of the data before multivariate calibration is performed by multiple linear regression (MLR). We used proximally sensed vis–NIR spectra from 10 different soil profiles and compared predictions of clay at short intervals down the profile. Predictions of clay content using 29 wavelet coefficients were more accurate (RMSE = 7.1%) than those from partial least squares regression (PLSR) using the original spectra with 208 wavelengths (RMSE = 7.9%) or the wavelet coefficients’ back-transformed spectra (RMSE = 8.1%). Hence, our wavelet approach combined with MLR produced simple, robust, and accurate calibrations of proximally sensed spectroscopic data.

Keywords Visible–near-infrared · Diffuse reflectance spectroscopy · Wavelets · Discrete wavelet transform · Proximal soil sensing

17.1 Introduction

Creating high-resolution digital soil maps for use in applications like precision agriculture requires good-quality data at high spatial resolutions (10 m or less). Soil analysis by conventional laboratory methods is expensive, time consuming, and laborious. Much work is being conducted worldwide to develop proximal soil sensors that can be used *in situ* to lessen the need for, or to complement, conventional soil analysis (Chapter 2). Although proximal soil-sensing techniques produce results that may not be as accurate as conventional laboratory analysis, they

R.A. Viscarra Rossel (✉)
CSIRO Land & Water, Canberra, ACT 2600, Australia
e-mail: raphael.viscarra-rossel@csiro.au

allow the collection of many more data using simpler, cheaper, and less laborious techniques. Furthermore, the information is produced in a timely manner. This is the rationale for proximal soil sensing (Viscarra Rossel and McBratney, 1998). In this research we used a portable visible–near-infrared (vis–NIR) diffuse reflectance spectrophotometer for proximal soil sensing to predict clay content.

Soil vis–NIR diffuse reflectance spectra are sensitive to both organic and inorganic soil composition, making vis–NIR spectroscopy a potentially useful and powerful tool for proximal soil sensing (Chapter 3). The technique is rapid, accurate, and more economical than are conventional methods of soil analysis. Furthermore, the technology is simple to use, measurements require only a small amount of sample preparation, it is non-destructive, and, when combined with multivariate calibrations, a single spectrum can be used to predict multiple soil properties. These qualities facilitate the collection of high-resolution soil information.

Visible–NIR spectra result from weak overtones and combinations of molecular vibrations that occur in the mid-infrared. These spectra are largely non-specific due to interferences from overlapping spectra of soil constituents that are themselves varied and interrelated. This lack of selectivity may be compounded by instrumental noise and drift, light scatter, and path length variations that occur during measurements. Chemometric methods may be used to treat the data and obtain multivariate calibrations by which soil property values can, from many spectroscopic predictor variables (or bands), be simultaneously predicted using a mathematical model or a pedotransfer function (PTF). Spectroscopic PTFs contain a large number of predictor variables that are collinear and, by nature, very redundant. Therefore, data compression techniques such as partial least squares regression (PLSR) (Wold et al., 1983) are often used for modelling and prediction.

Wavelet transforms have been used in several branches of scientific research, including soil science, to elucidate complex signals with multiscale structure. For example, wavelets can be used for signal processing and image analysis; to compress large datasets for more parsimonious representations of the data (and more efficient data storage, computation, and transmission); to smooth noisy data; and to detect irregularities.

The aim of this chapter is to use the wavelet transform for data compression before calibration by multiple linear regression (MLR). By using this approach, we hope to produce simpler, more robust, and accurate spectroscopic calibrations of proximally sensed spectroscopic data.

17.2 Materials and Methods

17.2.1 *The Soil Spectral Library*

The soils used in this study originated from different parts of Australia: New South Wales, Queensland, and Western Australia. There were a total of 1,361 soil samples from various depths down to 1 m. The spectra of 1,287 soil samples in the library

were collected in the laboratory, while the spectra of 74 soils were collected *in situ* in the field. For the laboratory-collected spectra, samples were air-dried, ground, and sieved to a particle size ≤ 2 mm. The clay content of all 1,361 soil samples was estimated using the hydrometer method outlined by Gee and Bauder (1986). The spectrometer used to collect the vis–NIR spectra was a portable spectrometer (AgriSpec Analytical Spectral Devices, Boulder, Colorado) with a spectral range of 350–2,500 nm. Before scanning, the spectrometer was calibrated with a Spectralon white sample. For each soil measurement, 10 spectra were averaged to improve signal-to-noise ratio. The Spectralon calibration was repeated after every 20 measurements. Reflectance was measured at 1 nm wavelength intervals, but because the data were very redundant, we only retained measurements at every 10 nm. We also removed excessively noisy portions of the spectra at the edges. As a result, the final spectra comprised measurements at 208 wavelengths from 380 to 2,450 nm. Reflectance measurements were transformed to apparent absorbance, $\log 1/R$.

17.2.2 Proximal Vis–NIR Sensing of Soil Profiles

In situ field measurements were made at 10 different locations in New South Wales. The soil at each of the sites was classified as Ferrosol, Podsol, Hydrosol, Dermosol, Chromosol, Black Vertosol, Grey Vertosol, Yellow Sodosol, Yellow Kandosol, and Lithocalcic Calcarosol according to the Australian Soil Classification (Isbell et al., 1997). Approximate WRB classifications are Ferralsol, Podzol, Gleysol, Planosol, Luvisol, Vertisol, Solonetz, Arenosol, and Calcisol (FAO, 1998). A schematic of the approximate measurement design at each profile is shown in Fig. 17.1.

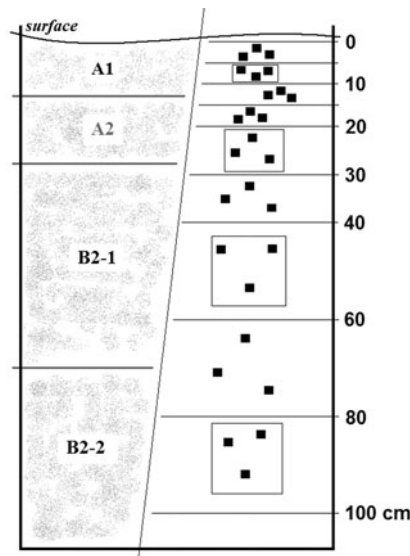


Fig. 17.1 Schematic of the approximate spectroscopic measurement and sampling design at each profile

Before taking the spectroscopic measurements at each depth, sample sites were cleared of stones, roots, and debris and their surfaces were evened out with a spatula, taking care not to smear the soil. Three replicate spectroscopic measurements were made at each depth. After averaging, there were a total of 76 spectra from the 10 profiles. Soil was also sampled at each depth where the spectra were collected and taken to the laboratory. Validation samples were taken at approximately regular intervals for each profile and measurements of clay content were made using the hydrometer method. There were 39 of these validation samples.

17.2.3 The Wavelet Transform

Each spectrum was padded to extend its total length to the nearest whole integer power of 2, that is, to 256. This was done by the common method of symmetrical reflection (e.g. Percival and Walden, 2000). Each spectrum was then analysed using the pyramid algorithm, as described by Lark and Webster (1999). This algorithm allowed us to extract 2^{m-2} sets of wavelet coefficients. The coefficients were exported and those that corresponded entirely to padding observations were removed. Wavelet coefficients were selected for compression and multivariate calibration by sorting them by their variance over the whole dataset and performing the multivariate calibrations one by one to select the optimal number of coefficients to be retained. Once selected, the remaining coefficients were set to zero. This technique is described in full by Viscarra Rossel and Lark (2009). The wavelet coefficients were also back-transformed for analysis of the denoised spectra.

17.2.4 Multivariate Calibrations

Multivariate calibrations of the selected (orthogonal) wavelet coefficients were done by MLR. The calibration models were validated by predicting clay content for the 39 validation samples. Predictions were assessed using the adjusted coefficient of determination (R_{adj}^2) and root mean squared error (RMSE). The RMSE was calculated as follows:

$$\text{RMSE} = \sqrt{\frac{1}{N} \sum_{i=1}^N (\hat{y}_i - y_i)^2},$$

where \hat{y}_i is the predicted value, y_i the observed value, and N the number of validation data.

MLR predictions of clay content using the wavelet coefficients were compared to PLSR predictions using the original spectra as well as the back-transformed wavelet coefficients. Predictions of ‘unknown’ clay contents at every depth for each of the 10 soil profiles were made using bootstrap aggregation MLR (bagging-MLR). The technique was also used to produce a measure of the uncertainty of the predictions.

Uncertainty was measured by 95% confidence intervals. Viscarra Rossel (2007) demonstrated the use of bagging with PLSR.

17.3 Results

17.3.1 The Soil Vis–NIR Spectral Library and Validation Samples

The soils in the spectral library were largely represented by black and grey Vertosols (Vertisols), Ferrosols (Ferralsols), Chromosols (Luvisols), Kurosols and Dermosols (Planosols), and Sodosols (Solonetz), but a smaller number of Podzols, Rudosols and Kandosols (Arenosols), Tenosols (Leptosols), and Calcarosols (Calcisols) were also represented. Their clay content ranged from 0 to 88% (Table 17.1).

The library also contained a diverse set of spectra, a sample of which is shown in Fig. 17.2a.

Multivariate calibration of clay content in the spectral library by PLSR, using two-thirds of the data to build the model and the remaining one-third to validate it, produced an R^2_{adj} of 0.83 and an RMSE of 7.9%. Figure 17.3 shows a scatter plot of the first two principal component scores of the spectra in the library. In Fig. 17.3, the grey points show the 1,287 laboratory-collected soil spectra, and the black points show the 74 in situ field-collected spectra of soils in the library.

Table 17.1 Statistics for soil clay content in the spectral library and in the validation samples

Clay percentage measurements	<i>n</i>	Mean	SD	Median	Min.	Max.
Spectral library samples	1,361	32.6	19.4	30.0	0	87.7
Validation samples	39	31.3	17.0	34.8	2.9	55.3

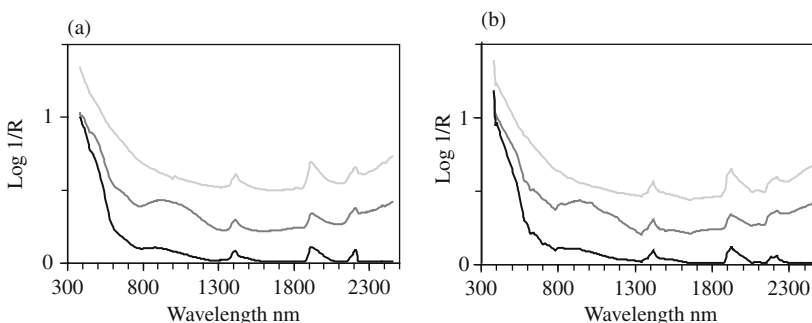
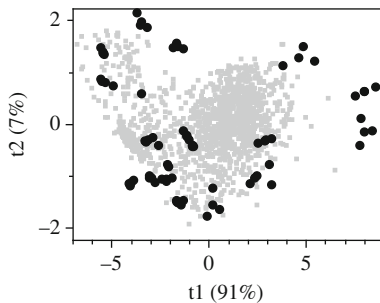


Fig. 17.2 (a) Original spectra; (b) back-transformed spectra from 29 wavelet coefficients

Fig. 17.3 Scatter plot of the first two principal component scores (t_1, t_2) showing the 1,287 laboratory-collected soil spectra (grey points) and the 74 in situ field-collected spectra (black points) of soils in the library

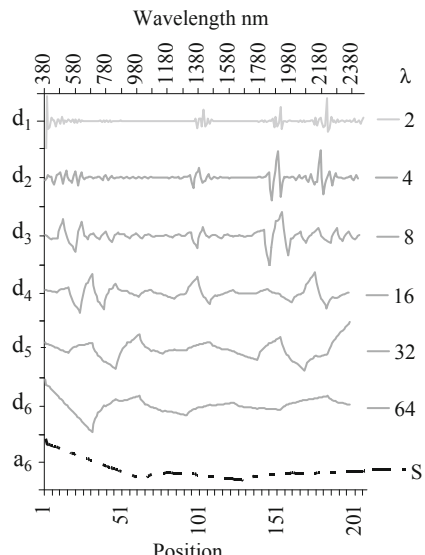


17.3.2 A Multiresolution Analysis (MRA)

Multiresolution analysis (MRA) of a vis–NIR spectrum in the library shows the detail (d_m), components of the wavelet transform at each scale (λ), and the approximation (or smooth) components (a_m). The MRA in Fig. 17.4 shows features of the spectrum at various scales, from the finest scale ($\lambda = 2$) showing the highest frequency wavelet coefficients to the coarsest scale ($\lambda = 64$) showing the lowest frequency wavelet coefficients.

The vis–NIR spectra in the library are relatively smooth with very little noise, which is evident only when looking at the finer wavelet scales ($\lambda < 8$) at the edges of the signal and at specific absorption features, such as those near 1,400, 1,950, and 2,200 nm (Fig. 17.4). Broader absorption features such as those near 550 and 950 nm, as well as those near 1,400, 1,950, and 2,200 nm, are more evident at coarser

Fig. 17.4 Multiresolution analysis (MRA). Approximation (a_m) and detail (d_m) components at each scale, λ , of a soil vis–NIR spectrum. Each component is centred about its own zero



scales ($\lambda > 8$) (Fig. 17.4). The wavelet coefficients at finer scales contain the high frequency, stochastic components of the original spectra, while those at the coarser scales contain the lower frequency, systematic information that may be important in regression.

17.3.3 The Wavelet Transform for Data Compression and Multivariate Calibrations

Spectral data compression using wavelets relies on the premise that the spectra can be quite accurately represented by a smaller number of wavelet coefficients; that is to say, like many natural phenomena, they have a sparse representation. Figure 17.5a shows that a multivariate calibration of 29 wavelet coefficients produced the smallest RMSE when used to predict the clay content of the validation samples.

Figure 17.5b shows the proportion of these wavelet coefficients retained at each scale. All the scaling coefficients were retained, as were the wavelet coefficients at the coarsest scales ($\lambda = 64$ and 32). Only 62% of the wavelet coefficients at $\lambda = 16$, 27% at $\lambda = 8$, 4% at $\lambda = 4$, and 1% at the finest scale 2 were retained (Fig. 17.5b).

MLR predictions of clay content for the 39 validation data using only 29 wavelet coefficients are shown in Fig. 17.6a. The spectra were compressed to less than 14% of their original size. PLSR predictions using the original spectra (208 wavelengths) are shown in Fig. 17.6b. Predictions of clay content using the 29 wavelet coefficients were more accurate (RMSE = 7.1% and $R_{\text{adj}}^2 = 0.83$) than the PLSR predictions using the original spectra (RMSE = 7.9% and $R_{\text{adj}}^2 = 0.78$) (Fig. 17.6).

Furthermore, the MLR technique was more straightforward and faster to implement than the full-spectrum PLSR. Bagging-MLR predictions of clay content with depth, for each of the 10 profiles, are shown in Fig. 17.7, together with their 95%

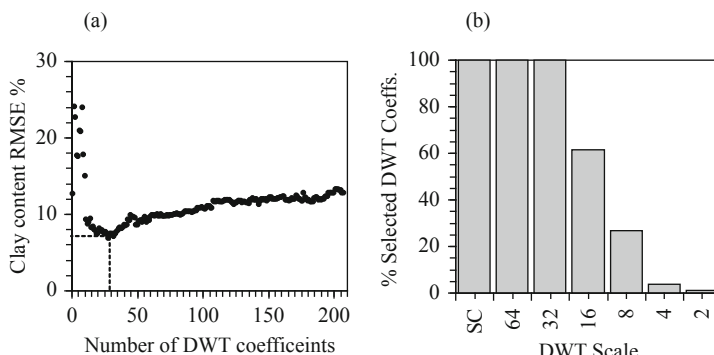


Fig. 17.5 (a) Root mean squared errors (RMSEs) of clay content predictions by multiple linear regression (MLR) using the wavelet coefficients ordered by variance (29 coefficients produced the smallest RMSE). (b) Proportion of these wavelet coefficients retained at each scale

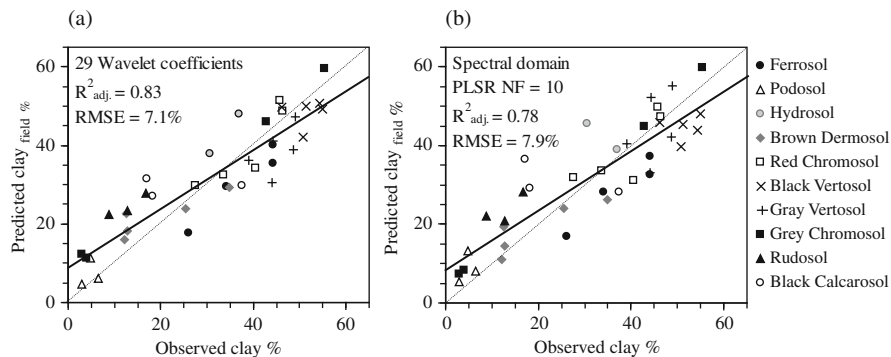


Fig. 17.6 Plots of observed vs. predicted clay content for the 39 validation data using (a) multiple linear regression (MLR) and 29 wavelet coefficients and (b) partial least squares predictions using the original spectra with 208 wavelengths

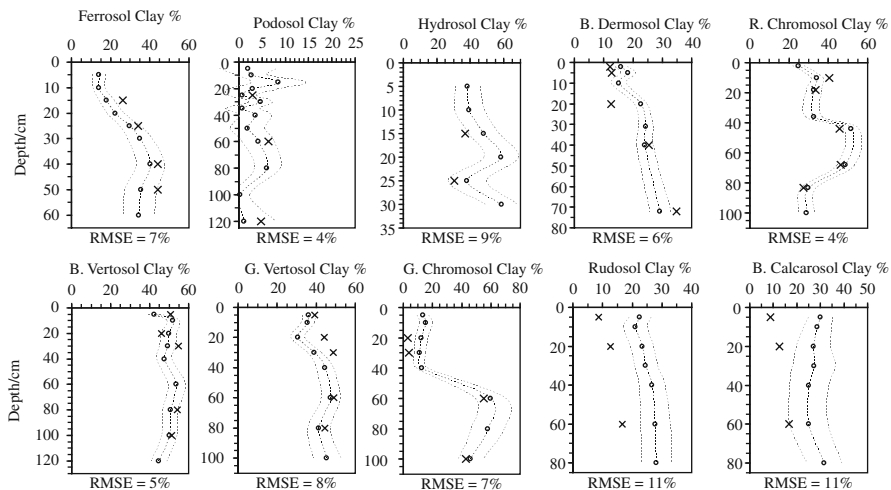


Fig. 17.7 MLR predictions using 29 wavelet coefficients, black points, enveloped by their 95% confidence intervals. Crosses show clay contents measured in the lab using the hydrometer method

confidence intervals and their individual RMSEs of prediction. Poorest predictions of clay content were obtained for the Hydrosol, Rudosol, and Calcarosol profiles, with RMSE $\geq 9\%$.

17.3.4 Denoising by Back-Transforming the Wavelet Coefficients

A sample of the denoised spectra produced by back-transforming the 29 wavelet coefficients to the spectral domain is shown in Fig. 17.2b. Their corresponding original spectra are shown in Fig. 17.2a. In this case, because the original spectra were

Table 17.2 Comparison of assessment statistics for predictions of clay content using the original spectra, the selected wavelet coefficients, and the back-transformed wavelet coefficients

	No. of predictors	Method	R^2_{adj}	RMSE (%)
Spectral domain	208	PLSR, NF = 10	0.78	7.9
Wavelet domain	29	MLR	0.83	7.1
Back-transformed wavelet	208	PLSR, NF = 11	0.72	8.1

NF refers to the number of factors used in the partial least squares regression (PLSR) models

relatively smooth, there was no apparent denoising. In fact, the spectra acquired some of the characteristic shape of the wavelet function (Fig. 17.2b). Predictions of clay content using the back-transformed spectra and PLSR were less accurate (RMSE = 8.1% and $R^2_{\text{adj}} = 0.72$) than predictions using the original spectra and the wavelet coefficients. These results are summarised in Table 17.2.

17.4 Discussion

Multivariate calibrations of spectroscopic data usually involve the use of large spectral libraries that need to be re-calibrated for different soil analyses. By transforming soil spectra into the wavelet domain and compressing to produce a smaller representation of the data, we may improve the efficiency of these calibrations as the models may be computed with simpler techniques and much reduced, parsimonious datasets. As this research has shown, the technique may also improve prediction accuracy for proximally sensed data. The discrete wavelet transform algorithm is fast and, coupled with a simple calibration technique, may also be useful for proximal on-the-go spectroscopic soil sensing, where the newly acquired spectrum may be transformed immediately after collection.

17.5 Conclusions

- A multiresolution analysis of soil diffuse reflectance spectra may be used to identify different spectral features that occur at different scales.
- The wavelet-transformed vis–NIR soil spectra were compressed to less than 14% of their original size, thereby producing a more parsimonious representation of the data.
- Multivariate calibration by MLR using 29 selected wavelet coefficients was more straightforward and faster than calibration by PLSR.
- Predictions of clay content using the wavelet-transformed proximally sensed spectra were more accurate (RMSE = 7.1%) than those from PLSR using the original spectra with 208 wavelengths (RMSE = 7.9%) or the back-transformed spectra (RMSE = 8.1%).

Acknowledgements We thank Dr. Stephen Cattle for his help with the collection and description of the soil samples.

References

FAO (1998) World reference base for soil resources. Food and Agriculture Organization of the United Nations, Rome

Gee GW, Bauder JW (1986) Particle-size analysis. In: Methods of soil analysis, Part 1. Physical and mineralogical methods. Agronomy monograph No. 9, 2nd edn. ASA-CSSA-SSSA, Madison, WI, pp 383–411

Isbell RF (1996) The Australian Soil Classification. Australian soil and land survey handbook. CSIRO Publishing, Melbourne, VIC

Lark RM, Webster R (1999) Analysis and elucidation of soil variation using wavelets. *Eur J Soil Sci* 50:185–206

Percival DB, Walden AT (2000) Wavelet methods for time series analysis. Cambridge University Press, Cambridge

Viscarra Rossel RA (2007) Robust modelling of soil diffuse reflectance spectra by ‘bagging-PLSR’. *J Near Infrared Spectrosc* 15:39–47

Viscarra Rossel RA, Lark RM (2010) Improved modelling of soil diffuse reflectance spectra using wavelets. *Eur J Soil Sci* 60:453–464

Viscarra Rossel RA, McBratney AB (1998) Laboratory evaluation of a proximal sensing technique for simultaneous measurement of clay and water content. *Geoderma* 85:19–39

Wold S, Martens H, Wold H (1983) The multivariate calibration method in chemistry solved by the PLS method. In: Ruhe A, Kagstrom B (eds) Lecture notes in mathematics, Proceedings of the conference on matrix pencils. Springer-Verlag, Heidelberg, pp 286–293

Chapter 18

Mapping Soil Surface Mineralogy at Tick Hill, North-Western Queensland, Australia, Using Airborne Hyperspectral Imagery

**T. Cudahy, M. Jones, M. Thomas, P. Cocks, F. Agustin, M. Caccetta,
R. Hewson, M. Verrall, and A. Rodger**

Abstract The use of airborne hyperspectral imagery for mapping soil surface mineralogy is examined for the semi-arid Tick Hill test site (20 km^2) near Mount Isa in north-western Queensland. Mineral maps at 4.5 m pixel resolution include the abundances and physicochemistries (chemical composition and crystal disorder) of kaolin, illite–muscovite, and Al-smectite (both montmorillonite and beidellite), as well as iron oxide, hydrated silica (opal), and soil/rock water (bound and unbound). Validation of these hyperspectral mineral maps involved field sampling (34 sites) and laboratory analyses (spectral reflectance and X-ray diffraction). The field spectral data were processed for their mineral information content in the same way as the airborne HyMap data processing. The results showed significant spatial and statistical correlation. The mineral maps provide more detailed surface composition information compared with the published soil and geological maps and other geo-science data (airborne radiometrics and digital elevation model). However, there is no apparent correlation between the published soil types (i.e. Ferrosols, Vertosols, and Tenosols) and the hyperspectral mineral maps (e.g. iron oxide-rich areas are not mapped as Ferrosols and smectite-rich areas are not mapped as Vertosols). This lack of correlation is interpreted to be related to the current lack of spatially comprehensive mineralogy for existing regional soil mapping. If correct, then this new, quantitative mineral-mapping data have the potential to improve not just soil mapping but also soil and water catchment monitoring and modelling at local to regional scales. The challenges to achieving this outcome include gaining access to continental-scale hyperspectral data and models that link the surface mineralogy to subsurface soil characteristics/processes.

Keywords Remote sensing · Hyperspectral mineral mapping · Airborne radiometrics · Digital elevation model

T. Cudahy (✉)

CSIRO Exploration and Mining, Australian Resources Research Centre, PO Box 1130,
Bentley, WA 6102, Australia
e-mail: Thomas.Cudahy@csiro.au

18.1 Introduction

There is a wealth of information on soils but much is dated, inaccurate, unavailable at appropriate scales, or relatively inaccessible. New airborne and space-borne sensors offer unprecedented detail, accuracy, rapid regional or global coverage.

[From the IUGS–UNESCO International Year of Planet Earth (2008), ‘Soils – Earth’s Living Skin’ (www.esfs.org/downloads/Soil.pdf)]

Soil mapping has largely been based on auger/spade methods to observe and measure the vertical characteristics of near-surface unconsolidated materials, including layering, texture, colour, organic matter, soil density, pH, electrical conductivity, and cation exchange capacity. Surface soil maps (www.asris.csiro.au/index_ie.html) typically represent interpolation between these ‘vertical’ sample points, often supplemented by spatially comprehensive data such as airborne and satellite optical imagery (Chapters 10 and 34), digital elevation models (DEMs), and airborne geophysics, especially gamma radiometric data.

McKenzie and Ryan (1999) recommend a quantitative approach for mapping soils, one that will then enable temporal monitoring and management of various environmental and agricultural issues. These issues range from the effects of climate change (e.g. desertification), carbon budgets (e.g. organic content on and within soils, including as carbon black), land use (e.g. water and wind erosion as well as groundwater acidity and salinity), and agricultural production (e.g. soil moisture, cation exchange capacity).

Digital measurement of soil information is now achievable through a range of laboratory, field, and airborne technologies, including reflectance spectroscopy (Chapters 3, 11, 12, 13, 14, and 17), gamma spectrometry (Chapters 27 and 28), ground-penetrating radar (Chapter 25), and electrical conductivity (Chapters 29 and 30). Typically, the measured data are statistically processed to identify any relationship with the target soil property (Chapters 13, 14, and 17). However, statistical relationships established for a given area (calibration suite) are rarely transferable universally. One of the reasons for this is the indirect relationship between the digital data and the target soil attribute. For example, the use of radiometric digital data to estimate clay content has been found to be correlated with the thorium (Th) channel (Chapter 27, Taylor et al., 2002), the potassium (K) channel (Thomas et al., 2003), or the ratio of the thorium and uranium (U) channels (Pracilio et al., 2006), depending on the soil type. In each case, the clay-size fraction contains an abundance of a mineral(s) that hosts these different radioactive elements, such as K in illite and Th in hematite or goethite.

Direct measurement of the species and abundance of soil minerals is generally not investigated in soil-mapping procedures, and yet mineralogy is a fundamental component of all soils and is an indicator for many important soil parameters, such as pH, redox potential, water/metal activities, and permeability. There are a few studies that have shown this link between mineralogy and soil properties, including one by Van der Merwe et al. (2002) of the mineralogy of melanic soils from South Africa. Using laboratory X-ray diffraction (XRD), they showed that soil pH is

correlated with clay composition. That is, increasing kaolin development is proportional to decreasing pH. In general, kaolins form under acid conditions, smectites under alkaline conditions, and illite can develop under alkaline and neutral conditions, provided there is sufficient K. Similarly, clay mineralogy affects the availability of soil nutrients. For example, Bajwa (1981) found that beidellite clay is the strongest fixer of K in tropical soils. In general, smectitic clays readily exchange cations (and have a high cation exchange capacity or CEC) such that they have high nutrient-holding capacity as well as high water-holding capacity. In contrast, kaolinite has low CEC and low water-holding capacity. With regard to soil types (Isbell, 1996), Vertosols, dominated by smectites, have a high CEC, whereas Ferrosols, comprising kaolinite and Fe oxides, have low CEC per unit weight. Thus accurate mapping of clay mineralogy will provide critical information in recognising potential fertility and types of soils.

Laboratory studies of the spectral reflectance and emission of minerals (Clark et al., 1990; Clark, 1999) have shown the potential for measuring specific minerals and their mineral physicochemistries (cation composition and crystal disorder). For example, Post and Noble (1993) showed that the change in Al content from beidellite to montmorillonite can be measured as a shift in the wavelength of the Al–OH absorption feature in the 2,200 nm region. The potential for using field spectral measurements to determine soil properties, such as the clay content for various levels of moisture content and different parent materials, has been examined (e.g. Chapters 12, 13, 14, and 16, Waiser et al., 2007).

Hyperspectral remote sensing systems, measuring a hundred or more discrete wavelengths, are able to capture the commonly subtle but diagnostic spectral signatures of specific minerals, including wavelength shifts of absorptions (e.g. positions of absorption features) like beidellite–montmorillonite. These hyperspectral systems, such as NASA's 224-channel airborne AVIRIS system (aviris.jpl.nasa.gov) and the Finnish AISA (Chapter 14), contrast with multi-spectral systems like Landsat TM and ASTER (www.ersdac.or.jp), measuring only 7–15 channels and at best identifying only mineral groups (Cudahy et al., 2005).

Using remote hyperspectral imaging systems, Ben-Dor et al. (2002, 2004) and Chabirillat et al. (2004) have shown that soil properties, such as soil water infiltration, organic matter, moisture, salinity, and clay content, can be mapped remotely, especially in drier climates where vegetation cover does not totally obscure the underlying soil. The other caveat for using optical remote sensing for soil mapping is that the measured mineralogy is from the top few micrometres only and that not all the important or characteristic soil parameters are exposed at the surface (e.g. duplex soils).

Regional maps of surface mineralogy are now becoming available to the mineral exploration industry in Australia (Cudahy et al., 2005). These are based on operational airborne hyperspectral systems, such as the Australian HyMap sensor (www.hyvista.com). A suite of hyperspectral satellite systems are also scheduled to be launched in the next 1–7 years (www.isiswg.org). Combined, these airborne and satellite hyperspectral technologies provide an opportunity to deliver high spatial resolution (≤ 30 m pixels) mineral maps at the continental scale.

This chapter explores the potential for mineral mapping in the Tick Hill test site ($21^{\circ}35' S$, $139^{\circ}55' E$), a $10\text{ km} \times 20\text{-km}$ area in north-western Queensland (Fig. 18.1). Specifically, the aims of this study are the following:

- To show examples of the types of mineral maps being generated by hyperspectral imagery for the mineral exploration industry which may also be of value for high-resolution digital soil surface mapping;
- To compare these mineral maps with other ‘soil-mapping’ data, including published soil and geological maps, airborne radiometrics, and digital elevation data; and
- To promote the vision of securing a high spatial resolution (<30 m pixel) mineral map of the Australian continent that would benefit a range of applications from environmental baseline mapping and monitoring of soils to mineral exploration.

18.2 Tick Hill Study Area

The Tick Hill area (Fig. 18.1) is located in the Mount Isa region of western Queensland. This area has a dry tropical climate with <500 mm rainfall per annum falling dominantly in the summer months. The topographic relief is subdued

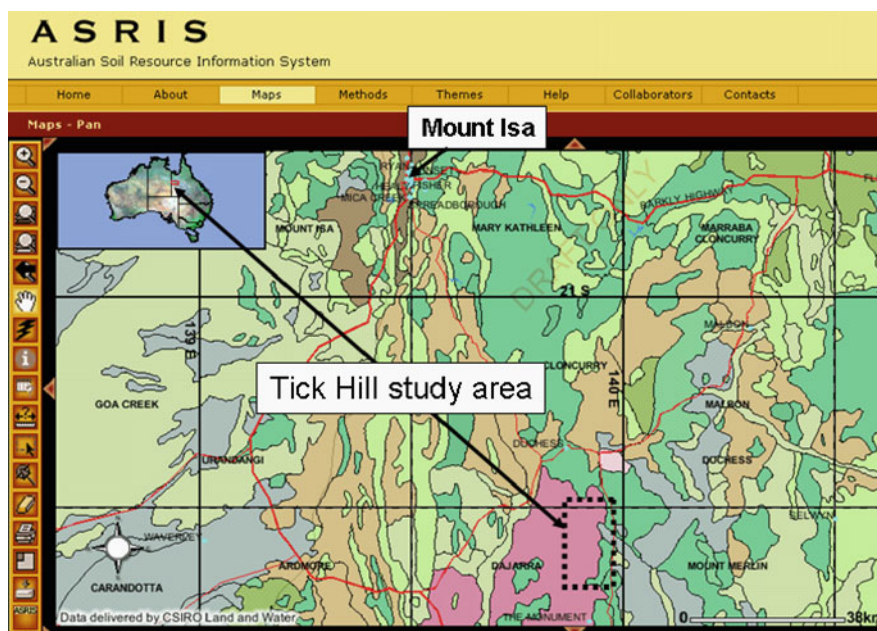


Fig. 18.1 ASRIS (www.asris.csiro.au) webpage screen capture showing the level 3 ‘dominant soil suborders’ of the Mount Isa region as well as the location of Tick Hill study area

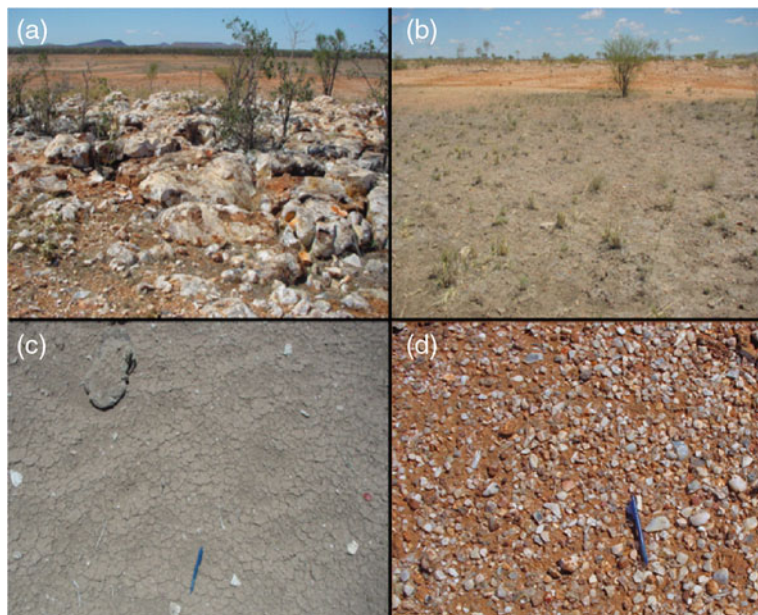


Fig. 18.2 Field photographs of the Tick Hill area. (a) Exposure of opaline silica (389190 mE; 7617437 mN, GDA94 MGA54); (b) depression of grey illite-rich soil in the foreground and a low rise of hematitic Al-smectite-rich soil with opaline silica in the background (388804 mE; 7617491 mN, GDA94 MGA54); (c) close-up of the grey illitic soil shown in (b); (d) close-up of the red Al-smectite soil with abundant opaline silica rock fragments shown in (a)

(<200 m) and the vegetation cover is limited (<25%) comprising narrow belts of green vegetation along the ephemeral drainage (e.g. *Eucalyptus* spp. and *Corymbia* spp.), while hardy bushes and dry grasses occur elsewhere (e.g. *Triodia* spp., also called spinifex grass, Neldner, 2001) (Fig. 18.2a, b). The geology comprises folded and metamorphosed Proterozoic felsic and mafic rocks, which hosted the now closed Tick Hill gold mine (Forrestal et al., 1998). Phanerozoic cover sequences also occur, including Tertiary rocks described as ‘laterite’ and ‘lateritic rubble’; Cambrian rocks described in part as ‘massive ferruginous sandstones’; and Cainozoic alluvium–colluvium of unconsolidated sand–silt–gravel (Fig. 18.3a).

The web-accessible digital ASRIS soil map of Australia (McKenzie et al., 2008) describes the soils of the Mount Isa region as developing over highly weathered bedrock (>50%), fresh bedrock (20–50%), and alluvial sediments (<20%). Soils typically lack an organic-rich A horizon. Soil types (Isbell, 1996) include Ferrosols (high iron content), Vertosols (shrink–swell clays), Kandosols (kaolin 1:1 clay minerals), Rudosols (rudimentary soil development), and Tenosols (weak soil development). In the Tick Hill study area, the mapped soil types (Fig. 18.3b) include Vertosols (VE), which are located in broad drainage lows evident in the associated DEM and are locally characterised mainly by high radiometric potassium response

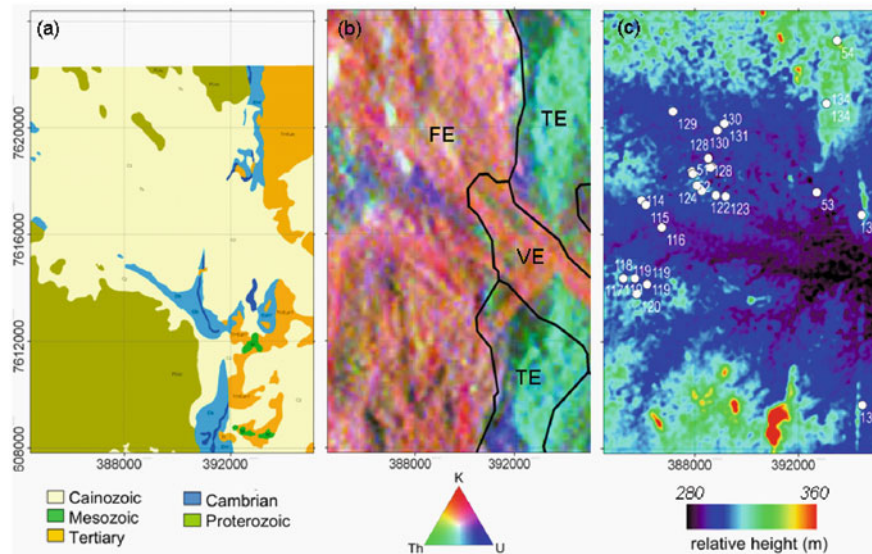


Fig. 18.3 Selected publicly available geoscience data over the Tick Hill study area. (a) The published 1:100,000-scale digitally available Dajarra geological map sheet showing only the major rock divisions based on their age of formation. (b) Ternary colour image of the airborne radiometrics, as well as ASRIS level 3 soil map units indicated by the black lines. (c) ASTER-derived digital elevation model with the location of the field sample sites

(Fig. 18.3c); Tenosols (TE), which are locally characterised by high radiometric thorium responses (Fig. 18.3b); and Ferrosols (FE), which are locally characterised by high radiometric potassium response (Fig. 18.3b).

18.3 Materials and Methods

18.3.1 Geoscience Mapping Data and Processing

The geoscience mapping data used in the information extraction of the Tick Hill area include the following:

- Airborne HyMap hyperspectral imagery collected in August/September 2006 at 4.5 m pixel resolution. The Tick Hill area was covered by 12 contiguous N–S flight lines of 512 pixel swaths each.
- ASTER digital elevation model at 30 m pixel resolution generated by the United States Geological Survey (USGS).
- Airborne gamma radiometric data collected at 200 m line spacing and resampled/interpolated to 50 m pixels (Jayawardhana and Sheard, 2000).
- Published 1:100,000 scale Dajarra geological map sheet (Geoscience Australia, 2008).

18.3.2 Airborne HyMap Data Processing for Mineral Mapping

The HyMap radiance-at-sensor data were processed to apparent reflectance by HyVista Corporation Pty Ltd using CSIRO's HYCORR software. HYCORR is essentially an IDL-based front-end widget to ATREM, based on 6S (Gao et al., 1993; Clark et al., 1993; <http://cires.colorado.edu/cses/atrem.html>), both of which are no longer publicly available or supported. Systematic, high-frequency, residual atmospheric absorption line features were not removed in the mineral-mapping processing as this typically involves the use of scene-dependent statistics, e.g. EFFORT correction within ENVI software (ITTIVIS, 2008). However, selected pixel spectra for presentation in this chapter were treated to remove this noise using a normalisation procedure based on the airborne and field spectra collected from the same sites.

The mineral information processing of the HyMap reflectance data was conducted using in-house CSIRO software, C-HyperMAP, and was designed to handle large-volume, multi-scene hyperspectral imagery. C-HyperMAP runs as an add-on to the commercial hyperspectral image-processing software IDL-ENVI (ITTIVIS, 2008) to capture the benefits of ENVI's image display and other functionality.

The underlying strategy for mineral information extraction using C-HyperMAP is based on measuring the diagnostic absorption features, including their depths, wavelengths, and geometries (full-width at half-height – FWHH – and asymmetry). Essentially, absorption depth (relative to the background continuum) is assumed to be proportional to the mineral abundance. That is, no absorption measured equates to no mineral present. The absorption wavelength is assumed to be proportional to the cation composition (e.g. Tschermak substitution, $[Al \leftrightarrow Si]_{\text{tetrahedral}} \leftrightarrow [Al \leftrightarrow \{Fe^{2+}, Mg\}_{\text{octahedral}}]$) of minerals like white mica (e.g. muscovite; Duke, 1994) and chlorite. For example, the level of Tschermak substitution in white mica was gauged using the wavelength of the continuum-normalised 2,200 nm absorption trough and determined with the first derivative of a fitted fourth-order polynomial between 2,120 and 2,240 nm. Chapter 17 describes the use of wavelets to model these (and other) absorption features.

Absorption bandwidth is assumed to be proportional to the crystal order/disorder. That is, the range of vibrational states (degrees of freedom) is increased (spread) with increasing disorder (long- and short-range molecular structural order). Multiple diagnostic features are used to mask in (or out) specific minerals and materials. For example, all pixels are measured for their green and dry vegetation contents and, if above a certain threshold, are masked out. This nulls many of the pixels available in a given image. Areas of standing water and deep topographic shading are also masked out. The images of masked absorption depth are converted to apparent percent abundance assuming that the USGS library spectra (USGS, 2008) represent 100% abundance and where no absorption recorded represents 0% abundance. Using this methodology, the detection limits typically start from 10 to 15% abundance. Details of all the algorithms used for the various mineral products can be obtained from Cudahy et al. (2008). Note that CSIRO has now developed methods to unmix the green and dry vegetation components at the pixel scale leaving as residual 'vegetation-free' pixels (Rodger and Cudahy, 2009).

18.3.3 Field Samples and Related Laboratory Analyses

Exactly 34 field samples from the Tick Hill area were sampled during two field campaigns in late 2006 and 2007. Samples included weathered and fresh rocks, as well as soils scraped by trowel from the top 5 mm of the surface. Following air drying in room conditions, all the field samples were measured using an Analytical Spectral Devices (ASD) FieldSpec Pro reflectance spectrometer (<http://www.asdi.com/>, Boulder, Colorado, USA). The contact probe of the ASD was used to measure the diffuse reflectance in the 350–2,500 nm region using an internal halogen light source. The data were calibrated using a Spectralon white reference standard provided by Labsphere (<http://www.labsphere.com/>).

These ASD reflectance spectra were used to confirm the spectral mineralogical signatures of the airborne HyMap imagery. Each spectrum was interpreted manually based on diagnostic spectral features. For example, kaolinite was identified through the development of a narrow (~18 nm FWHH) absorption at 2,206 nm coupled with smaller absorption at 2,160 nm. This manual spectral mineral interpretation was validated using X-ray diffraction (XRD) on all 34 soil samples.

Mineralogy detected using XRD relies on repetitive crystalline order, so relatively amorphous minerals (e.g. allophane and ferrihydrite) are difficult to detect. The key minerals targeted for detection by XRD were the clays, especially Al-smectites (montmorillonite versus beidellite), illite, and kaolin (kaolinite versus halloysite), as well as silica (opal–cristobalite). The 34 soil samples were prepared as random powders (<75 µm) mounted on circular holders. XRD patterns were obtained using a Philips X’Pert multi-purpose X-ray diffraction (MPD) system fitted with a Cu tube operated at 40 kV, 40 mA, and a curved graphite monochromator. All samples were scanned from 2° to 70° at 1.0°/min in 0.01° increments (all angles 2θ) at 1 or 2 s counting increments. First-pass mineral identification was facilitated using the Windows-based in-house search-match software XPLOT. Where quartz was identified in the diffraction patterns, this was used as an internal standard to correct for instrumental shifts in 2θ position.

From the first-pass spectral and XRD mineral interpretations, four samples were then selected for more detailed smectite clay analysis, namely the identification of beidellite versus montmorillonite using a modified Greene-Kelly test (Greene-Kelly, 1953). These samples were mixed with a 0.6% calgon (sodium hexametaphosphate) solution and allowed to settle to separate the clay fraction, which was dried on circular mounts before being Li saturated and heated overnight at 200°C. They were then treated with ethylene glycol and measured by XRD at a slower scan rate and a narrower angle range (2–30°). After heating, all smectites collapse to approximately 1 nm and after subsequent ethylene glycol solvation, beidellite expands to 1.7 nm, whereas the collapse of montmorillonite is irreversible. However, there is some concern that interactions with the sodium in the glass used as a substrate may have affected the results and lead to only a partial collapse of the montmorillonite (Volzone, 1992).

18.3.4 Field Validation of Airborne Mineral-Mapping Results

The accuracy of the mineral maps generated from the processed airborne HyMap imagery was validated using the field sample data. The field ASD spectra were first convolved to the HyMap band-pass configuration and then processed using the same algorithms implemented on the HyMap reflectance. For example, the Al-OH clay content was estimated by calculating the depth of a continuum-normalised, fitted fourth-order polynomial to the segment of the reflectance signature between the 2,120 and 2,245 nm range. To simplify the comparison between the airborne and field data, it was assumed that each field site was dominated by soil such that the contribution of the outcrop rock spectral mineralogical component in the field data was ignored. In addition, given the paucity of vegetation cover, the HyMap data were not unmixed of their vegetation component. Regions of interest (ROI) based on a sample average of 4–40 HyMap pixels were used to improve any geo-referencing errors between the field site positions (± 20 m) and HyMap pixels (± 50 m).

Two sets of sample site reflectance measurements were used to provide quantitative statistical correlation between the airborne and field data, whereas the remaining validation presented was based on spatial assessment of the remote and field measurements provided in the figures.

18.4 Results and Discussion

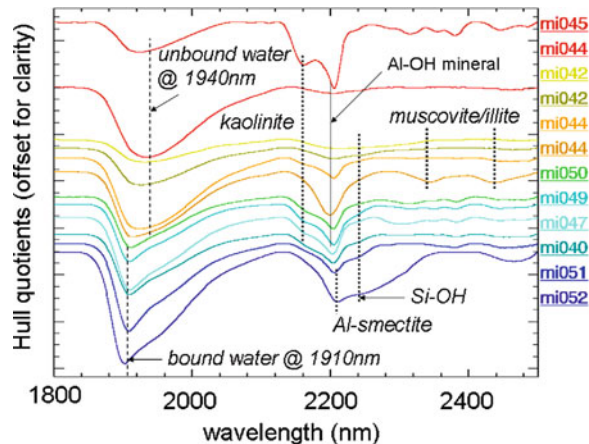
18.4.1 Field Samples

Figure 18.4 presents selected ASD reflectance spectra of field samples from the Tick Hill area. These continuum-removed spectra were prepared by normalising an interpolated hull, or continuum, that is mathematically draped over the spectra to highlight large and small absorption features. Multiple spectra from the same site (e.g. MI044) show the diversity of the spectral mineralogy at any one location. Most of the spectra show absorptions centred on 2,200 nm related to various clay minerals, including the following:

- Kaolinite, with diagnostic absorptions at 2,160 and 2,207 nm (e.g. sample MI045);
- Illite/muscovite, with diagnostic absorptions at 2,200, 2,350, and 2,450 nm (e.g. sample MI044-brown spectrum);
- Al-smectite, with diagnostic absorption at 2,200 nm only (e.g. samples MI051 and MI052).

Broad absorption around 2,250 nm (e.g. sample MI052 in Fig. 18.4) is related to Si-OH, confirmed by XRD analysis to be cristobalite, a common component of opaline silica. Bound (i.e. hydrogen bonded) water and unbound (free) water are

Fig. 18.4 Laboratory ASD reflectance spectra of selected soil samples from the Tick Hill study area. Key features are annotated



indicated by the geometry of absorption around 1,900 nm. Bound water produces a relatively narrow, short-wavelength ($\sim 1,907$ nm) absorption feature compared to unbound water. Bound water is evident in samples containing Al-smectite (e.g. MI052 and MI051) as well as poorly ordered kaolin (e.g. MI050, MI049, MI047, MI040) and to a lesser degree illite/muscovite (e.g. sample MI044-brown). In theory, illite can be spectrally separated from muscovite, assuming that illite contains abundant bound water and muscovite is relatively free of water. Unbound water is detected in samples with water ‘trapped’ in fluid inclusions in silica, as in possible vein quartz (e.g. sample MI044-red).

18.4.2 Airborne Versus Field Spectra

The reflectance spectra of field samples and matching HyMap pixels from five sites with different mineralogy are presented in Fig. 18.5. Note that the HyMap data (Fig. 18.5b) have only 126 spectral bands (~ 18 nm spectral resolution at 2,200 nm) and no bands in the intense water vapour absorption regions at 1,400 and 1,900 nm. In comparison, the ASD field reflectance spectra (Fig. 18.5a) have over 2,000 channels (~ 8 nm spectral resolution at 2,200 nm). Nevertheless, the same overall shapes and detailed absorption features can be recognised in both datasets. This includes the strong ferric oxide absorption of hematite–goethite at 900 nm evident in sample MI054 (red spectra) and the kaolin doublet at 2,160 and 2,206 nm in sample MI045 (green spectra).

18.4.3 Mineral Group Abundances

Maps of the airborne hyperspectral total Al–OH clay (Fig. 18.6a) and iron oxide (Fig. 18.6b) contents of the Tick Hill area show a high degree of similarity and are

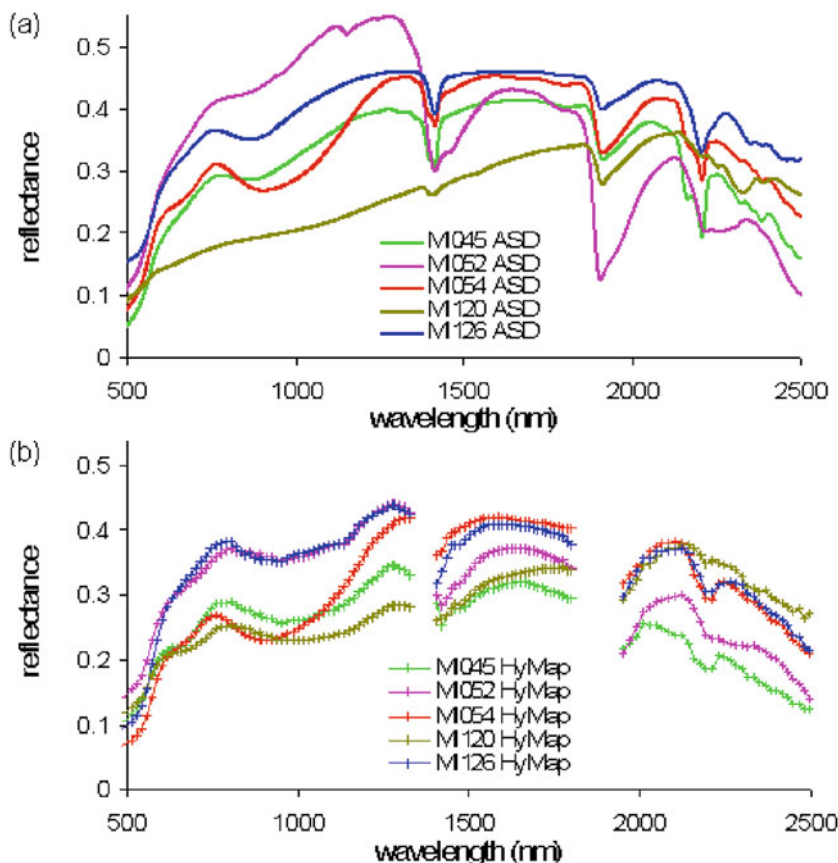


Fig. 18.5 Comparison of field sample reflectance spectra (a) and HyMap pixel reflectance spectra (b) for a selection of field sites that show iron oxide (e.g. MI054), kaolinite (e.g. MI045), illite–muscovite (MI126), Al-smectite plus cristobalite (e.g. MI052), and Al-smectite and a ferrous silicate (e.g. MI120). Note that the HyMap spectral bands (*crosses*) do not cover the strong atmospheric water vapour absorption regions at 1400 and 1900 nm

also consistent between each other and with their field validation soil data (coloured circles). For example, high abundances of clay and iron oxide are associated with the Tertiary ‘lateritic’ rocks and Cambrian ‘massive ferruginous sandstones’ (Fig. 18.3a) in the eastern third of the image. The similarity between the field and airborne mineral estimates is also provided in the scattergrams of Fig. 18.6c, d which show significant linear correlation, similar to the results of Cudahy et al. (2005). The Al–OH clay results approach the ideal $y = x$, which suggests that the correct assumptions were applied in this validation, especially in the use of only the soil ASD spectra, and the accuracy of the HyMap data reduction to reflectance. This is a very important result as it is critical to the hypothesis that the remote

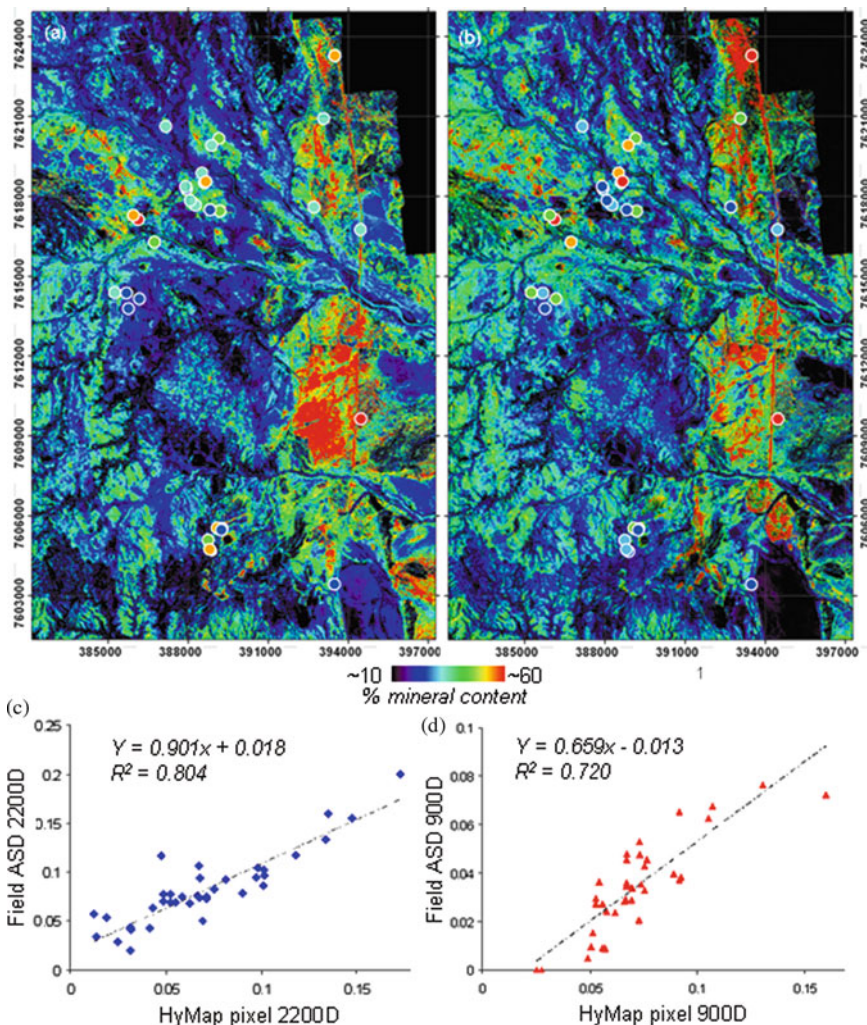


Fig. 18.6 (a) Total clay mineral content derived from the 2200 nm continuum-absorption depth measured from the HyMap data. (b) Total iron oxide mineral content derived from the 900 nm continuum-absorption depth measured from the HyMap data. (c) Scattergram of the field ASD spectra of soil samples versus the ROI HyMap spectra of the same areas, both processed using the same 2200 nm continuum-absorption depth. (d) Scattergram of the field ASD spectra of soil samples versus the ROI HyMap spectra of the same areas, both processed using the same 900 nm continuum-absorption depth. The GDA94 MGA54 grid shown is 3 km

mineral-mapping results are measuring the surface soils. The iron oxide results show that the airborne predictions are constantly overestimated, which is interpreted to be related to systematic residual water vapour errors in the HyMap data, prevalent in the 900 nm wavelength region. This could be compensated for by new data-processing methods now being developed.

18.4.4 Clay Mineral Abundances

Figure 18.7 presents the airborne hyperspectral estimates of the clay mineral contents for the kaolin group (i.e. kaolinite, halloysite, dickite, nacrite), the illite group (illite, muscovite, bramallite, paragonite, phengite, lepidolite), and Al-smectite group (montmorillonite and beidellite). These maps are mutually exclusive based on the current information extraction methodology. Close inspection of the field versus airborne clay mineral abundance maps (Fig. 18.7) shows a high degree of similarity. Note that the field and airborne mineral abundance measurements were processed and colour coded in the same way. This includes samples where no clay of a specific type (black dots) was apparent.

Kaolin minerals (Fig. 18.7a) are abundant in the Phanerozoic rocks, especially the Cambrian ferruginous sandstones and Tertiary laterites. Both of the rock units are commonly associated with the development of kaolin because of acid, well-drained conditions. It is unclear why this area was mapped in the ASRIS as a Tenosol (Fig. 18.3b) rather than a Kandosol or even a Ferrosol (Fig. 18.6b), especially as the airborne radiometric response shows this area to be relatively rich in thorium, which is commonly concentrated in ferruginous materials such as laterites (Dauth, 1997).

The Proterozoic ‘basement’ rocks, as well as the overlying alluvium–colluvium areas, are rich in illite as shown by the illite/muscovite map (Fig. 18.7b). These areas of spectrally mapped white mica are consistent with the high radiometric K

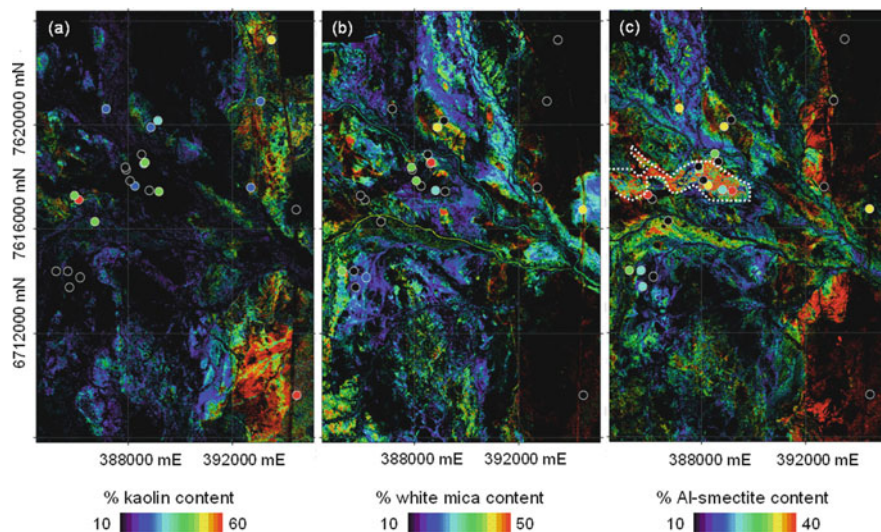


Fig. 18.7 Airborne hyperspectral-derived estimates of the apparent contents of (a) kaolin; (b) illite–muscovite; and (c) Al-smectite. Coloured dots are field spectral data that have been convolved to the HyMap band responses and then processed using the same HyMap algorithms to generate the clay mineral estimates. The colour coding for both the HyMap and field data is the same, with black equal to no clay detected

responses for this area (Fig. 18.3b). It is unclear why this area was mapped as a Ferrosol (Fig. 18.3b) as iron oxide abundance is low compared with other parts of the study area.

Al-smectite (Fig. 18.7c) is more widely distributed, with high abundances over a central corridor along the valley fill of alluvium–colluvium (Fig. 18.3a, c). Given that Al-smectite is characteristic of Vertosols, this area, mapped as Ferrosols, is arguably better described as Vertosols, especially as there is also evidence for shrink-swell effects (Fig. 18.2c).

These mineral maps (Fig. 18.7) show improved detail compared with the existing mapping data (Fig. 18.3). Particularly significant is the juxtaposition (near 385930 mE; 7617300 mN, GDA94 MGA54) of kaolin soils (which presumably formed in acid conditions) with Al-smectitic soils (presumably formed in more alkaline conditions). This could be explained by kaolinite developed in ‘unmapped’ Cambrian quartz sandstones, i.e. parent rock control, or changes in groundwater geochemistry.

18.4.5 Clay Mineral Physicochemistry

Remote hyperspectral data can provide measurements of mineral physicochemistry. Figure 18.8 presents the airborne hyperspectral-derived estimates of the physicochemistry of the Al-clay minerals, including kaolin ‘crystallinity’ (Fig. 18.8a), based

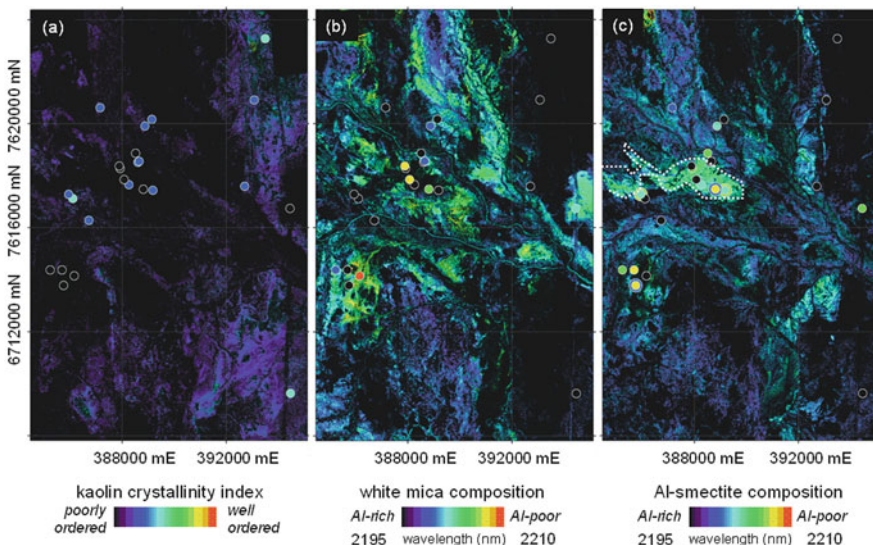


Fig. 18.8 Airborne hyperspectral-derived estimates of the apparent ‘crystallinity’ of (a) kaolin; the level of Tschermark substitution in (b) illite–muscovite; and (c) Al-smectite. Colour coding as for Fig. 18.7

on a spectral index involving the relative depth of the 2,160 nm absorption; illite composition (Fig. 18.8b), based on the wavelength of the 2,200 nm absorption which is correlated with the degree of Tschermak substitution; and the smectite composition (Fig. 18.8c), which is also related to Tschermak substitution and the presence of beidellite versus montmorillonite (Post and Noble, 1993).

The kaolin crystallinity index has proved valuable for mapping transported versus *in situ* regolith materials in Western Australia where transported materials such as alluvium–colluvium contain relatively poorly ordered kaolinite (Cudahy et al., 2005). The same pattern appears in the Tick Hill area with poorly ordered kaolin pervasively developed, especially in the Cainozoic sediments. Only windows of more well-ordered kaolin, associated with Cambrian sediments, protrude through this younger cover. The main points to note regarding the illite and smectite composition maps (Fig. 18.8b, c) and the smectite abundance (Fig. 18.7c) are the similarity between the field and airborne data and the area of abundant smectite along a corridor (marked by a white dotted line) between two drainage lows in the Cainozoic alluvium–colluvium (Fig. 18.3a, c). This abundant smectite has long wavelengths (Fig. 18.8c), which in theory would be associated with montmorillonite rather than beidellite.

XRD analysis of four smectite-rich samples (Table 18.1) found that both beidellite and montmorillonite are present in the soils. However, when the field sample XRD results are plotted (Fig. 18.8c), the longer wavelength smectites include the two beidellite-bearing soils (points with yellow cores and blue rims) as well as one of the montmorillonite-bearing samples (points with blue cores and green–yellow rims). The other montmorillonite sample is associated with shorter wavelength smectites. The reason for this unclear pattern may be the fact that mixed layer clays are common in these samples and that beidellite, unlike montmorillonite, is not found alone as the only smectite clay phase in any given soil.

18.4.6 Other Products

In addition to the clay mineral-mapping results, Fig. 18.9 presents predictions for the soil/rock water content (Fig. 18.9a); nature of water bonding (Fig. 18.9b); and the distribution of opaline silica (cristobalite, Fig. 18.9c). Note that all three of these maps show similarity with the field and laboratory data. For example, XRD analysis found cristobalite only in those samples mapped as having Si–OH absorption

Table 18.1 Interpreted clay mineralogy of selected soil samples as determined using X-ray diffraction

Sample	Major	Minor	Trace	Smectite mineralogy
MI114	Smectite + kaolinite		Mixed layer clay	Montmorillonite
MI120	Smectite	Kaolinite	Mixed layer clay	Beidellite + montmorillonite
MI122	Smectite + kaolinite	Illite	Mixed layer clay	Beidellite + montmorillonite
MI123	Kaolinite	Smectite	Mixed layer clay	Montmorillonite

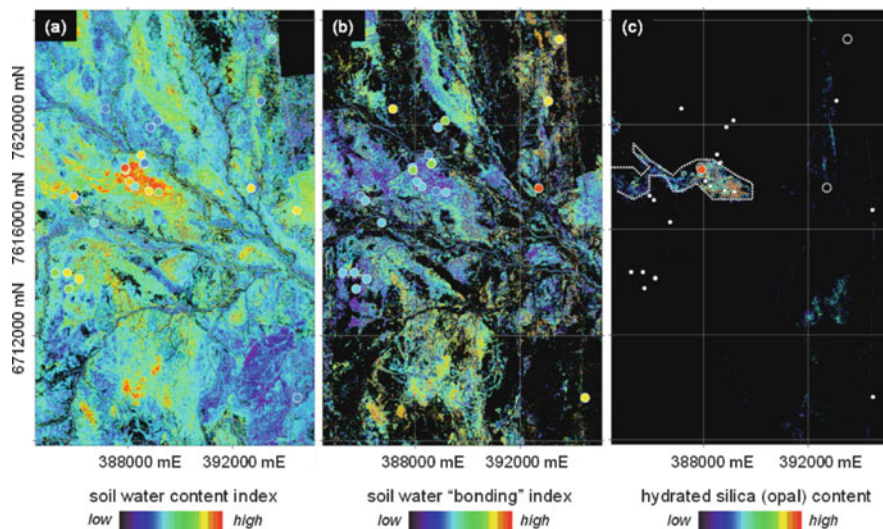


Fig. 18.9 Airborne hyperspectral-derived estimates of (a) the water content for the surface soils (and rocks), masked to remove pixels with abundant green and dry vegetation; (b) HyMap spectral index sensitive to bound/unbound water based on the geometry of the 1400-nm-long wavelength shoulder. Field validation sample data plot the wavelength position of the 1900 nm absorption ranging from 1907 nm (blue) to 1916 nm (red); (c) HyMap opal–cristobalite content based on the broad Si–OH 2250 nm absorption. The field validation data are XRD results with opal–cristobalite detected (red) or not present (black)

in the HyMap data (Fig. 18.9c). Outcrop and surface debris of opaline silica was also observed at these field sites. Positive results for the two water products occur despite the differences in time and surface conditions between the airborne acquisition (August 2006), field sampling (November 2007 and 2008), and laboratory measurements. Note also that different spectral parameters were used for deriving the water bonding. That is, the airborne product is based on the geometry of the 1,400-nm-long wavelength shoulder, whereas the field measurements are based on tracking the shift of the 1900 nm absorption band within the narrow range of 1,907–1,916 nm. Further independent analysis is required to confirm the nature of this water bonding.

18.4.7 Integrated Mineral Analysis

These mineral maps can be used in combination to provide more accurate predictions of soil composition. For example, abundant smectite (Fig. 18.7c) should in theory be associated with abundant bound water. This is the case in parts of the Cainozoic sediments (Figs. 18.3a and 18.9a, b), where there is also a spatial relationship with opaline silica (Fig. 18.9c) and, to a lesser degree, moderate levels of iron oxide (Fig. 18.6d, b). This mineralogical association can provide information about

the nature of the ground water fluids, in terms of both physicochemistry (alkaline, oxidised, dissolved Si, Fe, Mg, and Ca) and architecture (potential upward movement). The challenge now is to begin constructing 3D models that link this detailed surface mineralogy with subsurface ground water and soil-forming processes.

18.5 Conclusions

The hyperspectral mineral maps – generated as part of the government geological survey precompetitive geoscience data suite for enhancing mineral exploration – also have value for mapping soils. Key mineral maps include the abundance of clay minerals like kaolin, Al-smectite, and illite, which can be used as potential measures for soil pH, CEC, and permeability. The opportunity to measure both the soil water content and the nature of this water (bound versus unbound) may also be significant for understanding soils. The results from Tick Hill show that these hyperspectral maps provide mineralogical detail not evident in conventional geoscience maps or in other geophysical data such as airborne gamma radiometrics. The results show that although the current soil boundaries have some association with mineralogical boundaries, the current mapped soil types do not correlate with the surface mineralogy as mapped by hyperspectral imagery. There are a number of potential reasons for this, though the most likely are the assumptions used in interpreting the available geoscience data (radiometrics, DEM, geology). Given the importance of mineralogy in soil characterisation, and the lack of accurate mineralogical information provided by the currently available geoscience data, remote mineral mapping has the potential to provide complementary, valuable information for soil mapping. Given developments in hyperspectral data access, information extraction, and accuracy assessment, these mineral maps can also be used in the quantitative modelling and monitoring of soil properties for multi-temporal management of agriculture and water catchments from local to continental scales.

Acknowledgement This work is part of a larger collaborative mineral exploration study between CSIRO, Geological Survey of Queensland, Geoscience Australia, James Cook University, and Curtin University, with support from CSIRO Minerals Down Under Flagship, CRC Predictive Mineral Discovery, CRC Landscape Environment and Mineral Exploration, and the Queensland Government Smart Exploration/Mining initiatives. Ian Lau and Raphael Viscarra Rossel provided critical comment to the draft. To all of these people and organisations, we give our sincere thanks.

References

Bajwa MI (1981) Soil clay mineralogy in relation to fertility management: effect of soil mineral composition on potassium fixation under conditions of upland rice soils. *Nutr Cycl Agroecosyst* 2(3):299–303

Ben-Dor E, Goldshleger N, Braun O, Kindel B, Goetz AFH, Bonfil D, Margalit N, Binaymini Y, Karnieli A, Agassi M (2004) Monitoring infiltration rates in semiarid soils using airborne hyperspectral technology. *Int J Remote Sens* 25(13):2607–2624

Ben-Dor E, Patkin K, Banin A, Karnieli A (2002) Mapping of several soil properties using DAIS-7915 hyperspectral scanner data – a case study over clayey soils in Israel. *Int J Remote Sens* 23(6):1043–1062

Chabrilat S, Kaufmann HJ, Palacios-Orueta A, Escribano P, Mueller A (2004) Development of land degradation spectral indices in a semi-arid Mediterranean ecosystem. In: Ehlers M, Posa F, Kaufmann HJ, Michel U, De Carolis G (eds) *Remote sensing for environmental monitoring, GIS applications and geology IV*. Proceedings of SPIE 5574, pp 235–243

Clark RN (1999) Spectroscopy of rocks and minerals, and principles of spectroscopy. In: Rencz N (ed) *Remote sensing for the earth sciences: Manual of remote sensing*. Wiley, New York, pp 3–52

Clark RN, King TVV, Klejwa M, Swayze G, Vergo N (1990) High spectral resolution reflectance spectroscopy of minerals. *J Geophys Res* 95:12653–12680

Clark RN, Swayze G, Heidebrecht K, Goetz AFH, Green RO (1993) Comparison of methods for calibrating AVIRIS data to ground reflectance. *Proceedings of the 4th annual JPL airborne geoscience workshop*, Pasadena, October 25–29, vol I, pp 35–36

Cudahy TJ, Caccetta M, Cornelius A, Hewson RD, Wells M, Skwarnecki M, Halley S, Hausknecht P, Mason P, Quigley MA (2005) Regolith geology and alteration mineral maps from new generation airborne and satellite remote sensing technologies; and Explanatory notes for the Kalgoorlie–Kanowna 1:100,000 scale map sheet, remote sensing mineral maps. MERIWA report no. 252, 114 pp

Cudahy TJ, Jones M, Thomas M, Laukamp C, Caccetta M, Hewson RD, Rodger AR, Verrall M (2008) Next generation mineral mapping: Queensland airborne HyMap and satellite ASTER surveys 2006–2008. CSIRO exploration and mining open file report P2007/364, 120 pp

Dauth C (1997) Airborne magnetic, radiometric and satellite imagery for regolith mapping in the Yilgarn Craton of Western Australia. *Explor Geophys* 28:199–203

Duke EF (1994) Near infrared spectra of muscovite. Tschermak substitution and metamorphic reaction process. Implications for remote sensing. *Geology* 22:201–219

Forrestal PJ, Pearson PJ, Coughlin T, Schubert CJ (1998) Tick hill gold deposit. In: Hughes FE (ed) *Geology of the mineral deposits of Australia and Papua New Guinea*. Australian Institute of Mining and Metallurgy, Carlton South, VIC, pp 699–706

Gao B-C, Heidebrecht KB, Goetz AFH (1993) Derivation of scaled surface reflectances from AVIRIS data. *Remote Sens Environ* 44:145–163

Geoscience Australia (2008) Dajarra, Queensland 1:100,000 scale geology map sheet, www.ga.gov.au/meta/ANZCW0703003759.html

Greene-Kelly R (1953) Identification of montmorillonoids. *J Soil Sci* 4:233–237

Isbell RF (1996) *The Australian Soil Classification*. CSIRO Australia, Collingwood, VIC

ITTVIS (2008) <http://www.ittvis.com/ProductServices/ENVI.aspx>

Jayawardhana PM, Sheard SN (2000) The use of airborne gamma-ray spectrometry: a case study from the Mount Isa Inlier, northwest Queensland, Australia. *Geophysics* 65(6):1993–2000

McKenzie N, Grundy M, Webster R, Ringrose-Voase A (2008) Guidelines for surveying soil and land resources. Australian soil and land survey handbook series, 2nd edn. CSIRO Publishing, Melbourne, 576 pp

McKenzie NJ, Ryan PJ (1999) Spatial prediction of soil properties using environmental correlation. *Geoderma* 89:67–94

Neldner J (2001) A vegetation map for Northern Australia. Tropical Savannas CRC. http://savanna.cdu.edu.au/research/vegetation_map.html

Post JL, Noble PN (1993) The near-infrared combination band frequencies of dioctahedral smectites, micas and illites. *Clays Clay Miner* 41(6):639–644

Pracilio G, Adams M, Smettem KJ, Harper RJ (2006) Determination of spatial distribution patterns of clay and plant available potassium contents in surface soils at the farm scale using high resolution gamma ray spectrometry. *Plant Soil* 282:67–82

Rodger A, Cudahy TJ (2009) Vegetation corrected continuum depths at 2.20 μm : an approach for hyperspectral sensors. *Remote Sens Environ* 113:2243–2257

Taylor MJ, Smettem K, Pracilio G, Verboom W (2002) Relationships between soil properties and high-resolution radiometrics, central eastern Wheatbelt, Western Australia. *Explor Geophys* 33:95–102

Thomas M, Fitzpatrick RW, Heinson GS (2003) Mapping complex soil–landscape patterns using radiometric K%: a dry saline land farming area case study near Jamestown, SA. In: Roach IC (ed) *Advances in regolith*. CRC LEME, Canberra ACT, pp 411–416

USGS (2008) <http://speclab.cr.usgs.gov/spectral-lib.html>

Van der Merwe GME, Laker MC, Bühmann C (2002) Clay mineral associations in melanic soils of South Africa. *Aust J Soil Res* 40:115–126

Volzone C (1992) Improvements in the method to differentiate montmorillonite from other smectites. *J Mater Sci Lett* 11:921–923

Waiser TH, Lorgan CLS, Brown DJ, Hallmark CT (2007) In situ characterization of soil clay content with visible near-infrared diffuse reflectance spectroscopy. *Am J Soil Sci Soc* 71: 389–396

Wong MTF, Harper RJ (1999) Use of on-ground gamma-ray spectrometry to measure plant-available potassium and other topsoil attributes. *Aust J Soil Res* 37:267–277

Part IV

**Soil Sensing by Electromagnetic Induction
and Electrical Resistivity**

Chapter 19

Combining Proximal and Penetrating Soil Electrical Conductivity Sensors for High-Resolution Digital Soil Mapping

D.B. Myers, N.R. Kitchen, K.A. Sudduth, S. Grunwald, R.J. Miles, E.J. Sadler, and R.P. Udawatta

Abstract Proximal ground conductivity sensors produce high spatial resolution maps that integrate the bulk electrical conductivity (EC_a) of the soil profile. For meaningful interpretation, variability in conductivity maps must either be inverted to profile conductivity or be directly calibrated to profile properties. Penetrating apparent electrical conductivity (EC_{a-P}) sensors produce high depth resolution data at relatively fewer spatial locations. The objectives of this research were to (i) investigate the profile source of EC_a in claypan soils via a detailed examination of EC_{a-P} profiles; (ii) examine the potential for feature detection with EC_{a-P} in claypan soils; and (iii) determine if EC_a sensors can be calibrated to EC_{a-P} features. Two study areas were chosen representing the claypan soils of north-east Missouri, USA. Profile conductivity was measured at high depth resolution on soil cores using a miniaturised Wenner conductivity probe and in the field using a conductivity penetrometer. Proximal ground conductivity was mapped with one direct contact sensor and two non-contact sensors, providing five distinct coil/electrode geometries. Increasing EC_{a-P} was observed below the claypan, correlated with decreasing clay and water content and increasing bulk density. Depth to the claypan was successfully calibrated to derivative peaks on EC_{a-P} profiles ($R^2 = 0.72$, $p < 0.001$). Relationships between EC_a and EC_{a-P} features were poor ($R^2 \sim 0.21$) to good ($R^2 \sim 0.87$) on a field-specific basis. Results show that EC_{a-P} can be used for calibration of EC_a to the depth to claypan.

Keywords Claypan soils · Soil bulk apparent electrical conductivity · Penetrometer · Wenner mini-probe

D.B. Myers (✉)

Department of Soil and Water Science, GIS Core Research Laboratory, University of Florida, 2169 McCarty Hall, Gainesville 32611, FL, USA
e-mail: myersdb@ufl.edu

19.1 Introduction

Proximal bulk apparent electrical conductivity (EC_a) sensors can be used to produce high spatial resolution maps that integrate soil profile EC_a variation by a depth-response function. For meaningful interpretation, the conductivity data must either be inverted to approximate profile conductivity or be directly calibrated to profile properties. Penetrating apparent electrical conductivity (EC_{a-P}) sensors measure EC_a from a small soil volume localised to their sensing electrode. Penetrating sensors measure at high depth resolution, but at sparse locations compared to proximal EC_a sensors. These two types of EC_a sensors have synergistic potential. We examined two avenues for their combined use with a case study in the claypan landscapes of north-east Missouri, USA. Firstly, we examined the potential for EC_{a-P} to identify soil morphological features. Next we examined the calibration of EC_{a-P} features to the spatially dense EC_a data. We focus here on resolving the profile source of conductivity integrated by proximal EC_a sensors.

Three specific pathways of electrical conductance occur in soils: free water in large soil pores, hygroscopic or tightly interacting particle–water interfaces, and direct soil particle contact (Corwin and Lesch, 2005). As outlined by Corwin and Lesch (working in western US soils formed in semi-arid to arid environments), the magnitude of EC_a is dependent mainly on soil salinity, Na^+ saturation percentage, water content, and bulk density (BD). The claypan soils of Missouri exist in a humid, temperate environment. They are leached of salts and free carbonates and have a small concentration of exchangeable Na^+ ($< 2 \text{ cmol kg}^{-1}$). These variables are unlikely to affect EC_a . The experiments described in this work allowed the examination of the remaining factors important for influencing proximal EC_a variation in claypan soils.

Previous studies in claypan soils discovered the relationship between EC_a and depth to claypan (DTC) (Dolittle et al., 1994; Sudduth and Kitchen, 2006). These investigations speculated that depth to argillic horizon layer silicates was the primary cause of proximal EC_a variation. Several properties of the smectite clay mineralogy were considered to be important. Smectite and similar clay minerals might provide greater physical contact due to their size and platy structure, substantial interlayer water (which is usually present), and very large concentration of exchangeable cations. Clay content decreases below the claypan and therefore, if clay mineralogy were largely responsible for EC_a variation, then less conductivity response would be expected from there. However, greater below-claypan EC_{a-P} was detected during some of our early investigations with EC_{a-P} data (Sudduth et al., 2000). Confirmation of these observations on isolated samples is needed to understand the proximal EC_a response.

From our experiences with proximal EC_a and EC_{a-P} data, we suspected that profile conductivity features could be identified by penetrometer more objectively, at better depth resolution, and more quantitatively than by coring or augering. Mapping subsoil EC_{a-P} features via their relationship to EC_a would be more efficient than grid survey. An EC_a -to- EC_{a-P} feature calibration should provide the spatial and depth resolution needed for high-resolution soil mapping. We hypothesised that a

large gradient in the first derivative of the EC_{a-P} profile could be used to identify a claypan or other lithologic discontinuity. We examined the relationship between EC_{a-P} derivative peaks and observed depth to claypan in order to test this possibility. Further, we hypothesised that EC_a could predict the depth to EC_{a-P} first-derivative peaks.

The specific objectives of this research were to

- i. confirm the increase in EC_a below the claypan;
- ii. determine if EC_{a-P} data can be used to estimate depth to claypan; and
- iii. determine if EC_a sensors can be calibrated to EC_{a-P} features.

19.2 Materials and Methods

19.2.1 *Soil Landscapes, Measurements, and Observations*

Four agricultural fields in the claypan region of north-east Missouri were chosen for this study: three fields with a loess solum near Centralia, MO (fields A, B, and C) ($39^{\circ}13'43''$ N, $92^{\circ}8'20''$ W), and a field with a loess-till solum near Novelty, MO (field D) ($40^{\circ}1'46.5''$ N, $92^{\circ}11'19''$ W). Fields A, B, and C are located near the southern limit of the claypan region, while field D is at the northern limit, about 90 km away. Physical and chemical characterisation data by horizon were available from 44 profiles with claypan features. Field descriptions and horizon designations for these pedons were made by experienced soil morphologists. Observed depth to claypan was determined as depth to the Bt1 or the Bt2 horizon based on the field descriptions and lab data.

19.2.2 EC_{a-P} Measurement

Penetrometer EC_{a-P} (see Table 19.1 for EC_a abbreviations) and cone index (CI) were measured at the 44 claypan locations using a Veris¹ Profiler 3000 with an insulated shaft (Veris Technologies, Salina, KS, USA). Measurements of EC_{a-P} and CI were made on all fields in the late spring of 2007 and occurred within a few days of proximal EC_a measurements on fields B and D. However, EC_{a-P} and CI were measured on fields A and C approximately 18 months after the EC_a surveys. Gravimetric soil moisture (w) and BD determinations were made in 15-cm layers at the time of EC_{a-P} measurement.

Cone index and EC_{a-P} were measured to 92 cm, with five penetrations per site. Replicate EC_{a-P} profiles were pooled and fitted with locally weighted regression

¹ Mention of trade names or commercial products is solely for the purpose of providing specific information and does not imply recommendation or endorsement by the US Department of Agriculture, University of Missouri, or University of Florida.

Table 19.1 Bulk apparent electrical conductivity (EC_a) is a generic terminology that can be applied to a variety of sensors which can have multiple measurement channels. We differentiate the various EC_a sensors used in this study by the following abbreviations

Sensor	Symbol	Channel	Effective depth ^a	Sensor type	Coil/electrode geometry
DUALEM-2S	EC_a -Dsh	Shallow	2.2 m	Induction	2 m PCP ^b
DUALEM-2S	EC_a -Ddp	Deep	10 m	Induction	2.1 m HCP ^c
Geonics EM-38	EC_a -EM	Deep	5 m	Induction	1 m HCP
Veris 3150 MSP	EC_a -Vsh	Shallow	0.3 m	Wenner contact	0.7 m
Veris 3150 MSP	EC_a -Vdp	Deep	1 m	Wenner contact	2.2 m
Veris Profiler	EC_a -P	Single	—	Dipole contact	Cone electrode
Wenner mini-probe	EC_a -M	Single	—	Wenner contact	5 mm

^aDepth to 90% of total response (Sudduth and Kitchen, 2000)

^bPCP, perpendicular coplanar

^cHCP, horizontal coplanar

models. A Savitzky–Golay procedure was used to calculate the derivative of the fitted EC_a -P profile. A large peak in the first derivative, referred to as the transition peak, corresponds to the transition between the E horizon and the upper boundary of the claypan. Depth to the transition peak was determined for all of the fitted profiles. Clay-maximum depth translation was applied to each fitted EC_a -P profile independently in order to explore the landscape relationship in sub-claypan EC_a . Translated depth (D_t) indicates the depth at which a measurement occurs either above or below the claypan. Translated depth profiles were pooled into a single dataset and again fitted with a locally weighted regression.

19.2.3 EC_a -M Measurement

We developed a miniaturised Wenner array on a handheld probe (mini-probe) to measure EC_a (EC_a -M) on ex situ soil cores to confirm EC_a -P observations. Wenner mini-probe apparent electrical conductivity was measured every 1.25 cm. The mini-probe had 5 mm electrode spacing, 5 mm insertion depth, and was operated using the electronics from a Veris EC_a sensor. Veris supplied custom software accounting for the probe geometry. Measurements of EC_a -M were made on soil cores compressed into a steel channel which formed the cores into triangular prisms. This procedure repaired breaks and extrusion cracks in soil cores, consolidated loose soil, and formed two flat surfaces providing consistent contact for the mini-probe. Gravimetric soil moisture (w) of these cores was measured at 2.54 cm intervals.

19.2.4 Proximal EC_a Measurement

Three conductivity sensors were used to measure proximal EC_a with DGPS position on 10 m transects at 4–6 m intervals. Sensors were the DUALEM-2S

electromagnetic induction (EMI) sensor (Dualem, Inc., Milton, Ontario, Canada) in horizontal coplanar mode (EC_a -Dsh) and perpendicular planar mode (EC_a -Ddp) (2 m coil spacing); the Geonics EM-38 EMI sensor (Geonics Limited, Mississauga, Ontario, Canada) in horizontal coplanar mode (EC_a -EM), 1 m coil spacing; and the Veris 3150 rolling coulter Wenner array (Veris Technologies, Salina, KS, USA) with 0.7 m (EC_a -Vsh) and 2.2 m (EC_a -Vdp) electrode spacing. This combination of sensors provided five distinct coil/electrode geometries for EC_a measurement. Fields B and D had all EC_a surveys made within a relatively narrow window of 1 month in the spring of 2007. Surveys of fields A and C were made within 3 days in the fall of 2005.

The five proximal EC_a instrument geometries used for this study were unique (Table 19.1), but their depth-response functions were overlapping to one degree or another and their measurements were correlated (Sudduth and Kitchen, 2000). Partial least squares regression (PLSR) was used to model the EC_a relationship to EC_{a-P} features in order to mitigate correlation in the predictors and to capitalise on any orthogonality in their response to EC_{a-P} .

19.3 Results and Discussion

19.3.1 Soil Profile EC_a

The major morphological features found throughout the study fields were visible in the depth profile of EC_{a-P} or EC_{a-M} in a representative claypan site from field A (Fig. 19.1a). Firstly, the silty, granular, and low-density surface had very small EC_{a-P} . The remaining A horizons had greater EC_{a-P} , but still relatively smaller EC_{a-P} compared to the claypan and below. When an E horizon was present, it appeared as a zone of minimum conductivity. Conductivity abruptly increased in the transition to the Bt1 horizon, the claypan feature. Conductivity continued to increase below the claypan to 90 cm and beyond, even as clay content decreased.

Mean EC_{a-P} above and below the claypan for all 44 study locations was 20.9 and 47.4 mS m⁻¹ with standard errors 0.31 and 0.26 mS m⁻¹ respectively, and was significantly different ($p < 0.001$). This difference and the landscape trend in EC_{a-P} distribution were emphasised in pooled D_t profiles of EC_{a-P} (Fig. 19.2). The depth translation procedure allowed comparison of profiles on a coherent depth scale. These results verified large and increasing sub-claypan EC_{a-P} and emphasised the similarity of these soils to the theoretical bilayered earth discussed in the geotechnical literature (McNeill, 1980; Callegary et al., 2007).

Measurements of EC_{a-M} were highly correlated with EC_{a-P} measurements ($r = 0.82$), but were greater by a factor of 3.3 (Fig. 19.3). These results confirmed the EC_{a-P} sensor measurement and further indicated that as clay content decreases, profile EC_{a-P} increases – counter to the clay-source hypothesis. The greater magnitude of EC_{a-M} data relative to EC_{a-P} warrants further investigation but is potentially due to increased particle contact caused by the core-pressing procedure used in the EC_{a-M} measurement.

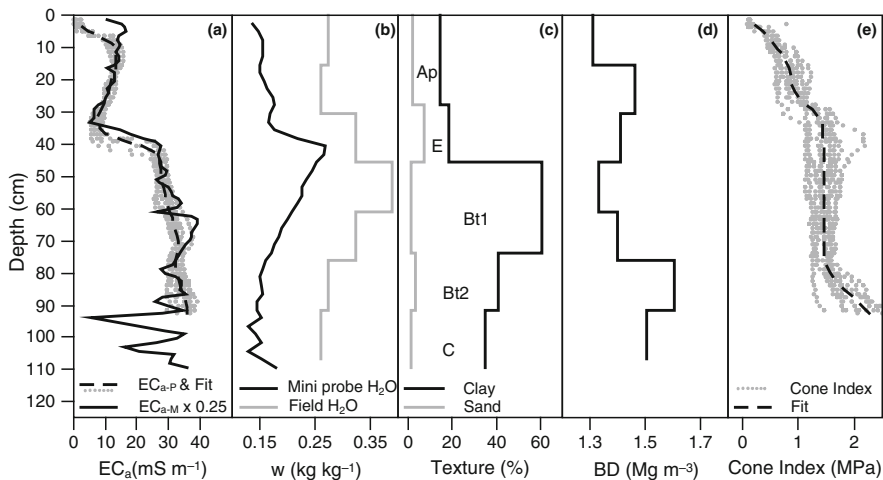


Fig. 19.1 Data from a representative claypan soil on field A. (a) Penetrometer electrical conductivity (EC_{a-p}) and scaled Wenner mini-probe conductivity ($EC_{a-M} \times 0.25$). (b) Field (taken with EC_{a-p}) and high-resolution (taken with EC_{a-M}) gravimetric soil moisture (w). (c) Percent clay and sand. (d) Bulk density (BD). (e) Cone index

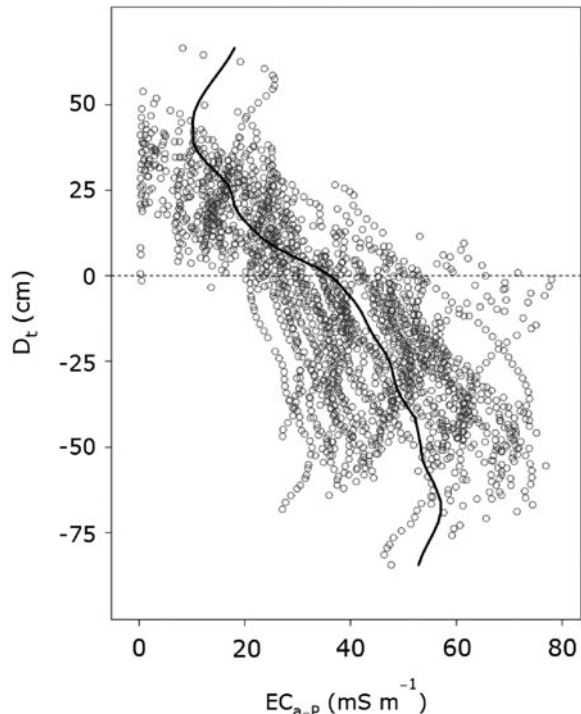
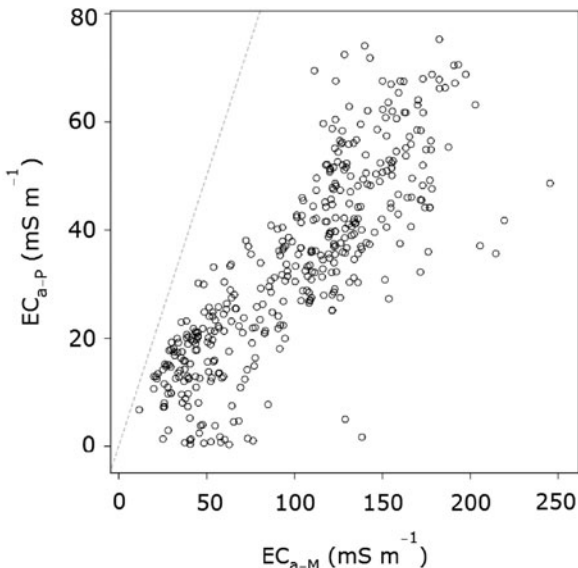


Fig. 19.2 Clay-maximum translated depth (D_t) profiles of EC_{a-p} from 44 locations in 4 claypan fields. The depth scale is translated such that the profile clay maximum for each location is at 0 cm (dashed horizontal line). Translated depth is positive above the claypan and negative below. Measurements of EC_a increase below the claypan ($D_t < 0$) as emphasised by the locally weighted regression (solid black line)

Fig. 19.3 Scatter plot showing the correlation between EC_a in claypan soil profiles measured in situ by penetrometer (EC_{a-P}) and ex situ by a Wenner mini-probe (EC_{a-M}). The Pearson correlation coefficient between these sensor measurements is 0.82 and EC_{a-M} is proportional to EC_{a-P} by a factor of 3.3



19.3.2 EC_{a-P} Predicted Depth to Claypan

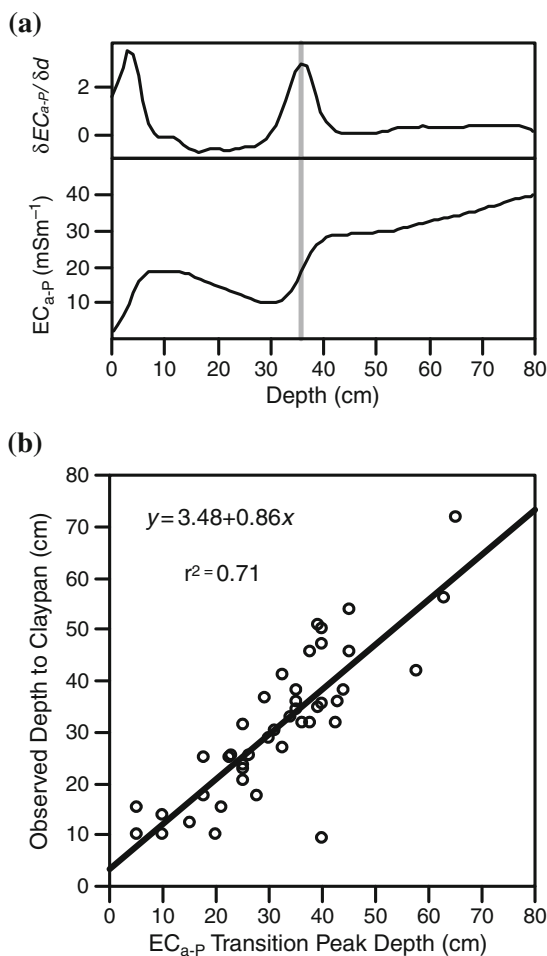
A major objective of this research was to examine the potential for using EC_{a-P} to rapidly identify and map subsoil features. The claypan is a critical soil morphological feature because it impacts hydrology, plant-available water capacity, water quality, subsoil fertility, root distribution, and crop yield (see Chapter 31). The claypan transition peak was clear on first-derivative plots of EC_{a-P} (Fig. 19.4a).

Claypan transition peaks indicate the depth at which an experienced soil morphologist would describe the E-Bt boundary. The EC_{a-P} sensor allows an objective and quantitative determination of the claypan and provides a continuous representation. Depth to claypan was significantly related to EC_{a-P} transition peak depth ($R^2 = 0.71$, $n = 44$, $p < 0.001$) (Fig. 19.4b). This result includes data from all four study sites spanning opposite ends of the Missouri claypan region. Based on these results, EC_{a-P} might be used to predict claypan depth anywhere within this area or in a similar soil region. The penetrometer can rapidly capture short-range spatial variability with multiple penetrations and may be more consistent and quantitative than a soil morphologist could be. This type of relationship is very useful for densifying investigations along transects or within an area (Drummond et al., 2005). Quantified EC_{a-P} feature observations can be efficiently collected at smaller intervals, while more time-intensive coring or augering can be performed at larger intervals.

19.3.3 Calibrating EC_a to EC_{a-P} Features

Severe correlation between proximal EC_a measurements requires a non-traditional approach to modelling. Partial least squares regression of transition peak depth as

Fig. 19.4 Penetrometer electrical conductivity (EC_{a-P}) and first derivative ($\delta EC_{a-P}/\delta d$) of a representative claypan soil profile. EC_{a-P} transition peak is identified by a vertical grey line. (b) Depth to EC_{a-P} transition peak is analogous to depth to claypan (DTC) and is compared to observed DTC by linear regression

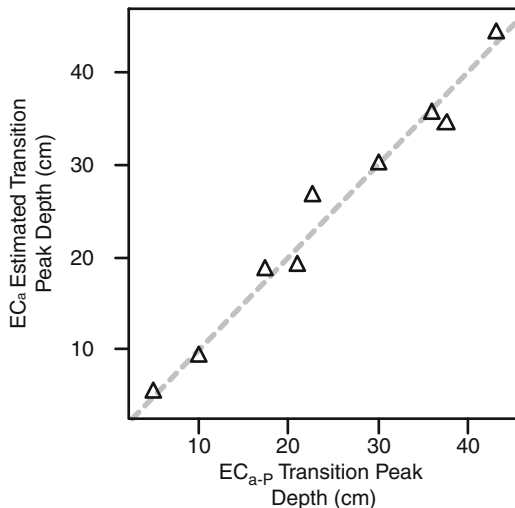


a function of EC_{a-EM} , EC_{a-Dsh} , EC_{a-Ddp} , EC_{a-Vsh} , and EC_{a-Vdp} produced varying results, from no significant model for field A to a very good relationship for field C (Table 19.2). The profiles from these four field sites were chosen, based on previous research needs, to represent the landscape variability present within each field. However, the field datasets differed in their realisation of this goal. Fields C and D have greater relief and a wider range of landscape positions and thus a wider range of DTC than does field A. Field B had a relatively wider range in DTC than did A, but had a lower number of profile samples concentrated in a fairly narrow range of DTC, and transition peak depth was poorly related to EC_a . Pooled results showed a moderate relationship (Table 19.2). A better stratified sample of EC_{a-P} profiles from within each field might produce better results. The potential for within-field mapping of EC_{a-P} features with EC_a data is shown in the site C results (Table 19.2, Fig. 19.5).

Table 19.2 Fit statistics and number of components for partial least squares regression models of EC_{a-P} transition peak as a function of five EC_a sensor measurements

Field	N	Intercept	Comp. 1	Comp. 1–2		Comp. 1–3		Comp. 1–4	
		RMSE	R^2	RMSE	R^2	RMSE	R^2	RMSE	R^2
A	16	12.38	—	—	—	—	—	—	—
B	7	17.67	−0.01	15.20	0.21	13.45	—	—	—
C	9	13.67	0.80	5.40	0.76	5.90	0.87	4.45	—
D	11	16.00	0.64	8.75	—	—	—	—	—
Pooled	43	13.71	0.37	10.67	0.39	10.48	0.43	10.12	0.44
									9.99

Fig. 19.5 Transition peak depth was modelled by five proximal EC_a measurements (see Table 19.2) using partial least squares regression. The resulting EC_a estimated transition peak depth is compared to measured transition peak depth from site C. Diagonal line is one-to-one



Multi-component PLSR models provided only minor gains in R^2 or root mean squared error for transition peak depth over single-component models. One or two components accounted for most of the variability within sites B, C, and D. This suggests that a single proximal EC_a instrument with dual-simultaneous investigation depths is sufficient for mapping transition peak depth. The pooled model included four components, potentially due to additional orthogonal variability in EC_a caused by temporal differences in temperature and soil moisture between EC_a surveys. This asynchrony in survey conditions is known to cause bias between surveys of the same field (Abdu et al., 2007).

19.3.4 Profile Sources of Proximal EC_a

According to Corwin and Lesch (2005), and discounting salinity and Na^+ saturation, the next most important factors determining profile conductivity are water content

and BD. As mentioned previously, lower EC_{a-P} values in surface soils are probably due to granular structure and silty texture which cause reduced particle contact and proximity (Fig. 19.1a). Minimum conductivity in the strongly leached E horizons may have been due to the high felsic mineral (e.g. quartz, feldspar) content and reduced contact of the silt-sized particles. The particle-contact pathway of EC_a may be dominating response above the claypan.

The large positive EC_{a-P} gradient at the transition peak coincides with the largest increase in clay and water content (Fig. 19.1b, c). Conversely, elevated concentrations of expanded smectite clays in the claypan cause a reduction in BD (Fig. 19.1c, d). These relationships suggest that within the transition zone, EC_{a-P} is more sensitive to the clay-bound soil–solution conductivity pathway (perhaps enhanced by large cation saturation) than to the particle-contact pathway. This is in contrast to what happens below the claypan where BD and CI are greater.

We found that clay and water content decreased below the claypan, while BD and CI both increased. These relationships suggest that below the claypan, EC_{a-P} is more sensitive to the particle-contact pathway than to the soil–solution or solution–particle pathway. Processes of cementation may be enhancing this effect. Structural units also tend to be larger in size with depth. Profile distribution of clay, bulk density, structure, and water content are confounded by soil genesis. Integrated processes of soil formation, including loess deposition, eluviation, illuviation, and subsoil densification, vary systematically with landscape. This combination of effects is probably responsible for success in the calibration of proximal EC_a to DTC and transition peak depth.

19.4 Conclusions

The spatial resolution of EC_a sensors and the depth resolution of EC_{a-P} sensors offer the potential to synergistically improve high-resolution soil mapping. Claypan soils are successfully handled in this way because they are essentially bilayered with respect to EC_a . Direct calibration of EC_{a-P} depth profile features to soil profile features such as depth to claypan is effective, but global or regional calibration of proximal EC_a to EC_{a-P} features is complicated by field-to-field and temporal variability in proximal EC_a measurements. In general, the multiple EC_a sensor geometries of the common commercially available platforms studied here do provide at least two orthogonal components of EC_a information. Finally, profile conductivity actually increases somewhat below the claypan, probably due to increased particle contact in denser soil. Response of EC_a to EC_{a-P} transition peak and DTC is due to the confounded processes of soil and landscape genesis rather than just depth to argillic horizon clay minerals. It is a combined effect of lesser EC_a near the surface, a profile minimum EC_a in E horizons, greater EC_a in the claypan, and even greater EC_a in the dense soil material below the claypan.

References

Abdu H, Robinson DA, Jones SB (2007) Comparing bulk soil electrical conductivity determination using the DUALEM-1S and EM38-DD electromagnetic induction instruments. *Soil Sci Soc Am J* 71:189–196

Callegary JB, Ferre TPA, Groom RW, (2007) Vertical spatial sensitivity and exploration depth of low-induction-number electromagnetic-induction instruments. *Vadose Zone J* 6:158–167

Corwin DL, Lesch SM, (2005) Apparent soil electrical conductivity measurements in agriculture. *Comput Electron Agric* 46:11–43

Drummond PE, Christy CD, Lund ED (2005) Using an automated penetrometer and soil EC probe to characterize the rooting zone. [CD-ROM]. In: Robert PC et al. (eds) *Proceedings of the 5th international conference on precision agriculture*, Minneapolis, MN, July 16–19, 2000, ASA, CSSA, and SSSA, Madison, WI

Dolittle JA, Sudduth KA, Kitchen NR, Indorante SJ (1994) Estimating depths to claypans using electromagnetic induction methods. *J Soil Water Conserv* 49(6):572–575

McNeill JD (1980) Electromagnetic terrain conductivity measurements at low induction numbers. *Geonics technical note TN-6*, Mississauga, Ontario

Sudduth KA, Hummel JW, Kitchen NR, Drummond ST (2000) Evaluation of a soil conductivity sensing penetrometer. 2000 ASAE international meeting, Milwaukee, WI, July 9–12. Paper no. 001043, ASAE, St. Joseph, MI

Sudduth KA, Kitchen NR (2006) Increasing information with multiple soil electrical conductivity datasets. 2006 ASABE international meeting, Portland OR, July 9–12. Paper no. 061055, ASABE St. Joseph, MI

Chapter 20

A Neural Network Approach to Topsoil Clay Prediction Using an EMI-Based Soil Sensor

L. Cockx, M. Van Meirvenne, U.W.A. Vitharana, F.M.B. Vancoillie, L.P.C. Verbeke, D. Simpson, and T. Saey

Abstract High-resolution proximal soil sensor data are an important source of information for optimising the prediction of soil properties. On a 10.5 ha arable field, an intensive EM38DD survey with a resolution of 2 m × 2 m resulted in 19,694 measurements of EC_a-H and EC_a-V. A large textural variation was present in the subsoil due to the presence of former water channels. Nevertheless, both EC_a-V and EC_a-H data displayed the same spatial variability. This spatial similarity indicated the strong influence of the subsoil heterogeneity on the EC_a-H measurements. Using variography, two scales of EC_a variability were identified: short-range (~35 m) variability associated with the channel pattern and wider within-field variability (~200 m). Using artificial neural networks (ANNs), prediction of the topsoil clay content was optimised (i) by using an input window size of 3, 5, 7, 9, and 11 pixels to account for local contextual influence and (ii) by including both EC_a-H and EC_a-V in the network input layer to isolate the response from the topsoil. The models were evaluated using R^2 and the relative mean squared estimation error (rMSEE) of the test data. The most accurate predictions were obtained using both orientations of the EM38DD sensor without contextual information ($R^2 = 0.66$, rMSEE = 0.40). The importance of EC_a-V on the topsoil clay prediction was expressed by a relative improvement of the rMSEE of 29%. For comparison, a multivariate linear regression (MVLR) was performed to predict the topsoil clay content based on the two orientations. The ANN models up to a window size of 5 pixels outperformed the MVLR, which resulted in an R^2 of 0.42 and an rMSEE of 0.63. ANN analysis based on both orientations of the EM38DD appears to be a useful tool to extract topsoil information from depth-integrated EM38DD measurements.

Keywords EM38DD · Artificial neural networks · Topsoil texture · Prediction · EM38

L. Cockx (✉)

Department of Soil Management, Research Group Soil Spatial Inventory Techniques,
Ghent University, Coupure 653, 9000 Gent, Belgium
e-mail: liesbet.cockx@ugent.be

20.1 Introduction

Nowadays highly detailed soil sensor data have become an interesting source of ancillary information to characterise within-field soil variability, a factor important for site-specific management. The non-invasive nature of proximal soil sensors allows the collection of high-resolution data in a short time. One of these proximal soil sensors is the EM38 (Geonics Ltd, Ontario, Canada) which measures the apparent soil electrical conductivity (EC_a) on the basis of electromagnetic induction (see Chapter 2). Under non-saline conditions, soil EC_a is influenced by a complex interaction of soil properties like texture (mainly the clay fraction), organic matter content, and soil moisture content (Cockx et al., 2007; Williams and Hoey, 1987). The EM38DD soil sensor consists of two EM38 units fixed perpendicular to each other, allowing the simultaneous measurement of soil EC_a in two orientations. The response of the sensor is a depth-integrated measurement of soil EC_a and each orientation has its own depth-response profile. Theoretically, the vertical orientation (EC_a -V) is mainly influenced by the subsoil, while the horizontal orientation (EC_a -H) receives a dominant influence from the topsoil. However, in soils with highly varying subsoil and homogeneous topsoil properties, the subsoil variability can dominate the EC_a -H measurements. To characterise the topsoil textural variability with the EM38DD, the influence of the subsoil on the EC_a -H measurements should be removed.

Since artificial neural network (ANN) analysis is able to model non-linear complex relationships between inputs and outputs without any a priori assumptions about the nature of the processes (Sy, 2006), this technique is used to estimate the topsoil clay fraction (referred to as *tclay* in this chapter) based on EC_a -H and EC_a -V data. Such data have already been used as an input in ANNs for estimating crop yield (Miao et al., 2006; Kitchen et al., 2003), but to our best knowledge the novel aspect of this research is the incorporation of the two orientations of the EM38DD sensor for soil texture estimations.

The aim of this study was to optimise topsoil clay predictions (i) by using a varying window size (of 3, 5, 7, 9, and 11 pixels) to incorporate contextual information of the input variables in the ANN and (ii) by including high-resolution data of both sensor orientations in the ANN. The results were compared to the ones obtained using multivariate linear regression (MVLR).

20.2 Materials and Methods

20.2.1 Study Site and Data Collection

The study site was a 10.5 ha arable field in the polder area of Belgium ($51^{\circ}16'17''$ N, $3^{\circ}40'35''$ E). In this area, predominantly sandy Pleistocene aeolian material is covered with Holocene alluvial loam to clay sediments, due to a series of marine

transgressions after the last glaciations. These marine transgressions occurred through water channels which were consequently filled with clayey material, resulting in large subsoil textural variation. These water channels formed a dominant pattern, up to 2 m deep, in the subsoil.

The EM38DD soil sensor was used to characterise soil variability; it was attached to an all-terrain vehicle and combined with a GPS. In this way, soil data (both EC_a -H and EC_a -V) were collected every second with an average resolution of 2 m \times 2 m, resulting in a total of 19,694 measurements. These EC_a data were processed to correct a lag between the GPS and the sensor; the noise present in the EC_a -H data was reduced using a Z-score filter – values deviating more than two standard deviations from their local mean (within a radius of 10 m) were replaced with the local mean EC_a value.

In 78 locations, soil samples were taken according to an EC_a -directed sampling scheme to ensure that the existing soil variability was captured. Due to the presence of former water channels, the sampling scheme had transect-like parts. The samples were analysed for subsoil and topsoil texture (indicated by the prefix *s*- and *t*-, respectively) using the pipette method.

20.2.2 Neural Network Analysis

The artificial neural network analysis mimics the capacity of biological neural systems to learn; nodes, equivalent to biological neurons, are organised into input, hidden, and output layers. The hidden layer controls the complexity of the relationship between input and output variables. Each node is connected to all the nodes in the next layer, and these connections have associated with them weights. For each node in the hidden layer, all input data, multiplied by their respective weight, are summarised and then used as an input in a non-linear transfer function. Neural networks are trained in an iterative process by optimising the weights of linkages connecting input and output variables so as to minimise differences between predictions and actual values (called back-propagation). For a detailed description on neural networks, refer to Haykin (1994).

In this study, we used a feed-forward back-propagation network with a *tangens hyperbolicus* as activation function and one hidden layer. Since soil texture data are compositional, two fractions, i.e. *tclay* and *tsand*, were estimated but only the results of *tclay* will be interpreted in this chapter. The dataset was randomly split into 10 sets of training ($n = 50$) and test data ($n = 28$), and each training set was initialised 10 times, resulting in 100 replicates per network model. To optimise the *tclay* predictions, the input of the network was altered in two ways. Firstly, contextual information was added to the network by using a window of input variables: a window size (WS) of 3, 5, 7, 9, and 11 pixels was tested. The latter systems were called contextual neural networks (CNNs) and abbreviated as WS3, WS5, Secondly, the relative importance of incorporating two orientations of the EM38DD sensor was determined by treating the EC_a -V data as unavailable (and using the

mean of the EC_a-V data as an input). The effect of changing the network input from two sensor orientations to one was tested for input window sizes of 1 (no contextual information), 3, and 5 pixels. Depending on the input, the number of neurons in the hidden layers changed according to the rule of Hecht-Nielsen (1987). The ANN analysis was performed using *LNNS*, an artificial neural network simulator developed at the Laboratory of Forest Management and Spatial Information Techniques and freely downloadable from <http://dfwm.ugent.be/forsit/>.

The performance of the ANN systems was determined by calculating the relative mean squared estimation error (rMSEE) and the coefficient of determination (R^2) of the predicted and the true test *tclay* concentration. The rMSEE is defined as the MSEE divided by the sample variance (Green et al., 2007) and the MSEE can be calculated as follows:

$$\text{MSEE} = \frac{1}{n} \sum_{\alpha=1}^n (z^*(\mathbf{x}_\alpha) - z(\mathbf{x}_\alpha))^2,$$

with n the number of samples, $z^*(\mathbf{x}_\alpha)$ the predicted value, and $z(\mathbf{x}_\alpha)$ the true test value. Using these two parameters, the ability of the ANN systems to reproduce both the variance of the measured data and the actual errors for the predictions was considered (Persson et al., 2002). An rMSEE value of 0 represents perfect prediction, while an rMSEE value of 1 signifies a prediction equivalent to using the mean value as predictor. A sensitivity analysis was performed to evaluate the relative importance of the EC_a-V data and the contextual information from neighbouring pixels in explaining the *tclay* variability. This was expressed by looking at the relative improvement (RI) of the rMSEE defined as follows:

$$\text{RI} [\%] = [(r\text{MSEE}_{\text{method1}} - r\text{MSEE}_{\text{method2}}) / r\text{MSEE}_{\text{method1}}] \times 100.$$

If RI < 0, then method 2 is superior to method 1; if RI = 0, there is no accuracy difference between both methods; and in case RI > 0, method 2 is worse than method 1.

20.2.3 Multivariate Linear Regression

As an alternative to the prediction of the *tclay* content based on EM38DD data, the use of MVLR was evaluated. Due to the limited soil dataset, the analysis was performed using all 78 soil samples. Nevertheless, the validation was conducted in an equivalent manner to the ANN, since the indices were calculated and averaged out for the 10 test sets. A stepwise MVLR was performed in SPSS 15.0 with EC_a-H and EC_a-V as predictor variables. In stepwise MVLR modelling, predictor variables are added one at a time to the regression to see if the model improves upon the addition of that variable. Adding the first predictor is based on the degree of correlation with the outcome and, because of this, the second predictor is fixed in the case of two-predictor variables.

20.3 Results and Discussion

The EC_a measurements are shown in Fig. 20.1, while Table 20.1 lists their descriptive statistics. Both orientations were clearly influenced by the former water channel pattern of the subsoil: in these channels the EC_a increased. On both maps, two dominant linear features (channels) of increased EC_a are present: one in the eastern part of the field (parallel to the boundary with clear side branches) and one diagonally crossing the western part of the field. A similar spatial variability was displayed in the two orientations but higher EC_a values were found in the subsoil and more noise was registered in the data of the topsoil. Nevertheless, the coefficient of variation ($CV = \text{standard deviation}/\text{mean}$) of both orientations was of the same order of magnitude and a Pearson correlation coefficient (r) of 0.84 was found between the EC_a -H and EC_a -V measurements.

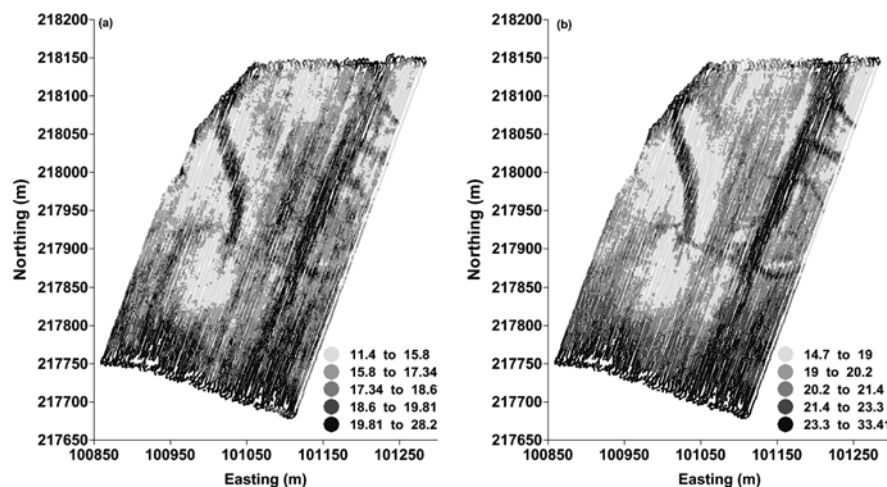


Fig. 20.1 Locations of the EC_a measurements: (a) EC_a -H, (b) EC_a -V, expressed in millisiemens per meter

Table 20.1 Descriptive statistics of EC_a ($n = 19,694$) and soil texture ($n = 78$)

	Mean	SD ^a	CV ^a	Min.	Med.	Max
EC_a -H (mS m^{-1})	18.13	2.80	0.15	10.90	18.10	30.30
EC_a -V (mS m^{-1})	21.22	2.83	0.13	14.70	20.7	33.40
<i>tclay</i> (%)	20.12	2.48	0.13	14.30	20.00	23.70
<i>sclay</i> (%)	9.07	4.12	0.45	3.20	7.70	22.10
<i>tsand</i> (%)	45.82	9.03	0.20	23.40	47.55	64.80
<i>ssand</i> (%)	74.17	12.10	0.18	31.70	76.95	92.90
<i>tsilt</i> (%)	35.06	7.29	0.21	20.80	33.30	54.20
<i>ssilt</i> (%)	16.80	9.20	0.55	3.70	15.05	46.30

^aSD: standard deviation, CV: coefficient of variation.

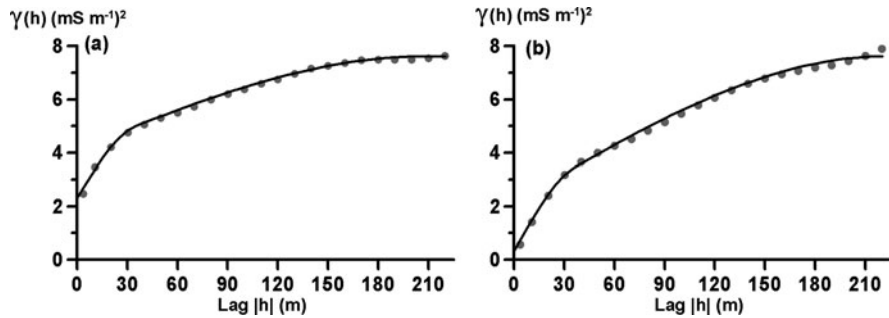


Fig. 20.2 Experimental variograms with a fitted model of (a) EC_a-H and (b) EC_a-V

A variogram analysis (Fig. 20.2) also led to the following results. The same spatial structure (double spherical model without directional effects) was used to model the spatial variability of EC_a-H and EC_a-V, while the relative nugget effect (RNE) of the horizontal orientation was much higher (30%) than the one with the vertical orientation (4%). However, the Z-score filter reduced the RNE of the EC_a-H data to 23%. Two scales of spatial textural variability were identified: a range of 35 m representing the variability within the creek pattern of the subsoil and a range of 200 m for the wider within-field variability. Based on these variograms, the sensor measurements were kriged to a map with a resolution of 1 m × 1 m.

Table 20.1 also illustrates that the topsoil texture was much more homogeneous than the subsoil texture, with the largest discrepancy for the silt and clay fractions. For the clay fraction, the CV of the topsoil was 13%, compared to a CV of 45% in the subsoil. A location map of the clay content of the samples showed that there was no channel pattern present in the topsoil: the highest *tclay* values were situated around a north-east line in the centre and in the bottom left corner of the field (Fig. 20.3).

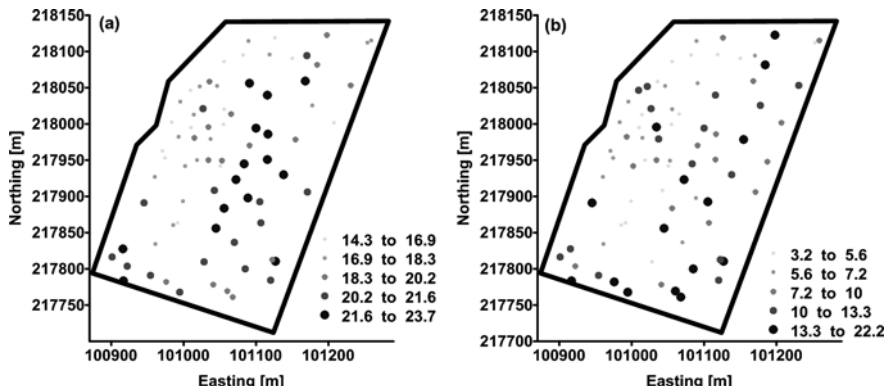


Fig. 20.3 Location maps of the soil samples analysed for (a) *tclay* and (b) *sclay*. The units are in %

Table 20.2 Correlation coefficients between EC_a and the soil textural fractions ($n = 78$)

	<i>tclay</i>	<i>tsilt</i>	<i>tsand</i>	<i>sclay</i>	<i>ssilt</i>	<i>ssand</i>
EC_a -H	0.59	0.73	-0.75	0.69	0.70	-0.71
EC_a -V	0.44	0.66	-0.66	0.68	0.70	-0.70

The subsoil clay content on the other hand followed the EC_a variability. The topsoil texture was mainly loam, while in the subsoil it ranged over five USDA textural classes (from sand to silt loam) (Vitharana et al., 2006).

The correlation coefficients between EC_a and the textural fractions are given in Table 20.2. Subsoil texture correlated similarly with EC_a -V and EC_a -H. This was an indication of the influence of the subsoil on the EC_a -H measurements. The clay fraction of the subsoil correlated even better ($r = 0.69$) with EC_a -H than did the topsoil clay content ($r = 0.59$).

The different ANN systems used to predict *tclay* were evaluated using the mean rMSEE of the test data (Fig. 20.4). The most accurate *tclay* prediction was achieved using EC_a -H and EC_a -V as input variables and no contextual information: the rMSEE was lowest (0.40) and 66% of the *tclay* variability was explained with this

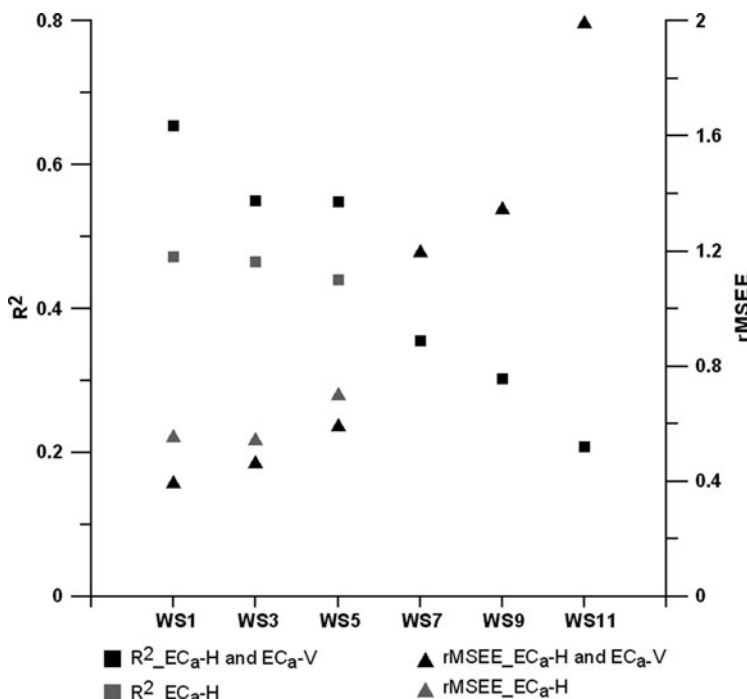


Fig. 20.4 Graph of the relative error (rMSEE) and R^2 of the ANNs/CNNs with the input variables indicated in the legend. The X-axis shows the input window size

ANN ($R^2 = 0.66$). Surprisingly, contextual information had a negative effect on the *tclay* predictions: increasing the input window size decreased the accuracy. The same trend was observed using the two indices: the rMSEE increased, while the R^2 decreased. Nevertheless, up to a window size of 5×5 pixels the differences were rather small. It was hypothesised that more contextual information increased the complexity of the network too much, resulting in generalisation problems. The advantage of including EC_a-V measurements in the network was illustrated by a decrease in relative error and an increase in R^2 ; the relative improvement of the rMSEE when using two sensor orientations instead of one was 29, 15, and 14% for windows of 1, 3, and 5 pixels, respectively. Since increasing the window size from 1 to 3 pixels deteriorated the validation indices on average by 15.5%, it was concluded that the effect of including both EM38DD orientations in the ANN was essential for optimising the *tclay* predictions.

Investigating the advantage of using a more complex technique like ANNs, a comparison was made with multivariate linear regression. A stepwise multivariate linear regression was performed with EC_a-H and EC_a-V as predictor variables. Both orientations contributed significantly to the model, and the following regression equation was found:

$$tclay = 13.25 + 1.53 \times EC_a\text{-H} - 0.99 \times EC_a\text{-V}.$$

The goodness of fit of the model (R^2) was 0.488 and the adjusted R^2 was 0.47. The goodness of fit of a univariate regression based on EC_a-H data was 0.37 (adjusted $R^2 = 0.36$), indicating that adding the vertical orientation improved the *tclay* prediction; however, the individual importance of each orientation was not assessed due to multi-collinearity concerns – variance inflation factors were 6.96. The model was validated based on the average indices of the 10 test datasets: the MVLR model had an rMSEE of 0.65 and 41% of the *tclay* variability was explained. So using ANNs clearly improved the clay predictions: for a WS of 1 the differences of rMSEE and R^2 between the two methods were even found to be significant ($p < 0.05$). The outperformance of ANNs could be attributed to the non-linear response of the sensor to soil conductivity with increasing depth. This non-linear process is too complex to be captured completely by an MVLR.

Based on this analysis, the most accurate *tclay* map was obtained using an ANN with WS = 1 and the EC_a-H and EC_a-V maps as input (Plate 20.1a). The resulting map demonstrated that the highest *tclay* was found in the centre of the field (as in Fig. 20.3). Although it was not evident from the location map, a water channel pattern with an increased clay percentage was also present in the west of the *tclay* map. In contrast to the result obtained using only the EC_a-H orientation, the subsoil channel pattern was substantially filtered out in the final output (Plate 20.1a versus Plate 20.1b). Moreover, the *tclay* map obtained using EC_a-H data only was more homogeneous; the standard deviation (SD) of the predictions was 1.43% and the maximum predicted *tclay* fraction was 21.0%. On the other hand, the MVLR result displayed larger *tclay* variability (SD of 1.54%) and no water channel pattern could be observed in the *tclay* map (Plate 20.1c). However, the accuracy of the MVLR method was not optimal. In all the maps a strong orientation can be seen, a feature arising from the fluvial history of the field.

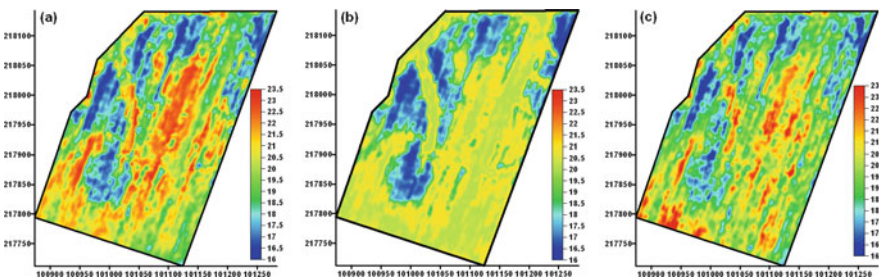


Plate 20.1 Map of *tclay*, predicted by (a) the ANN model with $WS = 1$ based on EC_a -H and EC_a -V, (b) the ANN model with $WS = 1$ based on EC_a -H, and (c) the MVLR model

20.4 Conclusions

Topsoil clay content predictions based on high-resolution measurements from the EM38DD sensor were optimised using a neural network analysis. We conclude that ANN models (including contextual information up to a window of 5×5 pixels) increased the accuracy of the topsoil clay prediction compared to an MVLR based on EC_a -H and EC_a -V data. MVLR was not an optimal method for *tclay* prediction based on EM38DD data, due to the non-linear response of the sensor to depth. ANNs on the other hand were able to capture this non-linearity and increased the topsoil textural information by optimally fusing the two orientations of the EM38DD sensor. The best ANN model included both orientations of the EM38DD sensor without contextual information; an R^2 of 0.65 was found and the rMSEE was 0.40.

References

Cockx L, Van Meirvenne M, De Vos B (2007) Using the EM38DD to delineate clay lenses in a sandy forest soil. *Soil Sci Soc Am J* 71:1314–1322

Green TR, Salas JD, Maritnez A, Erskine RH (2007) Relating crop yield to topographic attributes using spatial analysis neural networks and regression. *Geoderma* 139:23–37

Haykin S (1994) Neural networks: a comprehensive foundation. Macmillan College Publishing Company, New York

Hecht-Nielsen R (1987) Kolmogorov's mapping neural network existence theorem. In: Caudill M, Butler C (eds) Proceedings of the IEEE international conference on neural networks, vol 3, San Diego, CA, pp 11–14

Kitchen NR, Drummond ST, Lund ED, Sudduth KA, Buchleiter GW (2003) Soil electrical conductivity and topography related to yield for three contrasting soil–crop systems. *Agron J* 95:483–495

Miao Y, Mulla DJ, Robert PC (2006) Identifying important factors influencing corn yield and grain quality variability using artificial neural networks. *Precision Agric* 7:117–135

Sy NL (2006) Modelling the infiltration process with a multi-layer perceptron artificial neural network. *Hydrol Sci J* 51:3–19

Persson M, Sivakumar B, Berndtsson R, Jacobsen OH, Schjonning P (2002) Predicting the dielectric constant–water content relationship using artificial neural networks. *Soil Sci Soc Am J* 66:1424–1429

Vitharana UWA, Van Meirvenne M, Cockx L, Bourgeois J (2006) Identifying potential management zones in a layered soil using several sources of ancillary information. *Soil Use Manag* 22, 405–413

Williams BG, Hoey D (1987) The use of electromagnetic induction to detect the spatial variability of the salt and clay contents of soils. *Aust J Soil Res* 25:21–27

Chapter 21

Field Determination of Soil Moisture in the Root Zone of Deep Vertosols Using EM38 Measurements: Calibration and Application Issues

M.B. Hossain, D.W. Lamb, P.V. Lockwood, and P. Frazier

Abstract Electromagnetic induction sensors, such as the Geonics EM38, are used widely for monitoring and mapping soil attributes via the apparent electrical conductivity (EC_a) of the soil. The sensor response is the depth-integrated combination of the depth-response function of the EM38 and the local electrical conductivity $EC_a(z)$. In deep Vertosols, assuming that the depth-response function is not perturbed by the soil and that the volumetric moisture content $\theta(z)$ dominates $EC_a(z)$, the EM38 should be capable of predicting $\theta(z)$. A multi-height EM38 experiment was conducted over deep Vertosols to confirm the validity of the EM38 depth-response function, to test the hypothesis that the EM38 response was an additive combination of its depth-response function and $\theta(z)$, and to investigate if on-ground EC_a measurements could estimate average θ within the root zone. A simple model, involving mathematical summation of measured $\theta(z)$ from sectioned ‘calibration cores’ and the EM38’s known depth-response function, was found to explain 87 and 83% of the variance in measured EC_a for both horizontal and vertical dipole configurations, respectively. This included all data acquired at multiple sensor heights above the ground. However, a subsequent comparison of on-ground, EM38-derived EC_a and average θ from surface to 0.8 m ($\bar{\theta}_{0.8}$) and surface to 1.2 m ($\bar{\theta}_{1.2}$) demonstrated that $\bar{\theta}_{0.8}$ and $\bar{\theta}_{1.2}$ explained only 37 and 46% of the variance in EC_a for vertical dipole configuration measurements, compared to 55 and 56% of the variance for horizontal dipole configuration measurements. This result can be attributed to the small depth-specific changes in the $EC_a(z)$ and $\theta(z)$ relationship and the limited proportion of the depth-response function of the EM38 interacting with the soil volumes investigated. Whereas the best calibration over these depth ranges was achieved using a horizontal dipole configuration, further improvements in both dipole orientations might be achieved by calibrating, then deploying, the sensors while they are elevated tens of centimetres above the ground.

D.W. Lamb (✉)

Precision Agriculture Research Group, Cooperative Research Centre for Irrigation Futures,
University of New England, Armidale, NSW 2351, Australia
e-mail: dlamb@une.edu.au

Keywords Volumetric soil moisture · Electromagnetic induction · EM38 · Vertosol · Black Vertosol

21.1 Introduction

Electromagnetic induction (EMI) sensors such as the EM38 (Geonics, Ontario, Canada) offer the potential to measure numerous soil attributes without the need for destructive sampling. The EM38 consists of transmitting and receiving induction coils with an inter-coil spacing of 1 m. The single value of apparent electrical conductivity (EC_a) returned by the sensor at any given location is an integrated value based on a combination of the depth-related sensitivity of the instrument and the depth-dependent drivers of electrical conductivity (e.g. ion and moisture content) (McNeill, 1980).

Provided there is sufficient soil depth, variation in EC_a values will be primarily due to variations in clay content or volumetric moisture content (McBratney et al., 2005; Brevik et al., 2006). The relationship between soil moisture content and electrical conductivity has been established by many investigators ($R^2 = 0.96$, Kachanoski et al., 1988; $R^2 = 0.64$, Sheets and Hendrickx, 1995; $R^2 = 0.50\text{--}0.90$, Brevik et al. 2006). Hezarjaribi and Sourell (2007) used the EM38 to predict moisture content in a non-saline, loamy, sand soil and found a 56 and 35% relationship between total available moisture content and vertical and horizontal dipole EC_a values, respectively.

While the relationship between integrated EC_a and bulk soil moisture is well documented, varying the height of the EM38 sensor above a soil profile and factoring in the EC_a depth-response function should allow determination of the depth-related soil moisture profile rather than a single bulk moisture value. Hendrickx et al. (2002) and Borchers et al. (1997) have laid the foundations for the inversion of multi-height EM38 measurements to extract below-ground layer values of EC_a ; however, like numerous other workers, only the link between EM38-derived EC_a values and depth-related soil EC_a values has been investigated (e.g. Rhoades and Corwin, 1981). Rhoades and Corwin (1981) performed an experiment that compared the EC_a values generated by an EM38 at different heights above the ground with the integration of EC_a values at different depths acquired using a four-electrode EC sensor. They found that the integrated depth response of the EM38 explained 97% of the variance observed in the calculated EM38 reading based on integrating the multi-depth EC_a values. Although a very good relationship between volumetric soil moisture and EC_a has been established (e.g. Kachanoski et al., 1988, $R^2 = 0.96$; Reedy and Scanlon, 2003, $R^2 = 0.80$), none of this work has demonstrated a link between EM38-derived EC_a values and depth-related θ . Consequently, the objectives of this chapter are to

- confirm that the EM38-derived EC_a values are in fact an integration of the accepted depth-response function of the EM38 and $\theta(z)$ for deep Vertosols and
- determine the upper accuracy limit to calibrate on-ground EC_a measurements for predicting average volumetric soil moisture content from surface to 0.8 and 1.2 m, depths corresponding to accepted ‘root zones’.

21.2 Materials and Methods

21.2.1 Study Area

The experiment was conducted on a 2 ha block on Clark's Farm, an experimental property located at the University of New England, Australia (30°31.7' S, 151°37' E) with a deep, Black Vertosol.

21.2.2 EM38 Depth-Response Function

If the depth-response function of the EM38 is not perturbed by the $\theta(z)$ profile, the assumption of McNeill (1980) is correct that horizontal eddy currents induced by the primary field do not influence each other and the thickness of the individual contributing layers is identical, then the instrument's response should be proportional to the addition of the combined depth-response function and $\theta(z)$ according to the equation

$$EC_a \approx \sum_z k \times \theta(z) \times \phi^{V,H}(z).$$

Here, EC_a is the instrument (integrated) response in millisiemens per metre and k is the constant of proportionality between local $EC_a(z)$ at depth and $\theta(z)$ at the same depth, assuming that the relative contributions of all other EC-driving parameters remain fixed at depth. As set out by McNeill (1980), the depth-response function $\phi^{V,H}(z)$ is given as follows for both vertical and horizontal dipole orientations:

$$\phi^V(z) = \frac{4z}{(4z^2 + 1)^{\frac{1}{2}}} \quad (\text{vertical})$$

and

$$\phi^H(z) = 2 - \frac{4z}{(4z^2 + 1)^{\frac{1}{2}}} \quad (\text{horizontal}).$$

Note that raising the EM38 above the ground and collecting EC_a (Table 21.1) is equivalent to 'shunting' the volumetric moisture content profile lower down the EM38 depth-response function.

Exactly 17 'single-core' sites were established over the field site. Multi-height EM38 measurements of EC_a were first collected at each single-core location in both vertical and horizontal dipole configurations at seven heights above the ground surface (0, 0.2, 0.4, 0.6, 0.8, 1.0, and 1.2 m) using a specially designed polymer plastic 'ladder'. The ladder was constructed from lengths of 42-mm-diameter polyvinyl chloride (PVC) pipe segmented at heights corresponding to the ground surface (0 m) and at 0.2, 0.4, 0.6, 0.8, 1.0, and 1.2 m. The EM38 measurements were collected with the sensor axis (that is, the line between the sensor and receiver coils) orientated east–west. Prior to each measurement, the EM38 was nulled following the manufacturer's protocol. Soil cores (50 mm diameter and 1.7 m deep) were then

Table 21.1 The data combination process for linking multi-height EC_a and multi-depth volumetric moisture content using the depth-response function of the EM38 (vertical and horizontal dipole configurations)

Depth (m)	$\phi^V(z)$ or $\phi^H(z)x$	Sensor height (m)						
		0	0.2	0.4	0.6	0.8	1.0	1.2
0	0	2	$\theta(0.025)$					
0.1	0.37715	1.60777	$\theta(0.1)$					
0.2	0.64033	1.25722	$\theta(0.2)$	$\theta(0.025)$				
0.3	0.75661	0.97101	$\theta(0.3)$	$\theta(0.1)$				
0.4	0.76182	0.75061	$\theta(0.4)$	$\theta(0.2)$	$\theta(0.025)$			
0.5	0.70711	0.58579	$\theta(0.5)$	$\theta(0.3)$	$\theta(0.1)$			
0.6	0.62969	0.46356	$\theta(0.6)$	$\theta(0.4)$	$\theta(0.2)$	$\theta(0.025)$		
0.7	0.54982	0.37253	$\theta(0.7)$	$\theta(0.5)$	$\theta(0.3)$	$\theta(0.1)$		
0.8	0.47640	0.30400	$\theta(0.8)$	$\theta(0.6)$	$\theta(0.4)$	$\theta(0.2)$	$\theta(0.025)$	
0.9	0.41234	0.25169	$\theta(0.9)$	$\theta(0.7)$	$\theta(0.5)$	$\theta(0.3)$	$\theta(0.1)$	
1.0	0.35777	0.21115	$\theta(1.0)$	$\theta(0.8)$	$\theta(0.6)$	$\theta(0.4)$	$\theta(0.2)$	$\theta(0.025)$
1.1	0.31177	0.17927	$\theta(1.1)$	$\theta(0.9)$	$\theta(0.7)$	$\theta(0.5)$	$\theta(0.3)$	$\theta(0.1)$
1.2	0.27310	0.15385	$\theta(1.2)$	$\theta(1.0)$	$\theta(0.8)$	$\theta(0.6)$	$\theta(0.4)$	$\theta(0.2)$
1.3	0.24055	0.13331		$\theta(1.1)$	$\theta(0.9)$	$\theta(0.7)$	$\theta(0.5)$	$\theta(0.3)$
1.4	0.21306	0.11652		$\theta(1.2)$	$\theta(1.0)$	$\theta(0.8)$	$\theta(0.6)$	$\theta(0.4)$
1.5	0.18974	0.10263			$\theta(1.1)$	$\theta(0.9)$	$\theta(0.7)$	$\theta(0.5)$
1.6	0.16984	0.09104			$\theta(1.2)$	$\theta(1.0)$	$\theta(0.8)$	$\theta(0.6)$
1.7	0.15277	0.08127				$\theta(1.1)$	$\theta(0.9)$	$\theta(0.7)$
1.8	0.13804	0.07296				$\theta(1.2)$	$\theta(1.0)$	$\theta(0.8)$
1.9	0.12527	0.06585					$\theta(1.1)$	$\theta(0.9)$
2.0	0.11413	0.05972					$\theta(1.2)$	$\theta(1.0)$
2.1	0.10438	0.05439						$\theta(1.1)$
2.2	0.09579	0.04973						$\theta(1.2)$
2.3	0.08819	0.04565						
2.4	0.08145	0.04204						
$\sum_z \theta(z) \times \phi^{V,H}(z) \rightarrow$								

extracted and sectioned into a top sample of 0.05 m ($z = 0.025$ m) and 12 subsequent 0.1 m thick layers ($z = 0.1$ –1.2 m) for analysis of volumetric water content $\theta(z)$.

In the field experiment, the multi-height EC_a measurements derived from the 17 core sites were plotted against depth-weighted average moisture content $\sum_z \theta(z) \times \phi^{V,H}(z)$, following Table 21.1, using the measured $\theta(z)$ and calculated $\phi^{V,H}(z)$.

21.2.3 Field Calibration and Prediction of Average Moisture Content at Depth

For the field calibration work, the EM38 sensor was placed on the ground surface over (or adjacent to) the core sites, again with the sensor itself orientated east–west. For the first calibration dataset, EM38 measurements were conducted prior to

extraction of the cores and subsequent determination of average volumetric moisture content over the depth range 0–0.8 m ($\bar{\theta}_{0.8}$) and 0–1.2 m ($\bar{\theta}_{1.2}$). Calibration equations for both dipole configurations were derived using simple linear regression.

21.3 Results and Discussion

A plot of EC_a versus $\sum_z \theta(z) \times \phi^{V,H}(z)$ at different sensor heights above the ground for a single-core site is given in Fig. 21.1.

The data include both horizontal and vertical dipole orientations. Not surprisingly, the integrated EM38 response (measured in millisiemens per metre) decreases monotonically as the sensor is raised progressively above the ground. In Fig. 21.1, progressively raising the sensor above the ground corresponds to the data points (one for each dipole orientation) starting, in sequence, at the top right and finishing at the lower left. The measured EC_a values explained 99 and 97% of the variance observed in the $\sum_z \theta(z) \times \phi^{V,H}(z)$ values, with RMSE values of 1.38 and 2.57 mS m⁻¹ for horizontal and vertical dipole configurations, respectively. The R^2 and RMSE values were typical for all 17 test core locations investigated, as was the sequential trend in data points with increasing sensor height. The entire dataset of EC_a values, for every sensor height at the 17 core locations, is plotted against respective $\sum_z \theta(z) \times \phi^{V,H}(z)$ values in Fig. 21.2. The coefficients of determinations (R^2) for entire dataset (17 cores and 7 heights each) were 0.87 and 0.83, with RMSE of 6.01

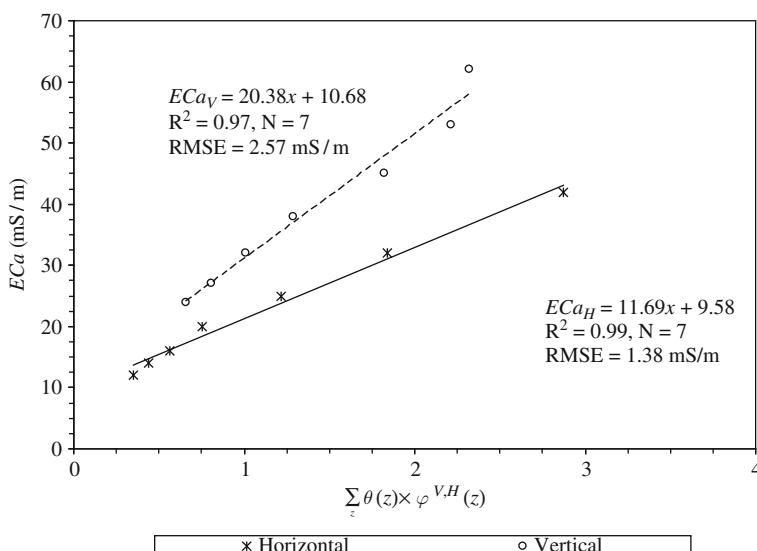


Fig. 21.1 EC_a versus $\sum_z \theta(z) \times \phi^{V,H}(z)$ for vertical and horizontal dipole configurations for a single-core site (EC_{aV} , vertical; EC_{aH} , horizontal). Sensor heights progress from 0 m (ground level, top right data point) through to maximum height (1.2 m, bottom left data point) in each plot

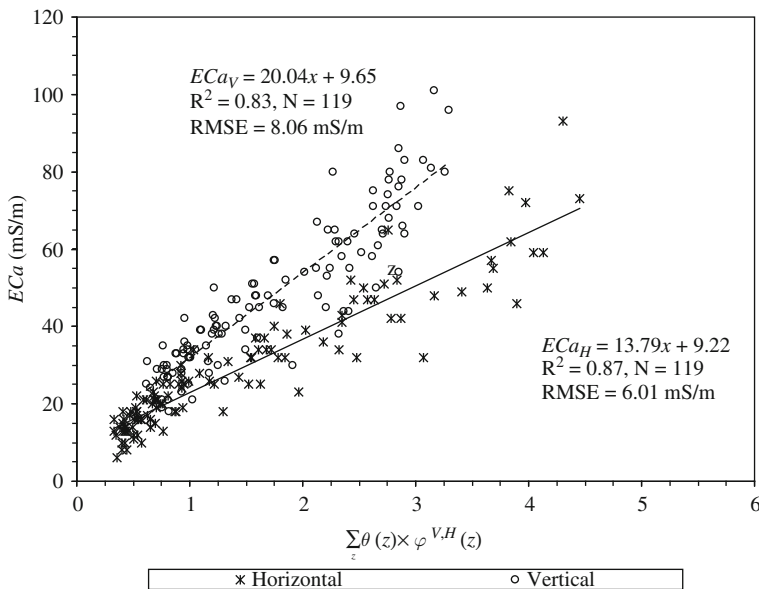


Fig. 21.2 EC_a versus $\sum_z \theta(z) \times \phi^{V,H}(z)$ for vertical and horizontal dipole configurations for all core sites (EC_{aV} , vertical; EC_{aH} , horizontal)

and 8.06 mS m^{-1} for horizontal and vertical dipole configurations, respectively. In all analyses, the response of EC_a to $\sum_z \theta(z) \times \phi^{V,H}(z)$ was highly significant ($p < 0.0001$).

A key finding from this correlation analysis is that the plots of Figs. 21.1 and 21.2 are all approximately linear. There is a suggestion of a curvilinear response at low EC_a , corresponding to the sensor located at maximum height above the ground. Here the EM38 is producing a slightly lower than expected response. However, the overall linearity supports the underlying assumption that the relative contributions of all EC_a -driving parameters at depth (for example salinity, moisture content, and clay content) remain the same. Any small, systematic deviation from linearity is likely to be attributed to small variations in the depth-related distribution of soluble salts and clay content in the profile. The layered earth model, whereby the contribution of each layer at depth is additive, is also verified, as is the fact that the depth-response function of the EM38 is not perturbed by the depth profile of the moisture (or ion) content under the conditions studied here. The significance of the constant k is also evident. It points to a direct link between $EC_a(z)$ and $\theta(z)$. For data collated from the 17 core sites, the values of k are 13.79 ± 0.49 and $22.04 \pm 0.93 \text{ mS m}^{-1}$ for horizontal and vertical dipole orientations, respectively. In the absence of any dissolved electrolytes, water has an intrinsic electrical conductivity of $5.5 \mu\text{S m}^{-1}$ (e.g. Marshall, 1987) and this generally increases linearly with increasing concentrations of ions (e.g. Lide, 2007). The slope of the conductivity-concentration curves for water varies with the specific acid, base, or salt. Thus, k

must represent the contribution of dissolved ions in water as well as the soil–water and soil–soil interfacial characteristics to the electrical conductivity. The linearity in Figs. 21.1 and 21.2 suggests that these contributing factors are relatively consistent throughout the deep Vertosol profiles investigated here, at least within the ‘penetration range’ of the EM38. The actual magnitude of k is found to vary depending on the dipole orientation of the EM38; however, the ratio of the k values for horizontal and vertical dipole configurations is approximately 0.6. This value is similar to the ratio of the horizontal to vertical integrated response of the EM38, calculated by integrating $\varphi^{V,H}(z)$ with respect to depth z for depths exceeding 0.5 m. Thus, k is attributed to a combination of the soil conductivity characteristics described above and the sensing volume of the EM38 in the specific dipole configuration to which it is employed.

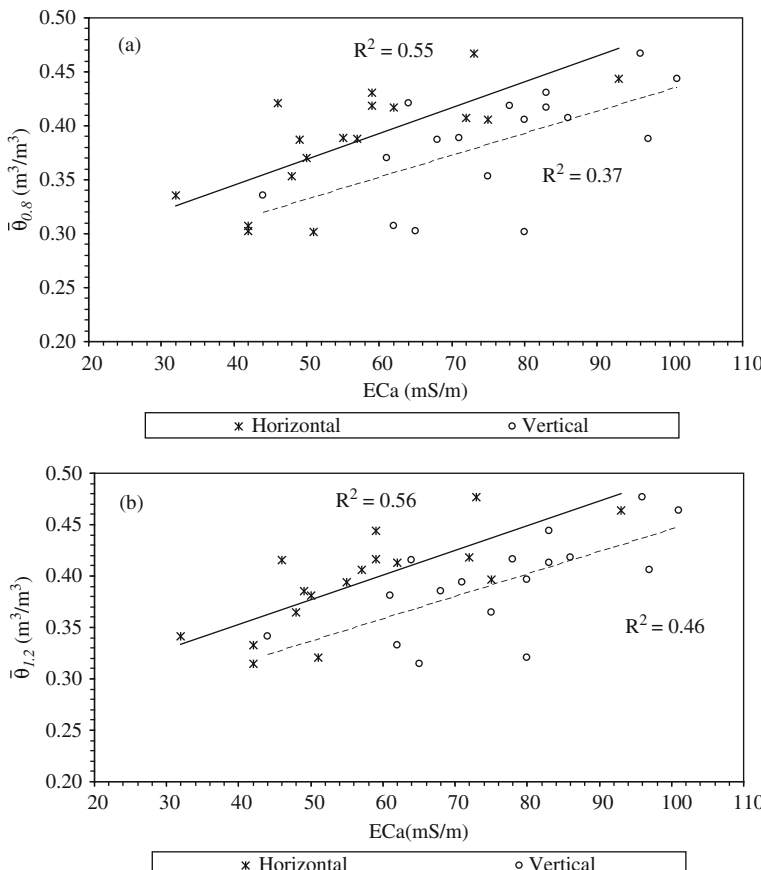


Fig. 21.3 Scatter plot of average volumetric moisture content at depths of (a) 0–0.8 m ($\bar{\theta}_{0.8}$) and (b) 0–1.2 m ($\bar{\theta}_{1.2}$) derived from the single-core calibration method versus EC_a measured by EM38 in both vertical and horizontal dipole orientations

Table 21.2 Derived linear calibration equations for prediction of θ by EM38 using the single-core calibration data, where $\bar{\theta}_{0.8}$ and $\bar{\theta}_{1.2}$ are average θ_v values over surface to 0.8 m and surface to 1.2 m depths, respectively, EC_{aH} and EC_{av} are on-ground EM38 measurements in horizontal and vertical dipole configurations, respectively, and n is the number of observations

EM38 dipole orientation	Regression equation	R^2	RMSE ($m^3 m^{-3}$)	p -value	N
Horizontal	$\bar{\theta}_{0.8} = 0.003EC_{aH} + 0.240$	0.55	0.034	0.000	17
	$\bar{\theta}_{1.2} = 0.002EC_{aH} + 0.255$	0.56	0.033	0.000	17
Vertical	$\bar{\theta}_{0.8} = 0.002EC_{av} + 0.224$	0.37	0.043	0.009	17
	$\bar{\theta}_{1.2} = 0.002EC_{av} + 0.225$	0.46	0.037	0.003	17

Scatter plots of $\bar{\theta}_{0.8}$ and $\bar{\theta}_{1.2}$ as functions of EC_a (both dipole configurations) are given in Fig. 21.3, and the derived calibration equations are listed in Table 21.2. The calibration equations summarised in Table 21.2 are all statistically significant ($p < 0.01$); however, both $\bar{\theta}_{0.8}$ and $\bar{\theta}_{1.2}$ explain more of the variance observed in the measured EC_a for the horizontal dipole configuration. This is not surprising, given that for depths of 0.8 and 1.2 m, 71 and 79% of the horizontal dipole configuration depth-response function $\varphi^H(z)$ contributes to the integrated signal – assuming a relatively uniform depth distribution of $\theta(z)$ – compared to a 47 and 62% contribution of the vertical dipole configuration depth-response function $\varphi^V(z)$. The remaining ‘unexplained’ variance in the equations in Table 21.2 is likely to be tied up with the fact that there is still a significant EM38 response (both dipole configurations) originating from below the depths ‘interrogated’ by our measurements of $\theta(z)$. This suggests that an improvement in instrument calibration (and subsequent estimation accuracy) might be achieved if the sensor were elevated above the ground. A second source of unexplained variance may be the fact that $\theta(z)$ was determined using core sampling. It has been demonstrated that the physical process of core sampling can alter the bulk density of the cores compared to the source soil profile, and this would subsequently alter the derived values of θ (Hossain, 2008).

21.4 Conclusions

In a field site characterised by deep Vertosols, multi-height EM38 measurements were used to confirm that the volumetric moisture content is the dominant factor in influencing the integrated EC_a response. Similarly, we confirmed that, in generating that integrated response, the known depth-response function of the EM38 was valid. Average volumetric moisture content at depths associated with the root zone of crop plants (surface to 0.8 and 1.2 m) was found to explain more of the variance associated with horizontal dipole configuration measurements than vertical dipole configuration measurements. An increase in accuracy is likely to result by conducting calibrations with the EM38 sensor elevated above the ground and by improved methods of determining volumetric moisture content (e.g. pits rather than cores).

Acknowledgements We would like to thank Cate MacGregor and George Henderson for their assistance with field work.

References

Borchers B, Uram T, Hendrickx JMH (1997) Tikhonov regularization of electrical conductivity depth profiles in field soils. *Soil Sci Soc Am J* 61:1004–1009

Brevik EC, Fenton TE, Lazari A (2006) Soil electrical conductivity as a function of soil water content and implications for soil mapping. *Precision Agric* 7:393–404

Hendrickx JMH, Borchers B, Corwin DL, Lesch SM, Hilgendorf AC, Schlué J (2002) Inversion of soil conductivity profiles from electromagnetic induction measurements: theory and experimental verification. *Soil Sci Soc Am J* 66:673–685

Hezarjaribi A, Sourell H (2007) Feasibility study of monitoring the total available water content using non-invasive electromagnetic induction-based and electrode based soil electrical conductivity measurements. *Irrigat Drainage* 56:53–65

Hossain MB (2008) EM38 for measuring and mapping soil moisture in a cracking clay soil. PhD thesis, University of New England, Australia

Kachanoski RG, Gregorich EG, Van Wesenbeek IJ (1988) Estimating spatial variations of soil water content using noncontacting electromagnetic inductive methods. *Can J Soil Sci* 68: 715–722

Lide DR (ed) (2007) CRC handbook of chemistry and physics, 88th edn. CRC Press, London

Marshall WL (1987) Electrical conductance of liquid and supercritical water evaluated at 0°C and 0.1 MPa to high temperatures and pressures: reduced state relationships. *J Chem Eng Data* 32:221–226

McBratney AB, Minasny B, Whelan BM (2005) Obtaining ‘useful’ high-resolution soil data from proximally sensed electrical conductivity/resistivity (PSEC/R) surveys. In: Stafford JV (ed) Precision agriculture ‘05. Wageningen Academic Publishers, The Netherlands

McNeill JD (1980) Electromagnetic terrain conductivity measurement at low induction numbers. Technical note TN-6. Geonics Limited, Mississauga, Ontario, Canada

Reedy RC, Scanlon BR (2003) Soil water content monitoring using electromagnetic induction. *J Geotech Geoenviron Eng* 129:1028–1039

Rhoades JD, Corwin DL (1981) Determining soil electrical conductivity–depth relations using an inductive electromagnetic soil conductivity meter. *Soil Sci Soc Am J* 45:255–260

Sheets KR, Hendrickx JMH (1995) Non-invasive soil water content measurement using electromagnetic induction. *Water Resour Res* 31:2401–2409

Chapter 22

Can the EM38 Probe Detect Spatial Patterns of Subsoil Compaction?

G. Hoefer, J. Bachmann, and K.H. Hartge

In memoriam of Karl Heinrich Hartge.

Abstract So far, an easy way of locating regions of subsoil compaction on the field scale has not been achieved using common soil physical methods. Our potential solution to this problem is to approximate the mechanical strength of the soil using K_0 (a stress-at-rest coefficient) and relate it to the apparent electrical conductivity (EC_a). Firstly, we prove the validity of the underlying assumption that the horizontal stress component characterises the compaction state of the soil. This consists of assigning penetration resistance (PR) values to the principal stress (σ_x) as a function of depth, normalised by a relation involving the PR value at the greatest accessible depth (0.8 m). Secondly, we evaluate how well non-destructive EC_a measurements (made with an electromagnetic induction meter) localise compacted areas. Results from two experimental sites located in the loess belt of northern Germany showed a strong correlation between penetration resistance and an electromagnetic induction meter, especially in areas with high PR values. We conclude that the geophysically based electromagnetic induction technique can be used to map spatial patterns of subsoil compaction in loess-derived soils.

Keywords Subsoil compaction · State of mechanical stress · Apparent electrical conductivity (EC_a) · Electrical conductivity

22.1 Introduction

Detecting the spatial pattern of soil properties on a field scale is still an open problem for soil physical investigations. This is mainly because specific measurements for a given location represent only the local compaction state of the soil and

G. Hoefer (✉)

Institute of Soil Science, Leibniz Universität Hannover, Herrenhäuser Str. 2,
30419 Hannover, Germany
e-mail: hoefer@ifbk.uni-hannover.de

K.H. Hartge is deceased.

ignore the spatial variability of soil physical properties. Special investigations on the mechanical strength of a soil can be accomplished in the laboratory, but are not very helpful for map making.

The use of non-destructive probes such as the EM38, GPR provides better spatial resolution, but they do not reveal the state of the mechanical stress and are too time consuming for field scale work.

To generalise the information obtained from penetration resistance data, Hartge and Bachmann (2004) proposed a simple, site-specific method of interpreting depth-dependent penetration resistance (PR). Results for loess profiles showed that the depth-dependent relation of PR for topsoil can be described in a systematic way so that deviations from the non-compacted reference state can be detected. PR-detected compaction increased with duration of land use (Bachmann and Hartge, 2006) or with land use intensity (Bachmann et al., 2006), e.g. changing from forest soil (reference) to agricultural soil. Increasing compression, e.g. by adding additional temporary loads at the soil surface, leads to a decrease in the depth-dependent void ratio, which coincides with a mean increase in the grain contact area. Bachmann and Hartge (2006) further reported that the horizontal stress component reflects the vertical penetration resistance as well as the shear resistance. Readings from both measurements may be used to represent the horizontal stress component, from which an estimate of the equivalent stress-at-rest coefficient K_0 can be made (where K_0 is the ratio of non-compacted state a and compacted state b ; Fig. 22.1). This compacted state can be sensed by using results of PR measurements.

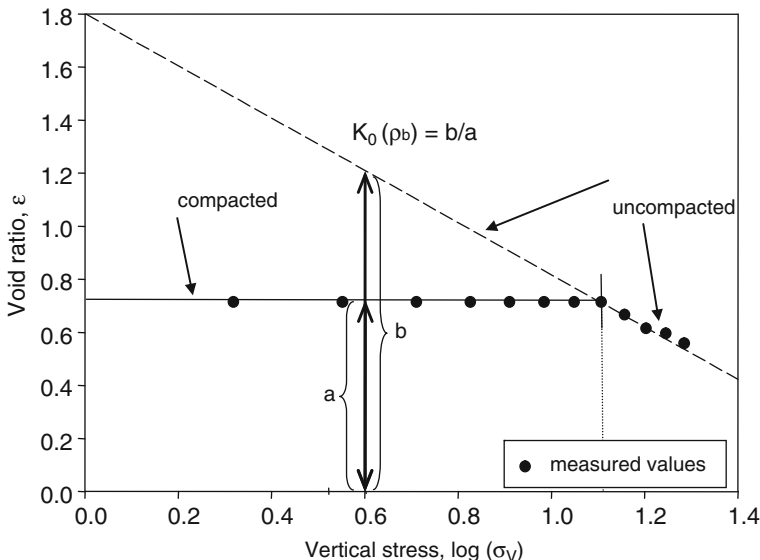


Fig. 22.1 Calculating the stress-at-rest coefficient K_0 by using depth-dependent soil bulk density data

The underlying assumption is that the vertical stress component for the lower-most layer assessed by PR measurements represents the hydrostatic stress situation, i.e. the stress at that depth is uniform in all directions.

The procedure described by Hartge and Bachmann (2004) proposed that drawing a straight line from the maximum depth towards the origin of the coordinates in the depth vs. PR plot gives, for a mechanically non-affected soil, values of the hydrostatic condition for each depth – i.e. values for the principal stress (σ_x) are available for each depth right up to the soil surface simply by linear interpolation (Fig. 22.2; a and b are the same as in Fig. 22.1). By assuming a hydrostatic stress situation, we establish a site-specific and easily definable base, which characterises a non-consolidated and mechanically undisturbed soil. Deviations from the ideal (hydrostatic) condition, which serves as the non-compacted reference, are considered to represent the depth-dependent compaction state of the soil, i.e. $K_0 > 1$ indicates compacted soil layers and $K_0 < 1$ indicates loose layers (Horn et al., 2007).

The question we considered was, Can a non-destructive geophysical technique with a short measurement time (seconds) detect inhomogeneities in the field, which can, in turn, be used as a guide to the compaction state of the soil?

The apparent electrical conductivity (EC_a) is a parameter that can be easily measured with an EM38 probe. The EM38 is widely used and can provide good spatial resolution of various soil characteristics (Domsch and Giebel, 2004) such as soil salinity (Doolittle et al., 2001), clay content and depth (Triantafyllis and Lesch, 2005), and yield (Kitchen et al., 2003). EC_a measurements can detect variability and heterogeneity in soil structures that correlate with traditional soil maps (Mertens and Welp,

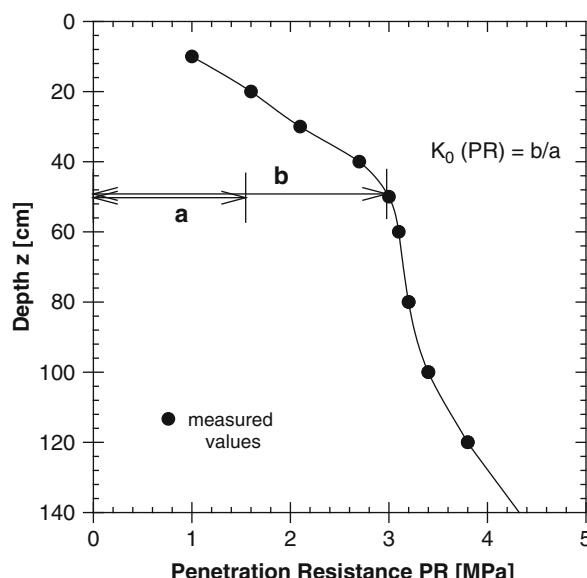


Fig. 22.2 Determination of the stress-at-rest coefficient K_0 by using vertical cone penetration data

2008) and can delineate management classes for precision agriculture (Vitharana et al., 2006).

Consequently, we sought to combine two simple field methods (PR and EC_a) to systematically interpret depth-dependent PR data. Our aim was to derive, from easily measurable data, parameters diagnostic of subsoil compaction. In this way, different degrees of subsoil compaction might be detected using non-destructive probing.

22.2 Materials and Methods

22.2.1 *Measurement of Penetration Resistance (PR)*

Subsoil compaction was assessed by measuring penetration resistance (PR) with a hand-driven Penetrologger (Eijkelkamp, Giesbeek, The Netherlands). This device combines an electronic penetrometer with a built-in datalogger for storage and processing. The penetration depth is measured continuously as the cone is pushed into the soil. The measuring range is 0–10 MPa (with a resolution of 0.01 MPa), and the measuring depth is from the soil surface down to 0.8 m (vertical resolution of 0.01 m). The penetration resistance is greatly influenced by soil water content, soil texture, speed of penetration, and the length and tip angle of the cone. We measured the PR at about 7000 measurement points; the penetration speed was either 0.03 or 0.04 m s⁻¹ with a 60° cone of 1 cm².

22.2.2 *Measurement of Apparent Electrical Conductivity (EC_a)*

The spatial variability of soil physical properties was assessed by measuring the apparent electrical conductivity (EC_a). The electromagnetic induction meter (EM38 probe; Geonics, Mississauga, Canada) induces an electromagnetic field in the ground and measures the apparent electrical conductivity of the soil. The EM38 reaches, on average, depths of exploration of 1.5 m in the vertical dipole mode and 0.75 m in the horizontal mode. The measured quantities are the apparent electrical conductivity in millisiemens per metre. Spacing between the transmitter and receiver coils was about 1 m and the operating frequency was 14.6 kHz. The range of measured conductivity was 0–200 mS m⁻¹ with a resolution of about ±0.1% of full scale and an accuracy of about ±5% at 30 mS m⁻¹.

22.2.3 *Study Sites*

Both sites under study (Schellerten and Ruthe) are located in northern Germany, south of Hannover (52°23' N, 9°44' E) in the German loess belt. Average annual precipitation is around 600 mm per year. The site at Schellerten is classified as a Weichselian loess (>1.8 m) over Jurassic clay, and the site at Ruthe also is a

Weichselian loess (> 1.2 m) but over Quaternary gravel (of the River Leine valley). The distance between sites is approximately 50 km. At both locations, typical Luvisols have developed. The texture at both sites is similar with approximately 10–15% clay, with a maximum of 20% in the B_t horizon, and 10–15% sand throughout the soil profile. The site at Schellerten is under agricultural cultivation with a rotation between sugar beet, potatoes, wheat, and rapeseed. Ruthe is also under agriculture, but with different types of cultivation and with a mixture of crops (e.g. wheat, barley) and vegetables (e.g. cauliflower, cabbage).

At Schellerten we measured apparent electrical conductivity (EC_a) at 1750 locations and penetration resistance (PR) at 1250 locations. The measured locations were situated on a regular grid (5 m, locally 1 m). In total, 10^5 single depth-dependent PR values were recorded. Measurements were done between April 1 and 5, 2005. At Ruthe, EC_a and PR measurements were made in October 2005 and April 2006. EC_a measurements were taken at 5000 locations on a field plot (42 × 70 m) with a nodal spaced 2 m (March and April 2006) and 3 m (October 2005) apart; PR values were measured at the same locations.

22.3 Results and Discussion

The determined statistical range for EC_a of about 15 m for Schellerten and 28 m for Ruthe was always larger than the grid size of 2–3 m at Ruthe and the grid size of 5 m at Schellerten.

Contour plots of clustered PR measurements showed that the maximum values are in the range 0.3–0.4 m, which corresponds to a layer of subsoil compaction beneath the ploughed surface layer. But high variation of the values in nearly all depth compartments showed that sole reliance on the Penetrologger to detect subsoil compaction can be done only for point data – it is not statistically possible to extend this data over a larger region with any precision.

In terms of frequency distribution, the EC_a values, as well as the cumulative values of the penetration resistance (PR) at depths from 0.0 to 0.8 m, are distributed normal to lognormal.

Contour plots of the EC_a values from the test fields at both campaigns were grouped into classes. The contour plots from Ruthe in 2006 were grouped into four classes (see Plate 22.1), where class one was with the lowest values and class four the highest. The results showed a clear structure of the EC_a data, indicating areas with higher absolute values at the lower margin of the field due to intensive trafficking (Plate 22.1). Contour plots at Schellerten showed a similar tendency.

The proposed hydrostatic stress–depth function is indicated by the line in Fig. 22.3. The figure shows that the mean of the measured values at 0.8 m (maximum values of the Penetrologger measurements) is around 3 MPa, which corresponds well to results for a great number of soil profiles from Middle Europe (Hartge and Bachmann, 2004).

The estimated compaction state of the soil, evaluated for the profile increment at depths from 0.3 to 0.4 m, is described by the area between the measured PR depth

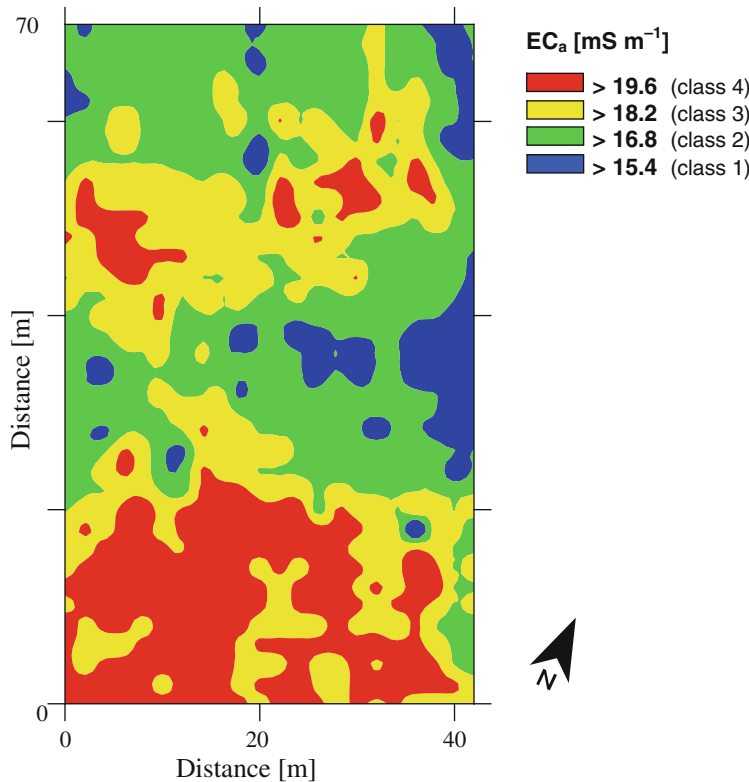


Plate 22.1 Contour plot of the EC_a values for Ruthe (EM38 vertical mode, April 2006)

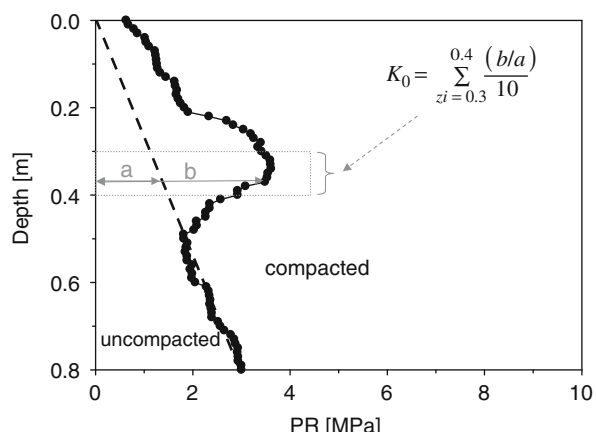


Fig. 22.3 Scheme for parameterising $K_0(\text{PR})$ over a depth of 0.3–0.4 m

function and the hydrostatic state and is expressed as $K_0(\text{PR})$. $K_0(\text{PR})$ is given here as the sum of the highest compacted area at depths between 0.3 and 0.4 m using a resolution of 0.01 m (a and b in Fig. 22.3 are the same as in Fig. 22.1).

To indicate the relation between PR and domains found by EC_a measurements, in each subplot, 10 locations were selected randomly. As an example, Figs. 22.4 and 22.5 show the depth-dependent PR (mean of 10 replicates) from subplots at Ruthe with the lowest (Fig. 22.4) and the highest (Fig. 22.5) EC_a values, respectively.

The PR–depth functions clearly indicate a local maximum at a depth of about 0.3–0.4 m. With increasing EC_a values of the subplots, the mean PR values and

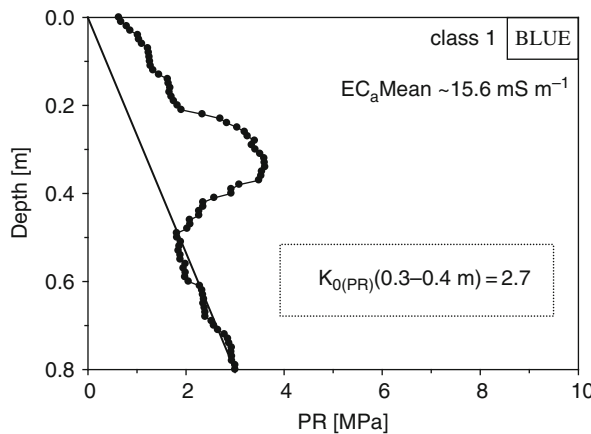


Fig. 22.4 Penetration resistance (PR) with depth for low values of EC_a (mean of 10 replicates, Ruthe, April)

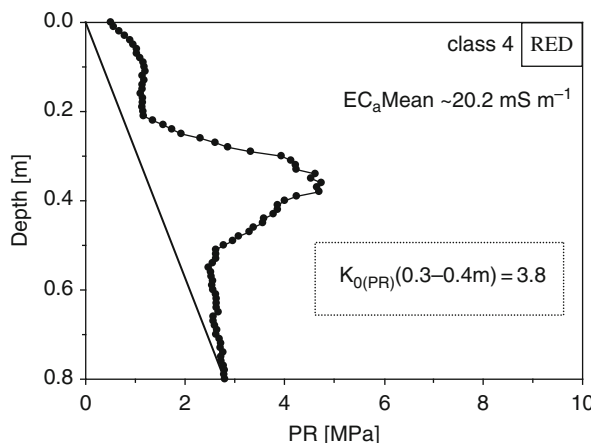


Fig. 22.5 Penetration resistance (PR) with depth for high values of EC_a (mean of 10 replicates, Ruthe, April)

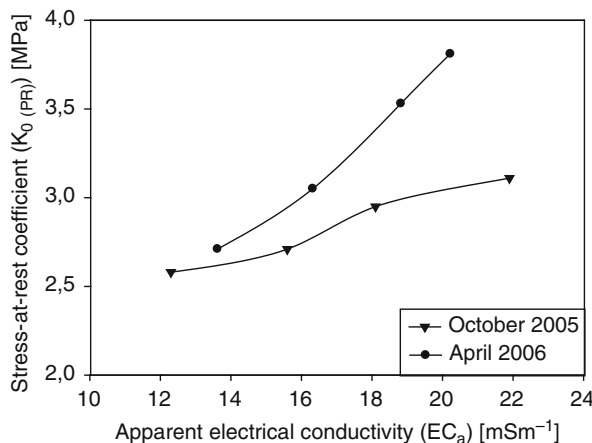


Fig. 22.6 Relationship between $K_0(\text{PR})$ and EC_a at Ruthe, subdivided into four classes

especially the $K_0(\text{PR})$ values in the compaction zone increased in the same rank order (Fig. 22.6).

This trend is observed both at experimental sites and for all measurement periods. The differences of the intensity and the distribution of the EC_a values are correlated with the average soil water content at the time of testing.

The PR values are slightly higher for autumn (lower soil water content) compared to spring (higher soil water content), without affecting the general PR characteristics.

Due to the instrument used, the reference measurement depth is 0.8 m (see Section 22.1), which was a fixed depth for all soils. Including only one reference depth may be considered arbitrary, but its reliability can be shown by the agreement between the postulated hydrostatic curve and measured PR at the base of the profile (0.8 m). Deviations are negligible near the soil surface and only increase slightly with increasing depth, except for the highly compacted zone (Figs. 22.4 and 22.5). However, no deviation occurs if the subsoil below the lowermost readings is non-compacted, as is generally found for the subarea with the lowest EC_a values.

22.4 Conclusions

Penetration resistance (PR) using hand-driven equipment such as the Penetrologger is easily measurable because the instrument is easy to handle, allows cost-effective measurements, and is readily transportable. Measurements can be performed quickly without extensive destruction of the site and the soil structure. This is the only method that can measure soil strength directly and in situ. A non-destructive method, which measures the apparent electromagnetic conductivity of a soil, is the EM38 probe. In general, a good correlation was found between the Penetrologger

values (PR) and those of the EM38 (EC_a), particularly over the depth range of 30–40 cm, which is generally the depth increment with the highest penetration resistance.

A reasonable agreement was also found for EC_a and the compaction state of the subsoil, $K_0(PR)$. Results show that $K_0(PR)$ is correlated with EC_a . This leads us to the conclusion that the non-destructive geophysically based EM38 technique can be used for detecting subplots with an extreme compaction or non-compaction state. However, up to now all our investigations have been made on loess-derived soils, which can be considered relatively homogeneous. Further investigations will show if this approach can be generalised.

Acknowledgement This chapter is dedicated to our colleague, mentor and fatherly friend Karl Heinrich Hartge. The authors want to thank especially Susanne K. Woche and Mary Beth Kirkham for improving the quality of the chapter.

References

Bachmann J, Contreras K, MacDonald AR, Hartge KH (2006) Comparison of soil strength data obtained in situ with penetrometer and with shear-vane. *Soil Tillage Res* 87:112–118

Bachmann J, Hartge KH (2006) Estimating soil stress distribution by using depth-dependent soil bulk-density data. *J Plant Nutr Soil Sci* 169:233–238

Domsch H, Giebel A (2004) Estimation of soil textural features from soil electrical conductivity recorded using the EM38. *Precision Agric* 5, 389–409

Doolittle J, Petersen M, Wheeler T (2001) Comparison of two electromagnetic induction tools in salinity appraisals. *J Soil Water Conserv* 56:257–262

Hartge KH, Bachmann J (2004) Ermittlung des Spannungszustandes von Böden aus Werten des Eindringwiderstandes von Sonden. *J Plant Nutr Soil Sci* 167:303–308 (in German)

Horn R, Hartge KH, Bachmann J, Kirkham MB (2007) Mechanical stresses in soils assessed from bulk-density and penetration-resistance data sets. *Soil Sci Soc Am J* 71:1455–1459

Kitchen NR, Drummond ST, Lund ED, Sudduth KA, Buchleiter GW (2003) Soil electrical conductivity and topography related to yield for three contrasting soil-crop systems. *Agron J* 95:483–495

Mertens FM, Welp SPG (2008) Spatial heterogeneity of soil properties and its mapping with apparent electrical conductivity. *J Plant Nutr Soil Sci* 171:146–154

Triantafilis J, Lesch SM (2005) Mapping clay content variation using electromagnetic induction techniques. *Comput Electron Agric* 46:203–237

Vitharana UWA, Van Meirvenne M, Cockx L, Bourgeois J (2006) Identifying potential management zones in a layered soil using several sources of ancillary information. *Soil Use Manage* 22:405–413

Chapter 23

Changes in Field Soil Water Tracked by Electrical Resistivity

**A. Besson, I. Cousin, G. Richard, H. Bourennane, C. Pasquier,
B. Nicoullaud, and D. King**

Abstract Recently, geophysical methods have been developed that can monitor soil characteristics spatially at high resolution. However, interpreting electrical measurements is difficult because geophysical data can be influenced by many soil variables, some of which vary over time. Our objective here was to use spatial measurements of electrical resistivity to define zones of homogeneity, to interpret them in terms of changing water contents, and to compare them with a soil map. Our underlying assumption was that the time variation of electrical resistivity at the field scale was only due to the dynamics of soil moisture in our studied field. Monitoring of soil electrical resistivity and soil moisture was performed at four dates during 2006 by two methods: by the use of the MUCEP (MultiContinuous Electrical Profiling) device, which gives measurements over a whole field, and by local gravimetric measurement of soil water content. Homogeneous zones were defined directly from measurements of the electrical resistivity and after ordinary kriging of the water content. Our analysis of spatial and temporal variability has permitted us to discriminate three temporally homogeneous zones, in terms of both electrical resistivity and water content, which were broadly related to the soil map. The use of electrical measurements enabled us to directly describe spatial and temporal changes in soil water content at the field scale and to describe some hydraulic processes, like lateral flows or upward capillary flows, that would be difficult to derive from soil maps.

Keywords Field scale · Time and space monitoring · Soil water content · Electrical resistivity

A. Besson (✉)

Unité de Science du Sol, INRA, Avenue de la Pomme de Pin, 45166 Olivet, France;
Department of Environmental Sciences and Land Use Planning, Université Catholique de Louvain,
Croix du Sud 2, BP 2, B-1348 Louvain-la-Neuve, Belgium
e-mail: Arlene.Besson@orleans.inra.fr

23.1 Introduction

Variability in the soil subsurface water content calls for a fine-scale description, both in space and time. It is commonly obtained by invasive measurements (gravimetric, TDR, and neutron probe). The last gives only a few isolated points of spatial or temporal information. In recent publications, geophysical and non-invasive methods – electric and electromagnetic methods – have been described that can quantify the characteristics of the soil, such as the soil water content, in a space continuum (Sheets and Hendrickx, 1995; Lambot et al., 2004; Guérin, 2005). One of them – the electrical resistivity or ER method, which is a technique that measures the resistance (in ohm.metre) of the soil – is well suited to characterise the soil subsurface and to describe soil properties, even when they are time dependent. Recent technical developments (Dabas et al., 2001) enable accurate, spatially continuous electrical estimates to be obtained at the field scale. However, electrical resistivity depends on several chemical and physical soil variables that can interact. Because of this, the effect of one soil parameter like soil water content on electrical resistivity is then hard to estimate.

Nevertheless, when temporal electrical measurements are made, they will be affected only by those soil parameters that vary with time, i.e. water content, temperature, and composition of the soil solution. If we were able in some way to correct for the effect of temperature and composition of the soil solution, electrical resistivity measurements of the soil could be interpreted in terms of water content.

Our study aimed at using the ER method to describe the spatial and temporal dynamics of soil water. Monitoring was done at the field scale using the MUCEP device, which gives spatially continuous measurements of electrical resistivity. Temporal analysis of these data enables us to define homogeneous zones of electrical resistivity and, as a consequence, of water content. We then compare the result with a conventionally prepared soil map, and discuss its usefulness for future investigations.

23.2 Materials and Methods

23.2.1 *Characteristics of the Soils Studied*

The study site is located in the Beauce region of France on a fallow field of 2 ha. The soils are Haplic Cambisols (WRB, 2007) formed on limestone materials. The differences between soils depend on the rock content and the thickness of the loamy-clay layer. From 39 boreholes, 8 soil units were defined on a soil map (Fig. 23.1).

23.2.2 *Soil Water Content Monitoring at the Field Scale*

Exactly 33 soil samples, located at different positions in the studied area, were taken at depths of 0–0.3, 0.3–0.5, 0.5–0.7, and 0.7–1.0 m on four dates in

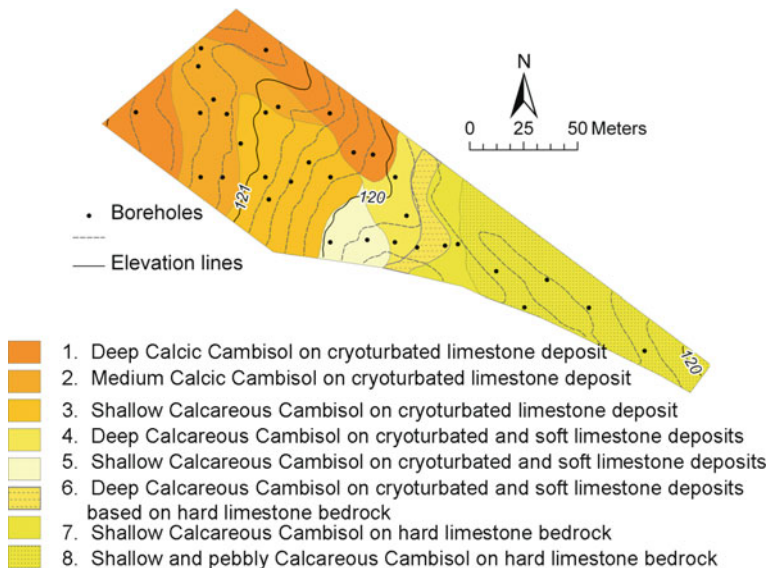


Fig. 23.1 Soil map of the study area. Black dots represent the locations of soil sampling

2006 (12/4, 1/6, 30/8, and 24/10). Because of systematic sampling, the samples were composed of a mixture of soil materials. Gravimetric water content w of the samples was determined. For comparison with the bulk electrical resistivity, mean values of soil water content were calculated for four depths: 0–0.3, 0–0.5, 0–0.7, and 0–1.0 m. The mean values were weighted by the layer thickness.

23.2.3 Electrical Monitoring Over Time

Electrical resistivity measurements were obtained at the field scale by the use of an MUCEP (multicontinuous electrical profiling) device (Fig. 23.2) on the same days as the soil water content monitoring.

MUCEP is a mobile soil electrical resistivity mapping system comprising a multi-probe system of three arrays (V1, V2, and V3) pulled by a cross-country vehicle. It also houses a resistivity meter (10 mA, 122 Hz) and a Doppler radar which triggers a measurement every 10 cm. The electrical measurement is an apparent resistivity defined as the integrated value of the real resistivity over the soil volume between the electrode arrays. Three arrays (V1, V2, and V3) are spaced 0.5, 1.0, and 2.0 m apart horizontally and hence give representative measures at increasing depths ('shallow', 'medium', and 'deeper'). The electrical profiles were spaced 2 m apart along parallel lines and were oriented SE–NW. All measurements were georeferenced by a dGPS (Trimble) device and recorded on a PC. At each sampling date and for each array, a minimum of 52,000 measurements

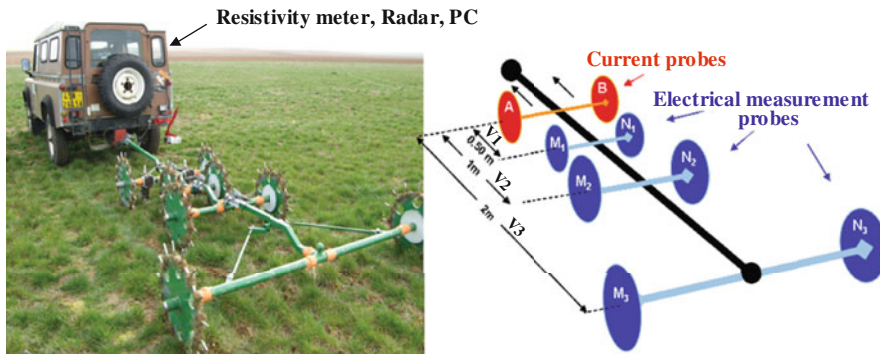


Fig. 23.2 The multicontinuous electrical profiling (MUCEP) device

were recorded. They were corrected for temperature by the equation of Keller and Frischknecht (1966):

$$ER_{T_{ref}} = ER_{T_m} [1 + \alpha(T_m - T_{ref})],$$

where $ER_{T_{ref}}$ is the corrected electrical resistivity at the reference temperature T_{ref} of 25°C, ER_{T_m} is the observed electrical resistivity at the measured temperature T_m , and α is the temperature coefficient (2%).

23.2.4 Spatial and Temporal Variability Analysis

For each date, the maps of water content and electrical resistivity were calculated by ordinary kriging with regular grids (5 m × 5 m for the water contents and 0.5 × 0.5 m for the electrical resistivity).

Spatial analysis of the temporal variability of soil water content and of electrical resistivity was undertaken by first calculating the normalised temporal mean map from the following equation:

$$\bar{X}_j = \frac{1}{4} \sum_{i=1}^4 \frac{x_{j,t_i} - \bar{x}_{t_i}}{s_{t_i}},$$

where x_{j,t_i} is the water content (or the electrical resistivity) at location j on date t_i and s_{t_i} is the standard deviation of the mean hydraulic or electrical state \bar{x}_{t_i} .

Negative (or positive) values for \bar{X}_j indicate that the water content or the electrical resistivity measured at location j on date t_i is always lower (or higher) than the spatial mean \bar{x}_{t_i} at t_i . Temporal maps were created with the same regular grids as the spatial maps; they carry no absolute unit.

23.3 Results and Discussion

23.3.1 Statistical Relationship Between Electrical Resistivity and Soil Water Content

For each date, a regression analysis was performed between the electrical resistivity measurements (V1, V2, and V3 arrays) and the corresponding soil water content of four soil layers (0–0.3, 0–0.5, 0–0.7, and 0–1.0 m). The linear determination coefficients and the Pearson correlation coefficient were calculated (Fig. 23.3).

Over a large range of soil water content, the determination coefficients were higher for the V1 array (about 40% for the soil layer of 0–0.7 m) than were for the other two (except in June). This suggests that the electrical resistivity measured by the V2 and V3 arrays was less sensitive to the soil water content measured within a depth of 1 m. We will therefore focus our analysis on the V1 array and on the soil water content of the 0–0.7 m layer in the following sections.

23.3.2 Spatial Analysis of the Experimental Data

Whatever be the date, the maps of electrical resistivity showed a similar spatial organisation in which three electrical zones can be defined (Fig. 23.4): high values

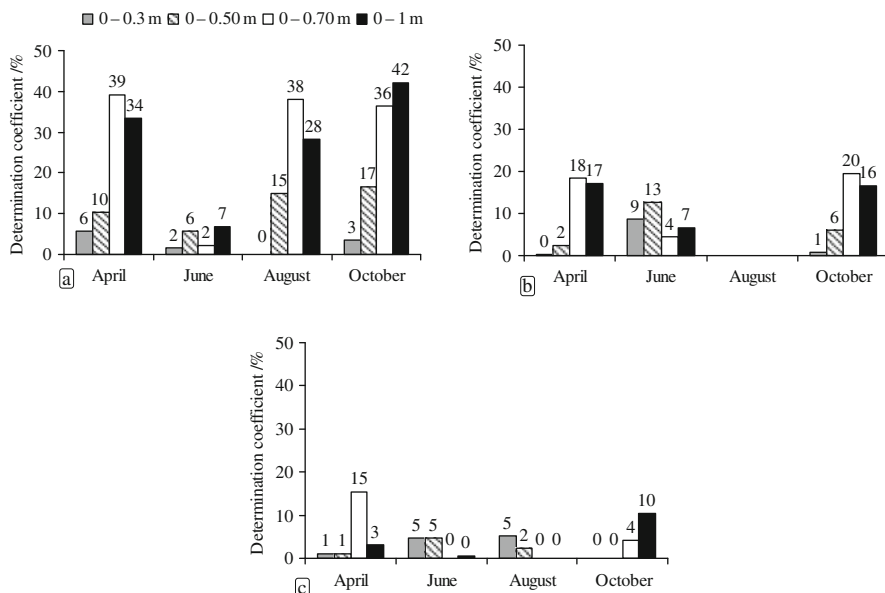


Fig. 23.3 Determination coefficient (R^2) of the linear relationship between the electrical resistivity measurements and the soil water content for each soil layer thickness (0–0.3, 0–0.5, 0–0.7, 0–1.0 m) for four dates. (a) V1 array; (b) V2 array; (c) V3 array

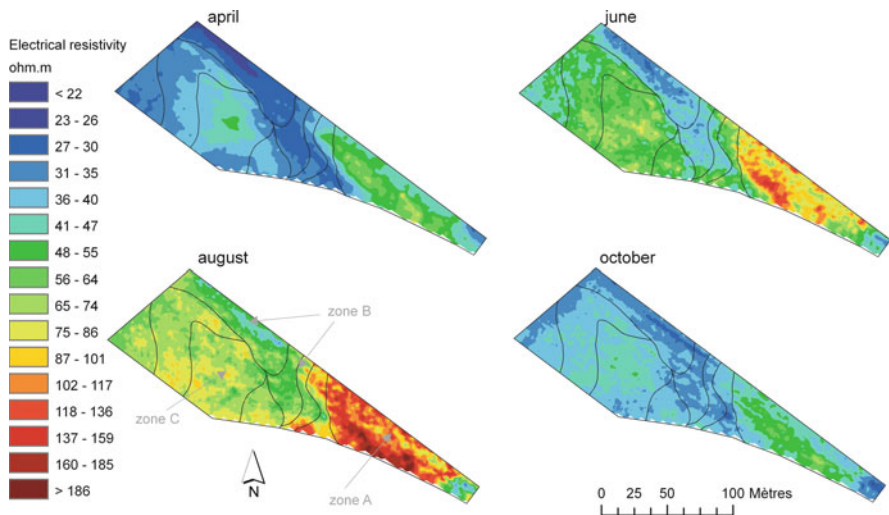


Fig. 23.4 Maps of electrical resistivity measured by the V1 array. Lines represent the limits of soil units and dots represent locations of soil water content measurements

on the south-east part of the study area (zone A), low values in the middle of the site (along a north-south corridor) and along the northern border (zone B), and intermediate values in the western part (zone C).

For all dates, the three zones (A, B, and C) in Fig. 23.4 can be related to areas on the soil water content map (Fig. 23.5). High electrical resistivity values match low soil water content values. This spatial organisation also corresponds to the soil types identified on the soil map (Fig. 23.1). Zone A corresponds to the shallowest soils, formed on the Beauce limestone bedrock. Zone B corresponds to deep soils

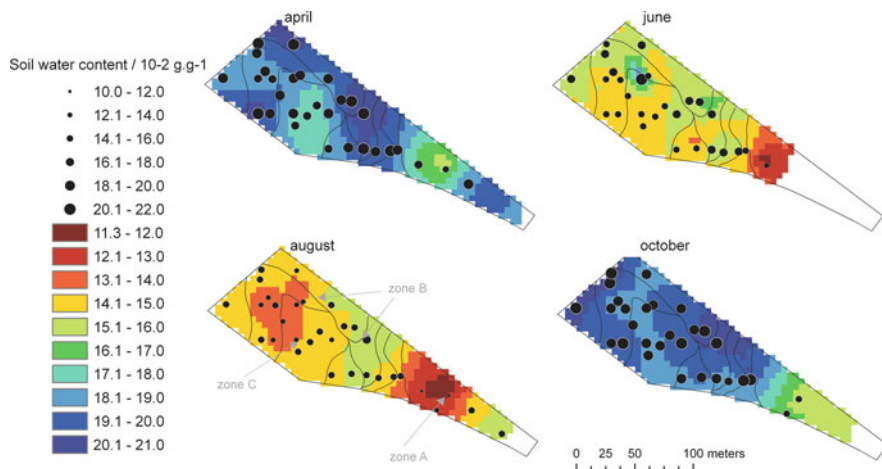


Fig. 23.5 Maps of water content measured between 0 and 0.70 m depth. Soil units are delineated by black lines. Black dots correspond to water content values locally measured after sampling

developed on the cryoturbated limestone deposit and on the soft limestone deposit. Zone C corresponds to soils thinner than 0.5 m developed on the cryoturbated limestone deposit.

Hence, the spatial variability of electrical resistivity depends not only on the soil water content but also on soil type and thickness of the loamy-clay layer. This confirms the view that temporal electrical measurements reveal only those soil parameters that vary with time, i.e. the water content.

23.3.3 Temporal Analysis of the Experimental Data

When we compare two values of electrical resistivity at the same location, the difference between them will not depend on the soil type (which is constant over the study) or on the soil temperature (which is corrected). We have already shown (Besson, 2008) that composition of the soil solution will not influence the results either. Only the water content can explain the difference between the values. We therefore make the hypothesis that temporal analysis of the electrical resistivity will help in assessing the temporal variability of the soil water content.

Estimating the spatial variability of water content is difficult because the sampling density of the prediction set is low (soil water content was not determined on the south-eastern part of the study zone because of the difficulty in sampling the hard Beauce limestone bedrock).

Zones B and C, identified on the electrical resistivity maps for each sampling date, are clearly evident on the temporal electrical resistivity map (Fig. 23.6a) and

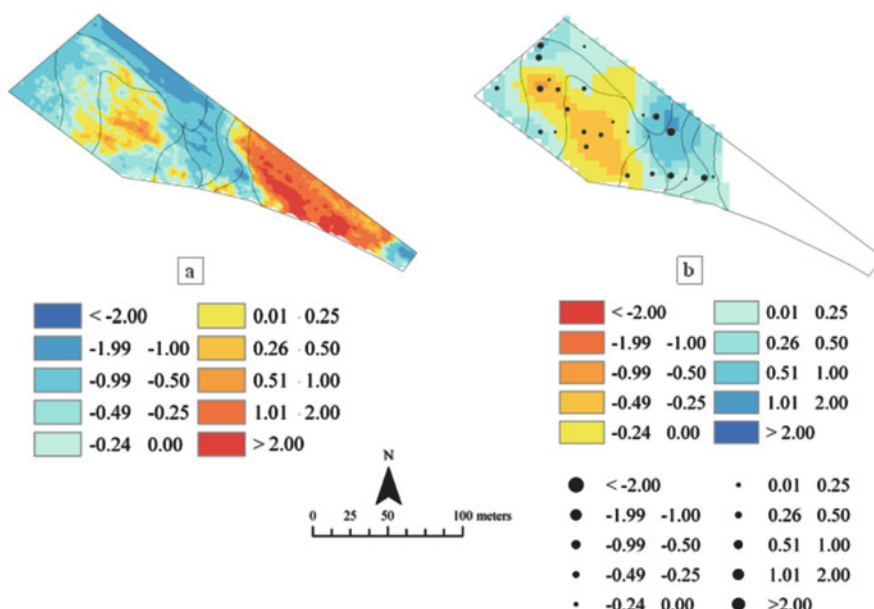


Fig. 23.6 Maps of temporal mean values of electrical resistivity measured by the V1 array (a) and the soil water content for the 0.07 m layer (b)

on the temporal soil water content map (Fig. 23.6b). Zone B corresponds to less than average temporal mean values for the electrical resistivity and to greater than average temporal values for the water content. (Negative values in Fig. 23.6 indicate values less than the mean.) On the other hand, zone C corresponds to higher temporal mean values for electrical resistivity and lower temporal mean values for the water content. In zone A, the temporal mean values for the electrical resistivity are high.

In summary, the zones of low electrical resistivity are similar to the zones of high soil water content and the same can be said, with shifted values, for zones B and C. In zone A, one assumes that the temporal mean values for the water content would be uniformly low.

23.4 Conclusion

Electrical resistivity measured by the MUCEP device is well suited to describe spatial and temporal soil hydraulic variability at a field scale. Its use allowed us to extrapolate temporal changes of water content to unknown zones. We could discriminate three electrical zones corresponding to the soil water content contrasts found on the soil hydraulic maps, with lower soil water content values being related to higher electrical resistivity values and to the soil units.

Analysis of the temporal means of electrical resistivity and water content showed a similar spatial organisation: the zones that present, over time, low soil water contents corresponded to those that present, over time, high electrical resistivity, and these zones can be related to the soil units. As far as soil hydrology is concerned, our temporal analysis of changes in water content shows that the flows in our studied field are probably only vertical, not lateral.

References

Besson A (2008) The influence of the soil water content and the composition of the soil solution on the electrical resistivity of undisturbed soil samples. Ph.D. thesis, INRA, Orléans, France, pp 91–110

Dabas M, Tabbagh A, Boisgontier D (2001) Multi-depth continuous electrical profiling for characterization of in-field variability. European conference on precision agriculture, Montpellier, France, 18–21 June 2001

IUSS Working Group WRB (2007) World reference base for soil resources. World soil resources reports no. 103. FAO, Rome

Guérin R (2005) Borehole and surface-based hydrogeophysics. *Hydrogeol J* 13:251–254

Keller GV, Frischknecht FC (1966) Electrical methods in geophysical prospecting. Pergamon Press, Oxford

Lambot S, Rhebergen J, van den Bosch I, Slob EC, Vanclooster M (2004) Measuring the soil water content profile of a sandy soil with an off-ground monostatic ground penetrating radar. *Vadose Zone J* 3:1063–1071

Lund ED, Christy CD, Drummond PE (1999) Practical applications of soil electrical conductivity mapping, In: Stafford IJV (ed) Precision agriculture '99. Proceedings of the European conference on precision agriculture. Sheffield Academic Press, Sheffield, pp 771–779

Sheets KR, Hendrickx JMH (1995) Non invasive soil water measurement using electromagnetic induction. *Water Resour Res* 31:2401–2409

Chapter 24

Is a Systematic Two-Dimensional EMI Soil Survey Always Relevant for Vineyard Production Management? A Test on Two Pedologically Contrasting Mediterranean Vineyards

G. Coulouma, B. Tisseyre, and P. Lagacherie

Abstract Thanks to recent technological developments, apparent soil electrical conductivity (EC_a) can now be mapped over large areas, providing new data for precision agriculture. However, in Mediterranean vineyards, rooting depth can be greater than usual and the volume of soil that needs to be explored is greater. This study examined two vineyard blocks in southern France and looked at the ability of an EC_a map, derived from a commercial mobile EMI system, to predict water-related vineyard variability [defined by variation in a normalised difference vegetation index (NDVI) map of the canopy]. To validate the EC_a -canopy relationship, electrical resistivity tomography (ERT) profiles and soil observations (42 soil cores sampled to 4 m depth) were made over seven representative transects across the two blocks. In one of the blocks, the EC_a map and the NDVI map were correlated, whereas only weak correlations were found for the other block. The examination of ERT data and soil observations in the first block showed a clear relation between soil electrical properties and soil properties known to influence vine water supply (e.g. bedrock depth) and a good discrimination of ERT measures at the measurement depth explored by EM38. In contrast, the second block showed lower ERT measurements and they were not directly related to any soil property that could cause variations in plant water. The contrasting responses between the two blocks demonstrate, as a prerequisite to EC_a survey, the importance of prior and local knowledge of soil patterns.

Keywords Electromagnetic induction (EMI) · Electrical resistivity tomography (ERT) · Apparent electrical conductivity (EC_a) · Map comparison method

G. Coulouma (✉)

INRA UMR LISAH, 2 place viala, 34060 Montpellier, France
e-mail: coulouma@supagro.inra.fr

24.1 Introduction

Electromagnetic induction (EMI) is a common geophysical method used for real-time, on-the-go soil sensing in precision agriculture (PA). EMI records in situ the soil's apparent electrical conductivity (EC_a), a measure strongly correlated with various soil properties such as moisture content, clay content, clay mineralogy, ionic strength of the soil solution, and bulk density (Corwin and Lesch, 2005; Samouëlian et al., 2005). High-resolution EC_a maps are now routinely produced over large areas by private companies for agronomic management (Chapter 2). This technique has recently been introduced into viticulture (Taylor et al., 2005), where the EC_a maps are assumed to give useful data for delineating vineyards into management zones reflecting plant vigour and yield.

However, such inferences from EC_a maps have been strongly questioned by some (McKenzie, 2000), and the limits of the technique need to be better defined, especially in viticulture. Certainly, most users do not recommend interpretation of EC_a maps without some auxiliary data or ground truthing. Several problems can arise when using EC_a for management: (i) the lack of well-identified relations between the EC_a signal and the local soil and material properties; (ii) difficulties encountered when the EMI sensor does not respond to locally limiting soil parameters, for example, high or low soil pH, or when it responds to non-soil factors, such as wire trellising; and (iii) issues with data quality associated with mobile platforms and post-processing of data. Here we will evaluate the relative importance of these questions and in so doing set out refined strategies for using this innovative technique.

This chapter presents results of a specific experiment in a vineyard in southern France. It concerns EMI and NDVI maps from commercial suppliers on two contrasting blocks of 1.2 ha each. In these non-irrigated and well-established vineyards, the NDVI data are considered suitable for accurately delineating permanent management zones based on vine water status. Additional EC_a measures and soil observations were made to interpret the EC_a maps and isolate the different possible permutations. This validation is expected to provide an evaluation of the utility of EC_a maps in vineyards where NDVI is unavailable, for example, in designing vineyards before planting, or maybe less relevant, in irrigated vineyards.

24.2 Materials and Methods

24.2.1 Location, Geology, and Pedology

The experimental sites, Block 96 and Block 64, were located near Narbonne ($43^{\circ}08'33''$ N, $3^{\circ}07'59''$ E, WGS84, Aude, southern France) on the 'La Clape' massif, a little Pyrenean thrust sheet of Cretaceous marine deposits. Two contrasting blocks were chosen with different soil types and materials (Fig. 24.1).

Block 96 is situated in a depression on marls and marlstones. It presents significant within-block soil variability characterised by (i) an outcrop of marlstone in the

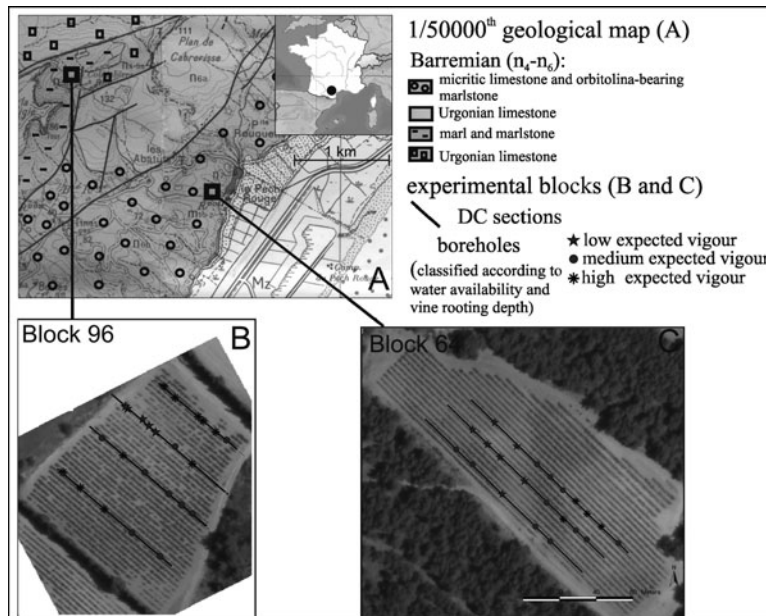


Fig. 24.1 Location and geological context of experimental blocks. (a) Presentation of the geological map. (b, c) Airborne images of the two experimental blocks with electrical resistivity tomography (ERT) transects in bold lines. Location of soil cores on the ERT transects is also shown

NW upper part and (ii) colluvial soils with or without coarse fragments of Urgonian limestone developed over an older loamy colluvial deposit in the southern part of the block. Block 64 is situated on a hillside. Its geological formation is composed of (i) interbedded micritic limestone and orbitolina-bearing marlstone in the upper part and (ii) important accumulations of red clay in the lower part of the block. Gravely soil is developed from and over micritic limestone. Colluvial soils with or without coarse fragments of limestone are present over the red clay in the lower part of the block.

24.2.2 Geophysical Surveys

EC_a maps were acquired from SIS John Deere. They were completed for the two blocks in June 2006 using an EMI sensor towed behind an all-terrain vehicle (ATV) and geo-referenced with an RTK-GPS receiver. Data acquisition was made every three vine rows (row spacing was 2.2–2.5 m). The depth of investigation was approximately 1 m and the signal was integrated across all the horizons. The final resolution of the EC_a map provided by SIS was 1 m², meaning that the raw

data were interpolated to sub-row dimensions. The raw EC_a survey data were not supplied.

To evaluate the validity of the EC_a survey, three additional geophysical datasets were created as follows:

- (1) Ninety EC_a measurements were made with a handheld Geonics EM38 in the vertical coil position (VCP) in May 2007. There were 40 measurements made over the two target blocks (Fig. 24.1) and another 50 measurements were made over five adjacent blocks located in the same vineyard where the SIS data were collected.
- (2) Two-dimensional electrical resistivity tomography (ERT) sections were made along three transects in Block 64 and four transects in Block 96 in May 2007. Locations of the transects are represented by bold black lines in Fig. 24.1b, c. ERT measurements were performed using a Wenner–Schlumberger array at an electrode spacing of 1 m. On each transect, 50 electrodes were used simultaneously to provide the apparent electrical resistivity over the profile (~ 0.5 m increments down the profile to a depth of 5 m). The soil electrical conductivity (EC) (Fig. 24.6) for each soil and layer was derived from the electrical resistivity measurement using an inverse method, i.e. the Gauss–Newton code Res2dinv as described by Locke (2002).
- (3) Isolated 1-m-spaced EC_a values were computed from the ERT dataset to simulate a 1D EC_a measurement to a depth of 1 m. This corresponded to the median depth of investigation (doi) of the EMI sensor used by the SIS John Deere.

Four types of geophysical data were therefore available on both blocks:

- (i) I-EC_a, an interpolated EC_a map from a mobile EM38 (doi ~ 1 m),
- (ii) P-EC_a point measurements from a handheld EM38 system (doi ~ 1 m),
- (iii) R-EC electrical conductivity along seven transects derived from ERT (doi ~ 5 m), and
- (iv) R-EC_a to a median depth of 1 m derived from an inverse algorithm of the ERT measurements.

All the data were geo-referenced. This dataset was designed to compare geophysical data from different sources to identify possible sources of error. Although the geophysical investigation dates were different for the commercial and manual measurements (June 2006 and May 2007), they both corresponded to very dry conditions, permitting valid comparisons.

24.2.3 Soil Survey

There were 22 soil cores in Block 64 and 20 soil cores in Block 96 sampled to a maximum depth of 4 m along the ERT sections. The depth of investigation was less

than 4 m in some areas due to shallow soils or subsoil constraints. The soil cores were described according to the STIPA system (Falipou and Legros, 2002), with classical observations (e.g. texture class, colour, and coarse fragments) for each soil horizon and material.

Soil materials within each block were different, varying in hardness and depth. Marlstone outcrops in Block 96, and micritic limestone or orbitolina-bearing marlstone in Block 64, dramatically limit rooting depth. The colluvial deposits in Block 96 and red clay in Block 64 are easily colonised by roots, allowing deep rooting in these areas. The water supply in colluvial soils depends on textural characteristics and coarse fragment proportion. In Block 64 an increase in the gravelly colluvial soil thickness over the red clay may reduce vine vigour. Each soil core was analysed according to material hardness and soil properties. Expert knowledge of the local environment, together with the soil core information, was used to delineate three distinct soil classes in each field. These three classes were related to the expected vigour (low, medium, and high) (Fig. 24.2). These expert-defined classes form a reference for the subsequent analysis.

The spatial patterns of the R-EC data in Block 64 were easily interpretable from the 22 soil cores, and a simple 2D model was developed to convert the ERT readings into soil texture/mineralogy maps. The model was applied to 220 simulated soil cores across the three transects to create 2D soil texture maps. For each simulated soil core, the presence of each different soil type was recorded. A value of EC_a , which corresponded to a median investigation depth similar to the EM38, was extracted from the ERT data along with the soil type information. This permitted expected frequency distributions of EC_a for each soil type to be generated.

For Block 96, the relationship between the soil texture/mineralogy and the ERT response was unclear, and so this analysis was not undertaken.

24.2.4 NDVI Maps of Vine Vigour and Map Comparison

Within-block vine vigour was estimated from NDVI images obtained from an airborne multi-spectral platform at 1 m^2 resolution. The images were provided by the Avion Jaune Company. The NDVI was resampled in Matlab with a moving

	class A	class B	class C
Block 64	gravelly soil over micritic limestone or marlstone	clayey gravelly soil over red clay	loamy soil over red clay
Block 96	gravelly soil over marlstone	clayey gravelly soil over loamy colluvial deposit	loamy soil over loamy colluvial deposit

soil water availability and rooting depth

Fig. 24.2 Presentation of the classification of soils and materials according to soil water availability and hardness. Three classes were expert defined; they are ranked from lowest (*class A*) to highest (*class C*) expected vigour

average window of $3\text{ m} \times 3\text{ m}$ to avoid row effects. In non-irrigated conditions in Mediterranean environments, vine vigour is directly related to rooting depth and soil properties which determine water availability.

The I- EC_a maps and NDVI maps of both blocks were classified into three equal quantiles and compared point to point with the Kappa method (Visser et al., 2006). The output coefficient K of the Kappa method ranges from -1 (inverse spatial patterns) to 1 (same spatial patterns). A value of 0 indicates that patterns observed on the maps are completely independent.

24.3 Results

24.3.1 Relations Between NDVI, Soil, and EC_a

Table 24.1 shows the mean NDVI values obtained from the expert-defined soil classes for both blocks. Low NDVI values were observed in soil class A for both blocks. Higher NDVI values were observed in class B and C soil types. Gravely soil over micritic limestone and marlstone drastically reduced the vine vigour. No significant differences in vine vigour were observed between class B and C soils. Obviously, this result shows that soil types may have a strong effect on vine vigour, through water availability and rooting depth. However, differences are less than expected between classes B and C. There may be two reasons for this result: (i) elevation, which may cause larger water accumulation in the lower part of the blocks, could enhance vine vigour in class B soils situated in the lower part of both blocks and (ii) the difference in vigour is too small and NDVI is not accurate enough to record this small variation.

However, this comparison identifies at least two different soil classes in both blocks and the EC_a survey should therefore constitute a relevant information source to delineate these different soil and vigour zones.

In order to check the relevance of EC_a maps for delineating vigour zones, the NDVI maps were compared to the EC_a maps in both blocks (Fig. 24.3). The K coefficient in Block 96 is very weak ($K = 0.008$), indicating no relationship between

Table 24.1 Mean NDVI values obtained from expert-defined soil class for both blocks (Block 64 and Block 96). Three soil classes are considered from the lowest (*class A*) to the highest (*class C*) expected vigour

Soil and material classes	NDVI	
	Block 64	Block 96
Class A	0.07 ± 0.02 (7) a	0.07 ± 0.01 (5) a
Class B	0.16 ± 0.04 (11) b	0.21 ± 0.07 (9) b
Class C	0.13 ± 0.04 (4) b	0.19 ± 0.03 (10) b

Mean \pm standard deviation (number of samples). Different small letters (a–b) represent a significant difference between means only within a same column (*t*-test, at $p < 0.001$ level)

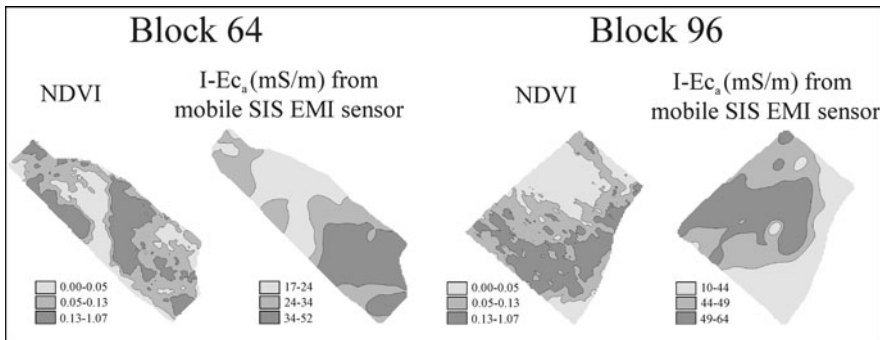


Fig. 24.3 NDVI and $I-EC_a$ maps for the two blocks. The four maps were realised using a classification into three equal quantiles

the EC_a and NDVI maps in this block. For Block 64, the K coefficient is higher ($K = 0.33$) but still low.

This result, in addition to map comparison (Fig. 24.3), highlights two different situations. For Block 96, the EC_a map seems to be irrelevant in delineating plant vigour zones. Conversely, for Block 64, some parts of the block show similar patterns for EC_a and NDVI and other parts no similarity, which explains a low K coefficient. Regarding the relationship between the soil classes and NDVI, a significant relation was not expected in both blocks due to the similar NDVI response of classes B and C. However, the significant difference in response observed between the two blocks is of concern, particularly the low K coefficient observed in Block 96. The EC_a maps seem to fail to delineate vine vigour, particularly in Block 96. The reasons which might explain this failure are investigated in the next sections.

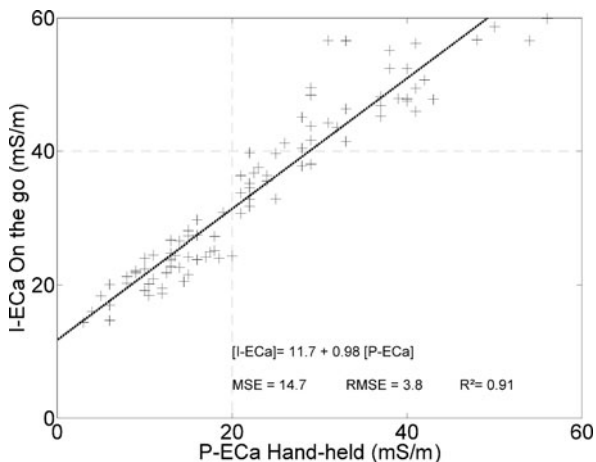
24.3.2 Differences Between Different EC_a Measurements

Among all the possible permutations that may explain the differences between the EC_a and NDVI maps, one is the accuracy and the quality of EC_a data provided by the SIS company. Map quality may be affected by the fact that the EMI sensor is mounted on a mobile platform (and subject to erratic shifting, which may induce error from external metal sources); alternatively, there may have been insufficient data density during surveying, or data smoothing and data interpolation may have been excessive. The following sections investigate the likelihood of these error sources.

24.3.2.1 Erratic Shifting with Mobile EMI

In the case of mobile platforms, erratic shifting behind the ATV may involve irregular change in EC_a due to a magnetic interaction with steel posts and trellis wire (Lamb et al., 2005). This effect is limited by handheld measurement where the

Fig. 24.4 Relationship between I- EC_a on the go and P- EC_a from handheld EM38

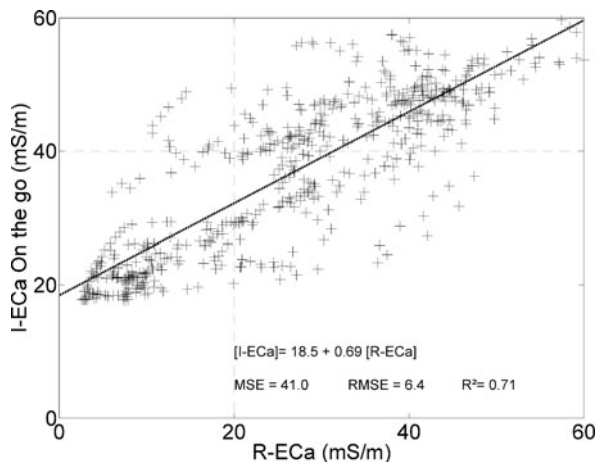


sensor is maintained carefully in the centre of the inter-rows. In order to quantify potential problems due to erratic shifting, a comparison between P- EC_a values from a handheld EM38 and I- EC_a from the mobile EM measured in both blocks and in five other blocks was made. Graphical results of the comparison are presented in Fig. 24.4. A high coefficient of determination ($R^2 = 0.91$) was observed between the systems and a slight offset of $\sim 12 \text{ mS m}^{-1}$. The offset is likely due to calibration error between the sensors (Sudduth et al., 2001) and small differences in soil moisture and temperature between the two measurement dates. The high coefficient of determination is encouraging, especially given that a comparison between the point (handheld) and interpolated (map) data will introduce some uncertainty with geo-location. The results lead to the conclusion that the EC_a map from the mobile EMI is comparable to the handheld EM38 measurements, and map quality is unlikely to be the source of gross error in the analysis.

24.3.2.2 Comparison Between R- EC_a and I- EC_a

As well as the handheld EM38 measurements, the EC_a map was compared to the 1 m R- EC_a data derived from the ERT. Figure 24.5 shows a plot of the two variables along the seven transects in the two blocks. Although there is a significant positive coefficient of determination ($R^2 = 0.71$), the lowest values of R- EC_a derived from the ERT are less than those of the I- EC_a derived from mobile EMI. These values correspond to EC between 1 and 10 mS m^{-1} on gravelly soil and limestone. As already shown by other authors (Dabas and Tabbagh, 2003; Sudduth et al., 2003), this result highlights the problems of signal attenuation in the case of low conductivity for EMI technology. However, regarding the magnitude of variation of EC_a values in these blocks, this problem concerns only a small range of data. Again, given the possible

Fig. 24.5 Relationship between I-EC_a on the go and R-EC_a from ERT measurements



errors with geo-location, data conversion, and temporal differences, the strong positive relationship between the I-EC_a map and R-EC_a data indicates that the EC_a map quality is not a major source of error. Furthermore it shows that fixing at 1 m, the median investigation depth represents an acceptable hypothesis to compare I-EC_a from EMI and R-EC_a from ERT.

24.3.3 Electrical Conductivity of Different Soils and Materials in the Two Blocks

Section 24.3.2 eliminated map quality as a potential error source contributing to the lack of concordance between the NDVI and I-EC_a maps observed in Section 24.3.1. The aim of this section is to focus on the relationship between EC_a values and soil properties in the two experimental sites to see if pedological knowledge helps in the interpretation of the NDVI and I-EC_a maps. The results of the ERT data model inversion are associated with soil cores in order to determine EC of different soil types.

Figure 24.6 shows electrical conductivity ranges of the different soil types observed in both blocks. The observed ranges of conductivity are similar to previous measurements recorded for these soil types (Telford et al., 1990). Strongly contrasted soil profiles gave large ranges in electrical conductivity in Block 64 ($1\text{--}115\text{ mS m}^{-1}$). In contrast, strongly contrasted soil profiles gave narrow ranges in electrical conductivity in Block 96 ($30\text{--}50\text{ mS m}^{-1}$). Although the soil types in Block 96 have contrasting texture and hardness, differences in conductivity are not significant except between the loamy colluvial deposits and gravelly soils (t -test at $p < 0.05$, data not shown).

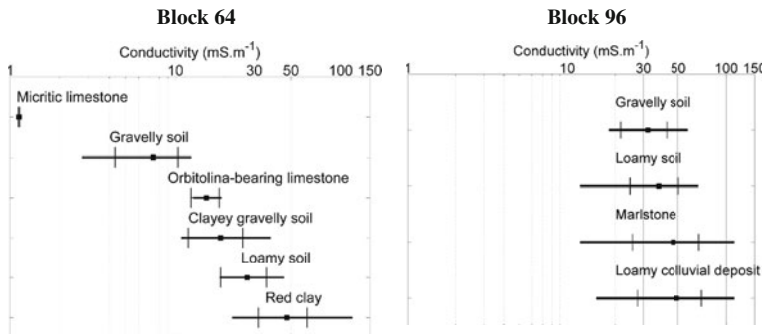


Fig. 24.6 Ranges of R-EC calculated for each soil and material on both fields. The mean conductivity is represented by a black square and the standard deviation by vertical lines

The high conductivity values of marlstone, which constitutes a vine rooting limit, are probably due to the high clay content, and the similar EC response on contrasting soil types may explain the lack of similarity between the NDVI and EC_a maps in Block 96. In Block 64, the EC data are able to differentiate several soil types, indicating that the EC_a data should be of use in this field, although some dissimilarities between the NDVI and EC_a maps still have to be addressed. In order to understand these dissimilarities, the following section focuses on a more detailed study of Block 64.

24.3.4 Soil Type Detection with EC_a Data

Plate 24.1 shows the predicted soil types, from our simple model relating the soil core information to the ERT data, overlain on the original 2D ERT map. The location and the depth of the actual soil cores are also indicated.

Figure 24.7 shows two examples of the distribution of EC_a values from the simulated soil data. Simulation was done to mimic the expected EMI sensor response and to compare (i) sites with red clay and no limitation to rooting depth to sites with micritic limestone that limits rooting depth and (ii) sites with a loamy soil over a red clay (which provides good soil moisture availability and good rooting depth) to sites with a deep gravelly clayey soil that may encounter problems with rooting depth or soil water retention when the coarse fragment percentage is high.

The first comparison shows two distinct distributions for the two soil types, which makes it easy to differentiate the soil types. The second example illustrates that even though some soil types are easily differentiated, there are still some contrasting soil types in the block that produce similar and overlapping EC_a distributions. This makes it almost impossible to differentiate all soil types in the block on the basis of EC_a alone. This explains why there are still some dissimilarities between the EC_a and NDVI maps in Block 64 and further highlights the need to understand the pedology of the block prior to interpreting the EC_a data.

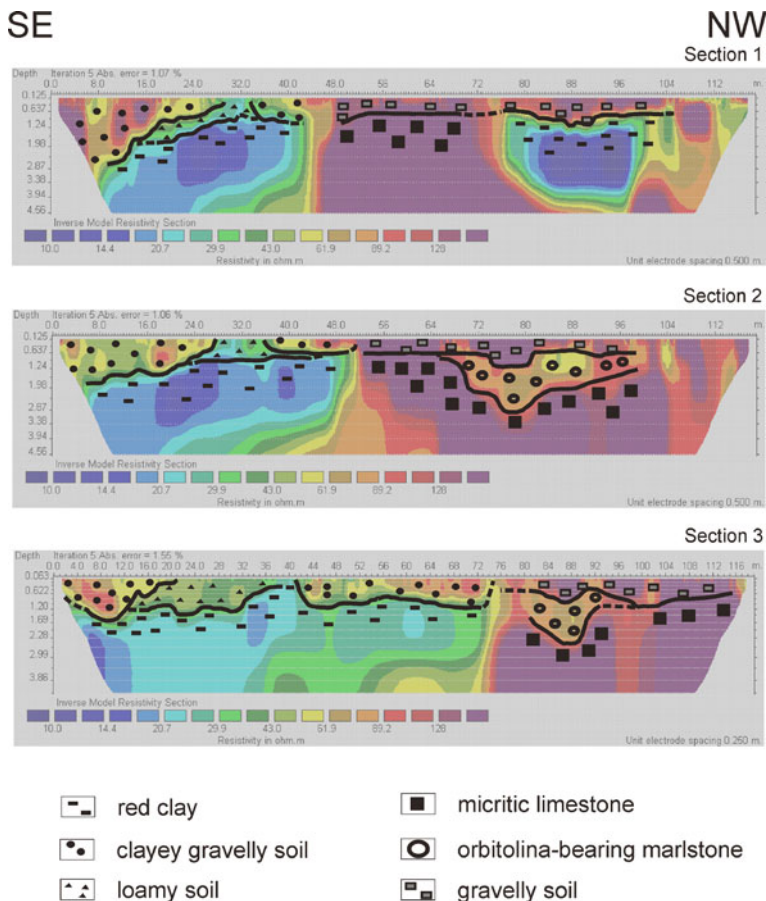


Plate 24.1 The three ERT transects calculated on Block 64 and results of the simple model applied to 220 simulated soil cores across the three transects to create 2D soil maps. The patterns in the horizontal and vertical ER data in Block 64 were easily interpretable from the 22 soil cores and a simple 2D model was developed to convert the ERT readings into soil texture/mineralogy maps

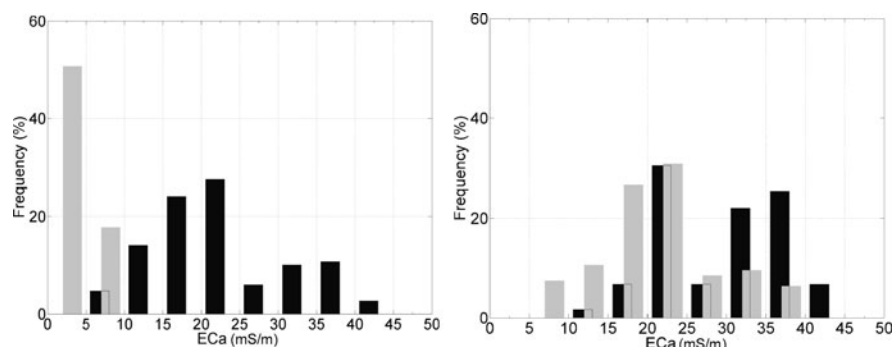


Fig. 24.7 Distribution of R-EC_a observed on Block 64 in two different pedological situations. (a) Micritic limestone (gray) and red clay (black), (b) clayey gravelly soil (gray) and loamy soil (black)

24.4 Discussion and Conclusions

This study examined the ability of EC_a (EMI) maps from a commercial, on-the-go EMI sensor to explain observed vineyard variability in two pedologically contrasting blocks. A preliminary comparison between vine vigour maps, derived from airborne images and expert-defined soil classes, showed that soil classification assisted in delineating differences in vine vigour. Vigour maps were also compared to the EC_a maps. A simple comparison of the spatial patterns in the two maps illustrated the potential difficulties in using EC_a maps as a surrogate to determine perennial management zones. Investigations were undertaken to identify the reasons for these dissimilarities. Results from these investigations showed the following:

- (i) The commercial EC_a data were highly correlated with manual handheld EC_a measurements. This indicates that the commercial EC_a map did not contain error or bias from the mode of sensor operation or the method of data analysis. It also points out the small effect that the vineyard trellis wire and steel posts have on the data.
- (ii) EC_a data provided by an invasive method (ERT) were correlated with the EC_a data from the non-invasive method (EMI) used in the commercial survey. However, in accordance with the literature, signal attenuation in the EMI data was observed in low-conductivity soils, leading to an over-estimation of EC_a values with EMI at these sites. In this particular instance, this problem occurred across only a small range of data and did not explain on its own the dissimilarities observed between the EC_a and vigour maps. In other conditions (with a majority of low-conductivity soils), this observation could be a significant drawback with EMI surveys.
- (iii) For one of the blocks investigated, Block 96, the different soil types, which drive plant vigour, exhibited very similar conductivity values. Therefore, the EC_a data can be considered ineffective for differentiating different soils where significant differences in vine vigour are observed. This result highlights a strong limitation of EC_a maps in determining vigour zones for soils with similar EC_a responses. For the second block, Block 64, the EC_a map was able to discern between two soil types (red clay versus micritic limestone). However, the results also showed, for this block, the poor ability of EC_a data to discriminate between two other soil types, loamy soil over red clay and loamy soil with deep clayey gravelly soil, that may induce significant differences in rooting depth and water availability.

In conclusion, these results show the extreme care that must be taken in using systematic EMI to delineate vineyard management zones in non-irrigated Mediterranean conditions. There are several points that need to be considered.

- (i) The depth of investigation of EMI may be of importance in non-irrigated conditions. Obviously, rooting depth changes drastically as a function of soil conditions. This aspect was not the purpose of our study; however, further

experiments should be conducted in order to study the potential improvement in using an EMI survey with a more suitable depth of investigation compared to a vine rooting system.

(ii) This study focused on EMI in dry conditions. These conditions may not be the best to differentiate soil properties in relation to vine vigour. Further work is needed to evaluate the usefulness of EMI in wet conditions. Another relevant approach would be based on two surveys, one under dry and the other under wet soil conditions, and an analysis of the differential EC_a . This new information could be relevant to differentiate soil characteristics which were not possible to discriminate with EC_a data collected only in dry conditions.

Finally this study points out the necessity that EC_a always needs to be interpreted with as much additional information as possible (and not by itself) to get the most benefit from the EC_a data.

Acknowledgement This experiment was carried out in the 'Pech Rouge' vineyards of the INRA experimental laboratory and was undertaken within the program 'Institut Languedocien de l'Eau et de l'Environnement'. We thank particularly Mr. O. Huttel for his help in ERT measurements and data inversion and J.L. Belotti for his help in soil sampling. The authors thank J. Taylor for assisting with the English as well as improving comments and analysis of our results.

References

Corwin DL, Lesch SM (2005) Apparent soil electrical conductivity measurements in agriculture. *Comput Electron Agric* 46:11–43

Dabas M, Tabbagh A (2003) A comparison of EMI and DC methods used in soil mapping – theoretical considerations for precision agriculture. In: Stafford J, Werner A (eds) *Precision agriculture*. Wageningen Academic Publishers, Wageningen, pp 121–127

Falipou P, Legros JP (2002) Le système STIPA-2000 d'entrée et édition des données pour la banque nationale de sols DONESOL II. Etude et Gestion des Sols 9:55–70 (in French)

Lamb DW, Mitchell A, Hyde G (2005) Vineyard trellising with steel posts distorts data from EM soil surveys. *Aust J Grape Wine Res* 11:24–32

Loke MH (2002) Tutorial: 2D and 3D electrical imaging surveys. Technical note, 2nd edn. Malaysia

McKenzie D (2000) Soil survey options prior to vineyard design. *Aust Grapegrower Winemaker Annu Tech Issue* 438a:144–151.

Samouelian A, Cousin I, Tabbagh A, Bruand A, Richard G (2005) Electrical resistivity survey in soil science: a review. *Soil Till Res* 83:173–193

Sudduth KA, Drummond ST, Kitchen NR (2001) Accuracy issues in electromagnetic induction sensing of soil electrical conductivity for precision agriculture. *Comput Electron Agric* 31: 239–264

Sudduth KA, Kitchen NR, Bollero GA, Bullock DG, Wiebold WJ (2003) Comparison of electromagnetic induction and direct sensing of soil electrical conductivity. *Agron J* 95:472–482

Taylor J, Tisseyre B, Praat J-P (2005) Bottling good information: mixing tradition and technology in vineyards. *Frutic '05 symposium*, Montpellier, France, Sept 12–16

Telford WM, Geldart LP, Sheriff RE (1990) *Applied geophysics*, 2nd edn. Cambridge University Press, Cambridge

Visser H, de Nijs T (2006) The map comparison kit. *Environ Model Software* 21:346–358

Part V

Radar and Gamma Radiometric Sensors

Chapter 25

Full-Waveform Modelling and Inversion of Ground-Penetrating Radar Data for Non-invasive Characterisation of Soil Hydrogeophysical Properties

S. Lambot, E. Slob, J. Minet, K.Z. Jadoon, M. Vanclooster, and H. Vereecken

Abstract We present a new technique for real-time, proximal sensing of the soil hydrogeophysical properties using ground-penetrating radar (GPR). The radar system is based on international standard vector network analyser technology, thereby setting up stepped-frequency continuous-wave GPR. The radar is combined with an off-ground, ultra-wideband, and highly directional horn antenna acting simultaneously as transmitter and receiver. Full-waveform forward modelling of the radar signal includes antenna propagation phenomena through a system of linear transfer functions in series and parallel. The system takes into account antenna–soil interactions and assumes the air–subsurface compartments as a three-dimensional multilayered medium, for which Maxwell's equations are solved exactly. We provide an efficient way for estimating the spatial Green's function as a solution of Maxwell's equations from its spectral counterpart by deforming the integration path in the complex plane of the integration variable. Signal inversion is formulated as a complex least squares problem and is solved iteratively using the global multilevel coordinate search optimisation algorithm combined with the local Nelder–Mead simplex method. The electromagnetic model has unprecedented accuracy for describing the GPR signal in controlled laboratory conditions, providing accurate estimates for both soil dielectric permittivity and electrical conductivity. The proposed method has been specifically designed for the retrieval of soil surface dielectric permittivity and correlated surface water content, which has been validated in field conditions. We also show that constraining the electromagnetic inverse problem using hydrodynamic modelling theoretically permits retrieval of the soil hydraulic properties and reconstruction of continuous vertical water content profiles from time-lapse GPR data. The proposed method shows great promise for field-scale, high-resolution digital soil mapping, and thereby for bridging the

S. Lambot (✉)

Earth and Life Institute, Université Catholique de Louvain, Croix du Sud 2, Box 2, B-1348 Louvain-la-Neuve, Belgium; Agrosphere (ICG-4), Institute of Chemistry and Dynamics of the Geosphere, Forschungszentrum Jülich GmbH, D-52425 Jülich, Germany
e-mail: sebastien.lambot@uclouvain.be; s.lambot@fz-juelich.de

spatial-scale gap between ground truthing based on soil sampling or local probes and airborne and spaceborne remote sensing.

Keywords Ground-penetrating radar · Multilayered media · Green's function · Full-waveform inversion

25.1 Introduction

Increases in global food and biofuel demands predicted for the next decades pose huge challenges for the sustainability and productivity of both terrestrial and aquatic ecosystems and the services they provide to society. Sustainable and optimal management of water and land resources relies strongly on knowledge of soil hydrological properties; such knowledge is essential in agricultural and environmental research and engineering as the properties control hydrological processes, contamination of surface and subsurface water, plant growth, sustainability of ecosystems and biodiversity, and climate. The soil is the interface between the earth and the atmosphere and it governs all the key processes of the hydrological cycle such as infiltration, run-off, evaporation, and energy exchanges with the atmosphere.

Characterising and monitoring the distribution of soil properties across the environment is therefore essential for developing site-specific management practices which match human activities with local environmental requirements. Obtaining soil information with the required spatiotemporal resolution is, however, complicated by the inaccessibility of the subsurface and its inherent variability. In addition, the inter-connectivity of different subsystems at different scales requires a holistic approach. Common techniques to characterise soil hydrological properties are suited either to small scales (<0.1 m), such as reference sampling methods or time domain reflectometry (TDR), or to large scales (>10 – 100 m), such as airborne and spaceborne passive microwave radiometry and active radar systems. Small-scale techniques are usually invasive, sometimes requiring boreholes, and may not be representative of the soil properties at the management scale. For the large-scale techniques, the characterisation is limited to the top few centimetres of soil and temporal resolution is relatively poor.

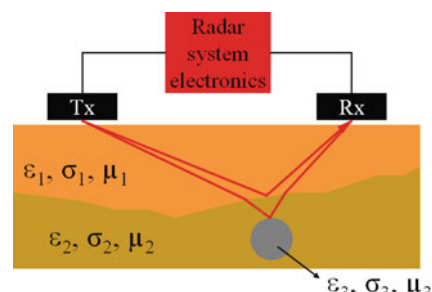
Non-invasive field-scale techniques are required in applications that include agricultural water management and soil and water conservation and to bridge the present scale gap between ground-truth measurements and remote sensing. Soil electrical sounding is commonly used as a technique to generate proxies of soil moisture and salinity or contaminants (Myers et al., Chapter 19). Soil electrical sounding can be performed by classical geo-electrical or electromagnetic induction techniques. Yet soil electrical conductivity is multivariate, depending simultaneously on water content, water salinity, texture, and structure. Its interpretation is therefore subject to large uncertainties that cannot be resolved by conductivity methods alone. Electrical soundings have been particularly successful in delineating management zones qualitatively or detecting contaminant plumes. Over the

last decade, ground-penetrating radar (GPR) has received increasing attention in environmental research and engineering applications (Richard et al., Chapter 26). Several GPR methods are available to identify soil dielectric permittivity, usually from determination of the GPR wave propagation velocity (Huisman et al., 2003). As the dielectric permittivity of liquid water overwhelms the permittivity of other soil components, soil dielectric permittivity constitutes an accurate surrogate measure of soil water content. In this chapter, we discuss common GPR techniques to characterise soil and we review our recent developments on the full-waveform modelling and inversion of proximal GPR (see also Grandjean et al., Chapter 7). The theory of the method is summarised and application examples are presented.

25.2 Ground-Penetrating Radar

GPR is a geophysical technique which is particularly appropriate to image the soil in two or three dimensions with high spatial resolution, up to a depth of several metres. GPR operates by transmitting high-frequency (VHF–UHF) electromagnetic waves into the soil (Fig. 25.1). Wave propagation is governed by the frequency-dependent soil dielectric permittivity ϵ (determining wave velocity), electrical conductivity σ (determining wave attenuation), magnetic permeability μ (determining wave velocity, affects attenuation), and their spatial distribution. Electromagnetic contrasts create partial wave reflections and transmissions that are measured by a receiving antenna, depending on the mode of operation (reflection or transmission). For non-magnetic materials, which are prevalent in the environment, μ is equal to the free-space magnetic permeability μ_0 . GPR has been primarily used to image the subsurface and detect buried objects. In the areas of unsaturated zone hydrology and water resources, GPR has been used to identify soil stratigraphy (Boll et al., 1996; Davis and Annan, 1989; Grandjean et al., 2006), to locate water tables (Nakashima et al., 2001), to follow wetting front movement (Vellidis et al., 1990), to identify soil hydraulic parameters (Binley et al., 2002; Cassiani and Binley, 2005; Kowalsky et al., 2005), to measure soil water content (Chanzy et al., 1996; Galagedara et al., 2005; Huisman et al., 2003; Lunt et al., 2005; Serbin and Or, 2004), to assess soil

Fig. 25.1
Ground-penetrating radar (GPR) basic principles. Tx is the transmitting antenna. Rx is the receiving antenna. Red lines represent wave propagation paths



salinity (al Hagrey and Müller, 2000), to monitor contaminants (Yoder et al., 2001), and to delineate soil compaction within agricultural fields (Petersen et al., 2005).

Quantitative information can also be derived from GPR data. Generally, GPR signal analysis is performed using ray-tracing approximations (Fig. 25.1) and tomographic inversion. Several methodologies are generally adopted for determining wave propagation velocity and retrieving soil water content from GPR data (Huisman et al., 2003):

- Determination of the wave propagation time to a known reflecting interface using single-offset surface GPR;
- Detection of the velocity-dependent reflecting hyperbola of a buried object using single-offset surface GPR along a transect;
- Extraction of stacking velocity fields from multi-offset radar soundings at a fixed central location (common midpoint method, CMP);
- Determination of the ground-wave velocity for surface water content retrieval using multi- and single-offset surface GPR;
- Determination of the surface reflection coefficient using single-offset off-ground GPR;
- Determination of the two-dimensional (2D) spatial distribution of water between boreholes using transmission tomography.

In particular, time-lapse GPR measurements have recently allowed monitoring of soil water dynamics between boreholes and inferring the soil hydraulic properties governing water flow. GPR can also be applied to monitor remediation amendments and processes, provided there is sufficient sensitivity of the GPR signal.

Although these techniques are well established, they still suffer from major limitations originating from the strongly simplifying assumptions on which they rely, particularly with respect to electromagnetic wave propagation phenomena. As a result, a bias is introduced in the estimates due to limited GPR model adequacy and, moreover, only a part of the information contained in the radar data is used, generally the propagation time. In addition, all these techniques are not appropriate in a real-time mapping context, as usually several measurements are needed at a given location.

To simultaneously estimate both the depth-dependent soil dielectric permittivity and the electrical conductivity, we must resort to the physical basis of GPR wave propagation. The relation between the subsurface constitutive parameters and the measured electromagnetic field is governed by Maxwell's equations. Reconstruction of the unknown constitutive parameters from the known field relies on inverse modelling. Inverting electromagnetic data has been a major challenge in applied geophysics for many years. Successful inversion is challenging, since it involves rigorous forward modelling of the 3D GPR–subsurface system, which is also computationally very time consuming. Moreover, the inverse problem needs to satisfy uniqueness and stability conditions, which are related to the information content of the radar data.

25.3 Full-Waveform Analysis of Proximal GPR Data

We have recently developed a full-waveform electromagnetic model for the particular case of zero-offset, off-ground GPR, i.e. a single antenna, situated at some distance above the soil, simultaneously plays the role of transmitter and receiver (Lambot et al., 2004a). The model includes propagation effects within the antenna and antenna–soil interactions (this is usually not accounted for using common GPR methods) and considers an exact solution of the 3D Maxwell's equations for wave propagation in multilayered media (only 1D solutions are usually considered). Both phase and amplitude information are used for model inversion, thereby maximising information retrieval from the available radar data, both in terms of quantity and quality. The technique was validated in a series of hydrogeophysical applications (Lambot et al., 2004a, b, c, 2006a). Recently, we integrated the method with hydrodynamic modelling to retrieve the soil hydraulic properties from time-lapse proximal radar data and monitor the dynamics of water content profiles (Lambot et al., 2006a). The radar model enhances high-resolution, shallow subsurface imaging by suppressing antenna and soil surface reflection effects which may be ambiguous or hide detailed information (Lopera et al., 2007).

25.3.1 GPR Forward Modelling

25.3.1.1 Antenna Equation in the Frequency Domain

The main advantage of vector network analyser (VNA) technology over traditional GPR systems is that the measured quantities constitute an international standard and are well defined physically with proper calibration of the system. Other advantages are the higher dynamic range and the possibility of avoiding transmission into specific, narrow frequency bands that may be against state regulations. The GPR signal to be modelled consists of the frequency-dependent complex ratio $S_{11}(\omega)$ between the returned signal and the emitted signal, ω being the angular frequency. The antenna is modelled using the block diagram depicted in Fig. 25.2 (Lambot et al., 2004c). It relies on the linearity of Maxwell's equations and assumes that the spatial distribution of the backscattered electromagnetic field measured by the antenna does not depend on the subsurface, i.e. only the amplitude and the phase change. This is expected to be a valid assumption if the antenna is not too close to the ground and if the soil can be described as a horizontally multilayered medium. The model consists of a linear system composed of elementary model components in series and parallel, all characterised by their own frequency–response function accounting for specific electromagnetic phenomena. The resulting transfer function relating $S_{11}(\omega)$ measured by the VNA to the frequency response $G_{xx}^\uparrow(\omega)$ of the multilayered medium is expressed in the frequency domain as follows:

$$S_{11}(\omega) = \frac{b(\omega)}{a(\omega)} = H_i(\omega) + \frac{H_t(\omega) G_{xx}^\uparrow(\omega) H_r(\omega)}{1 - H_f(\omega) G_{xx}^\uparrow(\omega)}, \quad (25.1)$$

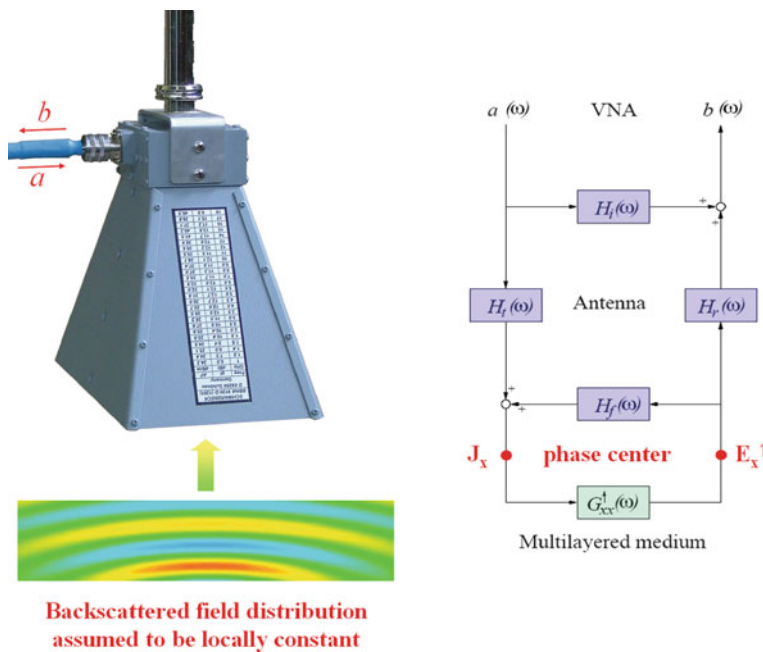


Fig. 25.2 Block diagram representing the VNA–antenna–multilayered medium system modelled as linear systems in series and parallel (Lambot et al., 2004c)

where $b(\omega)$ and $a(\omega)$ are the received and emitted signals, respectively, at the VNA reference calibration plane; $H_i(\omega)$, $H_t(\omega)$, $H_r(\omega)$, and $H_f(\omega)$ are the complex return loss, transmitting, receiving, and feedback loss transfer functions of the antenna, respectively; and $G_{xx}^\dagger(\omega)$ is the transfer function of the air–subsurface system modelled as a multilayered medium (referred to as Green’s function below). Due to inherent variations in the impedance between the antenna feed point, the antenna aperture, and air, multiple wave reflections occur within the antenna. Under the assumption above, these reflections can be accounted for exactly using the antenna transfer functions, which thereby play the role of frequency-dependent, global reflection and transmission coefficients. In this way, the proposed model inherently takes into account the multiple wave reflections occurring between the antenna and the soil.

25.3.1.2 Zero-Offset Green’s Function for Multilayered Media

The solution of Maxwell’s equations for electromagnetic waves propagating in multilayered media is well known. Following the approach of Lambot et al. (2004a), the analytical expression for the zero-offset Green’s function in the spectral domain (2D spatial Fourier domain) is found to be as follows:

$$\tilde{G}_{xx}^{\uparrow} = \left(\frac{\Gamma_n R_n^{\text{TM}}}{\eta_n} - \frac{\xi_n R_n^{\text{TE}}}{\Gamma_n} \right) \exp(-2\Gamma_n h_n), \quad (25.2)$$

where the subscript n equals 1 and denotes the first interface and first layer (in practice, the air layer); R_n^{TM} and R_n^{TE} are the transverse magnetic (TM) and transverse electric (TE) global reflection coefficients, respectively (Slob and Fokkema, 2002) accounting for all reflections and multiples from surface and subsurface interfaces; Γ_n is the vertical wavenumber defined as $\Gamma_n = \sqrt{k_{\rho}^2 + \xi_n \eta_n}$; k_{ρ} is the spectral domain transform parameter; $\xi_n = j\omega\mu_n$; $\eta_n = \sigma_n + j\omega\varepsilon_n$; and $j = \sqrt{-1}$.

The transformation of Eq. (25.2) from the spectral domain to the spatial domain is carried out by employing the 2D Fourier inverse transformation:

$$G_{xx}^{\uparrow} = \frac{1}{4\pi} \int_0^{+\infty} \tilde{G}_{xx}^{\uparrow} dk_{\rho}, \quad (25.3)$$

which reduces to a single integral in view of the invariance of the electromagnetic properties along the x and y coordinates. We developed a specific procedure to properly evaluate that singular integral in an optimal way (Lambot et al., 2007). As illustrated in Fig. 25.3, the integration path is deformed in the complex k_{ρ} plane by applying Cauchy's integral theorem. In addition to avoiding singularities (branch points and poles), the path minimises oscillations of the complex exponential part of the integrand, which makes integration faster.

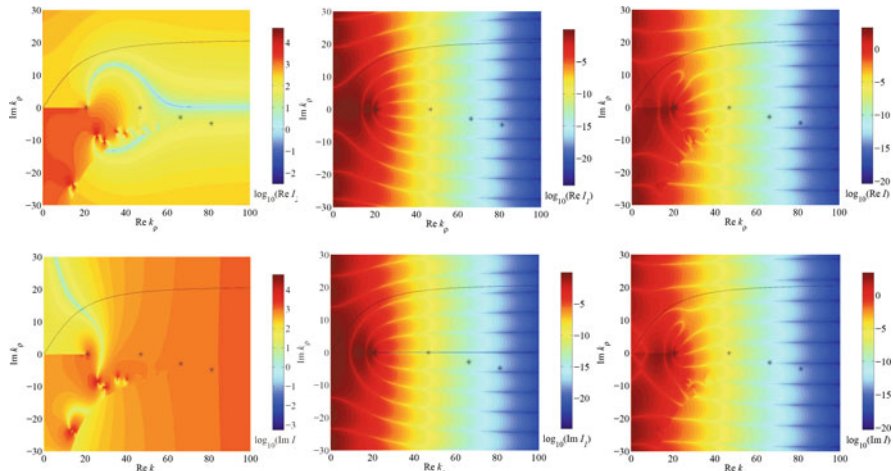


Fig. 25.3 Optimal integration path in the complex k_{ρ} plane for the real and imaginary parts of the two major components I_1 and I_2 of the integrand and for the full integrand I (Lambot et al., 2007)

25.3.2 Model Inversion

Inversion of the Green's function is formulated by the complex least squares problem as follows:

$$\min \phi(\mathbf{b}) = \left| \mathbf{G}_{\mathbf{xx}}^{\uparrow*} - \mathbf{G}_{\mathbf{xx}}^{\uparrow} \right|^T \mathbf{C}^{-1} \left| \mathbf{G}_{\mathbf{xx}}^{\uparrow*} - \mathbf{G}_{\mathbf{xx}}^{\uparrow} \right|, \quad (25.4)$$

where $\mathbf{G}_{\mathbf{xx}}^{\uparrow*} = G_{\mathbf{xx}}^{\uparrow}(\omega)$ and $\mathbf{G}_{\mathbf{xx}}^{\uparrow} = G_{\mathbf{xx}}^{\uparrow}(\omega, \mathbf{b})$ are vectors containing the observed and the simulated radar measurements, respectively, from which major antenna effects have been filtered using Eq. (25.1); \mathbf{C} is the error covariance matrix; and \mathbf{b} is the parameter vector containing the soil electromagnetic parameters and layer thicknesses to be estimated. As function $\phi(\mathbf{b})$ usually has a complex topography, we use the global multilevel coordinate search algorithm (Huyer and Neumaier, 1999), combined sequentially with the classical Nelder–Mead simplex algorithm, for minimising the function.

25.3.3 Model Validation and Applications

We performed radar measurements above a sandbox containing two sand layers subjected to various water contents, under which a metal sheet was installed as a perfect electric conductor to control the bottom boundary condition in the electromagnetic model (Lambot et al., 2004c). Radar measurements were performed in the range of 1–3 GHz, with a frequency step of 4 MHz. Figure 25.4 represents the modelled and measured Green's functions in the frequency domain for a specific water content. Figure 25.5 shows the inversely estimated relative dielectric permittivity as a function of the top layer's volumetric water content. In addition to the remarkable agreement between the measured and modelled data, we observe that

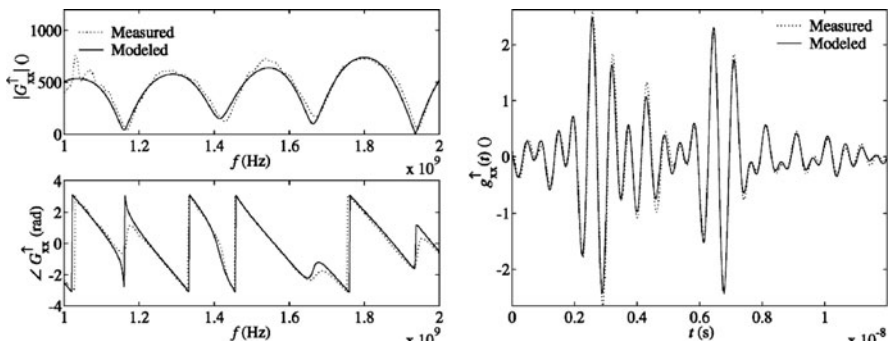


Fig. 25.4 Measured and modelled Green's functions for an antenna above a two-layered medium, with a perfect electric conductor as the bottom boundary condition (Lambot et al., 2004c). Radar data are presented in both the frequency (left) and time (right) domains

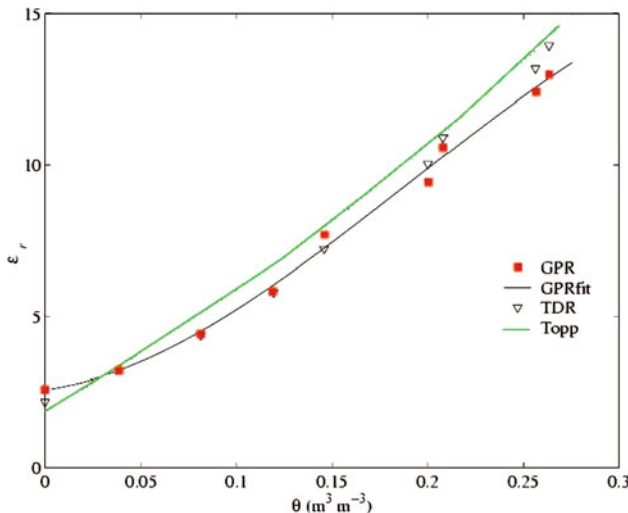


Fig. 25.5 Inversely estimated relative dielectric permittivity as a function of volumetric water content (Lambot et al., 2004c). GPR results are compared to reference TDR measurements. Topp's model is also shown

the inversely estimated dielectric permittivities are highly consistent with the different water contents and when compared to reference TDR measurements. These results demonstrate the accuracy of the GPR forward model, the uniqueness of the inverse solution for this specific inverse problem, and the stability of the inverse solution with respect to actual modelling and measurement errors. Remaining differences were partly attributed to the different operating frequency ranges of both systems (TDR and GPR) and to the different measurement scales. Accurate estimates were also obtained of the sand's electric conductivity and frequency dependence.

In Lambot et al. (2004a), we applied that GPR approach to monitor water content as a function of time and depth during a free drainage event in a 2-m-high laboratory sand column. The sand column was also equipped with TDR probes at two different depths. We subsequently used the water content time series obtained to identify the soil hydraulic properties, described by the Mualem–van Genuchten parameterisation, using hydrodynamic inverse modelling. We observed in particular that GPR was less sensitive than TDR to the small-scale soil heterogeneities (sedimentation layering) and the water dynamics was better described at the GPR characterisation scale. In another study (Lambot et al., 2004b), we identified from a single radar measurement, performed at a controlled outdoor test site, a continuous vertical water content profile in hydrostatic equilibrium with a water table. In that case the profile could be constrained using the Mualem–van Genuchten parameterisation as it corresponded to the characteristic water retention curve of the soil. As a result, only four parameters had to be inverted in order to reconstruct the whole continuous profile.

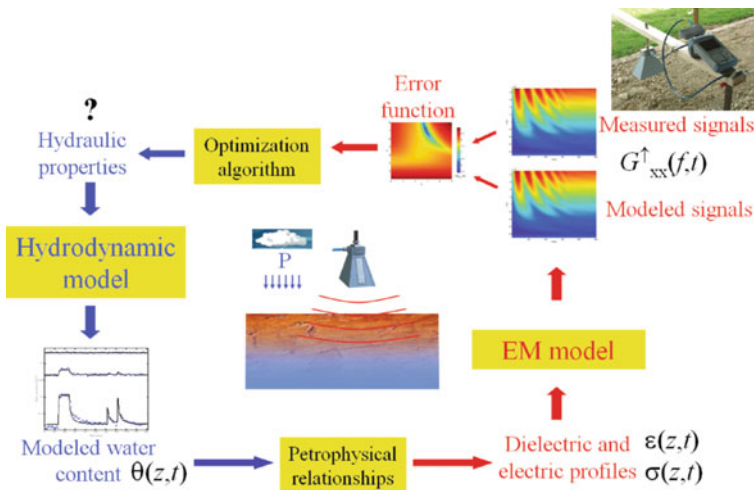


Fig. 25.6 Flowchart representing the integrated electromagnetic and hydrodynamic inversion of time-lapse radar measurements for estimating soil hydraulic properties and electrical profiles, where t is the time, z is the depth, and f is the frequency (Lambot et al., 2006a)

In Lambot et al. (2006b) and Jadoon et al. (2008), we tackled the issue of retrieving continuous electromagnetic profiles and soil hydraulic properties from time-lapse GPR data. The proposed inverse modelling flow chart is presented in Fig. 25.6. Electromagnetic inverse modelling is constrained by hydrodynamics and petrophysical laws, significantly reducing the complexity of the inverse problem. We demonstrated, using numerical experiments, the uniqueness of the inverse solution for a series of soils and hydrodynamic boundary conditions. Laboratory results (Lambot et al., 2009) demonstrated the promising prospects of mapping the shallow soil hydraulic properties at the field scale with high spatial resolution.

Finally, we have set out a proposal for mapping surface water content under field conditions (Lambot et al., 2006b). For that specific purpose, inversion of the Green's function is performed in the time domain, on a time window focused on the surface reflection only. We have shown that compared to the traditional surface reflection method, filtering antenna effects and performing full-waveform inversion provides valuable advantages compared to other existing techniques. In particular, antenna distortion effects are filtered out (resulting in increased accuracy), the antenna elevation does not need to be known a priori as it is inversely estimated as well, and, finally, it does not require measurements to be made above a calibrating perfect electric conductor situated at exactly the same height as the field measurements. Figure 25.7 represents an example of the real-time mapping GPR platform and shows a map of surface soil moisture acquired over a 16-ha agricultural field. About 3000 measurements were acquired. Full-waveform inversion for the retrieval of soil surface water content took less than 1 s on a field laptop.

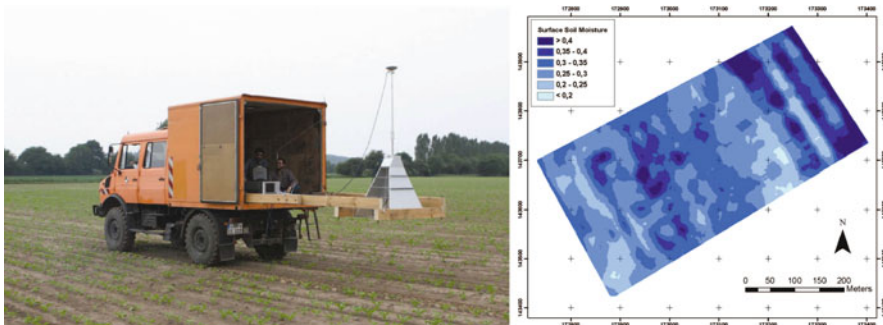


Fig. 25.7 Real-time mapping of surface soil water content using an ultra-wideband horn antenna operating in the range of 200–2000 MHz. (Left) Experimental set-up. (Right) Surface soil water content map for a 16-ha agricultural field (Walhain, Belgium)

25.4 Conclusions

In this chapter, we emphasised the need for non-invasive techniques for soil characterisation and monitoring at the field scale. GPR is increasingly used for such applications as it permits both high-resolution subsurface imaging and quantitative characterisation. Although traditional GPR techniques have been useful in many applications, more advanced technology and processing are still needed to benefit from the full potential of GPR for subsurface investigations. We have illustrated such progress in characterising the shallow subsurface from proximal measurements. The characterisation depth depends on the operating frequency range, the soil's electromagnetic properties and spatial distribution, and on the dynamic range of the radar system. The proposed method is particularly appropriate to characterise the top metre of the soil.

Acknowledgements This work has been supported by the Université Catholique de Louvain (Belgium), the Forschungszentrum Jülich GmbH (Germany), Delft University of Technology (The Netherlands), the Fonds National de la Recherche Scientifique (FNRS, Belgium), the Helmholtz Association (Germany), a Marie Curie Intra-European Fellowship within the 6th European Community Framework Programme (SENSOIL project), the Belgian Science Policy Office within the framework of the Stereo II Programme – project SR/00/100 (HYDRASENS) – and the DIGISOIL project financed by the European Commission under the 7th Framework Programme for Research and Technological Development, Area ‘Environment’, Activity 6.3 ‘Environmental Technologies’.

References

al Hagrey SA, Müller C (2000) GPR study of pore water content and salinity in sand. *Geophys Prospect* 48:63–85
 Binley A, Cassiani G, Middleton R, Winship P (2002) Vadose zone flow model parameterisation using cross-borehole radar and resistivity imaging. *J Hydrol* 267(3–4):147–159

Boll J, van Rijn RPG, Weiler KW, Steenhuis TS, Daliparthy J, Herbert SJ (1996) Using ground penetrating radar to detect layers in a sandy field soil. *Geoderma* 70:117–132

Cassiani G, Binley A (2005) Modeling unsaturated flow in a layered formation under quasi-steady state conditions using geophysical data constraints. *Adv Water Resour* 28(5):467–477

Chanzy A, Tarussov A, Judge A, Bonn F (1996) Soil water content determination using digital ground penetrating radar. *Soil Sci Soc Am J* 60:1318–1326

Davis JL, Annan AP (1989) Ground penetrating radar for high resolution mapping of soil and rock stratigraphy. *Geophys Prospect* 37:531–551

Galagedara LW, Parkin GW, Redman JD, von Bertoldi P, Endres AL (2005) Field studies of the GPR ground wave method for estimating soil water content during irrigation and drainage. *J Hydrol* 301:182–197

Grandjean G, Paillou P, Baghdadi N, Heggy E, August T, Lasne Y (2006) Surface and subsurface structural mapping using low frequency radar: a synthesis of the Mauritanian and Egyptian experiments. *J Afr Earth Sci* 44(2):220–228

Huisman JA, Hubbard SS, Redman JD, Annan AP (2003) Measuring soil water content with ground penetrating radar: A review. *Vadose Zone J* 2:476–491

Huyer W, Neumaier A (1999) Global optimization by multilevel coordinate search. *J Global Optim* 14(4):331–355

Jadoon KZ, Slob E, Vanclooster M, Vereecken H, Lambot S (2008) Uniqueness and stability analysis of hydrogeophysical inversion for time-lapse ground penetrating radar estimates of shallow soil hydraulic properties. *Water Resour Res* 44:W09421, doi:10.1029/2007WR006639

Kowalsky MB, Finsterle S, Peterson J, Hubbard S, Rubin Y, Majer E, Ward A, Gee G (2005) Estimation of field-scale soil hydraulic and dielectric parameters through joint inversion of GPR and hydrological data. *Water Resour Res* 41:W11425, doi:10.1029/2005WR004237

Lambot S, Slob EC, van den Bosch I, Stockbroeckx B, Vanclooster M (2004a) Modeling of ground-penetrating radar for accurate characterization of subsurface electric properties. *IEEE Trans Geosci Remote Sens* 42:2555–2568

Lambot S, Rhebergen J, van den Bosch I, Slob EC, Vanclooster M (2004b) Measuring the soil water content profile of a sandy soil with an off-ground monostatic ground penetrating radar. *Vadose Zone J* 3(4):1063–1071

Lambot S, Antoine M, van den Bosch I, Slob EC, Vanclooster M (2004c) Electromagnetic inversion of GPR signals and subsequent hydrodynamic inversion to estimate effective vadose zone hydraulic properties. *Vadose Zone J* 3(4):1072–1081

Lambot S, Weihermüller L, Huisman JA, Vereecken H, Vanclooster M, Slob EC (2006a) Analysis of air-launched ground-penetrating radar techniques to measure the soil surface water content. *Water Resour Res* 42:W11403, doi:10.1029/2006WR005097

Lambot S, Slob EC, Vanclooster M, Vereecken H (2006b) Closed loop GPR data inversion for soil hydraulic and electric property determination. *Geophys Res Lett* 33:L21405, doi:10.1029/2006GL027906

Lambot S, Slob E, Vereecken H (2007) Fast evaluation of zero-offset Green's function for layered media with application to ground-penetrating radar. *Geophys Res Lett* 34:L21405, doi:10.1029/2007GL031459

Lambot S, Slob E, Rhebergen J, Lopera O, Jadoon KZ, Vereecken H (2009) Remote estimation of the hydraulic properties of a sandy soil using full-waveform integrated hydrogeophysical inversion of time-lapse, off-ground GPR data. *Vadose Zone J* 8(3):743–754

Lopera O, Slob EC, Milisavljevic N, Lambot S (2007) Filtering soil surface and antenna effects from GPR data to enhance landmine detection. *IEEE Trans Geosci Remote Sens* 45(3):707–717

Lunt IA, Hubbard SS, Rubin Y (2005) Soil moisture content estimation using ground-penetrating radar reflection data. *J Hydrol* 307(1–4):254–269

Nakashima Y, Zhou H, Sato M (2001) Estimation of groundwater level by GPR in an area with multiple ambiguous reflections. *J Appl Geophys* 47:241–249

Petersen H, Fleige H, Rabbel W, Horn R (2005) Applicability of geophysical prospecting methods for mapping of soil compaction and variability of soil texture on farm land. *J Plant Nutr Soil Sci – Zeitschrift Fur Pflanzenernährung Und Bodenkunde* 168(1):68–79

Serbin G, Or D (2004) Ground-penetrating radar measurement of soil water content dynamics using a suspended horn antenna. *IEEE Trans Geosci Remote Sens* 42:1695–1705

Slob EC, Fokkema J (2002) Coupling effects of two electric dipoles on an interface. *Radio Sci* 37(5):1073, doi:10.1029/2001RS2529

Vellidis G, Smith MC, Thomas DL, Asmussen LE (1990) Detecting wetting front movement in a sandy soil with ground penetrating radar. *Trans ASAE* 33:1867–1874

Yoder RE, Freeland RS, Ammons JT, Leonard LL (2001) Mapping agricultural fields with GPR and EMI to identify offsite movement of agrochemicals. *J Appl Geophys* 47:251–259

Chapter 26

Using Proximal Sensors to Continuously Monitor Agricultural Soil Physical Conditions for Tillage Management

G. Richard, R. Rouveure, A. Chanzy, P. Faure, M. Chanet, A. Marionneau, P. Régnier, and Y. Duval

Abstract Homogeneity of crop establishment, which directly depends on physical conditions within the seedbed, is very important for crop yield. We did a field experiment to test the abilities of various sensors to characterise seedbed physical conditions and the possibility of continuously modifying the intensity of soil tillage with the objective of producing a uniform seedbed. The experiment was done on a silt soil with 19% clay and 74% silt in northern France. We created two initial soil structures (with and without clods >10 cm) and controlled water content (field capacity or less). A special cultivator was developed with a continuous-output GPS and a microwave ground-based radar sensor; it also carried a laser profile meter for soil surface characterisation, a capacitance probe for monitoring soil water content, and a load cell for measuring soil mechanical resistance. Each sensor was able to detect differences in soil physical conditions at the field scale. Because of the simultaneous effect of soil water content and soil structure on the geophysical parameters obtained with the sensors, it was not possible to obtain a continuous characterisation of the soil's bulk density, water content, clod-size distribution, or surface roughness (although the use of two radar angles of incidence might allow better assessment of soil surface roughness). For tillage control, seedbed conditions depended on initial soil conditions (water content and degree of compaction) and soil tillage tool characteristics (working depth and speed of rotation). Working depth and speed of rotation had opposite effects on the size of clods at the seedbed surface; within the seedbed, they could reduce initial soil variability. Seeding rate could be controlled by the same sensors if they were put in front of the seeder. Results of the experiment are relevant to spatial parameterisation of existing soil models.

Keywords Seedbed · Clod size · Water content radar · Microwave ground-based radar

G. Richard (✉)

INRA, UR272 Science du Sol, Centre de Recherche d'Orléans, 2163 Avenue de la Pomme de Pin, CS 40001, 45075 Orléans Cedex 2, France
e-mail: Guy.Richard@orleans.inra.fr

26.1 Introduction

Agricultural practices should simultaneously preserve the environment and the profit margins of farmers. Seedbed preparation and sowing are particularly important for mechanised cropping systems because of (1) energy needed for tillage, (2) cost of seeds, (3) dependence of crop yield on the homogeneity of crop establishment, and (4) erosion risk when the soil is bare. In the context of large fields, continuously finetuning soil tillage and sowing rates could limit the use of energy and seeds and lead to homogeneous crop emergence. Such a modulation (which is part of the precision agriculture concept) requires real-time measurement of soil characteristics that influence crop emergence (e.g. clod-size distribution, resistance to root penetration, and moisture content) and a dynamic control of the cultivator and seeder variables (e.g. working depth, forward speed, rotation speed, and sowing rate). It is difficult to continuously characterise soil conditions during tillage because of the operational constraints of an agricultural environment: a mobile machine with possible wind and rain, dust in dry conditions, and mud in wet ones. (Incidentally, this kind of spatial characterisation of soil properties is also relevant to spatial parameterisation of soil models, for example, erosion prediction at the catchment scale.) We have therefore undertaken a field experiment with two objectives: (1) to test the abilities of various sensors, with and without soil contact, to characterise seedbed physical conditions and (2) to evaluate the possibility of continuously modifying the intensity of soil tillage with the objective of producing a uniform seedbed. Several sensors were mounted on a special cultivator carrying continuous-output GPS, microwave ground-based radar sensor, laser profile meter for soil surface characterisation, capacitance probe for soil water content, and load cell for soil mechanical resistance. They were used before and after a tilling with a rotary harrow (using two working depths and two rotation speeds) on a field with contrasting initial soil structure and water content.

26.2 Materials and Methods

26.2.1 Description of the Sensors

All the sensors were mounted on the rear of a tractor over a special tillage tool whose operating depth was controlled by wheels rolling on the soil surface (Plate 26.1a, b). (1) An infrared rangefinder (HT 66 MGV 80; Wenglor) was installed 0.55 m above the surface to characterise surface roughness. It measured distance to the soil surface with a precision of 1 mm. (2) We developed a frequency-modulated continuous-wave radar (FMCW) which provided a cheaper solution than did a pulsed radar for short-range applications (distance <1 m). The FMCW radar transposes temporal variables into the frequency domain so that a short time delay Δt is transformed into a broad variation of frequency Δf , which is easier to measure (Noyman and Shmulevich, 1996; Skolnik, 1980). The radar has a carrier frequency of 10 GHz

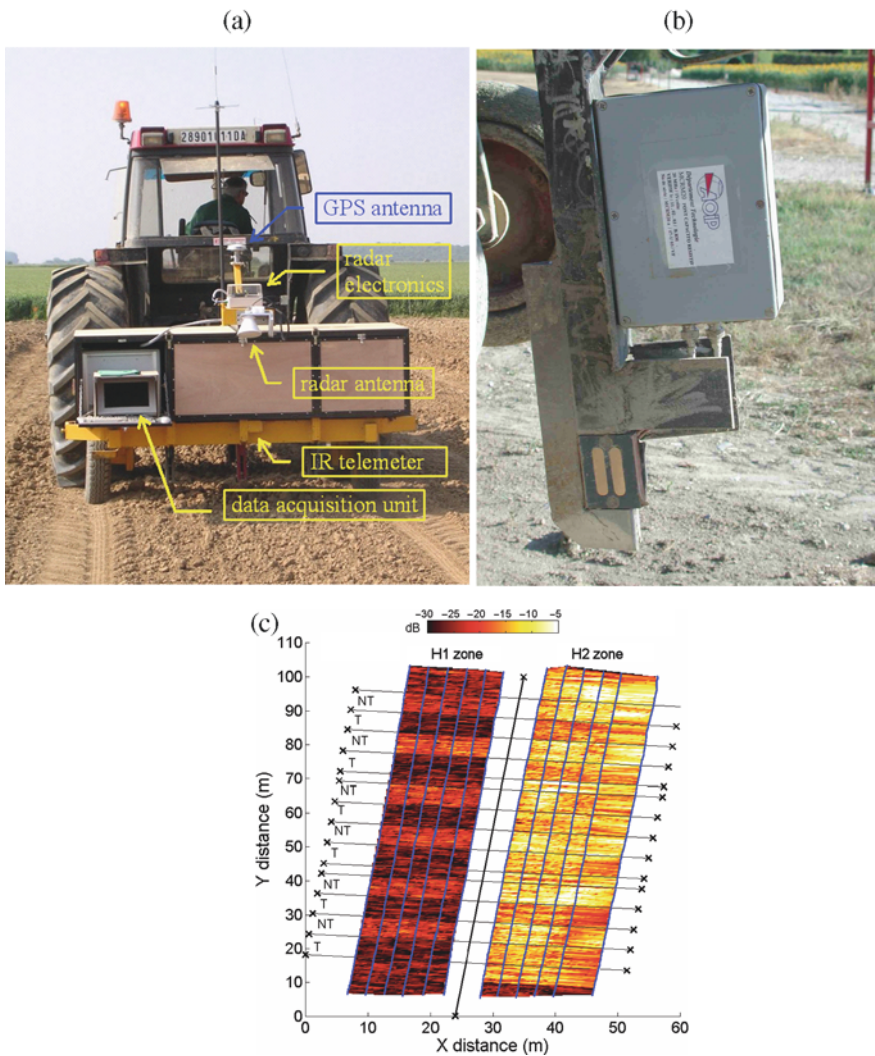


Plate 26.1 (a) Location of sensors on the tool behind the tractor. (b) Details of capacitance probe. (c) Map of relative scattering coefficient before soil tillage, obtained by radar with an incidence angle of 0°

(X band, horizontal polarisation) and a transmitted power of 18 dBm. It is monostatic, which means that a single-lens horn antenna is used for both transmitting and receiving. The antenna beam width was 10° . The radar was mounted 1.2 m above the soil surface and could be used at two angles of incidence, 0° and 20° . (3) The tillage tool had four rigid metallic pieces that penetrated the soil 10, 20, 30, or 40 cm. A pressure cell on each piece measured the resistance to forward movement. (4) A capacitance probe was mounted on the 10-cm piece to continuously measure

dielectric permittivity (Plate 26.1b). It consisted of two brass electrodes (5 cm long, 1 cm wide) enclosed within PVC. The volume of measurement was a bulb 1 cm thick (Bolvin et al., 2004).

26.2.2 Field Experiment

The experiment was conducted in 2004 in northern France at the INRA experimental centre of Estrées-Mons (Péronne, 50° N, 3° E, 85 m elevation). The field had an area of 5000 m² (50 m wide, 100 m long). The soil was a silt loam developed from loess (World Reference Base, Orthic Luvisol; FAO, 2006). The first 30 cm contained, per kilogram, an average of 190 g clay, 738 g silt, 50 g sand, 17 g organic matter, and 5 g CaCO₃; its pH was 7.6. Soil water contents at -10, -50, -100, and -1500 kPa matric potentials were 0.252, 0.213, 0.164, and 0.083 g g⁻¹, respectively.

Using a digging machine, the soil was deep tilled over the whole field in March 2004 to obtain a homogeneous, fragmentary structure over 30 cm deep. In April, plots 6 m wide were compacted using a heavy tractor in wet conditions, and these were separated by 6 m non-compacted plots to create a chequerboard pattern. Compaction was followed by a second deep tillage operation with the digging machine. In this way, we obtained two structures in the first centimetres of soil: (1) a fragmentary structure with fine earth and small clods (NT plots) after digging without compaction and (2) a fragmentary structure with many large compacted clods (T plots) after compaction and digging.

Irrigation was applied in May on one-half of the field to obtain two levels of water content: less than field capacity (non-irrigated, H1 or 'dry' plots) and near-field capacity (irrigated, H2 or 'wet' plots). Following irrigation, superficial tillage was then done to mimic seedbed preparation using a rotary harrow on both NT and T plots at a tractor velocity of 1.5 m s⁻¹. Two working depths (4 and 8 cm) and two speeds of PTO rotation (500 and 1000 rpm) were used in the length direction (four combinations).

26.2.3 Data Acquisition

All measurements were done twice in each plot, before and immediately after secondary tillage: (1) direct measurement of bulk density (membrane densitometer) and water content (gravimetric method) of the first 10 cm; (2) photography of soil surface to assess clod-size distribution by image analysis; seedbed sampling and dry sieving; (3) continuous recording of all the sensors with an acquisition frequency of 100 Hz at a tractor velocity of 1 m s⁻¹ (i.e. one measurement every centimetre). A kinematic GPS (global positioning system) with a precision of ±2 cm was used for geo-referencing in order to obtain a precise cartography of the measured data.

26.3 Results and Discussion

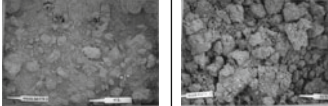
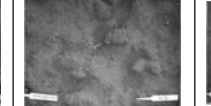
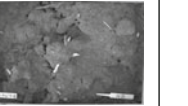
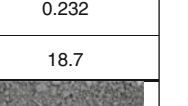
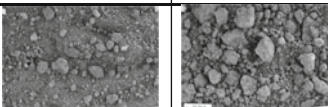
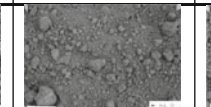
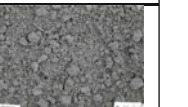
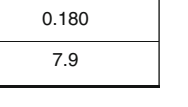
26.3.1 Soil Physical Conditions

Soil physical conditions obtained before and after tillage are presented in Table 26.1. Soil water content showed a strong contrast between plots H1 and H2: water suction was $>15,000$ kPa in the H1 plots and <100 kPa in the H2 plots. Before tillage, plots H1-T had a cloddy soil surface with high roughness, whereas plots H2-NT and H2-NT had a smooth, crusted soil surface due to irrigation. Soil surface roughness was reduced by secondary tillage. H1-T plots continued to have big clods (with some clods >8 cm diameter) after secondary tillage.

26.3.2 Radar Data

Plate 26.1c shows a plot of relative scattering coefficient before soil tillage using an incidence angle of 0° . Both soil surface roughness (characterised by the root mean square of the profile heights) and soil moisture had an effect on the backscattering coefficient, as shown in Fig. 26.1 for data obtained before tillage with an incidence angle of 0° . Results were similar with an incidence angle of 20° , but with a lower range of variation of the backscattering coefficient. On the other hand, the relative backscattering ratio (coefficient obtained at 20° incidence angle compared to that obtained at 0° incidence) depended on the soil surface roughness and was less sensitive to soil moisture (Fig. 26.2). We suggest that such a ratio might better discriminate between changes in soil surface structure, even if the ratio were not very sensitive to high surface roughness (e.g. a cloddy seedbed).

Table 26.1 Physical parameters of the plots of the field experiment before and after tillage. (Pictures after tillage correspond to a working depth of 4 cm and a PTO speed of 500 rpm; water content and rms height correspond to the mean of the four combinations)

	H1-NT plot	H1-T plot	H2-NT plot	H2-T plot
Before tillage				
Water content (0–5 cm) g g ⁻¹	0.077	0.020	0.220	0.232
RMS height with laser (mm)	12.8	27.6	10.5	18.7
After tillage				
Water content (0–2 cm) g g ⁻¹	0.083	0.036	0.124	0.180
RMS height (mm)	7.2	13.0	7.5	7.9

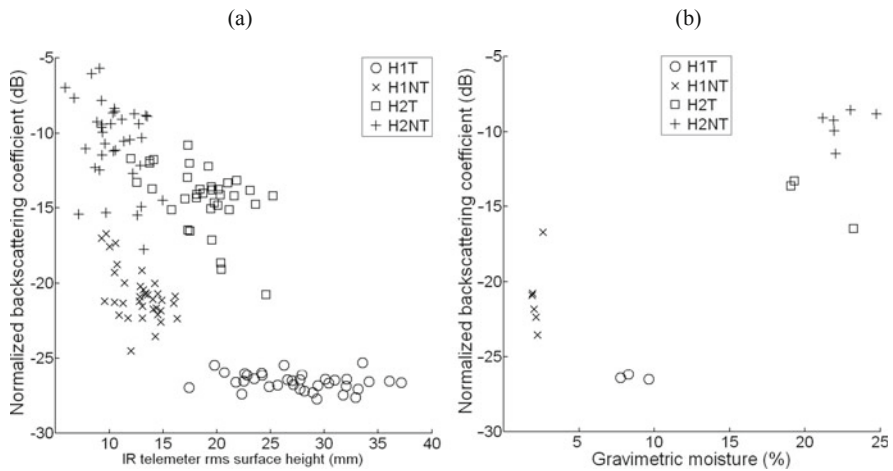


Fig. 26.1 Variations of the relative backscattering coefficient (radar angle of incidence of 0°) of plots before tillage as a function of the rms surface height (a) and gravimetric soil moisture (b)

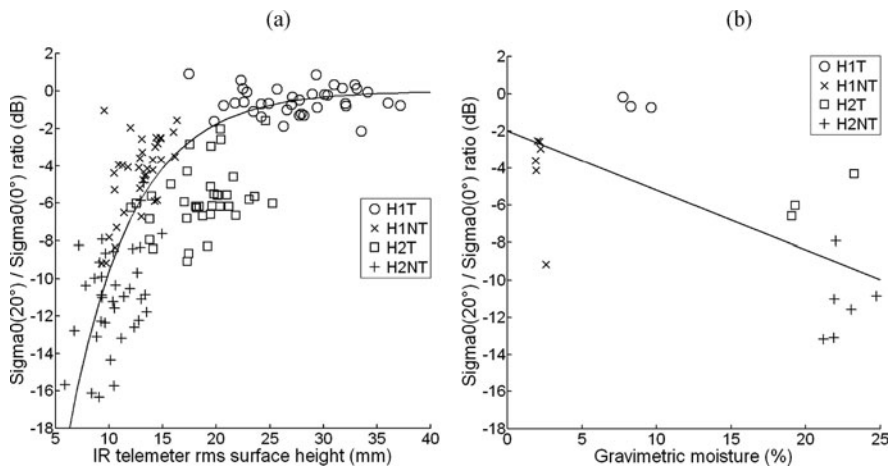


Fig. 26.2 Variations of relative backscattering ratios (coefficient obtained at 20° incidence angle compared to that obtained before tillage at 0° incidence angle) as a function of the rms surface height (a) and gravimetric soil moisture (b)

26.3.3 Capacitance Probe

Measurements performed with the mobile capacitance probe were strongly influenced by soil tillage history (Fig. 26.3). NT treatments led to a finer structure, allowing a good contact between the soil and the electrodes, and therefore to a higher signal.

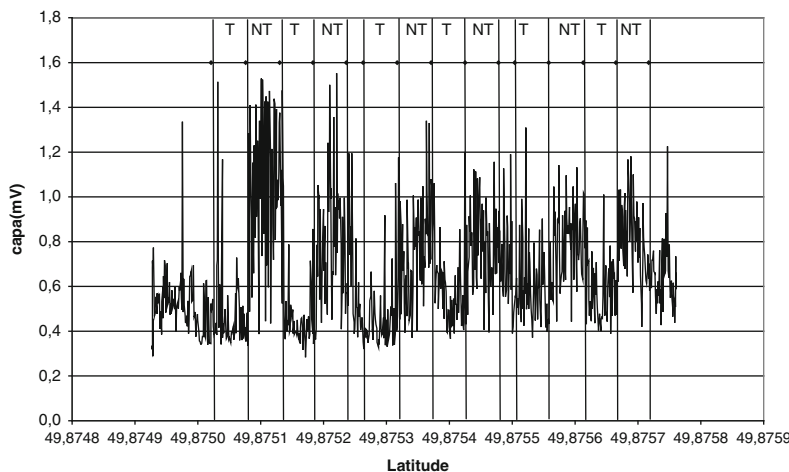


Fig. 26.3 Variation in voltage output from the capacitance probe as it is moved over a dry plot

26.3.4 Mechanical Resistance Probe

Both soil structure and soil water content had an effect on soil mechanical resistance (Fig. 26.4). Dry H1 plots had a higher resistance, particularly in the NT plots, i.e. in the plots with big clods. The difference between NT and T plots was not very pronounced in the wet H2 plots. It seems that the sensor was very sensitive to the size of the structural elements, in the same way as the comparison between sand and gravels.

26.3.5 Tillage Effects on Seedling Emergence

We have estimated the mortality of seedlings during emergence to characterise the seedbed structure. We have used (1) the measurements of clod-size distribution

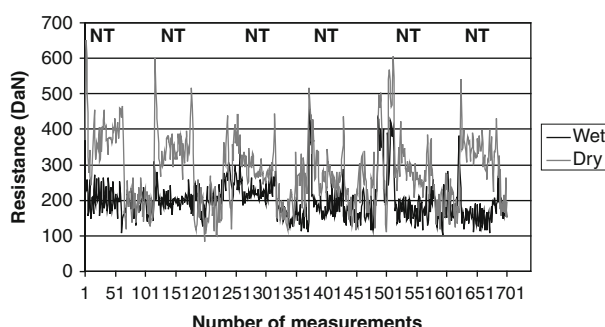


Fig. 26.4 Variation in soil resistance (daN) of the 0–20-cm layer in dry and wet plots before tillage

Table 26.2 Calculated seedling mortality during emergence as a function of seedbed structure in each plot of the field experiment (bold numbers indicate the minimum for two speed rotations and two tillage depths)

	H1-NT	H1-T	H2-NT	H2-T	Mean H1	Mean H2	Mean
<i>Within the seedbed</i>							
P1V1	10.1	23.1	13.2	18.9	16.6	16.0	16.3
P1V2	9.3	18.3	16.7	21.9	13.8	19.3	16.6
P2V1	13.4	25.6	16.1	21.1	19.5	18.6	19.0
P2V2	14.2	27.0	15.3	20.9	20.6	18.1	19.3
<i>Surface without crust</i>							
P1V1	4.7	20.2	4.7	6.1	12.5	5.4	8.9
P1V2	1.9	15.9	5.0	6.9	8.9	5.9	7.4
P2V1	4.5	19.5	4.9	5.7	12.0	5.3	8.7
P2V2	2.4	10.9	4.0	3.6	6.7	3.8	5.2
<i>Surface with crust</i>							
P1V1	30.4	34.4	31.3	33.1	32.4	32.2	32.3
P1V2	32.2	31.5	31.2	32.1	31.9	31.6	31.8
P2V1	22.5	36.1	30.8	30.1	34.8	30.5	32.6
P2V2	33.8	33.7	31.4	30.8	33.8	31.1	32.4

in the seedbed and at the seedbed surface and (2) data on mortality of sugar beet seedlings from Aubertot et al. (2002) and Dürr et al. (2001) (Table 26.2). The two measures in (1) were considered as a function of the presence, or not, of a crust due to rainfall at the surface of the seedbed. The crust corresponded to that area occupied by soil fragments with a diameter less than 2 cm; this situation was obtained after 20 mm of rainfall in this type of soil (Gallardo et al., 2006).

We calculated that tillage would result in a change in seedling mortality from 3 to 8.7%, as a function of initial soil physical conditions. The relative impact of initial structure was more important in dry conditions than in wet ones. Whatever be the water content, seedling mortality was reduced using the lowest tillage depth. Minimum mortality was obtained with the lowest speed rotation in wet conditions; it was the opposite in dry.

As a function of initial soil physical conditions, tillage characteristics induced, in a soil surface without any crust, an increase in mortality from 1 to 9.3% due to clods. Mortality was always lowest for the highest speed of rotation and deepest tillage, whatever be the initial soil conditions (except for non-compacted soil in dry conditions). Mortality due to clods and the crust at the soil surface was less variable. Lowest mortality was obtained with the deepest tillage and the lowest speed of rotation.

Finally, it was not possible to obtain a uniform seedbed in a field with various soil conditions (structure and water content). Speed of rotation and depth of tillage had an effect on seedbed quality, but was less important than the effect of soil water content. Consequently, the choice of tillage date, and therefore the choice of soil water content, remained the most important factor to take into account for seedbed quality.

26.4 Conclusions

A special cultivator was developed – with a continuous-output GPS, a microwave ground-based radar sensor, a laser profile meter, a capacitance probe, and a load cell – for continuously measuring soil physical conditions: water content and mechanical resistance in the first few centimetres, roughness, and clod size at the soil surface. Each sensor was able to detect differences in soil physical conditions at the field scale, but these always depended on soil water content and soil structure. Further work is needed to determine whether a multi-variable analysis would allow better identification of specific soil conditions. We suggest that using two radar angles of incidence might allow better determination of clod-size distribution. Seedbed conditions depended on initial soil conditions (water content and degree of compaction) and soil tillage tool characteristics (working depth and speed of rotation). Working depth and speed of rotation had opposite effects on the size of clods at the seedbed surface and within the seedbed; they could reduce initial soil variability but a uniform seedbed was never obtained. Seeding rate could be controlled by the same sensors if they were put in front of the seed drill. Results of the experiment are also relevant to work on spatial parameterisation of soil models, for example assessing soil hydraulic properties for erosion prediction.

Acknowledgements This work was carried out with the financial support of the INRA and Cemagref under the program GESPAS 'Gestion Spatialisée des AgroSystèmes' (Spatial management of agrosystems). The authors thank the staff of the INRA experimental unit of Estrées-Mons for their work with the field experiment. The authors thank Prof. A.R. Dexter for improving the English.

References

Aubertot JN, Dürr C, Richard G, Souty N, Duval Y (2002) Prediction of sugar beet (*Beta vulgaris* L.) seedlings emergence from beneath a crust. *Plant Soil* 241:177–186

Bolvin H, Chambarel A, Chanzy A (2004) Three-dimensional numerical modelling of a capacitance probe: application to measurement interpretation. *Soil Sci Soc Am J* 68:440–446

Dürr C, Aubertot JN, Richard G, Dubrulle P, Duval Y, Boiffin J (2001) SIMPLE, a model for SIMulation of PLant Emergence. *Soil Sci Soc Am J* 65:414–420

Gallardo-Carrera A, Léonard J, Dürr C, Duval Y, Boiffin J (2006) Effect of seedbed granulometry and soil moisture state on crusting development: an experimental study. 17th conference ISTRO, soil management for sustainability, 28/08–3/09/2006, Kiel, Germany

Noyman Y, Shmulevich I (1996) Ground surface sensing through plant foliage using an FM-CW radar. *Comput Electron Agric* 15:181–193

Skolnik MI (1980) Introduction to radar systems. Electrical engineering series. McGraw-Hill International Editions, New York

Chapter 27

Gamma Ray Sensor for Topsoil Mapping: The Mole

F.M. van Egmond, E.H. Loonstra, and J. Limburg

Abstract In general, farmers base their crop management decisions on a combination of their background knowledge, their experience with a field, and analysis of soil samples. Optimising agricultural production using precision agriculture requires detailed, high-resolution soil information. This level of detail is usually not available in current agricultural practice due to the cost of traditional soil sampling techniques. However, new sensor technology presents an opportunity to produce high-resolution soil maps, which can be used to support agricultural decision making and crop management. This chapter presents a highly sensitive sensor technology, based on the natural emission of gamma radiation from soil, which makes quantitative mapping of physical and chemical soil properties of the tillage layer possible. This method is shown to be capable of producing the high-resolution maps required for precision agriculture, and evidence is presented that in combination with precision agriculture techniques, it has already contributed to yield improvement.

Keywords Gamma ray sensor · Full-spectrum analysis · Precision agriculture · Digital soil mapping · Fluvisols

27.1 Introduction

In the interest of achieving optimum yields, precision agriculture practices deal with very detailed and spatially differentiated combinations of crop requirements and soil properties in a field. Significant variations in soil properties can exist within a field, and addressing these differences requires more detailed information about the cropping system than traditional agricultural practices allow.

F.M. van Egmond (✉)

The Soil Company, Leonard Springerlaan 9, 9727 KB Groningen, The Netherlands
e-mail: egmond@soilcompany.com

Precision agriculture uses high-resolution maps of physical and chemical soil properties, together with yield and crop biomass maps, to enable operational decision support in crop management and to derive variable rate application (VRA) maps. VRA maps show the localised doses of an application (e.g. fertiliser or lime) or indicate, for example, the amount of seed potatoes to be planted based on information from the site-specific soil conditions. Ideally, this information should be quantitative, accurate, and of high spatial resolution. The University of Groningen (RUG), Medusa Explorations, and The Soil Company (The Netherlands) have developed a sensor system (called the Mole) that is used commercially for the high-resolution mapping of physical and chemical soil properties of the tillage layer. The method is based on (natural) gamma radiation measurements and field or regional calibration with conventional soil sample analyses.

The fact that gamma radiation carries information on the mineral composition of soils and rocks has been known for a long time (Cook et al., 1996). Already in the early 1930s, gamma detectors were built and used for mineral (uranium) prospecting (de Meijer, 1998). With the advent of scintillation crystals, which replaced the early Geiger–Muller counter-based systems, it became possible to deconvolute the measured gamma radiation into a series of constituents, including the naturally occurring radioactive elements potassium (^{40}K), thorium (^{232}Th), and uranium (^{238}U).

However, it took researchers until the early 1990s to move from a qualitative interpretation of this information in terms of nuclide concentrations to a quantitative interpretation in terms of soil or soil mineral properties. A number of coincidental research findings have contributed to the development of this method.

Firstly, proper calibration methods were devised, which meant that absolute concentrations of radionuclides could be measured with field-based systems. At the same time, several studies were carried out to investigate correlations between radionuclide concentrations and the mineral properties of soil and sediment samples taken during vehicle, airborne, and underwater radiometric surveys (de Meijer, 1998; Cook et al., 1996; Pracilio et al., 2006). Strong correlations were found, for example, between the ^{232}Th radionuclide concentration and the clay content of the topsoil. Gamma radiation originating from depths as far down as 50 cm is able to reach the surface, while radiation originating from below that depth is attenuated by the overlying soil dry matter and soil moisture (Cook et al., 1996; Viscarra Rossel et al., 2007). As a general rule, it has been found that different soil and sediment types are characterised by unique fingerprints (van Wijngaarden et al., 2002; Cook et al., 1996; Pracilio et al., 2006) – i.e. each soil carries a unique concentration of the naturally occurring nuclides ^{40}K , ^{238}U , and ^{232}Th (C_{K} , C_{U} , and C_{Th}). Some years later it was found that relationships exist not only between radionuclides and physical soil properties (texture, grain size, etc.) but also between radionuclides and chemical soil properties (heavy metal pollution, fertilisers, nutrients, etc.) (van der Graaf et al., 2007; Viscarra Rossel et al., 2007).

In conjunction with the development of better spectrum analysis and fingerprinting methods, smaller and better gamma data acquisition systems were developed. Previous systems for measuring radioactivity have been converted into sensors for

measuring radioactivity-related soil properties. This chapter describes a method by which relatively low-cost, high-resolution soil maps can be produced by using these sensors and how farmers can use these maps in precision agriculture for yield improvement.

27.2 Equipment and Data Analysis Methods

In the past, most field gamma ray-logging systems were built from NaI scintillation crystals and used a ‘windows’ spectrum analysis to determine the concentration of the radionuclides. Our innovations, related to both the type of detector material used and the method of data analysis, have significantly improved the quality of gamma measurements (Koomans et al., 2007) and the level of detail and accuracy of the maps.

27.2.1 *Hardware*

Traditional gamma radiometers use crystals like sodium iodide (NaI), which are not the most efficient capturers of gamma radiation. They are also brittle and therefore accident-prone. Commercially available alternatives are bismuth germanate ($\text{Bi}_4\text{Ge}_3\text{O}_{12}$ or BGO) and caesium iodide (CsI). BGO has a low peak resolution, which rules out its use in cases where nuclear fallout radionuclides (such as ^{137}Cs) are the subject of interest. Furthermore, this material is rather expensive and prone to temperature instability. CsI is a very robust alternative to NaI and BGO. The higher density of CsI compared to NaI yields better efficiency, especially for smaller crystal sizes. The Soil Company’s sensor utilises a 70-mm \times 150-mm CsI crystal coupled to a photomultiplier unit and a 512-channel MCA system (Plate 27.1a). The system stores the full spectral information, which enables post-processing of the spectral data at a later stage.

27.2.2 *Spectral Data Analysis*

In order to convert the measured spectral information into concentrations of radionuclides, the ‘windows’ analysis method is frequently applied (Grasty et al., 1985). Here, the activities of the nuclides are found by summing the intensities of the spectrum found in a certain interval surrounding a peak. In the classic ‘windows’ approach, three peaks are used to establish the content of ^{232}Th , ^{238}U , and ^{40}K . A major flaw of the method is the limited amount of spectral information that is incorporated into the analysis. Another weakness is the inherent use of ‘stripping factors’ to account for contributions of radiation from nuclide A into the peak of nuclide B (Plate 27.1b).

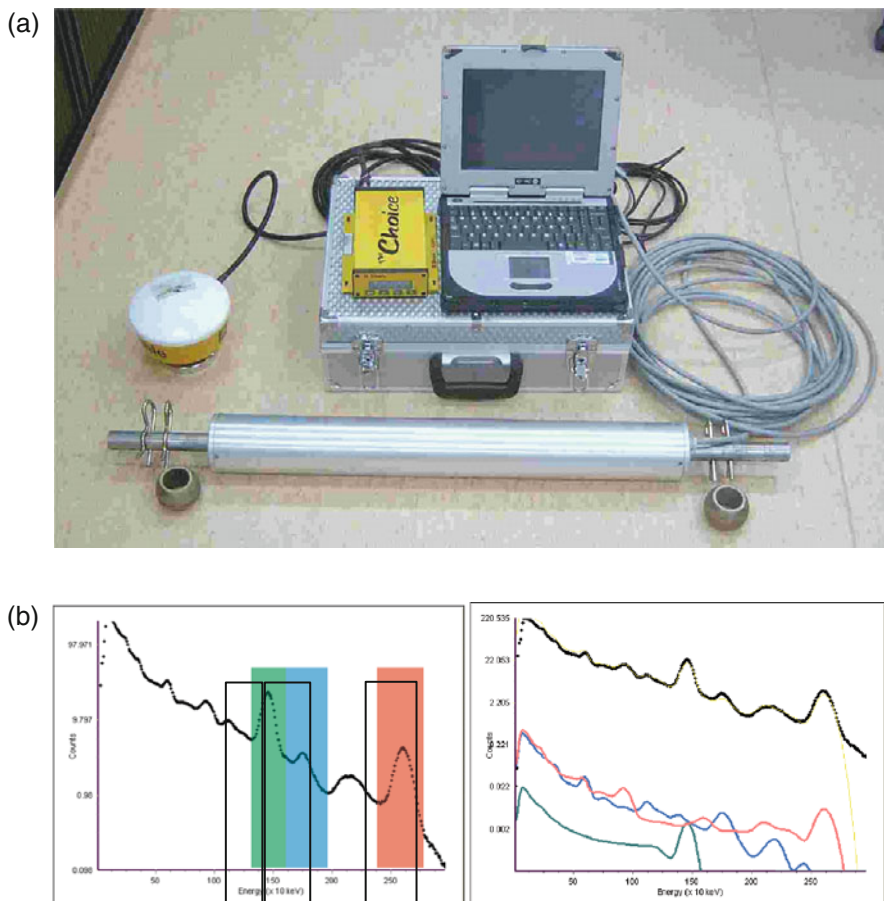


Plate 27.1 (a) The Mole system (The Soil Company, Groningen) consisting of a detector, a GPS, and a laptop. (b) Left: 'Windows' surrounding the ^{40}K , ^{238}U , and ^{232}Th peaks (left to right). Right: FSA analysis of a natural gamma spectrum. The measured spectrum (black dots) is fitted with a curve (yellow); green, blue, and red curves are standard spectra for ^{40}K , ^{238}U , and ^{232}Th , respectively

The Soil Company's Mole sensor system incorporates a different method to analyse gamma spectra. In contrast to the 'windows' method, our full-spectrum analysis (FSA) method incorporates virtually all of the data present in the measured gamma spectrum. With FSA, a chi-squared algorithm is used to fit a set of 'standard spectra' to the measured spectrum (see Plate 27.1b). (A standard spectrum is the pure response of the detector system used on a 1 Bq/kg source of a given radionuclide in a given geometrical setting.) The fitting procedure yields the multiplication factors needed to reconstruct the measured spectrum from the standard spectra of the individual nuclides. The multipliers are equal to the actual concentrations of the radionuclides in becquerel per kilogram that led to the measured spectrum. This method is described in detail by Hendriks et al. (2001). Hendriks showed that the

associated uncertainty in the FSA method is at least a factor of 1.7 less than that in the ‘windows’ method.

27.2.3 Fingerprinting and Soil Sampling

During field measurements, the Mole is placed on a tractor and driven across the field. A reading of the gamma spectrum and the GPS position is stored on a computer every second (Plate 27.1a). A constantly updated map, created on the go, shows the variation of the total count (spectrum) of gamma radiation ‘live’ in the field.

To translate the gamma data into soil maps, calibration with soil parameters is required. With this aim, soil samples are taken down to a depth of 25–30 cm (tillage depth), within a 2 m radius of the sensor. The locations of the soil samples are chosen based on the gamma variation in the data identified from the maps. The locations selected for soil sampling should reflect the overall soil variation in the field. At these sample sites, a gamma spectrum is measured for 5 min. The soil samples are analysed in the laboratory and the soil parameters are related to the corresponding gamma readings by regression analysis. The resulting regression equations allow the interpolated gamma readings to be translated into soil property maps. Soil sampling is conducted on the same day as the gamma survey of the field. The gamma spectrum analysis, regression, interpolation, map calculation, and quality control processes are conducted in the office.

The fingerprints of soil types and their properties depend on parent material, soil-forming processes, and age, among other things. In agriculture, soil nutrient levels are influenced by management practices and vary between different farming systems. Therefore calibrating the gamma data for soil nutrient maps has to be based on soil samples from that specific field or farm. However, physical soil properties and their natural gamma readings can be compared within a geological unit. To illustrate this, a dataset of soil samples and their gamma readings from an 800 ha farm on marine clays in Zeeland, The Netherlands, has been collected. The dataset consisted of 89 samples and was divided into a calibration dataset containing 46 samples and a validation dataset containing 43 samples. (Multiple) linear regression was performed using the calibration dataset and the best fits for each soil property are listed in Table 27.1. Soil texture (clay, silt, and loam) shows a good correlation when compared across the farm. However, soil nutrients like organic matter and magnesium show poor correlations on a farm scale, but these improve significantly when considered at field scale.

The Soil Company has gradually built a large database of soil samples and their gamma readings. This database is used to generate general spatial patterns of different soil properties and provides ‘extra’ regional sample data for the correlation of nuclides with physical soil properties (and sometimes organic matter and magnesium). For a graphical illustration of the data in Table 27.1, two of the correlations are plotted in Fig. 27.1. Similar plots can be made for other physical and chemical soil properties.

Table 27.1 Results of the separate calibration and validation of soil properties and gamma measurements for an 800-ha farm in Zeeland, The Netherlands

Soil properties	Calibration			Validation	
	Nuclide	N ^a	R ²	RMSE ^b	N ^c
Clay (<2 µm)	²³² Th	46	0.85	3.7	43
Fine silt (<16 µm)	²³² Th	46	0.80	6.8	43
Loam (<50 µm)	²³² Th	46	0.82	8.1	43
M0 (median grain size)	⁴⁰ K	46	0.84	9.5	43
Organic matter	⁴⁰ K, ¹³⁷ Cs	46	0.51	0.41	
Organic matter	⁴⁰ K, ¹³⁷ Cs	15	0.88	0.24	
Magnesium	²³⁸ U, ¹³⁷ Cs, ⁴⁰ K	46	0.65	15.2	
Magnesium	²³² Th, ¹³⁷ Cs	15	0.90	4.5	

^aNumber of samples used for calibration^bRMSE for clay, silt, loam, and organic matter is depicted in %; for M0 in µm; and for Mg in mg kg⁻¹ dry matter^cNumber of samples used for validation

In general, correlation plots had an R^2 ranging from 0.6 to 0.95. If the analysis explained less variance, the regression results were not used in the prediction of a soil property.

The gamma data from the field were interpolated using inverse distance weighting. Applying the regression equation from Fig. 27.1 to some of the gamma maps of this farm yielded the map of clay content shown in Fig. 27.2.

The intervals shown in the legend are comparable to the statistical error, and variation in the maps can therefore be considered as a significant variation. To check the reliability of a derived soil map, the map values on the sample locations were compared with the actual (measured) soil property values. The R^2 values between the predicted values and the sampled soil properties varied between 0.7 and 0.98. The image was compared to existing soil maps where available. In these cases, validation was performed by applying regression equations of the calibration dataset (Table 27.1, Fig. 27.1) to the gamma data of the separate validation dataset. For clay, this yielded an R^2 of 0.86 with an RMSE of 3.1% (Table 27.1). Results for validation of other soil properties in this dataset have an R^2 between 0.72 and 0.84, with RMSE between 5.4 and 13.3 (Table 27.1). The patterns in the soil maps corresponded well with the farmers' qualitative knowledge of the fields and confirmed their perception during tillage.

Maps of bulk density, water retention, etc. can be calculated using pedotransfer functions and the physical soil and organic matter maps. Maps of compaction risk, nematode risk, etc. can also be calculated based on information from agricultural research on the subjects (RBB, 1970).

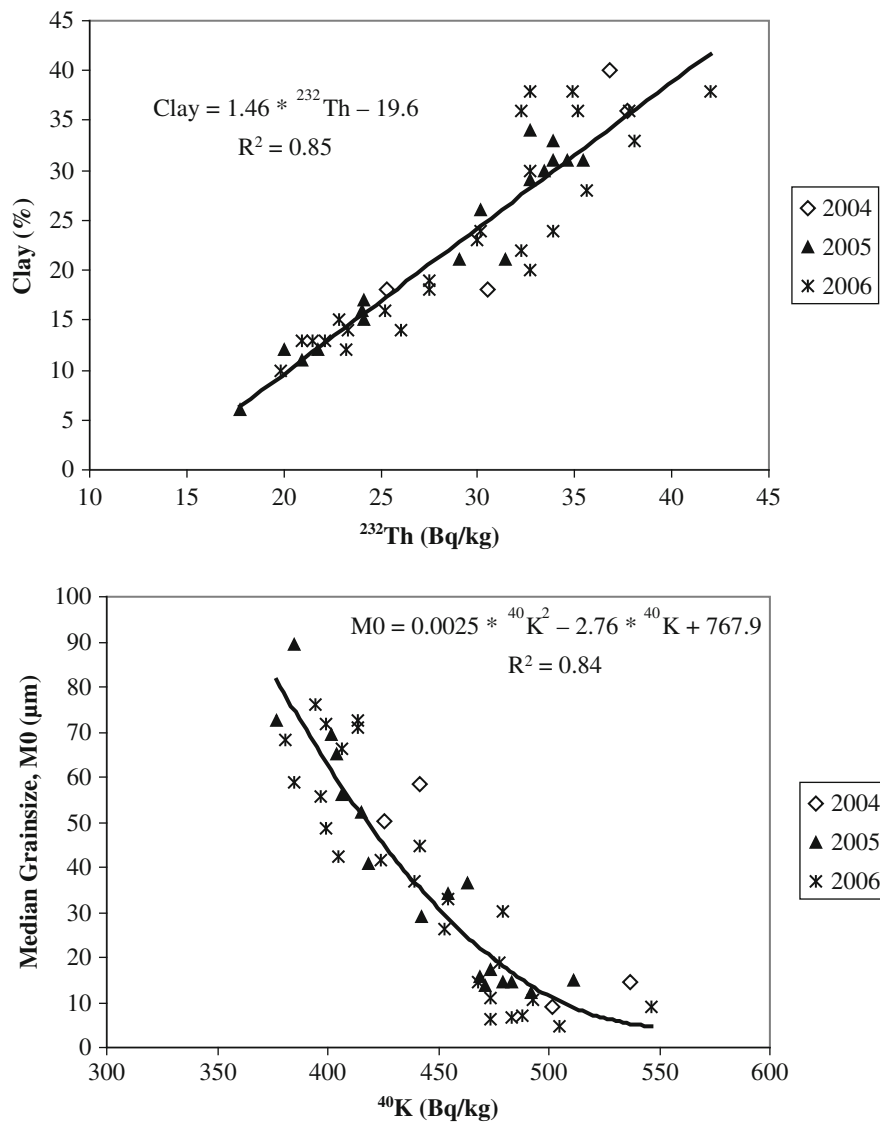


Fig. 27.1 Soil samples of clay content (%), top) and median grain size (M_0 , bottom) versus ^{232}Th and ^{40}K readings. Data from an 800-ha farm (Zeeland, The Netherlands) taken in three successive years

The standard set of reported maps from a field measurement consists of four types: regionally calibrated maps of physical soil properties, field or farm calibrated maps of chemical soil properties, maps calculated based on pedotransfer functions, and calculated risk maps.

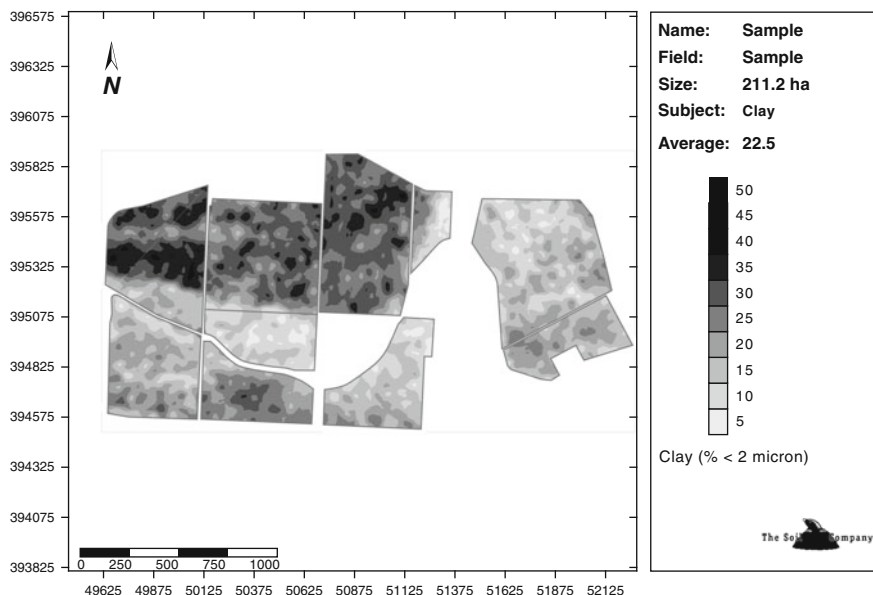


Fig. 27.2 Gamma-based map of the clay content of 10 fields (211 ha in total, Zeeland, The Netherlands) derived from the equation in Fig. 27.1

27.3 Applications

In The Netherlands, experience has been gained from several precision agriculture applications derived from or based on the gamma ray-based soil maps. Table 27.2 gives an overview of some of these applications and their general benefits.

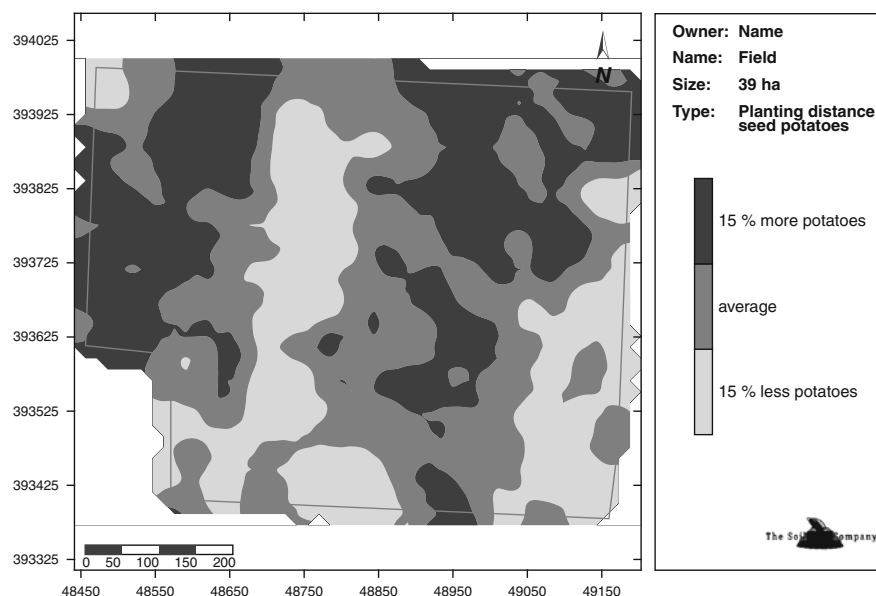
Clay maps from the Zeeland farm were used to reduce the amount of sugar beet seed needed by 13%, while maintaining the same yield. Another precision agriculture application used the clay content map to achieve a more homogeneous size distribution of seed potatoes. This is an attractive perspective for farmers, as seed potatoes in the 28–55 mm size range are worth more. The clay content map has been translated into a variable planting distance map (Fig. 27.3), and this has improved financial yields on average by 6% or 230 € ha^{-1} in a 4-year trial.

27.4 Future Developments

Currently research is being conducted on the integration of gamma ray sensing with other sensor techniques like EM38 (Chapters 29, 33, and 28). This can yield complementary data that can perhaps further enhance data-based decision making by farmers and offer new possibilities for precision agriculture. Improved data interpolation and sample location selection techniques are being automated to improve

Table 27.2 Tested precision agriculture strategies and their measured and perceived benefits in The Netherlands

Application	Base map(s)	Desired effect	Benefits
Variable planting distance	Clay content/water retention	Homogeneous size distribution of potatoes/broccoli Reducing amount of sugar beet seed	5% negative up to 15% positive financial benefit 13% reduction in cost while maintaining yield
Variable fertiliser amount	Nutrient or clay content	Saving fertiliser or improving yield	Up to 60% reduction in fertiliser 10% yield improvement consumer potatoes
Variable application compost	Organic matter	Reducing organic matter variation in field	Improved soil structure, water retention
Variable liming	pH and organic matter	More homogeneous pH	Improved sugar yield sugar beets
Variable nematode control	<i>Trichodorus</i> risk	Reduction in granular products	40–60% savings on chemicals
Variable tillage speed	Compaction risk	Less compaction due to tillage	Variable tillage patterns are highly recognisable

**Fig. 27.3** Map of recommended variable planting distance calculated from the gamma-based clay content map of Fig. 27.2

map quality and enable commercial implementation of the process. Additionally, alternative methods of data analysis are being examined for use instead of, or complementary to, the current regression analysis method to determine if or how gamma sensor measurements and their translation into soil data could be improved.

27.5 Conclusions

Sensor technology based on gamma ray sensing can be used for creating quantitative topsoil maps in conventional units that farmers are familiar with. The method is highly sensitive and is used to make high-resolution maps for precision agriculture. The patterns in the soil maps are recognisable to farmers and confirm their perception during tillage. The quantitative aspect of the soil property maps enables operational decision support for crop management. This work has shown that accurate sensor technology and precision agriculture can contribute to yield improvement.

References

Cook SE, Corner RJ, Groves PR, Grealish GJ (1996) Use of airborne gamma radiometric data for soil mapping. *Aust J Soil Res* 34:183–194

de Meijer RJ (1998) Heavy minerals: from 'Edelstein' to Einstein. *J Geochem Explor* 62:81–103

Grasty RL, Glynn JE, Grant JA (1985) The analysis of multi-channel airborne gamma-ray spectra. *Geophysics* 50:2611–2620

Hendriks PHGM, Limburg J, de Meijer RJ (2001) Full-spectrum analysis of natural γ -ray spectra. *J Environ Radioactiv* 53:365–380

Koomans RL, Limburg J, van der Graaf EJ (2007) Towards lightweight airborne gamma spectrometry. *Medusa Systems*. www.medusasystems.com

Pracilio G, Adams ML, Smettem KJR, Harper RJ (2006) Determination of spatial distribution patterns of clay and plant available potassium contents in surface soils at the farm scale using high resolution gamma ray spectrometry. *Plant Soil* 282:67–82

RBB (Rijkslandbouwconsulenten voor Bodem- en Bemestingsvraagstukken) (1970) Waardering van de Landbouwkundige Waarde van de Grond. 70/48, Wageningen

van der Graaf ER, Koomans RL, Limburg J, de Vries K (2007) In situ radiometric mapping as a proxy of sediment contamination: assessment of the underlying geochemical and -physical principles. *Appl Radiat Isot* 65(5):619–633

van Wijngaarden M, Venema LB, de Meijer RJ, Zwolsman JJG, Van Os B, Gieske JMJ (2002) Radiometric sand–mud characterisation in the Rhine–Meuse estuary Part A: Fingerprinting. *Geomorphology* 43:82–101

Viscarra Rossel RA, Taylor HJ, McBratney AB (2007) Multivariate calibration of hyperspectral γ -ray energy spectra for proximal soil sensing. *Eur J Soil Sci* 58:343–353

Chapter 28

Gamma Ray Sensing for Cadmium Risk Assessment in Agricultural Soil and Grain: A Case Study in Southern Sweden

M. Söderström and J. Eriksson

Abstract Cadmium (Cd) is a toxic metal, which is taken up by plants relatively easily. In Sweden, high Cd levels in soils and crops are encountered in agricultural areas where the soil parent material is rich in the metal. Farmers must produce grain with a Cd concentration below permissible limits, and the milling and food industry rates traceability as increasingly important. In this study, both airborne and proximal gamma ray sensing were tested in an area where high levels of Cd in soils and crops have been recorded. The hypothesis was that the occurrence of Cd in the topsoil and winter wheat grain would follow the variation of ^{238}U so that gamma ray sensing could thereby be used as a fast and cheap method for monitoring Cd in soils and crops. We found that the variability of Cd in the topsoil was considerable in the area and was very well correlated with ^{238}U . It seems possible to delineate areas of winter wheat that have a very low risk of high Cd. A working model for the practical application of the sensing technique is suggested.

Keywords Radioactivity · Geochemistry · Wheat · Cadmium · Uranium · Sweden · Risk classification

28.1 Introduction

High cadmium (Cd) concentration in grain can be a problem. For humans, grain food products are normally the main source of Cd (except for smokers). In Sweden, a certification system, ‘Swedish Seal of Quality’, is in place for quality and environmental control. A low Cd level in delivered grain is one criterion for certification. Currently, farmers with a soil Cd level above 0.3 mg kg^{-1} are required to analyse Cd in the crops. For soil Cd, one sample can at most represent 15 ha, and an analysis

M. Söderström (✉)

Department of Soil and Environment, the Precision Agriculture and Pedometrics Group,
Swedish University of Agricultural Sciences, PO Box 234, SE-532 23 Skara, Sweden
e-mail: mats.soderstrom@mark.slu.se

sample is valid for a maximum of 10 years. In some geographic areas, grain Cd often exceeds the currently permissible limit of $80 \mu\text{g kg}^{-1}$, and one crop sample can represent a maximum of 25 ha (alternatively, one analysis per 250 t of harvested grain is needed). Through the database of the certification system, it is possible to locate areas where high Cd levels occur, but the sampling procedure prevents a detailed analysis of the local spatial variability of Cd in crops and soil.

In a national soil survey ($n = 3,067$), the average Cd concentration in Swedish topsoil was 0.23 mg kg^{-1} , and 19% of the observations had $> 0.30 \text{ mg Cd kg}^{-1}$ (Eriksson et al., 1997). Cd uptake from soil to plants depends on many factors – e.g. plant species, cultivars, and various soil properties – but the most important is Cd concentration in the soil (Eriksson et al., 1996). In Sweden, high soil Cd areas are often found in areas where the parent bedrock at least partly is alum shale. The content of uranium (U) in the soil is also normally related to occurrences of this parent material. Since the 1960s, U has been mapped by airborne gamma ray measurements of the ^{238}U isotope by the Swedish Geological Survey (SGU), and recently comparable equipment mounted on a motor vehicle has become available. This equipment can be used for very detailed gamma ray scanning. The natural emission of gamma rays from rock outcrops and soil reflects both the type of bedrock and its weathering and the processes of soil development (e.g. IAEA, 2003; Wilford and Minty, 2007). In this study, the objective was to test whether airborne and proximal gamma ray measurements could be used in an area in southern Sweden rich in alum shale for detailed risk assessment of Cd in agricultural soils.

28.2 Materials and Methods

Data from airborne gamma ray spectrometry (^{238}U , ^{232}Th , and ^{40}K) are available in the SGU radiometric database. Currently, about 80% of Sweden has been mapped by this technique (SSI, 2007). In our study area, which is part of Östergötland County, the SGU radiometric data were obtained in N–W transects with 200 m spacing (Fig. 28.1). Approximately one measurement was taken for every 16 m of transect. Aircraft altitude was on average 60 m. Most of the detected signal originates from an ellipse on the ground (the footprint) with its major axis perpendicular to the flight path of about 200 m (Mats Wedmark, SGU, personal communication).

Ground-based gamma ray sensing was carried out from a 4WD motor vehicle at four agricultural fields in the area. The equipment used was ‘the Mole’, a gamma ray sensor for topsoil mapping developed by the University of Groningen and The Soil Company (Groningen, The Netherlands). Its use is described in Chapter 27. Data (^{238}U , ^{232}Th , ^{40}K , and ^{137}Cs) were collected approximately every 4 m along transects separated by about 12 m. The circular footprint had a diameter of 3–4 m. The measurements were made in February 2007 when the ground was covered by no more than 5 cm of fresh snow.

Digital geological maps of soil and bedrock at a scale of 1:50,000 are available for the study area from SGU (Fromm, 1976; Gorbatschev et al., 1976). The study area (Fig. 28.1) is in an area of southern Sweden where high Cd levels in soils and

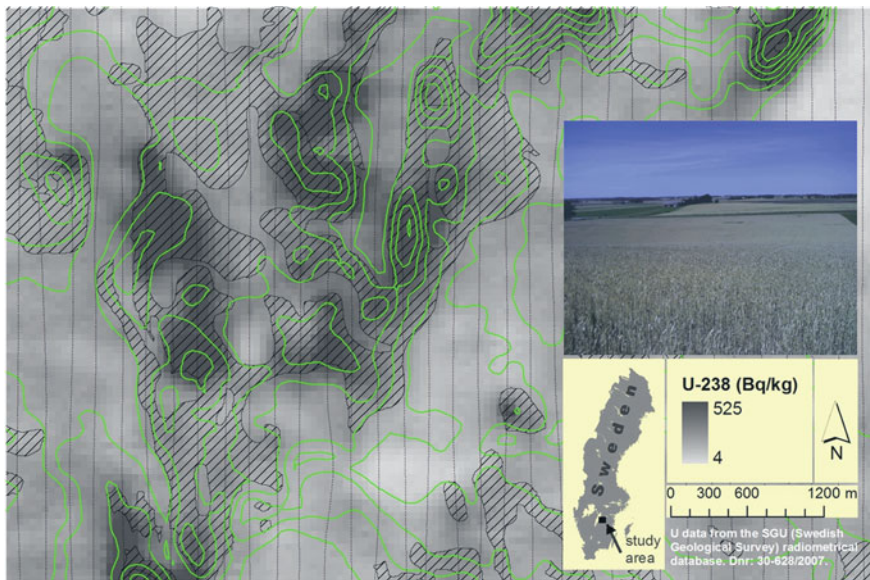
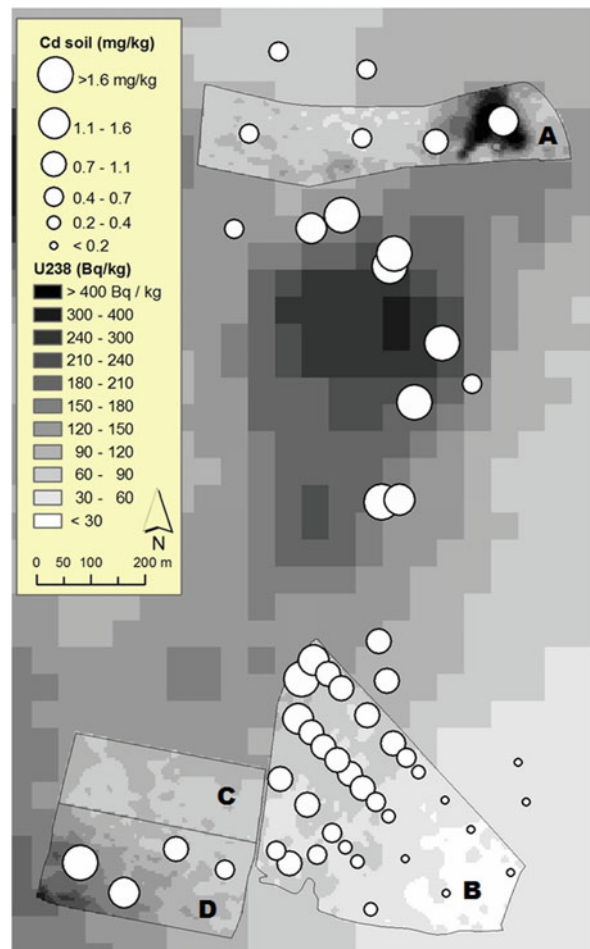


Fig. 28.1 Interpolated values of ^{238}U recorded from the air and measured along transects with 200 m spacing (dotted lines). Areas covered by glacial till are shown hatched, and 5 m elevation contours are drawn. The photo shows scenery typical of the area

crops have been recorded under the Swedish Seal of Quality certification system. The soil texture ranges from silty clay to sandy loam (Fromm, 1976). Most of the soils are Haplic Cambisols. The area is located in an E–W basin with a 0–20-m-thick soil cover underlain by Cambrian–Silurian bedrock, mainly limestone, sandstone, shale, and alum shale. Precambrian granitic bedrock covers the area north and south of the basin, just outside the study area.

Exactly 56 samples of topsoil (0–20 cm deep) were collected in one part of the study area (Fig. 28.2). Some 34 samples were obtained in 2001 from field B (Fig. 28.2) as part of an earlier unpublished study, while the rest were taken in 2006. A sample consisted of several sub-samples collected with a soil auger, but the sampling procedure differed between the surveys (2001: 7–10 sub-samples obtained from a circle of 3–5 m radius; 2006: 9 sub-samples obtained in a 3×3 grid covering 20 m \times 20 m). In 2007, 25 samples of winter wheat (*Triticum aestivum*) were collected (locations shown in Fig. 28.4). These samples were chosen to cover areas of high and low values of ^{238}U from the airborne survey (Fig. 28.1). Winter wheat grain samples obtained in 2006 were also used ($n = 34$). These were located in different soil types according to the SGU soil map. All grain samples consisted of nine sub-samples obtained in a 3×3 grid covering 20 m \times 20 m. At each sub-sample, 20 cm of the crop in two rows was cut. Soil Cd concentrations were determined after extraction with 7 M HNO_3 at 100°C (SIS, 1997). Grain Cd concentrations were determined after digestion in concentrated HNO_3 (suprapure) for 20 h at a final temperature of 135°C. Analyses were performed by ICP-MS.

Fig. 28.2 Cd in topsoil and $^{238}\text{U}_{\text{ground}}$ at four fields (A–D) scanned by the Mole ground sensor. The background map is based on ^{238}U from the SGU radiometric database (part of Fig. 28.1)



The maps in this report were created using ArcGIS 9.1 (ESRI Inc., Redlands, USA) with the extensions Spatial Analyst and Geostatistical Analyst. The interpolation method used was ordinary block kriging. Experimental variograms and fitting of variogram models were made in GS+ (Gamma Design, Plainwell, USA). The airborne data were interpolated to a 50-m \times 50-m grid, whereas the resulting maps of the ground-based data had a resolution of 5 m \times 5 m.

28.3 Results and Discussion

Figure 28.1 shows the interpolated ^{238}U values from the airborne measurements ($^{238}\text{U}_{\text{air}}$). High ^{238}U values coincided well with soils characterised as glacial till. The till with high ^{238}U content contains a large percentage of fragments from alum shale parent material.

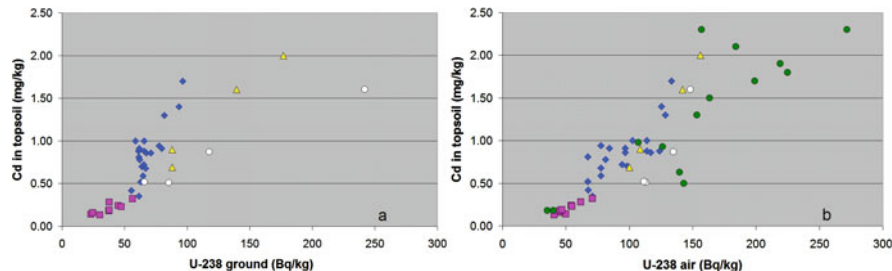


Fig. 28.3 Scatter plots of interpolated ^{238}U and topsoil Cd for (a) the ground sensor and (b) the SGU radiometric database. White circles, field A; pink squares, south-eastern part of field B; blue diamonds, north-western part of field B; yellow triangles, field D; dark green circles in diagram b, samples outside of fields A–D

Soil Cd concentrations in samples obtained in a smaller part of the study area are shown in Fig. 28.2. Detailed interpolated maps of the ground-based measurements of ^{238}U ($^{238}\text{U}_{\text{ground}}$) at four fields are displayed on top of the $^{238}\text{U}_{\text{air}}$ map. Figure 28.3a and b shows scatter plots of soil Cd vs. ^{238}U based on maps in Fig. 28.2. The correlation between soil Cd and the $^{238}\text{U}_{\text{ground}}$ map is fairly strong, but the relationship varies between the different fields or parts of a field. For example, the south-eastern part of field B consists of postglacial silt, which has a very low Cd concentration. Towards the north-east in the same field, there is an abrupt transition to a clayey soil, with high soil Cd concentration. Figure 28.3a shows that the correlation between $^{238}\text{U}_{\text{ground}}$ and Cd is different in the two parts of the field. The airborne measurements of U are also well correlated with soil Cd, despite the fact that a $^{238}\text{U}_{\text{air}}$ map provides more of a regional overview.

There is a clear positive correlation between the ^{238}U map and Cd in winter wheat in the 2007 samples (Figs. 28.4 and 28.5). However, a few of the samples that were taken at locations with very high ^{238}U values have a lower Cd content than expected. Cd in grain in the 2006 samples was more scattered and values were generally higher. Three samples had a Cd concentration of $120 \mu\text{g kg}^{-1}$, but at least for one of these the mapped ^{238}U value was not very high. This particular sample, however, was obtained close to an area with substantially elevated ^{238}U values.

The spread of values in the scatter plot of Fig. 28.5 may seem discouraging, but as was mentioned in Section 28.1, Cd uptake by a crop is complicated and depends on a number of variables. The wheat collected in 2007 was of the same cultivar (Olivin) and the samples were directed to fields that had sharp gradients from high to low $^{238}\text{U}_{\text{air}}$ values (Fig. 28.2). The samples from 2006, on the other hand, consisted of a mix of cultivars and the sampling was done without consideration of the variability of $^{238}\text{U}_{\text{air}}$. Local variations in soil properties – such as pH, clay content, and organic matter – may affect Cd uptake. Another problem with the comparison made in Fig. 28.5 is that a single airborne gamma ray measurement is an average over a large area on the ground. In this case, measurements are dense in the N–S direction (every 16 m), but the distance between the flight transects is about 200 m.

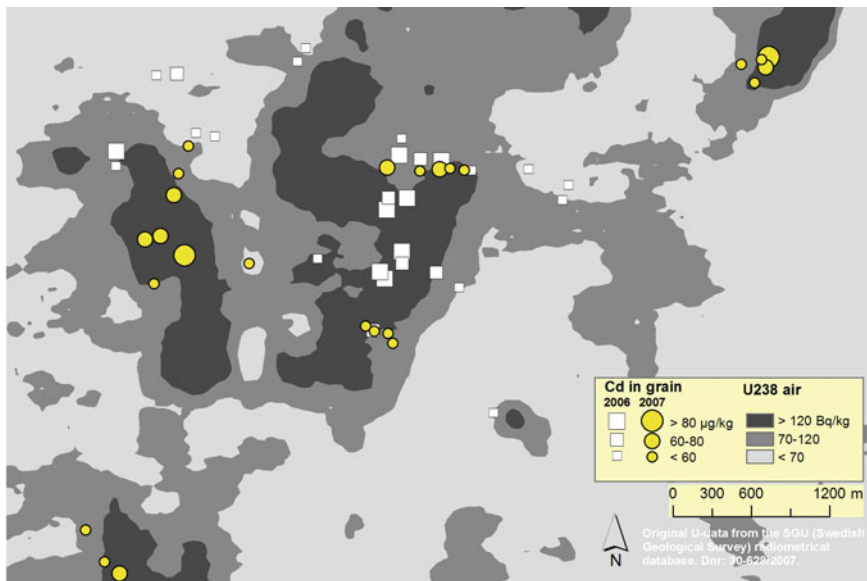


Fig. 28.4 Cd in winter wheat grain in 2006 and 2007. The background map is the $^{238}\text{U}_{\text{air}}$ map in Fig. 28.1 (airborne instrument), arbitrarily classified into three classes

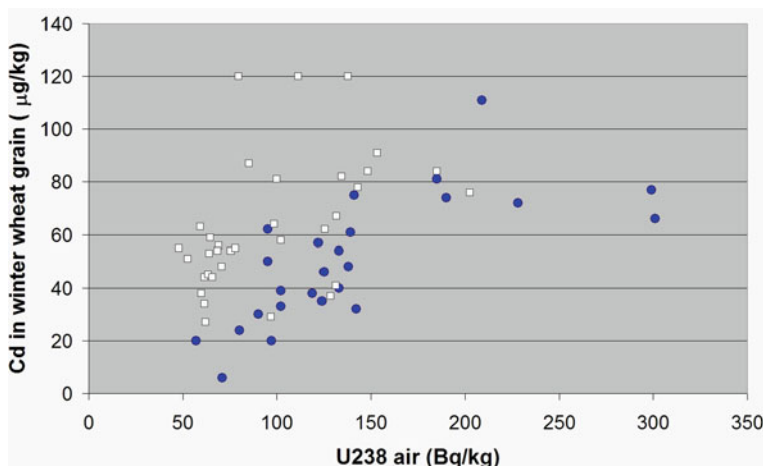


Fig. 28.5 Scatter plot of Cd in winter wheat grain in 2006 (white squares) and 2007 (dark circles) vs. values in the ^{238}U map in Fig. 28.1

The position of the measurement is also to some extent uncertain. Depending on the mapping method, estimated values at single pixels may differ.

Another interesting fact is that the uptake of Cd in the grain in the Östergötland study area is lower than expected from its soil Cd levels, which are high in some places. In other areas of Sweden with similar soil Cd concentrations, the Cd in

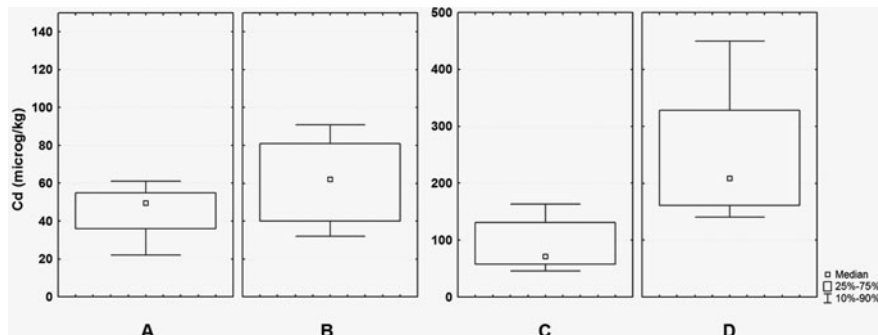


Fig. 28.6 Box plots of Cd in winter wheat at different levels of $^{238}\text{U}_{\text{air}}$ in (a) Östergötland $\text{U} < 85 \text{ Bq/kg}$; (b) Östergötland $\text{U} > 85 \text{ Bq/kg}$; (c) Skåne $\text{U} < 85 \text{ Bq/kg}$; (d) Skåne $\text{U} > 85 \text{ Bq/kg}$. Note the different scales on the y-axes

winter wheat is normally higher. Apparently, the Cd is less available to plants. In Fig. 28.6, a comparison is made between $^{238}\text{U}_{\text{air}}$ and Cd in winter wheat in the Östergötland study area and similar data from another problem area in southern Sweden (in south-eastern Skåne County). In the Skåne area, the $^{238}\text{U}_{\text{air}}$ values are similar or slightly lower than in the Östergötland area, but the uptake of Cd is much higher. In the Skåne area, however, there are other known sources of Cd than alum shale, e.g. occurrences of Cd-rich sphalerite in Cambrian sandstone (Söderström and Eriksson, 1996), which would not be recorded by ^{238}U measurements. In addition, the highest Cd values in Skåne were obtained during a year with very high precipitation, which has been reported to be an important uptake factor (Eriksson et al., 1996). Further work is needed to better understand the temporal (between-year) variations of Cd uptake in grain and the variation in uptake between varieties. This would improve the usefulness of the strong relationship encountered in this study between soil Cd and ^{238}U .

For farmers working under the quality certification system, it would be valuable if some fields could be classified as low risk for Cd in grain, without the need for analysing Cd in the soil. A system of ‘green cards’ for such areas has been suggested. In the studied area in Östergötland, it is evident that the alum shale is the primary source of Cd in the soil. The alum shale is also the source of uranium, and measurements of ^{238}U seem to work well as a proxy for soil Cd in this case. The variation of Cd is considerable, sometimes even within a field. Fields entirely located in areas with the lowest ^{238}U values, e.g. the light grey area in Fig. 28.4, should carry only a small risk for high Cd in either soil or crop. Conversely, fields wholly or partly located in areas of higher ^{238}U should be required to test for Cd in the soil. For such fields, a reasonable approach might be to use a detailed proximal gamma ray survey from a vehicle, together with a few samples for Cd analyses targeted according to the resulting map.

Given this framework, it seems reasonable to suggest that the described sensing techniques could be used for Cd risk classification of agricultural land in areas

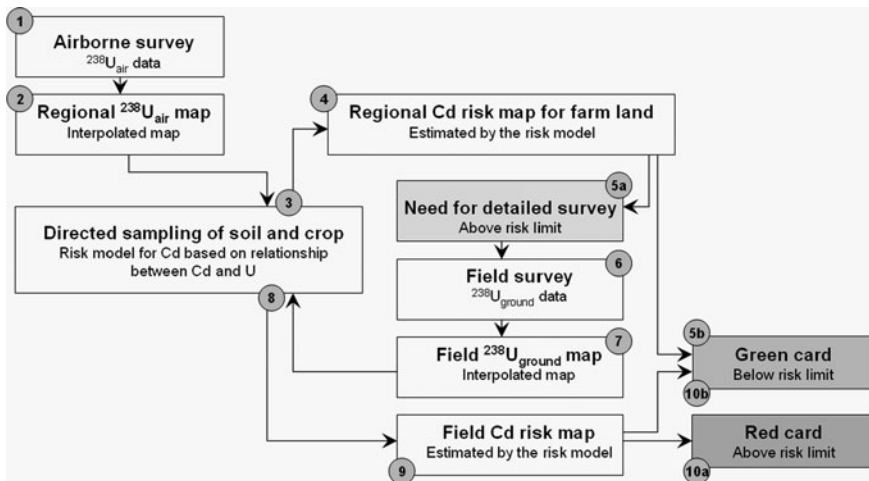


Fig. 28.7 Suggested steps of cadmium risk classification of agricultural land based on gamma ray sensing in areas where the main source of cadmium is uranium-rich bedrock, such as alum shale

such as this. A conceptual model of how these techniques could be applied in practice is shown in Fig. 28.7. The goal would be that farmland classified as low risk for Cd could receive a ‘green card’ and would not have to test for Cd in grain. In areas where the main source of Cd is U-rich bedrock, it should be sufficient to do this initial classification based on airborne gamma ray sensing combined with targeted sampling of soil and crop to develop a risk classification model for the area. Bearing in mind the differences in relationship between $^{238}\text{U}_{\text{air}}$ and Cd in wheat shown in Fig. 28.6, the sampling of Cd in soil and crop is crucial. It is advisable that such a risk model (step 3 in Fig. 28.7) be developed by a method that includes the uncertainty of the $^{238}\text{U}_{\text{air}}$ data, e.g. indicator kriging or fuzzy classification of the $^{238}\text{U}_{\text{air}}$ map.

Figure 28.8 is an example of a risk classification of agricultural land in the study area. In this case, agricultural land was derived from a vector polygon map used for management of EU agricultural subsidies in Sweden (Swedish Board of Agriculture, Jönköping, Sweden). Physical obstacles constitute boundaries of the polygons, which can be equivalent to one or a few fields. Owners of agricultural land that is judged being above a risk limit would need a detailed survey (boxes 6–9 in Fig. 28.7), e.g. by an instrument such as the Mole in combination with local samples of Cd. After the detailed survey, some additional areas could be given a ‘green card’ (box 10b in Fig. 28.7) or, if above a risk limit, a ‘red card’ (box 10a in Fig. 28.7). Grain from red card areas would always need to be controlled for Cd.

Although the results of this initial analysis of the co-variability between Cd in soil and crop and ^{238}U from gamma ray sensing are promising, it is suggested that further studies in areas with corresponding geological conditions should be conducted. Suitable methods for the development of risk maps in this context also need to be examined.

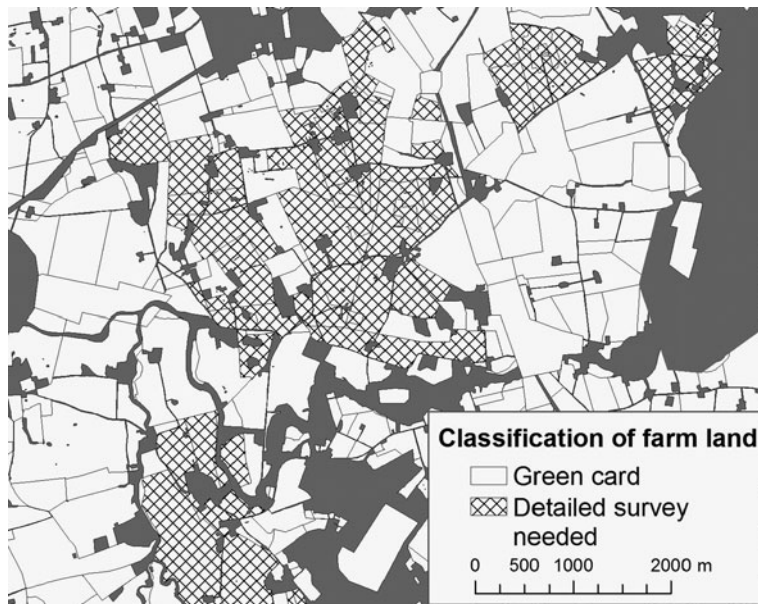


Fig. 28.8 Example of Cd risk classification of agricultural land in the Östergötland study area according to the model in Fig. 28.7. The cross-hatched areas correspond to box 5a in Fig. 28.7 and areas classified as ‘green card’ to box 5b. Dark grey areas indicate non-agricultural land

28.4 Conclusions

There is a risk that a national soil survey may depict, in very general terms, areas as having high Cd contents. The number of samples involved may be high, but the sampling density is often low and a single sample will represent a very large area. Our results indicate that both airborne and ground-based gamma ray measurements of ^{238}U can be used for more detailed assessment of Cd in soil, and thereby also in winter wheat grain, in areas where the main source of Cd is alum shale. Detailed maps from proximal gamma ray sensing from vehicles should be useful in detecting parts of fields with particularly high or low risk of high Cd in soil and crop. Cd uptake by crops is complicated and difficult to predict, but detailed knowledge of Cd in the soil improves our understanding of the spatial variability of Cd in crops. Precision in sampling of soil and crops for Cd analysis in alum shale areas could be improved if the sampling is targeted according to the variability of ^{238}U .

Acknowledgements Measurements with the Mole were carried out by The Soil Company, Groningen, The Netherlands. Mrs. Ann-Charlotte Nystedt provided the soil data for field B in Fig. 28.2. Financial support was given by the Swedish Foundation for Agricultural Research (SLF), the VL-Stiftelsen Foundation, and Agroväst AB.

References

Eriksson J, Andersson A, Andersson R (1997) Current status of Swedish arable soils. Swedish Environmental Protection Agency (Naturvårdsverket). Report 4778, Stockholm, Sweden. (In Swedish with English summary)

Eriksson J, Öborn I, Jansson G, Andersson A (1996) Factors influencing Cd content in crops – results from Swedish field investigations. *Swed J Agric Res* 26:125–133

Fromm E (1976) Description to the quaternary map – Linköping NO. Swedish Geological Survey (SGU). Serie Ae, No. 19. Stockholm, Sweden. (In Swedish with English summary)

Gorbatschev R, Fromm E, Kjellström G (1976) Description to the map of solid rocks – Linköping NO. Swedish Geological Survey (SGU). Serie Af, No. 107. Stockholm, Sweden. (In Swedish with English summary)

IAEA (2003) Guidelines for radioelement mapping using gamma ray spectrometry data. International Atomic Energy Agency (IAEA). IAEA-TECDOC-1363. Vienna, Austria

SIS (1997) Soil analysis – determination of trace elements in soils – extraction with nitric acids. Swedish Standards Institute (SIS). SS028311. Stockholm, Sweden

Söderström M, Eriksson JE (1996) Cadmium in soil and winter wheat grain in Southern Sweden. II. Geographical distribution and its relation to substratum. *Acta Agric Scand B* 46:249–257

SSI (2007) The radiation environment in Sweden. Swedish Radiation Protection Authority (SSI). Report 2007:02. (In Swedish with English summary)

Wilford J, Minty B (2007) The use of airborne gamma-ray imagery for mapping soils and understanding landscape processes. In: Lagacherie P, McBratney AB, Voltz M (eds) Digital soil mapping – an introductory perspective. *Developments in soil science*, vol 31. Elsevier, Amsterdam, pp 207–218

Chapter 29

Use of EM38 and Gamma Ray Spectrometry as Complementary Sensors for High-Resolution Soil Property Mapping

M.T.F. Wong, K. Wittwer, Y.M. Oliver, and M.J. Robertson

Abstract Apparent soil electrical conductivity (EC_a) is related to soil properties such as clay and water content, clay mineralogy, and depth to textural contrast – and hence to plant-available soil water storage capacity (PAWC). High spatial resolution sensing of EC_a , coupled with local field calibration, has been used to map expensive-to-measure soil properties, interpret yield maps, locate leaky areas for water and nitrate, and manage the land. Multiple factors affecting EC_a is a weakness of the method. Salinity interferes with data interpretation, and the method cannot distinguish between sandy soils and gravels which have similar and low EC_a . Therefore soil depth and PAWC cannot be estimated in shallow soils over gravels. Gamma ray spectrometry is relatively new to soil sensing and has shown promise to estimate clay content, PAWC, soil depth, and other soil properties. It is insensitive to common salt, but again it is difficult to interpret gamma ray emission data alone, as clays and gravels result in similarly strong signals. This work provides an approach to overcoming the weaknesses of the single-sensor data by developing a rule-based method for dual EM38–gamma radiometric sensor interpretation to infer soil properties. Simple rules are developed and used to identify soil types (ranging from coarse-textured sands to clay and areas of shallow soils <40 cm deep) and soil acidification risks. The rules are guided by the grower’s soil map and validated with published maps of soil pH and depth. The dual-sensor method overcomes the weakness of the single-sensor data and has the potential to compensate sparsely sampled measurements and estimate their spatial distribution at high resolution in complex field situations without the need for expensive and extensive direct sampling and measurements.

Keywords Dual sensors · EC_a · Gamma ray · Gravels · pH

M.T.F. Wong (✉)

CSIRO Land and Water, Underwood Avenue, Floreat, WA 6014, Australia

e-mail: mike.wong@csiro.au

29.1 Introduction

Apparent soil electrical conductivity (EC_a), or its reciprocal apparent soil electrical resistivity, measured, for example, by on-the-go EM38 sensing, has been used to estimate a range of expensive-to-measure soil properties such as plant-available soil water storage capacity (PAWC), clay content, and soil depth to hardpan at high spatial resolutions similar to those of yield maps (McBratney et al., 2005; Wong and Asseng, 2006). This high-resolution soil property mapping, combined with process modelling, has allowed the causes of spatial and seasonal variations in wheat yield to be determined to support management (Wong and Asseng, 2006, 2007). This approach of integrating detailed knowledge of the spatial distribution of soil properties with process modelling has also allowed field locations prone to deep drainage and nitrate leaching to be identified for targeted management (Wong et al., 2006). It has the potential to increase the impact of precision agriculture on both profits and the environment by allowing targeted site and season-specific management of variable yield and environmental performance across the farm (Stoorvogel and Bouma, 2005; Wong and Asseng, 2007).

For deep non-saline soils, EC_a is a function of temperature, clay content, mineralogy, moisture content, and bulk density (McBratney et al., 2005). Measurements of EC_a have been used to estimate soil depth to underlying hardpan due to contrast in soil texture and apparent electrical conductivities between the topsoil and the underlying clayey hardpan (Doolittle et al., 1994). Occurrence of salt in dryland and coastal environments is a common interference in the estimation of soil properties (other than salinity) in Australia and elsewhere. An additional weakness of EC_a -based methods is inability to distinguish between sandy soils and gravels because these materials have similar and low EC_a values. Soil depth and hence depth-limited PAWC therefore cannot be estimated in landscapes with shallow soils over gravels (Wong et al., 2008). Shallow soils over gravels are common in highly weathered landscapes (McKenzie et al., 2004). Shortcomings due to salinity and occurrence of gravels can be overcome by complementing EC_a -based methods with other sensors that are not subject to the same weaknesses.

Gamma ray spectrometry is a relatively new on-the-go soil property sensing technique that shows promise in high-resolution soil property mapping. While new to soil property sensing, it is commonly used for geological mapping and mineral exploration in Australia. Unlike EC_a survey, which can be done only proximally, the spectrometer can be carried on either ground or airborne platforms because γ -rays are little affected by air. The spectrometer measures natural γ -emissions from the top 30 to 45 cm (maximum depth that γ -rays can penetrate through to the soil surface and be measured) of the soil due to emitters such as ^{40}K and daughter radionuclides of ^{238}U and ^{232}Th . Association of these radionuclides with clays, gravels, and soil-forming materials led to variations in the concentrations of these emitters being used to estimate soil properties such as clay, potassium, organic carbon and iron contents, soil depth, and soil pH (Viscarra Rossel et al., 2007; Wong and Harper, 1999; Wong et al., 2008). Ambiguity in the interpretation of radiometric data arises when soils with varying gravel and clay contents occur across the surveyed area: both increases

in clay content and proximity of gravels to the soil surface result in strong signals. This problem is not encountered with EC_a -based methods since clays and gravels give rise to markedly different EC_a values.

This work seeks to overcome the weakness of the single-sensor technology by developing a rule-based method for dual EM38 and γ -radiometric data interpretation to infer soil properties. The initial rules for using these data to map soil properties (Wong et al., 2008) provide a basis for the work presented here. The aim is to progress the development of this rule-based method to use the grower's knowledge to identify texturally contrasting soils across a field and to compare these soils with reported values of soil pH and soil depth.

29.2 Materials and Methods

29.2.1 *Location and Soil*

The 200-ha field was 350 km north of Perth at Buntine, WA (116.57°E, 29.99°S). The average annual rainfall for Buntine is 333 mm, of which 238 mm falls in May–October (growing season). The main crops grown are wheat in rotation with lupin and canola. The grower produced a map of soil types in 2003 based on field observations and his knowledge. He used a GPS to approximately locate soil and field boundaries, and named these soil types as good sand (Eutric Regosol), medium sand (Eutric Regosol), poor sand (Ferrals Arenosol), gravels (Xanthic Ferralsol), and red clay (Ferrals Cambisol). This soil-mapping approach was chosen because these soil types are easily recognised by local growers and is cost effective. The field slopes to a salty creek which diagonally bounds the north-west of the field, which is mapped as good sand.

29.2.2 *EM38 and γ -Radiometric Survey*

We measured apparent soil electrical conductivity (EC_a) across the field in 2004 with electromagnetic induction equipment (Geonics EM38) in its vertical dipole mode (details in Wong et al., 2008). The EC_a survey was carried out on a 30-m line spacing with a quad bike in June 2004 when the soil was moist (75 mm of rain since the previous month). The EC_a data and exponential local variograms were used to krig values to a 5-m grid to produce a map of EC_a . The γ -ray emission survey was also carried out in 2004 on a 30-m line spacing with an Exploranium γ -ray spectrometer with a large (8 L) thallium-activated sodium iodide crystal scintillation detector (details in Wong et al., 2008). This survey was also done on a quad bike in February 2004 when the soil was dry (to minimise gamma ray attenuation). The site had received only 22 mm of rain in the previous 5 months. The spectra were resolved into individual emissions from potassium, thorium, and uranium according to their characteristic peaks. The individual emission data were kriged as above to map the surface counts from potassium, uranium, and thorium to a 5-m grid.

29.2.3 Sensor Response and Interpretation

Both EC_a and γ -ray emission measured on deep soils increase with increasing clay content (Wong and Asseng, 2006; Wong and Harper, 1999), provided there is no interference from salt, superficial rocks, and gravels. Under good conditions, coarse-textured soils with low clay content result in low values of both EC_a and γ -ray emission, while finer textured loams and clayey soils result in larger values of both EC_a and γ -ray emission which can be calibrated with local clay content to map this soil property (Wong and Harper, 1999). Presence of salt results in an increase in EC_a that is out of proportion to an increase in γ -ray emission; the reason is that salinity in dryland and coastal environments is dominated by sodium and calcium salts which have low radioactivity but high electrical conductivity in the presence of moisture. Shallow soils with layers of superficial gravels less than 45 cm from the soil surface result in increases in γ -ray emission not matched by increases in EC_a because gravels have similar EC_a values to sands but are strong emitters of γ -rays. This simple qualitative knowledge provides a basis for developing rules to interpret dual EC_a and γ -ray sensor data. We used the grower's knowledge of the field to determine the range of EC_a and γ -ray emission values typical of soils encountered across the field. This avoided expensive field calibrations against the geophysical data. The goodness of the method was then checked against published maps of soil depth over gravels and soil pH. Here soil pH is used as a surrogate for soil texture: coarser-textured soils are more leached, are more poorly buffered, and are at greater risk of acidification than are finer textured soils.

29.3 Results and Discussion

The area covered by low EC_a values ($<10 \text{ mS m}^{-1}$) represented 31% of the field (Plate 29.1a). This area could not be resolved more because of limits in the sensitivity of EM38 sensing. Correspondingly low γ -ray emission from ^{40}K (20–40 counts per 100 s) covered only 13% of the field (Plate 29.1b). Low sensitivity of EC_a measurements at $<10 \text{ mS m}^{-1}$ means that the method cannot discriminate between areas known by field observations and the grower to differ texturally (poor sand and medium sand) and between deep sandy soils and shallow soils over gravels (Plate 29.1c). While these soils cannot be resolved solely on the basis of their low EC_a values, ability to identify them is important because they had different crop yields that varied according to the season (Wong et al., 2008) and may benefit from site- and season-specific management.

Gamma radiometry is more sensitive to textural changes in sands than is EC_a sensing. The area with $EC_a < 10 \text{ mS m}^{-1}$ can be resolved into the component poor sand, medium sand, and shallow soil over gravels and mapped accurately with complementary γ -ray emission data and ground knowledge. The coarsest textured sand (poor sand) occurs where areas of low $EC_a < 10 \text{ mS m}^{-1}$ coincide with areas of low γ -ray emission from ^{40}K (20–40 counts per 100 s). Emission from ^{40}K is more sensitive to textural change, increasing to ~ 40 –80 counts per 100 s in the medium

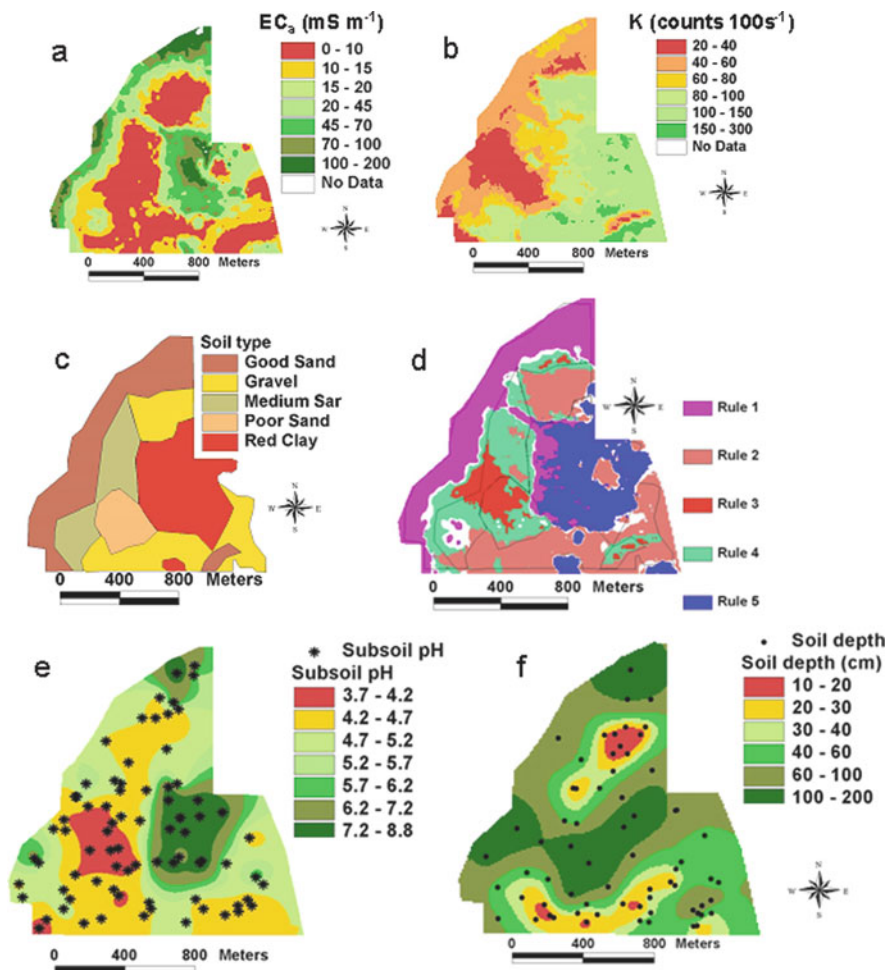


Plate 29.1 Apparent soil electrical conductivity measured by EM38 (a), γ -ray emission from ^{40}K (b), soil map of the field produced by the grower (c), field area covered by rules of dual EM38 and γ -radiometric sensor data interpretation shown in Table 29.1 (d), sample locations (stars and dots) and kriged subsoil pH in CaCl_2 (e), and soil depth (f). Reproduced from Wong et al. (2008) with kind permission of Springer Science and Business Media

sand, whereas EC_a mostly remains at $<10 \text{ mS m}^{-1}$, with small transition areas having EC_a values up to 15 mS m^{-1} . EC_a remains low ($<15 \text{ mS m}^{-1}$) in shallow soils over gravels but this area can be identified due to its high γ -ray emission from $^{40}\text{K} > 80 \text{ counts per } 100 \text{ s}$.

The red clayey soil is characterised by both high EC_a values $>20 \text{ mS m}^{-1}$ and high γ -ray emission from $^{40}\text{K} > 80 \text{ counts per } 100 \text{ s}$. In contrast, all sands have γ -ray emission from $^{40}\text{K} < 80 \text{ counts per } 100 \text{ s}$, but the finer textured ‘good sands’ also have EC_a values $>20 \text{ mS m}^{-1}$. Very high EC_a values measured along the west and

Table 29.1 Rules for dual EM38 and γ -radiometric sensor data interpretation

Rule number and description	EC_a (mS m^{-1})	^{40}K counts (100 s^{-1})	Grower's description of soil type
1. High–medium	>20	<80	Good sand
2. Low–high	<15	>80	Shallow gravelly
3. Low–low	<10	<40	Poor sand
4. Low–medium	<15	40–80	Medium sand
5. High–high	>20	>80	Red clayey

north-west boundary of the field, but which are not matched by high γ -ray emission from ^{40}K , mean that these soils are salt affected. The rules used to interpret the dual EM38 and γ -radiometric data are summarised in Table 29.1.

The areas of the field covered by the rules presented in Table 29.1 are in remarkably good accord with the grower's soil type map drawn without any prior knowledge of the EC_a and γ -ray emission maps (Plate 29.1d), which were available only 1 year later. This shows that the dual-sensor method is promising but is not a validation of the method since the range of geophysical values used in each rule was influenced by the grower's soil map. Independent kriged values of subsoil pH and soil depth across this field, reported by Wong et al. (2008), provide an indirect means of method validation. There was a good spatial match between extremely acidic subsoil (pH in CaCl_2 <4.2) and the area geophysically mapped as 'rule 3, poor sand' (Plate 29.1e). The accurate location of this area, corroborated by geophysics and subsoil pH measurements, is north-west of where the grower thought. Similarly, there was a good spatial match between the location of very acidic subsoils (pH 4.2–4.7) and the location geophysically mapped as medium sand and between the locations of neutral to alkaline soils (pH 6.2–8.8) and red clayey soil. Areas of soil with depths measuring <40 cm over gravels (Plate 29.1f) coincided with areas covered by rule 2 for shallow gravelly soils (Plate 29.1d). The remarkably good spatial agreement between measured subsoil pH and soil depth and the geophysically located 'soil type' suggests the validity of the method presented here. The next step is to test the method on fields in the region.

A spatially detailed assessment of soil properties is possible once the nature of the soil in each soil type polygon is unravelled. For example, once it is established that high γ -ray emission in an area is due to shallow gravels and not clayey soils, γ -ray attenuation theory can then be used to map variation in soil depth accurately at a spatial resolution of 5 m. This work, described elsewhere, solves the current inability of the currently used EC_a -based method of soil depth estimation (Doolittle et al., 1994) to estimate soil depth in this landscape (Wong et al., 2009).

29.4 Conclusions

A dual-sensor approach enabled different weaknesses of each individual sensor to be overcome. Apparently conflicting signals from EM38 and gamma radiometric surveys provide complementary information to interpret potentially ambiguous

single-sensor data. This interpretation of the dual sensor data is greatly aided by prior grower's and agronomist's knowledge and field observations to finetune the rules made. Independent soil property measurements indicate the validity and potential of the method. This approach should be generally applicable, but the actual sensor values used in rules to interpret the data are expected to vary in different landscapes due, perhaps, to differences in soil and landscape properties, giving rise to different EC_a and γ -radiometric responses. The use of dual sensors should be encouraged, as salts and gravels occur commonly in dryland environments and interfere with the interpretation of single-sensor data. The cost of each sensor system is of a similar order of magnitude, and it may be possible to run both sensors simultaneously to minimise mobilisation and operating costs. The approach presented here overcomes the weakness of the single sensor, such as the inability of EC_a -based methods to discern different types of sands, and between sands and gravels, which all have low EC_a values. It has the potential to compensate sparsely sampled measurements and estimate their spatial distribution at high resolution in complex field situations, without the need for expensive and extensive direct sampling and measurements.

Acknowledgement This work was co-funded by CSIRO and GRDC as part of their investment on Precision Agriculture (SIP09) and on amelioration of subsoil constraints (SIP08). We are grateful to the grower for sharing his knowledge of the field with us and mapping his field.

References

Doolittle JA, Sudduth KA, Kitchen NR, Indorante SJ (1994) Estimating depths to claypans using electromagnetic induction methods. *J Soil Water Conserv* 49:572–575

McBratney AB, Minasny B, Whelan BM (2005) Obtaining 'useful' high-resolution soil data from proximally-sensed electrical conductivity/resistivity (PSEC/R) surveys. In: Stafford JV (ed) Precision agriculture '05, Proceedings of the 5th European conference on precision agriculture. Wageningen Academic Publishers, The Netherlands, pp 503–510

McKenzie NJ, Jacquier D, Isbell R, Brown K (2004) Australian soils and landscapes: an illustrated compendium. CSIRO Publishing, Collingwood, VIC

Stoorvogel J, Bouma J (2005) Precision agriculture: the solution to control nutrient emission. In: Stafford JV (ed) Precision agriculture '05, Proceedings of the 5th European conference on precision agriculture. Wageningen Academic Publishers, The Netherlands, pp 47–55

Viscarra Rossel RA, Taylor HJ, McBratney AB (2007) Multivariate calibration of hyperspectral γ -ray energy spectra for proximal soil sensing. *Eur J Soil Sci* 58:343–353

Wong MTF, Asseng S (2006) Determining the causes of spatial and temporal variability of wheat yields at sub-field scale using a new method of upscaling a crop model. *Plant Soil* 283:203–215

Wong MTF, Asseng S (2007) Yield and environmental benefits of ameliorating subsoil constraints under variable rainfall in a Mediterranean environment. *Plant Soil* 297:29–42

Wong MTF, Harper RJ (1999) Use of on-ground gamma-ray spectrometry to measure plant-available potassium and other topsoil attributes. *Aust J Soil Res* 37:267–277

Wong MTF, Asseng S, Zhang H (2006) A flexible approach to managing variability in grain yield and nitrate leaching at within-field to farm scales. *Precision Agric* 7:405–417

Wong MTF, Asseng S, Robertson MJ, Oliver Y (2008) Mapping subsoil acidity and shallow soil across a field with information from yield maps, geophysical sensing and the grower. *Precision Agric* 9:3–15

Wong MTF, Oliver YM, Robertson MJ (2009) Gamma-radiometric assessment of soil depth across a landscape not measurable using electromagnetic surveys. *Soil Sci Soc Am J* 73:1261–1267

Part VI

Multisensor Systems and Other Sensors

Chapter 30

Field-Scale Draught Resistance and Soil Moisture Measurement in Australia Using a Tine-Based Force–Capacitance Sensing System

B.M. Whelan, Y. Sun, Q. Zeng, P. Schulze Lammers, and J. Hassall

Abstract A newly developed tine-based force/capacitance soil sensing system was used to measure draught resistance and soil moisture content across a 113-ha commercial-scale grain field at Gilgandra, NSW, Australia. Soil in the field ranged in USDA classification from sandy loam, clay loam, silty clay loam to clay. The field was at an average volumetric moisture content of 30%, and under these conditions the measured data ($\sim 15,000$ observations) showed a positive correlation between soil moisture content and draught force across the whole field ($r = 0.56$). The high moisture content at which the experiment was conducted and the range of soil texture encountered are believed to have contributed to high friction values between soil and probe. Importantly, the recorded draught force did show a strong correlation with historical soil EC_a ($r = 0.65$) or crop yield ($r = 0.54$) measured at a similar scale. The sensing system shows potential for providing fine-scale information on important yield-controlling parameters at a useful spatial scale when operated using standard farm machinery.

Keywords Draught force · Soil moisture · On the go · Crop yield

30.1 Introduction

The development of crop-sensing systems to monitor the quantity and quality of crop yield is revolutionising the way spatial and temporal variation in production output can be documented (Plate 30.1a). Correspondingly, there is a growing need for tools that can supply data at similar scales about variations in soil resource parameters that affect crop performance. At the field scale, the concept of site-specific crop management (SSCM) requires access to such information to improve decision making about resource use.

B.M. Whelan (✉)

Australian Centre for Precision Agriculture, University of Sydney, Sydney, NSW 2006, Australia
e-mail: b.whelan@sydney.edu.au

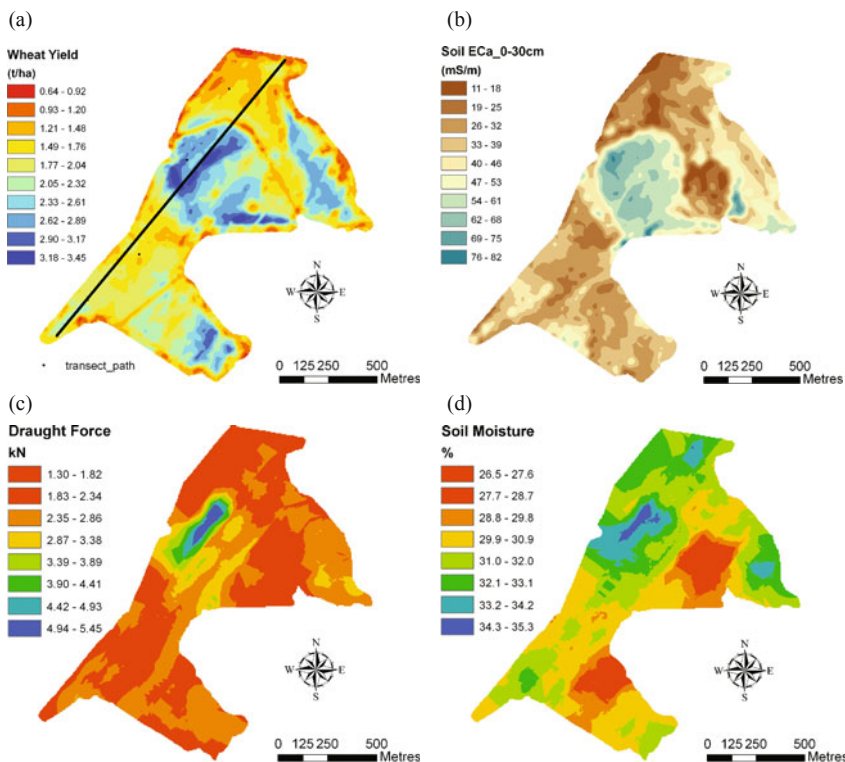


Plate 30.1 Data layer maps for the experimental field: 2005 crop yield (a); soil EC_a (b); measured draught force (c); and soil moisture (d)

To date there have been few instruments that can provide such data on variability in soil attributes at a commercial scale. The measurement of apparent soil electrical conductivity (EC_a) using electromagnetic induction or electrical resistivity techniques probably leads the way. However, soil EC_a is an integrated secondary property, the magnitude of which is controlled by cumulative contributions from clay content, clay type, soil moisture (and ergo soil structure/bulk density), and the ionic concentration of the soil solution. Extracting data on the variability in these important primary soil properties from the EC_a data across a field or a farm still requires site-specific calibrations. Direct, on-the-go measurements of primary soil properties would be much more desirable.

In Australia, irrigated land (including crops and pastures) occupies less than 1% of the total land used for agriculture (ABS, 2006). The overwhelming use of dry-land agriculture means that direct measurement of variation in soil moisture – or soil physical parameters that contribute to variability in available water-holding capacity (AWC) – across a field should be at the top of the development list. At present, matching the variation in moisture-controlling soil resource parameters to crop yield has been undertaken using EC_a, as a surrogate to direct physical soil

sampling (Taylor et al., 2007). However, in some cases, more specific soil attribute calibrations have been explored for individual sites, for example soil AWC in a Western Australian grain field (Wong et al., 2006).

Adamchuck (2004) provides a summary of early attempts to construct instruments to tackle the direct measurement goal, and since then a number of new in-ground, real-time sensors for the measurement of soil physical parameters and moisture content have been tested (e.g. Mouazen et al., 2005). Here, a recently developed tine-based force- and moisture-sensing system (Sun et al., 2006) is tested at the full-field scale using standard farm machinery. The aim was to explore, beyond the research plot scale, the functioning of the instrument and the degree of spatial variability in soil moisture and draught force.

30.2 Materials and Methods

Figure 30.1a is a schematic showing how the system is based on a horizontal cone penetrometer mounted on a pivoting force lever which is itself protected behind a fixed cutting tine. The force lever is attached to a load cell, which registers the draught force (F_2). The force at the tip of the cone (F_1) is here termed soil resistance.

Volumetric soil moisture content is measured using a fringe-capacitance sensor that is incorporated into the penetrometer shaft. Figure 30.1b shows the tine system mounted on a three-point linkage, while a close-up of the combined penetrometer is displayed in Fig. 30.2a. Figure 30.2b shows the unit operating under field conditions.

Laboratory calibration of the force and moisture sensors was carried out prior to field use. The linear relationships, shown in Fig. 30.3, were found to be as follows:

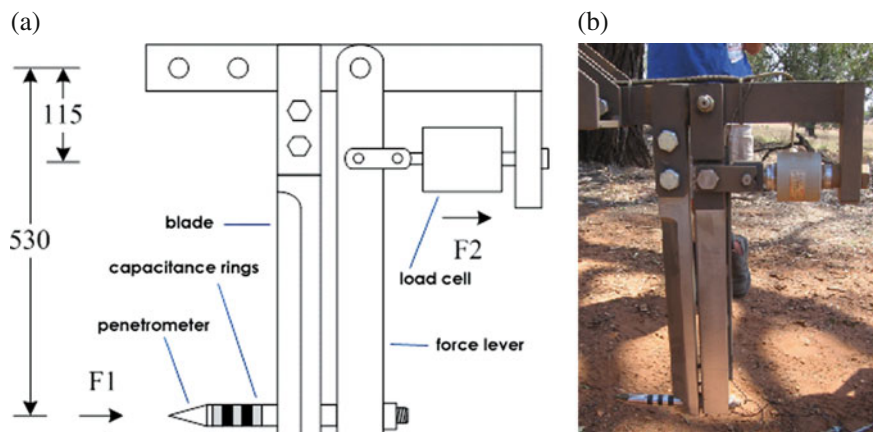


Fig. 30.1 Schematic of the soil sensing system (a) and the actual instrument (b)

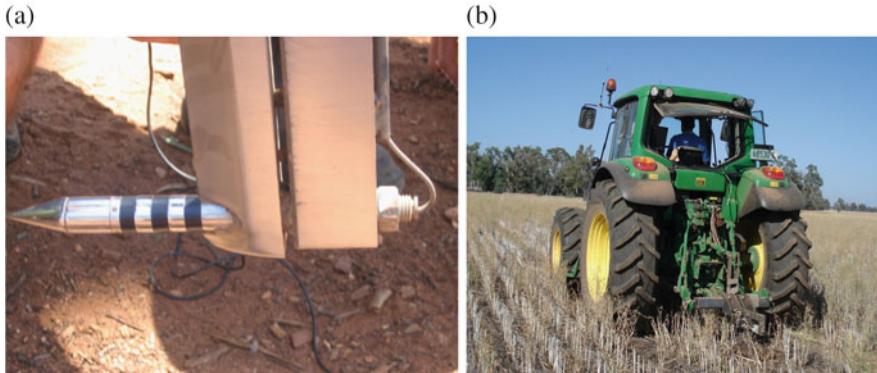


Fig. 30.2 The combined force and moisture penetrometer (a) and its in-field operation (b)

$$\theta = -0.05 + 0.62 \times \text{Output_Voltage}, \quad (30.1)$$

$$F2 = -1452.58 + 8146.94 \times \text{Output_Voltage}, \quad (30.2)$$

where the unit of $F2$ is newton and the Output_Voltage is the reading recorded from the individual sensors. The force $F1$ can be calculated as follows:

$$F1 = F2 \times \left(\frac{115}{530} \right). \quad (30.3)$$

The sensing system was mounted onto a tool bar attached to the three-point linkage and set to a penetration depth of 0.02 m. It was then used in a 113-ha commercial grain cropping field located south-east of Gilgandra, NSW, Australia. The field is managed using controlled traffic and minimum tillage, with a recent cropping history of wheat (2005) and canola (2006). The trial described here was conducted in

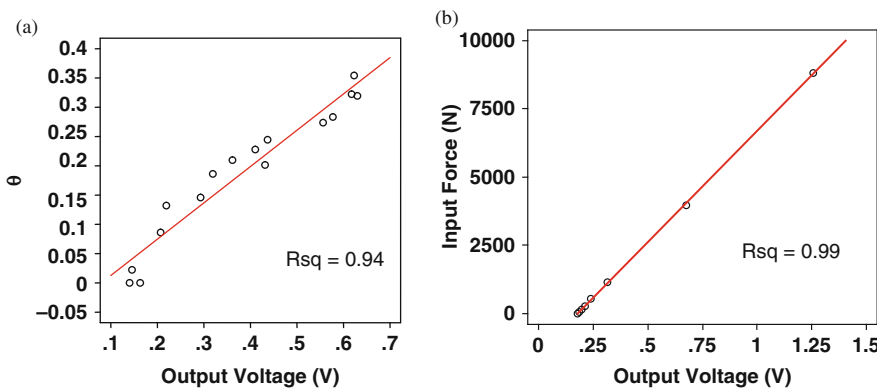


Fig. 30.3 Laboratory calibration results for (a) soil moisture and (b) force

July 2007 and consisted of a reasonably detailed spatial study of the whole field using replicated transects on a 100-m swath with the tractor travelling at an average speed of 6 km h⁻¹.

30.3 Results and Discussion

30.3.1 Transect

One transect ran the length of the longest axis in the paddock (see Plate 30.1a). This 1.8-km transect traversed changes in elevation and soil physical composition. Figure 30.4 shows the elevation recorded along the transect (a), the replicated output for the two sensors (b and c), and also a previous year's wheat crop yield (d) recorded along the same transect using a harvester-mounted yield-monitoring system. The replicated transects (531 and 524 observations, respectively) were conducted in opposing directions but for comparison displayed in a uniform direction. For analysis the transect was divided into four landscape stages delineated by the dashed lines in Fig. 30.4. The transect began on the top of a ridge (Stage 1); the recorded force then rose substantially as the transect entered a slight depression. The force reached a maximum in the base of the depression and fell again as the vehicle traversed the depression and climbed up and out (Stage 2). The observed moisture content mimicked the force readings through these stages, although with a smaller magnitude of change. The crop yield attributed to the region in Stage 2 rose to nearly double than that observed from the region in Stage 1.

Within Stage 3, the draught force and soil moisture were generally the lowest recorded in the paddock and this region also recorded a generally declining elevation and crop yield. The last half of Stage 3, however, was characterised by a slight plateau, and while the soil measurements remained relatively stable, the crop yield rose by 1 t ha⁻¹ across this region. In Stage 4, the force and moisture registered by the sensors gently increased as the terrain again dipped into a shallow depression. While the yield dropped entering this stage, it remained generally above that in Stage 3.

From a visual inspection of the data it is clear that the draught force changed in line with changes in terrain along the transect. Changes in crop yield also reflected changes in terrain and draught force. The moisture content appeared to be more independent. The mean measurements in each of these stages are recorded in Table 30.1 and provide quantitative confirmation of this assessment.

Soil profile sampling along the transect, at locations in the landscape indicated by the position of the numbers in Fig. 30.4a, provided the data in Table 30.2. Here it can be seen that the soil in Stage 1 is characterised by the lowest EC_a, CEC, combined clay and silt content, and Ca and Mg levels; it also had the highest bulk density. These attributes contribute to a sandy, poorly structured soil. In Stage 2, the draught force rose dramatically and the soil showed the highest EC_a, CEC, combined clay and silt content, Ca and Mg levels, and the lowest bulk density. The

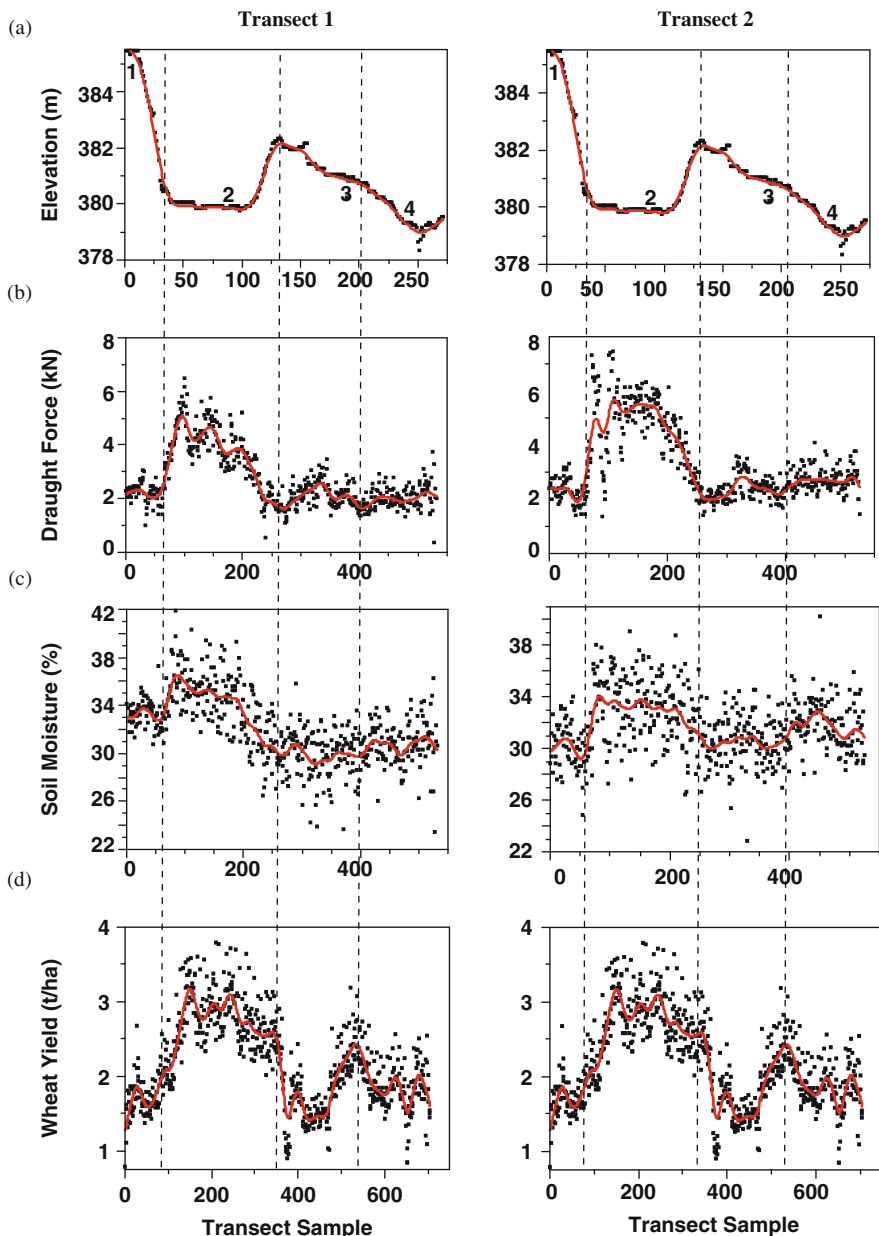


Fig. 30.4 Observations along the transect: (a) elevation, (b) draught force, (c) soil moisture, and (d) crop yield

Table 30.1 Calculated means for observations in the four stages along the transect

Stage	Mean elevation (m)	Mean draught force, $F2$ (kN)		Mean soil moisture (%)		Mean yield (t ha $^{-1}$)
		Transect 1	Transect 2	Transect 1	Transect 2	
1	384	2.2	2.3	33	30	1.67
2	380	3.7	4.7	34	33	2.70
3	381	2.1	2.3	30	31	1.75
4	379	2.0	2.7	31	32	1.92

Table 30.2 Soil sample data from each stage. Locations identified by numerals in Fig. 4a

Stage	Soil EC _a (mS m $^{-1}$)	pH		Mg		CEC	Clay (%)	Silt (%)	Sand (%)	AWC (%)	Texture class	
		(CaCl)	Ca	(mmol/kg)							BD	(USDA)
1	17.651	5.1	71.4	15		99.4	20	25	55	0.17	1.49	SL
2	74.285	6.2	205.8	61.3		283.2	40	43	17	0.21	1.27	ZCL
3	32.652	5.2	107.4	35.6		160.4	54	24	22	0.13	1.31	C
4	39.475	6.1	147.5	52.6		213.7	27	35	38	0.18	1.42	CL

soil in this area has attributes that contribute to a heavier soil with much improved soil structure and fertility.

The soil in Stage 3 had the highest clay content and the lowest potential AWC, which is reflected in the lowest mean moisture readings from the transects and the lowest mean yield. In Stage 4, the sample data showed a soil approaching the conditions found in the large depression and the magnitude of the force, moisture, and yield observations began to rise accordingly.

Simple linear correlation between the mean values measured in each stage (Table 30.3) showed that the force measurements from the two transects were significantly correlated (0.97), the moisture measurements were not (0.28), but that on both transects the force/moisture correlation was strong (0.77; 0.85). The crop yield was highly correlated with the force measurement (0.95; 0.99).

Table 30.3 Correlations between measured parameters in the duplicate transects and also previously measured soil EC_a and crop yield

	Elevation	Force trans 1	Force trans 2	Moist trans 1	Moist trans 2	Yield
Elevation	1.00					
Force trans 1	-0.21	1.00				
Force trans 2	-0.43	0.97*	1.00			
Moist trans 1	0.25	0.77	0.70	1.00		
Moist trans 2	-0.84	0.71	0.85	0.28	1.00	
Yield	-0.50	0.95*	0.99*	0.64	0.89	1.00

*Significant at $p < 0.05$

30.3.2 Whole Paddock

The data from the whole field sampling were used to estimate the global semivariogram parameters for the soil moisture and draught force (Fig. 30.5). The model parameters showed that the draught force exhibited the larger structural component and greater spatial autocorrelation.

These models were used to spatially predict estimates of both draught force and soil moisture onto a single 5-m grid across the whole paddock. Block kriging with local neighbours using the global variograms was performed in Vesper (Minasny et al., 2002) and the resulting maps are displayed in Plate 30.1c, d. Crop yield and soil EC_a previously gathered in 2005 have been predicted onto the same grid (Plate 30.1a, b), enabling a simple correlation between the soil parameters and the crop yield to be made across the whole paddock. Table 30.4 shows that there was a significant positive correlation ($r = 0.56$) between the two measured soil parameters and that the force measurement had a stronger relationship with soil EC_a and crop yield.

The significant positive relationship between draught force and soil moisture is not as predicted by laboratory experiments or small-scale field tests. However, here there is a substantial change in soil texture, moisture content, and terrain across this commercial sized field and these parameters are obviously interacting in some fashion, as evident in the repeatability of results shown in the transect experiment (Fig. 30.4). According to the USDA/FAO classification system, the soil across the

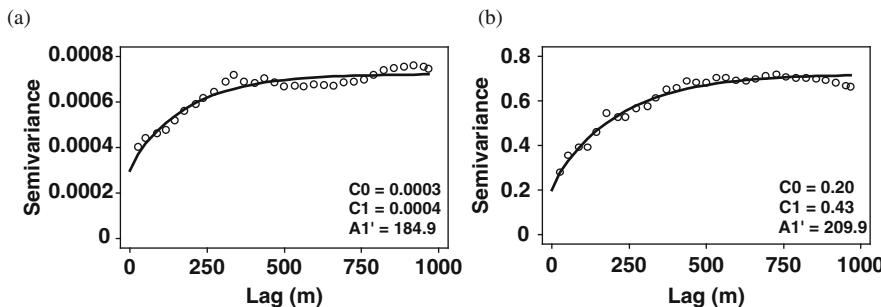


Fig. 30.5 Global semivariogram and associated exponential model parameters. (a) Soil moisture. (b) Draught force

Table 30.4 Whole-paddock correlations between measured soil draught force, soil moisture, and also previously measured soil EC_a and crop yield

	Soil moisture	Draught force	Soil EC_a	Elevation	Yield
Soil moisture	1.0				
Draught force	0.56*	1.0			
Soil EC_a	0.38*	0.65*	1.0		
Elevation	0.15*	-0.35*	-0.39*	1.0	
Yield	0.18*	0.54*	0.65*	-0.5*	1.0

*Significant at $p < 0.05$

transect ranges from a sandy loam (SL) in Stage 1 to a clay (C) in Stage 3. The soil in Stages 2 and 4 has a larger silt content (silty clay loam (ZCL), Stage 2; clay loam (CL), Stage 4). The soil moisture trace in Fig. 30.4 generally shows that soil with a higher silt content is holding more water as expected; however, these soils are also located in relative depressions along the transect.

Mulqueen et al. (1977) noted that the total force on a penetrometer comprised shear, compressive, tensile, and metal/soil friction components, which varied non-linearly with soil moisture content. Importantly, they noted that at high and very low moisture contents, the soil interacted with the penetrometer shaft and increased the measured resistance. The soil moisture contents at which the measurements were taken in this trial are much higher than those in previously published tests with this instrument (Schulze Lammers et al., 2008). The soil strength is highest in this field where the soil has the highest silt content and is generally wetter, leading to the possibility that the soil conditions were producing increased friction or 'grab' between the soil and the probe. At frequent inspections, soil was not found to be building up around the probe.

Such an observation in the soil moisture–draught resistance–texture interaction may be easily missed on small-scale experiments because they fail to cover a broad range of conditions. In this field the increasing draught resistance may well be associated with increasing silt content only at high field moisture contents. There is also the possibility that using standard machinery and operating speeds may influence the sensing systems and that in the wetter, more silty areas of the paddock the measurement depth may increase if the vehicle 'sank' further below the soil surface than at set-up conditions. It will be important to ensure that vehicle position relative to the soil surface is monitored in future applications to ensure accurate probe depth.

The data from the probe did show a significant positive correlation between crop yield and both draught force and soil moisture. The stronger relationship ($r = 0.54$) between crop yield and draught force was similar in magnitude to that observed between soil EC_a and crop yield ($r = 0.65$). The increased draught force is certainly reflecting an aspect of the soil/landscape that is associated with higher yield potentials. This is further confirmed by the significant positive relationship between soil EC_a and draught force ($r = 0.65$).

30.4 Conclusions

Ultimately, this experiment aimed to test the draught resistance–soil moisture instrument at field scale using standard machinery to investigate the potential for measuring soil parameters that could explain variability in crop yield. The sensor has shown that the measured draught force does bear a positive spatial relationship with crop yield over a commercial-sized field when measured at a similar scale. There was a positive relationship between draught force and soil moisture in this field, the reason for which requires further exploration. The spatial autocorrelation is greater in this field for the measured draught force compared with soil moisture content.

Acknowledgement This research was supported by the International Program Development Fund (University of Sydney) and the Grains Research and Development Corporation (GRDC).

References

Adamchuck VI, Hummel JW, Morgan MT, Upadhyaya SK (2004) On-the-go soil sensors for precision agriculture. *Comput Electron Agric* 44:71–91

Australian Bureau of Statistics (ABS) (2006) Water use on Australian farms 2004–2005, ABS publication 4618.0, www.abs.gov.au

Minasny B, McBratney AB, Whelan BM (2002) VESPER version 1.6. Australian Centre for Precision Agriculture, University of Sydney, www.usyd.edu.au/agric/acpa

Mounem AM, De Baerdemaeker J, Ramon H (2005) On-the-go sensor for measurement of dry bulk density referring to soil compaction. European conference on precision agriculture 2005, Uppsala, Sweden, pp 521–528

Mulqueen J, Stafford JV, Tanner DW (1977) Evaluation of penetrometers for measuring soil strength. *J Terramech* 14:137–151

Schulze Lammers P, Sun Y, Ma D (2008) Combined sensor for soil resistance and water content. First global workshop on digital soil sensing and mapping, Sydney, Australia

Sun Y, Ma D, Schulze Lammers P, Schmittmann O, Rose M (2006) On-the-go measurement of soil water content and mechanical resistance by a combined horizontal penetrometer. *Soil Tillage Res* 86:209–217

Taylor JA, McBratney AB, Whelan BM (2007) Establishing management classes for broadacre grain production. *Agron J* 99:1366–1376

Wong M, Oliver Y, Robertson M, Witwer K (2006) Technologies to estimate plant available soil water storage capacities at high spatial resolution. In: Turner NC, Acuna T, Johnson RC (eds) Ground-breaking stuff. Proceedings of the 13th Australian agronomy conference, Perth, Western Australia, Australian Society of Agronomy

Chapter 31

Sensor-Based Mapping of Soil Quality on Degraded Claypan Landscapes of the Central United States

N.R. Kitchen, K.A. Sudduth, R.J. Kremer, and D.B. Myers

Abstract Claypan soils (Epiqualfs, Stagnic Luvisols) in the central United States have experienced severe erosion as a result of tillage practices of the late 1800s and 1900s. Because of the site-specific nature of erosion processes within claypan fields, research is needed to achieve cost-effective sensing and mapping of soil and landscape properties that quantify the soil's current ability to produce crops and provide ecosystem services – the concepts of soil quality. In this research, EC_a sensors, aerial imagery, yield mapping, and a horizontally operated penetrometer were used for high-resolution mapping of soil quality indicators on a 36-ha claypan soil field in Missouri. Field areas experiencing the most erosion now have reduced grain production, lower plant-available water capacity (PAWC), and slower infiltration. These same areas have higher soil penetration resistance (at 30 cm), yet greater subsoil nutrients. The conclusion of this synthesis is that combining sensor-based information provides a much clearer picture of spatially important characteristics of claypan soil quality and can be used by land managers to target remediation of degraded soils and implement precision conservation practices.

Keywords Apparent soil electrical conductivity · Electrical conductivity · Erosion · Historical · Soil quality maps

31.1 Introduction

Highly contrasting textural layers that undulate at varying depths across a landscape can have a dominating influence on crop growth and hydrology. Soils with these characteristics provide an ideal setting for testing and evaluating sensors for high-resolution soil mapping. An example of such a soil type is the 4 million ha of

N.R. Kitchen (✉)

Cropping Systems and Water Quality Research Unit, USDA Agricultural Research Service,
University of Missouri, Columbia, MO 65211, USA
e-mail: Newell.Kitchen@ars.usda.gov

Epiqualfs (Stagnic Luvisols) or 'claypan soils' classified within the central United States as Major Land Resource Area 113 (MLRA 113). Claypan soils have an abrupt increase in clay, more than doubling from ~20% up to ~60% clay, between the topsoil (A or E horizon) and the initial argillic horizon. The depth of this claypan varies from 0 to 1.0 m, depending on landscape position and degree of erosion or downslope deposition. The low saturated hydraulic conductivity within the claypan leads to perched water tables, creating a high probability of run-off in most years during the winter and spring periods. As such, claypan soils are usually classified as somewhat poorly to poorly drained. Due to the high shrink–swell potential of smectitic clays, there is also a high probability of annual shrinkage cracks forming during late summer and early fall.

Much of the claypan soil landscape of the Midwest United States has been under cultivation only for about 100–120 years. Early in the 1900s, improvements in agricultural mechanisation allowed farmers to crop larger tracts. Additionally, soaring grain prices during the First World War resulted in plowing of previously grazed grasslands for the first time. However, under cultivation, intense storms caused devastating erosion that filled streams and rivers with sediment. It was not until the 1970s and later that conservation measures (e.g. tillage practices shifting to minimum and no-till) began to reduce the degrading effects of water erosion on these soils. So after only ~100 years of crop production, many claypan soil fields have experienced extensive soil quality degradation. Such degradation affects their current productivity and their long-term sustainability for food and biofuel production. Because of the site-specific nature of degradation within these fields, research is needed to achieve cost-effective sensing and mapping of soil and landscape properties that quantify the soil's current ability to produce crops and provide ecosystem services – the fundamental concepts of soil quality (Doran and Parkin, 1994).

Soil quality is complex due to the interaction of physical, chemical, and biological soil processes performing various functions. Adding to this complexity are changes in soil quality across landscapes. Further, the task of evaluating on-going agronomic and conservation effects on soil quality is daunting. Therefore, site-specific characterisation of soil quality is needed to provide a baseline understanding of the impact of past and future management, and can also be used for targeting remediation with precision agriculture methods. The objective of this chapter is to summarise our work on sensor measurements and methods that enable high-resolution mapping of soil quality indicators for claypan soils. The indicators examined include topsoil depth, yield and yield stability, hydraulic properties, surface soil carbon, nutrients, and soil compaction.

31.2 Materials and Methods

Investigations over 16 years on a 36-ha claypan soil field located in north-central Missouri, USA (39.2297 N, –92.1169 W), are summarised in this chapter. The soils on this field are generally classified as Adco (fine, smectitic, mesic aeric Vertic

Albaqualfs) and Mexico (fine, smectitic, mesic aeric Vertic Epiaqualfs) using the USDA–NRCS classification system. The field is typical of production-scale fields found in MLRA 113, managed in a corn (*Zea mays* L.)–soybean [*Glycine max* (L.) Merr.] crop rotation and mulch tilled. Details regarding the management employed on this field can be found in Lerch et al. (2005).

31.2.1 Soil EC_a

Under different soil conditions and during different years, we obtained soil EC_a using two different sensor systems – a non-contact, electromagnetic induction-based sensor (Geonics EM38) and a coulter-based sensor (Veris 3100).¹ EC_a surveys were usually run on transects spaced approximately 10 m apart with data being recorded at a 1 s interval (\sim 4–6 m data spacing) (see also Chapters 2 and 34). Data obtained by differential GPS were associated with each sensor reading to provide positional information with an accuracy of 1.5 m or better. From these datasets, methods were developed for estimating topsoil depth (Sudduth et al., 2003). At the time of an EC_a survey, 12–20 sampling sites were selected within the field to cover the range of EC_a values present. At these sites, a 120-cm-long soil core was obtained using a hydraulic soil-coring machine. Cores were examined within the field by a skilled soil scientist and pedogenic horizons identified. Cores were segmented by horizon for laboratory analysis of soil texture, soil organic C, bulk density, and other soil chemical properties. These soil measurements were related to soil EC_a . The EC_a data were also related to other soil quality characteristics as explained below.

31.2.2 Yield Mapping

This is one of the few field-scale experiments with more than 10 years of continuous, high-quality, spatially referenced, cleaned yield data. Although yield has been mapped, management has been conventional, with uniform inputs applied across the field. Thus, yield maps provide insight into yield variation and associated agronomic interpretations that occur due to spatial processes. Combines equipped with commercially available yield-sensing systems were used to collect data for 1993–2002 yield maps. Individual points where yield data were unreliable due to combine operation or yield sensor issues were removed. Cleaned yield data were interpolated with the geostatistical technique of block kriging. Further details on yield-mapping procedures can be found in Kitchen et al. (2005).

One way in which yield maps were used was by transforming them and soil test nutrient maps into a nutrient buffering index (BI) map. In essence, fertiliser

¹ Mention of trade names or commercial products in this publication is solely for the purpose of providing specific information and does not imply recommendation or endorsement by the U.S. Department of Agriculture.

additions and crop removal were examined relative to change in soil test. The BI is a quantity–intensity relationship ($\Delta Q/\Delta I$), where ΔQ is the net balance of a nutrient and ΔI is the change in soil test concentration. BI is interpreted as the quantity of nutrient balance change responsible for one unit of change in soil test value.

31.2.3 Claypan Hydraulic Properties

To relate EC_a to soil hydraulic properties, the lower (−1,500 kPa soil water pressure) and upper (after field capacity was reached) limits of PAWC were determined from sample profiles at various calibration points within the 36-ha field. Plant-available water was determined by the difference between the upper and lower values. Calculations were made on a 1.2 m basis. One hypothesis assessed whether EC_a could directly be used to estimate PAWC. A second hypothesis tested the idea that maximum PAWC could be approximated with a hypothetical two-layer soil profile composed of a topsoil layer (usually silt loam in texture) and a sub-layer (silty clay or clay in texture) to the bottom of the rooting depth. The texture-specific PAW fraction values needed to calculate profile available water are commonly available through the USDA–NRCS.

31.2.4 Soil Compaction

To enable efficient compaction mapping and targeting of remediation management, we developed a horizontally operated, multiple-depth penetrometer (Chung et al., 2006). Similar to the standard vertically operating cone penetrometer, this sensor measures the resistance of the soil to penetration by a series of prismatic cutting tips along a blade pulled through the soil. The multiple prismatic tips extend forward from the leading edge of the vertical blade and are spaced apart to minimise interference from the main blade and adjacent sensing tips. The design maximum operating depth was 0.5 m, and the upper limit and resolution of soil strength were 19.4 and 0.14 MPa, respectively.

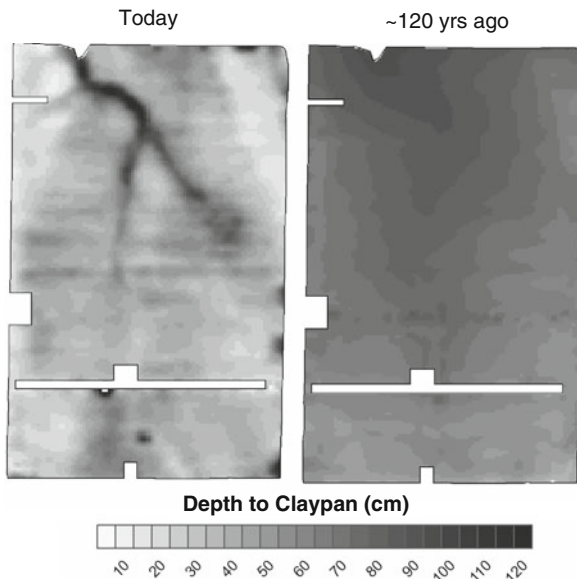
Since this chapter presents a synthesis of previously reported investigations, additional ‘Materials and Methods’ details will not be repeated here, but can be found in the cited papers.

31.3 Results and Discussion

31.3.1 Claypan Topsoil Depth

Because the claypan morphology presents a hostile environment for crop root growth, particularly the E horizon just above the claypan (Myers et al., 2007), the depth of soil above the claypan is an important indicator of soil quality. The

Fig. 31.1 *Left:* Topsoil depth for a 36-ha claypan soil field in Missouri developed from soil EC_a. *Right:* Modelled topsoil map of the same field, but prior to modern farming and tillage, using soil EC_a, bare-soil remotely sensed images, and profile descriptions of nearby uncultivated soil sites



relationship between topsoil depth and EC_a varies by field, soil moisture, temperature, and sensor type, but usually we have found regression R^2 values between 0.7 and 0.9. Applying a regression model developed from a calibration dataset allows transforming a field soil EC_a survey into a high-resolution topsoil depth map, as shown in the ‘today’ map of Fig. 31.1 (see also Chapter 20). Further, a combination of soil EC_a, bare-soil remotely sensed images, and profile descriptions of nearby uncultivated soil sites allowed us to develop a model estimating topsoil depth prior to cultivation (~120 years ago map of Fig. 31.1) (Lerch et al., 2005). The comparison vividly shows the extent of topsoil loss caused by farming during the past ~120 years. The majority of the field has lost topsoil, with an average loss of 13 cm. The lighter colour areas on the ‘today’ map highlight field areas that have experienced the greatest amount of erosion, losing up to ~45 cm of topsoil. The darker, narrow areas on the north end of the field define a drainage channel that has accumulated sediments. We find that the visual representation of historical erosion provided with this set of maps is extremely valuable in educational programs and to help reinforce the need for conservation practices.

Comparing the thin topsoil areas to yield maps has demonstrated the importance of topsoil to crop productivity and the instability of corn yield as shown in a 5-year average yield map and yield coefficient of variation map (Fig. 31.2). Low-yielding areas (darker areas in Fig. 31.2, *left* map) correspond to highest year-to-year corn yield variability (lighter areas on Fig. 31.2, *right* map), meaning yield is low and less predictable on thin topsoil areas.

Areas with low topsoil identified by soil EC_a have also been identified as creating the greatest on-going environmental concerns (Lerch et al., 2005) and therefore

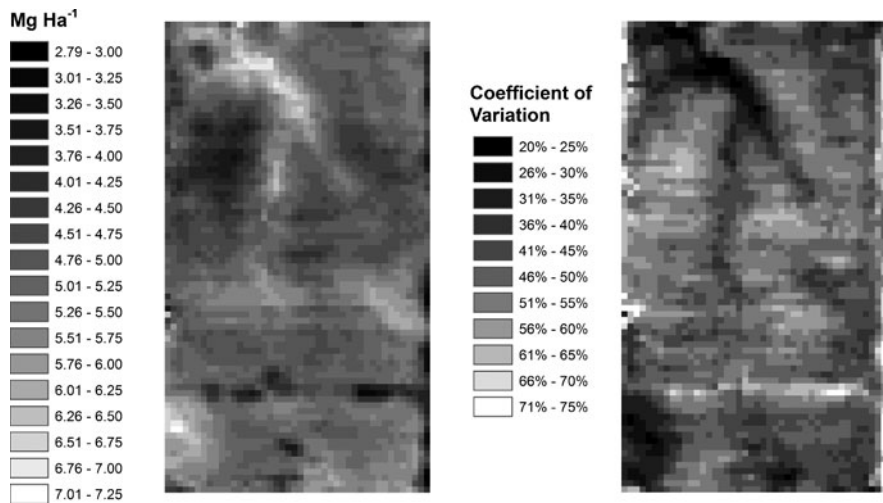


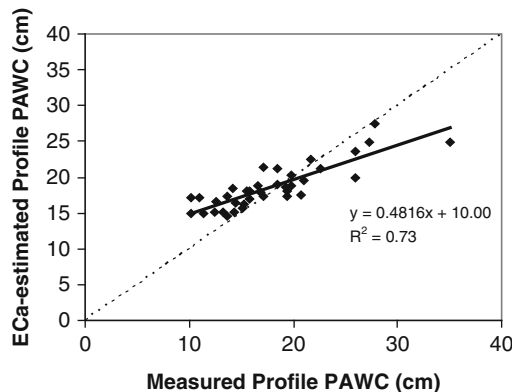
Fig. 31.2 Five-year (1993, 1997, 1999, 2001, and 2003) average corn yield map (left) and coefficient of variation (right) for a Missouri claypan soil field

should be high priority sites for targeting with precision conservation. In 2003, a precision agriculture system employing multiple production and environmental goals was developed and initiated on this field. The plan for this system was developed on the premise that mapped crop and soil information from sensors was fundamental to understanding what crops should be grown and what other management and conservation practices should be adopted. Precision nutrients, crop type and rotation, tillage, and herbicides are components embraced within this system and are described in detail in Kitchen et al. (2005). The plan calls for conservation practices targeted to degraded field areas to help remediate soil to a higher level of soil quality (Kitchen et al., 2005).

31.3.2 Claypan Hydraulic Properties

Another aspect of soil quality relates to hydraulic characteristics. As briefly described above, the claypan has dramatic effects on the hydrology of claypan soil watersheds. Understanding variability in the claypan depth over the landscape is essential for more accurately modelling soil water storage and infiltration rate, and therefore run-off potential. In our work reported by Jiang et al. (2007), soil EC_a using both electromagnetic induction and coulter-based EC_a sensors was applied in two separate procedures to estimate PAWC of claypan soils. In the first procedure, simple regression modelling between measured PAWC and EC_a showed a significant relationship with an R^2 of 0.67 and an RMSE of 30 mm. These results were derived from the significant relationship of EC_a to the lower limit of the profile PAWC, which is highly correlated with topsoil thickness. In the second procedure, PAWC was simplified by hypothesising a two-layer soil profile composed of a silt

Fig. 31.3 A two-layered soil profile obtained from soil EC_a was used to estimate plant-available water capacity (PAWC)



loam topsoil layer and a silty clay subsurface layer. The boundary between these layers (i.e. topsoil depth) can be conveniently estimated by EC_a as described in Section 3.1. Compared to measured PAWC, the results were promising (Fig. 31.3), with RMSE values of ~ 15 mm. With the two-layer approach, some underestimates of PAWC resulted from the underestimation of topsoil thickness, whereas overestimates were attributed to some soil profiles being short of field capacity at sampling due to slow recharge. So for similar claypan soil fields, we propose these to be quick and cost-efficient methods to quantify within-field profile PAWC with reasonable accuracy.

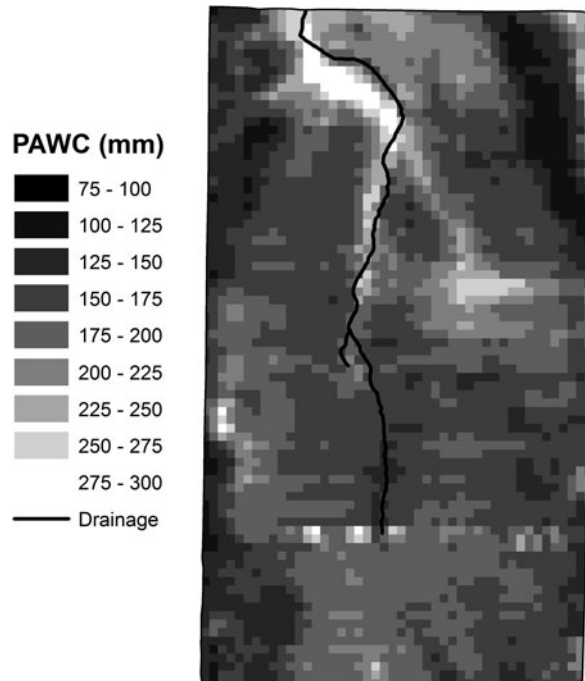
The two-layered approach was used to create a high-resolution map of PAWC (Fig. 31.4). Transforming the sensor information into a measure like PAWC allows one to view problem areas in a metric that has direct meaning to the crop's physiology. Such PAWC maps are also useful for site-specific decision making with regard to soil and water management.

In other work we have done, soil EC_a was negatively correlated with saturated hydraulic conductivity (K_s) (Jung et al., 2007) and bulk density in the 15–30 cm soil sampling depth (Jung et al., 2005) of claypan soils. While the EC_a – K_s relationship was weak, it could also be mapped to screen for variations in hydraulic conductivity at a field scale and isolate areas most prone to generating surface run-off (see also Chapter 32).

31.3.3 Soil Organic Carbon

Soil organic carbon has long been recognised as one of the most important characteristics for soil quality. While more direct sensor measurements have also been explored (see Chapter 13), in some situations, indirect sensing of soil organic carbon may be achieved. In work by Jung et al. (2007), soil EC_a was weakly correlated with surface soil organic carbon ($r = 0.70$) on claypan soils. This relationship was hypothesised as a reason EC_a and infiltration were related, as previously described (see also Chapters 12 and 15).

Fig. 31.4 High-resolution plant-available water capacity (PAWC) mapping can be obtained from soil EC_a surveys of claypan soils

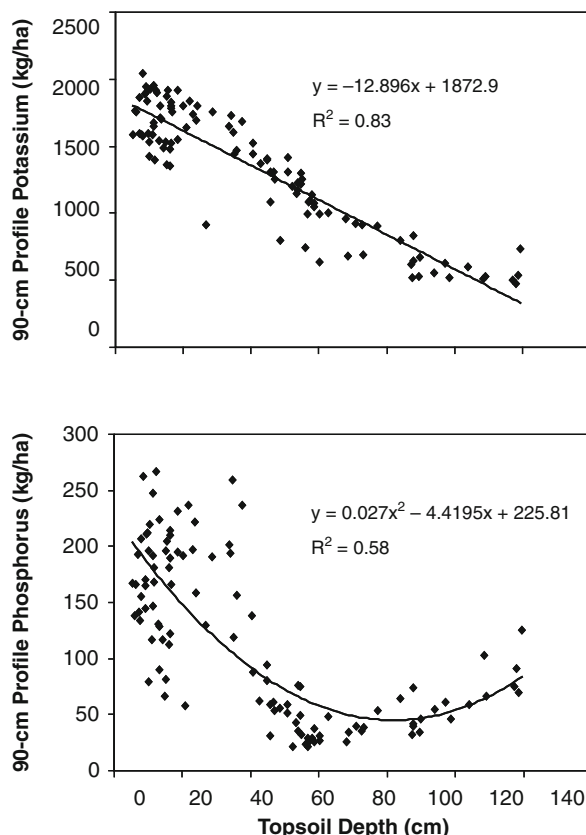


31.3.4 Nutrients

Another aspect of soil quality is a soil's ability to supply nutrients to plants. For convenience, typically only the surface ~20 cm of soils is sampled for nutrient analysis. However, the subsoil can be rich in nutrients and significantly contribute to crop nutrient needs. The challenge is assessing subsoil nutrients without costly deep soil sampling. We found that claypan topsoil depth was strongly related to profile soil nutrient content. After summing P and K soil test values over a 90 cm soil profile, a significant relationship to topsoil thickness was found (Fig. 31.5). Soil test K levels decreased with increasing topsoil thickness. Soil test P levels also decreased with topsoil thickness, but then slightly increased with deeper topsoil depth. This finding is significant because estimates of topsoil thickness using soil EC_a sensing may then be used to help estimate the total nutrients in the root zone and to predict the response of crop plants to fertiliser inputs. In related studies, we found a more probable response to P and K fertilisation where claypan soil topsoil depth was the greatest (Kitchen et al., 1999).

A second concept developed relative to nutrient management is using yield mapping and soil test results over time to create a site-specific nutrient BI. Here this is illustrated with potassium (K). This analysis showed that change in soil test K to sufficiency levels was impacted by BI, and this factor was variable within this field (Fig. 31.6). While K was not sustainable without fertiliser additions, not every

Fig. 31.5 Profile potassium (top) and phosphorus (bottom) have been shown to be highly related to topsoil depth on claypan soils



location in the field needed to receive the same amount to sustain K supply. Sites with a positive BI nearing 0 are the least buffered and should receive higher rates of fertiliser. At these locations, small amounts of removal cause large reductions in buffered nutrient. Fertiliser additions, whether maintenance or build-up applications, could be modified by the locally derived BI to provide an application rate that more efficiently meets the crop's need.

31.3.5 Soil Compaction

Due to their poor drainage, claypan soils are often wet in the spring. Thus, they are sensitive to traffic- and tillage-induced compaction problems that impact soil quality. Using an on-the-go horizontal penetrometer, maps of resistance for claypan soil fields have been produced. We found that compaction variations seem to be more strongly related to differences in soil properties than to traffic patterns. In Fig. 31.7 (~10 ha at the north end of the same field shown in the other figures), soil

Fig. 31.6 Potassium (K) buffering index created from net K removed (estimated from yield mapping) and change in soil test K

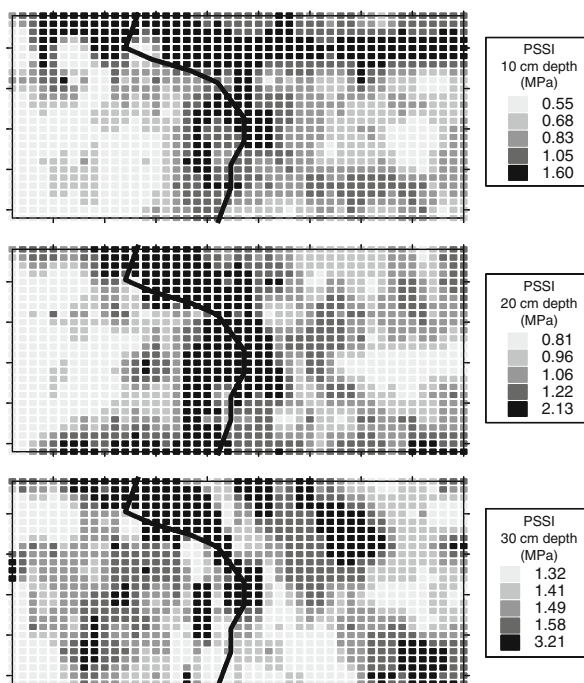
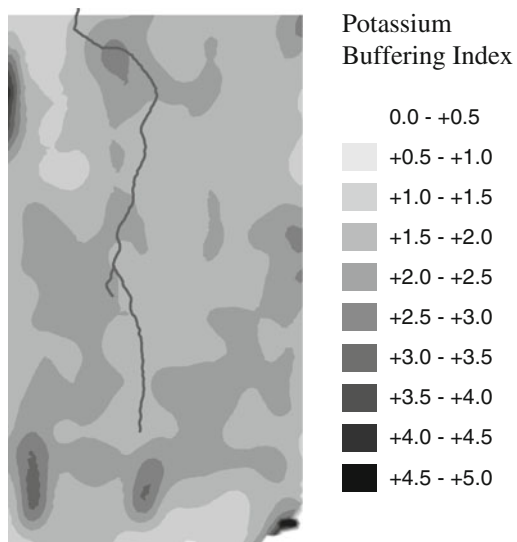


Fig. 31.7 Compaction variations in a typical claypan soil field, represented as prismatic soil strength index (PSSI) measured by a horizontally operating, multiple-depth penetrometer. The solid line represents the drainage channel

resistance at 10 cm was greatest near the drainage channel, which is what one would expect since this area stays wetter longer and would be more prone to compaction by machinery operations. At the 30 cm depth, soil resistance was greatest on the eroded side slopes. The sensor in this case would generally be within the claypan. In general, resistance using the sensor was higher at locations with lower EC_a , lower water content, and greater bulk density (see also Chapter 22).

31.4 Conclusions

Claypan soils vary greatly in their ability to produce crops and provide ecological service for minimal environmental impact. These soils lost resiliency when topsoil eroded over the last \sim 120 years of cultivation. The sensors and methods described in this chapter help define, with high resolution, the spatial variability of soil quality. These results can help land managers identify the practices needed and location for improved precision conservation.

References

Chung SO, Sudduth KA, Hummel JW (2006) Design and validation of an on-the-go soil strength profile sensor. *Trans Am Soc Agric Biol Eng* 49:5–14

Doran JW, Parkin TB (1994) Defining and assessing soil quality. In: Doran JW et al (eds), *Defining soil quality for a sustainable environment*. Soil Science Society of America special publication 35. Soil Science Society of America, Madison, WI, pp 3–21

Jiang P, Anderson SH, Kitchen NR, Sudduth KA, Sadler EJ (2007) Estimating plant-available water capacity for claypan landscapes using apparent electrical conductivity. *Soil Sci Soc Am J* 71:1902–1908

Jung WK, Kitchen NR, Sudduth KA, Kremer RJ, Motavalli PP (2005) Relationship of apparent soil electrical conductivity to claypan soil properties. *Soil Sci Soc Am J* 69:883–892

Jung WK, Kitchen NR, Anderson SA, Sadler EJ (2007) Crop management effects on water infiltration for claypan soils. *J Soil Water Conserv* 62:55–63

Kitchen NR, Spautz RE, Sudduth KA (1999) Can topsoil thickness help determine crop phosphorus and potassium nutrient needs? *Better Crops* 83:4–6

Kitchen NR, Sudduth KA, Myers DB, Massey RE, Sadler EJ, Lerch RN, Hummel JW, Palm HL (2005) Development of a conservation-oriented precision agriculture system: crop production assessment and plan implementation. *J Soil Water Conserv* 60:421–430

Lerch RN, Kitchen NR, Kremer RJ, Donald WW, Alberts EE, Sadler EJ, Sudduth KA, Myers DB, Ghidley F (2005) Development of a field-scale precision conservation system: water and soil quality assessment. *J Soil Water Conserv* 60:411–421

Myers DB, Kitchen NR, Sudduth KA, Sharp RE, Miles RJ (2007) Soybean root distribution related to claypan soil properties and bulk apparent soil electrical conductivity. *Crop Sci* 47:1498–1504

Sudduth KA, Kitchen NR, Bollero GA, Bullock DG, Wiebold WJ (2003) Comparison of electromagnetic induction and direct sensing of soil electrical conductivity. *Agron J* 95:472–482

Chapter 32

Proximal Sensing Methods for Mapping Soil Water Status in an Irrigated Maize Field

C.B. Hedley, I.J. Yule, M.P. Tuohy, and B.H. Kusumo

Abstract Approximately 80% of allocated freshwater in New Zealand is used for irrigation, and the area irrigated has increased by 55% every decade since 1965. The research described in this chapter therefore focuses on developing new techniques to map and monitor soil attributes relevant to irrigation water use efficiency. The apparent electrical conductivity (EC_a) of soils under a 33-ha irrigated maize crop was mapped using a mobile electromagnetic induction (EM) and RTK-DGPS system, and this map was used to select three contrasting zones. Within each zone, further EC_a values were recorded at a range of volumetric soil water contents (θ) to develop a relationship between EC_a , soil texture, soil moisture, and available water-holding capacity (AWC) ($R^2 = 0.8$). This allowed spatial prediction of AWC, showing that these sandy and silty soils had similar AWCs (~ 160 mm/m). High-resolution digital elevation data obtained in the EM survey were also co-kriged with TDR-derived θ to produce soil moisture prediction surfaces, indicating drying patterns and their relationship to topography and soil texture. There was a 12.5–13.1% difference in soil moisture to 45 cm soil depth between the wettest and the driest sites at any one time ($n = 47$). Spatial and temporal variability of soil moisture, indicated by these co-kriged prediction surfaces, highlights the need for a rapid high-resolution method to assess in situ soil moisture. The potential of soil spectral reflectance (350–2,500 nm range; 1.4–2 nm resolution) for rapid field estimation of soil moisture was therefore investigated. Soil spectra were pre-processed and regressed against known soil moisture values using partial least squares regression (R^2 calibration = 0.79; R^2 prediction using leave-one-out cross-validation = 0.71). These proximal sensing methods facilitate spatial prediction of soil moisture, information which could then be uploaded to a variable rate irrigator.

Keywords Available water-holding capacity · Co-krige · Digital elevation map · EM mapping

C.B. Hedley (✉)
Landcare Research, Manawatu Mail Centre, Private Bag 11052,
Palmerston North 4442, New Zealand
e-mail: HedleyC@LandcareResearch.co.nz; m.hedley@massey.ac.nz

32.1 Introduction

New Zealand reflects a global trend in which increasing gains in agricultural productivity are supported by increasing use and reliance on irrigation. This has led to over-allocation of freshwater for irrigation in parts of the country, mirroring the global situation. In addition, efficiency of water use is very low in some systems, for example, up to 50% of water can be wasted in flood irrigation systems. Centre-pivot irrigators, however, have the ability to apply exact depths of water accurately to a crop, and recent advances have been made towards individual nozzle control for variable rate irrigation. However, adequate decision support systems for variable rate irrigators are not available, and there is a need for real-time monitoring, decision, and control systems to be developed (DeJonge et al., 2007).

This decision support system would ideally provide real-time information to the irrigator about daily spatial soil water status, where soil water status is defined as the amount of water available to the crop. As crop yield is directly related to water stress, this not only addresses the need for sustainable freshwater use but also introduces cost efficiencies to the producer.

The total amount of water a soil can supply to a crop is usually measured by the volume it can hold between field capacity and wilting point, which can be assessed in the field (Hedley et al., 2005). Water status is the amount of this total available water that is available to a crop on any one day and is commonly expressed as millimetre water per millimetre rooting depth in soil. However, the spatial variability of this status, as indeed is the case for many soil properties, will vary across the landscape, a fact largely ignored before the 1980s (Cook and Bramley, 1998).

EM mapping is a proximal sensing method that maps soil variability on the basis of soil texture and moisture in non-saline conditions (Hedley et al., 2004; Chapter 34). The EM sensor records one weighted mean value for apparent soil electrical conductivity (EC_a) to a depth of 1.5 m, and this can be related directly to soil moisture (e.g. Huth and Poulton, 2007; Chapters 21 and 23) if soil moisture is the major variable affecting EC_a . EC_a has also been used to predict AWC (Waine et al., 2000; Hedley et al., 2005; Hezarjaribi and Sourell, 2007), AWC being the amount of water held by the soil between field capacity and wilting point. Field capacity is defined as the point where all macro-pores have drained and is measured in the field 2 days after a heavy rain (i.e. 2 days after an event which brings the soil to saturation). Wilting point is the lower limit of available water, the soil moisture content reached when a plant permanently wilts.

In comparison, direct soil moisture mapping has traditionally been accomplished by exhaustive point measurements – which is both time consuming and costly. Embedded sensors such as time domain reflectometry (TDR) are improvements, but require considerable time and effort for installation and measurement, and the data cannot be easily logged (Kaleita et al., 2005). A method of determination that does not require exhaustive manual measurements is therefore desirable for robust precision irrigation soil information support systems. Proximal sensing with a vis–NIR spectroradiometer allows rapid field collection of soil reflectance spectra,

which can then be related to a calibration set of soils for gravimetric soil moisture estimation (w) (Mouazen et al., 2005; Kaleita et al., 2005). Mouazen et al. (2005) used a tractor-drawn subsoiler chisel to carry an optical unit through the soil; this unit carried reflected light to a spectrophotometer (wavelength range 306–1,710 nm) attached to the tractor. A prediction correlation of 0.75 [root mean squared error of prediction (RMSEP) of 0.0250 kg/kg] was obtained for in-line field measurements compared with a prediction correlation of 0.98 [root mean squared error of cross-validation (RMSECV) of 0.0175 kg/kg] under laboratory conditions. Kaleita et al. (2005) used an HR2000 spectrometer (spectral resolution 0.065 nm; wavelength range 331–1,069 nm) to estimate w . Their results returned a lower R^2 validation of 0.63 for all soils and an improved R^2 validation of 0.71 when only the light-coloured soils were included.

This chapter reports on our progress in the development of proximal sensing methods to assess daily spatial soil moisture status for precision irrigation. It uses high-resolution EC_a data to predict AWC and high-resolution DEM to co-krige TDR values. TDR values are used to investigate spatial and temporal variability of soil moisture at the research site. The potential of backpack vis–NIR spectroradiometry for rapid, real-time mapping and monitoring of soil moisture is also discussed.

32.2 Materials and Methods

32.2.1 Study Site

A 33-ha irrigated maize crop was selected at a farm near Bulls, approximately 30 km north-west of Palmerston North, in the Rangitikei River Catchment, New Zealand. A 600-m centre-pivot irrigator is used at this site during periods of seasonal drought. The soils occur on a terrace surface and are mapped as Ohakea silt loams (Mottled, Immature Pallic Soil, New Zealand Soil Classification; Endoaquept, USDA NRCS classification; Stagnic Cambisol, FAO-WRB soil classification), characterised by silt loam topsoils and mottled subsoils to about 0.6 to >1.0 m above heterogeneous layers of sands and gravels. In some places, sand has blown onto this terrace soil from an adjacent sand dune, forming the Ohakea loamy sand (Mottled, Immature Pallic Soil; Endoaquept; Stagnic Cambisol). This soil is characterised by loamy sand topsoil over mottled silt loam subsoil over sands and gravels.

Soil classifications

Soil name	NZ	USDA	FAO
Ohakea silt loam	Mottled, Immature Pallic Soil	Endoaquept	Stagnic Cambisol
Ohakea loam sand	Mottled, Immature Pallic Soil	Endoaquept	Stagnic Cambisol

32.2.2 Electromagnetic Induction Mapping and Soil AWC

A Geonics EM38 electrical conductivity sensor with Trimble RTK-DGPS and Trimble Ag170 field computer onboard an ATV was used to map soil variability. The Geonics EM38 measured apparent soil electrical conductivity (EC_a) to a depth of 1.5 m, providing one mean weighted value that is primarily influenced by soil texture and moisture in non-saline soils (e.g. Hedley et al., 2004). Survey data points were collected at 1 s intervals, at an average ATV speed of 15 km h^{-1} , with a measurement recorded approximately every 4 m along transects 10 m apart. The EC_a map was produced using ordinary kriging in Geostatistical Analyst (ArcMap).

A method was then developed, based on that of Waine et al. (2000), to relate EC_a values to AWC. Three zones with low, intermediate, and high EC_a values were selected on the EC_a map and AWC estimated for each zone. AWC was estimated in the field by sampling three replicate soils in each zone for θ on days when the soils were at field capacity [soil moisture deficit (SMD) 0 mm], had an intermediate moisture content (SMD 40 mm), and were very dry (close to wilting point; SMD 130 mm). At an SMD of 130 mm, the very dry soil was losing water at no more than 1 mm per day and was assumed to be close to wilting point. Soils were cored to 600 mm (0–150, 150–300, 300–450, and 450–600 mm) and soil moisture was determined gravimetrically on the known volumes of soil. Handheld EC_a values were also recorded.

Soil samples were also collected for particle size analysis (0–150, 150–300, 300–450, and 450–600 mm). Percent sand, silt, and clay was determined by wet sieving the >2-mm soil fraction and by a standard pipette method for the <2-mm soil fraction; then one mean value for percent sand, silt, and clay to 600 mm was calculated for three replicates in each zone. This was then converted to a single number, using the fineness class developed by Waine et al. (2000) for UK soils. This fineness class provides a numeric ranking of soils (1–6 in 0.5 intervals for the 11 classes on a soil texture triangle) on the basis of increasing fineness of texture and provides a single numeric value for soil texture.

To check the applicability of this fineness class to New Zealand soils, a centroid value of percent sand, silt, and clay was obtained for each of the 11 classes in the New Zealand soil texture triangle (Fig. 32.1a), which is used for standard soil descriptions (Milne et al., 1995). Both UK and New Zealand soil particle classifications classify soil particle sizes as 0.06–2 mm (sand), 0.002–0.06 mm (silt), and <0.002 mm (clay).

The texture-weighting equation developed by Waine et al. (2000) to produce a line of best fit for UK soils was then applied to the New Zealand soil data, giving an R^2 of 0.96 (Fig. 32.1b), confirming its suitability for New Zealand soils. The texture-weighting equation developed for UK soils can therefore be used for New Zealand soils to define a numeric value (fineness class) for New Zealand soil textural classes in terms of the following:

$$\text{Fineness class} = -0.8981 (\text{Tw})^2 + 3.8704(\text{Tw}) + 1.9686 \text{ and texture weighting} \\ (\text{Tw}) = 0.03 (\% \text{clay}) - 0.004 (\% \text{sand}).$$

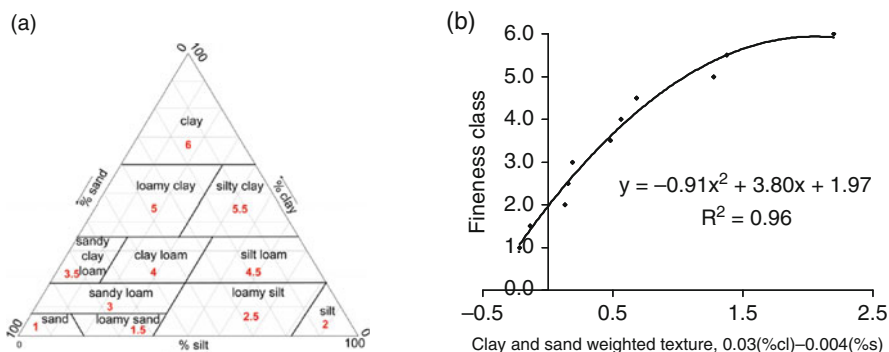


Fig. 32.1 (a) New Zealand soil texture triangle. Milne et al. (1995) defines 11 soil texture classes on the basis of percent sand, silt, and clay. Fineness class is shown for each soil texture class. (b) Fineness class developed for UK soils (Waine et al., 2000) applied to New Zealand soil texture classes

The fineness class determined for soils in this study was then plotted as a single value on the abscissa against θ on the y-coordinate to produce a texture–moisture graph. The texture–moisture graph displays curves of θ against soil texture for a range of soil moistures between field capacity and very dry (near wilting point), providing a field estimate of AWC. It can be used to predict AWC for other soils of known texture within this range. EC_a was measured each time field θ was measured and these EC_a values were plotted against the derived AWC value.

32.2.3 Soil Moisture Measurement

32.2.3.1 Time Domain Reflectometry (TDR)

Soil moisture θ was measured monthly by TDR ($n = 47$) between December and March to assess spatial and temporal variability of soil moisture.

32.2.3.2 Collection of Vis–NIR Soil Reflectance Spectra

A vis–NIR spectroradiometer was trialed for rapid field estimation of soil moisture. Ten replicate soil reflectance spectra were collected at 90 positions using an ASD FieldSpec Pro FR spectroradiometer (Analytical Spectral Devices). A prototype soil probe was used in which an internal light source was replaced with a higher intensity halogen lamp; it was based on the ASD plant probe (see Chapter 15). Using the prototype probe, attached via a fibre optic cable to the ASD FieldSpec Pro FR spectroradiometer in a backpack, reflectance spectra were collected (350–2,500 nm) from a freshly cut soil surface at a soil depth of 20 mm. These hyperspectral data were recorded at bandwidth intervals of 1.4–2 nm. After spectra had been obtained, soil samples were collected (20–50 mm) at each position to determine w .

32.2.3.3 Spectral Data Pre-processing

The hyperspectral data were pre-processed and then partial least squares regression was used for prediction and statistical correlation. Data pre-processing included (i) waveband filtering to remove the noisy data between 350–470 and 2,440–2,500 nm, (ii) smoothing (Savitzky–Golay), (iii) data reduction, (iv) derivative calculation, and finally (v) averaging of the 10 replicate spectra using SpectraProc v1.1 software (Hueni and Tuohy, 2006). The pre-processed data were then imported into Minitab 14 (Minitab, Inc., 2006) and a calibration model for prediction of soil moisture was developed using partial least squares regression.

32.3 Results and Discussion

32.3.1 Electromagnetic Induction Mapping and Soil AWC

The EC_a map delineated soil differences on the basis of texture and moisture, confirmed by soil pit examination, particle size analysis, and soil moisture measurements (Table 32.1). Three zones, representing areas of low, medium, and high EC_a values (zones A, B, and C, respectively; Fig. 32.2, Table 32.1), were then defined as three classes (using Jenks natural breaks) of a prediction surface produced using a spherical semivariogram and ordinary kriging (Geostatistical Analyst, ArcMap). These zones were ground truthed as Ohakea loamy sands in the orange-red zones (zoneA); Ohakea silt loams in the yellow-green zones (zoneB), and a natural low-lying ponding area where subsoils were more intensely mottled and soils were generally wetter (zone C) (Fig. 32.2).

Texture–moisture graphs (Fig. 32.3a) and a derived relationship between EC_a and AWC (Fig. 32.3b) were used to produce the AWC map (Fig. 32.4). In Fig. 32.3a, the top curve represents θ at field capacity and the lower curve represents θ when the soils were very dry (close to wilting point) for the textural range of sampled soils (therefore the difference between these two curves is a field estimate of AWC). AWC is then plotted against EC_a (Fig. 32.3b), using the handheld EC_a values which were recorded for each replicate at each time of sampling for soil moisture. This provided

Table 32.1 EC_a (20 August 2006 survey) zone characteristics

Zone	EC _a range (mS m ⁻¹)	Clay (%) ^a	Soil moisture (m ³ m ⁻³)			
			12/12/06	5/1/07	12/2/07	27/3/07
			Pre-irrigation			
Zone A	12.0–18.5	11	0.276	0.253	0.241	0.258
Zone B	18.5–26.0	23	0.297	0.276	0.258	0.285
Zone C	22.0–31.4	14	0.359	0.320	0.306	0.295

^aWeighted mean value for 0–600 mm soil depth

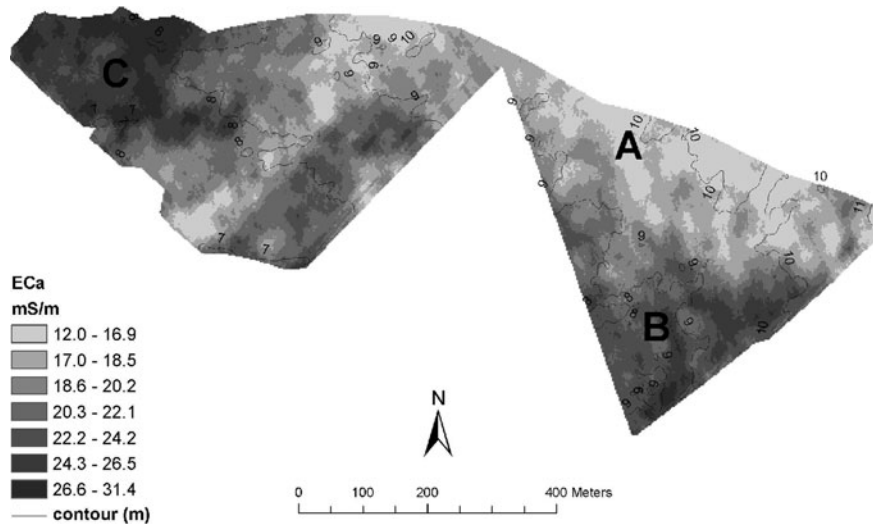


Fig. 32.2 EC_a map of the study area, showing zones A, B, and C

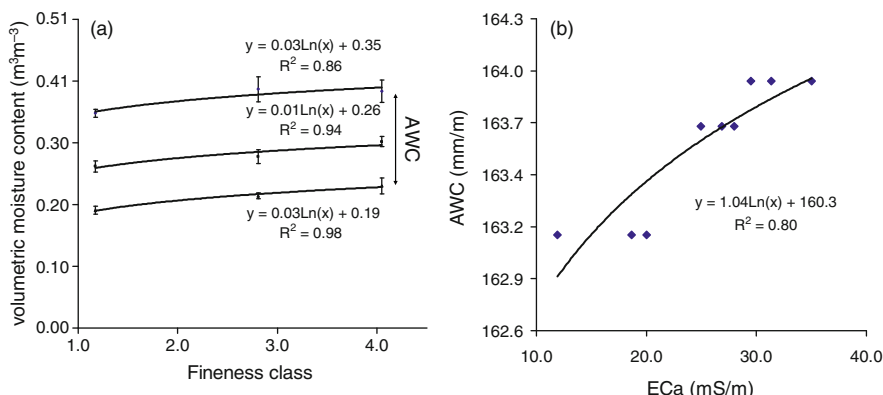


Fig. 32.3 (a) Texture-moisture graph, showing θ at field capacity (top curve), an intermediate moisture (middle curve), and when the soils were near wilting point (lower curve) for a range of soil textures. (b) Relation of AWC to EC_a for the study area

a relationship between AWC and EC_a ($R^2 = 0.8$), allowing spatial prediction of AWC using the EC_a data.

These sandy and silty soils have very similar AWCs (161–164 mm/m), i.e. these soils hold similar amounts of crop-available water at field capacity, as shown in Fig. 32.4.

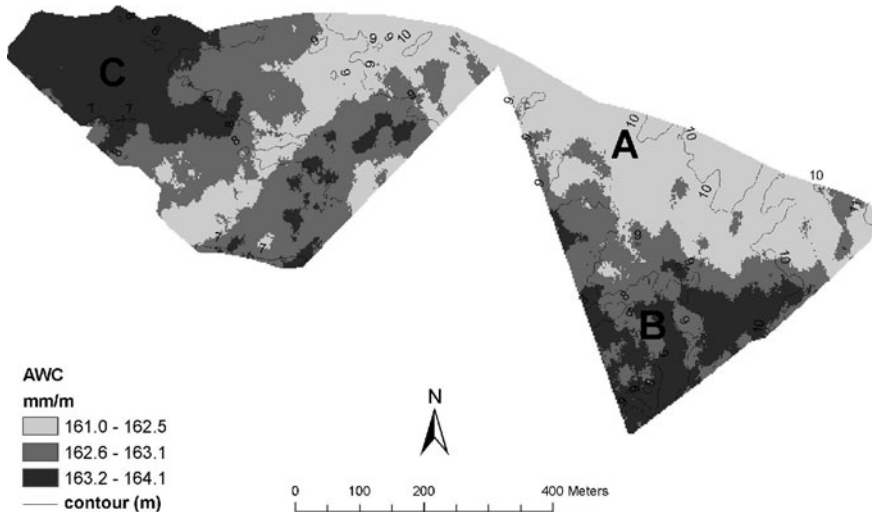


Fig. 32.4 AWC map of the study area

32.3.2 Soil Moisture Measurements

The TDR survey showed, however, that at any one time, soil moisture varied by $0.12\text{--}0.13\text{ m}^3\text{ m}^{-3}$ across this 33-ha maize field. We suggest that this is explained by (i) soil profile differences in texture, structure, and depth to gravels, and (ii) topographic position (Plate 32.1).

Sandy soils tend to have a greater proportion of larger pores, which drain faster than do smaller pores. Topographic position is also a controlling factor for drainage – soils in low-lying areas typically remain wetter for longer.

TDR values were co-kriged with high-resolution digital elevation data from the EC_a survey, and the prediction surface had a slightly smaller root mean squared error of prediction (2.78) compared with ordinary kriged TDR values (2.84).

32.3.3 Vis–NIR Soil Reflectance Spectra

Soil reflectance spectra were collected in the spring when the soils were close to field capacity, and soil surfaces exposed for collection of the spectra were very wet and in some cases smeared. Ten replicate spectra were obtained at each position. The collected spectra were then pre-processed and imported into Minitab 14 (Minitab, Inc., 2003) for principal component analysis (PCA) and partial least squares regression analysis (PLSR) against the measured data (see Chapter 15). A PCA score plot was used to observe the pattern of sample scattering. During PLSR processing, 12 samples which had standardised residuals ≥ 2.0 were removed as outliers.

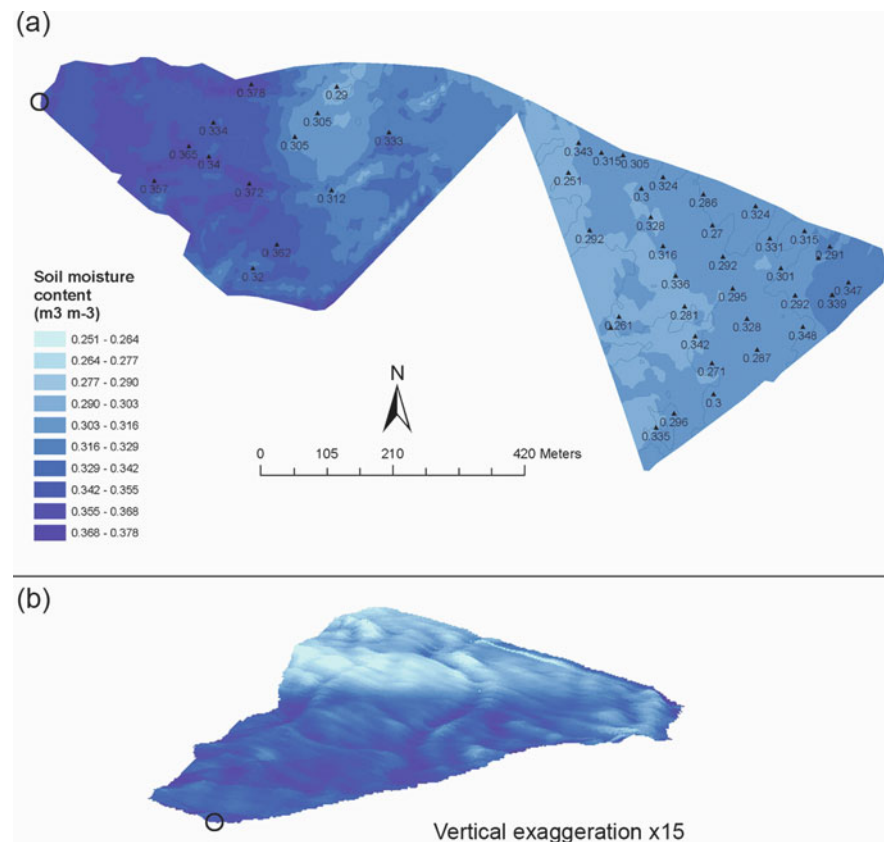


Plate 32.1 (a) Soil moisture prediction surface (13 Dec 2006) obtained by co-kriging TDR ($n = 47$) with high-resolution digital elevation data ($n = 9,350$). Point TDR values are shown (b) 3D soil moisture prediction surface (NW end) showing wetter soils in hollows and a drier area where sandy soils with low EC_a values exist (zone A). The black circle (o) shows the corresponding point on prediction surfaces in Plate 32.1a and b

An R^2 (calibration) of 0.79 and an R^2 (prediction using leave-one-out cross-validation) of 0.71 were obtained, with an RMSECV of 0.019 kg/kg and an RPD (standard deviation over RMSECV) of 1.85, the latter providing a measure of how large the error (RMSECV) is with respect to the range of w encountered during calibration. In comparison, Kaleita et al. (2005) obtained an R^2 (calibration) of 0.71 or lower when predicting field moisture from field-collected spectra and commented that one prediction model did not fit different soil types. Mouazen et al. (2005) used a calibration developed in the laboratory (cross-validation correlation 0.98, $R^2 = 0.96$), by adding known amounts of water to one soil, therefore minimising any other soil differences. However, if this method is to be successfully used in the field, it should be robust enough to predict soil moisture in soils where several soil

properties as well as soil moisture vary (for example, organic matter content, surface roughness, and texture). Mouazen et al. (2005) used the laboratory-developed calibration to predict in-line subsoiler chisel field reflectance measurements and reported a prediction correlation of 0.75 (RMSEP = 0.025 kg/kg; RPD = 3.376) in the field compared with 0.98 (RMSEP = 0.016; RPD = 5.115) in the laboratory. Our results suggest that field-collected spectra can be successfully used for calibration with a prediction correlation of 0.84 and a prediction error (RMSECV) of 0.019 kg/kg for this field site.

32.4 Conclusions

EC_a was used to spatially predict AWC ($R^2 = 0.80$), which shows that these soils store very similar amounts of plant-available water. TDR ($n = 47$), however, indicates that the spatial and temporal variability of soil moisture is significant, showing that drying patterns vary, which is most likely due to topography and soil profile differences. Ideally, therefore, the site should be characterised on a number of occasions during one drying cycle. Vis–NIR reflectance spectra are easily collected in the field and this method shows promise for rapid, accurate sensing of *in situ* soil moisture. Best practice precision irrigation scheduling decisions can then be made for utilisation of water stored in the soil profile, accounting for high-resolution spatial and temporal differences in soil water status.

Instruments Used

Geonics EM38 ground conductivity meter
Trimble RTK-DGPS
Trimble Ag170 field computer
ASD FieldSpec Pro FR spectroradiometer
Minitrave Kit 6050X3K1 TDR

Acknowledgements The authors would like to thank Hew and Roger Dalrymple for use of their farm. The research has been funded by the Agricultural and Marketing Research and Development Trust, New Zealand (AGMARDT), the New Zealand Vice-Chancellors' Committee, William Georgetti Trust, and The Sustainable Land Use and Research Initiative (SLURI), New Zealand.

References

Cook SE, Bramley RGV (1998) Precision agriculture – opportunities, benefits and pitfalls of site-specific crop management in Australia. *Austr J Exp Agric* 38:753–763

DeJonge CK, Kaleita AL, Thorp KR (2007) Simulating the effects of spatially variable irrigation on corn yields, costs, and revenue in Iowa. *Agric Water Manage* 92:99–109

Huth NI, Poulton PL (2007) An electromagnetic induction method for monitoring variation in soil moisture in agroforestry systems. *Austr J Soil Res* 45:63–72

Hezarjari A, Sourell H (2007) Feasibility study of monitoring the total available water content using non-invasive electromagnetic induction-based and electrode-based soil electrical conductivity measurements. *Irrigat Drainage* 56:53–65

Hueni A, Tuohy M (2006) Spectroradiometer data structuring, pre-processing and analysis - an IT based approach. *J Spat Sci* 51(2):93–102

Hedley CB, Yule IJ, Bradbury S (2005) Using electromagnetic mapping to optimise irrigation water use by pastoral soils. Proceedings of the joint international conference of the New Zealand Hydrological Society, International Association of Hydrogeologists, and New Zealand Society of Soil Science, Auckland, 28 November–2 December, New Zealand Hydrological Society, Wellington, New Zealand, CD-ROM

Hedley CB, Yule IJ, Eastwood CR, Shepherd TG, Arnold G (2004) Rapid identification of soil textural and management zones using electromagnetic induction sensing of soils. *Austr J Soil Res* 42:389–400

Kaleita AL, Tian LF, Hirschi MC (2005) Relationship between soil moisture content and soil surface reflectance. *Trans Am Soc Agric Eng* 48(5):1979–1986

Milne JDG, Clayden B, Singleton PL, Wilson AD (1995) Soil description handbook. Manaaki Whenua Press, Landcare Research, New Zealand, 157 pp

Mouazen AM, De Baerdemaeker J, Ramon H (2005) Towards development of on-line soil moisture content sensor using a fibre-type NIR spectrophotometer. *Soil Tillage Res* 80:171–183

Waine TW, Blackmore BS, Godwin RJ (2000) Mapping available water content and estimating soil textural class using electromagnetic induction. EurAgEng 2000, Warwick, UK, Paper 00-SW-044, European Society of Agricultural Engineers, UK

Chapter 33

Comparing the Ability of Multiple Soil Sensors to Predict Soil Properties in a Scottish Potato Production System

J.A. Taylor, M. Short, A.B. McBratney, and J. Wilson

Abstract A soil survey with two soil sensors – an electromagnetic induction (EMI) sensor and a gamma radiometer – was conducted on a farm in south-east Scotland. The collected sensor data were used to direct soil sampling on the farm. The soil samples were then regressed against the sensor output to identify how well the sensor output predicted individual soil properties. The gamma radiometer produced better prediction fits in the topsoil than did the EMI sensor; however, the EMI predicted clay content better in the subsoil. Combining the sensor outputs produced improved fits for the topsoil data but not the subsoil. Neither sensor, individually or combined, produced good fits of soil pH. For potato production systems, topsoil properties are the dominant production determinants; thus a gamma radiometer using current configurations would be the preferred sensor in a single-sensor system assuming that all costs were equal. The economics of single vs. multiple sensor surveys is still unclear.

Keywords Multi-sensor · Gamma radiometer · Electromagnetic induction · Soil texture

33.1 Introduction

Spatial information on soil properties is important for management in all agricultural systems. However, the majority of commercially available soil sensors do not directly map soil properties. Rather, they generally measure soil responses, such as the apparent soil electrical conductivity (EC_a) and naturally occurring γ -ray emissions, which are a function of various soil properties. Some of the soil properties that affect the sensor response(s) are temporally stable, for example clay content

J.A. Taylor (✉)

Australian Centre for Precision Agriculture, The University of Sydney, John Woolley Building A20, Sydney, NSW 2006, Australia
e-mail: precision.agriculture@sydney.edu.au

and clay mineral type, while others may be highly temporally unstable, such as soil moisture content, and vary on a daily/weekly basis; still other soil properties, such as organic matter content and soil pH, exhibit low temporal instability and can vary over monthly or yearly time frames. The result is that, without extensive calibration, it is often hard to decompose the sensor output directly into soil properties. The use of multi-temporal and/or multi-sensor systems may help overcome this problem.

Soilessentials Ltd has been providing commercial soil mapping for growers in the United Kingdom, particularly potato growers, for the past 8 years. A core part of their business revolves around providing growers with variable rate maps for lime application (pH remediation). Currently, these maps have been derived from a 50-m × 50-m square grid survey, together with spatial information in the form of EC_a maps (collected with a Geonics EM38DD sensor) and a digital elevation map. The EC_a responses of the EM38DD, however, are not directly linked to soil pH. The current approach by Soilessentials Ltd relies on a further correlation between texture and the rate of change in soil pH under intensive crop production, but correlations between the EMI response and pH have not been strong in previously collected data (hence the current use of a dense (50 m) square grid for pH and lime requirement mapping). In Australia, the incorporation of EC_a data, with appropriate ground truthing, into the lime requirement decision-making process has shown significant savings over conventional composite bulk soil sampling and uniform lime application (Adam Inchbold, chairman, Riverine Plains, Inc., pers. comm.). Soilessentials Ltd was interested in knowing if and how soil sensor data could be used to decrease the intensity of physical soil sampling without compromising the final pH map quality.

While the incorporation of EC_a data into soil property mapping has been shown to be profitable, the limitations of this approach are well understood and there are published accounts (McKenzie, 2000; Chapter 24), as well as anecdotal reports such as those of Soilessentials Ltd, of areas where using EC_a has not provided any benefit in the lime application process. To date, the use of data from other soil sensors – either instead of EC_a data or in combination with EC_a data – in generating variable rate lime application maps has not been reported. To investigate the potential of gamma radiometric data for mapping soil properties, particularly pH, a study was undertaken in eastern Scotland by Soilessentials Ltd in collaboration with the Australian Centre for Precision Agriculture (ACPA) at the University of Sydney. The objectives of the study were to compare gamma radiometric data with EC_a for making pH (lime requirement) maps and what further benefits may be gained from combining the data (i.e. using multi-sensor data) compared with analysing the data from individual sensors. The hypothesis here is that the two sensors will have different responses to soil properties and multivariate analysis may provide a better prediction of soil properties. As well as pH, the topsoil and subsoil texture (clay content) and the cation exchange capacity (CEC) of the topsoil fraction were also investigated.

33.2 Materials and Methods

33.2.1 *On-the-Go Soil Survey*

The survey was conducted in February 2006 at 'Stenton', a farm located near Pittenweem, Fife, Scotland, UK. An Omnistar HP GPS (global satellite navigation system receiver), Geonics EM38DD (electromagnetic induction sensor), and SAIC Exploranium GRS320 (gamma radiometer) were mounted on a quad bike. The EM38DD is a dual-dipole sensor and provides two EC_a readings in real-time from both the horizontal (EC_{ah}) and vertical (EC_{av}) dipoles. The EC_{ah} generates 80% of its signal response from 0 to 1.1 m, while the EC_{av} has a deeper penetration and generates 80% of its signal response from 0 to 2 m (Abdu et al., 2007). The GRS320 generates 256 discrete energy band readings which are aggregated into four regions of interest (ROI) relating to the total response (total count, TC) and peaks associated with the decay of potassium (K), thorium (Th), and uranium (U) in the spectra. The Omnistar HP is a carrier-phase receiver and was used to geo-locate the EM38DD and GR320 outputs as well as log the elevation. All data were logged using Farmsite (Farm Works Software, Hamilton, IN, USA). The survey was conducted at 10–15-m swathes and at a line speed of $\sim 10 \text{ km h}^{-1}$. The soil was at field capacity during the survey and the air temperature ranged from ~ 0 to 10°C .

The elevation data, two EM38DD outputs (EC_{ah} and EC_{av}), and four ROIs (TC, K, Th, U) from the GRS320 were interpolated onto a 5-m \times 5-m grid that covered the entire farm. Interpolation was done using block kriging (15 m \times 15 m blocks) with a local variogram function in VESPER (Minasny et al., 2005). The kriged outputs were displayed in ArcMap v9.1 (ESRI, Redlands, CA, USA, 2005).

33.2.2 *Manual Soil Sampling*

The kriged data for the seven variables were collated into a single file. A k -means cluster analysis was performed to generate six classes, and four locations were randomly selected from each of the six. This produced 24 soil sample locations across the farm.

Soil sampling was done 2 days after the on-the-go survey. A soil core was extracted to a depth of 0.9 m and subset into a topsoil (0–0.45 m) and a subsoil (0.45–0.9 m) fraction. The soil fractions were sent to a commercial laboratory (Lancrop Labs, Yorkshire, UK) for chemical and physical analysis. Properties measured were clay content, sand content, pH (1:5 soil:0.2 M CaCl_2), available P, exchangeable K, Mg, Ca, CEC in the topsoil and clay content, sand content, available P, exchangeable K, Mg, and pH (1:5 soil:0.2 M CaCl_2) in the subsoil. An error in geo-location during soil sampling resulted in one class receiving an extra sample at the expense of another. One location had a shallow rocky soil with no fraction below 0.45 m; so only 23 data points were available for the subsoil.

33.2.3 Multivariate Data Analysis

The seven sensor variables were kriged onto the 24 soil sample locations, using the same process described above, and joined to the laboratory soil data. Generalised linear regression (GLM) was performed in the *R* statistical package using the sensor variables as predictors of pH and clay content in the topsoil and subsoil fractions, and CEC in the topsoil fraction. Although with seven independent variables there are 127 possible regression equations, regression models were confined to (a) EC_{ah}, (b) TC, (c) elevation, (d) TC + EC_{ah}, (e) TC + EC_{ah} + elevation, and (f) a stepwise linear regression (SLR) which initially included all seven variables. This approach enabled a comparison of the accuracy of prediction using the individual data sources as well as selected combinations of data sources. The EC_{ah} variate was preferred to EC_{av} as it corresponded to the depth of soil sampling. TC was selected as a value that integrated all information in the γ spectra. The accuracy of prediction was determined using leave-one-out cross-validation (LOOCV). The observed and predicted values from the LOOCV were used to calculate the coefficient of determination, Lin's concordance coefficient (ρ_c) (Lin, 1989), and the root mean squared error (RMSE). For the stepwise linear regression, all the data were initially included and a mixed (forward and backward) approach was applied to eliminate correlated predictors. The remaining predictors (noted in Table 33.1) were then used in the LOOCV. The SLR and LOOCV analyses were also performed in the statistical package *R*.

33.3 Results and Discussion

The interpolated maps for three of the sensor outputs are shown in Plate 33.1. The total count (GRS320) and EC_{ah} (EM38DD) show some similarities in pattern but also some differences. The results from the LOOCV analysis are given in Table 33.1.

33.3.1 Comparison of the Usefulness of Individual Sensors

In general, the elevation data provided poor predictions of both topsoil and subsoil properties and, as an individual sensor in this locale, were inferior to the gamma radiometer and EMI instruments. Poor fits for topsoil pH were found with all three of the individual sensors, with the gamma radiometrics providing the best fit ($R^2 = 0.21$), but this cannot be considered satisfactory for any topsoil pH mapping or management application. The gamma radiometrics data provided the best fits (R^2 , ρ_c , and RMSE) for topsoil clay percent and CEC. The gamma radiometric model explained 70% of the variance in the topsoil clay data compared to 55% by the EC_{ah} model. Neither model showed either a scale or a location shift as evidenced by the similarity between R^2 and ρ_c . For topsoil CEC, the gamma radiometric model was far superior to the EC_{ah} model (R^2 of 0.48 and 0.09, respectively). It appears that the gamma radiometric data may have some relevance in mapping and managing general soil fertility. For the three topsoil parameters investigated here, the gamma radiometrics provided the best predictions (although the usefulness of the pH model is questionable).

Table 33.1 Coefficient of determination (R^2), Lin's concordance coefficient (ρ_c), and root mean squared error (RMSE) from the leave-one-out cross-validation using single-sensor output and combinations of multiple sensors for three topsoil and two subsoil properties. Topsoil properties are derived from 24 observations, subsoil pH from 23 observations, and subsoil clay percent from 22 observations. Bracketed values for the subsoil clay percent include an outlier ($n = 23$). Stepwise regression equations are indicated at the bottom of the table

Predictors							
Soil property	Statistics	EC _{ah}	Total count (gamma)	Elevation	Total count and EC _{ah}	Total count, EC _{ah} , and elevation	Stepwise linear regression
Topsoil clay %	R^2	0.55	0.70	0.17	0.82	0.80	0.78 ^a
Subsoil clay %	R^2	0.68 (0.29)	0.31 (0.25)	0.00 (0.00)	0.60 (0.27)	0.50 (0.22)	0.25 (0.10) ^b
Topsoil pH	R^2	0.26	0.20	0.00	0.27	0.23	0.15 ^c
Subsoil pH	R^2	0.26	0.05	0.64	0.21	0.20	0.52 ^d
Topsoil CEC	R^2	0.09	0.48	0.03	0.45	0.53	0.38 ^e
Topsoil clay %	ρ_c	0.52	0.68	0.12	0.81	0.79	0.78
Subsoil clay %	ρ_c	0.47 (0.27)	0.23 (0.19)	0.00 (0.00)	0.43 (0.25)	0.36 (0.21)	0.18 (0.09)
Topsoil pH	ρ_c	0.21	0.14	0.00	0.23	0.20	0.14
Subsoil pH	ρ_c	0.20	0.03	0.04	0.17	0.17	0.52
Topsoil CEC	ρ_c	0.07	0.45	0.01	0.42	0.51	0.37

Table 33.1 (continued)

Predictors						Stepwise linear regression
Soil property	Statistics	EC _{ah}	Total count (gamma)	Elevation	Total count and EC _{ah}	Total count, EC _{ah} , and elevation
Topsoil clay %	RMSE	4.33	3.56	5.93	2.76	2.88
Subsoil clay %	RMSE	6.84 (9.04)	8.93 (9.14)	11.10 (11.00)	7.26 (9.29)	7.84 (9.73)
Topsoil pH	RMSE	0.34	0.35	0.41	0.34	0.35
Subsoil pH	RMSE	0.41	0.47	0.53	0.43	0.44
Topsoil CEC	RMSE	4.65	3.42	5.01	3.56	3.29
						3.94

^aTopsoil clay ~ em38v + gammaU + gammaTh

^bSubsoil clay ~ em38v + gammaK + gammaTC + gammaU + gammaTh

^cTopsoil pH ~ em38h + gammaTC + gammaU + gammaTh

^dSubsoil pH ~ em38h + em38v + gammaK + gammaTC + gammaU + gammaTh + elev

^eTopsoil CEC ~ gammaTC + elev

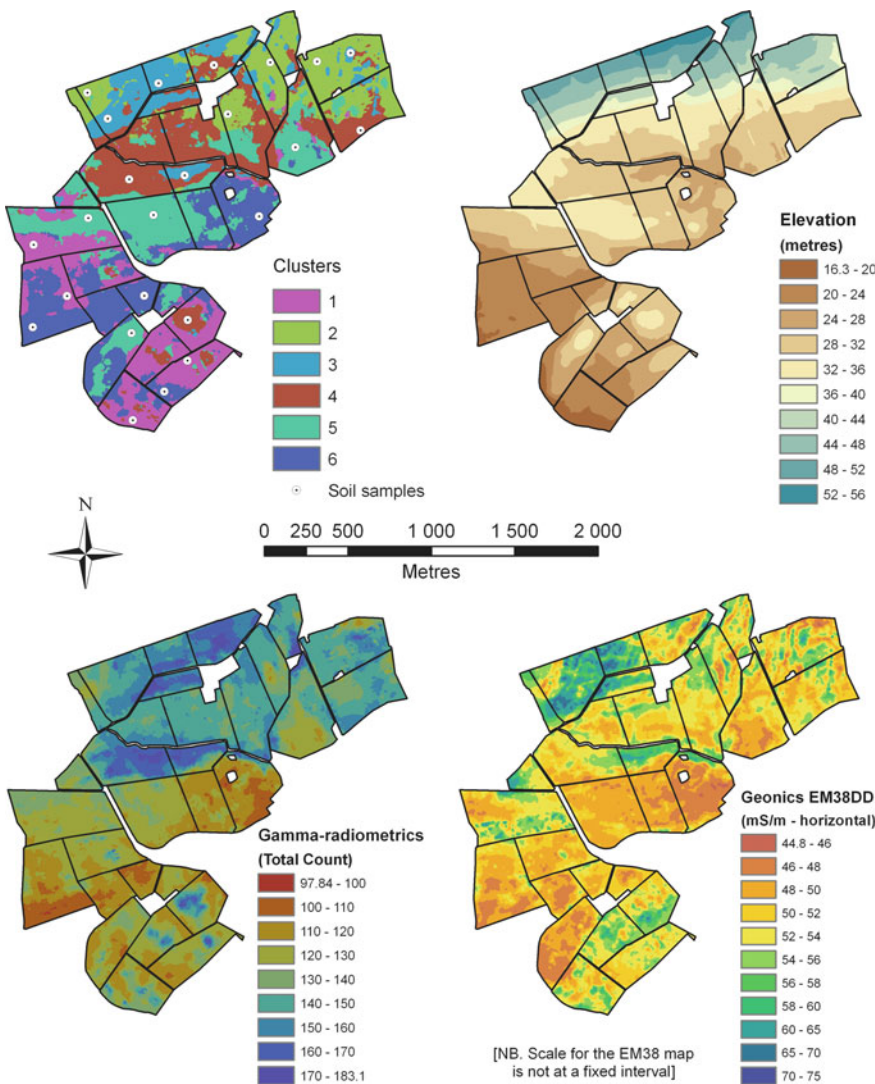


Plate 33.1 Maps of sensor output for the Stenton property. *Top left:* Clusters (6) and final soil-sampling locations; *top right:* elevation from the Omnistar HP GPS; *bottom left:* total count from the GRS320; *bottom right:* EC_ah from the EM38DD

For subsoil clay content, the EM38DD initially performed only marginally better than the gamma radiometrics (data in parentheses in Table 33.1). A closer investigation of the data revealed an extreme outlier (high subsoil clay percent) in the data. When this was omitted and the models rerun, the EM38DD (EC_ah) provided a much better fit and RMSE than did the gamma radiometrics. This latter result, and the results from the topsoil analysis, is not surprising, given the physics associated

with the depth of penetration of the two sensors. The elevation data again performed poorly in predicting subsoil clay content. Elevation data did provide the best R^2 fit for subsoil pH; however, this is a false fit, the result of chance and a severe scale shift. The true worth of the elevation model is indicated by the ρ_c value of 0.04.

33.3.2 Multi-sensors vs. Single Sensor

Multivariate models improved the prediction of topsoil clay content. There was little or no benefit in using multivariate models for predicting topsoil CEC or pH. In contrast, the stepwise multivariate model for subsoil pH was a significant improvement ($R^2 = 0.52$) on the individual sensor models, and the results appear to be robust ($\rho_c = 0.52$). This reasonable fit for subsoil pH comes despite poor fits for the three individual sensor models. The SLR model for subsoil pH retained all seven available variables in the model. The multivariate subsoil clay content models did not provide any improvement over the EC_ah model. The SLR models for both the topsoil and the subsoil clay contents selected the EC_av, U, and Th data. The subsoil SLR clay content model also included the other two gamma radiometric ROIs (TC and K). The reason for the 'step' model selecting the deeper penetrating EM38v data as a predictor (instead of the EC_ah data used in the expert-defined models) is unclear. Regardless, the EC_ah model provided better predictions than did the multi-sensor models for subsoil clay content.

33.3.3 Discussion

For potato production, the texture of the topsoil (0–30 cm) is particularly important for crop management and tuber development. In this context, for a single-sensor system the GRS320 (gamma radiometrics) may provide more useful information for the grower. It also provides a better indication of the fertility (CEC) of the soil. The gamma radiometer should exhibit a higher sensitivity to parent material and mineralogy than the EMI instrument, so this result is not unexpected although the translation of this response into improved model fits is welcome. The flip side to this is the inferior fit of the gamma radiometer data to the subsoil properties. For mapping subsoil properties, the deeper penetrating EMI instrument is better. The advantages of a shallower sensing EMI system for mapping topsoil texture (clay content) were not available for analysis in this study. It may be practical and more effective to run the dual-dipole EM38DD at an elevated height above the ground, for example at 0.5 m, so that the horizontal dipole maps the topsoil (0–0.5 m) and the vertical dipole the vadose zone (0–1.5 m).

A primary objective of the study was to investigate the ability of different individual and multi-sensor systems to map pH at a farm scale. With the exception of the SLR model of subsoil pH, none of the models provided useful information on soil pH. Mapping pH at the farm scale may be optimistic, given the differences in crop rotations, lime treatments, and management history between fields. It appears

that ground truthing the sensor output for pH needs to be done within field or management units. Thus a more intensive sampling strategy is needed for pH than for texture mapping. The significance of the moderate model fit for subsoil pH using all the available predictors is unclear. It may be an anomaly, although the ρ_c value does not indicate this. The subsoil pH may be more temporally stable than the topsoil pH and less influenced by management; however, further investigations are needed to validate and understand this response.

33.3.4 Other Considerations

This short investigation has focused only on a few soil properties. Many more, particularly chemical properties, were measured and will be investigated in future work. The GRS320 output has been analysed only as ROI data. Recent work by Viscarra Rossel et al. (2007) has shown that analysis of the full spectra, after appropriate data preparation, can improve prediction over the use of the ROIs. A partial least squares analysis of the spectral data is the next step in the data analysis to determine the fit of the GRS320 spectra relative to, and in combination with, the EM38DD data.

An appropriate model of the value of improved fits and RMSE is also required to determine if the cost of additional data collection and analysis is offset by the value of the information gained. That is, how profitable is a management decision made with the data? This model will vary with different cropping systems and between cropping regions.

As indicated before, the lack of fit between the sensor data and soil pH data is of some concern, given the desire for Soilessentials Ltd to use the information for variable lime application. The prediction of pH data may need more parameters, such as management history or other soil measurements. Zoning using different combinations of sensor data may be an alternative way of identifying differences within and across fields that may assist with differential management. This approach has not yet been tried with this dataset, but has been used in other studies to identify soil differences (Taylor et al., 2007).

33.4 Conclusions

Better predictions of topsoil clay content and topsoil CEC, an indicator of soil fertility, would indicate that the GRS320 may provide more relevant information for potato producers in this region of Scotland. However, combining the GRS320 with output from the EM38DD improved fits for texture over the single-sensor approach. The value of this extra information needs to be assessed in economic terms against the additional costs associated with data collection. Neither sensor, nor any combination of sensor data, provided good fits to the pH data at the farm scale.

Acknowledgements The authors would like to acknowledge the support of Roy Watson and Robert Ramsey at Soilessentials Ltd.

References

Abdu H, Robinson DA, Jones SB (2007) Comparing bulk soil electrical conductivity determination using the DualEM-1S and EM38-DD electromagnetic induction instruments. *Soil Sci Soc Am J* 71:189–196

Lin LI-K (1989) A concordance correlation coefficient to evaluate reproducibility. *Biometrics* 45:255–268

McKenzie DC (2000) Soil survey options prior to vineyard design. *Austr Grapegrower Winemaker* 438a:144–151

Minasny B, McBratney AB, Whelan BM (2005) VESPER version 1.62. Australian Centre for Precision Agriculture. The University of Sydney, NSW 2006. <http://www.usyd.edu.au/su/agric/acpa>

Taylor JA, McBratney AB, Whelan BM (2007) Establishing management classes for broadacre grain production. *Agron J* 99:1366–1376

Viscarra Rossel RA, Taylor HJ, McBratney AB (2007) Multivariate calibration of hyperspectral γ -ray energy spectra for proximal soil sensing. *Eur J Soil Sci* 58:343–353

Chapter 34

Spatial Variability and Pattern of Selected Properties of Agricultural Soils in the Czech Republic Measured by Indirect Proximal and Remote Sensing

M. Kroulik, J. Kumhalova, Z. Kviz, M. Zlinsky, M. Mimra, and V. Prosek

Abstract Spatial and temporal variabilities of soil properties were monitored within a 12-ha field over several consecutive years. Particle-size distribution, total carbon content (Ct), and pH were monitored. Soil samples were taken from points on a regular square grid. Additionally, the variability of soil properties was evaluated by proximal measurement methods including draft force measurements, soil electrical conductivity (EC_a), and crop yield mapping. Remotely sensed bare-soil satellite images were obtained and digital elevation models were made. All the observed variables showed spatial variability, but the spatial patterns of Ct, pH, EC, and crop yield were temporally stable. Results were processed using statistical and geostatistical methods. Variograms and their parameters were used to describe spatial dependencies between observed variables. Significant dependencies were observed between monitored soil properties and indirect methods, indicating utility in the proximal approach.

Keywords Draft force · EC_a · Crop yield · Flow accumulation · Soil properties

34.1 Introduction

The cost of sampling soil at a sufficient number of points to create maps of soil properties is still a limiting factor holding back the commercial expansion of precision agriculture. Soil is one of the most variable environmental media (Kolar and Kuzel, 1998), and to accurately describe spatial dependencies, a sufficient density of field sampling points is necessary. Grid-based soil sampling procedures are commonly used, but this approach is often not suitable for evaluating spatial relationships between observed variables (Basso et al., 2003). It seems desirable to

M. Kroulik (✉)

Department of Agricultural Machines, Czech University of Life Sciences, CZ-16521, Prague 6 – Suchdol, Czech Republic
e-mail: kroulik@tf.czu.cz

replace these high-intensive and time-consuming methods with quicker and more accurate monitoring methods (Hanquet et al., 2004). Cheap measurement methods that are able to provide high data densities and accurate results are therefore under intense development and are the subject of this book.

It is possible to monitor soil properties by means of current methods such as soil conductivity measurement, remote sensing (or aerial photos), and radiometry in different parts of the spectrum (see Chapter 2). In this way, site-specific application of fertiliser (and other components necessary for good plant growth) can be achieved using maps of soil properties and crop yield. Many economic methods of evaluating soil variability based on very simple measurement principles are available, and there is a real opportunity for the automation of these processes (Godwin and Miller, 2003; see also Chapter 26).

34.2 Materials and Methods

34.2.1 Experimental Field Description

Variability measurements of soil properties (from soil sampling) and indirect proximal and remote measuring methods (using methods to be described below) were performed on a 12-ha experimental field in Prague-Ruzyne, Czech Republic ($50^{\circ}05' N$, $14^{\circ}18' E$). The soil was a Haplic Luvisol (IUSS Working Group WRB, 2007), and its altitude ranged from 338 to 357 m a.m.s.l. Annual precipitation was 526 mm and average temperature was $7.9^{\circ}C$.

34.2.2 Soil Sampling and Soil Property Determination

Variability of soil properties was monitored annually in this experimental field beginning from 2002. Total carbon content (Ct), particle-size distribution, and pH were sampled at 70 locations by a global positioning system (GPS) on a regular 40-m \times 40-m grid over a depth range of 0–30 cm.

34.2.3 Proximal and Remote Measurement Methods

Soil variability was also studied by means of soil electric conductivity (EC_a) (in 2002, 2004, and 2005) and draft force measurements (2003, 2005, and 2007). For EC_a measurement, a contact method was used in which a measuring frame holding six electrodes was pulled by a tractor over the entire area of the field. Every 5s the output from the conductivity meter was recorded simultaneously with GPS position in a measuring unit on the tractor.

Draft force measurement was carried out by means of a measuring frame carrying one shovel and the force exerted on the shovel was measured using a dynamometer. The dynamometer output was also recorded simultaneously with the GPS position.

In 1 year, 2007, the draft force measurement was carried out with Fendt 933 Vario tractor with an electro-hydraulically controlled hitch, an arrangement that meant it was possible to record data from the hitch sensors simultaneously with the dynamometric measurement. In this way, two sets of draft force data could be obtained.

Crop yield variability was observed for two consecutive years in the same field. Winter wheat was grown in the field in 2002 and malting barley in 2003. A combine harvester, equipped with a crop yield monitor, was used for harvesting planted crops.

Digital panchromatic and multispectral pictures with spatial resolutions of 0.5 m (for the former) and 2.4 m (for the latter) were taken on 15 February 2002 by the QuickBird satellite. The pictures were first taken when the soil was bare (no crop in the field). Unsupervised classification for colour detection was used, in which darker colours were given a smaller index.

The topographical data were saved on a PCMCIA memory card on the combine harvester. Initially, a digital elevation model (DEM) was created from the point shapefile, specifically from the elevation data. This elevation model was further used to create a flow direction model and finally for a flow accumulation model. The flow accumulation model gives a map of accumulated flow to a particular cell. Detailed methodology can be found in Jenson and Domingue (1988).

34.2.4 Data Evaluation, Statistical, and Geostatistical Analyses

Values of draft force, conductivity, crop yield, colour index, and flow accumulation were collected from established sampling points only, and their mean values were calculated. Spatial interdependencies of monitored variables were also calculated and compared. Besides basic statistical outputs, the evaluation procedure also produced a Pearson product moment correlation coefficient.

All the data were standardised to zero mean and unit variance. To explore spatial relationships, experimental variograms were estimated. These variograms were fitted by model variograms and ordinary kriging interpolation was applied. Spatial cross-dependence was studied by means of cross-variograms for pairs of measured variables. The software used was ArcGIS 9.1 and GS + 5.1.1. The satellite picture was obtained from QuickBird Digital Globe (distributed by Eurimage/ARCDATA PRAHA, s.r.o.).

34.3 Results and Discussion

To evaluate temporal stability, observations of soil properties and crop yield were made in the same field over several years. The measurements were essentially stable, especially for C_t and pH which showed only small changes between the years. Statistically significant dependence ($p < 0.01$) was observed for the values of C_t ($r = 0.75–0.91$) and pH ($r = 0.81–0.98$).

Correlation analysis also showed a significant ($p < 0.01$) temporal stability for soil conductivity; however, the correlation coefficients in this case were rather low ($r = 0.39\text{--}0.63$).

By way of contrast, draft force values were not temporally stable, although a significant correlation existed between the draft force measured by a dynamometer and the draft force measured by the electro-hydraulic hitch ($r = 0.84$).

The crop yield values were temporally stable, showing a statistically significant ($p < 0.01$) r value of 0.34 between the years.

In cases where temporal stability was observed, average values were calculated (Table 34.1). The datasets were characterised by a range (expressed as minimum and maximum values) and by a coefficient of variation (CV), which showed a particular variability. The relationship between the tested pairs of variables was studied by means of correlation analysis. The correlation coefficients showing the dependence between the datasets are given in Table 34.2. The correlation coefficients show the relationships between soil properties and indirect measurement methods.

34.3.1 Geostatistical Analysis

In all cases, experimental variograms were fitted by a spherical model with nugget. The details of these isotropic variograms are given in Table 34.3.

According to some authors (Cambardella and Karlen, 1999; Lopez-Granados et al., 2002) it is possible to divide the spatial dependence pattern into three groups based on the nugget C_0 and sill variance ($C_0 + C$). A value of $C_0/C_0 + C$ less than 25% indicates a strong spatial relationship between Ct, pH/H₂O, EC, crop yield, particle-size distribution, and the colour index of the digital image. The values of pH/KCl, flow accumulation, and draft force showed a medium strong spatial dependence ($C_0/C_0 + C$ of 25–75%). Higher values of $C_0/C_0 + C$ could be explained (in the case of draft force) by the micro-variability of soil properties. A high nugget value for the draft force measurement underlines this finding.

The spatial relationship between variables measured over the sampling grids is also demonstrated by the variogram range (A_0), the distance at which the semivariance reaches the sill value.

Selected maps obtained from ordinary kriging using the isotropic variograms are presented in Fig. 34.1. Visual inspection of these maps shows that many of the variables returned high values mostly at the southern and south-western parts of the field. In some cases, the maps are remarkably similar.

Because spatial cross-variability can give good insight into soil variation at the field scale, experimental cross-variograms for all pairs of variables were calculated and fitted with spherical models (Fig. 34.2) wherever possible (i.e. wherever a defined structure could be identified and there was a significant correlation). No defined structure was found for the pairs of variables involving particle-size distribution (coarse sand), pH KCl with draft force 2005(a), pH H₂O with colour index, and draft force 2005(a) with flow accumulation. (Relationships between pH KCl and pH

Table 34.1 Summary statistics of the variables. Average values of C_t , pH, EC_a , and crop yield were used. (a) Draft force measured by the measuring frame; (b) draft force measured by the electro-hydraulically controlled hitch

Ct (mg C/g)	pH/ KCl H ₂ O	pH/ H ₂ O	Particle-size distribution (%)	Draft force (kN).				EC _a (mS m ⁻¹)	Crop yield, t ha ⁻¹ (wetness 0.14 g/g)	Flow accumulation	Colour index
				Clay and fine silt <0.01 mm	Silt 0.01– 0.05 mm	Fine sand 0.25 mm	Coarse sand 0.25–2 mm				
Mean	1.36	7.21	7.77	38.26	28.53	20.51	12.71	2.99	3.66	4.19	22.94
Median	1.37	7.28	7.83	38.95	28.85	18.55	12.50	2.98	3.68	4.08	23.04
SD	0.13	0.17	0.17	4.09	7.26	5.78	2.96	0.24	0.24	0.72	1.60
Variance	0.02	0.03	0.03	1.672	52.77	33.35	8.76	0.06	0.06	0.52	2.57
Skew	-0.34	-1.35	-1.26	-0.46	-0.29	0.61	1.07	0.62	0.47	17.26	7.00
CV (%)	9.65	2.34	2.16	1.69	25.47	28.16	23.29	7.85	6.61	0.83	0.79
Minimum	1.04	6.71	7.29	30.20	10.60	10.10	8.30	2.47	3.12	2.87	19.97
Maximum	1.59	7.42	7.97	46.30	43.10	32.30	20.80	3.80	4.35	6.50	28.26
Sample	70	70	70	28	28	28	28	70	70	70	70

Table 34.2 Correlation matrix between values

Particle-size distribution															
1	2	3	4	5	6	7	8	9	10	11	12	13	14	15	
1	0.39	1													
2	0.96	1													
3	0.52	1													
4	0.00	0.03	0.07												
5	0.57	0.22	<u>0.34</u>												
6	-0.54	<u>-0.31</u>	-0.45	-0.37	-0.80	1									
7	-0.36	<u>0.02</u>	<u>-0.06</u>	-0.26	-0.67	0.51	1								
8	<u>0.21</u>	0.08	0.05	<u>-0.10</u>	0.24	<u>-0.22</u>	<u>-0.04</u>								
9	<u>0.24</u>	0.39	0.41	0.24	0.26	-0.44	<u>-0.11</u>	1							
10	0.15	0.17	-0.25	0.28	-0.12	-0.10	0.09	0.01	1						
11	<u>0.24</u>	<u>0.23</u>	<u>0.26</u>	<u>-0.33</u>	<u>0.33</u>	<u>-0.18</u>	<u>-0.01</u>	<u>0.17</u>	0.84	1					
12	<u>0.27</u>	<u>0.22</u>	<u>0.23</u>	<u>0.03</u>	0.51	-0.50	<u>-0.31</u>	0.33	<u>0.14</u>	<u>0.10</u>	<u>0.12</u>	1			
13	0.39	-0.12	<u>-0.01</u>	0.13	0.38	-0.48	<u>-0.14</u>	<u>-0.02</u>	<u>-0.01</u>	<u>-0.19</u>	<u>-0.16</u>	0.43	1		
14	0.24	-0.17	-0.06	0.13	0.13	-0.23	-0.05	-0.10	-0.14	-0.34	<u>-0.23</u>	<u>0.19</u>	0.63	1	
15	-0.57	-0.20	-0.36	-0.07	-0.49	0.54	0.15	-0.03	-0.09	0.18	0.04	-0.35	-0.64	-0.57	1

Underlined, significant dependence at 90% confidence level; *bold italic*, significant dependence at 95% confidence level; *bold*, significant dependence at 99% confidence level

Colour index (15)

Flow accumulation (14)

Crop yield (14% wet) (13)

EC (12)

Draft force 2007 (11)

Draft force 2007 (10)

Draft force 2005 (9)

Draft force 2003 (8)

Fine sand

Coarse sand

Clay and Fine silt

pH/H₂O (3)

pH/KCl (2)

Ct (1)

Table 34.3 Parameters of the variogram model. (a) Draft force measured by measuring frame; (b) draft force measured by electro-hydraulically controlled nichich (values standardised to zero mean and unit variance)

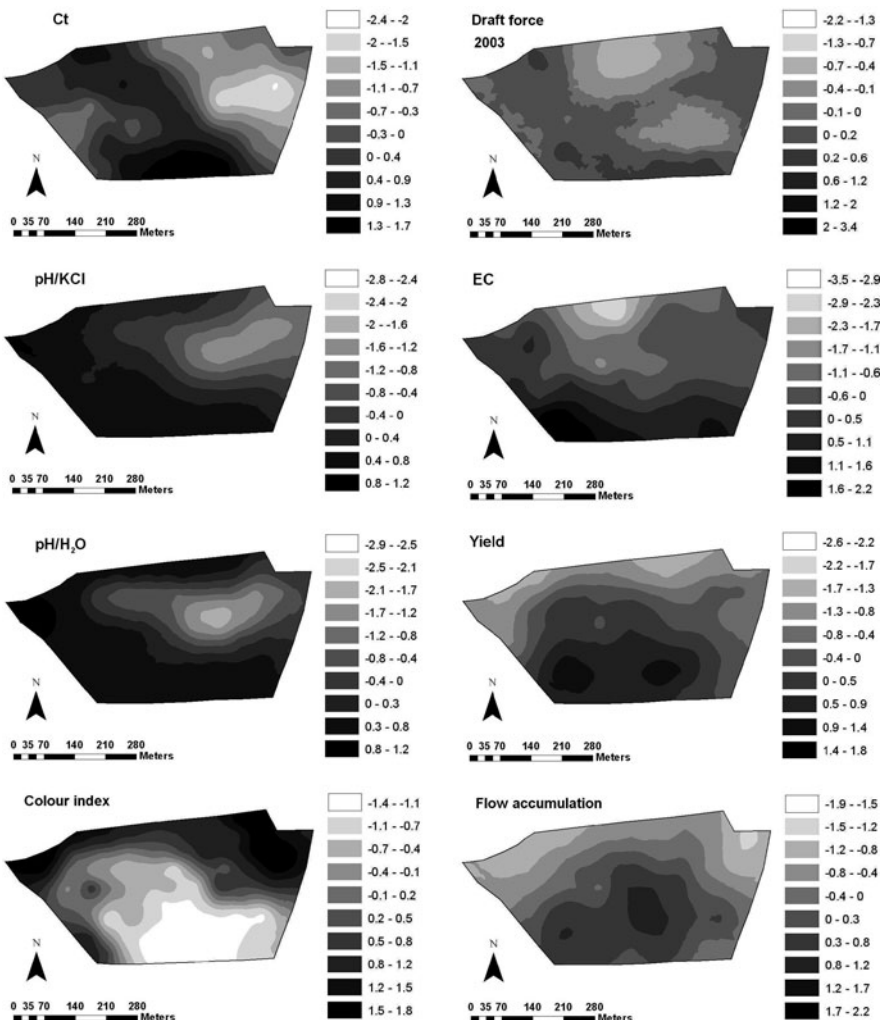


Fig. 34.1 Selected maps of kriged estimates (values standardised to zero mean and unit variance)

H₂O and draft force 2007(a) and draft force 2007(b) were not calculated because dependence was of course expected.) Selected cross-variograms are presented in Fig. 34.2.

In Table 34.4, the structural correlation coefficients of spherical variogram components ρ_{uv} , computed on the basis of following formula (Boruvka and Kozak, 2001), are presented:

$$\rho_{uv} = \frac{b_{uv}}{\sqrt{b_{uu}b_{vv}}},$$

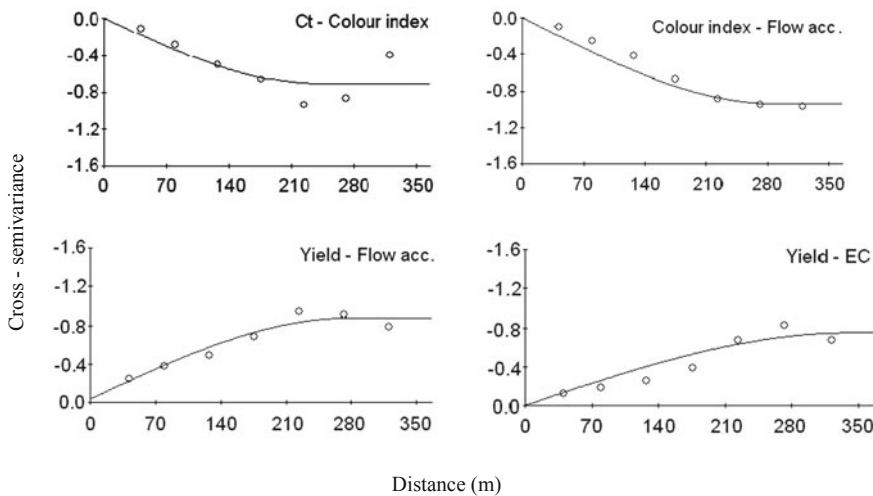


Fig. 34.2 Selected cross-variograms of variables

where b_{uu} , b_{vv} , and b_{uv} are the coefficients of structural components of the variogram and cross-variogram of two observed variables.

Except for pairs of variables involving draft force, all the calculated structural correlation coefficients were higher than, or at least equal to, the correlation coefficient given in Table 34.2. This means that a large part of the relationship between the variables was spatially based.

34.3.2 Discussion

Proximal and remote measuring methods will play an increasingly important role in the development of precision agriculture systems. The high density of the data measured, time and cost efficiencies, and routine measurement methods are vital factors in making precision agriculture a common practice. An important outcome from our work is that crop yield depends strongly on flow accumulation. According to Reuter et al. (2005), topography influences the textural, physical, and chemical properties of the soil. Marques da Silva and Alexandre (2005) also conclude that soil and topographic attributes can affect crop yield and its variability.

Topographical data, in combination with soil information, are key parameters that can explain much crop yield variability at the field scale. Topographical information can be especially helpful in managing and delineating sites where crop yields are sensitive to extreme weather conditions (Kravchenko and Bullock, 2000).

Kumhalova et al. (2008) found that the relation between crop yield and topography (elevation, slope, and flow accumulation) was stronger in dry years. From visual and statistical comparisons of maps of flow accumulation and crop yield, they

Table 34.4 Structural correlation coefficients of the spherical variogram components

showed that yield depended more on flow accumulation and field water redistribution in dry years than it did in wet years. They concluded from their experiments that the flow accumulation layer could be used for delineating certain management zones, although the dependence of crop yield on flow accumulation can vary from year to year, and is affected by weather conditions. In our work, we also found a strong spatial correlation between flow accumulation and colour index. Interestingly, we also found that draft force showed a negative correlation with flow accumulation – in 2007 at least – so that wet soils were weaker.

Data from soil sensors have the potential to be widely used in precision agriculture. In particular, measures of soil conductivity are a powerful handle for describing soil properties (Zhang et al., 2002; Godwin and Miller, 2003; see also Chapters 19 and 22). Soil EC_a measurements also offer a simple and cheap way for determining soil variability in the field, since soil electrical conductivity is affected in particular by soil wetness and texture (Godwin and Miller, 2003; see also Chapter 21). In addition, our results indicate relationships between EC_a and particle-size distribution, crop yield, draft force (2003), colour index, Ct, and pH.

Remote sensing is a quick way of acquiring important and detailed information about soil variability within a field. In our experience, information from the satellite image of the bare soil was of high value (see Chapter 14). Except for draft force, clay and fine silt content, coarse sand, and pH/KCl, significant correlations with the satellite image of the bare soil were found in all cases.

Knowledge of the draft force exerted during soil cultivation might be a useful tool. Results could be used for comparing energy consumption, checking machine performance, optimising settings, and assessing certain agro-technical interventions (see Chapter 30). As described by Kürsteiner (2003), measuring the force at the tractor tree-point hitch is usually carried out using a measuring frame inserted between the tractor and the attached machine. Working with such a frame can be difficult. Besides experimental frame, measurements can also be obtained from the serial stepped power pins which are normally used in the tractor for electronic hitch regulation (Schutte and Kutzbach, 2003). In our view, mapping soil properties during cultivation is an easy and natural step from monitoring the draft force of soil cultivation implements (Rothmund et al., 2003).

Figure 34.3 illustrates relationship between output tension values on the power pins (tensiometric gauges) and the draft force value for three different heights L (Fendt 933 Vario tractor). A linear correlation between the output tension and the draft force was evident, and the coefficient of determination (R^2) for the entire dataset ($n = 58$) was 0.99. Note how the slopes of the straight lines were influenced by hitch position.

Our measurements illustrate how modern electronic tractor components can be used for draft force measurement. At the same time, it must be acknowledged that draft force is influenced by many factors. Godwin and Miller (2003) noted deficiencies and disadvantages connected with the practical application of such measurements, pointing to the large number of factors that could influence measurements. For example, heavy agriculture machinery often crisscrosses a field, sometimes regularly, sometimes randomly. The repeated tracks compact the soil,

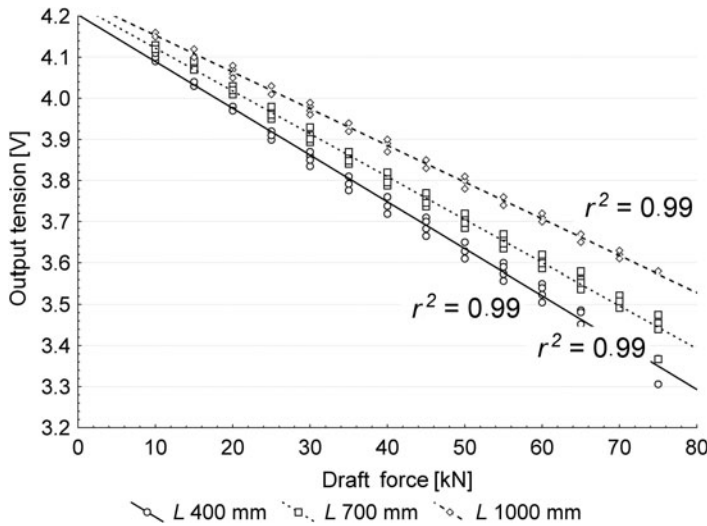


Fig. 34.3 Output tension values on the power pins related to the draft force value for three different heights L (tractor: Fendt 933 Vario)

and it suffers more or less irreversible structural changes. In this context, our measurements show that, as a result of conventional tillage, 96% of the total field area was run over with a machine at least once a year; this figure should be compared with values of 65 and 43% of the total field area when using conservation tillage and direct seeding, respectively. We calculate that 144% of the area covered was run over repeatedly for conventional tillage, 31% for conservation tillage, and only 9% for direct seeding. To a degree, this fact might explain the variability of the measured values and the low repeatability of the draft force values between years.

34.4 Conclusions

We have demonstrated certain advantages of using indirect (both proximal and remote sensing) methods for evaluating soil property variability. We have also demonstrated the potential of implementing them into precision farming systems. Correlation analysis applied to our measurements showed significant dependencies between observed variables. A high-resolution satellite image of bare soil gave remarkably good correlations with C_t , crop yield, EC_a , flow accumulation, and silt and fine sand content. EC_a showed a dependency on soil properties, and a correlation between crop yield and the satellite imagery was observed. Many factors can affect the proximal measurement methods, as was demonstrated in the case of our draft force measurements. The correlation coefficients between draft force and other observed variables fluctuated when datasets from different years were compared.

It is not possible to generalise our results completely. However, on the basis of our measurements, indirect measurement methods appear to have potential for

practical agricultural use. Temporal stability of Ct, pH, crop yield, and EC_a values suggests to us that periodic sampling is not necessary. Indirect measurement methods offer a way to simply and quickly describe soil variability; they allow soil properties to be sampled in cases when they cannot be estimated proximally.

Acknowledgement This research was supported by project MSM 604 6070905 and by the Ministry of Agriculture of the Czech Republic, project 0002700601.

References

Basso B, Sartori L, Bertocco M, Oliviero G (2003) Evaluation of variable depth tillage: economic aspects and simulation of long term effects on soil organic matter and soil physical properties. In: Stafford JV, Werner A (eds) Precision agriculture. Wageningen Academic Publisher, Wageningen, Netherlands, pp 61–67

Boruvka L, Kozak J (2001) Geostatistical investigation of a reclaimed dumpsite soil with emphasis on aluminum. *Soil Tillage Res* 59:3–4, 115–126

Cambardella CA, Karlen DL (1999) Spatial analysis of soil fertility parameters. *Precis Agric* 1:5–14

Godwin RJ, Miller PCH (2003) A review of the technologies for mapping within-field variability. *Biosyst Eng* 84:393–407

Hanquet B, Sirjacobs D, Destain MF, Frankinet M, Verbrugge JC (2004) Analysis of soil variability measurement with a soil strength sensor. *Precis Agric* 5:227–246

IUSS Working Group WRB (2007) World reference base for soil resources 2006, first update 2007. World soil resources reports no. 103. FAO, Rome

Jenson SK, Domingue JO (1988) Extracting topographic structure from digital elevation data for geographic information system analysis. *Photogramm Eng Remote Sensing* 54:1593–1600

Kolar L, Kuzel S (1998) Heterogenita pudnich vlastnosti. Final proceedings of the Racionalni pouziti hnojiv. KAVR, CZU Prague, Prague, Czech Republic, pp 76–83 (in Czech)

Kumhalova J, Matejkova S, Fifernova M, Lipavsky J, Kumhala F (2008) Topography impact on nutrition content in soil and yield. *Plant Soil Environ* 54:255–261

Kürsteiner B (2003) Rahmenlose Messung der Dreipunktkräfte am Traktor. Final proceedings of the agricultural engineering 2003. VDI Verlag GmbH, Hannover, Germany, pp 73–78

Kravchenko AN, Bullock DG (2000) Correlation of corn and soybean grain yield with topography and soil properties. *Agron J* 92:75–83

Lopez-Granados F, Jurado-Expósito M, Atenciano S, Garcia-Ferrer A, Sánchez de la Orden M, Garcia-Torres L (2002) Spatial variability of agricultural soil parameters in southern Spain. *Plant Soil* 246:97–105

Marques da Silva JR, Alexandre C (2005) Spatial variability of irrigated corn yield in relation to field topography and soil chemical characteristics. *Precis Agric* 6:453–466

Reuter HI, Kerssebaum KC, Wendroth O (2005) Spatial and temporal variability of soil properties with respect to relief information. In: Stafford JV (ed) Precision agriculture '05. Wageningen Academic Publisher, Wageningen, Netherlands, 433–440

Rothmund M, Zipprich M, Auernhammer H, Demmel M (2003) Zugkraftmessung bei der Bodenbearbeitung als ergänzende Information zur Standortbeschreibung. Final proceedings of the agricultural engineering 2003. VDI Verlag GmbH, Hannover, Germany, 305–310

Schutte B, Kutzbach HD (2003) Evaluierung von ortsspezifischen Zugkraftmessungen bei der Bodenbearbeitung. Final proceedings of the agricultural engineering 2003. VDI Verlag GmbH, Hannover, Germany, 299–304

Zhang N, Wang M, Wang N (2002) Precision agriculture – a worldwide overview. *Comput Electron Agric* 36 113–132

Part VII

Applications

Chapter 35

Inverse Meta-modelling of Yield-Monitor Data for Estimating Soil-Available Water-Holding Capacities at a Farm Resolution of 10 m

M.J. Florin, A.B. McBratney, and B.M. Whelan

Abstract Spatially dense, geo-referenced information is an integral component of precision agriculture (PA) management. Moreover, the value of temporally dense information is gaining recognition. An example of such valuable information is crop yield data. An intuitively appealing response to these information requirements is simulation modelling. In order to meet the temporal density and the spatial extent requirements of PA, simulation modelling is faced with a major challenge: that of capturing yield variation at a spatial resolution relevant to PA. Adequate computer power to run a representative number of simulations ($>1,000$) and suitable information to populate the models are the motivating challenges behind this study. Inverse meta-models were derived from the agricultural production simulator (APSIM) using neural network modelling to predict soil-available water capacity (AWC). Using as many years of yield data as was available for a dryland grain farm in Australia, ‘effective’ AWC maps with a resolution of 10 m were made by averaging maps estimated from different yield years. The AWC values were validated in terms of value for predicting spatially variable yield. The AWC maps were significantly different, depending on the year of yield data used. This demonstrated that the ‘effective’ component of the AWC values contains information about climate interacting with the soil, the crop, and the landscape. The AWC values proved useful for predicting yield using simple linear models ($0.48 < R^2 < 0.80$) rather than using APSIM. A conclusion from this study is that the inverse meta-modelling concept is an efficient way of extracting soil physical information that exists within crop yield maps. Further research attempting to enhance understanding about the ‘effective’ components of the AWC values and to improve the temporal consistence of the AWC values is important. A greater number of AWC scenarios, more years of yield data, and the inclusion of additional information into the meta-models are possible ways forward.

M.J. Florin (✉)

Australian Centre for Precision Agriculture, Faculty of Agriculture, Food and Natural Resources, The University of Sydney, Sydney, NSW, Australia; Plant Production Systems, Wageningen University, Wageningen, The Netherlands
e-mail: madeleine.florin@wur.nl

Keywords Inverse modeling · Meta-modelling · Soil-available water-holding capacity (AWC)

35.1 Introduction

In order to better match inputs with soil and crop requirements (which vary in space and time), site-specific crop management (SSCM) involves management of spatial units that are smaller than fields. Spatially dense, geo-referenced information is an integral component of SSCM.

Yield maps from many years are an example of such information. The use of simulation models can potentially provide a wealth of yield information satisfying both spatial and temporal requirements. Under this scenario, point-based crop growth simulation modelling would allow simulation of as many yield maps as desired across space and time. In order to meet the temporal density and the spatial extent required by PA, this modelling approach is faced with a major challenge: that of capturing yield variation at a spatial resolution relevant to PA. A large obstacle is the ability to obtain a representative number of simulations across an area of interest. Populating the required number of points and the computer power required for the simulations are particularly relevant issues. For these purposes, soil-available water capacity (AWC) is an important soil property that has proven to be difficult to estimate by means of available sensing techniques. Some examples of current research attempting to map soil water are described in this book (Chapters 21 and 32).

There are a number of publications within the PA and simulation modelling literature that address estimation of soil properties for input into simulation models at a resolution relevant to PA. Most of these studies take advantage of high-resolution yield information from a number of years and estimate site-specific soil properties with the inverse use of crop growth simulation models (inverse modelling or parameter optimisation). These studies document a range of different estimation procedures. Timlin et al. (2001) provided an example of this approach. These authors optimised available water-holding capacity across a single field for two separate years with a genetic algorithm that minimised the difference between yields simulated with a water budget/yield model and measured yields. Morgan et al. (2003) demonstrated a contrasting approach by using a forward model to create 'look-up' tables containing yield values as a function of plant-available water for a number of years. These tables were then used to match the 'yield-monitor' yields with plant-available water estimates. Maximum available water estimates were then obtained by averaging across years.

The spatial extent of these examples (a single field) is consistent with other studies in the literature. It would be potentially valuable to populate a point-based simulation model at fine resolution and at a greater spatial extent – for example a whole farm. This demand dramatically increases the number of points to simulate. A consequence is that the computer time and memory to run a point-based crop simulation model in the order of thousands of times is beyond a standard desktop computer.

Meta-modelling provides a possible solution to this computer power challenge. A meta-model is an approximation of a more complex simulation model in terms of transforming model inputs into model outputs (Kleijnen and Sargent, 2000). A clear advantage of using a meta-model rather than the original model is that the meta-model attempts to take only the significant relationships from the system under question and as a consequence input parameters and computing time are reduced.

The data requirements for inverse modelling in the context of high-resolution yield maps, and the computer processing power requirements for meta-modelling, point towards integration of inverse modelling and meta-modelling for estimating site-specific soil properties across farms. This is particularly the case where little detailed soil water information is available. Consequently the aims addressed in this chapter are as follows: (1) to create an inverse meta-model from APSIM to estimate soil hydraulic properties from yield-monitor data; (2) to generate ‘effective’ soil-available, water-capacity (AWC) maps across a whole farm at a spatial resolution of 10 m; and (3) to validate the inversely modelled hydraulic properties with respect to yield prediction.

35.2 Materials and Methods

The method consists of five steps:

- (i) Identifying some key assumptions;
- (ii) Gathering and generating available and necessary soil, crop, and landscape information;
- (iii) Creating inverse meta-models;
- (iv) Inversely estimating AWCs; and
- (v) Validating the estimates.

35.2.1 Key Assumptions

It is assumed that water is the most important limiting factor in the dryland grain-farming system under examination. A substantial amount of literature supports this assumption; for example, Irmak et al. (2002) demonstrated correlations between root-zone plant-available water and soybean yield. A consequence of this assumption was that hydraulic properties were the only model input considered in detail. The only hydraulic property considered was ‘soil-available water capacity’ (AWC) defined by the difference between ‘field capacity’ or the drained upper limit (DUL) and ‘wilting point’ or the lower limit (LL). In terms of model input requirements, previous research has demonstrated relationships between AWC and crop yield within APSIM (Wong and Asseng, 2006). For this study, AWC was assumed to be the same as plant-available water capacity (PAWC) (or extractable water).

35.2.2 Study Site and Available Data

A dryland grain farm, 'Brook Park', located 200 km north of Adelaide in South Australia was chosen for this study. A mean annual rainfall of 345 mm falls mostly during the winter. Soil types distributed across the farm include Planosols, Chernozems, and Durosols (FAO, 1998).

AWC scenarios and daily rainfall were the two main datasets required for creation of an inverse meta-model. The envisaged domain of applicability for the meta-model is all possible rainfall and AWC scenarios that might occur across the study site.

We generated 1,000 different, uniformly distributed AWCs using Latin hypercube sampling (LHS). Uniform distributions of DUL and LL at two depths (depth 1, 0–60 cm; depth 2, 60–90 cm) were generated.

We considered 20 years of rainfall data adequate to include a range of climate scenarios. Daily rainfall data were sourced from the SILO Data Drill (Jeffrey et al., 2001).

Spatially referenced yield information was required for application of the inverse meta-model. Yield-monitor data from seasons between and including 1999 and 2006 were obtained in its interpolated form such that it conformed to its respective section of a whole-farm 10-m grid. Fields were utilised for further study if three or more years of yield data were available.

35.2.3 Creating a Meta-model

APSIM is a point-based model that runs on a daily time step and is capable of yield prediction across areas (Keating et al., 2003). APSIM was run for 20 years of continuous wheat production for each of the 1,000 AWCs. A list of the parameters that were varied for model calibration is presented in Table 35.1.

Table 35.1 APSIM variables used for model calibration

Some APSIM variables	Aspect of crop growth environment described
U and Cona	Evaporation
SWCon	Saturated hydraulic conductivity (sort of)
Diffusivity constant and diffusivity slope	Unsaturated soil water movement
Curve number	Run-off
kl	Root length density and soil diffusivity
xf	Root advancement
Sowing date	Management environment – crop development
Sowing density/row spacing/sowing depth	Management environment – competition for resources
Cultivar	Management environment – crop development

Linear stepwise regression was used to determine which monthly rainfall, along with AWC, best predicted the APSIM yield output. Based on results from the regression, these variables were chosen as input into a neural network model designed to predict AWC and LL at two depths.

35.2.4 Estimating ‘Effective’ Hydraulic Properties

The neural network model was applied across the farm by replacing APSIM yield with yield-monitor yield. For seven fields, at least three different maps of ‘effective’ AWC were obtained. ‘Best’ estimates were then calculated by averaging the AWC derived from multiple years.

35.2.5 Validating ‘Effective’ AWCs

A year of yield data was excluded from the ‘best’ estimate of ‘effective’ hydraulic properties and was then used to validate the inversely modelled hydraulic properties from a yield prediction perspective. Stepwise linear regression was used to predict yield using the mean hydraulic properties and monthly rainfall data. Individual models were derived across the farm for fields that shared the same crop rotations.

35.3 Results and Discussion

The predictors used in the neural network model were APSIM-simulated wheat yield between and including 1979 and 1998, and monthly rainfall from June, July, August, and November. The neural network modelling resulted in an R^2 value of 0.51 for the meta-model.

Figure 35.1 illustrates the relationship between AWC and APSIM yield where the AWC is firstly derived from LHS and secondly from the inverse meta-model. In this figure, different shades of grey represent 20 different years.

There is scope to improve the fit of the meta-model. Some possibilities are to include greater than 1,000 different hydraulic scenarios for derivation of the meta-model and to incorporate some other APSIM parameters such as sowing dates, crop cultivars, and rooting depths.

Figures 35.2 and 35.3 illustrate estimated profile AWC maps that were derived from two individual years of yield data. These two figures demonstrate clearly that there are different relationships between AWC and yield under different climate years.

Figure 35.4 illustrates the ‘best’ estimates of AWC across the farm on a 10-m grid. It is important to note that there are some conceptual differences between these estimates and the actual AWC values across the farm. In the context of these differences, the estimates will be referred to as ‘effective’ AWCs. Firstly,

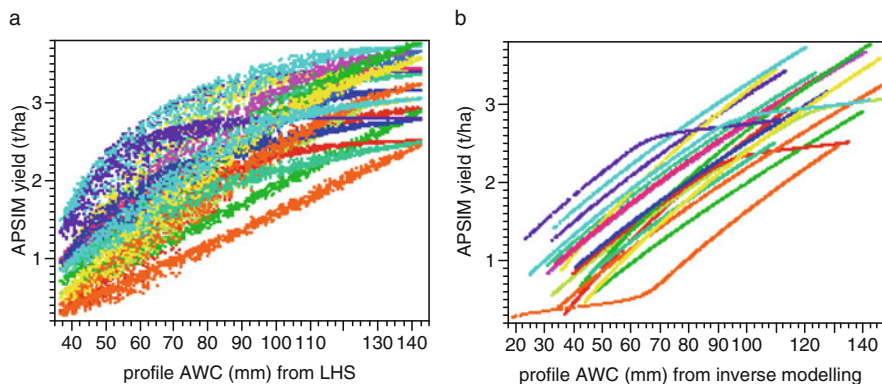


Fig. 35.1 Simulated yield versus profile AWC. (a) APSIM yield–AWC relationship (AWC from LHS); (b) APSIM yield–AWC relationship (AWC from inverse meta-model)

the different estimates between years suggest that the ‘effective’ component of the AWCs contains some information about climatic interactions with the crop, the soil, and the landscape. Some possibilities of additional information within the estimates are root growth, soil depth, soil structure, soil chemical properties, and topography. For example the assumption that root extraction front depths do not vary across space provides a possibility for information included in the ‘effective’ AWCs. The relationship between AWC and yield will necessarily be different if the extraction front depth of crop roots varies, as this soil and crop property impacts the rate at which crop roots can take up water.

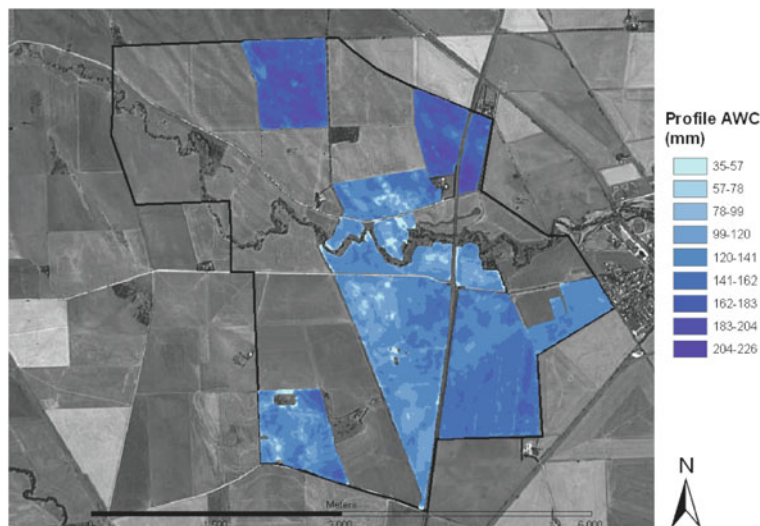


Fig. 35.2 Inversely modelled profile of AWC at 90 cm using 2005 yield data

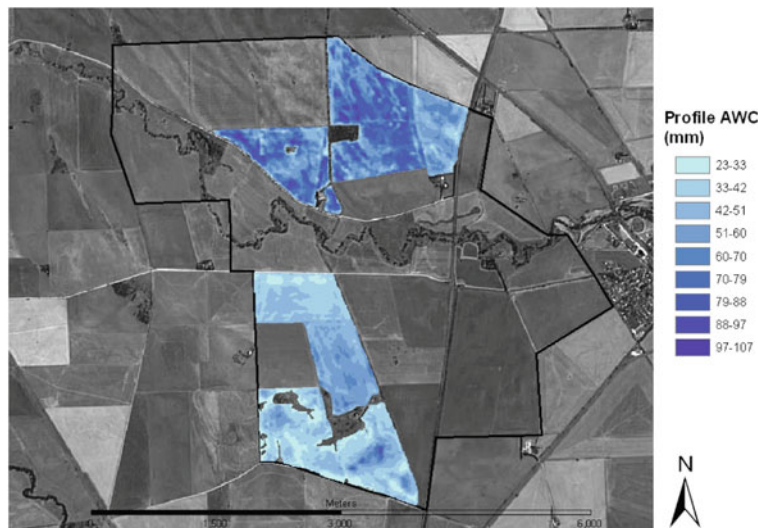


Fig. 35.3 Inversely modelled profile of AWC at 90 cm using 2006 yield data

The results and discussion so far imply that the incorporation of additional APSIM variables into the meta-models could enhance one's understanding about information that resides within the 'effective' AWCs. At this point, the value of the simplicity of the meta-model must be considered. If more parameters are incorporated into the modelling exercise, Ockham's razor would require that an equivalent

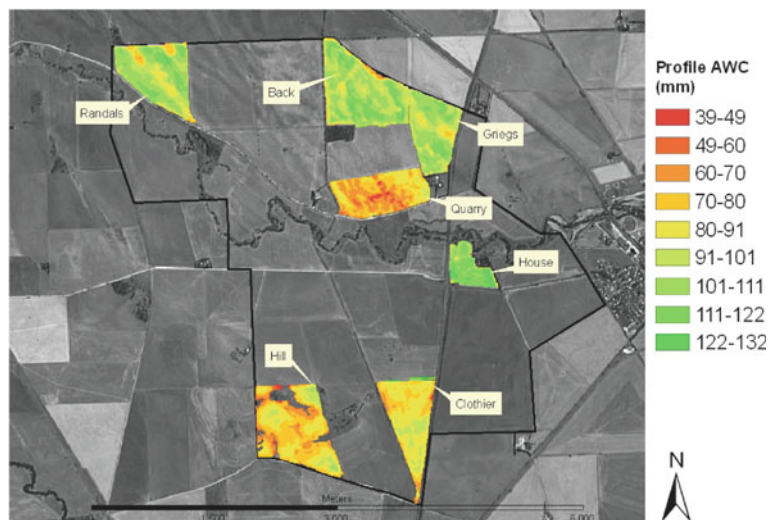


Fig. 35.4 'Best' estimates of profile of AWC at 90 cm based on averages for 3 or 4 years

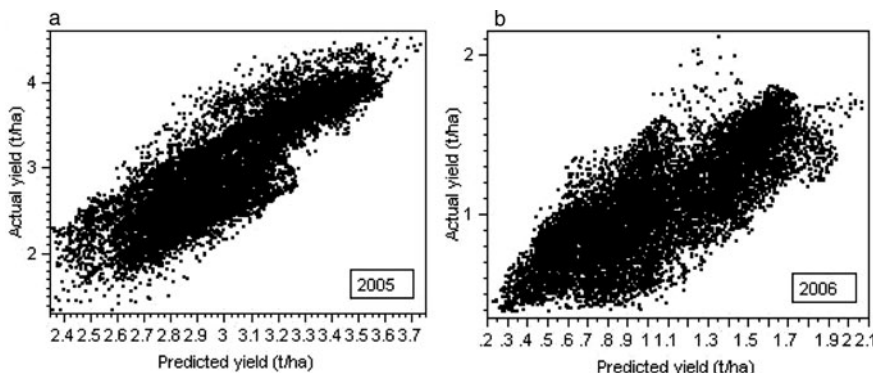


Fig. 35.5 An example of linear yield predictions compared with yield-monitor yields across two fields: (a) 'Griegs' and 'Hill' 2005; (b) 'Griegs' and 'Hill' 2006

gain in information is gained from the model. It is important to strike a balance between the number of parameters, accurate prediction, and the ease of model application.

Figure 35.5 depicts yield-monitor yield versus predicted yield for two separate years using a model that was derived for two of the fields on the farm. For these two fields, the model was based on yield data from 1999, 2002, 2005, and 2006. The R^2 values ranged between 0.48 and 0.80. The model performance varied between fields and between years.

These results suggest that simple yield prediction models are potentially useful as a means to relatively easily predict yield across whole farms. These models also make use of information that has been gained from the inverse modelling exercise, demonstrating the validity of the 'effective' AWC values for this purpose.

35.4 Conclusions

1. Inverse meta-modelling has proven to be very useful in terms of solving the computer power challenge that simulation modelling for PA brings. The inverse model was efficiently applied to a 10-m grid across a farm. It is imperative for future research to address the ability of meta-models to more closely approximate APSIM and other crop growth simulation models.
2. Yield-monitor data provided a source of information about AWC. 'Effective' hydraulic properties across a farm at a resolution of 10 m were extracted from the yield-monitor data using an inverse crop growth simulation model. Further understanding about the 'effective' component of the AWC values is required. It is possible that some additional information such as landscape variables would improve the AWC estimates. Many years of yield data are required to improve and to gain confidence in this process.

3. Value has been gained from the inversely modelled hydraulic properties for yield prediction using simple linear models. This approach could be applied across whole farms under different climate scenarios, resulting in yield information at a spatial and a temporal resolution useful for PA. Model validation with more than 1 year of yield information is required and the amount of variability predicted could be improved.

Acknowledgements The authors would like to acknowledge the Grains Research and Development Corporation for funding this work and Malcolm Sargent for providing his farm as a study site and the yield-monitor data.

References

FAO (1998) World reference base for soil resources. Food and Agriculture Organization of the United Nations, Rome

Irmak A, Batchelor WD, Jones JW, Irmak S, Paz JO, Beck HW, Egeh M (2002) Relationship between plant available soil water and yield for explaining soybean yield variability. *Appl Eng Agric* 18:471–482

Jeffrey SJ, Carter JO, Moodie KB, Beswick AR (2001) Using spatial interpolation to construct a comprehensive archive of Australian climate data. *Environ Model Softw* 16:309–330

Keating BA, Carberry PS, Hammer GL, Probert ME, Robertson MJ, Holzworth D, Huth NI, Hargreaves JNG, Meinke H, Hochman Z, McLean G, Verburg K, Snow V, Dimes JP, Silburn M, Wang E, Brown S, Bristow KL, Asseng S, Chapman S, McCown RL, Freebairn DM, Smith CJ (2003) An overview of APSIM, a model designed for farming systems simulation. *Eur J Agron* 18:267–288

Kleijnen JP, Sargent RJ (2000) A methodology for fitting and validating metamodels in simulation. *Eur J Operat Res* 120:14–29

Morgan CLS, Norman JM, Lowery B (2003) Estimating plant-available water across a field with an inverse yield model. *Soil Sci Soc Am J* 67:620–629

Timlin D, Pachepsky Y, Walthall C, Loehel S (2001) The use of a water budget model and yield maps to characterize water availability in a landscape. *Soil Tillage Res* 58:219–231

Wong MT, Asseng S (2006) Determining the causes of spatial and temporal variability of wheat yields at sub-field scale using a new method of upscaling a crop model. *Plant Soil* 283:203–215

Chapter 36

Reconstructing Palaeotopography at the Beginning of the Weichselian Glacial Stage Using an Electromagnetic Induction Sensor

T. Saey, M. Van Meirvenne, D. Simpson, U.W.A. Vitharana, L. Cockx, and H. Vermeersch

Abstract During the last glacial period (Weichselian), wind-blown loess was deposited over the undulating landscape of central Belgium, which had been formed in surfacing Tertiary marine sediments. Since valleys were covered with a thicker loess layer than were elevated areas, the present topography is much flatter. Reconstructing the palaeolandscape at a detailed scale is almost impossible by conventional procedures based on soil augering. Therefore, the use of the EM38DD electromagnetic induction sensor was evaluated as an alternative for mapping the depth to the Tertiary clay substrate. On our 2-ha study site, strong non-linear relationships ($R^2 = 0.85$) were found between the apparent electrical conductivities (EC_a) measured by the vertical orientation of the EM38DD and the depth to the Tertiary clay (z_{clay}) on the one hand and between the combination of the EC_a s measured by the vertical and horizontal orientations of the EM38DD and z_{clay} on the other hand. These predictions were validated by independent observations of the depth to the Tertiary clay, and r values of 0.84 (using only the measurements in the vertical orientation) and 0.85 (using both measurements in the vertical and horizontal orientations), with an average error of 0.26 m, were found. Our dense EC_a measurements (2 m \times 2 m resolution) allowed us to build a three-dimensional surface of the depth to the Tertiary substrate, reconstructing the palaeotopography beneath the loess cover and revealing distinct erosion patterns. The continuity of these was confirmed by an analysis of surface flow patterns on the reconstructed palaeotopography. The non-invasive, quick, and cost-effective electromagnetic induction sensor offers new possibilities in reconstructing and analysing the Quaternary palaeotopography beneath the loess cover.

Keywords EM38DD · Apparent electrical conductivity · Palaeolandscape · Erosion patterns

M. Van Meirvenne (✉)

Research Group of Soil Spatial Inventory Techniques, Department Soil Management,
Ghent University, Coupure 653, 9000 Ghent, Belgium
e-mail: marc.vanmeirvenne@ugent.be

36.1 Introduction

During the last glacial period (Weichselian, 80–10 ka BP), the periglacial undulating landscape of central Belgium, formed in surfacing Tertiary marine sands and clays, was covered by niveo-aeolian loess, with a thickness ranging from only a few decimetres on hilltops up to several tens of metres in valleys (Hubert, 1976; Vanwalleghem et al., 2005). As a consequence, the palaeotopography became much flatter, and since slope processes have modified the thickness of this loess layer even further, the palaeotopography cannot be reconstructed on the basis of the present topography (Leverington et al., 2002). Yet, a precise and accurate representation of landforms and niveo-aeolian loess sediments offers us a fundamental picture of Pleistocene periglacial environments (Smith et al., 2006). The extent to which conventional invasive methods, such as augering, can be employed for quantifying the small-scale soil variability is limited by the expense and labour associated with obtaining soil samples (Stroh et al., 2001). As an alternative, soil-adapted geophysical sensors, like the EM38DD, have proved their worth (Doolittle et al., 1994; Cockx et al., 2007; Chapters 19, 20, 21, 22, 29, 31, 32, and 33).

The objective of this study was to evaluate, using the EM38DD sensor, two methodologies for mapping the palaeotopography at shallow depths (<3 m) beneath the loess cover. As a test case, we used a 2-ha study site in central Belgium where the palaeolandscape prior to the deposition of the loess cover was formed in Tertiary marine clay. More information can be found in Saey et al. (2008, 2009).

36.2 Materials and Methods

36.2.1 Study Site

The 2-ha research site ($50^{\circ}47'58''$ N, $3^{\circ}24'41''$ E) is located in Heestert, Belgium, in the European loess belt. It is situated on a hillside with an average slope of 7% and elevation of 30–40 m a.s.l. The soil type was a Luvisol according to the WRB classification system (FAO/ISRIC/ISSS, 1998) and was characterised by an argic horizon at a depth of between 0.3–0.35 and 1.3–1.4 m.

During the last glacial stage (Weichselian, 80–10 ka BP), wind-blown loess was deposited over the periglacial undulating landscape of central Europe. Due to the deposition of the loess, the relief of the Tertiary (generally clayey) substrate became smoother, making it impossible to reconstruct the small-scale differences in depth to the Tertiary substrate based on the present topography.

36.2.2 Electromagnetic Induction Sensing

We used the EM38DD, which is a dual-dipole sensor with one dipole oriented horizontally and the other vertically, yielding two soil EC_a measurements with their

own depth-response profile. The cumulative EM38 responses $R_v(z)$ and $R_h(z)$ from the soil volume below a depth z (m) were given by McNeill (1980) as follows:

$$R_v(z) = (4z^2 + 1)^{-0.5}, \quad (36.1)$$

$$R_h(z) = (4z^2 + 1)^{0.5} - 2z. \quad (36.2)$$

Due to the quasi-exponential form of the cumulative response curves, the depth of exploration (DOE) can be arbitrarily defined as the depth where 70% of the response is obtained from the soil volume above this depth (and 30% from below this depth). Therefore, the DOE for the horizontal orientation (0.76 m) proves to be approximately half of the DOE of the vertical orientation (1.55 m).

36.2.3 Mobile EC_a Measurement Equipment and EC_a Mapping

An EM38DD sensor was mounted on a sled pulled by an all-terrain vehicle (ATV) driven at a speed of 6–10 km h^{−1}. Every second, EC_a -V and EC_a -H measurements were recorded by a field computer. A Trimble AgGPS332, with Omnistar correction, was used to geo-reference the EC_a measurements with a pass-to-pass accuracy of approximately 0.10 m. Measurements were made along parallel lines 2 m apart, guided by a Trimble lightbar system. Additionally, at each EC_a measurement point, the soil surface elevation was acquired with the Trimble AgGPS332 (accuracy ± 0.30 m).

Table 36.1 shows the summary statistics of the EM38DD measurements obtained at the study site. The mean of the EC_a -V values is higher than the mean of the EC_a -H values, as a result of the larger weighting the former gives to deeper soil layers. However, the coefficient of variation of these same signals was smaller. This indicates that in this two-layered soil, the subsoil can be considered more conductive and less heterogeneous than the topsoil.

Ordinary kriging (OK) (Goovaerts, 1997) was used to interpolate the EM38DD measurements to a grid of 0.5 m \times 0.5 m. A maximum of 64 neighbours was used within a circular search area with a radius of 20 m around the location being interpolated. The spatial structures of EC_a -V and EC_a -H were modelled by Gaussian variogram models. The parameters are given in Table 36.2. The interpolated EC_a maps are shown in Fig. 36.1a, b. Large differences in EC_a were found over short distances, with a similar pattern between EC_a -V and EC_a -H.

Table 36.1 Descriptive statistics of EC_a -V and EC_a -H measured with the EM38DD (n , number of observations; m , mean; s^2 , variance; CV, coefficient of variation)

	n	m (mS m ^{−1})	Min. (mS m ^{−1})	Max. (mS m ^{−1})	s^2 (mS m ^{−1}) ²	CV (%)
EC_a -H	8562	33	6	86	243	47
EC_a -V	8562	67	29	127	408	30

Table 36.2 Variogram parameters for the variables $EC_a\text{-}V(mS\ m^{-1})$, $EC_a\text{-}H (mS\ m^{-1})$, $Z (m)$, and $z_{\text{clay}}^* (m)$ modelled with EM38DD measurements together with 56 calibration observations (C_0 , nugget variance; $C_0 + C_1$, sill; a , range of Gaussian variogram models)

	C_0	$C_0 + C_1$	$a (m)$
$EC_a\text{-}V$	5	225	20
$EC_a\text{-}H$	5	145	20
Z	0.001	0.601	35
$z_{\text{clay}}^* (EC_a\text{-}V + 56 \text{ calibration observations})$	0.005	0.225	20
$z_{\text{clay}}^* (EC_a\text{-}V \text{ and } EC_a\text{-}H + 56 \text{ calibration observations})$	0.005	0.215	20

36.2.4 Depth to Tertiary Clay Observations

Two transects ABCD and EF were laid out in such a way that both the largest and the lowest EC_a measurements of field 1 were visited equally (Fig. 36.1a). Along the 225 m of transect ABCD, 46 observation points were located at 5 m intervals, while along the 42 m of transect EF, 15 points were selected at 3 m intervals. At each of these 61 points, the depth to the Tertiary clay (z_{clay}) was observed by augering with a gouge auger. Figure 36.2b shows z_{clay} in respect to elevation for transect ABCD, together with the present-day soil surface. At most locations, a clearly observable demarcation was present between the loess topsoil and the Tertiary clay. However, between points B and C, a mixture of loess–clay was found on top of the clayey substrate at some locations. This mixture was as much as 0.5–0.6 m thick. At the first 42 sampling points along this transect, the Tertiary clay substrate was present within the first 1.6 m. At 14 observation points along transect EF, the Tertiary substrate was located between 1.5 and 3 m below the soil surface. Due to the extent of the loess cover below the 3.5 m maximum augering depth, at the last four sampling points on transect ABCD and the last sampling point on transect EF, the exact z_{clay} at these points could not be discerned.

36.2.5 Relationship Between $EC_a\text{-}V$ and Depth to Tertiary Clay

In a two-layered model where silty soil (loess) is located above clayey material, the relationship between the depth to the clay substrate (z_{clay}) and the $EC_a\text{-}V$ can be modelled using the McNeill (1980) cumulative response $R_V(z_{\text{clay}})$ from the soil below z_{clay} (Eq. (36.1)). The main assumption of the model is that the EC_a for loess and clay is fairly uniform throughout the field. Therefore, at each z_{clay} the corresponding $EC_a^*\text{-}V$ can be modelled, given the apparent conductivity values of homogeneous Quaternary loess ($EC_a\text{-}loess$) and Tertiary clay ($EC_a\text{-}clay$):

$$EC_a^* - V = [1 - R_V(z_{\text{clay}})] (EC_a - \text{loess}) + [R_V(z_{\text{clay}})] (EC_a - \text{clay}). \quad (36.3)$$

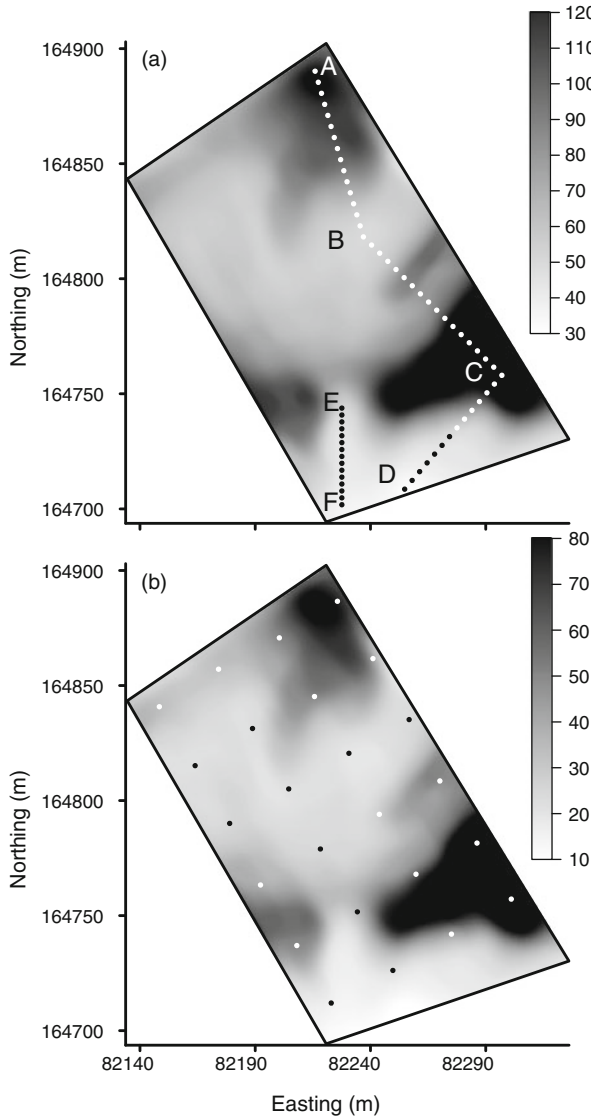


Fig. 36.1 (a) Interpolated EC_a-V (mS m⁻¹) showing calibration points (dots) on transects ABCD and EF. (b) Interpolated EC_a-H (mS m⁻¹) showing validation points (dots)

Inversely, z_{clay}^* can be modelled, given the EC_a-V measurements. Therefore, $R_V(z_{\text{clay}}^*)$ was calculated, given the EC_a-V measurements, EC_a-loess, and EC_a-clay:

$$R_V(z_{\text{clay}}^*) = \frac{(\text{EC}_a - V) - (\text{EC}_a - \text{loess})}{(\text{EC}_a - \text{clay}) - (\text{EC}_a - \text{loess})}. \quad (36.4)$$

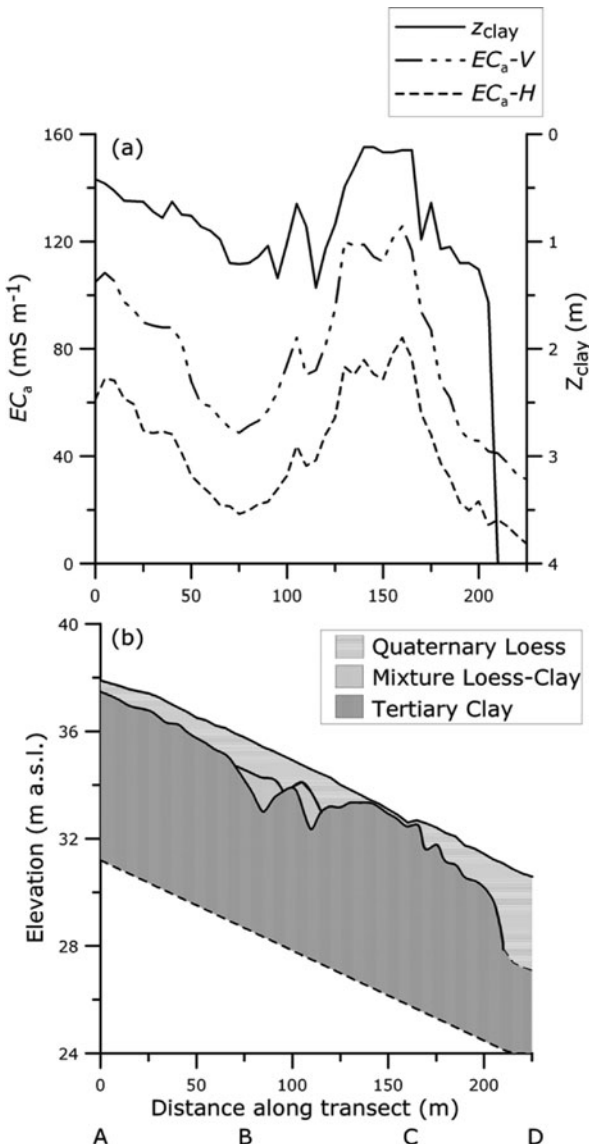


Fig. 36.2 (a) EC_a -V, EC_a -H, and z_{clay} measurements along the 225-m transect ABCD. (b) Profiles of the three layers encountered along this transect

This calculated $R_v(z_{\text{clay}}^*)$ can be input to Eq. (36.1) to obtain the modelled z_{clay}^* :

$$z_{\text{clay}}^* = \left[\frac{1}{4R_v(z_{\text{clay}}^*)^2} - \frac{1}{4} \right]^{0.5}. \quad (36.5)$$

To fit a theoretical relationship to the $z_{\text{clay}} - EC_a - V$ data points based on the McNeill (1980) cumulative depth response, the sum of the squared differences between z_{clay} and z_{clay}^* must be minimised:

$$\sum_{i=1}^n \left[z_{\text{clay}}(i) - z_{\text{clay}}^*(i) \right]^2 = \min, \quad (36.6)$$

with i being the number of observation and n the total amount of observations. The value of z_{clay}^* was modelled with Eqs. (36.4) and (36.5), given the $EC_a - V$ measurements. The modelling parameters EC_a -loess and EC_a -clay were iteratively adjusted to obtain the smallest sum of the squared differences between z_{clay} and z_{clay}^* .

Figure 36.2a shows the $EC_a - V$, $EC_a - H$, and z_{clay} profile measured along transect ABCD. It is clear that the EC_a profiles behave similarly to the z_{clay} values as shown in Fig. 36.2b. The 42 z_{clay} observations of transect ABCD and the 14 observations of transect EF were compared with their nearest EC_a measurements. The fitting of the McNeill relationship to the $z_{\text{clay}} - EC_a - V$ data points was done by minimising the sum of the squared differences between z_{clay} and z_{clay}^* by iteratively altering the modelling parameters EC_a -loess and EC_a -clay in Eqs. (36.3) and (36.4).

36.2.6 Relationship Between the Combined EC_a -V and EC_a -H and Depth to Tertiary Clay

The cumulative response from the Quaternary topsoil and the Tertiary subsoil can be calculated as $1 - R(z_{\text{clay}})$ and $R(z_{\text{clay}})$, for the vertical and horizontal dipole modes, respectively [Eqs. (36.1) and (36.2)]. For each EC_a -V and EC_a -H measurement, z_{clay}^* can be modelled by solving a system of non-linear equations. Therefore, the automated function FSOLVE based on the Levenberg–Marquardt algorithm (Marquardt, 1963) in the high-level language and interactive environment Matlab (MathWorks, Natick, Massachusetts, USA) was used, given the conductivity values of homogeneous Quaternary topsoil (EC_a -loess) and Tertiary clayey subsoil (EC_a -clay):

$$EC_a - V = [1 - R_v(z_{\text{clay}}^*)](EC_a - \text{loess}) + [R_v(z_{\text{clay}}^*)](EC_a - \text{clay}). \quad (36.7)$$

$$EC_a - H = [1 - R_h(z_{\text{clay}}^*)](EC_a - \text{loess}) + [R_h(z_{\text{clay}}^*)](EC_a - \text{clay}). \quad (36.8)$$

To fit these theoretical relationships to the $z_{\text{clay}} - EC_a$ data, the sum of the squared differences between z_{clay} and z_{clay}^* was minimised:

$$\sum_{i=1}^n \left[z_{\text{clay}}(i) - z_{\text{clay}}^*(i) \right]^2 = \min, \quad (36.9)$$

with n being the number of observations. The parameters EC_a -loess and EC_a -clay were iteratively adjusted to obtain the smallest sum of the squared differences between z_{clay} and z_{clay}^* .

36.3 Results and Discussion

36.3.1 Relationship Between EC_a -V and Depth to Tertiary Clay

The optimal values of EC_a -loess and EC_a -clay were 17 and 129 mS m^{-1} , respectively, with an R^2 of 0.85 (Fig. 36.3). Therefore, the following $z_{\text{clay}} - EC_a$ -V relationship was used to predict z_{clay}^* :

$$z_{\text{clay}}^* = \left[\frac{1}{4 \cdot \left(\frac{(EC_a - V) - 17}{129 - 17} \right)^2} - \frac{1}{4} \right]^{0.5} \quad (36.10)$$

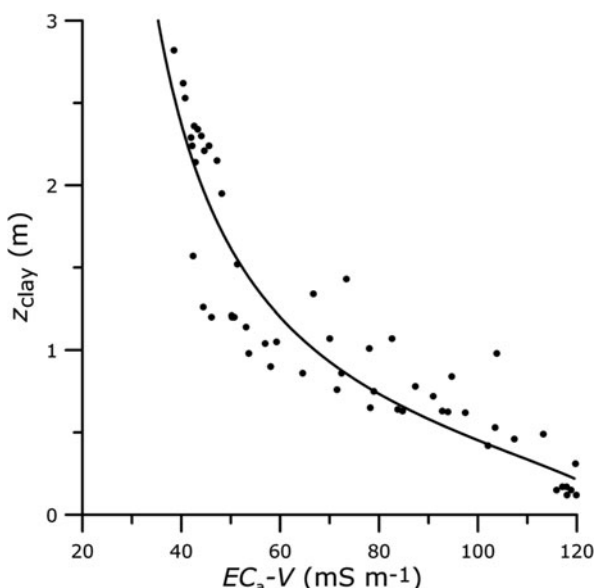


Fig. 36.3 z_{clay} as a function of EC_a -V along study transects ABCD and EF with fitted McNeill curve

36.3.2 Relationship Between the Combined EC_a -V and EC_a -H and Depth to Tertiary Clay

The obtained values of EC_a -loess and EC_a -clay were 12 and 125 mS m⁻¹, respectively, with an R^2 of 0.85. So, at each measurement point, EC_a -V and EC_a -H were linked to z_{clay}^* by using Eqs. (36.1), (36.2), (36.7), and (36.8) as follows:

$$EC_a\text{-V} = 12 + \frac{113}{(4z_{\text{clay}}^*{}^2 + 1)^{0.5}}, \quad (36.11)$$

$$EC_a\text{-H} = 12 - 226 \cdot z_{\text{clay}}^* + 113 \cdot (4z_{\text{clay}}^*{}^2 + 1)^{0.5}, \quad (36.12)$$

This system was solved at each location to z_{clay}^* with Matlab using the Levenberg–Marquardt algorithm (Marquardt, 1963).

36.3.3 Validation of Predicted Depth of Tertiary Clay

An independent validation was performed to evaluate the predictive quality of the models. Three indices were used as validation criteria: the mean estimation error (MEE), the root mean squared estimation error (RMSEE), and the Pearson correlation coefficient r . The MEE and RMSEE were obtained from the following equation:

$$MEE = \frac{1}{n} \sum_{i=1}^n [z_{\text{clay}}^*(i) - z_{\text{clay}}(i)], \quad (36.13)$$

$$RMSEE = \sqrt{\frac{1}{n} \sum_{i=1}^n [z_{\text{clay}}^*(i) - z_{\text{clay}}(i)]^2}, \quad (36.14)$$

with n denoting the total number of validation observations. The accuracy of the proposed models to predict z_{clay}^* was evaluated by investigating at 24 locations. These were taken at the centres of 24 grid cells projected over the study site. The observed depths were compared with the model predictions (Fig. 36.4). A strong correlation between predicted and measured depths (0.84 using only the measurements in the vertical orientation and 0.85 using the combined measurements in the horizontal and vertical orientations) and a low RMSEE (0.26 m) indicated that both procedures predicted z_{clay}^* with a similar accuracy. However, on average, both procedures overestimated z_{clay} with a bias of 0.12 m, as indicated by the MEE.

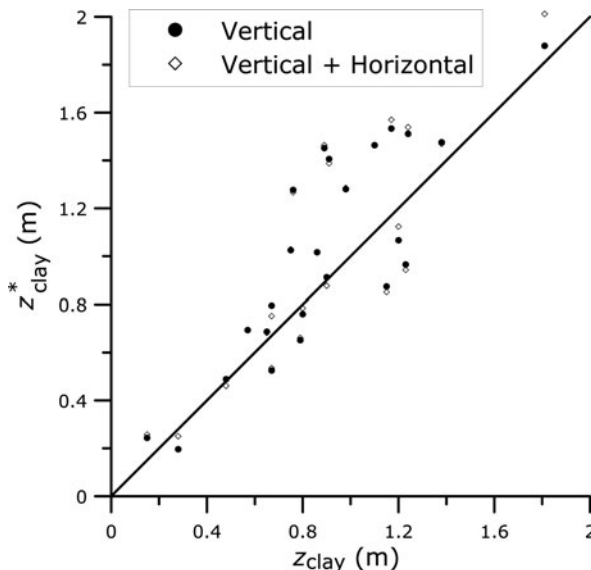


Fig. 36.4 Scatter plot of predicted depth to the Tertiary clay (z_{clay}^*) versus the observed depth (z_{clay}) for both procedures ($n = 24$)

36.3.4 Palaeotopography Beneath the Loess Cover

The soil surface elevation (Z) of the fields was interpolated (Table 36.2) and visualised in Plate 36.1. The EC_a measurements with the EM38DD were converted into z_{clay}^* for both procedures. The interpolated z_{clay}^* maps (Table 36.2) were subtracted from the interpolated Z map and the resulting $Z - z_{\text{clay}}^*$ maps are shown in Plate 36.1b, c. A comparison of the current topography (Plate 36.1a) with the palaeotopography represented by the Tertiary clay (Plate 36.1b and c) reveals the palaeolandscape beneath the loess cover to be less smooth. A pattern of shallow gullies emerged in the Tertiary substrate, despite its clayey composition. These gullies combine into one major gully that ends in what seems to be a wider valley. To evaluate the continuity of these flow pathways, the Idrisi Kilimanjaro modules RUNOFF and WATERSHED were applied to the palaeotopography surfaces. The results are visualised in Plate 36.1b and c. A clear accumulation of flow lines, representing past surface flow patterns, emerges. Hubert (1976) reported the occurrence of strong erosion during the glacial stages of the Pleistocene. Valleys were filled with thick loess sediments, while elevated locations received a thinner layer. Subsequent erosion modified the thickness of the loess further, increasing the thickness of the valley loess by colluvial deposits.

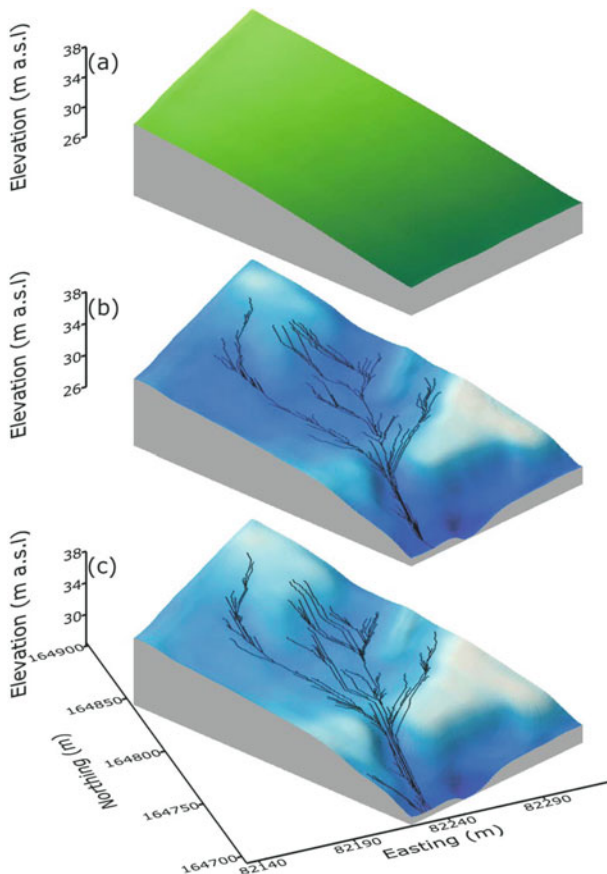


Plate 36.1 (a) Elevation of the current soil surface. (b) $Z - z_{\text{clay}}^*$ predicted using only the EC_a-V measurements. (c) $Z - z_{\text{clay}}^*$ predicted using the combined EC_a-V and EC_a-H measurements. Both (b) and (c) are shown with simulated flow lines

36.4 Conclusions

The EC_a measurements of the EM38DD sensor proved suitable for predicting z_{clay} . The relationship between z_{clay} and EC_a was found to be well represented by the theoretical response curve proposed by McNeill (1980). With the EM38DD, a number of soil auger observations are required to calibrate the EC_a measurements to z_{clay} . Therefore, applying both EC_a measurements instead of only the measurements with the instrument in the vertical orientation did not improve the accuracy of the z_{clay} predictions.

We can conclude that the combination of high-density EMI sensor measurements with direct observations of the depth of the Tertiary clay beneath the Quaternary loess cover for shallow depths (<3 m) proved to be a successful method for reconstructing the palaeotopography at the beginning of the last glacial period. Additionally, the reconstructed palaeotopography showed realistic patterns of surface processes, which could be modelled as a continuous flow process by a flow run-off model.

Acknowledgement This research was supported by the Fund for Scientific Research – Flanders (FWO-Vlaanderen).

References

Cockx L, Van Meirvenne M, De Vos B (2007) Using the EM38DD soil sensor to delineate clay lenses in a sandy forest soil. *Soil Sci Soc Am J* 71:1314–1322

Doolittle JA, Sudduth KA, Kitchen NR, Indorante SJ (1994) Estimating depth to clays using electromagnetic induction methods. *J Soil Water Conserv* 49:572–575

FAO/ISRIC/ISSS (1998) World reference base for soil resources. World soil resources report no. 84. FAO, Rome

Goovaerts P (1997) Geostatistics for natural resources evaluation. Oxford University Press, New York, NY

Hubert P (1976) Verklarende tekst bij het kaartblad: Zwevegem 97E. Hoste-Staelens, Gent

Leverington DW, Teller JT, Mann JD (2002) A GIS method for reconstruction of late quaternary landscapes from isobase data and modern topography. *Comput Geosci* 28:631–639

Marquardt D (1963) An algorithm for least-squares estimation of nonlinear parameters. *SIAM J Appl Math* 11:431–441

McNeill JD (1980) Electromagnetic terrain conductivity measurement at low induction numbers. Technical note TN-6. Geonics Limited, Mississauga, Canada

Saey T, Simpson D, Vitharana U, Vermeersch H, Vermang J, Van Meirvenne M (2008) Reconstructing the paleotopography beneath the loess cover with the aid of an electromagnetic induction sensor. *Catena* 74:58–64

Saey T, Simpson D, Vermeersch H, Cockx L, Van Meirvenne M (2009) Comparing the EM38DD and DUALEM-21S sensors for depth-to-clay mapping. *Soil Sci Soc Am J* 73:7–12

Smith MJ, Rose J, Booth S (2006) Geomorphological mapping of glacial landforms from remotely sensed data: an evaluation of the principal data sources and an assessment of their quality. *Geomorphology* 76:148–165

Stroh JC, Archer S, Doolittle JA, Wilding L (2001) Detection of edaphic discontinuities with ground-penetrating radar and electromagnetic induction. *Landscape Ecol* 16:377–390

Vanwalleghem T, Poesen J, Nachtergael J, Verstraeten G (2005) Characteristics, controlling factors and importance of deep gullies under cropland on loess-derived soils. *Geomorphology* 69:76–91

Postscript: Where to from Here?

Developing and utilising proximal soil sensors has turned into a new field of study in soil science, a predictable development when we consider that the data collected can provide key information for solving a wide range of environmental and socio-economic challenges. This book sheds light on diverse work on the subject being carried out throughout the world. While Section 1 provided overviews of current research, here we aim to summarise the key messages emerging from the remaining sections. For each section, we set out suggestions for future work, and at the end we sketch some initiatives that have already begun.

Soil Sensing and Sampling

Although soil scientists have been trying to measure soil properties using proximal soil sensors since the early 1900s, the sensors involved have evolved enormously. Sensors are now smaller, faster, and more accurate; they consume less energy and can be wireless. Examples are the ion-sensitive field effect transistors used to measure soil pH and soil nutrients. It is pleasing to see that two large projects are underway from the European Commission, DigiSoil and iSoil, the aim of which is to develop integrated soil-sensing systems for digital soil mapping. Soil sampling is important for PSS, especially for designing the sensor sampling locations and sampling for calibration.

Future Work

- Where, when, and how do we sample using proximal soil sensors?
- Which technique is most suitable for each soil property?
- What is the most efficient strategy for ‘calibration sampling’? Do we need to consider geographic space as well as covariate space?

Soil UV, Visible, and Infrared Spectral Sensing

There is much interest in using soil visible and infrared spectroscopy because it is cheap and rapid, and the measurements can be made *in situ* in field conditions.

Another major reason for this interest is that, unlike most other sensing techniques, several soil properties can be measured from a single scan. This multi-attribute feature of reflectance spectroscopy relies on a single spectrum holding information about multiple soil constituents, and this has been clearly shown in our book. Although soil mineral content can be measured directly from the spectra, for the most part the techniques rely on correlations; therefore, to be quantitatively useful, the spectra need to be related to a set of known reference samples through a calibration model. We have learned that the set of reference samples used in the models need to be representative of the range of soils in which the models are to be used and that the techniques for analysing the spectra and developing the multivariate models need to be robust.

Future Work

- Need to develop theoretical multivariate calibrations that use soil knowledge.
- Identify the underlying mechanisms that allow prediction of soil properties from spectra, particularly those involving secondary (or indirect) correlations.
- Which are best, local or global calibrations? And does this depend on the soil property?
- Are there cleverer algorithms than conventional ones like PLSR to process and analyse soil spectra?
- Need to move soil visible and infrared spectroscopy to the field.
- Need research to combine spectral PSS with hyperspectral remote sensing.
- Develop the use of spectra directly into soil mapping and modelling.

Soil Sensing by Electromagnetic Induction and Electrical Resistivity

Electromagnetic induction and electrical resistivity are really two different means of measuring the soil's electrical conductivity. The EMI method is perhaps the most widely used sensor and now, with multiple frequencies, several depth ranges can be measured simultaneously. With direct resistivity instruments, this same result is achieved by having several pairs of electrodes spaced at varying inter-electrode distances. The major advantage of the former over the latter is that no physical contact is required, a clear advantage in hard dry soil. On the other hand, the direct resistivity method is easier to interpret and measurements are not interfered with by the presence of metal in the vicinity of the instrument. Soil electrical conductivity is affected by several soil properties, particularly moisture content, clay content, and salinity – so calibration and inference are always required.

Future Work

- Better inversion techniques for reconstructing soil profiles such as Bayesian inversion
- A sound theory on interpreting the EC_a data, which incorporates soil knowledge

Radar and Gamma Radiometric Sensors

Both ground-penetrating radar and gamma radiometrics provide new avenues for measuring and inferring soil properties. Radar has been used in soil studies for more than 20 years, largely in North America for detecting horizon boundaries and topsoil thickness. It has the potential to calculate, on the run, soil moisture content through measuring the soil's dielectric constant, an achievement that would in turn make it easier to infer other soil properties. Ground-based hyperspectral gamma radiometry is more recent and its use is not widespread, so the technique is not well known among soil scientists. Nevertheless, it demonstrates great usefulness in its ability to discriminate soil materials, texturally and mineralogically.

Future Work

- Better signal and reconstruction methods for deriving soil properties, particularly soil moisture, directly from radar signals
- Understanding the gamma attenuation due to moisture content and the depth range of response for different soil materials

Multi-sensor Systems and Other Sensors

Every soil-sensing technology has strengths and weaknesses, and no single sensor can measure all soil properties. It is therefore important when measuring a suite of soil properties to select a set of sensors that complement each other. Integrating multiple proximal soil sensors of both types in a single multi-sensor platform can provide a number of operational benefits over single-sensor systems: robust operational performance, increased confidence (as independent measurements are made on the same soil), extended attribute coverage, and increased dimensionality of the measurement space.

Future Work

- Data fusion algorithms to produce information from the multi-sensor data
- Develop efficient algorithms that can handle high spatial resolution datasets

Applications

A major application of proximal soil sensing has been precision agriculture. However, there are other applications. For example, detailed spatial information furnished by proximal soil sensors can be used to reconstruct palaeoenvironments.

Because it can make closely spaced observations without much difficulty, proximal soil sensing is naturally suited to high-resolution mapping (~ 20 m or less). This means it is ideal for sites that call for careful management. Potential areas of application, besides precision agriculture, include contaminated site assessment, geotechnical site assessment, and sites of special scientific interest.

Future Work

- High-resolution mapping of soil carbon for sequestration purposes
- Application of multi-sensors for contaminated site assessment
- Investigation of soil diversity–plant biodiversity relationships

Initiatives

FP7 Projects iSoil and Digisoil

The largest current investment in proximal soil sensing is under the European Commission's Framework 7 research initiative. There are two large projects, iSoil and Digisoil (www.isoil.ufz.de and www.digisoil.brgm.fr), which aim to develop proximal soil sensing for digital soil mapping. The projects, funded at around 3.5 million euro each, comprise consortia from a number of European countries, with some external scientific advisors. The projects are investigating some of the key technologies reported in this book. Useful findings will begin to flow from 2010 onwards.

IUSS WG-PSS

The IUSS Working Group on Proximal Soil Sensing (www.proximalsoilsensing.org) was formed in July 2008. The working group operates under the auspices of both the Pedometrics Commission and the Soil Physics Commission of the International Union of Soil Sciences (IUSS). Its purpose is to enable greater interaction and collaboration between scientists and engineers with a common interest in applying state-of-the-art sensing technologies to the study of soil processes and spatio-temporal soil variability.

Global Soil Spectral Library

An initiative to develop a global soil visible and infrared soil spectral library was started in April 2008. The Global Soil Spectral Library (www.proximalsoilsensing.org/global-spectroscopy/) aims to develop a collaborative network for

soil spectroscopic research to further its development and encourage its adoption in soil science.

Australia
January, 2010

Raphael Viscarra Rossel
Alex McBratney
Budiman Minasny

Index

A

- Aeolian material, 246
- Airborne radiometrics, 214, 216, 223
- Allophanic, 179–180, 182–184, 188
- Allophanic, New Zealand
 - Manawatu Region, 180
 - Andic Cambisol, 180
- Allophanic, New Zealand
 - Taupo–Rotorua Region, 179, 182–184
 - Vitric Andosol, 179
- Alluvium, 215, 223–225
- Alum shale, 334–336, 339–341
- Apparent electrical conductivity (EC_a), 8, 18, 23–26, 78, 106, 115–116, 119, 122–123, 234–242, 246–253, 256–262, 267–272, 284–294, 344–348, 354, 357, 359–361, 365–370, 373, 376–383, 387–389, 398, 401, 403, 406–407, 424–433, 436
- Apparent soil electrical conductivity, 122, 246, 344–345, 347, 354, 376, 378, 387
- APSIM, 415–420
- Artificial neural networks, 246–248
- ASD FieldSpec Pro FR
 - spectroradiometer, 155, 379, 384
- Attenuated total reflection (ATR), 144–150
- Autocorrelation, 122, 124–125, 128, 154, 360
- Available water holding capacity, 354, 414

B

- Bagging, 36, 204–205, 207
- Batcombe series, 71
- Belgium, 96, 245–246, 309, 424
- Black Vertosol, 203, 208, 257
- Boreholes, 276, 300, 302
- Broadbalk, 71, 73–74

C

- Cadmium, 192–193, 196–197, 333–341
 - calcisol, 55, 203, 205
- Calibration, 4, 9–13, 19, 30, 35–36, 38–44, 68, 80–81, 86, 88, 97–99, 109, 111–113, 119, 122, 124–125, 128, 136–140, 143–151, 153–157, 161–162, 166, 168–175, 180–182, 184, 186–188, 202–205, 207, 209–210, 212, 234, 255–262, 290, 303–304, 324, 327–328, 346, 354–356, 366–367, 375, 377, 380, 383–384, 388, 416, 426–427, 435–436
- Capacitance probe, 314–315, 318–319
- Carbon, 16–17, 19, 32–33, 36–37, 39–41, 43, 92–93, 96–97, 134–138, 140, 144–148, 151, 160, 165–175, 177–189, 195, 212, 234, 344, 364, 369, 398, 438
- Case AFS yield monitoring system, 413–421
- Chemometrics, 35, 136–137, 166, 169–170, 202
- Chernozem, 416
- Chromic Luvisols, 71
- Chromosols, 55, 203, 205, 208
- Classification, 17, 55, 98, 122, 125, 127, 167, 179–180, 203, 287, 289, 294, 333, 339–341, 360, 365, 377–378, 399, 424
- Clay
 - mineral abundances, 223–224
 - mineral physicochemistry, 224–225
 - tertiary marine clay, 424, 426–432
- Claypan soils, 154–155, 162, 234, 238–240, 242, 364, 367–372
- Clod size, 314, 316, 321
- Co-krige, 377, 382

Compacted state of the subsoil [K_0 (PR)], 266, 270–273

Conductivity, electrical, 16–18, 23–24, 78, 106, 112, 115–116, 122, 212, 233–242, 246, 256, 260–261, 267–269, 272, 284, 286, 291–292, 299–302, 344–347, 354, 376, 378, 387, 407, 423, 436

Cost modelling, 5

Crop growth simulation modelling, 414

Crop yield
monitoring, 399

Cross-variogram, 399–400, 404–405

Crystallinity, 224–225

Czech Republic, 397–409

D

Data integration, 93

Data mining, 36, 107–108

Depth to claypan (DTC), 234–235, 239–240, 242, 367

Dermosols, 55, 203, 205, 208

Diagnostic screening, 191–198

Diffuse reflectance infrared spectroscopy (DRIFTS), 134

Diffuse reflectance spectrophotometers, 202

Diffuse reflectance spectroscopy, 16, 19, 29–44, 134, 141, 154, 166, 191–198

Digilab FTS7000 FTIR/FTNIR (Varian, Inc., Palo Alto, CA), 135, 169

Digital elevation map, 388

Digital elevation model, 175, 212, 216, 399

Digital soil mapping, 10, 49–62, 90, 103–109, 111, 119, 154, 233–242, 299, 435, 438

Discrete wavelet transform, 209

Dissemination, 109

Draft force, 398–408

Draught force, 69–70, 354–355, 357–361

Dual sensors, 348–349, 356, 388, 390, 394

Durosol, 416

Dynamometer, 69, 71, 398, 400

E

EC_a
soil properties, 78, 246, 284, 291, 344, 354, 387–388

Electrical conductivity, 16–18, 23–24, 78, 106, 112, 115–116, 122, 212, 233–242, 246, 256, 260–261, 267–269, 272, 284, 286, 291–292, 299–302, 344–347, 354, 376, 378, 387, 407, 423, 436

Electrical and electromagnetic sensors, 17–18

Electrical resistivity, 16–18, 78, 95–96, 275–282, 285–286, 344, 354, 436

Electrical resistivity tomography (ERT), 285–287, 290–295

Electrochemical sensors, 17, 22–23, 77–86

Electromagnetic induction (EMI), 16–18, 74, 95, 105, 112, 122, 237, 246, 256, 268, 284, 300, 345, 354, 365, 368, 378–381, 389, 423–434, 436

EM38, 8, 18, 55, 113–118, 246–248, 253, 256–262, 265–273, 286–287, 290, 330, 343–349, 365, 378, 384, 388–390, 392–394, 424–426, 432–433

EM38DD, 246–248, 252–253, 388–390, 393–395, 424–426, 432–433

EMI conductivimeter, 290

EM mapping, 376

ENVI, 123, 125, 217

Epiqualfs, 155, 364–365

ER, 276, 293

Erosion, historical, 367

Erosion patterns, 104, 423

ESAP, 122–127

EU FP7, 104

F

False negative ratio, 193–194, 196–198

False positive ratio, 193–194, 196–198

Ferrosols, Calcic, 203, 205, 208, 213, 215–216, 223–224

Field capacity, 316, 366, 369, 376, 378–382, 389, 415

Field scale, 38, 42, 107, 154, 172, 265–266, 276–277, 299–300, 308–309, 321, 327, 353–362, 365, 369, 405

Filter-based variable filter array spectrometer, 146–151

Filter-based VFA spectrometer, 146–147

Fixed rank kriging (FRK), 51, 61

Flow accumulation, 399–403, 405–408

Fluvial Recent, 180, 184–186, 188

Fluvial Recent, New Zealand
Manawatu Region, 180
Stagnic Fluvisol, 180

Force, draft, 398–407

France, 18, 276, 284, 316

Freshwater, 376

FTIR/ATR spectroscopy, 145–147, 151

FT-IR DRIFT, 29

Full spectrum analysis, 326

Full-waveform inversion, 308

Fuzzy k -means, 12

G

Gamma radiometer, 51, 55, 62, 325, 389–390, 394
Gamma ray
sensing, 330, 333–341
sensor, 323–332, 334
Geochemistry, 224
Geophysical techniques, 93, 100, 106, 267, 301
Geophysical transfer functions, 106–107
Geophysics, 19, 95, 103–109, 212, 302, 348
Geostatistics, 8–9, 50, 55, 57, 105, 107, 336, 365, 378, 380, 399–400
Glacial till, 335–336
Gravels, 42, 215, 269, 285, 287–288, 290–294, 319, 344–348, 377, 382
Green's function, 304–306, 308
Ground-penetrating radar, 16, 95, 98, 105, 212, 299–309, 437
GRS spectrum, 55, 395

H

Haplic Cambisols, 276, 335
Haplic luvisol, 398
Heavy metals, 192–198, 324
High-resolution, 3–13, 21, 29–44, 49–62, 68, 71, 90, 99, 104–106, 109, 111, 178, 201–202, 214, 233–242, 246, 253, 284, 299, 303, 324–325, 343–349, 363, 367, 369–370, 377, 382–383, 414–415, 438
Hydraulic properties, 92, 94, 99, 299, 302–303, 307–308, 364, 366, 368, 415, 417, 420
Hypercube sampling, 10–11, 111–119, 416
Hyperspectral imaging, 166–167, 213
Hyperspectral mineral mapping, 211, 227

I

Illite, 32–33, 98, 212–213, 215, 218–221, 223–225
Inference model, 89
Infrared profiler, 203
In situ measurement, 19, 42–43, 178, 186
Instruments used, 384
Inverse modelling, 99, 302, 307–308, 414–415, 418, 420
Ion selective electrode (ISE), 16–17, 22, 24, 78–79
Ion selective field effect transistor (ISFET), 17, 22, 144
Irrigation, 81, 92, 255, 316–317, 376–377, 380
ISOIL, 90, 103–109, 435, 438

K

Kaolinite, 32–33, 213, 218–219, 221, 223–225
Kriging
ordinary, 8, 278, 336, 378, 380, 382, 399–400, 425
regression, 154–156, 160–162

L

Latin hypercube sampling, 10–11, 111–119, 416
Leave-one-out cross validation, 181, 390
Leptic Calcisol, 55
Limestone, 276, 280–281, 285, 287–288, 290, 292–294, 335
Loam, 71, 81, 145–146, 155, 180, 246, 251, 256, 276, 281, 285, 287, 291–294, 316, 327–328, 335, 346, 361, 366, 369, 377, 380
Loess soils, 242, 316, 426, 432
Logarithmic transformation, 56
Luvisol, 55, 71, 203, 205, 269, 316, 362–363, 398, 424
orthic, 316

M

Management zones, 24, 284, 294, 300, 407
Map
soil, 4, 12, 16, 26, 55, 68, 105–107, 109, 201, 212, 215–216, 267, 276, 280, 293, 325, 327–328, 330, 347–348, 367
yield, 24, 344, 365–368, 414–415
Map comparison method, 287–289
Marlstone, 284–285, 287–288, 292
Mean squared prediction error, 51, 53–54
Mechanical resistance probe, 319
Mechanical sensors, 17–18, 20–22
Mediterranean soils, 283–295
Meta-modelling, 413–421
Microwave ground-based radar, 314
Mid-infrared diffuse reflectance spectroscopy, 16, 19, 29–30, 39, 134–135, 167, 192
Mid-infrared (mid-IR), 16–17, 19, 37, 39, 134, 143–151, 154, 166, 169, 202
Missouri, 154–155, 234–235, 239, 364, 367–368
Moran statistic, 125
MUCEP device (Multi-Continuous Electrical Profiling), 276, 278
Multilayered media, 99, 300, 303–305
Multiple linear regression (MLR), 35–36, 85, 151, 202, 207–208, 327
Multi-resolutional models, 57

Multi-sensor, 388, 394, 437–438
 Multivariate calibration, 19, 35–36, 39, 202, 204–205, 207–208, 436

N
 NDVI, 123, 125–127, 284, 287–289, 291–292
 Near-infrared diffuse reflection spectroscopy, 34
 Near infrared (NIR), 16–18, 36–38, 133–141, 144, 154, 166–167, 169–170, 178, 202
 Neural networks, 36, 245–253, 417
 NIRSystems model 6500 scanning NIR monochromator (FossNIRSystems, Eden Prairie, MN), 136
 Nitrate, 17, 19, 22–23, 25–26, 39, 77–86, 144–150, 344
 Nitrogen, 16–17, 19, 23, 26, 39, 78, 85, 125, 133, 135–138, 144, 177–189
 Non-invasive methods, 276, 294
 Normalised differences vegetation index (NDVI), 123, 125–127, 284, 287–289, 291–292
 Nugget effect, 52, 250
 Nutrient management, 370

O
 Oil carbon mapping, 175
 On-site analysis, 133–141
 On-the-go soil sensors, 17, 26
 Optical and radiometric sensors, 17–19
 Ordinal logistic regression, 193, 196, 198
 Organic matter, 17, 19, 21, 24–26, 32–33, 37–38, 40, 42–43, 92–94, 104, 139–140, 143–151, 154–155, 157–158, 160, 166, 175, 178, 182–183, 195, 198, 212–213, 246, 316, 327–328, 331, 337, 384, 388

P
 Palaeolandscape, 424, 432
 Partial least squares, 35, 96, 145, 156, 167, 169, 172, 175, 181, 202, 208–209, 237, 239, 241, 380, 382, 395
 Partial least squares regression, 35, 167, 181, 202, 209, 237, 239, 241, 380, 382
 Particle-size distribution, 398, 400–403, 407
 Pasture, 55, 177–189, 354
 Pedophysics, 103
 Penetration resistance (PR), 21, 266–269, 271–272
 Penetrologger, 268–269
 Penetrometer, 21, 234–235, 239–240, 268, 355–356, 361, 366, 371–372

pH, 16–17, 23–26, 68, 78, 80–82, 84, 95, 155, 159, 212, 227, 265–266, 268, 313–321, 344–348, 354–355, 388, 390–392, 394–395, 435, 438

Phosphorus, 17, 38, 86, 371
 Physicochemistry, 224–225, 227
 Planosol, 203, 205, 416
 Plant available soil water storage capacity (PAWC), 344, 366, 368–370, 415
 Plant-available water content, 239, 344, 369–370, 384, 414–415
 Pneumatic and acoustic sensors, 17, 22
 Poorly drained soils, 364
 Portable spectrophotometers, 43
 Potassium, 17, 19–20, 22–23, 25–26, 39, 55, 77–78, 80–83, 86, 193, 212, 215–216, 324, 344–345, 370–372, 389
 Precision agriculture, 15–16, 22, 27, 38, 42, 50, 74, 81, 95, 121–129, 154, 201, 268, 284, 314, 323–325, 330–331, 344, 364, 388, 397, 405, 407, 437–438
 Prediction, 4–5, 11, 13, 19, 30, 36–37, 39–43, 50–61, 85, 96–97, 112, 116, 119, 122, 125, 127, 156, 167–168, 171, 173–175, 177, 180–188, 196–198, 202, 204, 207–208, 222, 225–226, 245–253, 262, 281, 314, 328, 377, 380–384, 388, 390, 394–395, 415–417, 420, 431, 433, 436
 Prescription maps, 16
 Principal component analysis, 181, 193, 382
 Profile sources of proximal EC_a, 241–242
 Proximal sensing, 3–4, 43, 78, 375–384
 Proximal sensor, 313–321
 Proximal soil sensing (PSS), 15–16, 19, 42–43, 78–86, 172, 201–202, 435–438
 Pumice, New Zealand
 Taupo–Rotorua Region, 179, 182–184
 Vitric Andosol, 179

R
 Radar, 16–17, 19, 95, 98–99, 105, 212, 278, 299–309, 314–315, 317–318, 437
 Radioactivity, 324–325, 346
 Rapid measurements, 77–78, 109, 435
 Real-time mapping, 99–100, 302, 308–309, 377
 Redox, 212
 Remote sensing, 4, 99, 123–124, 127, 134, 141, 165–166, 173–175, 213
 Resistivity, electrical, 16–18, 78, 95–96, 275–282, 285–286, 344, 354, 436

Response surface, 10–11, 121–128
Risk classification, 339–341
Root density, 178, 180–181, 185, 188–189
Rothamsted, 69, 71
RTK-DGPS, 378, 384
Rule-based method, 345

S
Salinity, 18, 24, 55, 95, 99, 106–107, 122, 212–213, 234, 241, 260, 267, 300, 302, 309, 344, 346, 436
Sampling, 4–5, 7–13, 15, 23–24, 26, 50, 57, 68, 83, 99, 105, 107–108, 111–119, 121–129, 145, 153–155, 166–167, 169, 173, 175, 192, 203, 226, 247, 256, 262, 277, 280–281, 300, 316, 327, 334–335, 337, 340, 354–355, 357, 360, 365, 369–370, 378, 380, 388–390, 395, 397–400, 416, 426, 435
Sawyers field, 71–72
Scorpan, 107
Scotland, 388–389
Seedbed, 314, 316–317, 319–321
Semivariogram, 156–158, 160, 162, 360, 380
Sensing technologies, 26–27, 90, 98, 154, 437–438
Sensor
 draft force, 398–408
 electromagnetic induction, 18, 237, 256, 365, 389, 423–434
 fusion, 22
 used, 286
Site-specific crop management, 353, 414
Smectite, 32–33, 98, 213, 215, 218–221, 223–226, 234
Sodium, 17, 19, 78, 81–83, 218, 325, 345–346
Sodosols, 55, 203, 205
Soil analysis, 19, 30, 37, 39, 81, 141, 192, 201–202, 393
Soil available water holding capacity (AWC), 354–355, 359, 376–383, 414–419
Soil bulk-apparent electrical conductivity (EC_a), 16, 18, 23, 78, 112, 115–116, 233–242, 246, 256, 267–269, 272, 284, 286, 291–292, 344–345, 347, 354, 376, 378, 387, 436
Soil carbon, 140, 165–175, 177–189, 364, 438
Soil compaction, 17, 99, 265–273, 302, 364, 366, 371–373
Soil contamination, 191–194
Soil core, 43, 84–85, 134, 178–180, 184, 186, 189, 233, 236, 257, 285–287, 291–293, 365, 389
Soil depth, 18, 106, 178, 185–187, 256, 344–348, 364–367, 369–371, 375, 380, 418
Soil electromagnetic properties, 306
Soil fertility, 26, 239, 390
Soil hydraulic properties, 92, 94, 99, 299, 302–303, 307–308, 366, 415
Soil mapping, 3–13, 20, 41, 49–62, 90, 103–109, 111, 119, 154–155, 178, 212–214, 227, 233–242, 323–332, 334, 345, 363, 388, 435–436, 438
Soil mineralogy, 33, 39, 43, 144, 212, 324, 436
Soil moisture, 18, 43, 84, 96, 98, 173, 180, 212, 235–236, 238, 241, 246, 255–262, 290, 292, 300, 308, 317–318, 321, 353–361, 367, 376–380, 382–384, 388, 437
Soil nitrate sensor, 144
Soil nitrogen, 85
Soil nutrients, 16, 22, 77–86, 213, 327, 370, 435
Soil pH, 16–17, 23–26, 68, 78, 80–82, 84, 95, 155, 159, 212, 227, 265–266, 268, 313–321, 344–348, 388, 390–392, 394–395, 435, 438
Soil properties, 16–17, 19, 22, 24–25, 35–39, 42, 49, 55, 78, 81, 90, 92–94, 99, 104–108, 111, 154–162, 166, 173, 181, 192, 202, 212–213, 246, 265, 276, 284, 287–288, 291, 300, 314, 323–325, 327–329, 334, 337, 344–345, 348, 354, 371, 376, 387–388, 395, 397–400, 407, 414–415, 435–437
Soil quality indicators, 364
Soil quality maps, 363–373
Soils
 Arenosol, 8, 203, 205, 345
 Ferralsol, 203, 205, 345
 Gleysol, 203
 Luvisol, 55, 71, 203, 205, 269, 316, 362–363, 398, 424
 Planosol, 203, 205, 416
 Podzol, 203, 205
 Solonetz, 55, 203, 205
 Vertisol, 203, 205
Soil sampling, 3, 11, 15, 23–24, 41, 83, 99–100, 103, 105, 111–112, 119, 122, 155, 167, 169, 277, 327–330, 354–355, 369–370, 388–390, 397–398, 435

Soil sensing, 4, 15–17, 19, 27, 50, 68, 74, 79–82, 85–86, 105, 154, 172, 201–202, 209, 284, 355, 435, 437–438

Soil texture, 17, 22, 25–26, 38, 43, 92, 94–96, 98, 146, 155, 182, 246–247, 249, 268, 287, 293, 327, 335, 344, 346, 360–361, 365, 376, 378–379

Soil thickness, 287, 368–370, 437

Soil water content, 16–17, 42, 94–95, 99, 186, 268, 272, 276–282, 301–302, 309, 314, 316–317, 319–320

Solonetz, 55, 203, 205

Spatial covariance function, 51–53

Spatial mapping, 18

Spatial random effects (SRE) model, 52

Spatial statistics, 51

Spectral reflectance, 95, 155, 177–189, 193, 213

Spectrophotometer, 43, 149–150, 168–169, 202, 377

State of mechanical stress, 266

Stress-at-rest coefficient (K_0), 266–267, 272

Subsoil compaction, 265–273

Subsoil nutrients, 370

Surface Optics Corporation model SOC-400 FTIR, 135–136

Sweden, 40, 333–341

T

Tephric Recent, 179, 182–184

Tephric Recent, New Zealand

- Taupo–Rotorua Region, 179, 182–184
- Vitric Cambisol, 179

Time domain reflectometry (TDR), 300, 376, 379

Time and space monitoring, 275

Topsoil texture, 247, 250–251, 394

Transition peak depth, 239–242

Tschermark substitution, 217, 224–225

U

Uranium, 19–20, 55, 212, 324, 334, 339–340, 345, 389

Urban soils, 191–198

V

Variable rate technology, 144, 388

Variogram, 11, 50, 52, 119, 250, 336, 389, 400, 403–406, 425–426

Vegetation index, 123, 126

Veris 3100, 18, 365

Vertisols, 205

Vertosol, 203, 205, 208, 213, 215, 224, 255–262

Vine rooting depth, 287–288, 292, 294, 366, 376, 417

Vineyards, 283–295

Visible–near-infrared (vis–NIR), 16, 19, 29–32, 36–43, 167, 192–198, 201–209, 376, 379, 382–384

Vis–NIR spectroradiometer, 376–377, 379

Visual and near-infrared reflectance, 17, 178

Volumetric soil moisture, 256, 355

W

Water content, 16–17, 19, 37, 39, 42, 94–95, 99–100, 107, 112, 182–183, 186, 225–226, 234, 241–242, 258, 268, 272, 276–282, 300–303, 306–309, 314, 316–317, 319–320, 373

Wavelet analysis, 145, 147

Wavelets, 35, 57, 147, 175, 201–209, 217

Wenner mini-probe, 236, 238–239

Wheat, 71, 73, 269, 335, 337–340, 344–345, 357–358, 399, 416–417

Whole farm, 414–416, 420

Wilting point, 376, 378–381, 415

Y

Yield map, 344, 365–368, 370, 372, 414–415

Yield mapping, 365–366, 370, 372